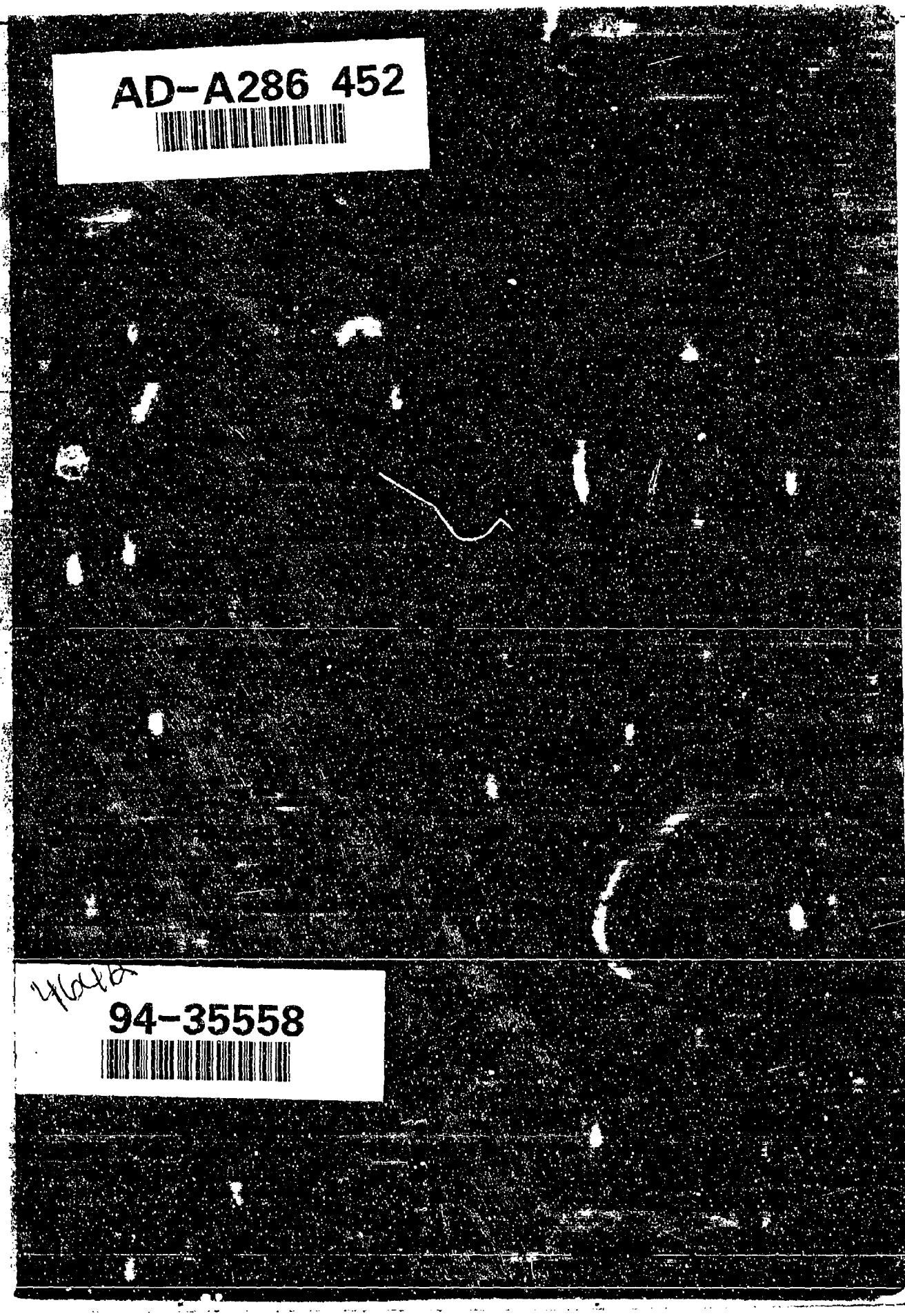
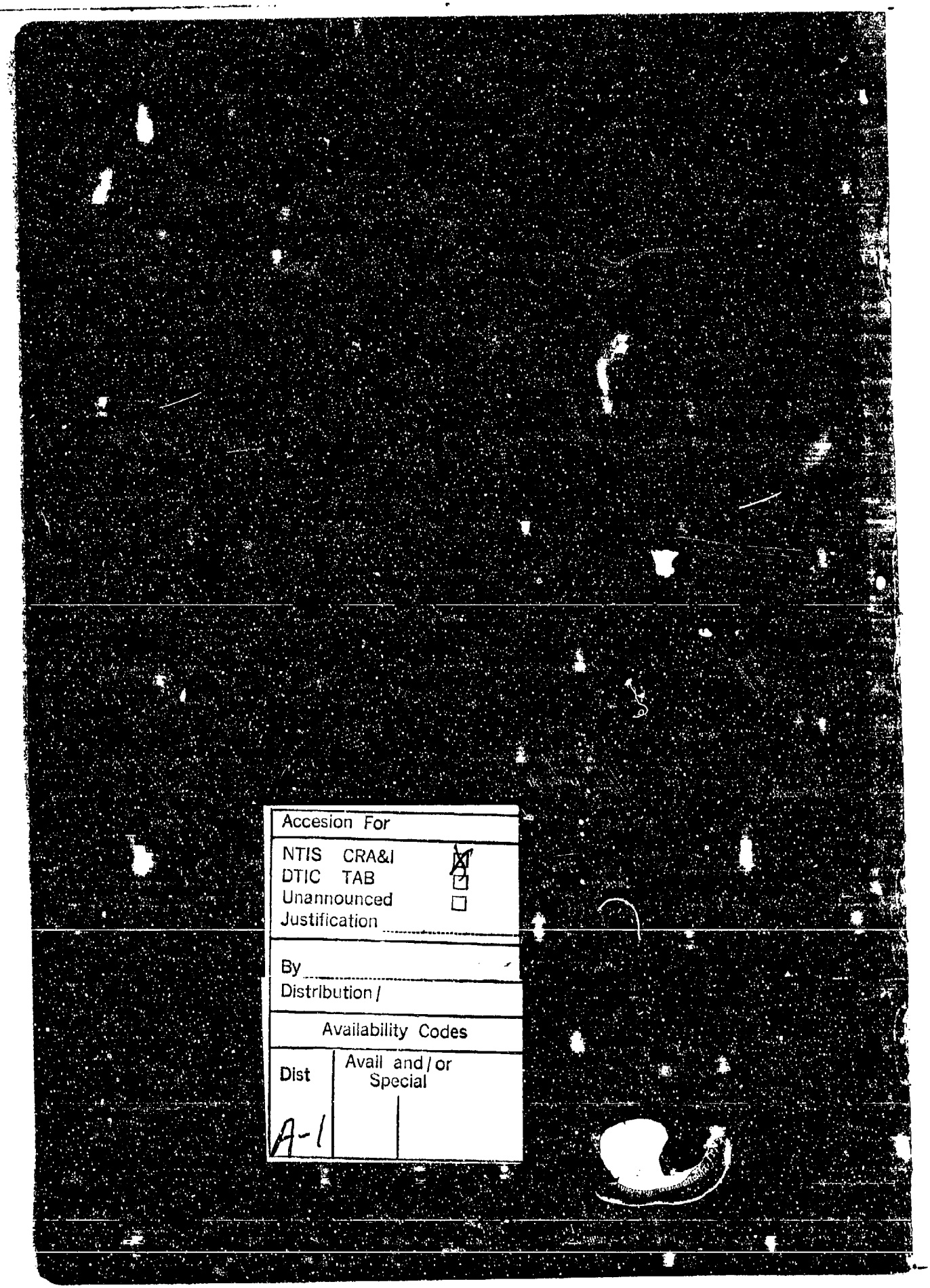
AD-A286 452



94-35558



Accesion For

NTIS CRA&I ☒
DTIC TAB ☐
Unannounced ☐
Justification

By

Distribution /

Availability Codes

Dist	Avail and / or Special
A-1	

DRAFT SF 298

1. Report Date (dd-mm-yy) 10 Oct 94	2. Report Type conference proceedings	3. Dates covered (from... to) 29 June - 2 July 1994
4. Title & subtitle 4th International Symposium on Stratified Flows		5a. Contract or Grant # N00014–94-J-9018
		5b. Program Element #
6. Author(s) Emil Hopfinger, Bruno Voisin, Genevieve Chavand, editors		5c. Project # 5202
		5d. Task # EUR
		5e. Work Unit #
7. Performing Organization Name & Address Laboratoire des Ecoulements Geophysiques et Industriels, Institut de Mecanique de Grenoble, B.P. 53 X - 38041 Grenoble Cedex 9 France		8. Performing Organization Report #
9. Sponsoring/Monitoring Agency Name & Address Office of Naval Research Europe PSC 802 BOX 39 FPO AE 09499-0700		10. Monitor Acronym ONREUR
		11. Monitor Report #
12. Distribution/Availability Statement A		
13. Supplementary Notes 4 volumes		
14. Abstract		
15. Subject Terms stratified flows		

Security Classification of			19. Limitation of Abstract	20. # of Pages	21. Responsible Person (Name and Telephone #)
16. Report Unclassified	17. Abstract Unclassified	18. This Page Unclassified	Unlimited		Mike Shear, 011-44-0171-514-4921

Friday – July 1 – Morning

8:45 – 9:30 **General Session**

Mixing and transport in a stratified lake
J. Imberger

	Session A5 INTERNAL WAVES		Session B5 LAKES AND OCEAN BASINS
9:30	Laboratory measurements of gravity wave, critical layer interactions – 185 *D. P. Delisi, T. J. Dunkerton*	9:30	Investigation of the vertical water exchange in the Baltic Sea – 244 *R. V. Ozmidov, A. V. Ozmidova*
9:45	Nonlinear internal waves in observations from shelves: manifestations of soliton-like behaviour – 9 *A. N. Serebryany*	9:45	Turbulent mixing in the oceanic boundary layer due to internal wave reflection from sloping terrain – 100 *D. N. Slinn, J. J. Riley*
10:00	Stratified flow over an obstacle: nonlinear wave interactions in the lee wave field – 54 *K. G. Lamb*	10:00	Internal tidal amphidromes in Vestfjorden – 167 *J. H. Nilsen, T. A. McClimans*
10:15	Inertia-gravity wave propagation in a jet region – 265 *M.-P. Lelong, T. J. Dunkerton*	10:15	Observations and modelling of stratified flow in the sound between Denmark and Sweden – 169 *J. S. Møller, E. B. Rasmussen, A. C. Ellegaard*
10:30	Lagrangian coordinates, gravity wave spectra, and the dichotomy of buoyancy subrange theory – 2 *J. Weinstock*	10:30	The variability of vertical finescale temperature structures in Lake Geneva, Switzerland – 202 *S. M. Zhang, U. Lemmin, E. J. Hopfinger*
10:45 – 11:15	**COFFEE BREAK**		
11:15	Internal solitary waves with oscillatory tails – 80 *R. Grimshaw*	11:15	A numerical investigation of stratified circulation over abrupt topography on the Norwegian continental shelf – 171 *W. P. Budgell, B. Hackett, L. P. Roed P. E. Bjerke*
11:30	A numerical study of the three-dimensional internal waves excited in the flow of a stratified fluid – 212 *H. Hanazaki*	11:30	Diapycnal diffusivity measured by microstructure and tracer techniques - A comparison – 183 *A. Wüest, D. C. van Senden, J. Imberger, G. Piepke, M. Gloor*
11:45	Internal waves generated by a translating and oscillating sphere – 223 *P. Dupont, B. Voisin*	11:45	Observations of mixing in a stratified lake – 101 *P. F. Hamblin, C. L. Stevens, G. A. Lawrence*
12:00	Non-linear internal gravity waves: the local and the global view of the phase-space – 204 *V. Zeitlin*	12:00	Wind forcing of internal waves in long narrow stratified lakes – 64 *C. Stevens, G. Lawrence, P. Hamblin, E. Carmack*
12:15	The structure of the turbulent wake and the random internal wave field generated by a moving sphere in a stratified fluid – 44 *P. Bonneton, J.-M. Chomaz, E. J. Hopfinger, M. Perrier*	12:15	Stratified flow in a lagoon – 66 *P. Péchon, J.-M. Janin, F. Lepeintre*
12:30	The wake regimes influence on hydrodynamic characteristics of the submerged sphere in the stratified fluid – 39 *O. D. Shishkina*	12:30	Vertical and horizontal structure of a density current in an small lake – 102 *E. Roget, J. Colomer*

12:45 -- 2:00 **LUNCH**

Friday – July 1 – Afternoon

2:00 – 3:30 **General Session**

Turbulence and mixing at density interfaces
H. J. S. Fernando

Particle-driven gravity currents
H. E. Huppert

3:30 – 4:00 **Poster Presentation GP3**

1. Experimental study of regular background and ship internal waves interaction in the thermocline – 40
O. D. Shishkina

2. Effect of stratification on the hydrodynamic loads acting on a submerged cylinder advancing in water waves – 35
I. V. Sturova

3. Lee waves and hydrodynamical loads due to the motion of a submerged horizontal circular cylinder in a three-layer fluid – 172
O. A. Arntsen

4. Stratified flow over three-dimensional topography – 181
Y. Kadri, P. Bonneton, J.-M. Chomaz, M. Perrier

5. On the amplification of internal-wave surface manifestations due to subsurface shear current – 218
V. I. Shrira, V. V. Voronovich

6. Interaction and generation of waves in a two-layer fluid flowing over uneven bottom – 92
M. Funakoshi

7. Steepening of the leading and back faces of solitary internal wave-depressions and its connection with tidal currents – 10
A. N. Serebryany

8. Capillary-gravity interfacial waves – 124
F. Dias

9. Turbulent mechanisms in stratified fluids – 193
J. M. Redondo, M. A. Sanchez, I. R. Cantalapiedra

10. Interfacial resistance and mixing in stratified channel flows – 122
P. Prinos, V. Dermissis

11. Sea-strait type flows and breaking up phenomena of interface by vertical jets – 253
T. T. Numan

4:00 4:30 **COFFEE BREAK AND POSTER VIEWING**

Session A6
INTERNAL WAVE BREAKING

4:30 A numerical study of the breaking of an internal soliton and its interaction with a slope – 8
K. Saffarinia, T. W. Kao

4:45 Decay of internal solitary waves and a comparison of timescales of dissipation and dispersion – 41
H. Sandstrom, N. S. Oakey

5:00 Vertical mixing of passive scalars due to breaking gravity waves – 50
V. Schilling, D. Etling

5:15 A numerical study of wave-breaking in stratified flow over obstacles – 72
M. F. Paisley, I. P. Castro

5:30 The dynamics of internal waves produced by parametric instability: an experimental study – 233
D. Bénielli, J. Sommeria

5:45 Stratified turbulence produced by internal wave breaking – 129
P. Bourunt-Aubertot, J. Sommeria, C. Staquet

6:00 Internal wave breaking and the nonlinear critical layer – 201
N. G. Potylitsine, W. R. Peltier

6:15 On the breakdown into turbulence of propagating internal waves – 215
P. N. Lombard, J. J. Riley

Session B6
GRAVITY CURRENTS

4:30 The dynamics of sedimenting surface-gravity-currents – 195
T. Maxworthy

4:45 The internal slab-collapse problem – 154
J. Bühler, S. J. Wright, T. Dreier

5:00 Experiments on 3-D turbulent density currents – 67
G. C. Christodoulou, F. E. Tzachou

5:15 Mixing at the front of gravity currents – 232
M. H. Garcia, J. D. Parsons

5:30 Laboratory observations of gravity currents and internal bores – 225
S. Mausshardt, H. Yeh, C. Grandinetti

5:45 Shear instabilities in arrested salt-wedge flows – 109
N. Yonemitsu, G. E. Swaters, N. Rajaratnam, G. A. Lawrence

6:00 Dilution of dense bottom plumes in turbulent currents – 69
O. Petersen, T. Larsen

6:15 Mixing in lock-release gravity currents – 182
J. Hacker, P. F. Linden, S. B. Dalziel

8:00 **BANQUET**

GENERAL SESSION

MIXING AND TRANSPORT IN A STRATIFIED LAKE

Jörg Imberger

Centre for Water Research
and
Department of Environmental Engineering
The University of Western Australia
Nedlands 6009 Australia

Reference ED 883 JI

To be published
Proceedings of the Fourth International Symposium on Stratified Flows, Grenoble, July 1994.

1. PHYSICAL LIMNOLOGY: INTRODUCTION

Physical limnology is the study of the motion and mixing of water in a lake, reservoir, wetland or stream. In this article I shall confine my comments to lakes and reservoirs. A lake is a holding basin for water which usually enters the lake via a set of streams. Solar radiation imparts heat at the surface stabilising the water column. Evaporation, sensible heat transport and long wave radiation at the surface of a lake can either add to impart additional heat or, as is the case in the fall, add to lead to a net cooling causing convection immediately beneath the water surface. Wind at the surface imparts momentum which leads to a general motion in the lake and turbulent kinetic energy which energizes mixing of the surface layer. Additional forcing is imparted by river inflows and overflows or selective outflows. The inflows and outflows may act to increase or decrease the stability of the water column depending on the temperature structure and the physical configuration of this forcing.

In general, the motion in a lake is the result of the balance between all the disturbing and restoring forces listed above. However, due to the configuration of the applied forces the water column responses may be categorised into the following flow regimes.

Immediately beneath the water surface there is a layer which is being actively mixed by the action of the wind or is undergoing stratification due to solar radiation; this is called the diurnal surface layer. Beneath this surface layer there is the subsurface layer which is the stratified buffer between the surface layer and the water immediately beneath. The pressure fluctuations, due to the turbulence in the surface layer, excite internal waves in the subsurface layer which break and sustain an active level of turbulence in the presence of a usually strong stratification. Together the surface and subsurface layers respond strongly to the meteorological forcing at the time and grow and decay depending on the conditions overhead. The water beneath the subsurface layer is strongly stratified to a depth of up to 30 meters, below which the strength of stratification rapidly decreases. The strongly stratified region is called the metalimnion and this acts, due to the strong stratification, as a wave guide for a spectrum of internal waves. The stratification is due to seasonal heating and the point where the stratification gradient peaks is called the seasonal thermocline. The weakly stratified fluid below the metalimnion is called the hypolimnion and in this the water tends to remain quiescent, not because of the stability of the water column, but rather due to the absence of large forcing. The exception to this statement occurs during strong winds when the barotropic forcing becomes strong enough to initiate a general circulation in the lake as a whole. Adjacent to the lake bottom we again find a turbulent layer, the benthic boundary layer. The benthic boundary layer is energized by the currents overhead, internal wave energy reflecting off the sloping bottom and internal waves breaking due to shoaling. The degree to which any of these features may be observed in a lake, at a particular time, depends on the climate and the immediate weather conditions.

The article by Imberger and Patterson (1989) gives a full account of physical limnology, but emphasises advection and mixing. Hutter (1991) gives an excellent foundation to the theory of internal seiches and waves. Imboden and Wüest (1994) review the traditional mixing ideas and compare these with the results from tracer experiments. A particularly useful reference on the benthic boundary layer may be found in Garrett *et al.* (1993), while Gargett (1989) provides an excellent overview of mixing in the ocean. With respect to mixing, the reader is also referred to the review article on chaos by Ottino (1990) and the general review of turbulent mixing in stratified fluids by Fernando (1991). For a basic yet extremely thorough overview of internal waves, the reader is referred to the books by Phillips (1977) and Turner (1979). The two articles by Gregg (1989) and (1993) provide a very recent update on the ideas of how internal waves lead to mixing in a stratified water body. In this context the Proceedings of the three speciality workshops on internal waves held in Hawaii are also recommended (Müller &

Henderson, 1989, 1991, 1993). The relevance of the physical processes to ecological processes is discussed by Imboden (1990).

The contents of this article are a synopsis of a more detailed very recent article (Imberger 1994), which I prepared for an anniversary volume in honour of the limnologist Margalef. I have shortened the text, as the original article was written for a different audience and I have added some more technical material, but no attempt was made to alter the structure.

2. THERMAL CHARACTERISTICS

The physical response of a lake to a surface wind stress, a river inflow or an outflow via a river or offtake tower is strongly dependent on the thermal stratification present in the lake. This thermal stratification may be predominant in only the vertical direction, or it may be biased in the direction of the long axis of the lake as is the case in throughflow reservoirs. In addition the overall density stratification caused by the thermal stratification may be either enhanced or weakened by a layering in chemical constituents.

The motion in a stratified lake is thus the result of a delicate interplay between the four dominant disturbances (wind, inflow, outflow, differential heating), the potential energy of the resident stratification, the bathymetry of the lake and the earth's rotation if the lake is large. This interplay between the disturbing and restoring forces is reviewed in Imberger (1985), Imberger and Patterson (1989), Imboden and Wüest (1994).

The seasonal variability of the thermal regimes of a lake are now well documented and a great many papers exist with examples of the seasonal variation of the thermal stratification in a particular lake. In winter the lake water is usually cold and reasonably homogeneous, in spring there is a general warming of the surface waters which leads to a peak stratification towards the latter half of summer. During autumn, surface cooling gives rise to penetrative convection which progressively cools and deepens the surface layer. Strong winds often assist this deepening process until finally the water becomes well mixed.

Numerical models have been developed for the prediction of the seasonal thermal cycle; these are described in Imberger and Patterson (1989). However, the models are not able to fully bridge the spectral range of scales of motion, from the basin scale to the turbulent large wave number motions; this range spans scales from 10^4 m to 10^{-4}m. The smallest grid sizes that have been used in estuarine and lake modelling (Stronach *et al.* 1993) are about 100 m to 500 m. All processes smaller than this have been lumped together and modelled with different closure schemes. The simplest of these closure schemes is the assumption of a constant eddy exchange coefficient (Casulli & Cattani 1994). More sophisticated closure schemes have been used in the geophysical content (Mellor & Yamada 1982; Fukushima & Watanabe 1990; Zic 1990). These authors used a k-ε scheme modified to account for the buoyancy flux in the turbulent kinetic energy equation. Such models appear to reasonably successfully predict the bulk properties of small scale phenomena such as gravity currents (Fukushima & Watanabe 1990; Hürzler *et al.* 1994(a) and 1994(b)), but even for such flows the turbulent properties are reproduced only poorly.

For lake simulations as a whole such models appear to completely miss the point. Field data in lakes (Imberger & Ivey 1993) and in the ocean (Gregg *et a;*. 1993; Kudryavtsev & Soloviev 1990) suggests, at least in the stratified metalimnion, the water offers very low internal frictional resistance with vertical exchange coefficients for both momentum and mass being close to molecular; the momentum transport which does take place is dominated by internal wave transport. This means that internal friction is usually not an important dynamical

consideration, therefore using complicated closure schemes based on shear turbulence but which neglect internal waves, is of questionable value. The turbulent transport which does exist is, however, crucial from a biological point of view as it is this transport, albeit small and patchy, which nourishes the plankton in the surface layer with nutrients contained in the deeper water, circulates material from the benthic layer to the lake water column and cycles organisms within the surface layer exposing them to a changing light climate.

Uittenbogaard (1988) has clearly shown that in order to correctly describe the mean fluxes in the stratified water column we must account for the energy store in the internal wave field. This realization has been discussed for a considerable time now in the oceanographic literature (Imberger & Patterson 1989; Gargett 1989; Gregg 1989; Gregg *et al.* 1993; Garrett & Munk 1979). We review this material in the following sections where we also suggest recipes for the inclusion of internal waves energy as an integral part of a model; to date there is no such model available.

3. SURFACE LAYER

Surface layer energetics are discussed and reviewed fully in Imberger and Patterson (1989). An update of the most recent methodology for estimating surface exchange coefficients is given in the article on gas exchange processes by MacIntyre *et al.* (1994). A description of the internal boundary layer may be found in Garratt (1990) and a general review on surface fluxes is given in Frenzen and Vogel (1992).

The surface layer is defined as the layer of water extending from the surface, where the waves form and break, down to a depth where the direct influence of the surface wind and surface heat fluxes stops.

Under certain wind conditions a second surface layer forms immediately below the surface layer; pressure fluctuations in the surface layer induce internal waves in the underlying fluid which radiate down into the water column causing active mixing for many meters below the diurnal thermocline. We call this the subsurface layer (Zic & Imberger 1994; Wijesekera & Dillon 1991). The surface and subsurface layer are important for the growth of plankton. Since plankton grow in the surface layer in response to light, any coherent motion in the surface layer which sweep plankton through a cyclic light regime are most important. Further, the nutrient supply for the plankton growth comes from the subsurface layer via the turbulence flux sustained by the internal wave field there.

Models based on the turbulent kinetic energy equation appear to work remarkably well (Spigel *et al.* 1986) and are able to accurately predict the rate of deepening of the surface layer and also the mean temperature of the surface layer water. This is true even though models of this kind completely neglect the spatial variation of the turbulence within the layer, neglect an explicit description of the leakage of internal energy from the base of the thermocline, neglect the presence of coherent motions, but at the same time contain constant energy conversion coefficients. The conclusions which may be drawn from this apparent success is that either all the neglected factors are implicitly accounted for, the models have not been verified over a wide enough range of conditions, or the neglected factors do not contribute significantly to the deepening of the surface layer. As shown below it is most likely the first and last conclusion which are consistent with very recent observations. It is important to note, however, that the neglected mechanisms, particularly the presence of coherent motions, may have major implications for the growth of plankton.

These models assume a constant fraction of the rate of the working of the wind is transported to the water column. This suggests that the turbulent boundary layer immediately below the water surface is in equilibrium and thus should contain similarity profiles for all the turbulent properties. The dissipation of turbulent kinetic energy is the variable most often measured and the evidence here is still somewhat conflicting. Soloviev *et al.* (1988), Lombardo and Gregg (1989), Imberger (1985), and Shay and Gregg (1984) all find that similarity is essentially present with $\varepsilon kz/u_*^3$ being close to one and ε/B ranging between 0.4 and 0.8. Here k is the von Karman constant, z is the distance from the surface, B is the buoyancy flux and ε is the rate of dissipation of turbulent kinetic energy. On the other hand, Gargett (1989) examined data from the north-east Pacific and found that, for periods of rapidly increasing wind speed, $\varepsilon \sim z^{-4}$, a much faster decay with depth. The likely explanation for the relatively much larger dissipation values near the surface is the presence of plunging jets due to wave breaking. Zedel and Farmer (1991) found that bubbles resulting from breaking waves could penetrate down to 13 metres for wind speeds of about 12 ms^{-1}. If we exclude the area immediately under the breaking wave zone it appears that similarity is preserved for times when the wind speed is relatively steady.

The assumption that the energy loss due to internal wave leakage is captured by the dissipation at the base of the billow layer is probably poor at best. Zic and Imberger (1994), Stevens and Imberger (1994), and Wijesekera and Dillon (1991) have presented data showing that strong leakage occurs during the initial deepening period but when active billowing sets in energy is no longer communicated into the metalimnion; parameterization of this leakage is, however, still poorly understood.

During strong heating periods the model of Spigel *et al.* (1986) assumes a rapid decay of the dissipation field. This seems to have been verified by Imberger (1985) and Kudryavtsev and Soloviev (1990). The case where the buoyancy flux is roughly in equilibrium with the wind has not received any attention (see Imberger & Patterson 1989 where this point was previously made).

Langmuir circulation (Langmuir 1938) has recently received a great deal of attention in the oceanographic literature. This follows the earlier documentation by Weller *et al.* (1985) and Thorpe and Hall (1982). The papers by Weller and Price (1988), Smith (1992), Osborn *et al.* (1992), and Soloviev (1990) all point to a consistent picture. Langmuir's cells exist as opposing vortex rolls, the size of which grow under neutral conditions with wind speed keeping a depth to width ratio at about 1:1. The downwelling zone between two opposing rolls is more confined than the upwelling zone and is also the plane of a relatively strong horizontal jet in the direction of the wind. The vertical growth of the cells is inhibited when the base of the cell reaches the diurnal thermocline and the aspect ratio can then grow to 1:3 or 1:4. In the downward convergent zone the dissipation is considerably larger than in the rest of the cell and this may further explain the higher dissipation values documented by Gargett (1989). Osborn *et al.* (1992) make the point that Langmuir circulation may be present, as evidenced by bubble plume spacings, even though there is no surface evidence. The longitudinal structure is characterised by points where the surface manifestations converge and the rolls pair. Further, Thorpe and Hall (1982) and Soloviev (1990) show that Langmuir cells are interrupted longitudinally by temperature gradient sheets which have a spacing of many 100's of meters.

The physical mechanism responsible for the formation of Langmuir cells is believed to be the production of longitudinal vorticity by the interaction of the cross-wind vorticity of the wind shear layer and the vertical vorticity of the periodic variation due to the wave Stoke's drift (Leibovich 1977; Leibovich & Radhakrishnan 1977). This theory has undergone many modifications, the latest being the inclusion of a finite thickness of the diurnal surface layer and realistic boundary conditions of the water surface. Cox and Leibovich (1993) have shown that

these inclusions lead to a realistic finite estimate for the scale of the Langmuir circulation. Thorpe (1992) performed a stability analysis of adjacent parallel vortex rolls and showed that a longitudinal instability is possible which results in pairing at length scales of 100's of meters; in good agreement with observations.

As evidenced by the success of the energy models (Section 3.2), Langmuir cells are of lesser importance for the production and redistribution of the turbulent kinetic energy or the modification of the entrainment velocity at the base of the surface layer. However, the circulation induced by cells is extremely importance for the growth of plankton (Patterson 1991) and the distribution of bubbles and the associated gas exchange (MacIntyre *et al.* 1994; Thorpe 1984).

4. MAIN WATER BODY

4.1 Currents, Eddies, Internal Waves and Intrusions

Now let us turn to the problem of understanding the transport processes in the main body of the lake. Before we can do this we must discuss, at least briefly, the nature of the composite motions in a stratified water body. This is a vast topic and we shall only give a brief overview and then show how to establish a simple recipe for the flux of mass and momentum in the water column between the surface layer and the benthic boundary layer.

In general, motions in lakes are energized by the wind acting on the lake surface and through differential cooling at the surface (Monismith *et al.* 1986). The momentum input from these two sources leads to currents, eddies, intrusions and internal waves; intrusions are internal waves with long periods (Lemckert & Imberger 1993). Eddies form mainly in large lakes through the action of currents, induced by Kelvin waves, sweeping the water past headlands. This gives birth to large pancake shaped eddies at headlands and these traverse the lake carrying with them mass. Ivey and Maxworthy (1992) have given graphic evidence from laboratory experiments of the formation and propagation of such eddies. When established the currents, eddies, intrusions and internal waves combine to trigger patches of turbulence throughout the lake.

This scenario is best illustrated by example. During the recent BITEX experiment, thermistor chains were place in the southern part of Lake Biwa. These chains recorded the temperature from 20 thermistors, spaced approximately uniformly over the water depth, at the measurement site. The lake has a depth of over 90 meters and a surface area of around 300 km^2. and the array of chains were located in 50 meters of water. The temperature was sampled at 2 second intervals, averaged over 14 seconds and then recorded. The recording continued over a period of 4 weeks during which the weather was mostly calm and sunny. However, on day 247 a major typhoon, with wind speeds up to 25 ms^{-1} passed almost directly overhead. A more minor typhoon was again experienced on day 252.

The temperature from the thermistor located at a depth of 22 m, in the middle of the metalimnion, is shown in Figure 4.1.1(a). Between days 236 and 247 the temperature showed small undulations with a frequency of about 2 days; otherwise the signal was relatively quiescent. The typhoon which passed on the evening of day 247 induced a sharp ramp-like increase in temperature which was followed by strong undulations for the next 6 days after which they decayed. The second typhoon on day 252 further energised the oscillations. The signal was low passed (2 hour cut off) and the results are shown in Figure 4.1.1(b). The smoothed signal shows the Kelvin wave oscillation more clearly. Spectral analysis revealed

that these long waves had a period of 41 hours which is similar to that previously measure by Okuda *et al.* 1994.

A spectrogram was constructed from the temperature record shown in Figure 4.1.1(a) using a 2 day window and a 1 hour window shift. This is shown in Figure 4.1.1(c). Inspection of this spectrogram reveals very clearly the scenario discussed above. Before the main typhoon passed the site energy levels were low, only weakly correlated with the phase of the Kelvin wave and there was little energy above 10^{-4} Hz. However, after the storm had excited the large Kelvin waves, the internal wave energy levels became strongly correlated with the phase of the Kelvin wave; energy levels rose strongly during periods of downwelling due to the Kelvin wave. At the same time energy penetrated to frequencies beyond 10^{-3} Hz, in particular, immediately after the storm where there was substantial energy to 10^{-2} Hz. These data were accompanied by an intense sampling programme of microstructure flux measurements; the times of these measurements are shown at the base of Figure 4.1.1 and these data are presently being analysed. Preliminary analysis clearly shows elevated levels of dissipation of turbulent kinetic energy during periods of elevated internal wave activity.

The character of the motion in the water column is graphically illustrated in Figure 4.1.2 which shows the isotherms for a brief period immediately after the passage of the typhoon; the water column was filled with a mixture of long mode one and two waves, undular bores, free internal waves and turbulence. The turbulence is thus clearly the result of the shear induced by the composite motion and the local weakening of the stability of the water column by the straining due to internal waves.

A major consideration in this scenario is the role internal waves play in the distribution of energy. If we have an internal wave which has an energy density (energy per unit volume of water) of say E (Joules m^{-3}), then this energy will only ultimately decay through the action of the dissipation of turbulent kinetic energy ε. Thus we may write:

$$\frac{dE}{dt} = -\varepsilon \rho_0 , \qquad (4.1.1)$$

so that the time it takes for the wave to decay may be estimated from :

$$t_d \sim \frac{E_0}{\varepsilon_0 \rho_0} , \qquad (4.1.2)$$

where ε_0 is the initial rate of dissipation.

Now for waves as shown in Figure 4.1.1(a), $E_0 = 20$ J m^{-3} and a typical dissipation rate was 10^{-9} m^2 s^{-3} so that the time taken for the wave to decay is about 230 days. This is a very long time! Much longer than what is observed in Figure 4.1.1(b), which indicates a decay time of around 3 days. This implies that the reflection process at the boundaries is far from perfect and large dissipation must occur at the reflecting sites. Further, since the dissipation processes involve wave breaking, we expect a dispersion of the frequency content of the reflected waves and this is possibly the site for the formation of the solitary waves seen in Figure 4.1.2 (Kao *et al.* 1985; Gan & Ingram 1992).

In summary, internal waves distribute mean kinetic energy very effectively throughout the lake. In the water column this composite nonlinear wave field leads to turbulence through what appears to be two distinct actions. First, shear induced instability and second, weakening of the stability of the water column due to nonlinear internal wave straining. At the boundaries the internal waves again induce turbulence in two distinct ways. First the waves reflect and so

intensify the energy density (Phillips 1977) and second, the nearly horizontal internal waves shoal and break as they propagate towards the shore. I shall now discuss each of these four mechanisms separately.

4.2 Shear Flow Turbulence

In order to understand the role of shear, consider the very simplest configuration—that of a uniform mean shear flow in a linearly stratified fluid. The problem is completely specified by the parameters :

S ,	N^2 ,	ν ,	κ ,	t ,	$q'(0)$,	$\ell_c(0)$
s^{-1}	s^{-2}	$m^2 s^{-1}$	$m^2 s^{-1}$	s	ms^{-1}	m ,

where S is the shear, N^2 is the buoyancy frequency, ν the viscosity, κ is the molecular diffusion coefficient, t is the time, $q'(o)$ is the initial RMS of the velocity fluctuations and $\ell_c(o)$ is the initial RMS scale of the motion.

To conform with convention we choose the first three dimensional numbers as $Ri = N^2/S^2$, $T = St$ and $Pr = \nu/\kappa$. The Richardson number Ri has a simple physical interpretation if one examines the energetics of mixing. Suppose we have a layer of the linearly stratified fluid of thickness ℓ_c which is partially mixed so that the new buoyancy frequency in the patch is N_2 and the new shear is S_2. Thus the ratio of the potential energy required to mix the water column to that available from the mean kinetic energy released by the mixing is given by :

$$\frac{\Delta PE}{\Delta KE} = \frac{2\gamma N^2}{\beta(2-\beta)S^2} = \frac{2\gamma}{\beta(2-\beta)} Ri . \qquad (4.2.1)$$

where γ and β are the mixing fraction; a value of one means $N_2^2 = 0$ and $S_2 = 0$.

Now dissipation occurring during the mixing event may be estimated by noting that the dissipation per unit mass must scale, from as $\rho_0 u^3/\ell_c$, so that the energy lost to dissipation over the time it takes to mix the fluid is given by :

$$\varepsilon \ell_c \frac{\ell_c}{u} \sim \rho_0 \frac{u^3}{\ell_c} \cdot \ell_c \cdot \frac{\ell_c}{u} \sim \rho_0 u^2 \ell_c \sim \rho_0 \left(\frac{\partial u}{\partial z}\right)^2 \ell_c^3 \sim \Delta KE \qquad (4.2.2)$$

since the time scale for releasing the kinetic energy is given ℓ_c/u (Tennekes and Lumley, 1972) and u the velocity characterising the larger scale motions in the mixing event is given by $u \sim \left(\frac{\partial u}{\partial z}\right)\ell_c$.

Thus if $Ri < \frac{(2-\beta)\beta}{2\gamma}$ there is sufficient energy available from the mean kinetic energy field to overcome the necessary potential energy required to achieve the mixing, but there must be an excess energy available to supply the energy for the dissipation. Stability analysis (Yih, 1980) tells us that the flow is stable for $R_i > 1/4$. Suppose the value 1/4 forms the stability boundary then according to the above model, whenever there is complete mixing of the fluid column, 50% of the kinetic energy is released to dissipation and 50% is used to lift the mixed fluid parcel resulting in a change of potential energy. On the other hand, when the mixing is only

partial and the process may be modelled more closely by taking the limit β and γ tending towards zero, then the division of energy is 75% of the released kinetic energy going to dissipation and only 25% of the released energy is utilised to lift the fluid parcel. This is an important result as most experimental evidence on mixing efficiency points to a conversion ratio close to the latter value (Ivey & Imberger 1991).

The evolution of the flow must also depend on the initial conditions imposed as these are the conditions from which the flow evolves. Thus, unless the turbulence quickly "forgets" the history of its origin, the initial conditions will be important in determining the flow characteristics. This influence may be captured by introducing the nondimensional parameters:

$$Fr_t(0) = \frac{q'(0)}{N^{1/2} \ell_c^{1/2}(0)}, \tag{4.2.3}$$

$$Re_t(0) = \frac{q'(0)\,\ell_c(0)}{\nu}. \tag{4.2.4}$$

Thorpe (personal communication) has shown, using a linear stability analysis, that the linear shear flow is stable for all values of Ri so if ℓ_c is to be non-zero, the profile must be unstable to finite values of $Fr_t(0)$ and $Re_t(0)$. Numerical experiments carried out by Holt *et al.* (1992) starting with a finite disturbance, show that provided Ri is sufficiently small, ℓ_c grows with time, indicating that the linear shear case is unstable to finite initial disturbances. Ivey *et al.* (1994) analysed the results from a large number of these and further numerical experiments for the case where the Richardson number was small enough to cause active growth of the turbulence. Under these circumstance, they found that for a wide range of Prandtl numbers and Richardson numbers ≤ 0.21 the displacement scale was given by:

$$\ell_c = 8\,\ell_p\,K^{\frac{1}{4}}(S\,t)^n, \tag{4.2.5}$$

where

$$n = 1.9\,(0.21 - Ri) \qquad (Ri \leq 0.21), \tag{4.2.6}$$

independent of the initial conditions or the Prandtl number and,

$$\ell_p = \left(\frac{\nu}{N}\right)^{1/2}, \tag{4.2.7}$$

which we shall call the primitive length scale. Comparison between this prediction and the numerical data used to derived the above correlation is shown in Figure 4.2.1.

The dissipation of turbulent kinetic energy ε and the buoyancy and the momentum fluxes at a point are further population parameters which again must be functions of the set of dimensionless groups. Ivey *et al.* (1994) showed:

$$\varepsilon = 8\,\nu S^2 (St)^{2n} \quad ; \quad (R_i \leq 0.21). \tag{4.2.8}$$

$$B = \overline{g'w'} = 13\,\nu\,S^2 Ri\,(St)^{2n} \quad ; \quad (R_i \leq 0.21) \tag{4.2.9}$$

$$M = \overline{u'w'} = \nu S[8 + 13\,Ri]\,(St)^{2n} \quad (Ri < 0.21)\,. \tag{4.2.10}$$

The vertical mass eddy exchange coefficient may thus be written:

$$K_\rho = \frac{B}{N^2} = 1.6\,Ri\,\frac{\varepsilon}{N^2} = 1.6\,\frac{\varepsilon}{S^2} \tag{4.2.11}$$

so that the ratio of the mass to the momentum eddy coefficients becomes:

$$\frac{\kappa_\rho}{\kappa_m} = \left(\frac{13}{8 + 13\,Ri}\right)\,, \tag{4.2.12}$$

indicating for active turbulence , $Ri < 0.21$, there is very little difference between the mass and momentum transfer coefficients. This is of course not the case when Ri becomes large; under such circumstances momentum will continue to be transferred by the internal waves (Kim and Mahrt 1992), but the mass flux ceases. However, under such circumstances the concept of a transfer coefficient is no longer useful and it is better to calculate the momentum flux directly by, say, wave ray tracing techniques (Phillips 1977). Further study is required for the case where Ri is at first less than the critical value and is then suddenly increased. Only empirical results are available on the mass and momentum transfers during the ensuing collapse of the turbulence.

It is, however, interesting to note that many authors have developed formulae, especially for the mass transfer coefficient (4.2.11) in terms of only the Richardson number of the flow and these formulae have been used with some success in describing flows in estuaries, lakes and even the ocean (Odd & Rodger 1978; Simpson & Sharples 1991). The fact that these formulae appear to yield useful results means that, in the field, there are other factors which limit the growth of the turbulent scale ℓ_c and so prevent the continued growth of the turbulence. This conjecture needs a thorough evaluation.

For practical application of (4.2.11) and (4.2.12) it is useful to enquire whether it is necessary to track the whole history of the turbulent event, or is it possible to take a local approach as suggested by (4.2.11) which does not depend explicitly on time, but time enters only through the dissipation ε, a "local" parameter.

4.3 Some Local Concepts; generalization to other flows

The key towards a generalisation of the above discussion beyond a simple shear flow is the realisation that there may be variables of the turbulent flow itself in terms of which all the other characteristics of the flow may be described. Further, if these fundamental variables are such that they may be either easily measured or derived from the mean flow then we are in a position to once again close the equations of motion and derive the transfer of mass and momentum. Again from dimensional analysis such parameters exist and are given by (Imberger 1994):

$$Fr_t = \left(\frac{\ell_0}{\ell_c}\right)^{\frac{2}{3}} = \left(\frac{\varepsilon}{g'^{\frac{3}{2}}\ell_c^{1/2}}\right)^{1/3} = \left(\frac{\varepsilon}{N^3\ell_c^2}\right)^{1/3} \qquad (4.3.1)$$

which reduces to the familiar form $Fr_t = \left(\frac{u}{N\ell_c}\right)$, if we now also assume that the whole range of scales in the flow is active so that $u \sim (\varepsilon\ell_c)^{\frac{1}{3}}$.

Similarly, the Reynolds number,

$$Re_t = \left(\frac{\ell_c}{\eta}\right)^{\frac{4}{3}} = \left(\frac{\varepsilon\ell_c^4}{\nu^3}\right)^{1/3} . \qquad (4.3.2)$$

Again, for active turbulence this leads to the more traditional definition of the Reynolds number :

$$Re_t = \left(\frac{u_c\ell_c}{\nu}\right) . \qquad (4.3.3)$$

The Grasshof Gr_t is defined by :

$$Gr_t = \left(\frac{\ell_c}{\ell_p}\right)^4 = \left(\frac{\ell_c^3 g'}{\nu^2}\right) \sim \left(\frac{N^2\ell_c^4}{\nu^2}\right) , \qquad (4.3.4)$$

and the strain Froude number is defined by :

$$Fr_\gamma = \left(\frac{\ell_0}{\eta}\right)^{\frac{2}{3}} = \left(\frac{\varepsilon\ell_c}{g'\nu}\right)^{1/2} , \qquad (4.3.5)$$

where the strain rate, $\gamma = \left(\frac{\varepsilon}{\nu}\right)^{1/2}$. (4.3.6)

Given the above definitions it is now possible to construct an activity diagram. This is shown in Figure 4.3.1 and the type of motion is reflected by the position of the data on this diagram. Ivey *et al.* (1994) used these parameters to derive general relationships for the various turbulent quantities. These are reproduced in table 4.3.1. The special case of shear driven turbulence in a linearly stratified fluid discussed above is given by the $Fr_t = 1/2\ Ri^{-1/2}$. Thus for a value of the Richardson number of 0.21, $Fr_t = 1.1$ again indicating that for the stationary state the value of the Froude number is near one and the mixing efficiency is a maximum (Ivey & Imberger 1991).

The exact nature by which the internal waves interact among themselves and with the turbulence is at this stage not clear; the activity diagram, first advocated by Gibson (1986), is, however, a convenient tool to parameterise the turbulent fluxes under a wide range of conditions. As mentioned earlier a major mechanism, in addition to the enhanced shear produced by the internal waves, is the reduction of the local stability due to internal wave straining. In Figure 4.3.2 we show results from Javam *et al.* (1994), who compiled the flow due to two internal wave rays crossing and interacting. Clearly visible is the build up of a small region in the middle of the crossing where there is extensive vertical stretching of the isopycnals; laboratory experiments carried out by Teoh *et al.* (1994) using similar configuration with approximately the same Reynolds and Froude number showed that the regions of stretching are also the points where turbulent spots are formed. Clearly, internal waves can thus produced turbulence by focussing the shear or by decreasing the stability by stretching the isopycnals; one increases the disturbance force and the other decreases the stability. Both lead to the formation of turbulent spots where mass and momentum transport takes place.

4.4 Estimating the Values of ε and ℓ_c

The biggest difficulty in the closure question for a lake is thus no longer estimating the mixing efficiency, but rather finding the distribution and intensity of the mixing patches. Turbulence in the field involves many instability mechanisms other than the simple linear shear flow discussed above. Turbulence may be generated within a stratified fluid by two or more waves interacting (wave-wave instability), internal waves being trapped by the background shear (critical layer absorption), heavier fluid being somehow moved above lighter fluid (convective instability), or internal waves breaking by shoaling or shear steepening (wave breaking) (see Phillips (1977) and Turner (1979) for further details).

A number of methods of increasing complexity suggest themselves for estimating the dissipation ε in the main fluid body and thus the patch intensity and distribution:

a) The simplest assumption is to assume that the overall water body under consideration is in equilibrium with the external forcing and there are no patches. All the energy introduced by the wind, not utilized to mix the surface layer, is distributed by the internal wave field into the metalimnion and hypolimnion where it is ultimately converted to dissipation and buoyancy flux. This approach was suggested by Imberger *et al.* (1978) and is successfully operating in the numerical model DYRESM; in that model the energy input from the inflowing river and the outflow are also added. The weakness of this algorithm is that we do not know, a priori, what fraction of the total internal wave energy is dissipated at the boundaries, and what is dissipated internally, nor is the assumption of continuous dissipation representative of field evidence.

b) In the ocean the internal wave spectrum is in equilibrium and the flux of energy from large scales to small scales is mainly through wave-wave interaction. With this assumption it is possible to relate the dissipation to the shear at a 10 m scale and the actual buoyancy frequency. Gregg (1989) has suggested the formula:

$$\varepsilon = 7 \times 10^{-10} \left\langle \frac{N^2}{N_0^2} \right\rangle \left\langle \frac{S_{10}^4}{S_{GM}^4} \right\rangle, \qquad (4.4.1)$$

where $N_0 = 0.0052\ s^{-1}$, S_{10} is the shear observed at 10 m scale and $S^4_{GM} = 3.92 \times 10^{-5}$ $(N / N_0)^2$. This formula cannot be expected to work in lakes or estuaries since there is no equilibrium internal wave spectrum, but appears to yield excellent results in the ocean.

c) In general, we must resort to numerical calculations of the large scale internal wave field and use the cascade mechanism to route the energy down to small scales. In a separate model we may calculate the spectrum of free internal waves; this can be done by propagating the waves after they have formed, allowing them to interact, energizing them from the larger field computed in the first model, and accounting for all reflections and frequency transformations. Given this information it is possible to use wave-wave interaction theory to calculate the energy flux moving to smaller scales and then equate this to the dissipation. Such a model is presently not available, but is being constructed by the author and his colleagues.

Let us now turn to the other variable ℓ_c, the length scale required to determine the efficiency of mixing. Again there are a number of ways of approaching the estimation of this variable.

a) Oceanographers have noted that most energetic mixing episodes have the property that Fr_t is close to one. There are good reason why this should be so (Imberger & Ivey 1991). Detailed documentation of a collapsing intrusion was recently given by Lemckert & Imberger (1994) who show that as an intrusion travelled through a lake $Fr_t = 1$, but the Reynolds number Re_t became progressively smaller until viscosity finally damped all turbulence. If this is the case, then $R_f = 0.23$ and we may calculate the buoyancy flux directly from turbulent kinetic energy budget (Ivey & Imberger 1991). A very simple model thus follows. It may be assumed that the dissipation is given from above and the buoyancy flux is used to calculate the mass and momentum transport over the time step. A simple scheme would be to ignore the collapse process and only account for the active transport periods.

b) One could assume that the mixing in the lake, when active, is modelled by simple shear flow. If this is the case then K_ρ follows directly from ε and R_i through (4.2.11) without the knowledge of ℓ_c. The dissipation ε follows, however, directly and is given by $3.2\ \varepsilon^{1/2}\ S^{-3/2}$. Once the decay equations have been found it will be possible to also model episodes where the Ri suddenly increases from a low to a higher value.

5. BENTHIC BOUNDARY LAYER AND GRAVITY CURRENT

5.1 The Benthic Boundary Layer

In Section 4.1 we saw that a great deal of energy supplied by the wind to the internal wave field is lost not internally in the water column, but rather at the boundary, implying we should see active turbulence adjacent to the lake bottom. This is further supported by the observation that in both the ocean and in lakes the basin scale average vertical exchange coefficient is around $10^{-4}\ m^2\ s^{-1}$ (Imberger & Patterson 1989; Garrett 1991; Hondzo *et al.* 1991) whereas microstructure observations would suggest a value between 10^{-6} and $10^{-5}\ m^2\ s^{-1}$; (Gregg *et al.* 1993; Imberger & Ivey 1991) again indicating that there must be other flux paths by which mass is transported vertically through the lake. Such a conclusion has important consequences for the biologist since if the dominant flux path is along the benthic boundary layer and then into the main water body horizontally via intrusions then particles will be periodically recycled through the benthic boundary layer. In other words particles will experience a cycling through water of low and high oxygen content.

Many observations have been made documenting the occurrence of turbulence at the lake bottom (for example Imberger & Ivey 1991; Ivey & Boyce 1982; Thorpe *et al.* 1990). Excellent reviews exist for the analogous problem in the ocean.

5.2 Sources of Energy

If the benthic boundary layer is to remain turbulent then there must be a source of turbulent kinetic energy which overcomes the dissipation. Originally, Armi (1978) and Munk, (1966) postulated that ocean currents sweeping the water over a rough bottom, could be one source. Long internal Kelvin waves may be dissipated by such action; their period is much longer than the time h/u_* it takes to establish the turbulence in the layer. At present no experimental data appear to exist in lakes for the development of such stress driven layers.

A more likely source of energy for the maintenance of turbulence in the benthic boundary layer is the smaller internal waves. Two mechanisms may be cited as possible sources. First, wave reflection leading to energy intensification and then turbulence and second, internal wave breaking due to shoaling. A very clear explanation of the first mechanism may be found in Phillips (1977) who discusses the linear theory and Thorpe (1987) who provides the first order correction due to non-linearities. The turbulent spots may form at or away from the boundary and as shown by Ivey and Nokes (1989) this turbulence is able to transport mass vertically.

The second mechanism is usually associated with large internal waves shoaling on a sloping boundary. Such waves may break leading to active turbulence. The energy remaining is reflected in the form of solitary internal waves (Whitham 1974) and these then propagate away in their own right (see Figure 4.1.1). This is a vast subject and the reader is referred to the review articles by Chu and Chou (1989) and Boyd (1989).

Eriksen (1985) and later Garrett and Gilbert (1988) postulated a boundary turbulence model for the ocean which conceptually was most attractive. The idea was that the spectrum of internal waves propagating towards a boundary is modified by wave reflection whenever the waves encounter a boundary. The increased energy density, wave steepness and rate of strain are assumed to push energy into the breaking part of the spectrum. These authors then simply assumed that the energy which went outside the breaking boundary in the spectrum was lost to turbulence. The experiments discussed by Van Haren *et al.* (1992) and Thorpe *et al.* (1990) were an attempt to verify this model, however, the evidence is inconclusive.

In summary a number of plausible mechanisms exist which may be used to explain the existence of a turbulent benthic boundary layer. These are bottom currents, internal wave reflection and internal wave shoaling. So far, however, there is no simple recipe to predict either the thickness of the benthic boundary layer nor the dissipation rates within it. This is a top priority for further research given that the benthic boundary layer is the interface between the bottom sediments and the water column and perhaps, even more importantly, given that it is most likely the main conveyer of fluid, particles and dissolved materials between the deep and shallow waters.

5.3 Boundary Layer Fluxes

Given the existence of a turbulent benthic boundary layer around the lake bathymetry, it is natural to enquire what role this turbulent layer plays with respect to the flux paths of material throughout the lake. This problem has attracted much attention starting with the pioneering work of Phillips (1970) who showed that in linearly stratified fluid a shear flow dispersion layer is set up next to a sloping boundary. Recent contributions are discussed fully in Garrett (1991) and Garrett *et al.* (1993). The dynamics underlying the transport of water through the

benthic boundary layer were derived by Imberger and Ivey (1993) via a perturbation analysis which allowed a unification of previous theories, particularly those of Salmun *et al.* (1991) and Woods (1991). A number of different scenarios are possible.

First, suppose that the energy source for this turbulence ceases with the passage of the group of internal waves which provided the energy. The turbulence will then collapse, leaving behind a volume of water close to the boundary which is relatively well mixed compared to the water immediately adjacent in the main body of the lake. Such a mixed volume will then collapse and intrude horizontally into the lake, the speed and thickness of the intrusion depending on the initial density difference and volume of the boundary water (cf Imberger *et al.* (1976) and Lemckert & Imberger (1994)).

Second, if the source of energy remains active for some time, but the energy is focussed locally onto a relatively small part of the boundary (as would be the case if a long internal wave train continued to beach there), then a local mixing boundary layer will form. The mixing will set up a horizontal density anomaly between the fluid in the boundary layer and the interior of the lake, and an intrusion will form. This is equivalent to stirring locally near the boundary in a stratified water body. Common experience leads to the conclusion that the stirred area becomes a source of intermediate density water which then intrudes horizontally into the lake (De Silva & Fernando 1992). The process is also analogous to that induced by differential mixing at the surface layer (Ivey & Maxworthy 1992).

Third, if the boundary layer extends over an alongshore distance which is large compared to the thickness of the benthic boundary layer then a continuous flux is maintained. In such cases the temperature gradient in the main part of the lake is imposed on the boundary via a turbulent boundary layer. In this layer the gradients normal to the bottom are small due to the turbulence, but the gradient along the slope is the same as in the interior. By simple analogy with the original solution derived by Phillips (1970) a density current is established which is driven by the tendency of the constant density surfaces to return to the horizontal; near the lake bottom the fluid moves up the slope and near the top of the benthic boundary layer the fluid moves downwards.

On the other hand, if the stratification in the lake is non-linear, as would normally be the case due to the stronger stratification in the metalimnion then, since the shear dispersion mechanism transport is proportional to the mean longitudinal temperature gradient, there would be a strong heat transfer near the level of the thermocline and progressively weaker heat transfer above and below. This would mean that the boundary layer above the thermocline would cool, and immediately below the thermocline it would warm. Garrett (1990), Woods (1991) and Salmun *et al.* (1991) showed that in order for this flow to achieve a steady state, a convection is induced in the boundary layer which brings warm water down from near the surface to arrest the cooling above the thermocline, and cold water up from the bottom to arrest the warming just below the thermocline.

Imberger and Ivey (1993) derived the dynamics of this combined shear dispersion and convection mechanism. The induced flow along the boundary converges at the thermocline and thus vents into the interior of the lake, leading to an effective basin average vertical exchange coefficient K_B given by

$$K_B = 8.3 \times 10^{-6} \frac{h^9 \cos^2\theta \sin^3\theta}{\varepsilon^3 \ell} \left(\frac{g}{\rho_0} \frac{d\Lambda}{dZ}\right)^2 , \qquad (5.3.1)$$

where h is the benthic boundary layer thickness, θ is the bottom slope angle, A is the density of the water column, Z is the vertical distance, ε is the dissipation of turbulent kinetic energy in the boundary layer and ℓ is the lake hydraulic radius (A/P) where A is the area of the lake at height Z and P is the associated perimeter. Equation (5.3.1) appears to lead to reasonable estimates of the bulk vertical transport and boundary layer thickness.

In large lakes or the ocean where the earth's rotation becomes important, MacCready and Rhines (1993) (see also the discussion in Garrett *et al.* (1993)) have shown that an Ekman suction may be superimposed on the above flow which may act to oppose the gravitation transport, so leading to a zero flux boundary condition.

6. FUTURE DIRECTIONS

6.1 Field Work

Over the last 10 years our ability to measure physical parameters over the whole range of scales (10^{-3} m to 10^{5} m) has increased dramatically. It will soon become possible to mount new experiments which quantitatively map processes occurring in a lake. Examples of such, much needed, experiments are,

(a) The quantification of the energy and mass flux paths throughout the whole lake.
(b) Sources of energy for the benthic boundary layer and factors which determine its thickness.
(c) Verification of the mass flux in the benthic boundary layer.
(d) Energy cascade from internal waves to turbulent patches.
(e) Leakage of internal wave energy from the base of the surface layer.
(f) Formation of solitary waves due to seiches encountering a changing topography.
(g) Formation of gyres due to topographic constraints.
(h) Entrainment into gravity and turbidity currents.
(i) Horizontal dispersion in the hypolimnion.

(j) Dynamics of Langmuir circulation.

(k) Mass flux in the benthic boundary layer and the venting in the thermocline; impact on the iron, manganese, nutrient and carbon cycles.

(l) Influence of the mixing in the subsurface layer on the nutrient supply to the surface layer.

(m) Cycling of plankton by coherent motions in the surface layer and its influence on the population selection of the plankton.

(n) The importance of gyres in the transportation of carbon and nutrients from side arms to the main body of the lake.

(o) Importance of shear stress on the growth of plankton and other particles in the surface layer.

(p) The role of the intermittent turbulence in the interior of a lake on the flocculation of particles.

6.2 Laboratory and Numerical Experiments

The introduction of particle image velocimetry (PIV), laser induced fluorescence (LIV) and miniature sensors for temperature, conductivity and velocity measurements mark a quantum jump in our ability to study fundamental fluid mechanical processes in the laboratory. This should see a renaissance for the hydraulic engineer, but the signs are otherwise; most groups have abandoned their laboratories at the encouragement of funding agencies who see the world's solutions in closure schemes and the computer screen. Without doubt this mistake must be rectified over the next few years. Further, simulations using the full Navier Stokes equations (example Lin *et al.* (1994) and Javam *et al.* (1994)) are now at the point where they can effectively complement the laboratory.

The following are examples of where such a joint approach of numerical and experimental may be expected to lead to major advances in the very near future,

(a) Internal wave-wave interaction.
(b) Critical layer absorption
(c) Breaking of internal solitary waves
(d) Breaking of internal waves on the sloping bottom.
(e) Turbulence induced by internal waves reflecting from a sloping bottom.
(f) Entrainment into gravity and turbidity currents.
(g) Quantification of horizontal transport due to the formation of gyres.
(h) Energy cascade in an internal wave spectra and transfer from basin scale seiching to internal waves.
(i) Energy leakage from the base of the surface layer.
(j) Quantification of coherent motions in the surface layer.

6.3 Numerical Modelling

The need to introduce model equations is clearly necessitated by the very large scale range in lakes; a 0.2 m^3 the present full simulation capability (Holt *et al.* 1992) is a long way from a lake with volume of 10^8 m^3. It is unlikely that such volumes will be amenable to full solutions even with massively parallel computers. We may expect, therefore, continued strong development of models which capture the major processes active in a lake, yet run fast enough that meaningful simulations can be completed.

The major need appears to be how to account for the energy store in the internal wave field and then how to dissipate this energy so as to properly apportion a certain amount to increasing the potential energy of the water column. The following is a concept of how this may be achieved. First, the basin scale motions should be computed with a model such as described by Casulli and Cattani (1994). Such models can now deal relatively comfortably with 2×10^6 grid points when run on a fast workstation. For a lake with dimensions 6 km × 1 km × 30 m this means a resolution of close to 12 m × 12 m × 0.05, fine enough to resolve all basin scale motions together with intrusions and the bulk of the internal wave spectra. Present development has as one of its objectives to verify the hydrostatic pressure assumption of each grid point and correct the pressure for the influence of the vertical acceleration when necessary.

Second, at each grid point of the first model the directional internal waves spectra is stored. At each time step the energy in the internal waves is propagated, reflected, modified due to wave-wave interaction and decreased due to dissipation as appropriate. Such algorithms need to be developed but in principle are already clear from the vast literature on internal waves. The net result would be an updating of the internal wave spectra at each grid point and at each time step. Third, and this is still the area of greatest unclarity, the energy available from the internal

wave energy cascade must be added to that available from the mean shear and this is used, as discussed in 4.3, to calculate the buoyancy flux and the Reynolds stress. It may be expected that when complete such models will yield detailed descriptions of the transport in the lake and so form a suitable base for water quality process models.

ACKNOWLEDGEMENT

Lorraine Dorn typed the document and compiled the reference list and Jennifer Angelatos created the figures. This work was supported by the Centre for Environmental Fluid Dynamics.

Armi L, Some evidence for boundary mixing in the deep ocean, J Geophys Res 1978; 83: 1971-1977.

Boyd JP, New directions in solitons and nonlinear periodic waves, In: JW Hutchinson and TY Wu (Eds), *Advances in Applied Mechanics*, Academic Press Cambridge 1989; 27: 2-76.

Casulli V, Cattani E, Stability, accuracy and efficiency of a semi-implicit method for three-dimensional shallow water flow, to appear in Computers & Mathematics with Applications 1994.

Chu CK, Chou RL, Solitons induced by boundary conditions In: JW Hutchinson and TY Wu (Eds), Advances in Applied Mechanics, Academic Press Cambridge 1989, 27: 283-302.

Cox SM, Leibovich S, Langmuir circulations in a surface layer bounded by a strong thermocline, J Phys Oceanogr 1993; 23: 1330-1345.

De Silva IPD, Fernando HJS, Some aspects of mixing in a stratified turbulent patch, J Fluid Mech 1992; 240: 601-625.

Eriksen CC, Implications of ocean bottom reflection for internal wave spectra and mixing, J Phys Oceanogr 1985; 15: 1145-1156.

Fernando HJS, Turbulent mixing in stratified fluids, Ann Rev Fluid Mech 1991; 23: 455-493.

Frenzen P, Vogel CA, The turbulent kinetic energy budget in the atmospheric surface layer: A review and an experimental reexamination in the field, Boundary-Layer Meterol 1992; 60: 49-76.

Fukushima Y, Watanabe M, Numerical simulation of density underflow by the k-e turbulence model, J Hydrosci Hydr Engng 1990, 8(1): 31-40.

Gan J, Ingram RG, Internal hydraulics solitons and associated mixing in a stratified sound, J Geophys Res 1992; 97: 9669-9688.

Gargett AE, Ocean turbulence, Ann Rev Fluid Mech 1989; 21: 419-451.

Garratt JR, The internal boundary layer – A review, Boundary-Layer Meterol 1990; 50: 171-203.

Garrett C, How effective is boundary mixing? J Geophys Res 1990; 95: 3181-3188.

Garrett C, Marginal mixing theories, Atmosphere-Ocean 1991; 29(2): 313-339.

Garrett C, Gilbert D, Estimates of vertical mixing by internal waves reflected off a sloping bottom, In: JCJ Nihoul and BM Jamart (Eds) Small-scale Turbulence and Mixing in the Ocean, Elsevier 1988; 405-424.

Garrett C, MacCready P, Rhines P, Boundary mixing and arrested Ekman layers: rotating stratified flow near a sloping boundary, Ann Rev Fluid Mech 1993; 25: 291-323.

Garrett C, Munk W, Internal waves in the ocean, Ann Rev Fluid Mech 1979; 11 339-369.

Gibson CH, Internal waves, fossil turbulence, and composite ocean microstructure spectra. J. Fluid Mech. 1986, 168: 89-117.

Gregg MC, Scaling turbulent dissipation in the thermocline, J Geophys Res 1989; 94: 9686-9698.

Gregg MC, Seim HE, Percival DB, Statistics of shear and turbulent dissipation profiles in random internal wave fields, J Phys Oceanogr 1993; 23(8): 1777-1799.

Holt SE, Koseff JR, Ferziger JH, A numerical study of the evolution and structure of homogeneous stably stratified sheared turbulence, J Fluid Mech 1992; 237: 499-539.
Hondzo M, Ellis CR, Stefan HG, Vertical diffusion in small stratified lakes: Data and error analysis, J Hydr Engng 1991; 117(10): 1352-1369.
Hürzeler BE, Ivey GN, Imberger J, Spreading model for a turbidity current with reversing buoyancy from a fixed volume release, Submitted J Aust Mar Freshw Res 1994(a).
Hürzler BE, Imberger J, Ivey GN, Dynamics of a turbidity current with reversing buoyancy, Submitted ASCE, Hydr Div 1994(b).
Hutter K, Salvade G, Spinedi C, Zamboni F, Bauerle E, Large scale water movements in lakes, *Aquat Sci* 1991; 53: 100-135.
Imberger J, The diurnal mixed layer, Limnol Oceanogr 1985; 30: 737-770.
Imberger J, Physical Limnology: An Update, to appear In: R. Margalef (Ed) "*Limnology Now, A Paradigm of Planetary Problems*", Elsevier Science Publishers, 1994.
Imberger J, Ivey GN, Boundary mixing in stratified reservoirs, J Fluid Mech 1993; 248: 477-491.
Imberger J, Ivey GN, On the nature of turbulence in a stratified fluid, Part 2: Application to lakes, J Phys Oceanogr 1991: 21: 659-680.
Imberger J, Patterson JC, Physical limnology, In: Advances in Applied Mechanics, JW Hutchinson and TY Wu (Eds) Academic Press Cambridge 1989; 27:303-475.
Imberger J, Patterson J, Hebbert B, Loh I, Dynamics of reservoirs of medium size. J Hydraul Div, ASCE 1978, 104: 725-743.
Imberger J, Thompson RORY, Fandry C, Selective withdrawal from a finite rectangular tank, J Fluid Mech 1976: 78 489-512.
Imboden DM, Mixing and transport in lakes: Mechanisms and ecological relevance, In: M.M. Tilzer and C. Serruya (Eds) Large Lakes, Ecological Structure and Function, 47-80, 1990
Imboden DM, Wüest A, Mixing mechanics in lakes, to appear in A Lerman (Ed) Lakes, Springer New York (1994).
Ivey GN, Boyce FM, Entrainment by bottom currents in Lake Erie, Limnol Oceanogr 1982; 27(6): 1029-1038.
Ivey GN, Imberger J. On the nature of turbulence in a stratified fluid. Part I: The energetics of mixing, J Phys Oceanogr, 1991, 21, 650-658.
Ivey GN, Koseff JR, Imberger J. Mixing in a stratified shear flow, submitted to J Phys Oceanogr 1994.
Ivey GN, Maxworthy T, Mixing driven by internal Kelvin waves in large lakes and the coastal ocean, Proc 11th Australasian Fluid Mechanics Conference, Hobart, Tasmania 1992; 1: 303-306
Ivey GN, Nokes RI, Vertical mixing due to the breaking of critical internal waves on sloping boundaries, J Fluid Mech 1989; 204: 479-500.
Javam A, Armfield SW, Imberger J. Numerical study of internal wave-wave interaction. J. Fluid Mech, 1994 (to be submitted)
Kao TW, Pan F-S, Renouard D, Internal solitons on the pycnocline: generation propagation and shoaling and breaking over a slope, J Fluid Mech 1985; 159: 19-53.
Kim J, Mahrt L, Momentum transport by gravity waves, J Atmos Sci 1992; 49(9): 735-748.
Kudryavtsev VN, Soloviev AV, Slippery near-surface layer of the ocean arising due to daytime solar heating, J Phys Oceanogr 1990; 20(5): 617-628.
Langmuir I, Surface motion of water induced by wind, Science 1938; 87(2250): 119-123.
Leibovich S, On the evolution of the system of wind drift currents and Langmuir circulations in the, Part 1: Theory and averaged current, J Fluid Mech 1977; 79(4): 715-743.
Leibovich S, Radhakrishnan K, On the evolution of the system of wind drift currents and Langmuir circulations in the ocean, Part 2. Structure of the Langmuir vortices, J Fluid Mech 1977; 80(3): 481-507.
Lemckert CJ, Imberger J, Axisymmetric intrusive gravity currents in linearly stratified reservoirs, J Hydr Engng (ASCE) 1993, 119(6): 662-679
Lemckert CJ, Imberger J, Turbulence within inertia-buoyancy balanced axisymmetric intrusions, J Geophys Res 1994, (in press).

Lin C-L, Ferziger JH, Koseff JR, Monismith SG, Single triad resonant interactions in linearly stratified fluids, submitted to Journal of Fluid Mechanics, 1994.
Lombardo C, Gregg MC, Similarity scaling of viscous and thermal dissipation in a convecting surface boundary layer, J Geophys Res 1989: 94(C5) 6273-6284.
MacCready, P, Rhines PB, Slippery bottom boundary layers on a slope, J Phys Oceanogr 1993; 23: 5-22.
MacIntyre S, Wanninkhof R, Chanton JP, Trace gas exchange across the air-water interface in freshwater and coastal marine environments. Chapter 3 in PA Matson and RC Harriss (Eds) Methods in Ecology: Biogenic Trace Gas Emissions from Soil and Water, Blackwell Scientific, (in press) 1994.
Mellor GL, Yamada T, Development of a turbulence closure model for geophysical fluid problems, Rev Geophys and Space Phys 1982; 20: 851-875.
Monismith SG, Imberger J, & Morison ML, Convective motions in the sidearm of a small reservoir, Limnol Oceanogr 1990, 35(8): 1676-1702. ?????1986
Müller P and Henderson D (Eds) (1989) Parameterization of Small-Scale Processes, Proc 'Aha Huliko'a Hawaiian Winter Workshop University of Hawaii at Manoa.
Müller P and Henderson D (Eds) (1991) Dynamics of Oceanic Internal Gravity Waves Proc. 'Aha Huliko'a Hawaiian Winter Workshop University of Hawaii at Manoa.
Müller P and Henderson D (Eds) (1993) Statistical Methods in Physical Oceanography, Proc 'Aha Huliko'a Hawaiian Winter Workshop University of Hawaii at Manoa.
Munk WH, Abyssal Recipes, Deep Sea Res 1966; 13: 707-730.
Odd NVM, Rodger JG, Vertical mixing in stratified tidal flows, J Hydr Div 1978; 104: 337-351.
Okuda S., Imberger J, Kumagai M. (Eds) *Physical Processes of Lake Biwa*:. Coastal and Estuarine Studies (1994, in press).
Osborn T, Farmer DM, Vagle S, Thorpe SA, Cure M, Measurements of bubble plumes and turbulence from a submarine, Atmosphere-Ocean 1992; 30(3): 419-440.
Ottino JM, Mixing, chaotic advection, and turbulence, Ann Rev Fluid Mech 1990; 22: 207-253.
Patterson JC, Modelling the effects of motion on primary production in the mixed layer of lakes, Aquat Sci 1991; 53: 218-238.
Phillips OM, On flows induced by diffusion in a stably, stratified fluid, Deep-Sea Res 1970; 17; 435-443.
Phillips OM, The Dynamics of the Upper Ocean, Cambridge University Press 1977.
Salmun H, Killworth PD, Blundell JR, A two-dimensional model of boundary mixing, J Geophys Res 1991; 96(C10): 18447-18474.
Shay TJ, Gregg MC, Turbulence in an oceanic convective mixed layer, Nature 1984; 310 : 282-285.
Simpson JH, Sharples J, Dynamically-active models in the prediction of estuarine stratification, In: D Prandle (Ed) Dynamics and exchanges in Estuaries and the Coastal Zone 1991: 101-113 Springer-Verlag New York.
Smith JA, Observed growth of Langmuir circulation, J Geophys Res 1992; 97(C4): 5651-5664.
Soloviev AV, Coherent structures at the ocean surface in convectively unstable conditions, Nature 1990; 346: 157-160.
Soloviev AV, Vershinsky NV, Bezverchnii VA, Small-scale turbulence measurements in the thin surface layer of the ocean, Deep-Sea Res 1988; 35(12: 1859-1874l.
Spigel RH, Imberger J, Rayner KN, Modeling the diurnal mixed layer, Limnol Oceanogr 1986; 31(3): 533-556.
Stevens CL, Imberger J, Downward propagating internal waves generated at the base of the surface layer of a stratified fluid, Geophys Res Letters 1994 (in press).
Stronach JA, Backhaus JO, Murty TS, An update on the numerical simulation of oceanographic processes in the waters between Vancouver Island and the mainland: The GF8 Model. Oceanogr Mar Biol Annu Rev 1993, 31: 1-86.
Tennekes H, Lumley JL, A First Course in Turbulence, Massachusetts Institute of Technology Press, 1972 , pp 300.

Table 4.3.1

Regime	$R_{\rho w}$	R_f	b	K_ρ
$Fr_T > 1$	0.3	$\frac{1}{1 + 3.3\,Fr_T^2}$	$0.3\varepsilon^{1/3} L_c^{4/3} N^2$	$0.3\varepsilon^{1/3} L_c^{4/3}$
$Fr_T < 1$ $10 < \varepsilon/\upsilon N^2 < 100$	$0.0012\left(\frac{\varepsilon}{\upsilon N^2}\right)^{1.2}$	$\frac{1}{1 + 800\,(\varepsilon/\upsilon N^2)^{-1.2}}$	$0.0012\,\frac{\varepsilon^{2.2}}{(\upsilon N^2)^{1.2}}$	$0.0012\,\frac{\varepsilon^{2.2}}{\upsilon^{1.2} N^{4.4}}$
$Fr_T < 1$ $\varepsilon/\upsilon N^2 > 100$	0.3	0.25	0.3ε	$0.3\left(\frac{\varepsilon}{N^2}\right)$

Summary of suggested parameterization for the properties of a turbulent shear flow for different flow regimes and $Pr > 1$. (After Ivey, Koseff and Imberger 1994).

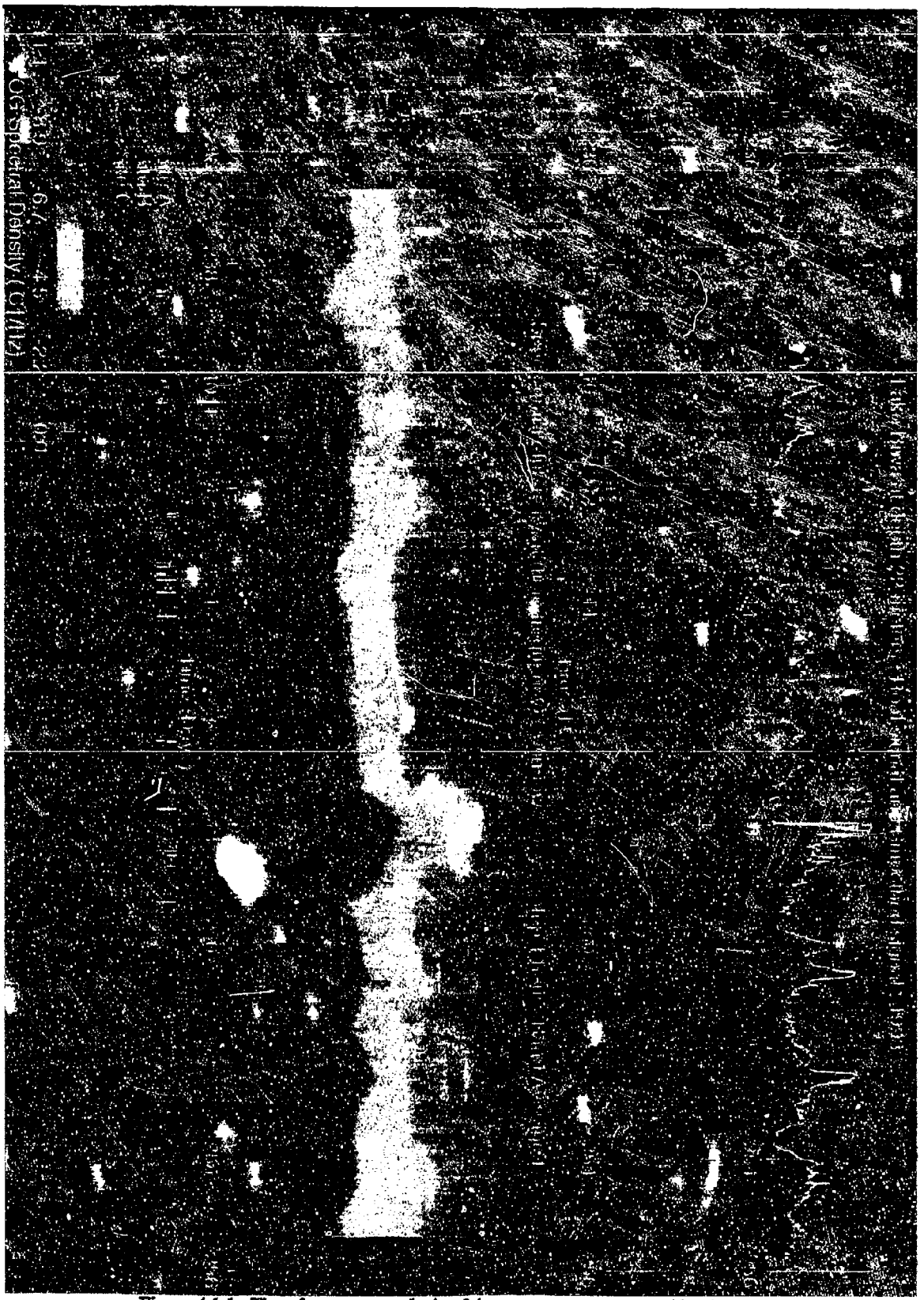


Figure 4.1.1. Time frequency analysis of the temperature measured by the thermistor located at 22 meters. (a) Raw temperature, (b) Low pass temperature, (c) Spectrogram.

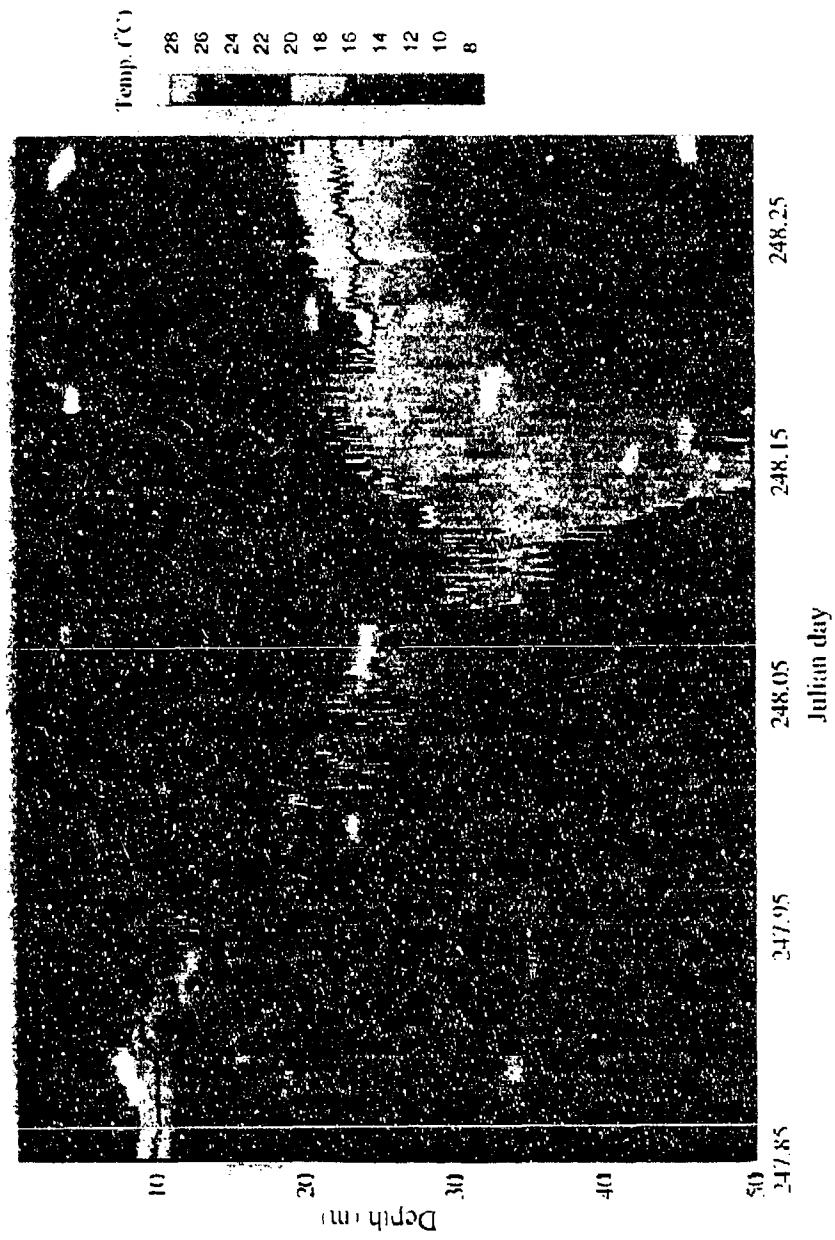


Figure 4.1.2. Isotherms for the period immediately after the typhoon passed over Lake Biwa. Clearly shown are hydraulic jumps, undular bores, mode one and two oscillations and the presence of high frequency waves.

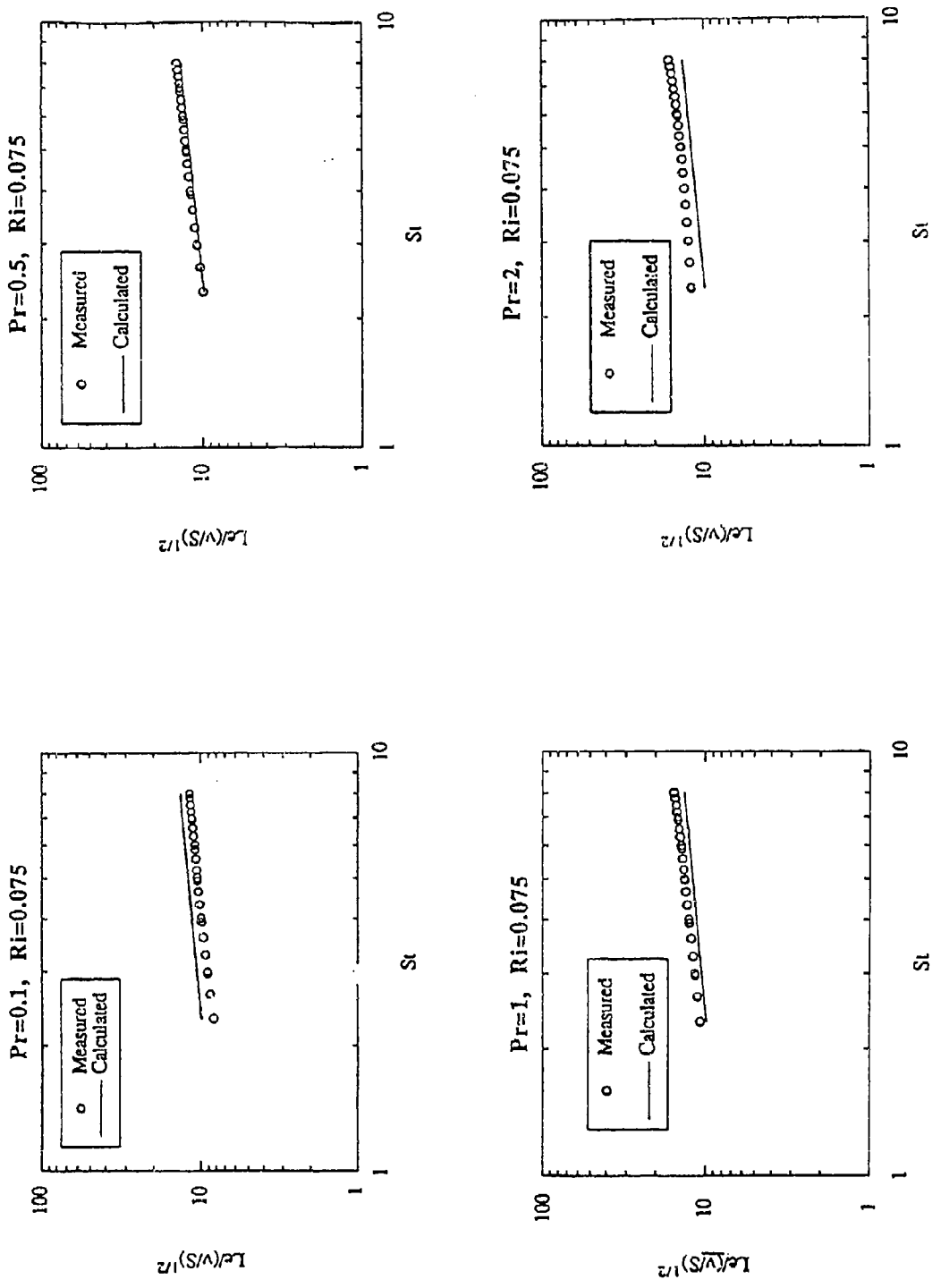


Figure 4.2.1. Non dimensionalised length scale versus non-dimensional time for different Richardson and Prandtl numbers. Round open ended circles are the numerical data, full line represents the empirical fit as discussed in the text (after Ivey et al. 1994).

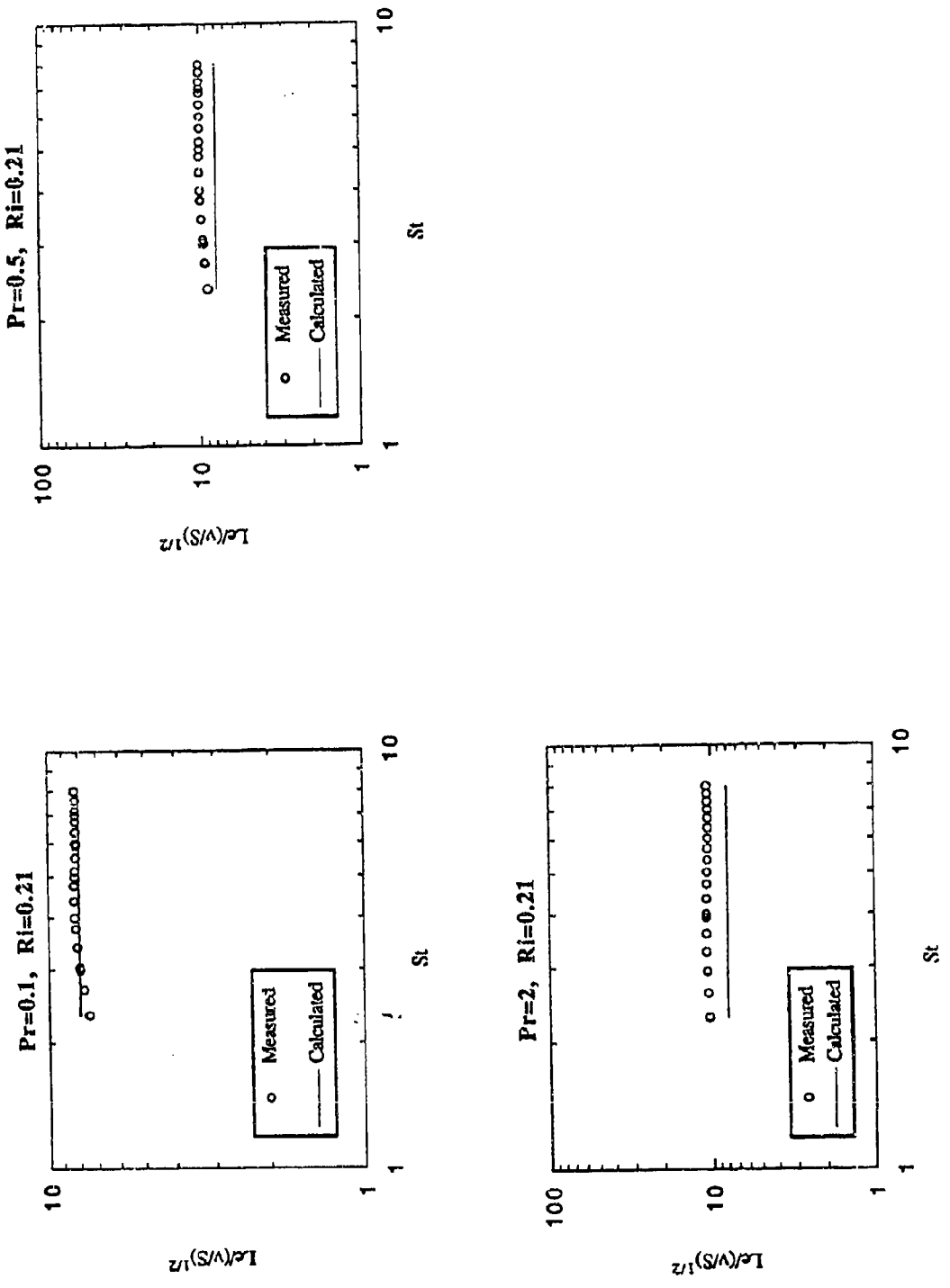
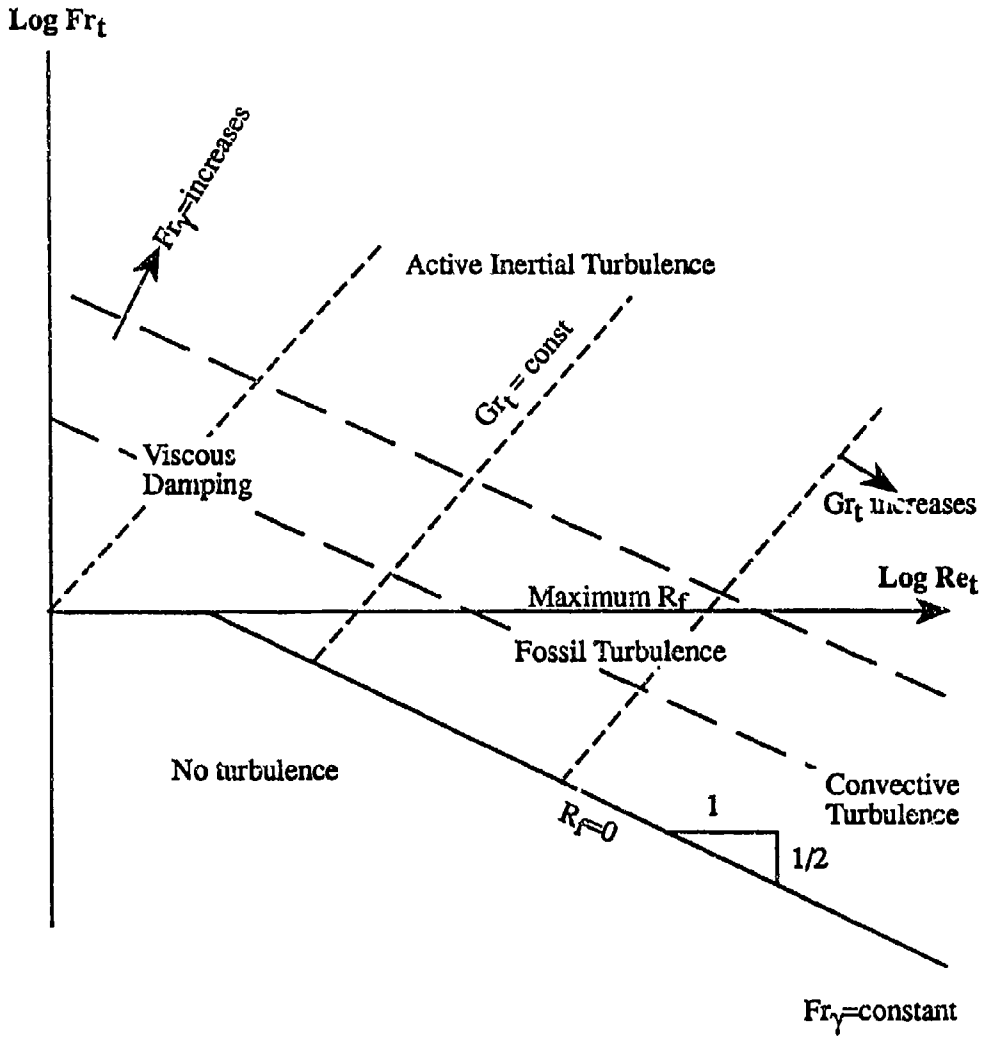


Figure 4.2.1. continued

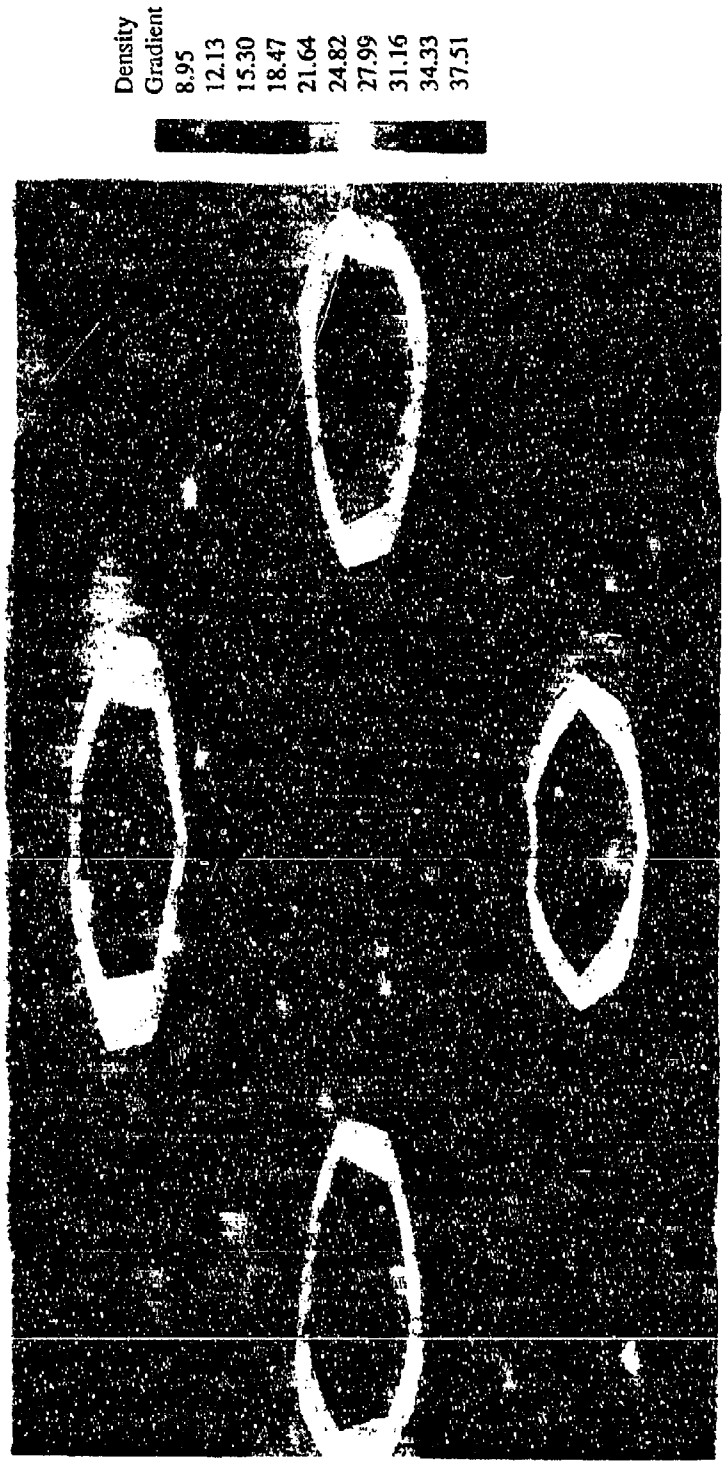


4.3.1. Activity diagram showing the relationship between Frt, Ret, Grt and Frg.



(a)

Figure 4.3.2. The density field for two intersecting internal waves generated locally in a stratified fluid. (a) Isopycnal from numerical simulation (Javam et al.). Parameters are: frequency w = 0.4 rad/s, buoyancy frequency N = 1 rad/s, flow Reynolds number = 1.4 x 104; Froude number = 0.8 and Richardson number = 6.25. (b) Density gradient image from numerical simulation. (c) Rainbow Schlieren image obtained from laboratory (Teoh et al.)



(b)

Figure 4.3.2. continued



(c)

Figure 4.3.2. continued

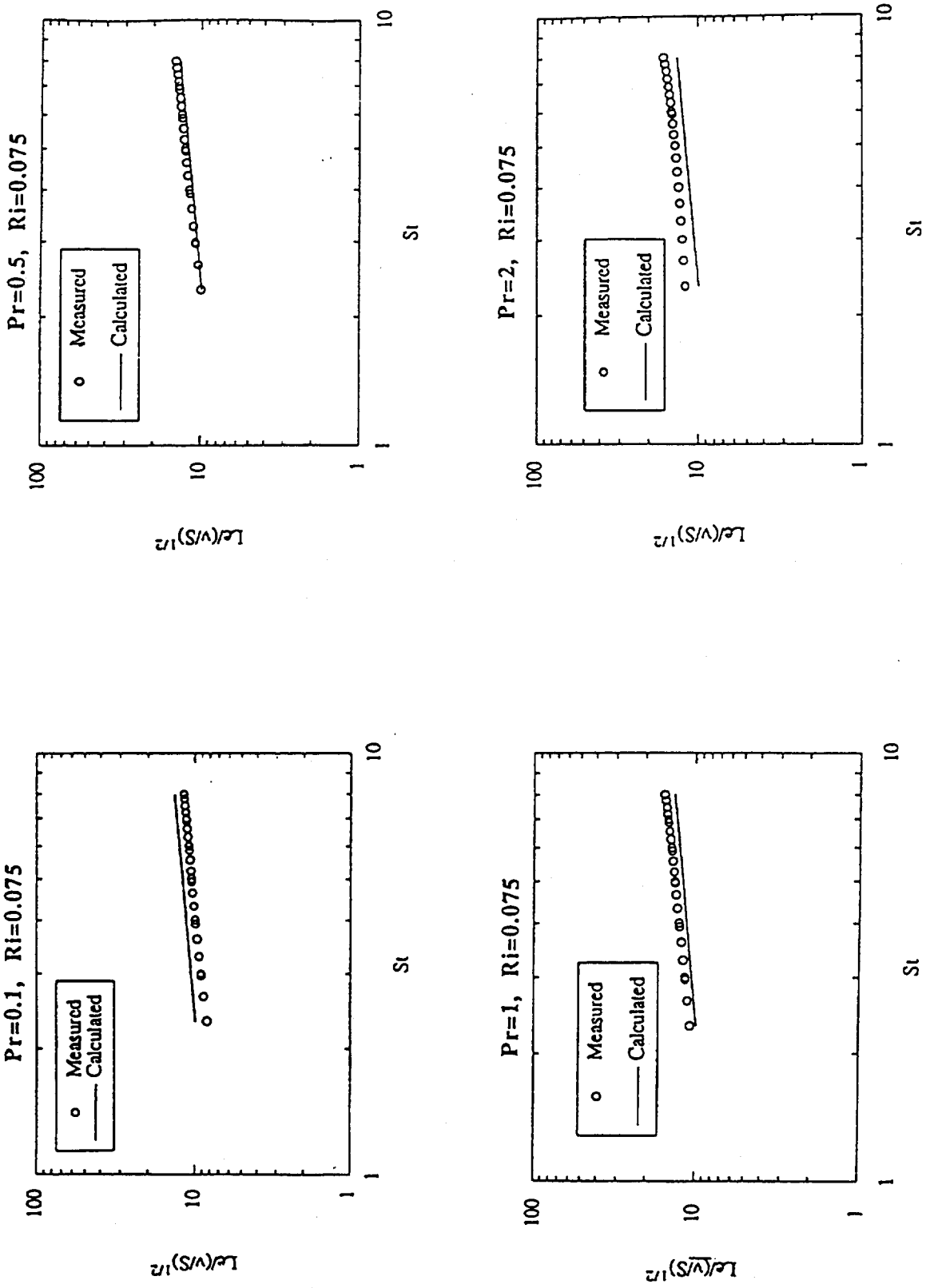


Figure 4.2.1. Non dimensionalised length scale versus non-dimensional time for different Richardson and Prandtl numbers. Round open ended circles are the numerical data, full line represents the empirical fit as discussed in the text (after Ivey et al. 1994).

Laboratory Measurements of Gravity Wave, Critical Layer Interactions

Donald P. Delisi and Timothy J. Dunkerton
Northwest Research Associates, P O Box 3027, Bellevue WA 98009-3027

ABSTRACT

Laboratory measurements of gravity wave, critical layer interactions are presented. The measurements were obtained in an annular, salt-stratified water tank. A vertical shear is added by rotating a lid on the water surface. Internal gravity waves are generated by moving the bottom floor of the tank vertically. The gravity waves propagate up into the tank and interact with their critical level, the level where the wave phase speed equals the mean flow speed. Measurements are presented for two categories of bottom-wave forcing: experiments with a single, monochromatic bottom wave and experiments with two monochromatic bottom waves.

INTRODUCTION

Gravity waves occur naturally in the ocean and the atmosphere. They are important in transporting momentum and for generating turbulence, thereby producing mixing. One mechanism for the breakdown of a gravity wave into turbulence occurs when the wave approaches its critical level, which is defined as the level where the horizontal phase speed of the wave equals the mean flow speed (Booker and Bretherton, 1967). When this occurs, the wave's vertical propagation is modified, wave energy is transferred to the mean flow, and turbulence can be generated.

Most of our present understanding of gravity wave, critical level interactions has come from theoretical and numerical studies (see e.g., Bretherton, 1966; Lindzen, 1981; Fritts, 1984; Maslowe, 1986; and Dunkerton and Robins, 1992, to name a few). In addition, there have been attempts at observational studies of this phenomenon (e.g., Merrill and Grant, 1979).

In the laboratory, studies of gravity wave, critical level interactions under controlled conditions have been reported by Bretherton et al., 1967; Thorpe, 1973; Koop, 1981; Koop and McGee, 1986; and Delisi and Dunkerton, 1989. In these experiments, the reported results have typically been qualitative in nature, and most experiments were limited by the physical dimensions of the test facility, which limited the duration of the interactions.

THE EXPERIMENTAL FACILITY

The experimental facility used in these experiments is described in detail in Delisi and Dunkerton (1989). Our facility is a modification of a laboratory wave tank developed by Plumb and McEwan (1978). A schematic of the facility is given in Figure 1. The tank is annular, with an outer diameter of 1.8 m, an inner diameter of 1.2 m, and a depth of 40 cm.

The bottom floor of the tank is moved vertically by 32 stepper motors. Each stepper motor drives a vertical piston which moves acrylic plates on the bottom floor of the tank. A

rubber sheet on top of the acrylic plates acts as a water seal and as a flexible membrane for the floor. A computer controls the stepper motors, thus driving each section in a prescribed way. In this manner, we can specify the motion of the bottom floor as one or more waves which propagate around the bottom of the tank with known amplitudes, wavelengths, and phase speeds. In these experiments, the computer controlled the floor to move as either a single, monochromatic wave or as two monochromatic waves, with different phase speeds. Wavenumber two was used in all the experiments.

To perform an experiment, we fill the tank with a known stratified salt water profile, rotate a floating lid on the water surface to create a vertical shear profile, then propagate one or two waves on the bottom floor of the tank by moving the floor vertically with the stepper motors. Flow measurements include density data from an oscillating conductivity probe, mean and instantaneous velocity profiles from streak photographs of neutrally buoyant particles, 35-mm and video pictures of shadowgraph flow visualization which show the turbulent regions, and, in some cases, instantaneous velocities using Digital Particle Imaging Velocimetry (Willert and Gharib, 1991).

Typical initial velocity and density profiles are shown in Figure 2. The velocity profile shows a nearly constant velocity at the top, where the lid has mixed the fluid, and a nearly exponential velocity profile beneath the mixed region. The initial density profile shows two, linearly stratified density layers. To minimize the depth of the mixed layer generated by the rotating lid, we placed a high-N region at the top of the tank, next to the rotating lid. The Brunt-Vaisala frequency, N, for this layer is 1.62 sec^{-1}, where $N = (g/\rho\, d\rho/dz)^{1/2}$, g is the acceleration due to gravity, ρ is density, and z is the vertical coordinate. N for the bottom layer is 1.02 sec^{-1}.

RESULTS

One Wave Results

Several, different experimental configurations were investigated using single wave forcing. In the experiments reported here, we propagated a single wave on the bottom with a peak-to-peak amplitude of 4.0 cm and a phase speed of 4.5 cm/sec. The movement of the bottom floor was not exactly sinusoidal, but was asymmetric to match the propagating wavefronts in a nonsheared, linearly stratified fluid. This asymmetry in the forcing function mimicked the generated gravity wave and, therefore, reduced the higher harmonics that would be generated by using a sinusoidal wave.

The velocity profiles for these runs were obtained by digitizing instantaneous streak photographs. An important experimental question was to determine how repeatable conditions remained from run to run when the experimental conditions were nominally the same. Figure 3 shows velocity profiles from two nominally identical runs at the same time during each run. To within the experimental accuracy, the agreement is quite good, indicating that the data are reproducible from run to run.

Videotapes and 35 mm photographs of shadowgraph visualization clearly show regions of overturning and turbulence as a function of time. An example of a 35 mm photograph is shown in Figure 4. This photograph shows a side view of the tank, with the bottom of the mixed layer at the top of the photo and an overturning region about mid-way down in the tank. A clock is shown at the bottom, and the oscillating conductivity probe is shown (with its

shadow) in the right-most part of the picture. The flow is from left to right. The overturnings shown in this photo have a wavelength of about 10.9 cm, and an amplitude of about 2.1 cm. With the videotapes, we see that these overturnings begin as small perturbations which grow with time, and then collapse. Richardson number estimates, obtained from the velocity and density measurements, along with the observed growth and decay, indicate that the instabilities are Kelvin-Helmholtz (K-H) in nature.

From the photograph in Figure 4 and the videotapes of the shadowgraph visualizations, we can determine the vertical extent of the breaking regions as a function of time. Figure 5 shows the observed regions of turbulence vs time after the start of the bottom floor along with contours of constant density from the conductivity probe for the first ten wave cycles of an experiment. (Note that time is increasing from right to left in Figure 5. This is consistent with the photograph in Figure 4 in which the flow is from left to right.) The overturning regions in Figure 5 first appear near the top of the tank and progress downward, toward the bottom floor, as time progresses. For $t > \sim 13$ min, most of the observed turbulence occurs in mixing regions in the bottom half of the tank (Delisi and Dunkerton, 1989), with only sporadic, patchy turbulence being observed in the top half of the tank. The mixing regions occur once every wave cycle.

The evolution of the mean velocity profile (Figure 6) shows that the initial velocity profile is modified by a velocity ledge which progresses downward with time, similar to the overturning regions (Figure 5). The mean flow modifications shown in Figure 6 are qualitatively similar to those predicted by numerical simulations (Dunkerton and Robins, 1992), although the overturning regions in those simulations are characterized as convective overturning rather than K-H. In our laboratory experiments, the initial K-H overturning is observed during the time the ledge is a feature in the mean flow; the mixing regions appear to occur when the velocity in the lower part of the tank is more nearly constant.

Two Wave Results

In these experiments, we forced the bottom with two waves, one with a phase speed of 4.5 cm/sec, and the second with a phase speed of. 3.5 cm/sec. Each wave had a peak-to-peak amplitude of 3.0 cm. With these choices, the bottom forcing has a beat period of 4 minutes.

The overturning regions for this case are shown in Figure 7. In this figure, time progresses from left to right, and only observed regions of turbulence are displayed. This figure shows that the regions of turbulence appear to bifurcate around $t \sim 13$ min, with regions of turbulence appearing in the top and the bottom regions of the tank. The shadowgraph visualizations show that, at early times ($t < \sim 13$ min), the breaking regions are K-H, as in the one-wave case. For the two-wave case, $t > \sim 13$ min, K-H overturning continues at a depth of around 17 cm while a mixing region, similar to that in the one-wave case, appears in the lower portion of the tank. The K-H regions in the upper part of the tank appear more or less periodically throughout the lifetime of the experiment. This is in contrast to the turbulent regions in the bottom of the tank, which appear in packets of three. The time interval between these packets is due to the beating of the two bottom waves.

The evolution of the mean flow for the two-wave case (not shown), averaged over one beat period, is similar to the one-wave case in that a velocity ledge progresses downward toward the floor during the time the initial K-H overturning is observed. Thereafter, the mean velocity is nearly constant with time.

ACKNOWLEDGEMENTS

The authors thank Lee E. Piper for his assistance in performing the experiments and Wilbur F. Pierce IV for assistance in analyzing the data. This study was supported by the Air Force Office of Scientific Research under contracts F49620-92-C-0005 and F49620-92-C-0033.

REFERENCES

BOOKER, J. R. and BRETHERTON, F. P. 1967 The critical layer for internal gravity waves in a shear flow. *J. Fluid Mech.* **27**, 513-539.

BRETHERTON, F. P. 1966 The propagation of internal gravity waves in a shear flow. *Q. J. R. Met. Soc* **92**, 446-480.

BRETHERTON, F. P., HAZEL, P., THORPE, S. A., and WOOD, I. R. 1967 Appendix to the paper by Hazel P, The effect of viscosity and heat conduction on internal gravity waves at a critical level. *J. Fluid Mech.* **30**, 775-783, (Appendix on pp. 781-783).

DELISI, D. P. and DUNKERTON, T. J. 1989 Laboratory observations of gravity wave critical-layer flows. *Pure and Appl. Geophys.* **130**, 445-461.

DUNKERTON, T. J. and ROBINS, R. E. 1992 Radiating and nonradiating modes of secondary instability in a gravity-wave critical layer. *J. Atmos. Sci.* **49**, 2546-2559.

FRITTS, D. C. 1984 Gravity wave saturation in the middle atmosphere: A review of theory and observations. *Rev. Geophys. and Space Phys.* **22**, 275-308.

KOOP, C. G. 1981 A preliminary investigation of the interaction of internal gravity waves with a steady shearing motion. *J. Fluid Mech.* **113**, 347-386.

KOOP, C. G. and MCGEE, B. 1986, Measurements of internal gravity waves in a continuously stratified shear flow. *J. Fluid Mech.* **172**, 453-480.

LINDZEN, R. S. 1981 Turbulence and stress due to gravity wave and tidal breakdown. *J. Geophys. Res.* **86C**, 9707-9714.

MASLOWE, S. A. 1986 Critical layers in shear flows. *Ann. Rev. Fluid Mech.* **18**, 405-432.

MERRILL, J. T. and GRANT, J. R. 1979 A gravity wave-critical level encounter observed in the atmosphere. *J. Geophys. Res.* **84**, 6315-6320.

PLUMB, R. A. and MCEWAN, A. D. (1978), The instability of a forced standing wave in a viscous stratified fluid: A laboratory analogue of the quasi-biennial oscillation. *J. Atmos. Sci.* **35**, 1827-1839.

THORPE, S. A. 1973 Turbulence in stably stratified fluids: A review of laboratory experiments. *Boundary-Layer Meteorol.* **5**, 95-119.

WILLERT, C. E. and GHARIB, M. 1991 Digital particle image velocimetry. *Exp. in Fluids* **10**, 181-193.

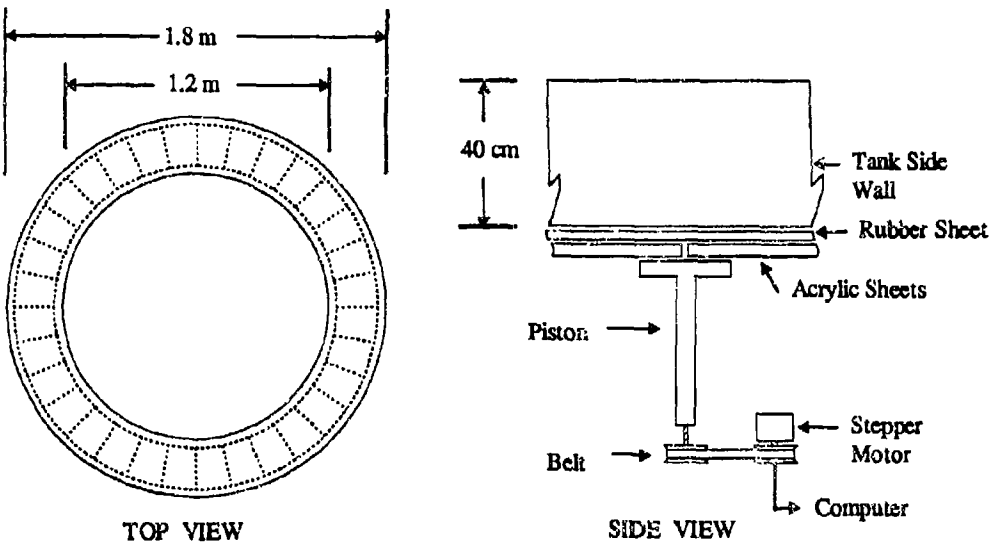


FIG 1. Schematic drawing of the experimental facility. The side view shows one of the 32 piston assemblies used to move the bottom floor.

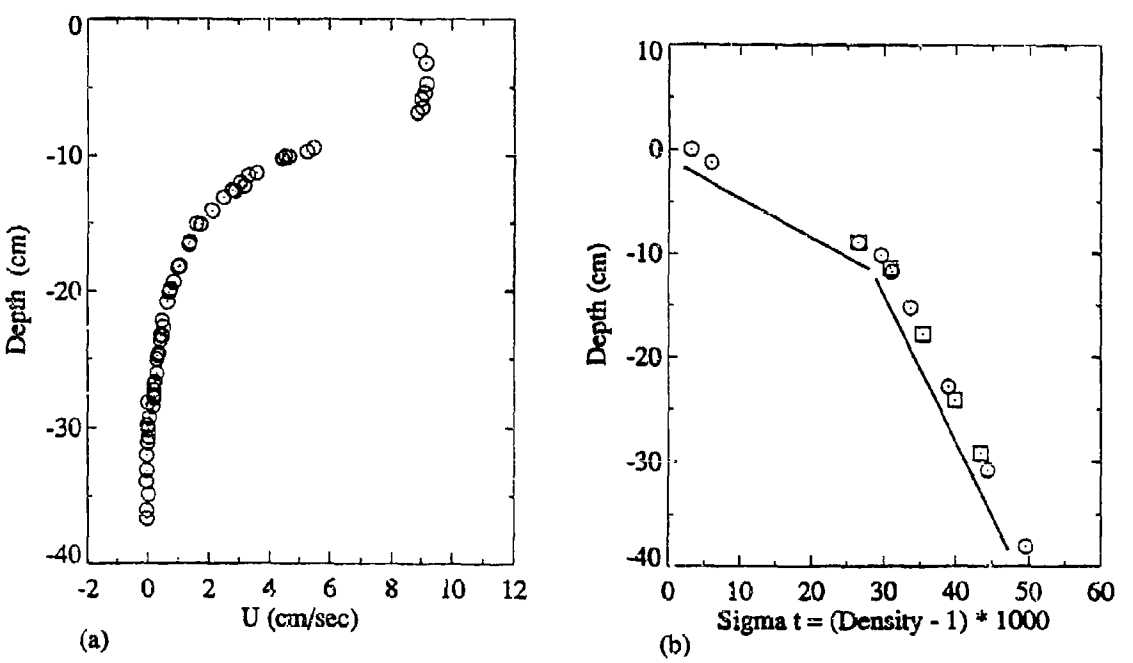


FIG 2. Typical initial (a) velocity and (b) density profiles before a two-wave experiment. In the density profile, circles are measurements taken during the filling of the tank; squares are probe samples taken after filling the tank; and straight lines are drawn for comparison to linearity.

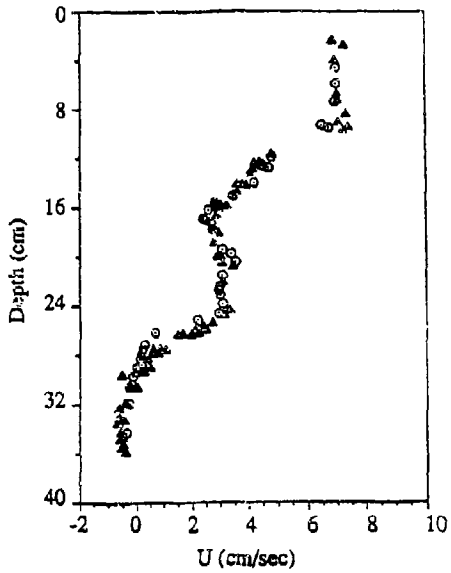


FIG 3. Two instantaneous, particle velocity profiles measured at 4 min, 55 sec after the start of the bottom floor in two different, but nominally identical, runs.

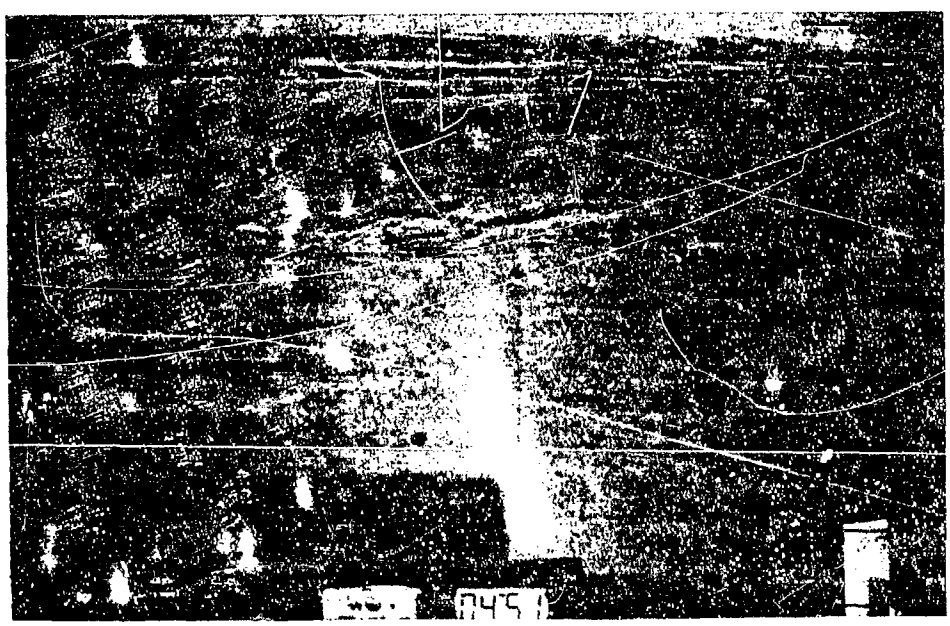


FIG 4. Shadowgraph visualization of Kelvin-Helmholtz overturning in a one-wave experiment.

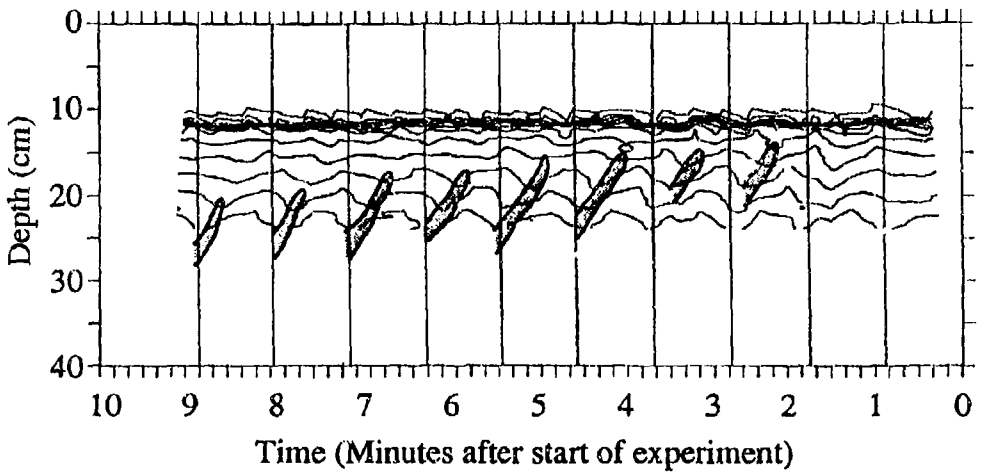


FIG 5. Contours of constant density and regions of observed wavebreaking (shaded) for a one-wave experiment. Vertical lines indicate times of the wave crest.

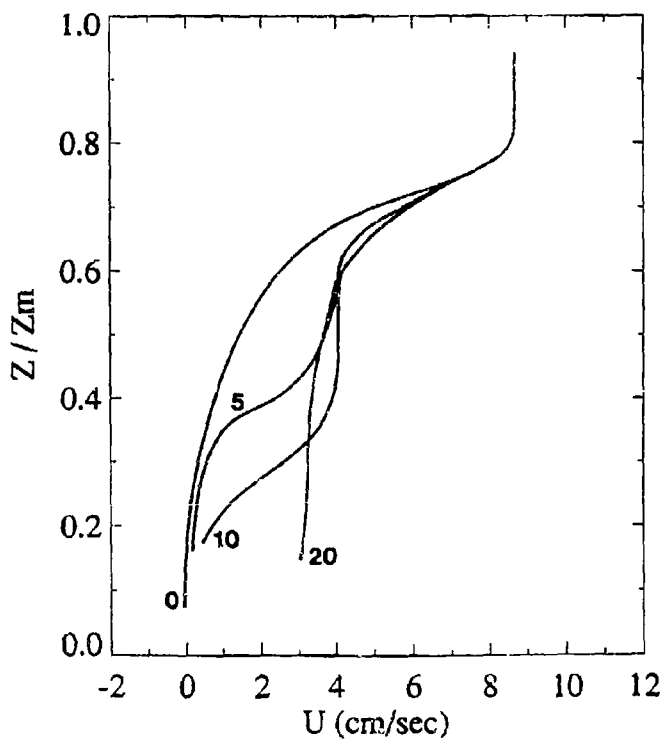


FIG 6. The evolution of the mean flow velocity profile for a one-wave experiment. The mean flow is the average over one wave cycle. Time is minutes after the start of the experiment.

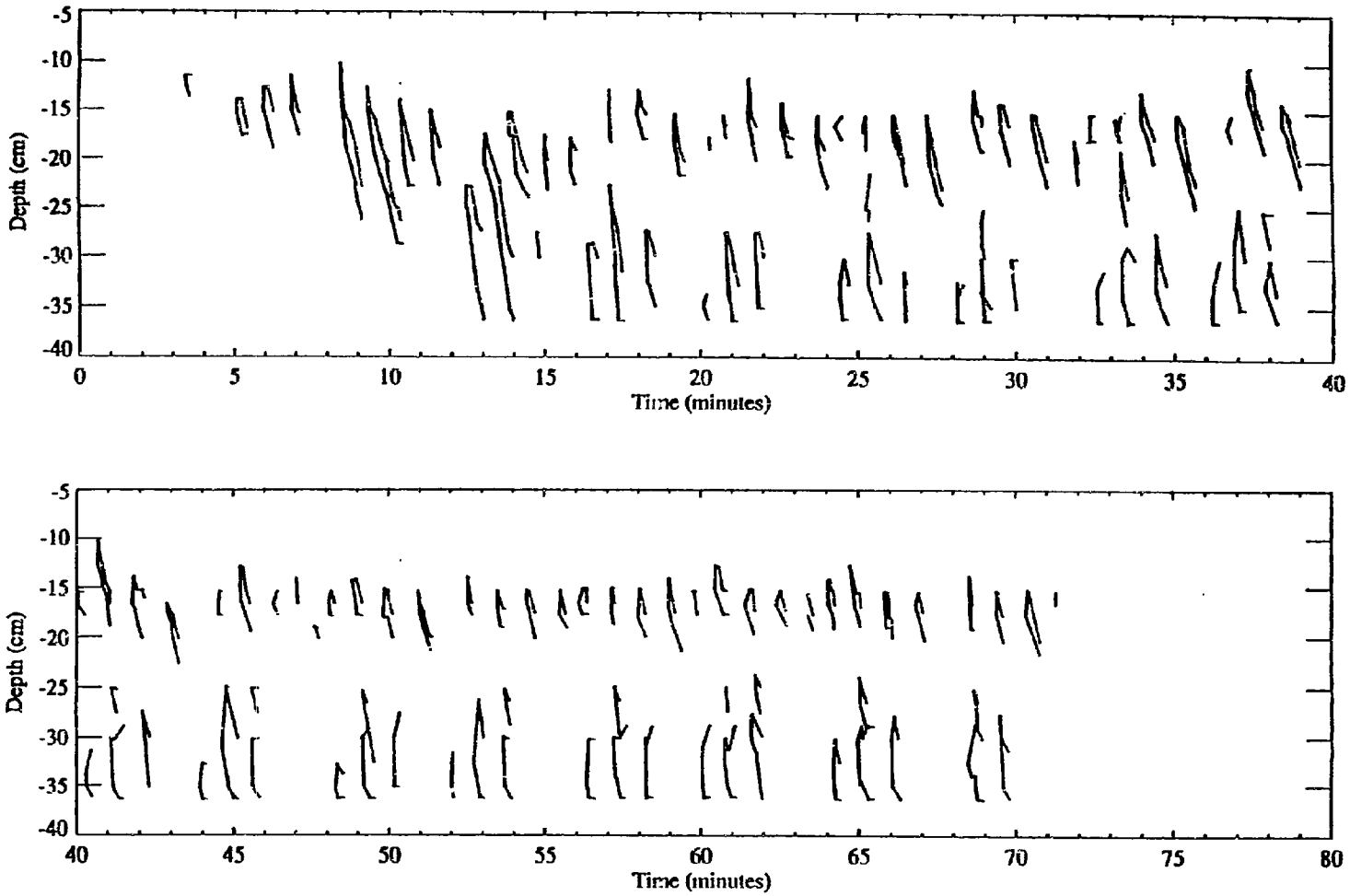


FIG 7. Observed regions of turbulence in a two-wave experiment. Time is minutes after the start of the experiment.

NONLINEAR INTERNAL WAVES IN OBSERVATIONS FROM SHELVES: MANIFESTATIONS OF SOLITON-LIKE BEHAVIOUR

A. N. SEREBRYANY

N.N.Andreev Acoustics Institute, Moscow 117036, Russia

1. Abstract

Wide spreading of nonlinear internal waves are shown on the base of long-term observations on the sea shelves of former Soviet Union. Measurements of intense internal waves by antennae of distributed temperature sensors on the Caspian Sea and the Sea of Japan are tested for revealing manifestations of soliton's features. The discrepancy between linear internal wave dispersion relationship of the first mode and measured wave parameters are shown to be caused by nonlinearity of observed waves. The observations revealed that wave propagation speed exceeds its value for linear waves and depends on amplitude. Examples of typical soliton manifestations such as waves on sharp step-like internal bore and wave-predecessors are presented.

2. Introduction

Stratified flows on a shelf result in appearance of solitary internal waves, brilliant phenomenon of geophysical hydrodynamics. Our 15-years experience of internal waves field observations on the sea shelves of former Soviet Union give grounds to say that solitary internal waves are a phenomenon which often occurs in the dynamic processes of oceanic margins. We carried out long-term observations during summer seasons on the shelves of the Caspian, Black and Barents Seas, the Sea of Japan and on the Pacific Coast of Kamchatka. As a result, a great amount of data on internal waves (including internal solitary waves) under different oceanographic conditions as well as in various geographical places, was collected. Everywhere, both in sea with strong tide, and in practically nontidal sea, we observed intense internal waves, pooled in trains, or solitary,regular or without any periodicity emerging in time and moving towards the shore. Three of the numerous examples of these waves records are shown on Fig. 1 and Fig. 2.

In many cases nonlinearity of observed intense waves is evident (for example due to characteristic non-sinusoidal shape of wave profiles), but it is interesting to know how close these observed waves are to solitons.

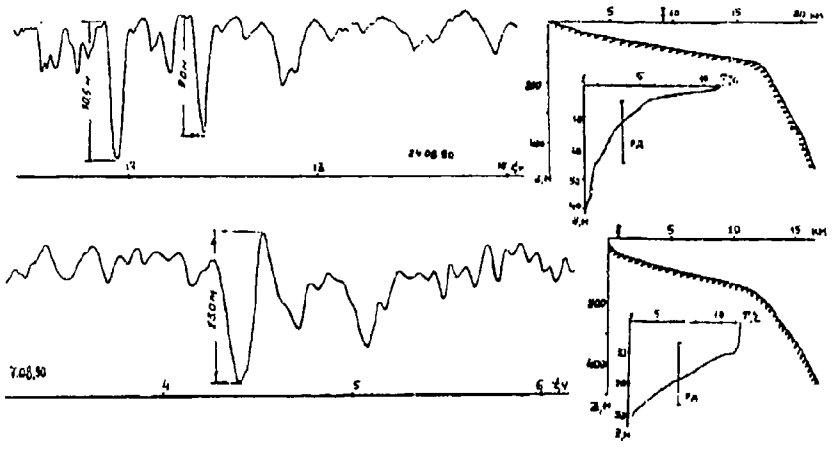


Figure 1: Internal waves trains observed on the shelf of the Pacific Coast of Kamchatka. In inlet temperature profiles and distributed sensor positions,as well as bottom relief of the places of observations are shown.

Solitons have some specific features which may be observe at the modern level of field experiment. These properties are the following: higher phase speed relative to linear wave, definite relationship between amplitudes of waves and their characteristic horizontal scale, the dependence of wave speed against amplitude, and others. At present are known some observations of large-amplitude internal waves in the ocean and on the shelves in which some soliton's features have been revealed [1-4].

In this paper we concentrate mainly on the results of internal waves measurements on shelves of The Caspian Sea and The Sea of Japan. In these experiments the data were obtained by means of antennae of space-delivered distributed sensors. The antenna consisting of 3-7 distributed sensors allows us to measure phase velocity and direction of propagation, as well as amplitude for each observed wave. This instrument gives us the possibility to obtain hard-to-reach in the field experiment data and to compare them with soliton's parameters.

3. Elevation of linear wave speed

In our previous measurements we often observed one interesting peculiarity. When comparing dispersive relationship of linear internal waves with that of frequency and wave vector observed experimentally we noted the tendency of experimental points to lay above the theoretical curve of the first mode. This feature indicates that phase speed for the observed waves is larger then speed of linear waves. We can suppose that two main causes are responsible for this effect. The first one is connected with the situation when internal waves are travelling with co-directional current and consequently the doppler effect takes place. Besides, it may be also the effect of shear current which will elevate the experimental points above the curve. The second reason of the observed elevation may be connected with the nonlinearity of the waves.

Let us consider the data on internal waves obtained in the coastal zone of the Sea of

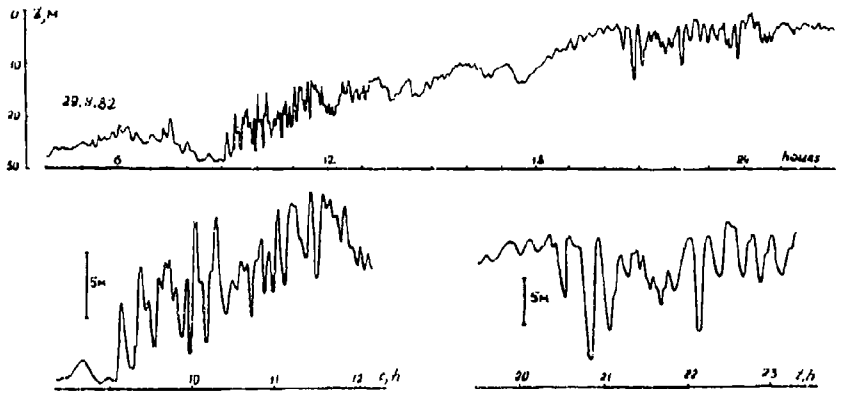


Figure 2: Two following on shore internal waves trains consisting of waves-elevations and depressions respectively and separated by a 12 hour interval. This effect turned out to be possible due to significant change of the mean thermocline position from the bottom to the subsurface layer.

Japan. Unfortunately we do not have data for the current. But it should be mentioned that the cross to shore current component in this place is never large while the internal waves travel nearly perpendicular to shore line. So, for the waves analyzed in our case we may assume the current factor to be small. This may help us to find the influence of nonlinearity factor on the discrepancy of observed data. Fig. 3 shows numerically calculated dispersive curve for linear internal waves of the first mode and also the experimental points. In our case each point corresponds to the mean value of parameters (period and length) for waves composing clearly seen trains of intense waves selected for the analysis. Let us discuss the measured parameters for the analyzed frequency of 3.75 circle/hour in more detail. In seven cases the points lay above the curve. The greater deviation to the left from the curve points to larger elevation of the observed speed above the linear one. This deviation which we connect with the possible nonlinearity could be tested if we found some way to evaluate the nonlinearity of the observed waves. As measure of nonlinearity we take the Ursell's parameter (parameter, characterizing relation between nonlinearity and dispersion in the wave). In terms of KdV equation the Ursell's parameter is calculated as $Ur = (\alpha/\beta)AL^2$, where α and β are the coefficients of nonlinearity and dispersion of the media, A is the height, and L is the characteristic horizontal wave scale. We can compare the calculated Ursell's parameters with velocities of observed waves on frequency 3.75 circle/hour (see inset of Fig. 3). Despite the limited data we can notice the following tendency: the larger the Ursell's parameter (i.e. the larger nonlinearity of the wave), the larger it's phase speed. So, our assumption that deviation of observed parameters of intense waves above dispersion curve of linear internal waves is to be connect with their nonlinearity is confirmed.

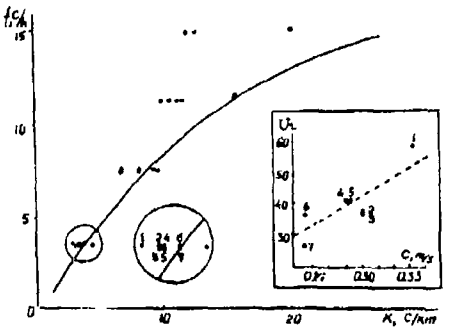


Figure 3: Dispersion curve of linear internal waves of the first mode and parameters of the observed waves (points). The points under detailed consideration are shown in circle. In right inlet relationship between Ursell's parameters and observed phase velocity are shown.

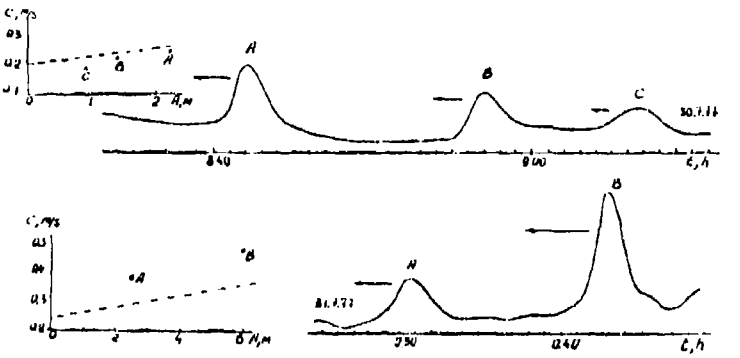


Figure 4: Manifestation of the speed-amplitude dependency in observed internal waves. (a)-Train of waves rank-ordered in heights and velocities. (b)-Larger wave B is catching up with leading low amplitude wave A. To the left experimental points and calculated dependency for KdV solitons are shown.

4. The wave speed-amplitude dependency

It is interesting to find out whether the dependence if any between the observed intense internal wave and the amplitude and phase speed is similar to that which takes place in case of solitons? Revealing the speed-amplitude dependence in field experiment is possible only for the waves which are travelling under identical background conditions. Due to this limitation one can compare only the waves which are close in time. As a rule they are waves pooled in trains. Fig. 1a shows a wave train on the shelf of the Caspian Sea moving above thermocline flanked on the bottom. The train consist of three waves rank-ordered in heights (from 2.2 m to 0.9 m). All the waves are moving in the same direction. The distance between the crests of the first two waves A and B is larger then the distance between crests of waves B and C. It is indirect evidence that the waves are moving with different speeds. The observed speeds are lowering with decreasing of heights from 0.23 m/s to 0.17 m/s (here and to follow for phase speed estimations the method

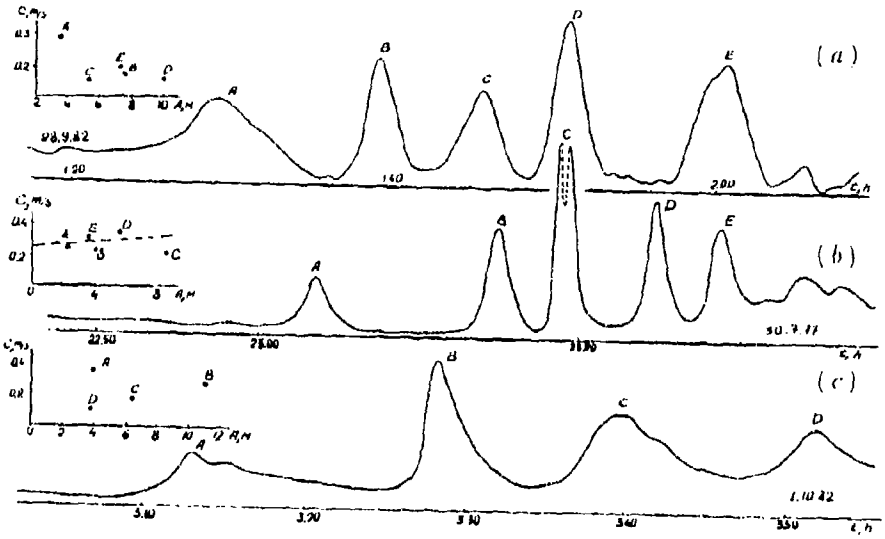


Figure 5: Trains and wave-predecessors: examples of measurements in the Sea of Japan (a,c) and in the Caspian Sea (b).

of phase triangles are used). The comparison is revealing a good qualitative agreement between linear law of speed-amplitude dependence for KdV solitons and the observed data, though real waves are moving with slower speeds. Fig. 4b shows another example where two solitary internal waves are moving on a sharp thermocline elevated above the bottom as compared with the previous occasion. Both waves are moving in the same direction too, but the higher wave is behind the leading smaller wave. The higher wave has larger speed (0.47 m/s against 0.37 m/s) and is catching up with the leading lower wave. This pair of solitary waves were recorded after a passage of internal bore when a strengthening of bottom current coincided with the direction of wave propagation. If we take into account the correction for co-directional current of 0.2 m/s, we obtain a good agreement with theory. So, for the examples considered we can see a clear manifestation of speed-amplitude dependency.

5. Wave-predecessors

There is a feature which is observed for internal wave trains moving on near bottom thermocline. It has been noticed that sometimes in front of a train is moving low amplitude solitary leading internal wave with relative high speed (comparing with other waves of the train). We will call this wave a wave-predecessor because, as a rule,it is the first wave emerging on a calm thermocline and some time later trains of intense waves or internal bores appear to follow it.

Fig. 5 shows the examples of the records of internal wave trains with wave-predecessors. In Fig. 5c we can see the train involving four waves in which all waves except the first one are rank-ordered in speed and height. The very high speed of the wave-predecessor differs greatly from that calculated for KdV solitons. Other examples of wave-predecessors are shown on Fig. 5a,b. Each recorded group consists of a predecessor and four waves

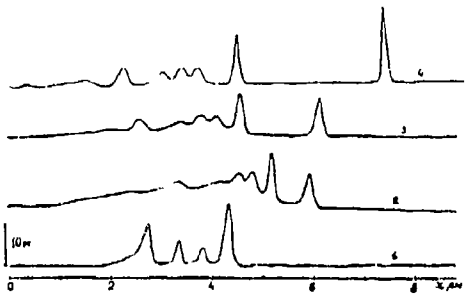


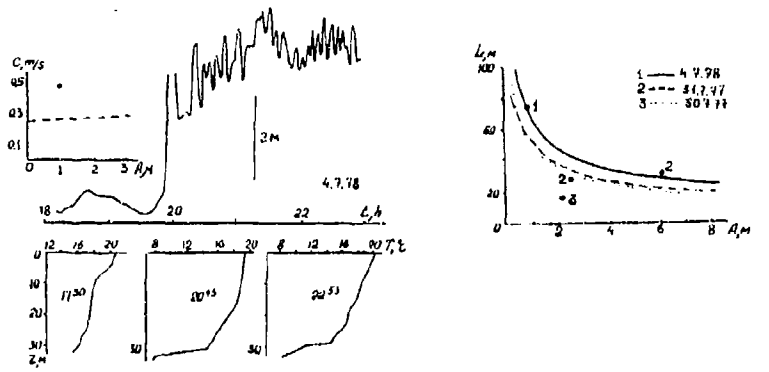
Figure 6: The results of numerical modeling by Liu [5]. Transformation of starting soliton's packet (1) without (4) and with consideration for shoaling and dissipation effects (2 and 3).

involved in the train. Waves in train have no ordering of amplitudes. Predecessors are at a distance in front of the trains. The peculiarity of this two groups is in their similarity despite the fact that one record was obtained in the Caspian Sea and the other in the Sea of Japan.

The leading wave with relative low amplitude does not agree with KdV equation model. However for better agreement between the model and observed data it is necessary to add in the right part of KdV equation some terms accounting for dissipation processes and the influence of inclined bottom, so called shoaling effect. The influence of these factors (dissipation due to horizontal turbulent viscosity and shoaling effect) on internal trains evolution was clearly demonstrated in the work of Liu [5] by means of numerical modeling for conditions of the New York Bay. Dissipation and shoaling effects, as Liu showed, lead in some moment to the stage when the leading wave becomes lower than the following waves. The relative influence of these both factors on train's evolution is illustrated by Liu in Fig. 6. Taking into consideration this results, we can treat the observed wave-predecessor as soliton which has run ahead and lost its own large amplitude due to strong dissipation.

6. Waves on a step-like bore

Short-period waves on a step-like internal bore are striking example of manifestation of soliton-like waves in the nature. Consider bore's record obtained in The Caspian shelf (Fig. 7a). A slightly pronounced thermocline in the bottom layer is observed before the emergence of internal bore. The sharp step has passed, followed by a thin layer of cold water emerged near the bottom. So a strong bottom thermocline has been generated and short-period waves were moving on it during a long time. If we take into consideration advection due to bottom current of 0.2 m/s then the observed high speed of waves equal to 0.17 m/s is reasonable enough. The parameters of waves on step like internal bore are in a good agreement with KdV solitons (see Fig. 7b).



(*a*) (*b*)

Figure 7: (a) Characteristic manifestation of internal solitons: short-period waves on a step-like bore. At the bottom temperature profiles for the different moments of bore's passing are presented. (b) Calculated amplitude-length (horizontal scale) relationship for KdV solitons and appropriate observed parameters.

7. Conclusions

On the basis of considered examples we find the features, which point to soliton character of the observed waves and give grounds for us to identify them with solitons. Speaking about finding soliton's features we are underlining the factor of qualitative agreement, that may be the main one for identification of soliton in real environment. In the quantitative comparison with the KdV equation we do not have the complete agreement in all parameters, though in some occasions the agreement with theory is good. This peculiarity is reasonably well accounted for by the background factors which have not been included into the consideration (for example, currents,proximity of bottom and etc.). Nevertheless, soliton properties in internal waves on the shelves are shown to be sufficiently well pronounced not to be shadowed by factors of external environment and its variability.

References

[1] Pingree R. D. and G. T. Mardell (1985) *Solitary internal waves in the Celtic Sea.* Progr. Oceanogr. **14**, 131-111.

[2] Apel J. R. *et al.* (1985) *The Sulu Sea internal soliton experiment.* J. Phys. Oceanogr. **15**, 1625-1651.

[3] Holloway P. E. (1987) *Internal hydraulic jumps and solitons at a shelf break region on the Australian North-West Shelf.* J. Geophys. Res. **92**, 5405-5116.

[4] Sandstrom H. and J. A. Elliott (1984) *Internal tide and solitons on the Scottian Shelf: a nutrient pump at work.* J. Geophys. Res. **89**, 6415-6426.

[5] Liu A. K. (1988) *Analysis of nonlinear internal waves in the New York Bight.* J. Geophys. Res. **93**, 12317-12329.

STRATIFIED FLOW OVER AN OBSTACLE: NONLINEAR WAVE INTERACTIONS IN THE LEE WAVE FIELD

Kevin G. Lamb

Department of Physics, Memorial University of Newfoundland
St. John's, Newfoundland, CANADA A1B 3X7

Abstract

Determining the internal gravity waves generated by the two-dimensional flow of a stratified fluid over an obstacle is an important problem. Recent calculations using a fully nonlinear, inviscid numerical model show that nonlinearities can substantially modify the nature of the flow field in certain parameter regimes (Lamb 1994). An approximate nonlinear spectral model has been developed which qualitatively reproduces the behaviour of the fully nonlinear model. This model is used to explore the nature of the nonlinear wave generation process.

Introduction

In Lamb (1994) a primitive equation numerical model was used to investigate two dimensional stratified flow over a single smooth obstacle. A rigid lid was used and the fluid had a nondimensional depth of one away from the obstacle. Far upstream the flow had a constant horizontal velocity also nondimensionalized to one and a constant buoyancy frequency N. Froude numbers

$$F = \frac{\Pi}{N} \tag{1}$$

between 0.5 and 1.0 were considered. It was shown that in certain parameter regimes large amplitude waves could be generated through a nonlinear mechanism.

Nonlinearities in this problem arise from two sources: i) the nonlinear terms in the governing equations, and ii) the nonlinear nature of the boundary condition over the obstacle. Among other effects the presence of an obstacle results in larger depth averaged flow and mean stratification over the obstacle which effects wave propagation. Figure 1 shows the mode one and two waves for two model runs with $F = 0.666$, one with an obstacle and one with a depression. The lower boundary is at

$$z = h(x) = \frac{a}{1 + (x/D)^2}, \tag{2}$$

with the half width $D = 0.17$ and the amplitude $a = 0.12$ for the obstacle and -0.12 for the depression. The flow is from left to right. The linear solution (Baines 1979) for the obstacle case is shown for comparison. Both model runs show a similar highly nonlinear behaviour. The nonlinearly generated waves include three dominant types, the generation of which are strongly coupled. A large mode-one wave, attached to the downstream side of the obstacle, oscillates in amplitude. With each oscillation a long mode-one wave is generated which propagates upstream. A large mode-two wave is also generated. It propagates against the

flow but is advected downstream. Downstream of the obstacle a train of mode-two waves is formed along with a lee-wave field of large amplitude mode-one waves having an upstream phase speed and a downstream group velocity. These mode-one waves break for obstacle amplitudes well below the breaking amplitude predicted by the steady-state Long's model solution (Lamb 1994).

When the linearized equations are solved (Baines 1979) in the model domain subject to the nonlinear lower boundary condition

$$w = (1+u)h'(x) \qquad \text{at } z = h(x), \tag{3}$$

(u and w are the horizontal and vertical velocity perturbations) rather than the linear one

$$w = h'(x) \qquad \text{at } z = 0, \tag{4}$$

the behaviour is almost identical to the linear solution.

The similarity of the obstacle and depression cases, for which the depth averaged flow and stratification are increased and decreased respectively, together with the approximately linear behaviour which occurs when the nonlinear terms in the governing equations are switched off, suggest that it is the nonlinearities in the governing equations which are responsible for the nonlinear wave generation. In order to investigate this a truncated spectral model has been developed in which the obstacle is removed and forcing terms, used to approximate its effect, are added to the governing equations. This model qualitatively reproduces the behaviour observed in the full nonlinear numerical model. It has the advantages over the full nonlinear model of allowing one to turn off different terms (e.g., forcing of mode-two waves) enabling one to investigate the cause of the behaviour, and it allows parameter space to be more rapidly explored.

The Spectral Model

In the numerical model used in Lamb (1994) a forcing term was used to quickly accelerate the flow from rest in order to mimic an impulsive start. Here, the forcing term is dropped and it is assumed that initially the isopycnals are flat and the velocity field is irrotational with an upstream flow speed of one. In terms of the total streamfunction $z+\psi$ the model equations can then be written as

$$\frac{\partial}{\partial t}\nabla^2\psi = -\frac{\partial}{\partial x}\nabla^2\psi + b_x + J(\psi, \nabla^2\psi), \tag{5a}$$

$$b_t = -b_x - N^2\psi_x + J(\psi, b). \tag{5b}$$

Here

$$b = g\rho' \tag{6}$$

where g is the gravitational constant and $\rho_o(1+\rho(z)+\rho'(x,z,t))$ is the density. The density perturbation ρ' is initially zero and

$$\rho = -\frac{N^2}{g}z. \tag{7}$$

J is the Jacobian operator

$$J(Q,R) = Q_x R_z - Q_z R_x. \tag{8}$$

With a rigid lid at $z = 1$ and a lower boundary at $z = h(x)$ given by (2). The inviscid boundary conditions are

$$\psi(x,1,t) = 0, \tag{9a}$$

$$-\psi_x = \Big(1 + \psi_z\Big)h'(x) \qquad \text{at } z = h(x), \tag{9b}$$

$$\psi, b \to 0 \quad \text{as } x \to \pm\infty. \tag{9c}$$

The first step in deriving the spectral model is to place the lower boundary at $z = 0$ and replace the lower boundary condition (9b) with the linearized lower boundary condition

$$\psi(x,0,t) = -h(x). \tag{10}$$

New dependent variables Ψ and B are introduced via

$$\psi = \Psi + h(x)(z-1), \tag{11a}$$

$$b = B - N^2 h(x)(z-1). \tag{11b}$$

The boundary conditions for Ψ are

$$\Psi(x,0,t) = \Psi(x,1,t) = 0. \tag{12}$$

The governing equations become

$$\begin{aligned}\frac{\partial}{\partial t}\nabla^2\Psi = &-\Big(1+h(x)\Big)\frac{\partial}{\partial x}\nabla^2\Psi + B_x + J(\Psi,\nabla^2\Psi) + h''(x)\Psi_x \\ &- \Big(h'''(x) + N^2 h'(x) + h(x)h'''(x) - h'(x)h''(x)\Big)(z-1) \\ &+ \Big(h'(x)\nabla^2\Psi_z - h'''(x)\Psi_z\Big)(z-1),\end{aligned} \tag{13a}$$

$$\begin{aligned}B_t = &-\Big(1+h(x)\Big)B_x - \Big(1+h(x)\Big)N^2\Psi_x + J(\Psi,B) \\ &+ \Big(h'(x)B_z + N^2 h'(x)\Psi_z\Big)(z-1).\end{aligned} \tag{13b}$$

One effect of the transformation has been to transfer the forcing from the boundary conditions to forcing terms in the governing equations (McIntyre 1972).

These rather complicated equations involve a number of nonlinear terms which are quadratic in h, Ψ and B. Dropping those which involve h and are zero away from the obstacle results in a much simpler set of equations, namely

$$\frac{\partial}{\partial t}\nabla^2\Psi = -\frac{\partial}{\partial x}\nabla^2\Psi + B_x + J(\Psi,\nabla^2\Psi) - \Big(h'''(x) + N^2 h'(x)\Big)(z-1), \tag{14a}$$

$$B_t = -B_x - N^2\Psi_x + J(\Psi,B). \tag{14b}$$

These equations are the same as the original equations (5) for ψ and b except for the forcing term in the vorticity equation. Linearizing (14) gives the linear problem

$$\frac{\partial}{\partial t}\nabla^2\Psi = -\frac{\partial}{\partial x}\nabla^2\Psi + B_x - \Big(h'''(x) + N^2 h'(x)\Big)(z-1), \tag{15a}$$

$$B_t = -B_x - N^2\Psi_x. \tag{15b}$$

The initial conditions for (13), (14) and (15) are those of irrotational flow and flat isopycnals. In terms of Ψ and B these are

$$\nabla^2\Psi(x,z,0) = -h''(x)(z-1), \tag{16a}$$

$$B(x,z,0) = N^2 h(x)(z-1). \tag{16b}$$

The solution of (15)–(16) with the boundary conditions (13) recovers the classical linear solution (e.g., Baines 1979).

The advantage of using Ψ and B as dependent variables is that Ψ has homogeneous boundary conditions. In addition,

$$B(x,1,t) = 0, \tag{17}$$

and, for the linear problem

$$B(x,0,t) = -N^2 h(x-t). \tag{18}$$

which becomes zero near the obstacle for large time. This latter equation does not hold for the nonlinear problems. With a particular choice of terrain following isopycnals as initial conditions, the initial condition and, for the linear problem, the bottom boundary condition become zero.

The spectral model is obtained from equations (13) by setting

$$\Psi = \sum_{n=1}^{\infty} \frac{a_n(x,t)}{n\pi}\sin(n\pi z), \tag{19a}$$

$$B = \sum_{n=1}^{\infty} b_n(x,t)\sin(n\pi z), \tag{19b}$$

$$z - 1 = -2\sum \frac{\sin(n\pi z)}{n\pi}. \tag{19c}$$

a_n and b_n are the amplitudes of the mode-n horizontal-velocity and density waves. Substituting (19) into (13) results in coupled PDE's for the a_n's and b_n's. The model is then truncated to M modes by eliminating all terms involving a_n and b_n with $n > M$. The resulting $2M$ coupled nonlinear equations comprise a new approximate nonlinear model which is referred to as the spectral model. The corresponding model based on equations (14) is called the simple spectral model. Solutions of the two models are very similar (at least for the parameter values considered). For $F > 0.5$ we set $M = 3$. The behaviour of

the first two modes, which is of most interest, is not significantly different if more modes are included. The statement that mode-n is not forced means that both the forcing term proportional to $h''' + N^2 n' + hh''' - h'h''$, is set to zero and that a_n and b_n are initially zero. In that case, in the absence of nonlinearities, a_n and b_n would remain zero. The equations for the a_n and b_n are solved numerically using second-order differencing in time and space with a leapfrog time stepping scheme.

Results

Using obstacles given by (2) there are three parameters in the problem: the obstacle amplitude a, the obstacle half width D, and the Froude number F. Consider the case $F = 0.666$, $a = 0.12$ and $D = 0.17$. These are the same parameter values used for the obstacle case shown in figure 1. In figure 2 the spectral model results are compared with the numerical model results at $t = 100$. The mode-one and two horizontal velocity waves a_1 and a_2 are shown. For the numerical model a_n is given by

$$u = \frac{1}{1 - h(x)} + \sum_{n=1}^{\infty} a_n(x,t) \cos\left(n\Pi \frac{z - h(x)}{1 - h(x)}\right) \tag{20}$$

where u is the total horizontal velocity. Away from the obstacle a_n can be identified as the mode-n horizontal-velocity wave.

The behaviour of modes one and two are qualitatively similar in the numerical and spectral models. Upstream of the obstacle ($x < 0$) the amplitude of the mode-one waves initially decreases as the obstacle is approached, but then increases dramatically. This increase is referred to as growth of the upstream waves. Linear theory predicts a monotonically decreasing amplitude (figure 1). Downstream of the obstacle, linear theory predicts a stationary lee wave field with a wavelength of 1.79 and approximately constant amplitude between $x = 0$ and $x \approx 50$. Both nonlinear models show waves with almost twice this wavelength. Some of the waves are considerably larger than the linear waves. Both models include a nonlinearly generated train of large amplitude mode-two waves. There is one large mode-two waves for each mode-one wave upstream of the obstacle.

While there is substantial qualitative agreement between the two nonlinear models there are differences. The waves in the numerical model are significantly larger than those in the spectral model, presumably because the linearized boundary condition underestimates the forcing due to the obstacle. In addition, the upstream propagating waves produced by the spectral model include a small, negative columnar disturbance.

Solutions of the simple truncated model based on (14) are remarkably similar. For the above case the biggest difference by $t = 100$ is that the last two upstream propagating mode-one waves to have left the obstacle are about 25% smaller.

When only the mode-one wave is forced the behaviour is qualitatively similar to the base case, although the growth of the upstream propagating waves is significantly reduced (by about two thirds). Interestingly the large mode-two waves between $x = 0$ and $x \approx 30$ are virtually identical to those in the base case. When only the mode-two wave is forced the

mode-one waves are greatly reduced in amplitude everywhere while the mode-two waves are very similar to the linear waves. This shows that the mode-one forcing is the key forcing term and that forcing of the mode-two wave enhances the nonlinear behaviour.

Summary

Two spectral models have been derived based on the idea of linearizing the lower boundary condition and transferring the wave forcing from the boundary condition to the governing equations. The simplest of the two is based on (14). These equations are identical to the initial equations (5) with the addition of a forcing term in the vorticity equation. After the Fourier Series expansion (19) and the truncation to a finite number of modes the forcing terms are zero on the upper and lower boundaries and have the effect of forcing a finite number of waves. These forced waves are identical to the waves generated in the linear problem. The full spectral model is more complex and includes terms which model some of the effects of the nonlinear nature of the lower boundary condition. For example, in (13) factors of $1 + h(x)$ appear which model the increased depth averaged flow speed and stratification over the obstacle. The full spectral model improves the agreement with the full nonlinear model, but not very significantly.

The qualitative features of the nonlinear wave generation process for Froude numbers between 0.5 and 1.0 are reproduced by the spectral model. Both mode-one and mode-two waves are nonlinearly generated when only the mode-one waves are forced. This shows that nonlinear interactions among the mode-one waves are directly responsible for the mode-two wave generation. This occurs over the obstacle at the upstream edge of the mode-one lee-wave field. The mode-two waves then interact with the mode-one waves. This results in growth of the upstream propagating mode-one waves and also in a lee-wave train of mode-one waves which are both larger and longer than the stationary, linear, mode-one lee waves. These large mode-one waves reduce the obstacle amplitude required for wave breaking. Direct forcing of the mode-two waves amplifies the nonlinear behaviour, in particular the growth of the upstream propagating mode-one waves, but does not qualitatively change it. The increased mean flow speed and stratification strength over the obstacle is not of fundamental importance for the obstacles and Froude numbers considered here.

Acknowledgements. This work was funded by a grant from the Natural Sciences and Engineering Research Council of Canada.

References

BAINES, P. G. 1979 Observations of stratified flow over two-dimensional obstacles in fluid of finite depth. *Tellus* **31**, 351 371.

LAMB, K. G. 1994 Numerical simulations of stratified inviscid flow over a smooth obstacle. *J. Fluid Mech.* **260**, 1–22.

McINTYRE, M. E. 1972 On Long's hypothesis of no upstream influence in uniformly stratified or rotating flow. *J. Fluid Mech.* **52**, 209–243.

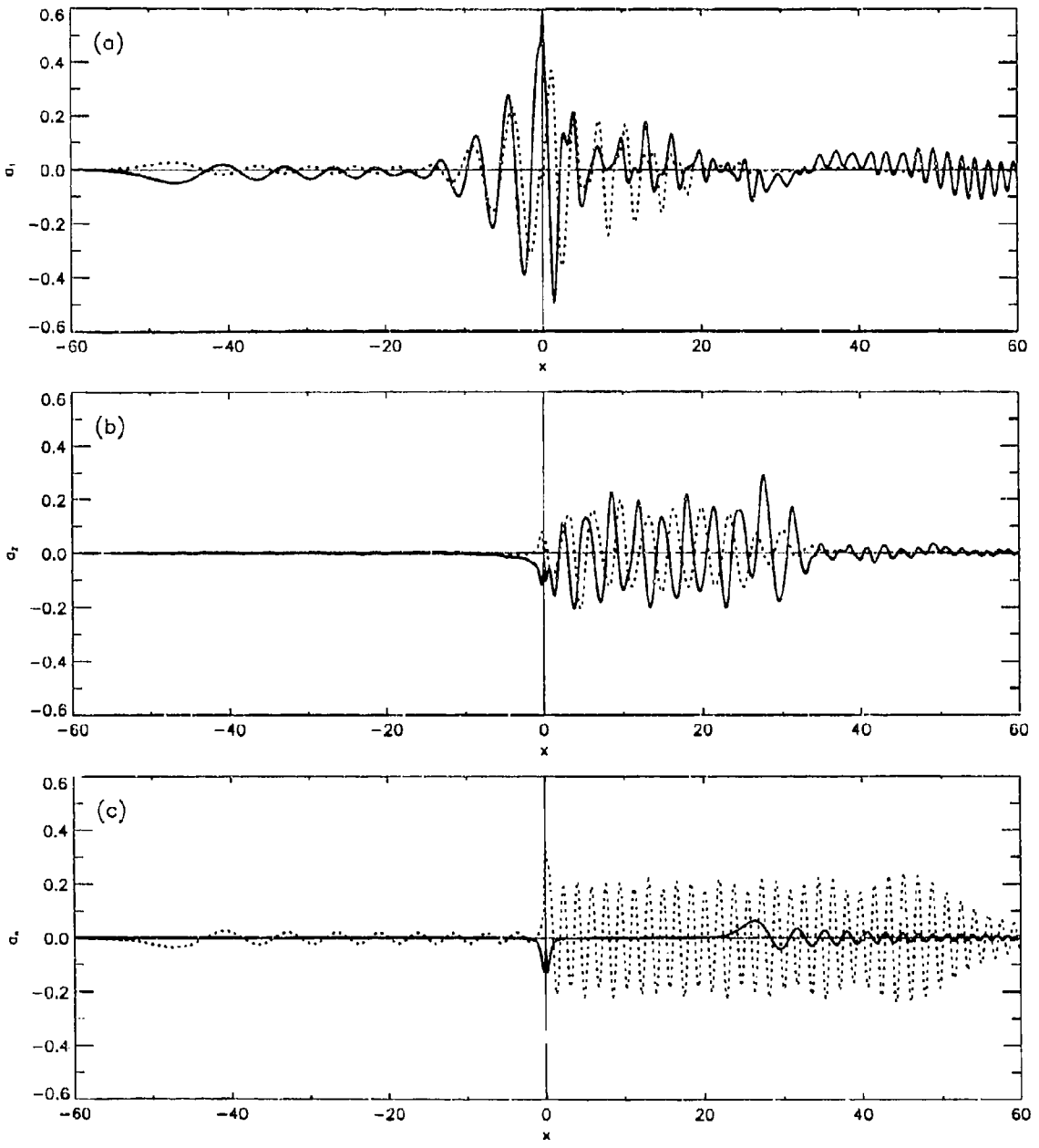


Figure 1. Comparison of waves generated by flow over an obstacle, $a = 0.12$, (solid curve) and a depression, $a = -0.12$, (dashed curve) for $F = 0.666$ and $D = 0.17$ (a) a_1. (b) a_2. (c) Linear solution for obstacle case. Lower resolution used for depression case results in unresolved short waves for $x > 30$.

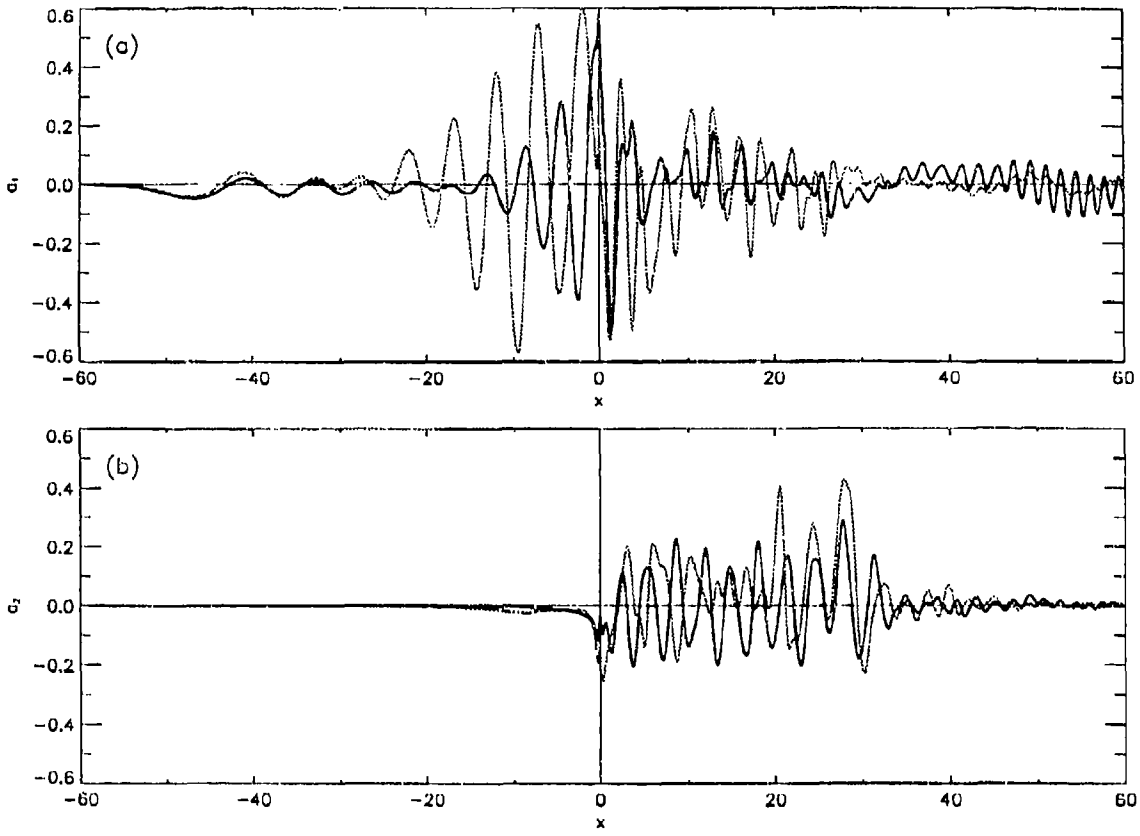


Figure 2. Comparison at $t = 100$ of the results of the numerical model (gray curve) and the spectral model (solid curves) for the case with $a = 0.12$, $F = 0.666$ and $D = 0.17$. a) a_1. b) a_2.

INERTIA-GRAVITY WAVE PROPAGATION IN A JET REGION

M.-Pascale Lelong and Timothy J. Dunkerton
Northwest Research Associates
Bellevue, Washington USA

Internal gravity waves are a common feature of middle atmosphere mesoscale flows; they are known to play an important role in transporting momentum, heat and constituents in the earth's atmosphere. In the lower stratosphere and upper troposphere, near-inertial waves dominate the gravity wave spectrum. These inertia-gravity waves (henceforth IGW) distinguish themselves from high frequency gravity waves by their short vertical wavelength (~1-2 km), large horizontal scale (~200-1000 km) and long periods (several hours or more). Whereas the high-frequency part of the gravity wave spectrum tends to saturate principally via convective instability, it is believed that IGW undergo breakdown via Kelvin-Helmholtz instability. The relative importance of the ensuing mixing, however, remains to be established.

Here, we present the results of some high-resolution, three-dimensional numerical simulations designed to address the issue of mixing efficiency following the breakdown of IGW.

The numerical model is a three-dimensional, pseudo spectral code for the Navier-Stokes equations with the Boussinesq approximation. Boundary conditions are triply-periodic. The time-stepping is performed with a second order Adams-Bashforth algorithm. A third order Adams-Bashforth version has also been implemented. The computational domain has horizontal dimensions of $1000km$ and vertical dimension of $10km$. A spectral resolution of 128^3 wavenumbers is typically used. For the cases involving a mean flow, sponge layers at the top and bottom domain boundaries are used. These layers effectively ensure that waves propagating upward will not reenter the computational domain through the bottom boundary.

The propagation and breakdown of an IGW is first examined in a shear-free environment. The problem is then generalized to investigate the propagation characteristics of IGW in the presence of a mean zonal jet $U(y, z)$ where y and z are longitudinal and vertical coordinates respectively. Linear as well as nonlinear cases are considered. The breakdown is also examined as the horizontal orientation of the wave relative to the jet is varied.

This particular problem constitutes one aspect of some ongoing research on the role of inertia-gravity waves in stratosphere/troposphere exchange.

LAGRANGIAN COORDINATES, GRAVITY WAVE SPECTRA, AND THE DICHOTOMY OF BUOYANCY SUBRANGE THEORY

J. Weinstock
Aeronomy Laboratory, NOAA
325 Broadway
Boulder, CO 80303

ABSTRACT. It is shown that Lagrangian coordinates are equivalent to use of particle propagators. Both account for nonlinear advection in the same way. Relatedly, it is found that Stokes drift has an equivalence to solution of the Navier-Stokes and immediately reveals the structure and significance of perturbation theory -- inluding quasilinear, weak wave interactions, and so-called strong wave interactions. These elementary relations are then applied to derive the vertical wavenumber spectra of broad band of random gravity waves, the related scale dependence of diffusivity, and the connection of this spectrum and diffusivity to buoyancy subrange theory.

1. Introduction

Lagrangian coordinates provide a convenient and general tool for understanding and calculating the nonlinear behavior of gravity waves (e.g., Andrews and McIntyre, 1978; Weinstock, 1976; Allen and Joseph, 1989) -- including gravity wave saturation and spectra. The first part of our article concerns such coordinates. The purpose is to show that Lagrangian coordinates are entirely equivalent to particle propagators, and, relatedly, that Stokes drift has an equivalence with solution of the Navier-Stokes equation and immediately reveals the structure and significance of perturbation theory -- including quasilinear theory, weak wave interactions and the so-called strong wave interactions. Much of this discussion appears in a recent book (Weinstock, 1993) to which we refer for proofs of some relations. One motivation for stressing the relationship between Stokes drift and solutions of the Navier-Stokes equation is to take advantage of recent interest of the former to help explain our previous work with the latter. The other motivation is that the former provides a simplification of the latter.

The second part of our paper is to use these Lagrangian considerations to calculate the spectrum of a broad band of random gravity waves, the related scale dependence of diffusivity, and the connection of this spectrum and diffusivity to buoyancy subrange theory. Emphasized is that the scale dependence of the diffusivity is more than a theoretical concept but has a major influence on transport in stably stratified turbulence. Also emphasized is how this scale may help resolve a defect of buoyancy subrange theory.

2. Lagrangian Coordinates and Particle Propagators

To demonstrate the equivalence between Lagrangian coordinates and particle propagators, and how they help solve the Navier-Stokes equation, we begin with that equation in the familiar form:

$$\frac{\partial \underset{\sim}{u}}{\partial t} + \underset{\sim}{u} \cdot \underset{\sim}{\nabla}\, \underset{\sim}{u} = -\frac{\underset{\sim}{\nabla} p'}{\rho_o + \boxed{\rho'}} - \frac{g\rho'\hat{z}}{\rho_o + \boxed{\rho'}} + \nu \nabla^2 \underset{\sim}{u}\,, \tag{1}$$

where $\underset{\sim}{u} \equiv \underset{\sim}{u}(\underset{\sim}{R},t)$ denotes the total (local) fluid velocity at position $\underset{\sim}{R}$ at time t, p' is the pressure fluctuation, ρ' is the particle density fluctuation, ρ_o is the average background density, g is the acceleration of gravity, ν is molecular viscosity, and $\hat{z}$ denotes a unit vector

along the vertical direction. The small squares around the ρ' terms on the right side of (1) denote that these terms are to be neglected compared with the nonlinear advection term, $\underset{\sim}{u} \cdot \underset{\sim}{\nabla}\, \underset{\sim}{u}$. Therefore, advection is the only nonlinearity to be considered hereafter.

It is convenient to write (1) in the condensed form

$$\left(\frac{\partial}{\partial t} + \underset{\sim}{u} \cdot \underset{\sim}{\nabla}\right) \underset{\sim}{u} = \underset{\sim}{E}(\underset{\sim}{R},t)\,, \tag{2}$$

$$\underset{\sim}{E}(\underset{\sim}{R},t) \equiv -\frac{\underset{\sim}{\nabla} p'}{\rho_0} - g\frac{\rho'}{\rho_0} - \nu\nabla^2 \underset{\sim}{u}\,,$$

where $\underset{\sim}{E}(\underset{\sim}{R},t)$ simply denotes the sum of all the terms on the right side of (2), and is a linear function of wave fluctuations. It is shown in App. A that a formally exact solution of (2) is given as follows:

$$\underset{\sim}{u}(\underset{\sim}{R},t) = \underset{\sim}{u}[\underset{\sim}{R}_L(-t),0] + \int_0^t dt_1 \underset{\sim}{E}[\underset{\sim}{R}_L(t_1-t), t_1]\,, \tag{3}$$

$$\frac{\partial \underset{\sim}{R}_L(t)}{\partial t} = \underset{\sim}{u}[\underset{\sim}{R}_L(t), t]\,, \tag{4}$$

where $\underset{\sim}{u}[\underset{\sim}{R}_L(-t),0]$ denotes the initial value of $\underset{\sim}{u}(\underset{\sim}{R},t)$ with $\underset{\sim}{R}$ replaced by the Lagrangian coordinate $\underset{\sim}{R}_L(-t)$ and the second term in (3) is the t_1 integral of $\underset{\sim}{E}(\underset{\sim}{R},t_1)$ but with the usual coordinate $\underset{\sim}{R}$ replaced by the Lagrangian coordinate. The Lagrangian coordinate $\underset{\sim}{R}_L(t)$ is defined by (4) as the solution of Newtons equation for the motion of a particle, or air parcel, $\underset{\sim}{R}_L(t)$ in the fluid velocity field $\underset{\sim}{u}$. The (Lagrangian) coordinate $\underset{\sim}{R}_L(t)$ is expressed in terms of the wave velocity field by eqn. (4). The minus t occurs because the Lagrangian operator is $\partial/\partial t + \underset{\sim}{u}\cdot\underset{\sim}{\nabla}$ rather than $\partial/\partial t - \underset{\sim}{u}\cdot\underset{\sim}{\nabla}$ and displaces particles backward in time.

What (3) states is that the (nonlinear) solution of the Navier-Stokes equation is given exactly by the solution of the linearized equation but with the coordinate $\underset{\sim}{R}$ everywhere replaced by a Lagrangian coordinate $\underset{\sim}{R}_L(t)$. Since linearized solutions are often fairly easy to obtain, (3) provides a general means of extending such (linear) solutions to nonlinear ones. Correspondingly, (3) combined with (4) implies that the Lagrangian velocity $\underset{\sim}{u}[\underset{\sim}{R}_L(t), t]$ is the basic quantity needed to solve the nonlinear Navier-Stokes equation -- since it determines $\underset{\sim}{R}_L(t)$.

What we particularly wish to emphasize is that Lagrangian coordinates are equivalent to use of a particle propagator. To demonstrate this, we show that the Lagrangian velocity $\underset{\sim}{u}[\underset{\sim}{R}_L(t), t]$ can be written as

$$\underset{\sim}{u}[\underset{\sim}{R}_L(t), t] = \exp\,(\underset{\sim}{\xi}\cdot\underset{\sim}{\nabla}^+)\,\underset{\sim}{u}(\underset{\sim}{R},t) \tag{5}$$

$$\underset{\sim}{\xi} \equiv \underset{\sim}{R}_L(t) - \underset{\sim}{R}_L(0) \equiv \int_0^t dt_1 \underset{\sim}{u}[\underset{\sim}{R}_L(t_1), t_1] \tag{6}$$

where, physically, $\underset{\sim}{\xi}$ is just the displacement of a particle from its initial position. The symbol $\underset{\sim}{\xi}$ was used in a related context by Andrews and McIntyre (1978). The superscript +

on ∇ is to note that, in the case of incompressibility, ∇ in (5) operates only on $u(R,t)$ to its right and not on ξ;

A pedestrian way to verify (5) is to expand $u[R_L(t), t]$ in a Taylor-McLauran expansion about $R_L(t) = R$ and, at the same time, to expand the exponential of (5) in a power series in $\xi \cdot \nabla^+$, and, afterwards, compare both sides of (5) term by term.

It is the exponential term $\exp\left(\xi \cdot \nabla^+\right)$ that is referred to as a particle propagator. According to (5), this propagator simply states that the usual Eulerian coordinate R is everywhere replaced by the Lagrangian coordinate $R_L(t)$. In other words, the propagator is equivalent to (being in) Lagrangian coordinates. The advantage of the propagator is that the transformation (to Lagrangian coordinates) is given in an explicit mathematical form which readily allows for mathematical manipulations (so as to derive nonlinear wave properties in a fairly simple way). For example, the straight-forward power series expansion of the propagator in ascending powers of $\xi \cdot \nabla$ yields perturbation theory, and immediately determines Stokes drift and other results -- as shown in the next section.

3. Stokes Drift and the Navier-Stokes Equation:

To show that Stokes drift is closely related to a solution of the Navier-Stokes equation, and, at the same time, yields perturbation theory we take the straight-forward power series expansion of the exponential propagator (5) as follows:

$$u[R_L(t), t] = u(R,t) + \xi \cdot \nabla u + \frac{1}{2}\xi \cdot \left(\xi \cdot \nabla\right)\nabla u$$

Quasilinear — Weak wave interaction (TRIADS)

$$+ \frac{1}{3!}\xi \cdot \left(\xi \cdot \left(\xi \cdot \nabla\right)\nabla\right)\nabla u + \frac{1}{4!}\left(\xi\right)^4 \vdots \nabla^4 u + \ldots, \qquad (7)$$

Higher order terms

where we again use $u = u(R,t)$ to condense the notation. These ordered ξ terms constitute perturbation theory.

Before discussing the various ξ terms in (7), we note that $\overline{u[R_L(t), t]} - \overline{u(R,t)}$ is the difference between averaged Lagrangian and Eulerian velocities, which, by definition, is the Stokes drift; here the superbar denotes a suitable average over space or time. Therefore, the Stokes drift u_s is the sum of all the ξ terms on the right side of (7). It is given by

(8)

$$u^s \equiv \overline{u[R_L(t), t]} - \overline{u(R,t)} = \left[\overline{\xi \cdot \nabla u} + \frac{1}{2}\overline{\xi \cdot \left(\xi \cdot \nabla\right)\nabla u} + \frac{1}{3!}\overline{\xi \cdot \left(\xi \cdot \left(\xi \cdot \nabla\right)\nabla\right)\nabla u} + \ldots\right]$$

4. Stokes Drift, Perturbation Theory, and Time Secularities

Each of the higher order terms can be shown to have a time secularity -- the third term varying as t, the fourth term as t^2 and so on, as, for example, $\overline{\xi \cdot \left(\xi \cdot \left(\xi \cdot \nabla\right)\nabla\right)\nabla u} \sim t$ -- so that after a sufficient time has elapsed each one of the infinite number of higher order terms will exceed the first and second terms in magnitude. What saves this expansion is that the sum of this infinite (9)

number of terms is itself finite (just like, for example, the sum $\sum_{n=0}^{\infty} (-t)^n/n! = e^{-t}$ is finite at large t). It is this

sum that is referred to as "strong" wave interactions: It is equivalent to a re-normalization. Let us next see what strong interactions yields for the gravity wave dispersion relation and for the vertical wavelength spectrum.

5. Strong Interactions

To derive a nonlinear dispersion relation from (7) we set $\underset{\sim}{u}$ equal to a Fourier wave component $\underset{\sim}{u}_{\underset{\sim}{k}} \exp\left(i\underset{\sim}{k}\cdot\underset{\sim}{R}_L + i\omega t\right)$ where $\underset{\sim}{u}_{\underset{\sim}{k}}$ is the velocity amplitude of the wave, $\underset{\sim}{k}$ its wavevector and ω its frequency. What occurs in the nonlinear wave equation (3) with (4) is $\underset{\sim}{u}[\underset{\sim}{R}_L(t), t] \equiv \exp\left(\underset{\sim}{\xi}\cdot\underset{\sim}{\nabla}^+\right)\underset{\sim}{u}$ for which (7) gives us (e. g., Weinstock, 1976; Dupree, 1966 or 1967) the APPROXIMATION

$$\exp\left(\underset{\sim}{\xi}\cdot\underset{\sim}{\nabla}\right)\underset{\sim}{u} \approx \left[\exp\left(i\omega_\Delta t - t\underset{\sim}{k}\cdot\underset{\approx}{D}\cdot\underset{\sim}{k}\right)\right]\underset{\sim}{u}_{\underset{\sim}{k}}\exp\left(i\underset{\sim}{k}\cdot\underset{\sim}{R}_L + i\omega t\right) \qquad (10)$$

$$\omega_\Delta \equiv \langle k\cdot\overline{\xi}\rangle/t\,, \qquad \underset{\approx}{D} \equiv \frac{1}{2}\left(\overline{\xi\xi}\right)/t \qquad (11), (12)$$

where $\underset{\approx}{D}$ is a diffusivity tensor and ω_Δ is a nonlinear frequency shift.

Returning to (12), we note that a similar expression between diffusivity and mean square particle displacements was used in the theory of Brownian motion (Einstein, 1926), and, afterwards, to describe atmospheric diffusion (Taylor, 1921). From (10) one can obtain the following algorithm to convert a linear dispersion relation to a nonlinear one:

$$\underset{\text{LINEAR DISPERSION RELATION}}{\omega} \rightarrow \underset{\text{NONLINEAR DISPERSION RELATION}}{\omega + \omega_\Delta + i\underset{\sim}{k}\cdot\underset{\approx}{D}\cdot\underset{\sim}{k}} \qquad (13)$$

However, the validity of (13) is limited, because of the approximation of neglecting nonlinear loss terms. For gravity waves, the nonlinear dispersion relation is

$$\left(k_z + i\beta\right)^2 + \frac{ik_z+\beta}{H} = \frac{k_x^2 N^2}{\left(\omega + \omega_\Delta + id_w\right)^2} \qquad (14)$$

where $d_w \equiv \underset{\sim}{k}\cdot\underset{\approx}{D}\cdot\underset{\sim}{k}$, and β is the imaginary part of the vertical wavenumber -- the growth-length. This relation applies to a broad spectrum of random waves, but not, for example, to a monochromatic wave.

Equating the real and imaginary parts of both sides of (14) there results $(\omega + \omega_\Delta)^2 = k_x^2N^2/k^2$, assuming $2k_zH \gg 1$, and $\beta \cdot k_z \gg 1$, with growth rate β given by $\beta = (2H)^{-1} - k^2 d_w/|k_z|(\omega+\omega_\Delta)|$ where the absolute value occurs because we are only concerned with wave propagating energy upwards, and, therefore, with vertical phase speeds that are negative; i.e., $\omega/k_z = -|\omega/k_z|$. It can be seen that the growth is reduced by the nonlinear diffusivity term in d_w and that the frequency is shifted.

6. Spectral Equation

To begin with, we find that evolution equation for an upward propagating spectrum of gravity waves can be written as

$$\frac{\partial F(k_z, z)}{\partial z} = \left[\frac{1}{H} - \frac{k_z^3}{\Omega} D_{zz}\right] F(k_z, z), \tag{15}$$

$$D_{zz} \equiv \Omega (N/\Omega)^{m-2} (HN^2)^{-1} \int_{c_i k_z}^{\infty} dk_z' \, F(k_z', z) k_z'^{-1},$$

where $F(k_z, z)$ is the spectrum of horizontal velocity for a broad band of random gravity waves and D_{zz} denotes the vertical diffusivity tensor. A formal derivation of (15) has been given (Weinstock, 1990). Attention is called to the scale dependence of D_{zz}, which is to be treated more fully in Sec. 7. At saturation, $\partial F(k_z, z)/\partial z = 0$, for which solution of (15) yields, with use of $c_i^4 = 0.25$, $\Omega/N = 2^{4c_i}$,

$$F(k_z, z) = 0.2 \left(\frac{\Omega}{\Omega_0}\right)^{2-m} N^2 k_z^{-3} \tag{16}$$

where $m = s/2$ is the power law of the frequency spectrum. Thus k_z spectrum agrees with the buoyancy wave spectrum observed in both ocean and atmosphere.

7. SCALE DEPENDENT TRANSPORT

It was pointed out in the previous section that the diffusivity caused by gravity waves, depends on the scale of the matter being diffused. The purpose of this and the next section is to point out that this scale dependence has a major influence on vertical transport in stably stratified fluids, and, additionally, provides a possible explanation, and correction of a defect of buoyancy subrange theory (Lumley, 1964; Weinstock, 1978, 1985).

We begin with D_{zz}, the vertical element of diffusivity $\underline{\underline{D}}$ defined by (12). For the case of a gravity wave band whose velocity is

$\underline{u}(R, t) = \int dk_z \int dk_x \int d\omega \, \underline{u}_k(z) \exp[i(k_z z + k_x x + \omega t)]$ -- where $\underline{u}_k(t)$

is the Fourier amplitude at height z of a gravity wave with wavevector $\underline{k}$ and frequency ω -- the $\hat{z}\hat{z}$ element of (12) can be shown to be given by (Weinstock, 1976; 1993).

$$D_{zz}(k_z, z) = \int_{\omega}^{N} d\omega' \int_{c_i k_z}^{\infty} dk_z' \, \frac{S(k_z', \omega') \omega'}{2HN^2 k_z'} \left(1 - \frac{\bar{k}_x k'}{\bar{k}_x k}\right)^2 \tag{17}$$

where $\bar{k}$ is an average wavevector of the band and it is required that $Hk_z \gg 1$, $\omega \ll N$. For simplicity, we use in (17) the separability approximation $S(k_z, \omega) = F(k_z) S_2(\omega)$ (Garrett and Munk, 1975) with the frequency spectrum normalized to unity and expressed as $S_2(\omega) = (m-1)\Omega^{m-1}\omega^{-m}$.
In that case, the ω' integration is elementary and (17) reduces to

$$D_{zz}(k_z, z) = \left(\frac{N}{\Omega}\right)^{\frac{m-1}{2}} \frac{\Omega}{HN^2} \int_{c_i k_z}^{\infty} dk_z' \, \frac{F(k_z', z)}{k_z'} \tag{18}$$

in the limit of $\Omega \ll \omega \ll N$.
Finally, with k_z restricted to lie in the saturated, or equivalently, the strong wave interaction region of

the spectrum we substitute (16) in (18) to obtain the desired diffusivity expression

$$D_{zz}(k_z, z) = \frac{(\sin\theta)}{145\,(Hk_z)}\left(\frac{k_R}{k_z}\right)^2 \frac{\epsilon_o}{N^2} \quad ; \left(k_R \equiv \left(\frac{N^3}{\epsilon_o}\right)^{\frac{1}{2}}\right) \qquad (19)$$

where k_R is referred to as the bouyancy wavenumber, the factor $(145)^{-1}$ comes from the estimate $N/\Omega_o = 240$, $C_1^3 \approx 0.25$ in the free atmosphere and θ is the latitudinal angle. Here, the (vertical) scale of the mass being diffused is represented by $L_z \equiv 2\pi/k_z$.
It can be seen in (19) that D_{zz} increases as L_z^3 with increasing L_z -- a fairly rapid increase. This equation re-states the logical and widely-known idea that atmospheric diffusivity generally increases with the size of the object being diffused: Logical because the larger the diffussee the larger the atmospheric fluctuations that can diffuse it.

Equation (19) also has the well-known ϵ_o/N^2 behavior associated with diffusion is stratified turbulence. The dimensionless factor multiplying ϵ_o/N^2 is sometimes reffered to as the efficiency factor. This factor is of interest in itself (it has been measured) and so we re-write (19) as

$$D_{zz} = E_{ff}\left(\frac{\epsilon_o}{N^2}\right), \qquad (20)$$

$$E_{ff} \equiv \frac{(\sin\theta)}{145\,(Hk_z)}\left(\frac{k_R}{k_z}\right)^2. \qquad (21)$$

Since $Hk_z >> 1$, it follows that $E_{ff} < 1$ even if L_z is many times as large as the bouyancy length $L_R \equiv 2\pi/k_R$.

We consider the following examples:

Example 1:

In the mesosphere, $L_R \approx 500$ m and $H \approx 6000$ m, so that $E_{ff} \leq 0.3$ for a diffussing mass whose vertical scale is as large as 7000m. The atomic oxygen layer is such a mass.

Example 2:

In the upper ocean typical values for L_R and H are 1m and 20km, respectively, so that Eff ≤ 0.13 for L_z/L_R as large as 100; i.e., for scales 100 times the buoyancy length.

Roughly speaking the efficiency in (21) does not exceed unity unless L_z/L_R exceeds 10^3 in the upper ocean and 20 in the mesosphere. Such a relatively small efficiency is consistent with oceanic observations (e.g. Oakey, 1982; Gregg, 1987).

In sum, strong wave interaction theory is consistent with observations of both k_z spectra and vertical transport in oceans. Another theory that predicts a k_z^{-3} spectrum is the buoyancy subrange theory (Lumley, 1964; Weinstock, 1978, 1985). We next compare the two theories and in particular, explain a seeming inconsistency of the latter theory with regard to the diffusion efficiency it predicts.

8. BUOYANCY SUBRANGE THEORY - A DICHOTOMY

For a brief critique of the status of buoyancy subrange range theory we recall that Lumley (1964) predicted E(k), the scalar kinetic energy density spectrum of ~~the in~~ stratified turbulence, to be

$$E(k) = \alpha \epsilon(k)^{2/3} k^{-5/3}, \qquad \epsilon(k) = \epsilon_o \left[1 + (k/k_R)^{-4/3}\right]^{3/2}, \tag{22}$$

where we note $k \approx k_z$ when $k << k_R$, $\alpha \simeq 1.5$ is the Kolmogorov constant and $\epsilon(k)$ is the spectral transfer rate. The same spectral variation was later found for the temperature spectrum (Weinstock, 1985). These predictions are consistent with observations of temperature spectra (e.g., Gregg, 1977) and kinetic energy spectra (e.g., Gargett et al., 1981). Nevertheless, (22) differs substantially from oceanic spectra when k is very much smaller than k_R the so-called weak wave interaction region -- (22) varying as k^{-3} whereas oceanic spectra vary as k_z^{-2} when $k_R/k >> 20$. Relatedly, (22) violates the underlying locally inertial condition $k\epsilon(k)\partial\epsilon(k)/\partial k << 1$ upon which it [(22)], is based. Thirdly, as pointed out by Holloway (1989), if one takes $Eff \sim \epsilon(k)/\epsilon_o$ then (22) gives values of Eff which greatly exceed unity when $k_R/k >> 1$ ------ -- in seeming disagreement with oceanic measurements of Eff (e.g., Oakey, 1982; Gregg, 1987). These discrepancies and violation were removed (Weinstock, 1978) by explicitly including a gravity wave influence not accounted for in the original theory. With this inclusion, it was shown that $\epsilon(k)$ is approximately given by

$$\epsilon(k) = \epsilon_o \begin{cases} \left(1 + \dfrac{5\alpha^{3/2}a}{12}(1 - R_f^{-1})\left[\dfrac{3 - 3(k/k_R)^{1/3}}{1 + 0.2(k/k_R)^2} + 0.5\right]\right)^3, & \text{for } k \le k_R \\ \left(1 + \dfrac{5\alpha^{3/2}a}{12}(1 - R_f^{-1})\left[\dfrac{0.6(k/k_R)^{-5/3}}{1 + 0.2(k/k_R)^2}\right]\right)^3, & \text{for } k \ge k_R \end{cases} \tag{23}$$

where a is an anisotropy factor, and R_f is the flux Richardson number. It can be seen that this modified E(k) satisfies the locally inertial condition when $k << k_R$, and, additionally, when combined with (22), no longer varies as k^{-3} in the weak wave interaction region of $k_R/k >> 20$. Furthermore, the diffusion efficiency hardly exceeds unity when $k_R/k >> 1$. However, (23) does not always give a k^{-3} spectrum in the buoyancy subrange the k region $0.1k_R \le k \le k_R$ for oceans.

To put this all together, we have two buoyancy subrange theories; (22) and (23). The former theory always gives the observed k^{-3} spectrum in the buoyancy subrange but also implies much too large a diffusivity efficiency. The latter theory which includes gravity waves, implies a more reasonable diffusivity efficiency but does not always give the k^{-3} spectrum. We note that one would have a complete and inconsistent theory if we could combine the correct features of each theory -- use (22) for spectra and use (23) for diffusivity considerations. Such a possibility may be justified by the fact that both theories make the wrongfull assumption of isotropy at $k << k_R$. In actually, at such small k, the spectrum is dominated by gravity waves and vortical modes and is, therefore, extremely ANISOTROPIC. Indeed, (22) resembles what is expected for horizontal motion and spectra whereas (23) more resembles vertical motion and spectra; i.e., if we write $E(k) \equiv E_H(k) + E_\perp(k)$, ---------- where $E_H(k)$ AND $E_\perp(k)$ --- respectively denote the horizontal and vertical parts of E(k) then (22) becomes

$$E_H(k) = \alpha \epsilon(k)^{2/3} k^{-5/3}, \qquad (k < k_R) \tag{24}$$

when $k << k_R$. Furthermore, and most importantly, (24) no longer overestimates the diffusion efficiency since that efficiency pertains to vertical motion whereas (24), and (22), pertain to horizontal motion (when $k << k_R$). A more fundamental approach to stratified turbulence is to divide the spectral balance equation into horizontal and vertical components in the

manner done by Riley et al. (1981) for the fluctuation equations and for the mean square energies. That would be a formidable problem involving as it would wave-wave interactions.

Because of this complication, one can view the buoyance and subrange theory (22), or more correctly, (24), as being nothing less than remarkable in that it correctly predicts so much of both kinetic and potential energy spectra by an elementary consideration of buoyance. Of course, we again note, one need have in mind that, (22) can pertain only to horizontal motion and not to vertical motions when $k << k_B$. It may be possible to prove this a priori from the horizontal energy balance equation.

REFERENCES

Allen, K.R. and Joseph, R.I., (1989) 'A canonical statistical theory of oceanic internal waves', J. Fluid Mech., 204, 185-228.

Andrews, D.G. and McIntyre, M.E., (1978) 'An exact theory of nonlinear waves on a Lagrangian mean flow', J. Fluid Mech., 89, 609-646.

Balsley, B.B. and Carter, D.A., (1982): The spectrum of atmospheric velocity 8km and 86km, Geophys. Res. Lett., 9, 465-468.

Balsley, B.B. and Garello, R., (1985) 'The kinetic energy density in the troposphere, stratosphere, and mesosphere, Radio-Scince', 20, 1355-1361.

Dewan, E.W., Grossbard, N., Good, R.E., and Brown, J., (1984) 'Spectral analysis of 10m resolution scalar velocity profiles in the stratosphere', Geophys. Res. Lett., 11, 80-83.

Dewan, E.W. and Good, R.E., (1986) 'Saturation and the "universal" spectrum for vertical profiles of horizontal scalar winds in the atmosphere', J. Geophys. Res., 91, 2742-2448.

Dupree, T.H., (1966) 'A perturbation theory for strong plasma turbulence', Phys. Fluids, 9, 1773.

Endlich, R., Singleton, R.C., and Kaufman, J.W., (1969) 'Spectral analysis of detailed vertical wind speed profiles', J. Atmos. Sci.

Fisz, M., (1963), 'Probability Theory and Mathematical Statistics', Chapter 4, John Wiley, New York.

Gardner, C.S., (1989) 'Sodium flouresence lidar applications in atmospheric science and astronomy' Proc. IEEE.

Hines, C.O., (1991) 'The saturation of gravity waves int he middle atmosphere. Part II: Development of Doppler-spread theory', J. Atm. Sci., 48, 1360-1379.

Hines, C.O., (1992)

Justus, C.G. and Woodrum, A., (1973) 'Upper atmospheric planetary-wave and gravity-wave observations', J. Atmos. Sci., 30, 1267-1275.

Müller, P., 1988: Vortical motions. In: Small-Scale Turbulence and Mixing in the Ocean, edited by J.C.J. Nikoul and B.M. Jamart, 285-301, Elsevier, New York.

Smith, S.A., Fritts, D.C., and VanZandt, T.E., (1987) 'Evidence for a saturated spectrum of atmsopheric gravity waves' J. Atmos. Sci., 44, 1404-1410.

Taylor, G.I., (1921) 'Diffusion by continuous movements', Proc. London Math Soc., 20, 196-202.

Vincent, R.A., (1984) 'Gravity wave motions in the mesosphere', J. Atmos. Terr. Phys., 46, 119-128

Weinstock, J., (1976) 'Nonlinear theory of gravity waves. I. Saturation and enhanced diffusion', J. Geophys. Res., 81, 633-652.

Weinstock, J., (1984) 'Gravity wave saturation and eddy diffusion in the middle atmosphere', J. Atmos. Terr. Phys., 46, 119-128.

Weinstock, J., (1990) 'Saturated and unsaturated spectra of gravity waves and scale-dependent diffusion', J. Atmos. Sci., 47, 2211-2225.

GARGETT, HENDRICKS, SANFORD, OSBORN & WILLIAMS (1981), J. PHYS. OCEANOGR. 11, 1258-1271.

GREGG, M.C. (1987), J. GEOPHYS. RES. 92, 5249-5286

HOLLOWAY, G. (1984), IN OCEAN CIRCULATION MODELING ED. BY ANDERSON AND WILLEBRAND REIDEL ACADEMIC PUBLISHERS. 513-548

CALEY, M.S. (1982), J. PHYS. OCEANOGR. 12, 256-271

KELLY, MCINTYRE, W. STRAUGHAN IN NONLINEAR PROPAGATION OF INTERNAL WAVES EDITED BY [illegible] AMER. INST. PHYS. 88-112

Internal Solitary Waves with Oscillatory Tails

by

R. Grimshaw
Department of Mathematics
Monash University
Clayton, Victoria 3168, Australia

Abstract

Traditionally internal solitary waves have been conceived as genuinely isolated waves which decay to zero in the far–field. Recently, however, it has been recognized that, quite commonly, this is not necessarily exactly so, and internal solitary waves may not be truly isolated, and instead decay to non–zero small–amplitude oscillations in the far–field. This occurs generically whenever the linear spectrum contains wave phase speeds which can resonate with the solitary wave speed. For internal solitary waves this can occur via mode–mode interactions leading to the conclusion that only mode one internal solitary waves can be truly solitary. Analytical methods for determining the structure of these non–local solitary waves will be reviewed.

§1. Introduction

Solitary waves are traditionally conceived as localized disturbances of permanent form and propagating with constant speed. One of the classical prototypes is the solitary–wave solution of the Korteweg–de Vries (KdV) equation

$$u_t + 6uu_x + u_{xxx} = 0 \tag{1}$$

given by $u = u_0(x - c_0 t)$ where

$$u_0(x) = 2\gamma^2 \mathrm{sech}^2 \gamma x, \quad c_0 = 4\gamma^2 . \tag{2}$$

Importantly in the present context note that in the tail of the solitary wave, as $|x| \to \infty$, $u_0(x) \sim 4\gamma^2 \exp(-2\gamma |x|)$. Thus the KdV–solitary wave (2) is a genuine solitary wave, with exponential decay in the tail regions. Further, the KdV equation has been invoked to describe small–amplitude long water waves in the absence of surface tension, and more generally small–amplitude long waves in a wide variety of physical systems involving shallow fluids, including density–stratified fluids (e.g., Benney, 1966).

However, it has recently been recognized that so–called solitary waves may not be genuinely localized, and in fact are accompanied by co–propagating oscillatory tails which persist with non–zero amplitudes (see, for instance, the reviews by Boyd, 1989, 1990, who has called these waves "nanopterons"). This situation may occur in a variety of physical situations including the case of solitary water waves in the presence of surface tension, where a combination of numerical work by Hunter and Vanden–broeck (1983), Vanden–broeck (1991) and Vanden–broeck and Dias (1992), and analytical work by Amick and Kirchgassner (1989), Iooss and Kirchgassner (1990), Beale (1991), Sun (1991) and Dias and Iooss (1993) has lead to the following general picture. In the absence of any surface tension, there exist solitary water waves of elevation, which can be described by the KdV–solitary waves (2) in the limit of small amplitude. However when the Bond number τ (measuring the effect of surface tension) is greater than $1/3$, these exist solitary gravity–capillary waves of depression, which can again be described by the KdV–solitary waves (2) in the limit of small–amplitude. But when the Bond

number τ lies between 0 and 1/3 there exist two kinds of solitary wave: one kind contains waves of both depression and elevation with decaying oscillations in the tail region; the other kind consists of a solitary wave core of elevation accompanied by non–decaying tail oscillations. It is this latter non–local solitary wave with which we are concerned here.

The reason for the appearance of the non–decaying tail oscillations when $0 < \tau < 1/3$ can be readily understood on physical grounds from the linear spectrum. Solitary water waves are supercritical when $\tau = 0$; that is, their speed is greater than the linear long–wave speed, which is the maximum phase speed of small–amplitude sinusoidal waves. Hence it is not possible for sinusoidal short–wavelength water waves to co–propagate with solitary water waves, and so no tail oscillations are found. A similar situation occurs when $\tau > 1/3$ since now the solitary waves are subcritical, and all small–amplitude sinusoidal waves are supercritical. On the other hand, when $0 < \tau < 1/3$ solitary waves of elevation are supercritical, but can co–exist with small–amplitude sinusoidal capillary waves with the same phase speed. It is the existence of this resonance that is responsible for the non–decaying tail oscillations, although it is often a delicate task to establish that the amplitude of the tail oscillation is in fact non–zero since the mechanism involved is intrinsically nonlinear.

Similar considerations can be applied to other physical systems to determine when non–decaying tail oscillations might be expected to co–exist with a solitary wave core. A simple example is the singularly–perturbed KdV equation

$$u_t + 6uu_x + u_{xxx} + \epsilon^2 u_{xxxxx} = 0 , \tag{3}$$

which has been proposed by Hunter and Scheurle (1988) as a model for gravity–capillary waves when τ is just less than 1/3 . Note that for $0 < \tau < 1/3$ the KdV equation (1) cannot be expected to be a valid model since it is derived on the assumption that only long waves are present, and cannot account for the short wavelength oscillatory tails. The linear spectrum for sinusoidal waves of phase speed c and wavenumber k is

$$c = -k^2 + \epsilon^2 k^4 . \tag{4}$$

By considering the limit $k \to 0$ we see that solitary waves will be supercritical with positive speeds. But then there will be a resonance with small–amplitude short–wavelength waves whose wavenumber $k \approx \epsilon^{-1}$ as $\epsilon \to 0$. Interestingly, in this limit $\epsilon \to 0$ the amplitude of the tail oscillations is exponentially small (but non–zero), and the calculation of this amplitude requires the techniques of exponential asymptotics (see, for instance, Pomeau et. al., 1988, or Grimshaw and Joshi, 1994) who use the technique of Borel–summation to calculate the exponentially small quantities. Indeed, it can be showen that as $\epsilon \to 0$, the non–local solitary wave solution of (3) is given by

$$u \sim u_0(x) + \frac{b}{\epsilon^2} \exp\left[-\frac{\pi}{2\epsilon\gamma} \right] \sin\left[\frac{|x|}{\epsilon} - \delta \right] , \tag{5}$$

where we are using the frame of reference in which the wave is stationary, and $u_0(x)$ is the KdV–solitary wave (2). The amplitude b and phase δ are related by the relation $b \cos\delta \approx 62.74$, so that (5) defines a 2–parameter family with parameters γ and δ say. The expression (5) agrees with the numerical results of Boyd (1991). Note that (5) is a symmetric non–local solitary wave, and hence the tail oscillations must be supported by energy sources and sinks as $|x| \to \infty$. Here the group velocity for waves of wavenumber $k \approx \epsilon^{-1}$ is $2\epsilon^{-2}$ and hence there must be an energy source as $x \to -\infty$ and a sink is $x \to \infty$. If instead, equation (5) is solved with a localized initial condition, the solution will consist of a solitary wave with co–propagating oscillations to the right only (Benilov et. al., 1993). Such non–local solitary waves cannot be exactly steady since they continually lose energy to this radiation.

§2. Internal waves

Akylas and Grimshaw (1992) have explored the implications of these ideas for solitary waves in density–stratified fluids of shallow depth. Here we summarize their results, and then discuss some conceptual models which illustrate the basic ideas. First we note that in the absence of an underlying rotation the linear spectrum typically consists of an infinite set of modes for each of which the phase speed of linear long waves is a monotonically decreasing function of the wavenumber k (see Figure 1). For each wave mode of mode number n and linear long–wave phase speed c_n ($n = 1, 2, 3, \ldots$) it might now be expected that these exists a supercritical internal solitary wave (i.e. its speed is greater than c_n) which in the small–amplitude long–wave limit is governed by a KdV equation (e.g. Benney, 1966). For the mode $n = 1$, this is indeed the case since a solitary wave of speed greater than c_1 cannot resonate with any small–amplitude sinusoidal wave. However, for the modes $n \geq 2$ there exists a resonance with short–waves of the modes $n - 1, \ldots, 1$. For instance, an internal solitary wave of mode number $n = 2$ will have a resonance with mode number 1 and wavenumber k_1 (see Figure 1). Thus in general internal solitary waves of mode number $n \geq 2$ are non–local and are accompanied by co–propagating sinusoidal waves of mode numbers less than n. Indeed, Vanden–broeck and Turner (1992) have confirmed numerically that mode–2 internal solitary waves are accompanied by mode–1 oscillatory tails. A similar situation occurs for equatorial Rossby solitary waves (Boyd, 1989) and in other physical systems.

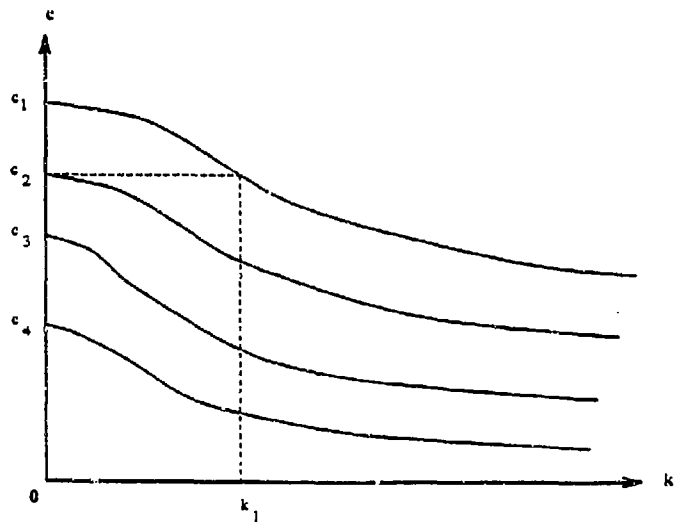


Figure 1: A schematic plot of the linear spectrum for internal waves.

Akylas and Grimshaw (1992) adapt the Borel–summation technique of Pomeau et. al. (1988) (see also Grimshaw and Joshi, 1994) to calculate the amplitude of the oscillatory tails since in the limit of small–amplitude solitary waves, these are exponentially small. We shall not describe the method here because of its complexity but will state the outcome. In the next section, however, we will outline the procedure for a conceptual model. To describe the salient features of non–local internal solitary waves we first consider the linear spectrum for waves of phase speed c and wavenumber k. The modal equations are

$$(\rho_0 \phi_z)_z + \rho_0 \left[\frac{N^2}{c^2} - k^2 \right] \phi = 0, \quad 0 \leq z \leq h, \tag{6a}$$

$$\phi = 0, \quad z = 0, h. \tag{6b}$$

Here the modal function is $\phi(z)$, $\rho_0(z)$ is the basic density field, $N^2(z) = -g\rho_{0z}/\rho_0$ is the buoyancy frequency, and the fluid occupies a channel of height h. In the long–wave limit $k \to 0$, these define an infinite set of long–wave modes $f_n(z)$, with long–wave phase speeds c_n, $n = 1, 2, 3, \ldots$. In general, for $0 \le k \le \infty$, the modal problem (6a, b) defines an infinite set of dispersion curves (see Figure 1). For a given long–wave mode of mode number n (≥ 2), the resonant modes and wavenumbers are obtained from (6a, b) by fixing $c = c_n$ and solving for the wavenumbers k. There exist n real wavenumbers k_{n-1}, k_1, 0 with corresponding modal functions $\phi_{n-1}(z)$, $\ldots$, $\phi_1(z)$, $\phi_0(z)$ where we note that $\phi_0(z) = f_n(z)$. There also exist an infinite set of pure imaginary wavenumbers which represent evanescent disturbances and these need not be considered further.

It can then be shown that symmetric non–local internal solitary waves are given by, keeping only the significant dominant terms, and using a frame of reference in which the wave is stationary,

$$\psi \sim \epsilon a \operatorname{sech}^2(\epsilon\gamma x)\, f_n(z) + b \exp\left[-\frac{\pi k_{n-1}}{2\epsilon\gamma}\right] \sin(k_{n-1}|x| - \delta)\phi_{n-1}(z) \tag{7}$$

Here ψ is the stream function and ϵ is a small parameter defining the small–amplitude long–wave limit. The first term in (7) is the leading term in an asymptotic expansion in powers of ϵ^2 which defines the solitary wave core. The amplitude a of the solitary wave is proportional to γ^2 by a well–known formula involving integrals of $f_n(z)$ (Benney, 1966), while the speed of the solitary wave is asymptotically given by $c_n + \epsilon^2 v$ where v is likewise proportional to γ^2. The second term in (7) is the leading term in the exponentially small tail oscillation for the resonance with mode $n - 1$. There are similar but exponentially smaller terms corresponding to resonances with modes $n - 2, \ldots 1$. The amplitude b and phase δ are related by $b \cos\delta = C_{n-1}$ where C_{n-1} is a numerical constant. Thus (7) defines a two–parameter family of non–local solitary waves with parameters γ and δ. There is an obvious similarity with the non–local solitary wave solution (5) of the singularly perturbed KdV equation (3).

§3. A model system

A conceptual model for non–local internal solitary waves is a coupled KdV–system. In the frame of reference of a wave of speed c, this is

$$-cu + 3u^2 + u_{xx} + (pv_{xx} + quv + \tfrac{1}{2}rv^2) = 0, \tag{8a}$$

$$-(c - \Delta)v + 3v^2 + v_{xx} + \lambda(pu_{xx} + ruv + \tfrac{1}{2}qu^2) = 0, \tag{8b}$$

Such systems have been derived by Gear and Grimshaw (1984) for strongly interacting internal wave modes, but here we shall regard the system (8a, b) as a qualitative model for an internal solitary wave (the u–mode) interacting resonantly with sinusoidal waves (the v–mode). The system is energy–conserving with energy density $\frac{1}{2}\lambda u^2 + \frac{1}{2}v^2$ and for linear stability we choose $\lambda > 0$. It is convenient to regard λ as a coupling parameter, and for $\lambda = 0$ the linear spectrum has two modes, $c = -k^2$ (the u–mode) and $c = \Delta - k^2$ (the v–mode). Without loss of generality we choose $\Delta > 0$ so that there is a potential resonance between a long–wave u–mode, and a short–wave v–mode of wavenumber $k = k_0 = \Delta^{\frac{1}{2}}$. For $0 < \lambda p^2 < 1$ the spectrum has the same qualitative features and the resonant wavenumber $k_0 = \{\Delta/(1 - \lambda p^2)\}^{\frac{1}{2}}$. Interestingly,

for $\lambda p^2 > 1$ there is no resonance for the u–mode, and presumably there is then a local solitary wave solution for this mode.

First we consider small–amplitude long waves and show that the u–mode solitary wave is non–local with an oscillatory tail of v–mode sinusoidal waves. We shall confine our attention here to symmetric waves. The asymptotic expansion for the solitary wave core (u_s, v_s) is given by

$$u_s \sim \epsilon^2 u_0 + \epsilon^4 u_1 + \dots, \quad v_s \sim \epsilon^4 v_1 + \dots, \quad c \sim \epsilon^2 c_0 + \epsilon^4 c_1 + \dots, \tag{9a}$$

where

$$u_0 = 2\gamma^2 \operatorname{sech}^2 \epsilon\gamma x, \quad c_0 = 4\gamma^2, \tag{9b}$$

$$u_1 = \frac{\lambda}{\Delta}\left\{-\frac{p}{2}(2q - 5p)c_0 u_0 - \frac{1}{8}(q-6p)(q-10p)u_0^2\right\} \tag{9c}$$

$$v_1 = \frac{\lambda}{\Delta}\left\{-pc_0 u_0 - \frac{1}{2}(q-6p)u_0^2\right\} \tag{9d}$$

Here ϵ is a small parameter characterizing the solitary wave amplitude. This expansion can be continued in powers of ϵ^2 without any oscillatory tail being detected. This is because these tails are exponentially small with respect to ϵ and hence cannot be found by expansions of the form (9a). To find the tail oscillations we observe that $u_0, u_1 \dots$, and $v_1, \dots$, are singular in the complex x–plane at $x = \pm i\pi/2\epsilon\gamma$, $\pm 3i\pi/2\epsilon\gamma, \dots$, and this motivates us to consider the solution structure near these points. Thus let

$$x = \frac{i\pi}{2\epsilon\gamma} + z, \tag{10}$$

so that as $|\epsilon z| \to 0$

$$u_s \sim -\frac{2}{z^2} - \frac{\lambda}{2\Delta z^4}(q-6p)(q-10p) + \dots + 0(\epsilon^2), \tag{11a}$$

$$v_s \sim -\frac{2\lambda}{\Delta z^4}(q-6p) + \dots + 0(\epsilon^2). \tag{11b}$$

Next we consider the inner problem in which u and v are functions of the complex variable z through the transformation (10). The equations are then just (8a, b) with x replaced by z, and we note that c is $0(\epsilon^2)$ and so to leading order the terms proportional to c may be omitted. The inner problem is to be solved with the matching condition that (u, v) are given by (11a, b) as $|z| \to \infty$ in $Re\ z \geq 0$, $Im\ z < 0$, and the symmetry condition that $Im\ (u, v) = 0$ on $Re\ z = 0$. We seek a solution in the form of a Laplace transform

$$(u, v) = \int_\Gamma \exp(-zs)(U(s), V(s))ds \tag{12}$$

where the contour Γ runs from 0 to ∞ in the half–plane $Re\,(zs) > 0$. A solution is then sought in the form

$$(U, V) = \sum_1^\infty (a_n, b_n)s^{2n-1} \tag{13}$$

Here $a_1 = -2$, $b_1 = 0$ and more generally substitution of (13) into (12) and term–by–term evaluation shows that as $|z| \to \infty$

$$(u, v) \sim \sum_1^\infty (u_n, v_n)z^{-2n} \tag{14}$$

where $(u_n\ ,\ v_n) = (2n-1)!(a_n\ ,\ b_n)$. It is readily verified that (14) agrees with the matching condition (11a, b) and in effect the Laplace transform (12) is a Borel–summation of the asymptotic series (11a, b). Further, substitution of (12) and (13) into the equations (8a, b) shows that as $n \to \infty$, $a_n \sim -pK(-k_0)^{-2n}$ $b_n \sim K(-k_0)^{-2n}$ so that the series (13) converge only for $|s| < 1$. Here we recall that k_0 is the resonant wavenumber $\{\Delta/(1-\lambda p^2)\}^{\frac{1}{2}}$ and K is a numerical constant whose exact value depends on λ , p , q and r . It follows that $(U\ ,\ V)$ have a pole singularity near $s = ik_0$, where

$$(U\ ,\ V) \approx \frac{(p\ ,\ -1)K}{2(s - ik_0)}. \tag{15}$$

The contour Γ must now be chosen to avoid the imaginary s–axis, and to be explicit we choose Γ to lie in $Re\ s > 0$. Also the expression (12) cannot satisfy the symmetry condition and must be amended by the addition of a sub–dominant term so that

$$(u\ ,\ v) \sim \int_\Gamma \exp(-zs)(U(s),\ V(s))ds + \tfrac{1}{2}ib(-p\ ,\ 1)\exp(-ik_0 z + i\delta)\ . \tag{16}$$

Here b , δ are real constants to be determined, and we note that $|\exp(-ik_0 z)|$ is smaller than any power of z^{-2n} as $|z| \to \infty$ in $Re\ z \geq 0$, $Im\ z < 0$. The symmetry condition is now applied by deforming Γ to the axis $Re\ s = 0$, and deforming the contour around the pole at $s = ik_0$. We find that

$$b\cos\delta = \pi K\ . \tag{17}$$

The final step is to bring the solution (16) back to the real x–axis using (10). Taking account of a corresponding singularity at $x = -i\pi/2\epsilon\gamma$ we get, in $x \geq 0$,

$$(u,\ v) \sim (u_s,\ v_s) + b(-p,\ 1)\ \exp(-(\pi k_0/2\epsilon\gamma)\sin(k_0 x - \delta) \tag{18}$$

where we recall that $(u_s\ ,\ v_s)$ are given by (9a, b) and define the solitary wave core. Note the similarity of this expression with the result (7) for internal solitary waves obtained by Akylas and Grimshaw (1992).

§4. Algebraic tail oscillations

The analysis of §3 was for small–amplitude long waves and we showed that the tail oscillations are then exponentially small with respect to a parameter characterizing the small–amplitude solitary wave core. Here we show that when the solitary wave core is of finite–amplitude the tail oscillations are algebraically small with respect to the coupling parameter λ . Suppose then that $0 < \lambda << 1$, and put

$$(u\ ,\ v) \sim \sum_0^\infty (u_n\ ,\ v_n)\lambda^n\ , \qquad c \sim \sum_0^\infty c_n \lambda^n \tag{19}$$

It is readily seen that

$$(u\ ,\ v) = (2\beta^2\mathrm{sech}^2\beta x\ .\ 0)\ ,\ c_0 = 4\beta^2\ , \tag{20}$$

corresponding to a u–mode solitary wave. Note that in comparison to (9a, b) $\beta = \epsilon\gamma$. Substitution of (19) into (9a) shows that

$$-c_0 u_1 + 6u_0 u_1 + u_{1xx} + pv_{1xx} + qu_0 v_1 - c_1 u_0 = 0\ , \tag{20a}$$

$$(c_0 - \Delta)v_1 + v_{1xx} + (pu_{0xx} + \tfrac{1}{2}qu_0^2) = 0\,, \tag{20b}$$

The general solution for v_1 is

$$v_1 = A\sin k_0 x + B\cos k_0 x - \frac{1}{2k_0}\int_{-\infty}^{\infty} f(x')\sin k_0|x-x'|\,dx', \tag{21a}$$

where

$$f(x) = pu_{0xx} + \tfrac{1}{2}qu_0^2\,. \tag{21b}$$

Here, recalling that $0 < \lambda << 1$, the resonant wavenumber $k_0 = (\Delta - c_0)^{\frac{1}{2}}$ and we note that we must now assume that $0 < c_0 < \Delta$. If $c_0 > \Delta$ then there are no tail oscillations. To determine the constants A, B we impose a symmetry condition on v_1, and then find that, as $|x| \to \infty$

$$v_1 \sim b_1 \sin(k_0|x| - \delta)\,, \tag{22a}$$

where

$$b_1\cos\delta = L = -\frac{1}{2k_0}\int_{-\infty}^{\infty} f(x)\cos k_0 x\,dx \tag{22b}$$

Next, with v_1 determined we can similarly solve (20a) for u_1, and find that, as $|x| \to \infty$,

$$u_1 \sim -\alpha b_1 \frac{(\Delta - c_0)}{\Delta}\sin(k_0|x| - \delta)\,. \tag{23}$$

Note that the tail oscillations again form a 1–parameter family with the phase δ being the free parameter, and the amplitude b then given by (22b). But in contrast to the results of §3 the amplitude of the tail oscillations is now $0(\lambda)$ when β is finite, and hence only algebraically small.

It is interesting now to consider the limit $\beta \to 0$ in (22b); that is, we put $\beta = \epsilon\gamma$ and let $\epsilon \to 0$. The solitary wave core (20) then agrees with (9a, b) as expected. However,

$$L = -\frac{\beta^2}{6k_0}\{k_0^2(q-6p) + 4\beta^2 q)\}\int_{-\infty}^{\infty}\mathrm{sech}^2\beta x\cos k_0 x\,dx\,, \tag{24a}$$

and so

$$L \sim -\frac{\pi k_0^2}{6}(q-6p)\exp(-\pi k_0/2\epsilon\gamma)\,. \tag{24b}$$

Although, on combining (24b) with (22a, b), we see that the tail oscillations are now exponentially small as $\epsilon \to 0$, and the form of the expressions (22a) and (23) agree with (18), the constant L does not in general agree with K. The reason is that in the limit $\epsilon \to 0$ all terms in the solitary wave core expansion (u_s, v_s) are needed to calculate the tail oscillation amplitude, and a technique such as the Borel–summation method described in §3 is needed.

References

T.R. Akylas and R.H.J. Grimshaw, 1993: "Solitary internal waves with oscillatory tails", J. Fluid Mech., **242**, 279–298.

C.J. Amick and K. Kirchgässner, 1989: "A theory of solitary waves in the presence of surface tension", Arch. Rat. Mech. Anal., **105**, 1–49.

J.T. Beale, 1991: "Exact solitary water waves with capillary waves at infinity", Comm. Pure Appl. Maths., **44**, 211–247.

E.S. Benilov, R. Grimshaw and E.P. Kuznetsova, 1993: "The generation of radiating waves in a singularly perturbed Korteweg–de Vries equation", Physica D., **169**, 270–278.

D.J. Benney, 1966: "Long nonlinear waves in fluid flows", J. Maths. & Phys., **45**, 52–63.

J.P. Boyd, 1989: "Weakly nonlocal solitary waves", in Mesoscale/Synoptic Coherent Structures in Geophysical Turbulence, ed J.C.J. Nihoul and B.M. Jamart, Elsevier, 103–112.

J.P. Boyd, 1990: "New directions in solitons and nonlinear periodic waves: polynoidal waves, imbricated solitons, weakly nonlocal solitary waves, and numerical boundary value algorithms", Adv. Appl. Mech., **27**, 1–82.

J.P. Boyd, 1991: "Weakly non–local solitons for capillary–gravity waves: fifth–degree Korteweg–de Vries equation", Physica D., **48**, 119–146.

F. Dias and G. Iooss, 1993: "Capillary–gravity waves with damped oscillations", Physica D., **65**, 399–423.

R. Grimshaw and N. Joshi, 1994: "Weakly non–local solitary waves in a singularly perturbed Korteweg–de Vries equation", SIAM J. Appl. Maths., (to appear).

J.K. Hunter and J–M. Vandenbroeck, 1983: "Solitary and periodic gravity–capillary waves of finite–amplitude", J. Fluid Mech., **134**, 205–219.

J.K. Hunter and J. Scheurle, 1988: "Existence of perturbed solitary wave solutions to a model equation for water waves", Physica D. **32**, 253–268.

G. Iooss and K. Kirchgässner, 1990: "Bifurcation d'ondes solitaires en présence d'une faible tension superficielle", C.R. Acad. Sci. Paris, **311**, 265–268.

Y. Pomeau, A. Ramani and B. Grammaticus, 1988: "Structural stability of the Korteweg–de Vries solitons under a singular perturbation", Physica D., **31**, 127–134.

S.M. Sun, 1991: "Existence of a generalized solitary waves with positive Bond number smaller than 1/3", J. Math. Anal. Appl., **156**, 471–504.

J–M. Vandenbroeck, 1991: "Elevation solitary waves with surface tension", Phys. Fluids, **A3**, 2659–2663.

J–M. Vandenbroeck and F. Dias, 1992: "Gravity–capillary solitary waves in water of infinite depth and related flows", J. Fluid Mech., **240**, 549–577.

J–M. Vandenbroeck and R.E.L. Turner, 1992: "Long periodic internal waves", Phys. Fluids, **A4**, 1929–1935.

A numerical study of the three-dimensional internal waves excited in the flow of a stratified fluid

by Hideshi Hanazaki
National Institute for Environmental Studies,
Tsukuba, Ibaraki 305, Japan

Abstract

Three-dimensional flow of a linearly stratified Boussinesq fluid is studied numerically. The flow is assumed to be confined in a rectangular channel. Near resonance of the first vertical internal wave mode, it was found that the reflection of the internal wave at the side wall is *'abnormal'* in the sense that reflection angle is larger than the incident angle and a third wave perpendicular to the side wall is generated. The waves become straight crested(two-dimensional) as this third wave becomes longer. The whole mechanism is similar to the *'Mach reflection'* observed in the general stratified fluid in which the usual soitary waves are generated. In the case of the linearly stratified Boussinesq fluid, the abnormal reflection occurs even though the wave has a sinusoidal profile and not a $sech^2$ profile. This suggests that the abnormal reflections similar to the Mach reflection always occur when the wave amplitude is large enough, irrespective of the wave profile.

1 Introduction

It has been known by laboratory experiments that the three-dimensional upstream waves generated by an obstacle on a shallow water becomes two-dimensional with their crests perpendicular to the side wall of the channel. As an explanation for this phenomenon, 'Mach reflection' (Miles, 1977a,b) has been proposed (Ertekin, 1984; Pedersen, 1988). Similar two-dimensionalization occurs in the internal waves generated in the subcritical flow of a linearly stratified Boussinesq fluid (Hanazaki, 1989).

However, close examinations of those phenomena have not been done experimentally or numerically. In a recent paper Hanazaki (1994) showed that the upstream-advancing internal waves generated by an obstacle in a two-layer fluid becomes straight-crested because of the Mach reflection. In that case, the upstream wave-profile is similar to the $sech^2$ solitary wave even when the flow is subcritical and the theory by Miles (1977a,b) is qualitatively applicable irrespective of the flow is near resonance or subcritical. On the contrary, internal waves excited in the subcritical flow of a linearly stratified Boussinesq fluid have sinusoidal profiles and it was thought that the two-dimensionalization is the result of the diffference in the propagation speed of the lateral modes.

The remaining problem is to see what occurs in the near-resonant flow of a linearly stratified Boussinesq fluid, where the linear theory(dispersion relation) can not be applied.

For the same size of the obstacle, waves of larger amplitude are excited in this system, compared to those in the two-layer fluid. In a two-dimensional flow, similar difference exists and the nonlinearity of the wave is described only by the 'strongly' nonlinear equation (Grimshaw & Yi, 1991). We will see that the Mach reflection and the subsequent two-dimensionalization of the wave occur in this large-amlitude wave system.

2 Results

We have solved the Navier-Stokes equation with the Reynolds number 1000 based on the topography height. The linearly stratified Boussinesq fluid flows through a rectangular channel whose dimension is $80D \times 40D \times D(x \times y \times z)$. The number of grid points used for the finite-difference computation is $400 \times 80 \times 100(x \times y \times z)$. A circular topography is located on the bottom of the channel at $(x, y, z) = (0, 0, 0)$. It has a horizontal scale of radius $5D$ and has a height of $0.1D$. In this study, Froude number F is defined by $F = U/C_1 = \pi U/ND$, where C_1 is the phase (=group) velocity of the linear long wave of the first vertical mode ($n = 1$). (In the field of the linearly stratified Boussinesq fluid, inverse Froude number defined by $K = ND/\pi U$ is often used.) In this study the Froude number is varied between 0.9 and 1.4 (from slightly subcritical to supercritical).

In Figure 1, we show the time development of the amplitude$[A_1(X, Y, T)]$ of the first vertical internal wave mode when $F = 0.95$. Here, A_1 was calculated from the velocity in the x-direction assuming that the physical quantities such as the velocities are the sum of the contribution from the each vertical internal wave mode. Initially, at $Ut/D = 40$, the waves are curved backward. As time proceeds, the waves (especially the foremost waves) becomes gradually straight crested.

To see this mechanism more clearly, the corresponding contour is shown in Figure 2. At $Ut/D = 40$, the far-most end of the wave does not reach the side wall of the channel and the waves are strongly curved backwards. At $Ut/D = 80$, the far-most end of the wave reaches the side wall and the reflection begins there. We note here that the reflection angle is larger than the incident angle. We also note that the amplitude of the reflected wave is smaller than the incident wave. As time proceeds($Ut/D = 120, 160, 200$) there appears a third wave perpendicular to the side wall, whose length becomes monotonically larger with time. This makes the foremost wave straight-crested or 'two-dimensional.' As the third wave propagates upstream, the incident angle becomes smaller, but the reflection angle is always larger than the incident angle.

The mechanism is quite similar to the 'Mach reflection' observed in the two-layer fluid (Hanazaki, 1994), where the waves of $sech^2$-profile are generated. In the present case, a phenomenon similar to Mach reflection occurs even when the waves are sinusoidal and the Miles' theory for the solitary waves can not be applied. This means that the phenomenon similar to the Mach reflection occurs not only for the solitary wave of $sech^2$ profile but also for the other large-amplitude wave systems.

To see if the same phenomenon occurs for other Froude numbers, we show in Figure 3 the contour of $A_1(X, Y, T)$ at $Ut/D = 200$ for various Froude numbers. We see that it occurs for all the other near-resonant Froude numbers ($F = 0.9, 1.0, 1.1$). Reflected waves are much weaker than the incident waves and the reflection angle is always larger than the incident angle. On the contrary, when $F = 1.4$(supercritical), the reflection angle coincides with the incident angle. The amplitude of the reflected wave is large and almost

equal to the amplitude of the incident wave. These show that the reflection in this case is the 'normal' reflection. We see no upstream-moving of the Mach stem in this case.

3 Conclusion

We found that the abnormal reflection similar to the Mach reflection occurs also in the near-resonant flow of a linearly stratified Bousssinesq fluid, where only the sinusoidal waves are generated. The abnormal reflection makes the foremost wave straight crested or 'two-dimensional.' This suggests that the abnormal reflection occurs always when large-amplitude waves are generated, irrespective of the wave profile. Further theoretical studies might be necessary to clarify the mechanism of this phenomenon.

4 References

Ertekin, R. C. 1984 Soliton generation by moving disturbances in shallow water: Theory, computation and experiment. PhD dissertation, University of California, Berkeley.

Grimshaw, R. & Yi, Z. 1991 Resonant generation of finite-amplitude waves by the flow of a uniformly stratified fluid over topography. *J.Fluid Mech.* **229**, 603-628.

Hanazaki, H. 1989 Drag coefficient and upstream influence in three-dimensional stratified flow of finite depth. *Fluid Dyn. Res.* **4**, 317-332.

Hanazaki, H. 1994 On the three-dimensional internal waves excited by topography in the flow of a stratified fluid. *J.Fluid Mech.* **263**, 293-318.

Miles, J. W. 1977a Obliquely interacting solitary waves. *J.Fluid Mech.* **79**, 157-169.

Miles, J. W. 1977b Resonantly interacting solitary waves. *J.Fluid Mech.* **79**, 171-179.

Pedersen, G. 1988 Three-dimensional wave patterns generated by moving disturbances at transcritical speeds. *J.Fluid Mech.* **196**, 39-63.

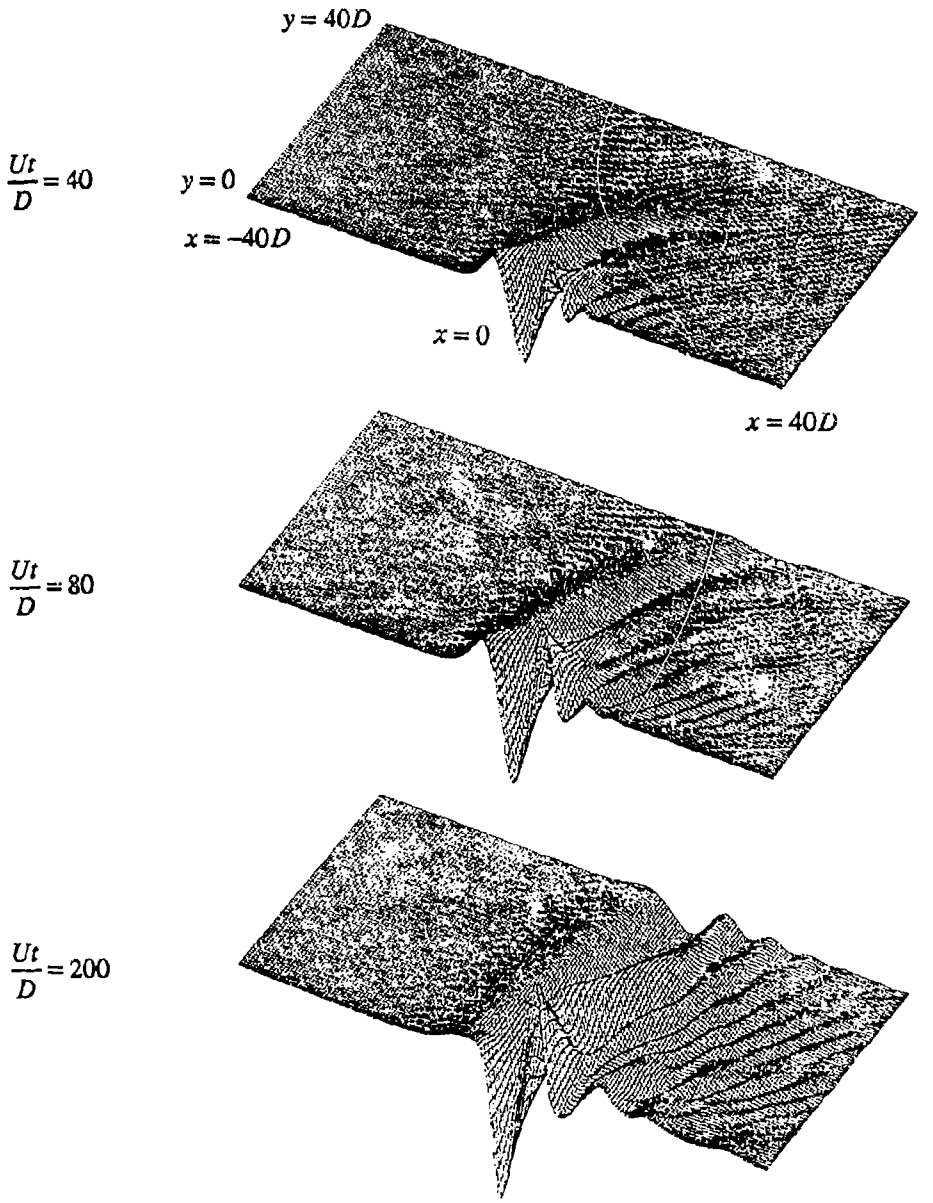


Figure 1. Time development of the first vertical mode (n=1) when F=0.95.

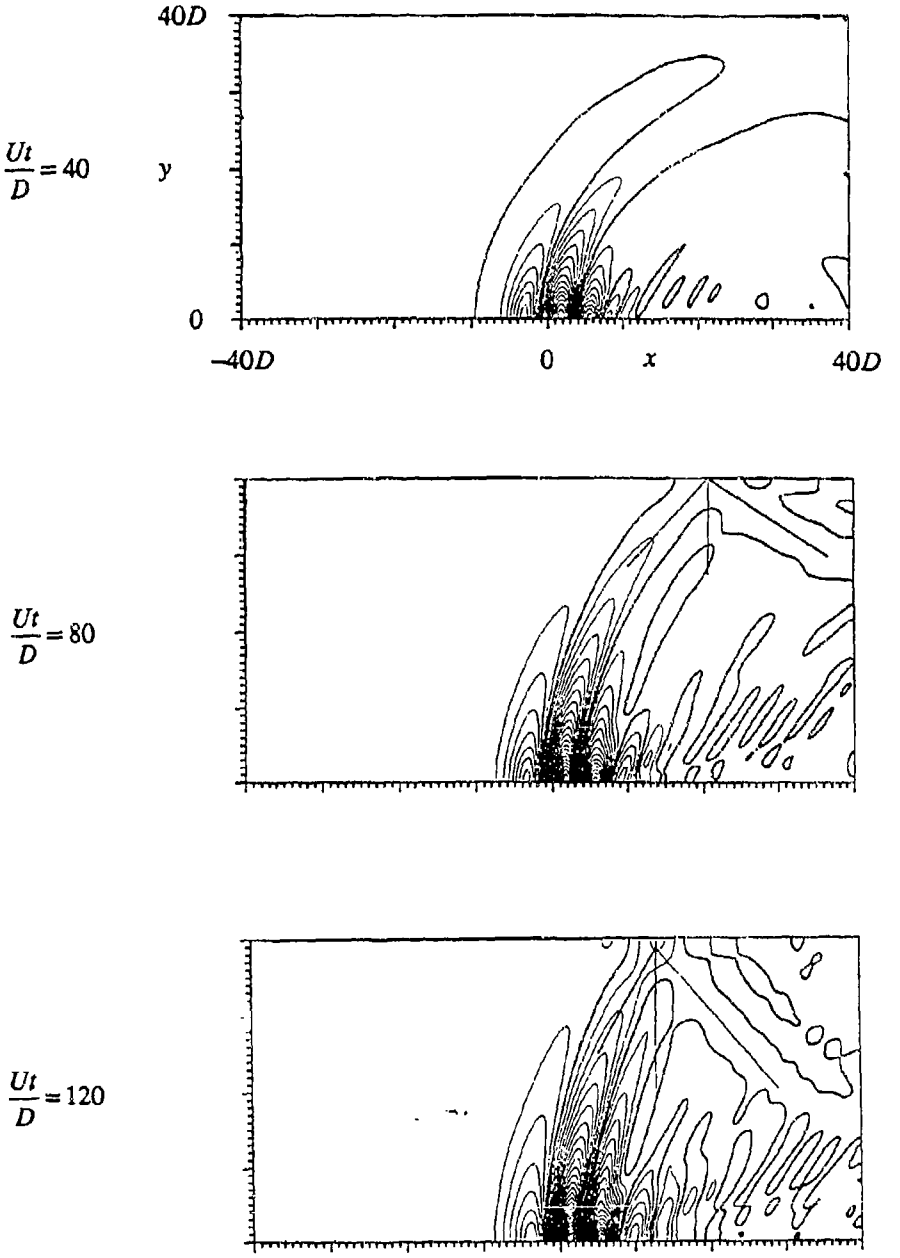


Figure 2. (to be continued. For caption see the next page.)

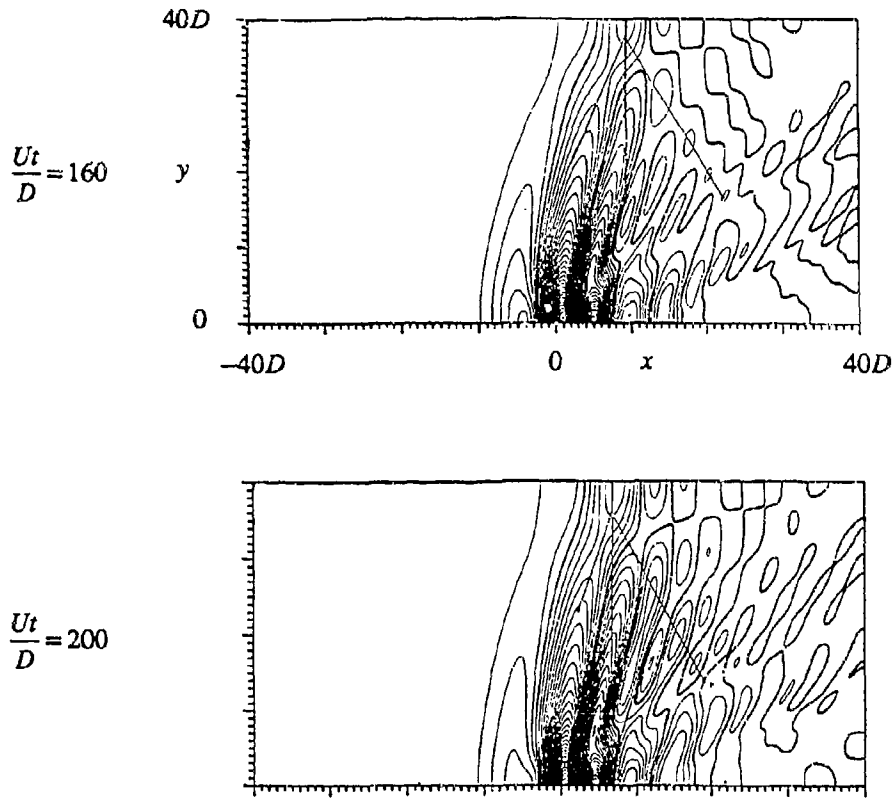
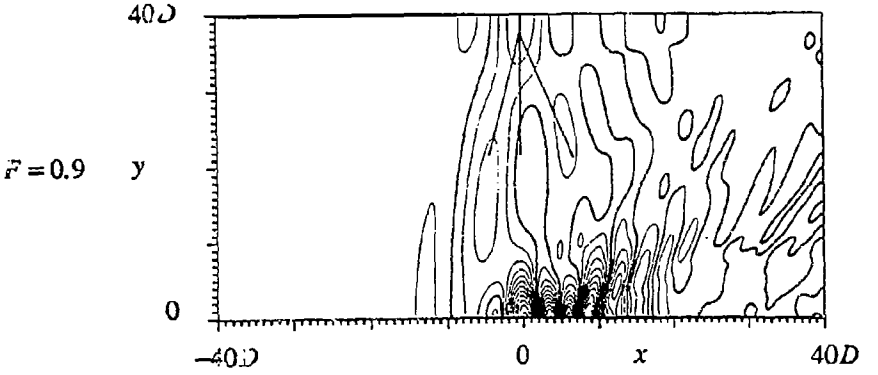


Figure 2. Time development of the contours of the first vertical mode (n=1) that corresponds to Figure 1 (F=0.95).



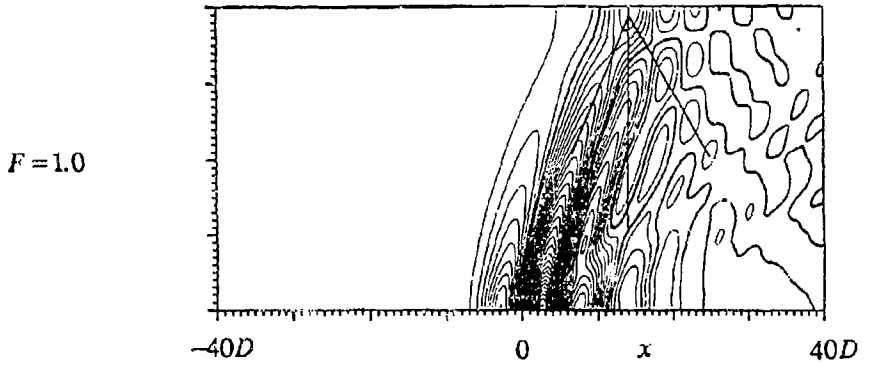
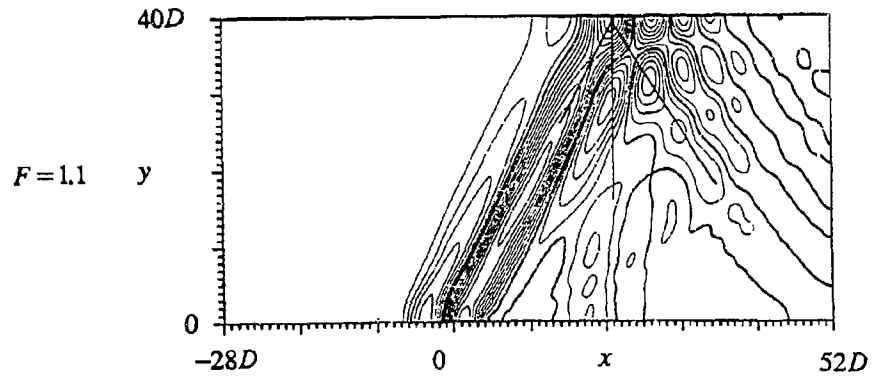


Figure 3. (to be continued. For caption see the next page.)



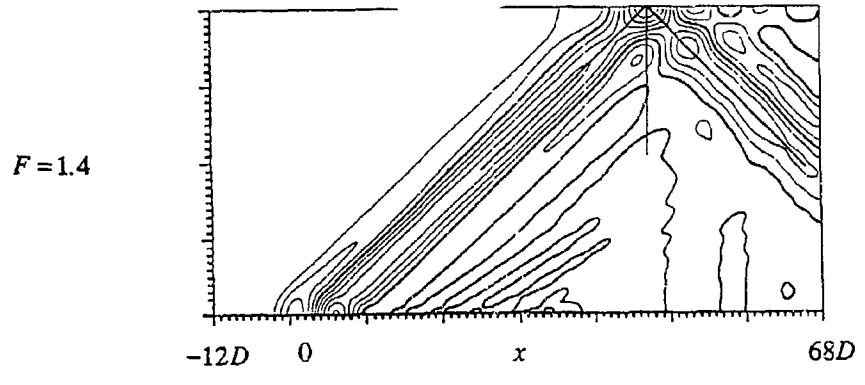


Figure 3. Contours of the first vertical mode (n=1) for various Froude numbers at time Ut/D=200.

Internal waves generated by a translating and oscillating sphere

PASCAL DUPONT* AND BRUNO VOISIN

LEGI/IMG, CNRS-UJF-INPG, BP 53, 38041 Grenoble Cedex 9, France

At high Reynolds and Froude numbers, lee waves due to the horizontal motion of a body in a stratified fluid are superseded by random waves generated by its wake. The origin of these waves lies in the buoyant collapse of the large-scale coherent structures of the wake, and can be modelled as a source moving at the velocity of the body and of strength oscillating at the frequency of vortex shedding. In the present paper two parallel studies of the associated wave field are described. The first of these is theoretical and considers localized and extended models of the source, while the second is experimental and involves a vertically oscillating and horizontally translating sphere. Oscillation frequencies both smaller and larger than the Brunt–Väisälä frequency are considered, and reasonably good agreement between theory and experiment is obtained concerning, e.g., the shape of the surfaces of constant phase, the streamwise evolution of the wavelength, and the domain of existence of the waves. Calculations are then presented for a realistic turbulent wake, and comparison with available experimental results is performed.

1. Introduction

A body moving horizontally in a stratified fluid generates several systems of internal waves, each of which is associated with a distinct perturbation of the basic stratification. In this respect, the important parameters are the Froude number $Fr = U/Na$, which represents the ratio of inertial forces to buoyancy forces, and the Reynolds number $Re = Ul/\nu$, which represents the ratio of inertial forces to viscous forces, with U the velocity of the body, a its transverse radius, l its axial length, N the Brunt–Väisälä frequency and ν the kinematic viscosity. In particular, experiments over the past twenty years (Lin & Pao 1979; Gilreath & Brandt 1985; Hopfinger *et al.* 1991; Bonneton *et al.* 1993; Lin *et al.* 1993) have shown that, at sufficiently high Fr and Re, lee waves generated by the motion of the body are superseded by random waves generated by its wake, and have traced back the origin of these waves to the large-scale coherent structures of the wake.

The modelling of this phenomenon was discussed by Voisin (1994*b*). In the Reynolds and Froude numbers range involved, the wake is turbulent and develops initially as in a homogeneous fluid. Coherent structures, in the form of vortex loops or turbulent bursts, are released periodically behind the body at the frequency ω_0 of the near wake spiral instability; after a dimensionless time $Nt_c \approx 3$ they collapse impulsively under the influence of buoyancy, generating internal waves. As far as these waves are concerned, a

* also at SPEA/GMEI/CNRM, Météo-France, 42 avenue Coriolis, 31057 Toulouse Cedex, France

turbulent wake is thus amenable to a series of impulses, of alternating signs so as to take into account its geometry, periodically spaced in both space and time, and separated from one another by a distance $\pi U/\omega_0$ and time π/ω_0. Two equivalent views of this series arise naturally: a source moving at velocity U and emitting impulses at time intervals π/ω_0; a source moving at velocity U and of strength oscillating at the frequency ω_0 and at all its odd harmonics. The first view is appropriate at small axial distances from the body, when the waves generated by each collapse have not yet had time to interfere; then each impulse can be considered individually. Conversely, the second view is appropriate at large axial distances, when interference has taken place; then the collective effect of all the impulses is observed, resulting in a predominance of the fundamental frequency ω_0.

A first step towards assessment of this interpretation was carried out by Bonneton *et al.* (1993), who studied each coherent structure individually. The present paper investigates the second, collective, aspect. Specifically, § 2 describes a theoretical approach of internal waves generated by the simplest practical realisation of a horizontally translating source of oscillatory strength, i.e., a sphere both translating horizontally and oscillating vertically. Then § 3 compares the results of this theory with experiments, and § 4 applies them to a realistic turbulent wake.

2. Theoretical background

2.1. Source model

In a homogeneous fluid, a sphere of radius a moving at velocity $\mathbf{u}_0(t)$ along a path $\mathbf{x}_0(t)$, with $\mathbf{u}_0(t) = \mathrm{d}\mathbf{x}_0/\mathrm{d}t$, can be modelled either approximately, for $R \gg a$, as the dipole

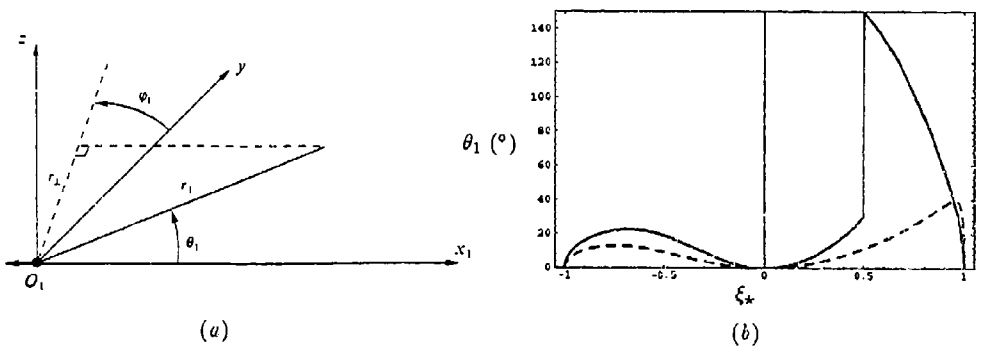
$$m_\mathrm{d}(\mathbf{x}, t) = -2\pi a^3 \mathbf{u}_0 \cdot \nabla\delta(\mathbf{X}), \tag{1}$$

or exactly, for all R/a, as the surface distribution of sources

$$m_\mathrm{s}(\mathbf{x}, t) = \frac{3}{2}\mathbf{u}_0 \cdot \frac{\mathbf{X}}{a}\delta(R - a), \tag{2}$$

where $\mathbf{x} = [x, y, z]$ denotes position, with $r = |\mathbf{x}|$, t denotes time, $\mathbf{X} = \mathbf{x} - \mathbf{x}_0$ is the position relative to the centre of the sphere, $\mathbf{u} = [u, v, w]$ the fluid velocity and $m = \nabla \cdot \mathbf{u}$ the source strength (rate of volume outflow from the source). Use of these models in a stratified fluid was introduced by Miles (1971) and Gorodtsov & Teodorovich (1982), respectively, on the assumption that the Froude number be large, so that the flow around the sphere is locally unaffected by gravity. Experiments suggest, however, that these models remain valid even for moderate values of Fr, the only difference being the replacement of the far-field condition $R \gg a$ by the compactness condition $a \ll \lambda$, with λ the wavelength of the waves (see, e.g., Voisin 1994*a*). Another approximation implicit in (1) and (2) is that the Reynolds number Re be moderate, so that no wake is formed.

In the system of coordinates shown in figure 1*a*, of origin O_1 equal to the mean position of the centre of the sphere, x_1-axis horizontal and directed opposite to the mean motion, and vertical z-axis, a motion composed of horizontal translation at velocity U and vertical oscillation of frequency ω_0 and amplitude h corresponds to the path $\mathbf{x}_0(t) = -Ut\mathbf{e}_x -$



(*a*) (*b*)

FIGURE 1. Determination of the wave field of a horizontally translating source of oscillatory strength; (*a*) system of coordinates and (*b*) graphical solution of equation (8) for the parameter $\xi_* = \xi/|\sin\varphi_1|$, for (——) $\Upsilon/|\sin\varphi_1| = 0.5$ and (---) $\Upsilon/|\sin\varphi_1| = 1.2$.

$h\sin(\omega_0 t)\mathbf{e}_z$, where $\mathbf{e}_x$ and $\mathbf{e}_z$ are unit vectors along the x_1- and z-axes, respectively. Small oscillations $h \ll a$ can be neglected in the position of the source but not in its velocity, so that (1) and (2) become

$$m_{\mathrm{d}}(\mathbf{x},t) = 2\pi a^3 \left[U\frac{\partial}{\partial x} + h\omega_0\cos(\omega_0 t)\frac{\partial}{\partial z}\right]\delta(x_1)\delta(y)\delta(z), \tag{3}$$

$$m_{\mathrm{s}}(\mathbf{x},t) = -\frac{3}{2}\left[U\frac{x_1}{a} + h\omega_0\cos(\omega_0 t)\frac{z}{a}\right]\delta(r_1 - a). \tag{4}$$

This approximation is straightforward for the surface source; for the dipole it follows from remarking that $m_{\mathrm{s}}(\mathbf{x},t)$ is asymptotic to $m_{\mathrm{d}}(\mathbf{x},t)$ in the limit of large wavelengths $\lambda \gg a$, as can be seen by comparing their spectra

$$m_{\mathrm{d}}(\mathbf{k},t) = -2\mathrm{i}\pi a^3[Uk + h\omega_0\cos(\omega_0 t)m], \tag{5}$$

$$m_{\mathrm{s}}(\mathbf{k},t) = -6\mathrm{i}\pi a^3[Uk + h\omega_0\cos(\omega_0 t)m]\frac{j_1(\kappa a)}{\kappa a}, \tag{6}$$

defined by

$$m(\mathbf{x},t) = \frac{1}{(2\pi)^3}\int m(\mathbf{k},t)\mathrm{e}^{-\mathrm{i}\mathbf{k}\cdot\mathbf{x}}\,\mathrm{d}^3\mathbf{k}, \tag{7}$$

where $\mathbf{k} = [k,l,m]$ is the wavenumber vector, with $\kappa = |\mathbf{k}| = 2\pi/\lambda$, and $j_1(z) = (\sin z)/z^2 - (\cos z)/z$ is the spherical Bessel function of order 1.

The sphere can thus be modelled as the linear superposition of two sources, both in uniform horizontal motion, and whose strengths are constant and oscillatory, respectively. For oscillation velocities $h\omega_0$ large compared with the translation velocity U the second component becomes large compared with the first component (i.e., lee waves); in what follows this is only the situation that we shall consider and lee waves will accordingly be omitted. In terms of the dimensionless parameters introduced, e.g., by Davies *et al.* (1994), we have: moderate Reynolds number $Re = 2Ua/\nu$, large Froude number $Fr = U/Na$, small Keulegan–Carpenter number $Ke = h/a$ and large velocity ratio $h\omega_0/U$.

2.2. Wave field

Internal waves generated by the uniform horizontal motion of a source of oscillatory strength have been studied both theoretically (Stevenson & Thomas 1969; Redekopp 1975; Rehm & Radt 1975; Peat & Stevenson 1975) and experimentally (Stevenson & Thomas 1969; Peat & Stevenson 1975; Davies *et al.* 1994). Emphasis was on the determination of the surfaces of constant phase. Here we adopt the approach exposed in Voisin (1994*a*), in which the amplitude and the phase are obtained jointly.

Waves are ruled by the frequency ratio $\Upsilon = \omega_0/N$, and are expressed in terms of the auxiliary variable ξ, which in spherical coordinates $(r_1, \theta_1, \varphi_1)$ (see figure 1*a*) satisfies the equation

$$\tan\theta_1 = \frac{\xi^2(\sin^2\varphi_1 - \xi^2)^{\frac{1}{2}}}{\Upsilon\sin^2\varphi_1 - \xi^3}\,\mathrm{sgn}(\Upsilon - \xi), \tag{8}$$

subject to the condition $|\xi| < |\sin\varphi_1|$. The solution of this equation defines two systems of waves, sum waves with positive ξ and difference waves with negative ξ, each of which system is itself separated into transverse and divergent components. Both systems are contained within wavefronts, parts of which are caustics, and which correspond to the maxima or jumps $(\Xi_\pm, \Theta_\pm)$ observed in figure 1*b*. The analytical expression of $\Xi_\pm$ and $\Theta_\pm$ was given in Voisin (1994*a*) and will not be repeated here. For each wave system the divergent and transverse components merge on the caustic; associated ranges of ξ are $-|\sin\varphi_1| < \xi < \Xi_-$ for divergent difference waves, $\Xi_- < \xi < 0$ for transverse difference waves, $0 < \xi < \Xi_+$ for transverse sum waves and $\Xi_+ < \xi < |\sin\varphi_1|$ for divergent sum waves.

The name of those components refers to the shape of their horizontal curves of constant phase, shown in figure 2*a*. For $\Upsilon > 1$ difference waves are upstream facing and sum waves downstream facing; both of them have cusps on the caustic where divergent and transverse waves meet, and extend only downstream. For $\Upsilon < 1$ difference waves and transverse sum waves remain essentially unchanged, while divergent sum waves, starting up from the caustic, tend towards infinity downstream as $|y| \to |z|(1-\Upsilon^2)^{\frac{1}{2}}/\Upsilon$, come then back towards regions of smaller x_1 and finally extend upstream.

The derivation of the characteristics of the waves is straightforward and yields, for the frequency and wavenumber vector,

$$\omega = N\xi, \qquad \mathrm{k} = \frac{N}{U}\left[\Upsilon - \xi, \xi\frac{|\Upsilon - \xi|\cos\varphi_1}{(\sin^2\varphi_1 - \xi^2)^{\frac{1}{2}}}, -\frac{1-\xi^2}{\xi}\frac{|\Upsilon - \xi|\sin\varphi_1}{(\sin^2\varphi_1 - \xi^2)^{\frac{1}{2}}}\right]. \tag{9}$$

The vertical displacement ζ, related to the vertical velocity w by $w = \partial\zeta/\partial t$, follows similarly from replacing in Voisin (1994*a*) the monopolar moment m_0 of the source by the spectrum $m(\mathrm{k}, t)$. The resulting expressions, combining (5), (6) and (9), fail to describe the vicinity of the caustics, where they diverge; a more elaborate description of this vicinity, involving Airy functions (Lighthill 1978, § 4.11), was not attempted.

3. Sphere experiments

Experiments were conducted in a transparent tank 50 cm wide, 50 cm deep and 400 cm long. A heavy sphere of radius 1.12 cm was towed horizontally through a linearly strati-

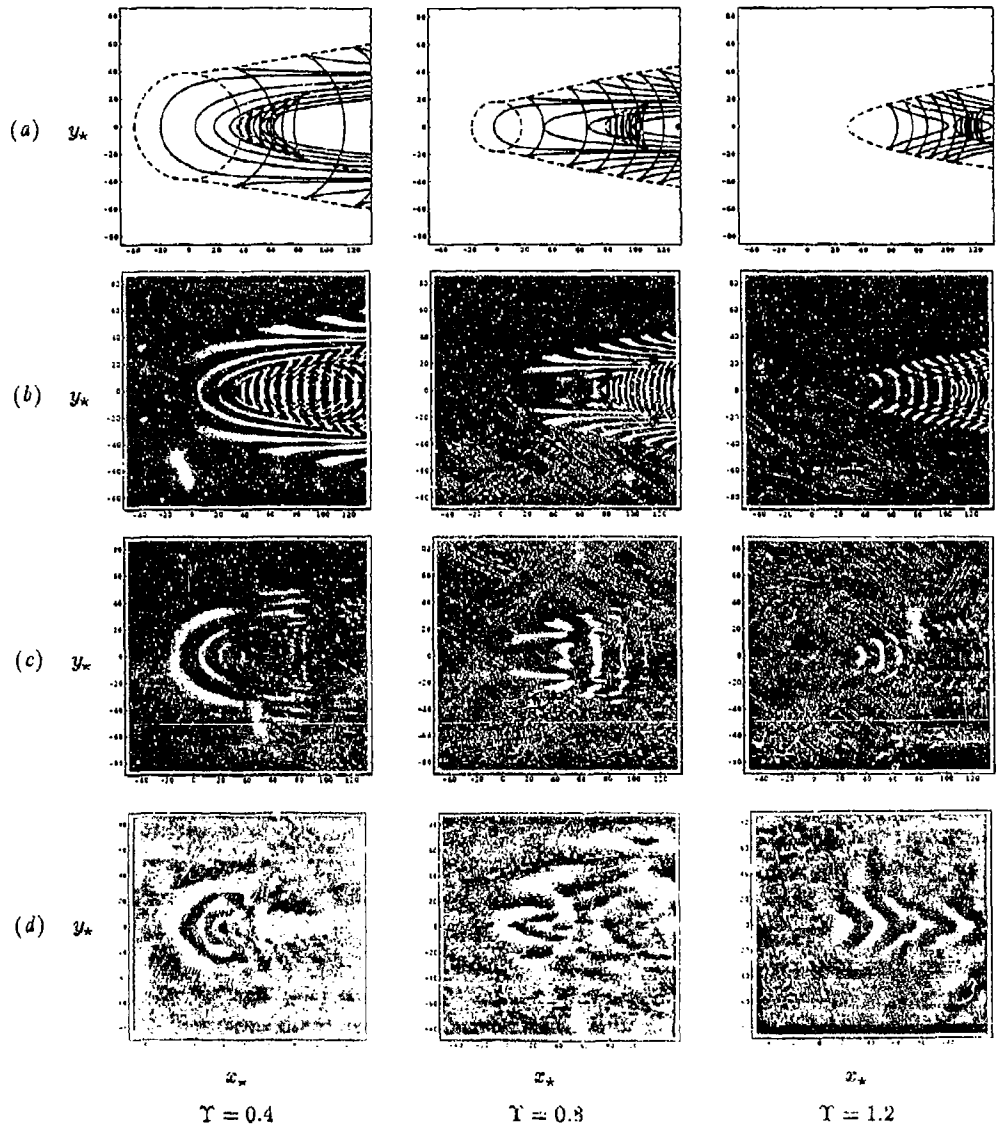


FIGURE 2. Vertical displacement field generated by horizontal translation of a vertically oscillating sphere, for $\Upsilon = 0.4$, 0.8 and 1.2, with $Fr = 0.25$ and $Ke = 0.6$. Dimensionless coordinates $\mathbf{x}_* = N\mathbf{x}/U$ are used, with $z_* = 24$ (except for $\Upsilon = 0.4$, in which case $z_* = 17$). (*a*) shows (——) the first few lines of constant phase of each wave system and (- - -) the associated wavefronts; for $\Upsilon < 1$ these fronts comprise a circle, whose upstream and downstream halves correspond to divergent and transverse sum waves, respectively. The theoretical displacement field is shown in (*b*) for the dipole and in (*c*) for the surface source, while (*d*) is the experimental visualization; gray scale units are arbitrary.

fied fluid, a vertical sinusoidal oscillation being superimposed on the uniform horizontal translation of the support of the sphere. The towing and visualization techniques were identical to those used by Bonneton *et al.* (1993). Five frequency ratios $\Upsilon = 0.4$, 0.6, 0.8, 1.01 and 1.2, both smaller and larger than 1, were selected. Other parameters were chosen so that three of the four conditions mentioned in § 2.1 be satisfied: moderate Reynolds number, small Keulegan–Carpenter number, large velocity ratio. The Froude number was then fixed by experimental requirements.

Experimental results are summarized in figure 2. Two factors appear to distort them significantly: the presence of lee waves, easily recognized by their hyperbolic curves of constant phase, and the reflection of the waves on the walls of the tank. Lee waves are all the more pronounced as Υ is small, since the velocity ratio $h\omega_0/U = \Upsilon Ke/Fr$ is, for given Fr and Ke, proportional to Υ. For a discussion of the effects and occurrence of tank wall reflections the reader is referred to Graham & Graham (1980).

The first conclusion to be drawn from figure 2 is the inadequacy of the dipolar representation (3) of the sphere, since the displacement field shown in figure 2*b* is dominated by high-amplitude difference waves which are absent from experiments. The reason for this lies in the compactness condition $a \ll \lambda$, which is not satisfied by the short difference waves. Alternatively, this can be explained by remarking that the dipolar spectrum (5) varies as κa, overemphasizing the contribution of large wavenumbers, while the surface source spectrum (6) varies as $j_1(\kappa a)$ and is thus a maximum at $\kappa a \approx 2$ (Abramowitz & Stegun 1972, ch. 10). Only the surface source model can thus be expected to yield satisfactory agreement with experiments.

This agreement is first qualitative, and concerns the structure of the wave field. As shown in figure 2*d*, divergent sum waves are dominant for $\Upsilon = 0.4$; as Υ increases and reaches 0.8 transverse sum waves appear at some distance downstream, and finally for $\Upsilon = 1.2$ they supersede divergent waves in the vicinity of the sphere. This results from the combination of several factors: position of the wavefronts $\theta_1 = \Theta$ within which each wave system is found; amplitude associated with these systems in the spectrum $m(\mathbf{k}, t)$ of the source; restrictions imposed on the domain of observation of the waves by the presence of lee waves and by tank wall reflections. These arguments can be made quantitative, e.g., by plotting the function $j_1(\kappa a)$ as a function of x_1 for $y = 0$ (not shown here). As Υ increases from 0.4 to 1.2, zones of rapid phase variations (nay inversions) appear near the caustics. This is attributable to an interference between transverse and divergent sum waves, of similar wavelengths in that zone.

The evolution of the wavefronts with Υ, i.e., their narrowing as Υ increases, is confirmed by experiment. Their position is difficult to determine because of the perturbation of the wave field by the lee waves and by the wall reflections. For relatively small x_1, however, this perturbation is negligible, and the theoretical and experimental wavefronts differ by a lateral distance of the same order as the diameter of the sphere. A possible explanation for this is the diffraction of the waves outside the caustics, a phenomenon not taken into account in the formulae used to compute the theoretical wave field.

More quantitatively, figure 3*a* compares, for $\Upsilon = 0.6$, the theoretical and experimental values of the axial wavelength $\lambda_x = 2\pi/|k|$ in the plane $y = 0$, measured from several images similar to figure 2*d*. The number of experimental runs compensates for the relatively poor precision of the method. Good agreement is obtained with the interpretation

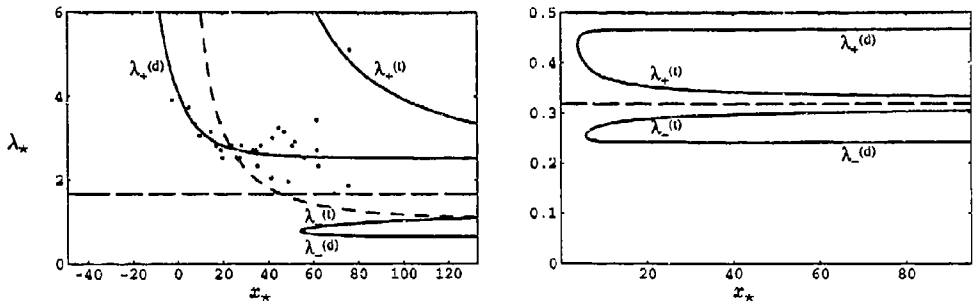


FIGURE 3. Dimensionless axial wavelength $\lambda_* = (N\lambda_x)/(2\pi U)$ versus dimensionless downstream distance x_* in the plane $y = 0$, for (a) $\Upsilon = 0.6$ and $z_* = 24$ and (b) $\Upsilon = \pi$ and $z_* = 0.6$; (——) theoretical curves, $(\cdot)$ experimental points, (– – –) lee wave length, (— —) spatial period of the source path.

of the wave field in terms of mainly divergent sum waves. As $Nx_1/U \to \infty$ we have for divergent difference waves, transverse waves and divergent sum waves, respectively,

$$\lambda_x \sim 2\pi \frac{U}{\omega_0} \left(\frac{1}{\Upsilon + 1}, 1, \frac{1}{|\Upsilon - 1|} \right), \tag{10}$$

indicating that the axial wavelength of transverse waves tends towards the spatial period $2\pi U/\omega_0$ of the path of the source. Figure $3a$ shows that this period is never observed in the wave field.

4. Wake application

Application of the preceding analysis to a realistic stratified turbulent wake, created by horizontal motion at velocity U' of a body of transverse radius a' and axial length l', supposes that the various parameters arising in this analysis be expressed in terms of those associated with the wake. According to the discusion of § 1, the velocity U and frequency ω_0 of the source equivalent to the wake are identical to the velocity U' of the body and to the frequency ω_0' of the near wake spiral instability. Similarly, the radius a of this source represents in some phenomenological way the radius of the coherent structures before their collapse, and will be assumed to be of the same order as the radius a' of the body. The amplitude h of the oscillations is just a device to reproduce experimentally a source of oscillatory strength and, as this strength, depends on the precise dynamics of the collapse. Hereafter these approximations will be used and primes will be omitted.

The main conclusion of §§ 2 and 3 was the strong dependence of the wave field on the frequency ratio $\Upsilon = \omega_0/N$, which can be expressed in terms of the Strouhal number $St = a\omega_0/\pi U$ as $\Upsilon = \pi StFr$. In the Reynolds and Froude numbers range considered in the literature, the Strouhal number is 0.2 for towed bodies and 1.0 for self-propelled bodies (see, e.g., Voisin 1994*b*). A sphere towed at a Froude number $Fr = 5$ corresponds thus to $\Upsilon = \pi$, value that we adopted in figures $3b$ and 4 to compute the axial wavelength

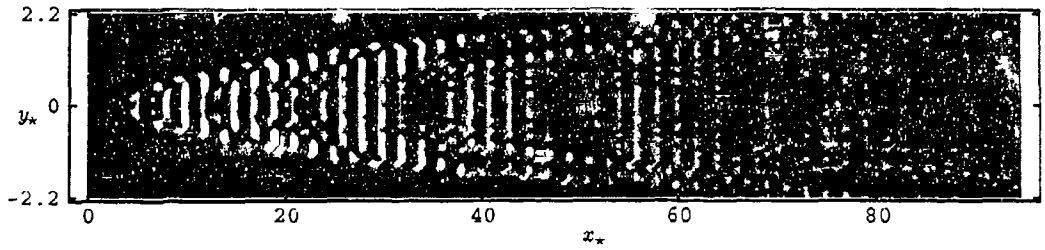


FIGURE 4. Vertical displacement field generated by uniform horizontal translation of a vertically oscillating sphere, for $\Upsilon = \pi$, $Fr = 5$ and $z_* = 0.6$.

and vertical displacement field, respectively; these are to be compared with figures 8 and 9 of Bonneton *et al.* (1993).

Comparison between the theoretical and experimental wavefronts has already been successfully performed by Gilreath & Brandt (1985) and Bonneton *et al.* (1993) and will not be repeated here. As this wavefront is passed all waves are observed nearly simultaneously, with axial wavelengths close to one another and tending rapidly towards the asymptotic values (10), which themselves do not differ much from the spatial period $2\pi U/\omega_0$ of the wake. Then, consistently with Hopfinger *et al.* (1991), Bonneton *et al.* (1993) and Lin *et al.* (1993), a régime is reached in which the wavelength is independent of the Froude number and identical to the mean spacing of the coherent structures, which in terms of the diameter $2a$ of the body means $\lambda_x/2a \sim St^{-1} \approx 5$.

It is tempting to associate this régime with the coherent wave régime reported by Bonneton *et al.* (1993) and already distinguishable in the results of Hopfinger *et al.* (1991). In particular, $\lambda_x/2a$ is roughly of the same order as the wavelength of the first coherent waves identified by Bonneton *et al.* (1993). However, the associated wave field, shown in figure 4, exhibits a very complicated phase structure resulting from the interference between the four wave systems, and differs from the more or less organized structure observed by Hopfinger *et al.* (1991) and Bonneton *et al.* (1993). This makes the present interpretation just tentative.

We finally point out that the analysis exposed in the present paper relies entirely on the assumption that advection of the coherent structures before the collapse is negligible, so that the process of emission of the waves is impulsive. There may, however, be situations where advection is significant before the collapse. Then each structure generates not an impulsive wave field but a lee wave field, as reported by Sysoeva & Chashechkin (1991) for a towed sphere and by Dupont & Kadri (1994) for a bell-shaped obstacle.

The authors gratefully acknowledge the advice and guidance of Prof. E. J. Hopfinger. Experiments were carried out by one of the authors (P. D.) during a one-year stay within the SPEA team of the Centre National de Recherches Météorologiques; thanks to all of them for their kindness and invaluable help.

References

ABRAMOWITZ, M. & STEGUN, I. A. (eds.) 1972 *Handbook of Mathematical Functions.* Dover.

BONNETON, P., CHOMAZ, J.-M. & HOPFINGER, E. J. 1993 Internal waves produced by the turbulent wake of a sphere moving horizontally in a stratified fluid. *J. Fluid Mech.* **254**, 23–40.

DAVIES, P. A., BOYER, D. L., FERNANDO, H. J. S. & ZHANG, X. 1994 On the periodic motion of a circular cylinder through a linearly stratified fluid. *Phil. Trans. R. Soc. Lond.* A **345**, 353-386.

DUPONT, P. & KADRI, Y. 1994 Internal gravity waves generated by advected coherent structures of the wake of a mountain. (in preparation).

GILREATH, H. E. & BRANDT, A. 1985 Experiments on the generation of internal waves in a stratified fluid. *AIAA J.* **23**, 693–700.

GORODTSOV, V. A. & TEODOROVICH, E. V. 1982 Study of internal waves in the case of rapid horizontal motion of cylinders and spheres. *Fluid Dyn.* **17**, 893–898.

GRAHAM, E. W. & GRAHAM, B. B. 1980 The tank wall effect on internal waves due to a transient vertical force moving at fixed depth in a density-stratified fluid. *J. Fluid Mech.* **97**, 91–114.

HOPFINGER, E. J., FLOR, J.-B., CHOMAZ, J.-M. & BONNETON, P. 1991 Internal waves generated by a moving sphere and its wake in a stratified fluid. *Exp. Fluids* **11**, 255–261.

LIGHTHILL, M. J. 1978 *Waves in Fluids.* Cambridge University Press.

LIN, J.-T. & PAO, Y.-H. 1979 Wakes in stratified fluids. *Ann. Rev. Fluid Mech.* **11**, 317–338.

LIN, Q., BOYER, D. L. & FERNANDO, H. J. S. 1993 Internal waves generated by the turbulent wake of a sphere. *Exp. Fluids* **15**, 147–154.

MILES, J. W. 1971 Internal waves generated by a horizontally moving source. *Geophys. Fluid Dyn.* **2**, 63–87.

PEAT, K. S. & STEVENSON, T. N. 1975 Internal waves around a body moving in a compressible density-stratified fluid. *J. Fluid Mech.* **70**, 673–688.

REDEKOPP, L. G. 1975 Wave patterns generated by disturbances travelling horizontally in rotating stratified fluids. *Geophys. Fluid Dyn.* **6**, 289–313.

REHM, R. G. & RADT, H. S. 1975 Internal waves generated by a translating oscillating body. *J. Fluid Mech.* **68**, 235–258.

STEVENSON, T. N. & THOMAS, N. H. 1969 Two-dimensional internal waves generated by a travelling oscillating cylinder. *J. Fluid Mech.* **36**, 505–511.

SYSOEVA, E. YA. & CHASCHECHKIN, YU. D. 1991 Vortex systems in the stratified wake of a sphere. *Fluid Dyn.* **26**, 544–551.

VOISIN, B. 1994*a* Internal wave generation in uniformly stratified fluids. Part 2. Moving point sources. *J. Fluid Mech.* **261**, 333–374.

VOISIN, B. 1994*b* Internal wave generation by turbulent wakes. In *Proc. Meeting-Workshop on Mixing in Geophysical Flows, Effects of Body Forces in Turbulent Flows, Barcelona, December 16–18, 1992* (in press).

NON-LINEAR INTERNAL GRAVITY WAVES: THE LOCAL AND THE GLOBAL VIEW OF THE PHASE-SPACE

V. Zeitlin

IPSL-LMD, B.P.99,Université P. et M. Curie, 4, pl. Jussieu, 75252 Paris Cedex 05, France

...

Abstract

The dynamics of a stratified fluid is studied in the Boussinesq approximation. The 2-d case of one vertical and one horizontal dimensions is taken, being a situation encountered in a number of theoretical and experimental studies. The resulting dynamical system describing non-linear internal gravity waves or, in other words, the internal wave - vortex interactions has a peculiarity of having an infinity of integrals of motion constraining the initial dynamical variables. It is shown that this is a reflection of a deep geometric nature of the system. This latter is used 1) to eliminate perturbatively the constraints and to arrive to a set of the proper dynamical variables neccessary for a weak turbulence approach; 2) to formulate a variational principle and to study a global stability of the system.

Introduction

Stratified fluid in the Boussinesq approximation provides a conceptually and practically important example of the wave - vortex intraction. Indeed, the internal gravity (buyoancy) waves dominate in the limit of small perturbations, while in the opposite limit we have a system of vortices that advects density. The parameter which controls dynamical behaviour of the system is the Brunt -Väisälä frequency $N = -g\frac{dlog\rho_0}{dy}$, where $\rho_0(y)$ is the background density stratification in the vertical direction and will be taken to be exponential (a constant N) for simplicity. In terms of vorticity (ω) and buyoancy ($\xi = -g\frac{\rho-\rho_0}{\rho_0}$, g - gravity acceleration) variables the system of dynamical equations restricted to the vertical $x-y$ plane takes the following form:

$$\dot{\omega} + J(\omega,\psi) + \xi_x = 0, \;\; \dot{\xi} + J(\xi,\psi) - N^2\psi_x = 0\,. \qquad (1)$$

Here J denotes the Jacobian in x, y variables, ψ is the stream-function. It easy to see that in the case of strong stratification ($N \to \infty$) one can use a perturbation theory to study non-linear corrections to the regime of freely propagating internal gravity waves. Thus this system is a natural candidate for a weak-turbulence approach [1] and indeed, certain attempts in this direction (see, for example, [2]) have been undertaken. However, the problem is that the dynamics governed by (1) possesses a peculiar property of having an infinity of integrals of motion. Namely, there are two infinite families of conserved quantities: any function of $\xi - N^2y$ integrated over the domain of the flow is conserved itself as well as being weighted with vorticity:

$$I_{F,G} = \int [F(\xi - N^2y) + \omega G(\xi - N^2y)]dxdy \qquad (2)$$

The physical origin of these conserved quantities is the advection of density in the Boussinesq approximation. From the mathematical viewpoint they are so-called Casimirs and reflect the fact that the original system may be treated as a generalized Euler equation related to some infinite-dimensional Lie algebra [3] and thus preserves all the invariants of the corresponding symmetry group action.The presence of an infinity of integrals means that the original dynamical variables ω and ξ are severely constrained

and in order to avoid the problem of the compatibility of these constraints with standard statistical assumptions of the weak turbulence approach it would be better to work from the very beginning with the variables which are free of constraints. In order to find these variables we need to understand better the above- mentioned symmetry transformations. Their study will be the subject of the first part of the paper and will allow us to find explicitely the unconstrained variables. The analysis of this part is essentially perturbative, i.e. local. The second part of the paper contains the global analysis in the sense that it allows to study a behaviour of trajectories of the dynamical system in terms of quasi-Lagrangian variables still provided by the aforementioned geometric background.

The local description of the phase-space

Consider the following transformation of the dynamical variables:

$$\delta\omega = J(\chi,\omega) + J(\lambda,\xi) - N^2\lambda_x, \quad \delta\xi = J(\chi,\xi) - N^2\chi_x\,, \tag{3}$$

where χ, λ are some infinitesimal functional parameters. It is easy to check that these transformations leave the Casimirs (2) invarant. Now, the presence of the Casimirs means that the time evolution of our dynamical system (1) takes place not in the whole space of original variables ω , ξ but rather on the surface of constant Casimirs embedded into this latter. This means that the original phase-space is foliated into a family of these surfaces. The fact that the transformations (3) do not change the Casimirs means that any such surface is a *symmetric* manifold. In fact, it is a so-called co-adjoint orbit of the group of symmetry transformations given in their infinitesimal version by (3). Any point of such a manifold may be reached by a finite group transformation from any other point. This means that by applying all possible symmetry transformations to some fixed initial point one obtains the whole manifold which gives a possibility to get unconstrained dynamical variables: they are the co-ordinates on this symmetric manifold - the parameters of symmetry transformations applyed to some given initial point in the phase space ω_0, ξ_0. Hence, what we need is an explicit form of the finite

transformation corresponding to (3). It has been found in [3], [8] and has the following form:

$$\omega(x,y) = \omega_0(X,Y) - J(\Lambda, \xi_0(X,Y) - N^2 Y)\ ,\ \ \xi(x,y) = \xi_0(X,Y) - N^2(Y-y). \quad (4)$$

Here X, Y are related to the original coordinates by an area-preserving change of variables $J(X,Y) = 1$, $\Lambda(x,y)$ is an arbitrary function. We see that the transformation of buyoancy variable is closely related to the fact that the combination $\xi - N^2 y$ - a "total buyoancy" is being simply advected (cf. (1)) while the transformation of vorticity is more complicated being a combination of the advection and adjustment due to buyoancy. Thus, we are close to our goal, the last obstacle being the incompressibility constraint $J(X,Y) = 1$, otherwise the (Lagrangian) variables X, Y and the additional function Λ would solve the problem. Unfortunately, as it is well-known, there is no way to get rid of the incompressibility constraint for arbitrary area-preserving change of variables. However this may be done perturbatively for special orbits (i.e. for special choice of Casimirs' values). Namely, taking the orbit corresponding to $\xi_0 = 0$ we reduce (4) to

$$\omega(x,y) = \omega_0(X,Y) + J(\Lambda, N^2 Y)\ ,\ \ \xi(x,y) = -N^2(Y-y). \quad (5)$$

Then, we note that for area-preserving changes of variables not far from identity we may use a generating function which solves explicitely the incompressibility constraint:

$$X = x + S_Y(x,Y) \quad , Y = y - S_x(x,Y)\ . \quad (6)$$

Introducing this into (5) we get

$$\omega(x,y) = \omega_0(x+S_Y(x,Y), y - S_x(x,Y)) + J(\Lambda, N^2 y - S_x(x,Y))\ ,\ \ \xi(x,y) = N^2 S_x(x,Y). \quad (7)$$

In fact, the nonlinearity of this transformation has become infinitely high since instead of Y one has to introduce $y - S_x(x,Y)$ as an argument of S everywhere in (7) in a nested way. To cope with this non-polynomial behavior we shall make use of the smallness of N^{-1}, i.e. we hereafter suppose that stratification is strong. Introducing a scaled variable $\zeta = N^2 S_x$ we can solve perturbatively the second equation in (5) and

get

$$\xi(x,y) = \zeta + \sum_{n=1}^{\infty} \frac{1}{(n+1)!}(-N^2)^{-n}\frac{\partial^n \zeta^{n+1}}{\partial y^n} = \zeta + N^{-2}\zeta\zeta_y + O(N^{-4}). \qquad (8)$$

The condition $\xi_0 = 0$ means that our system has no closed isolines of total buyoancy and the perturbative use of generating function supposes that there are only small deviations from this regime. We may further simplify our system by fixing $\omega_0 = 0$. This means (still assuming the validity of generating function description) that only small fluctuations around the vortexless state are possible during the dynamical evolution. This regime is fully compatible with the picture of weakly non- linear buyoancy waves. Thus, rescaling the variable $N^2\Lambda = \sigma$ we have:

$$\omega = \sigma + N^{-2}J(\sigma,\zeta) + O(N^4) \qquad (9)$$

Hence, we have got explicit expressions for old variables in terms of new unconstrained ones ζ and σ. By introducing them into original system (1) we get a system of dynamical equations in terms of these variables and may therefore apply a standard philosophy of weak turbulence without worrying about compatibility with constraints. Note that although we can always come back to original dynamical variables and original equations (1) the fact that the new variables and the old ones are related non-linearly means that applying Gaussian statistics to the new variables results in a non-Gaussian one for the original variables.

The global picture of the phase-space

Let us consider in more detail the origin of the Casimir invariants. To do this we need to remind some facts related to the abstract Euler equation. Given an arbitrary Lie algebra g (which may be thought of as, for example, some matrix algebra in the finite-dimensional case or an algebra of differential operators in the infinite-dimensional case) wi' 'ructure relations

$$[e_A, e_B] = C^C_{AB}e_C,\ e_A \in g, A = 1,2,\dots, \qquad (10)$$

where the vectors e_A form a basis in g, C^C_{AB} are structure constants and summation over repeated indices is assumed hereafter, we may define a (non-degenerate) metric

$$< e_A, e_B > = g_{AB} \tag{11}$$

i.e. a mapping from the vector space g to its dual g^*. Therefore for any element $\omega \in g^*$ given by its coordinates $\omega_A, A = 1, 2, ...$ we may construct the following equation which is called an abstract Euler equation:

$$\dot{\omega}_A + g^{BC} C^D_{AB} \omega_D \omega_C = 0, \tag{12}$$

here g^{BC} is the inverse of g_{BC}. Eq. (12) is an equation for a variable that belongs to the linear space g^* . The (infinitesimal) action of the Lie group related to (10) is defined in g^*:

$$\delta\omega_A = C^D_{AB} \omega_D \chi^B \tag{13}$$

where χ^B is a set of parameters. This action is called a co-adjoint action and a manifold obtained by applying (exponentials of) all possible transformations (13) is a co-adjoint orbit. As it is easily seen, a dynamical evolution (12) is, in fact, a co-adjoint action of the group and, hence, preserves any invariant of this action (a Casimir invariant) $C(\omega)$:

$$\frac{\partial C}{\partial \omega_A} C^D_{AB} \omega_D = 0. \tag{14}$$

The crucial fact is that the abstract Euler equation (12) is equivalent [4] to the geodesic equation on the Lie group (if it exists) corresponding to the Lie algebra g. The latter is a tangent space to this group at the vicinity of the identity element and a metric defined on g may be transported to any point of the group manifold by the (right) group action. In this way the group as a whole acquires a Riemannian structure, eq. (12) being a geodesic equation written at the vicinity of unity. Let us remind the corresponding formulas for the covariant derivative [4]:

$$\begin{aligned} \nabla_{e_A} e_B &\equiv \nabla_A e_B = \Gamma^C_{AB} e_C; \\ \Gamma^C_{AE} &= \frac{1}{2}(C^C_{AB} - g^{CD} C^E_{AD}\, g_{EB} - g^{CD} C^E_{BD}\, g_{EA}), \end{aligned} \tag{15}$$

here Γ^C_{AB} are the coefficients of a symmetric connection compatible with the metric. The components of the curvature tensor are:

$$R_{KLMN} = - < \nabla_K \nabla_L e_M - \nabla_L \nabla_K e_M - \nabla_{[e_K, e_L]} e_M, e_N > \tag{16}$$

while the sectional curvature which enters the Jacobi equation for geodesic variation and whose sign is responsible for the separation or convergence of neighbouring geodesics is given by

$$K(\xi, \eta) = R_{KLMN} \xi_K \eta_L \xi_M \eta_N, \tag{17}$$

where ξ and η are the tangent vector to the geodesic and a vector of geodesic deviation, respectively.

The basic infinite-dimensional example of this construction which was first treated in [4] is the Lie algebra (and the Lie group, respectively) of area-preserving diffeomorphisms. For periodic boundary conditions the elements e_n may be realized as the differential operators

$$e_n = e^{in \cdot x} n \times \frac{\partial}{\partial x}, \tag{18}$$

where n and x are 2-d vectors, n denoting Fourier-indices: $n \equiv (n_1, n_2)$, $x \equiv (x_1, x_2)$ and $\times$ denotes the skew product: $n \times m \equiv n_1 m_2 - n_2 m_1$. This gives

$$[e_n, e_m] = n \times m \, e_{n+m}. \tag{19}$$

Taking the inverse Laplacian in Fourier-space as a metric

$$g_{nm} = n^{-2} \delta(n + m) \tag{20}$$

and structure constants following from (19) one reproduces the equation of vorticity advection in 2-d ideal hydrodynamics [5].

In order to relate this construction to the stratified fluid equations (1) we have to make some extension of the original algebra (19) which is called a semi- direct product of symplectic diffeomorphisms and functions, a construction which has been repeatedly discussed in the literature [6], [7], [8]. It consists in adding to the e_n from (19) their commuting counterparts $e_{n'}$:

$$[e_{n'}, e_{m'}] = 0 \tag{21}$$

such that

$$[e_n, e_{m'}] = n \times m \, e_{(n+m)'}. \tag{22}$$

With e_n realized by (18), the $e_{n'}$ may be taken as the elements of a Fourier-basis for functions, $e_{n'} = e^{in'\cdot x}$ in order to reproduce (21), (22). While the variables ω_n related to e_n correspond as before to vorticity, the new variables, say $\xi_{n'}$, related to $e_{n'}$ appear. If the old metric, i.e. the inverse Laplacian, is preserved for the e_n-sector, and there are no mixed components: $g_{nm'} = 0$, the immediate consequence of (21), (22) is the advection of the variable $\xi(x)$:

$$\dot{\xi} + J(\xi, \psi) = 0 \tag{23}$$

while a term bilinear in ξ appears in the vorticity equation

$$\dot{\omega} + J(\omega, \psi) - J(\xi, \hat{M}\xi) = 0 \tag{24}$$

where we have introduced an operator $\hat{M}$ which is determined by the components $g_{m'n'}$ of the metric. There is a number of physically relevant equations resulting, with a proper choice of $\hat{M}$, from (23), (24) - e.g. 2-d MHD equations or equations for the axi-symmetric flows with swirl [9]. For our purposes it is sufficient to take $\hat{M} = 1$, in which case the additional term in the vorticity equation vanishes identically. There are no linear terms appearing in (1) in thus obtained equations so the next step is to further generalize the algebra (19), (21), (22) by means of a so called central extension. Indeed, one may add a term $in_1\delta(n + m')$ to the r.h.s. of (22) and have no contradiction with the Jacobi identity. This means that a new (unity) generator e_0 trivially commuting with all other ones may be added to g without destroying the Lie-algebraic structure. This means, in turn, that a new coordinate ω_0 should be added to $g*$. It is easy to see that it is trivially conserved and may be identified, after a proper rescaling, with N^{-1} in the resulting Euler equations (1).

Thus, we have shown that our basic dynamical equations indeed have a deep geometric nature and may be treated as geodesic equations on some infinite dimensional manifold. Note that in comparison with a geodesic interpretation of the pure hydrodynamics which is essentially the Lagrangian picture, here we have additional coordinates related to buyoancy (one may think about this latter as of the velocity component in

the third, auxiliary, direction) and to the new co-ordinate ω_0. The set of these co-ordinates gives a global picture of the phase-space and one may address the problem of global stability by estimating the divergence of the nearby trajectories (geodesics) in this global phase-space with the help of the Jacoby equation, i.e. by calculating sectional curvatures. Due to the presence of the symmetry group it is sufficient to calculate these latter in the vicinity of unity, i.e. according to (16). Knowing the structure constants and the metric we have all neccessary tools to do this. The detailed curvature calculation will be presented elsewhere, but we can expect that strong enough stratification will suppress the divergence of the neighbouring trajectories, playing the same stabilizing role as strong β in the case of non-linear Rossby waves dynamics [9].

Conclusions

We have shown that a stratified 2-dimensional fluid in the Boussinesq approximation has a geometric nature which manifests itself on the dynamical level by the presence of an infinity of the integrals of motion. The proper use of this geometric background allows one to find the proper unconstrained dynamical variables in the limit of strong stratification. From the other hand a global behaviour of the dynamical trajectories of the systems may be analyzed starting from the variational principle based on the same geodesic interpretation of the system.

References

[1] G. Falkovich, V.L'vov and V.E. Zakharov "Kolmogorov spectra of turbulence" Springer, 1993.

[2] E.N.Pelinovsky and M.A.Raevsky, Atm. Ocean Physics **13**, 187 (1977).

[3] V. Zeitlin, Phys.Letters A **164**, 177 (1992).

[4] V.I.Arnold, Ann. Inst. Fourier **16**, 319 (1966).

[5] V. Zeitlin, Physica D **49**, 353 (1991).

[6] D.Holm, J.E.Marsden, T.Ratiu, and A.Weinstein, Phys. Reports **123**, 1 (1985).

[7] B.A.Khesin and Yu.V.Chekanov, Physica D **40**, 119 (1989.

[8] V.Zeitlin, Journal of Phys.A **25**, L171 (1992).

[9] V.Zeitlin and R.Pasmanter "On the differential geometry aproach to geophysical flows" - to be published in Phys.Letters A

The structure of the turbulent wake and the random internal wave field generated by a moving sphere in a stratified fluid

By P. Bonneton[1], J.M. Chomaz[2], E. Hopfinger[3] and M. Perrier[4]

[1]IMFT, avenue du Professeur Camille Soula, 31400 Toulouse, France
[2]LADHYX, Ecole Polytechnique, 91128 Palaiseau-Cedex, France
[3]LEGI-IMG, BP 53, 38041 Grenoble-Cedex, France
[4]METEO-FRANCE, 42 avenue Coriolis, 31057 Toulouse, France

Abstract

We present experimental results on the structure of the turbulent wake of a sphere and on the frequencies associated with the vortex shedding in a stratified fluid. The strong correlation between the random internal wave field emitted by the wake and the coherent structures of the turbulent wake is demonstrated.

1. Introduction

In this paper probe measurements are presented which give novel information about the internal wave field and the turbulent wake generated by a moving sphere in a stratified fluid. It completes previous work, which dealt with the structure of the near wake (Chomaz et al. (1993)a, hereinafter referred to as CBH), the far wake (Chomaz et al. (1993)b) and the internal wave field (Bonneton et al. (1993), hereinafter referred to as BCH). In this paper we focus on the temporal evolution of the turbulent wake structure and its interactions with the random internal wave field.

Experiments were conducted in two different water towing tanks of respective sizes 0.5x0.5x4 m^3 and 1x3x20 m^3. These tanks were filled with a linear salt stratification $N \in [0.67, 2.02$ rad/s], $N=(-g/\rho\, d\rho/dt)^{1/2}$. Four spheres of radii R={1.12, 2.5, 3.6, 5.0 cm} were used in the experiments, and their velocities U ranged from 1 to 50 cm/s. The Froude number ($F=U/NR$) was varied between 0.8 and 12.7, and the Reynolds number ($Re=U(2R)/\nu$), between 380 and 30000. When, for a given stratification and a given sphere, the velocity is varied, the two dimensionless numbers F and Re vary together ; the linear relation is $Re(F)=Re(1)F$, where $Re(1)=2R^2N/\nu$ is the Reynolds number for F=1. In this paper, a set of experiments is characterized by its Re(1) value. The experimental methods have been presented in detail in CBH and BCH.

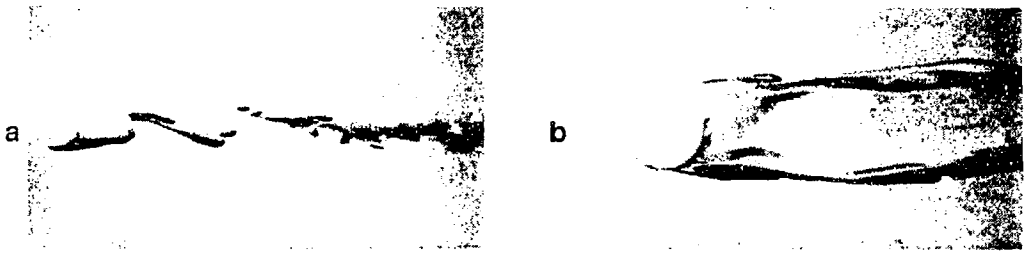


Figure 1. Fluorescent dye visualizations in (a) the vertical central plane, and (b) the horizontal central plane, for F=2.0 and Re(1)=329 (R=1.12 cm).

2. Wake instability

CBH showed that for F >4.5 (3D regime) the stratification has no effect on the close wake (Nt<3). Like in a homogeneous fluid a regular spiral instability occurs with a fixed Strouhal number of 0.17. On the opposite, for F<1.5 (SLW regime), the wake is dominated by a very strong lee wave of maximum amplitude R/2, which suppresses the wake instability. Between these two regimes, a more complex regime (T regime) exists, where the wake recovers progressively its behaviour in homogeneous fluid as F increases. Figure 1 shows that this instability does not correspond to a spiral instability but to a vertical oscillation. Lin et al. (1993) observe a symmetric vortex shedding because they used a shadowgraph technique which is not suited to analyse precisely the structure of three dimensional wakes. The shadowgraph picture integrates the information along each ray and the global symmetry of the picture they obtained does not imply that the wake is locally symmetric with respect to the median horizontal plane.

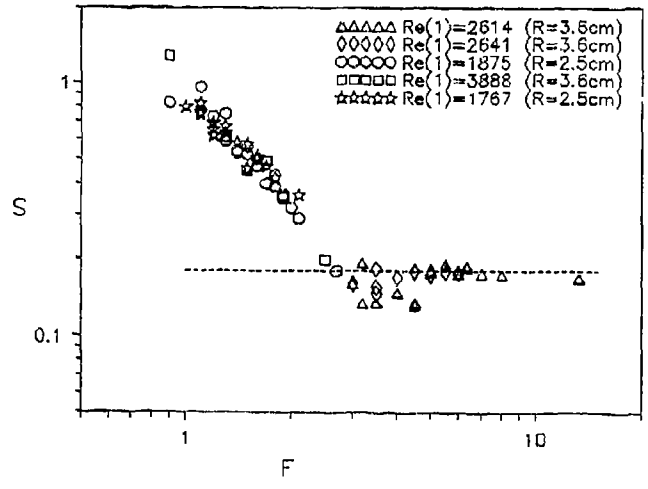


Figure 2. Strouhal number of low-frequency instabilities of the wake as a function of the Froude number, determined from spectral analysis of probe signals. The probe is located at z=0 and x=3R.

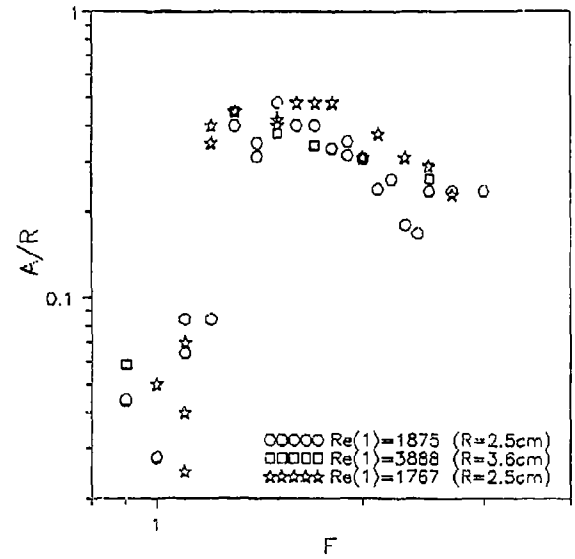


Figure 3. Instability amplitude A, normalised by R, as a function of F, measured with a conductivity probe at the location z=0 and x=3R.

New conductivity probe measurements have been carried out to complete the CBH's analysis of this regime. The Strouhal number (S=2fR/U) of the wake instabilities is plotted on figure 2 as a function of F. The oscillatory instability occurs for F=0.9 (SLW regime), but as indicated on figure 3, its amplitude is very small until F=1.2. Moreover, for F$\in$ [0.9,1.2], the instability is intermittent and very sensitive to perturbation, such as oscillations of the sphere at the start up. The oscillatory instability is strongly established for F>1.2 and its Strouhal number decreases like $1/F^{3/2}$ until F=3. The data dispersion for F$\in$ [3,4.5] is probably related to the transition between the oscillatory instability and the spiral instability. These instabilities do not depend on the Reynolds number, excepted for the critical Froude number F_c, at which the instability starts (see table 1), and contrary to Lin et al. 's (1992) analysis, can not be associated with Kelvin-Helmholtz instability.

Re(1)	3888	1875	329
F_c	0.8	0.9	1.4

Table 1. Critical Froude number for onset of oscillatory instability as a function of Re(1).

3. Turbulent wake structure

In this chapter we present results concerning the temporal evolution of turbulent wakes for T and 3D regimes. A single-electrode conductivity probe was pulled behind

the sphere at several locations behind the sphere. We made also some measurements of the vertical velocity w and the density ρ at the same location inside and outside the wake. Some results are reproduced from work by Thual et al. (1987).

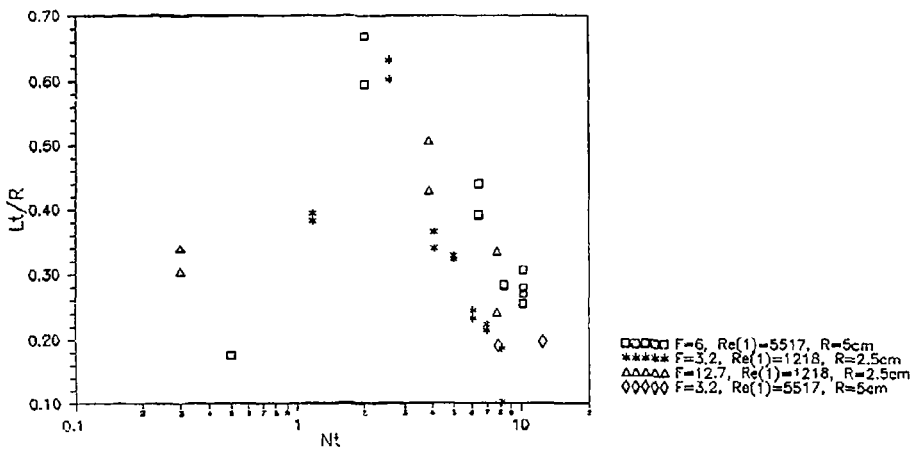


Figure 4. Overturning length scale normalised by R, as a function of Nt.

The overturning length scales $Lt = -2\langle \rho'^2 \rangle^{1/2}/(d\rho/dz)$, where ρ' is the density fluctuation, are plotted versus Nt in figure 4. Similar to what is observed in homogeneous turbulence, Lt increases first with time, until $Nt_c \approx 2.5$ and then starts to decrease. This transition corresponds to the maximum of the vertical wake thickness determined by Lin et al. (1992). For $Nt > Nt_c$, the wake feels the stratification effects and loses its axisymmetry. The decrease of Lt with time is indicative of the decrease of the amplitude of vertical motions which are progressively suppressed by stratification.

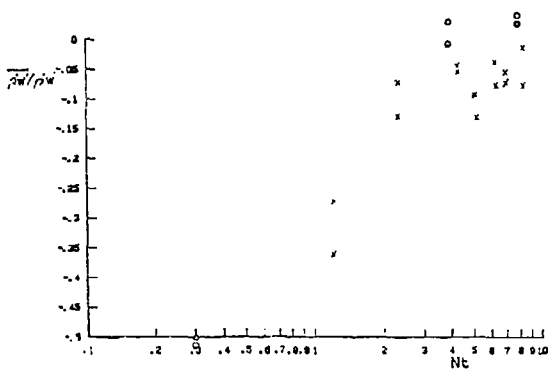


Figure 6. w' and ρ' correlation, as a function of Nt ; o, F=10/π ; x, F=40/π ; Re(1)=1218, R=2.5 cm and N=1.13 rad/s.

Figure 5 shows the temporal evolution of the co-spectrum and quad-spectrum of w' (the vertical velocity fluctuation) and ρ' , inside the wake (a,b,c,d,e,f,g) and outside

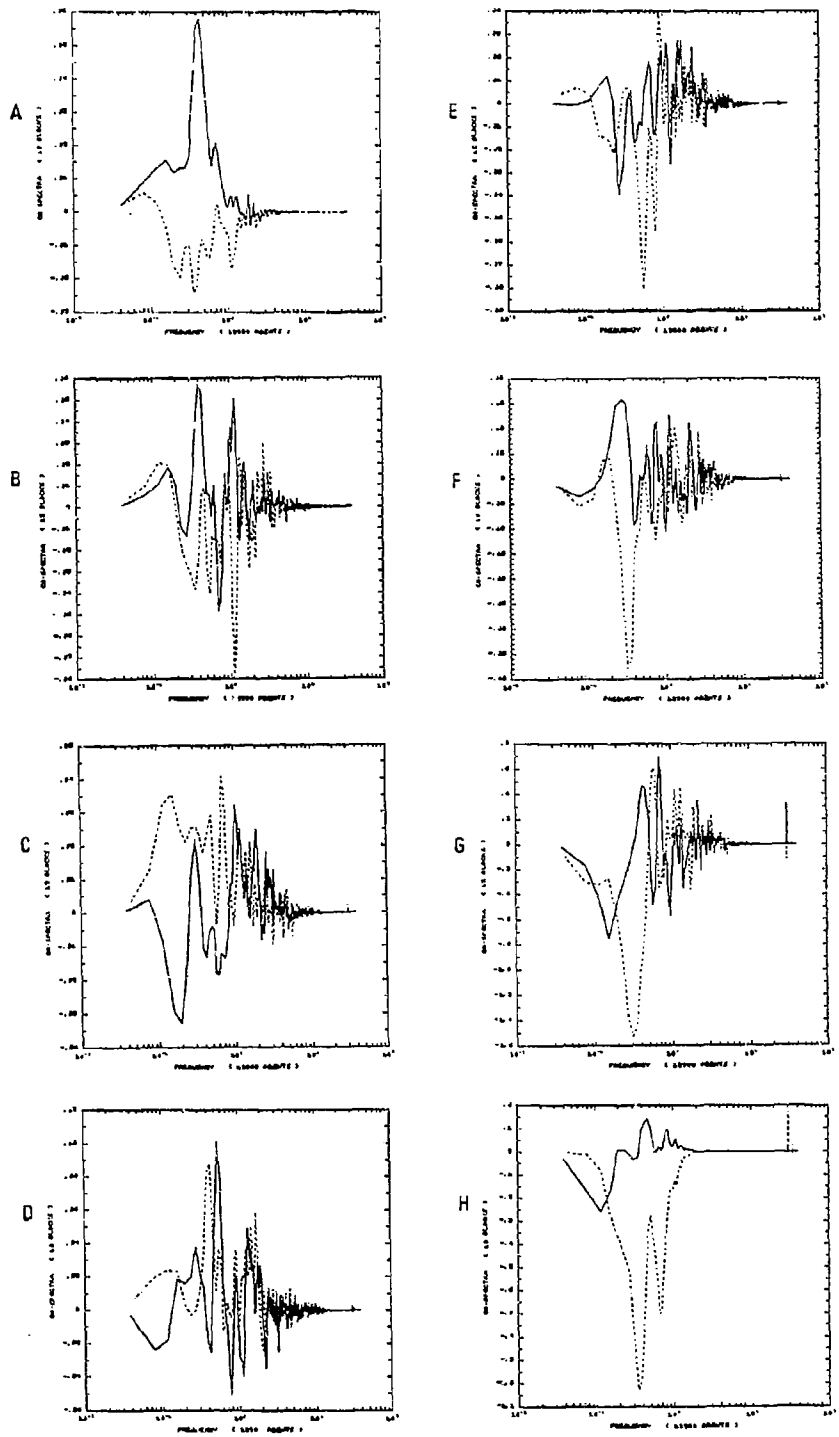


Figure 5. Co-spectrum (solid line) and quadrature-spectrum (dashed line) of w' and ρ', for F=10/π (Re(1)=1218, R=2.5 cm and N=1.13 rad/s), inside the wake at the location z=0 : (a) Nt=1.2 ; (b) Nt=2.2 ; (c) Nt=4 ; (d) Nt=5 ; (e) Nt=6 ; (f) Nt=7 ; (g) Nt=8 ; and outside the wake at the location z=2R : (h) Nt=7.

the wake (h). In figure 5 (a) the quadrature-spectrum is close to zero and the co-spectrum exhibits a significant peak which corresponds to the wake instability with a dimensionless frequency of 0.2. This implies that w' and ρ' are correlated inside the turbulent region. For $Nt \geq Nt_c$ (figures 5b,c and d), we note that the spectrum is not dominated by the wake instability. Figure 6 shows that w' and ρ' are correlated for $Nt < Nt_c$ and decorrelated for $Nt > Nt_c$. For $Nt \geq Nt_{w=}6$ (figures 5 e, f and g), we observe that the quad-spectrum is large compared to the co-spectrum. This indicates that w' and ρ' oscillate in phase quadrature as required for internal waves. Thus for $Nt \geq Nt_w$, the wake is dominated by internal wave motions. The quadrature-spectrum shows a peak which corresponds to the wake instability frequency. This confirms the fact previously described in BCH, that the random internal wave field is generated by the collapse of the coherent structure periodically emitted by the turbulent wake. The dimensionless time Nt_w corresponds also to the time of the appearance of internal wave outside the turbulent wake (see BCH).

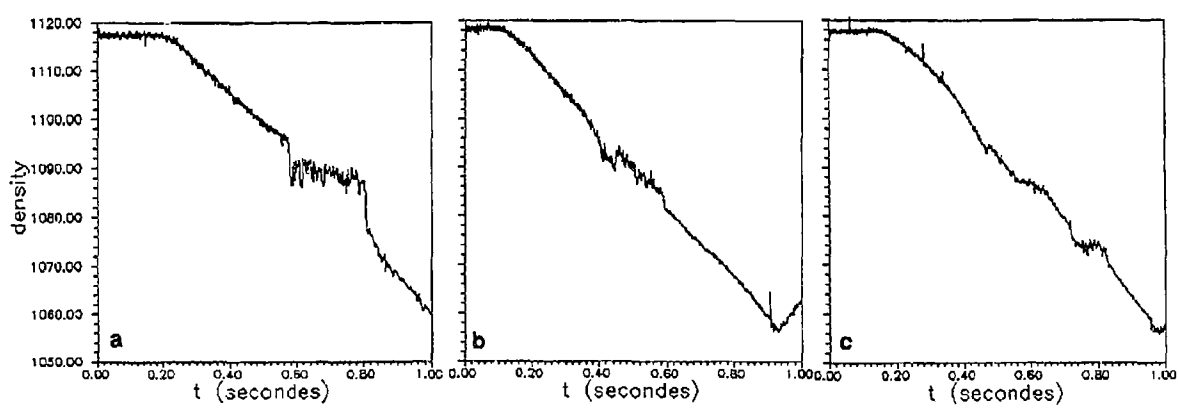


Figure 7. Vertical density profile for F=6 (Re(1)=31552, R=5cm, N=1.22 rad/s); (a) Nt=2 ; (b) Nt=6.5 ; (c) Nt=12.

To improve our understanding of the collapse phenomenon we measured the vertical density profile of the wake at different locations (figure7). A conductivity probe was pulled behind the sphere and was driven down across the wake with a constant velocity: 43.7 cm/s. In figure 7a, for Nt close to Nt_c, we observe that the wake has been entirely mixed by the turbulent motions. Figure 7b, obtained at $Nt > Nt_c$, shows that the density profile is close to the initial linear stratification, and that density perturbations are located in a narrow layer which corresponds to a collapsed wake. For $Nt > Nt_w$ (figure 7c) we observe density perturbations outside the wake, which are associated to the random internal wave propagation.

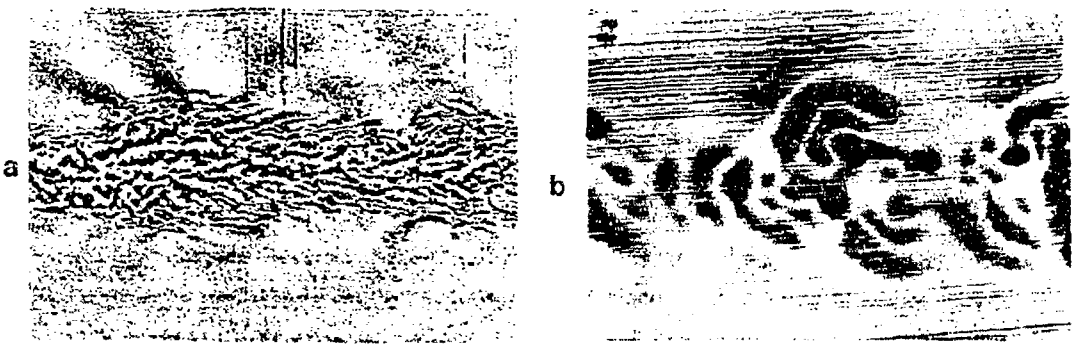


Figure 8. Random internal wave for $F=20/\pi$ and $Nt=11$. (a) shadowgraph side view, Re=12624 (R=2.5cm); (b) laser-induced-fluorescence visualization in a horizontal plane at z=3R below the centre of the sphere, Re=1611 (R=1.12cm).

4. Random wave field

We have shown in the previous chapter that internal waves are predominant inside the wake for $Nt>Nt_W$. BCH showed that these waves are also emitted outside the wake at the same time and demonstrated that these random waves behave like transient internal waves emitted by bodies started impulsively. The phase structure typical of impulsive waves is illustrated in figure 8. The shadowgraph side view (figure 8a) shows, outside the wake, black and white fringes which characterize the random wave isophases. Figure 8b presents a horizontal visualization of these waves which appear as semicircular concentric phase line patterns.

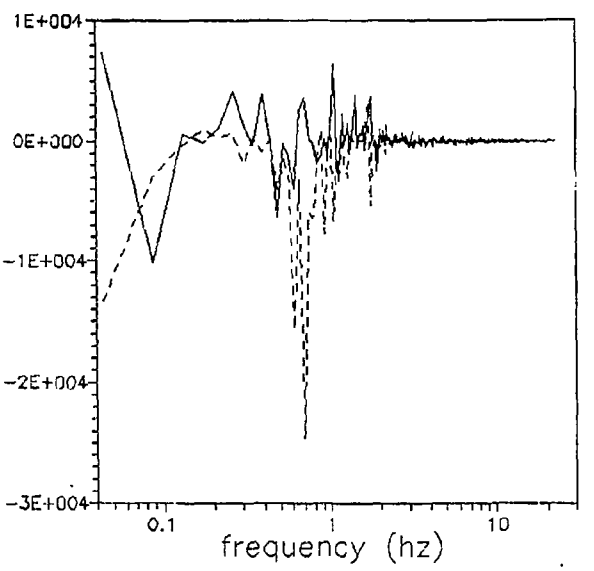


Figure 9. Co-spectrum (solid line) and quadrature-spectrum (dashed line) between ρ' measured at z=2R and z=5R. x=50R, F=6 (Re(1)=5474, R=5cm).

To improve our knowledge concerning the vertical structure of these waves, we have pulled behind the sphere at x=50R (Nt=8.3), a set of four conductivity probes located at z=2R,3R,4R and 5R. Spectral analysis of probe signals indicates that whichever z, wave spectra are dominated by the frequency which corresponds to the frequency of the wake instability. There is no frequency gap, but a phase gap between the signals. This is due to the slope of the isophases (see figure 8a). In particular, as shown in figure 9, internal waves at z=2R and 5R oscillate in phase quadrature. This corresponds to an angle between the vertical and the isophase of 43° which is in agreement with shadowgraph visualizations (figure 8a).

References

Bonneton, P., Chomaz, J.M. and Hopfinger, E. 1993 Internal waves produced by the turbulent wake of a sphere moving horizontally in a stratified fluid. *J. Fluid Mech.* **245**, 23-40.

Chomaz, J.M., Bonneton, P. and Hopfinger, E. 1993a The structure of the near wake of a sphere moving horizontally in a stratified fluid. *J. Fluid Mech.* **245**, 1-21.

Chomaz, J.M., Bonneton, P., Butet, A. and Hopfinger, E. 1993b Vertical diffusion of the far wake of a sphere moving horizontally in a stratified fluid. *Phys. Fluids* **A5**, 2799-2806.

Lin, Q., Lindberg, W.R., Boyer, D.L. and Fernando, H.J.S. 1992 Stratified flow past a sphere. *J. Fluid Mech.* **240**, 315-354.

Thual, O., Butet, A., Perrier, M. and Hopfinger, E. 1987 Sillage d'une sphère en milieu stratifié. *Rapport D.R.E.T.*

THE WAKE REGIMES INFLUENCE ON HYDRODYNAMIC CHARACTERISTICS OF THE SUBMERGED SPHERE IN THE STRATIFIED FLUID

OLGA. D. SHISHKINA

Institute of Applied Physics, Russian Academy of Sciences,
46 Ul'janov st., Nizhny Novgorod 603600, Russia [1]

ABSTRACT

Results of experimental study of the thermocline stratification influence on drag parameters of horizontally and uniformly driven sphere are represented. The sphere with a diameter of about thermocline thickness was towed at a depth of the thermocline center. The Reynolds and the Froude number ranges were respectively $1.6 * 10^3 \leq Re \leq 1.1 * 10^4$ and $0.3 \leq Fi \leq 2.0$. Analysis of the mode structure of the lee–wave field is provided. Maximum increase of the drag coefficient value ΔCx is obtained for regimes of the first mode effective generation. Considerable drag coefficient decrease for $Fi \geq 1.0$ caused by the wake turbulization is confirmed by internal waves characteristics measurements. The certain difference between lee waves and collapse waves is observed.

The comparative analysis results of drag coefficient versus Froude number both for two – layered and continuously stratified liquid in the range of Froude numbers $Fi \sim 1$ are presented. Comparison of $\Delta Cx\,(Fi)$ dependences showed an existence of linear dependence of Froude numbers Fi for continuously stratified fluids and square dependence between Fi for the two – layered liquid and an exponential stratification.

1. Introduction

The effect of fluid stratification on drag parameters of a submerged sphere moving uniformly in the horizontal direction has been investigated both theoretically and experimentally.

Research of Hanazaki (1988) is devoted to numerical studies of the relationship between the drag coefficient Cx and the parameters of three – dimensional flow of viscous incompressible exponentially stratified fluid. Calculations were performed for the constant Reynolds number $Re = 200$ and yielded the results close to the experimental ones for mentioned conditions.

There are few experimental works conserning study of drag on uniformly driven solid bodies in a stratified fluid.

In the work by Nikitina (1959) experiments on drag value measurements of a ship model mowing at a free surface of a two – layered fluid with various layers thickness has been fulfilled. The drag coefficient values were not estimated in this paper.

Two papers are available now (Mason 1977; Lofquist & Purtell 1984) dealing with experimental dependences of the coefficient Cx versus the Froude number for a sphere moving in an exponentially stratified fluid, as well as of its variations ΔCx relatively to the value Cx_0 in a homogeneous fluid.

Fluids with more complicated stratification profiles were not treated experimentally from this viewpoint.

[1] E-mail: olga@hydro.nnov.su

A limit of exerimental data is also the reason of any correlation analysis absence for the drag coefficient as a function of Fi for different stratification cases.

2. Experimental equipment

The aim of present experiment was to confirm and evaluate the influence of thermocline – wise stratification on the drag force and the drag coefficient of a submerged solid sphere.

All the experiments have been fulfilled in a thermostratified laboratory tank 1.6 m wide, 1.2 m deep and 5 m long. Horizontally homogeneous thermal stratification, provided in the fresh water, presented a scale model of the ocean thermocline.

Stratification – making system consists of a refrigerating machine connected with heat–exchangers arranged horizontally along the tank walls inside the tank. It provides the lower water layers temperature of about $4 \div 6°C$ and upper layers with the temperature of $18 \div 20°C$. As a result of the system's action and due to natural convection in heated and cooled water layers a scale model of natural ocean thermocline is provided in the tank. The thermocline of a thickness $d = 0.17H$ has its center's depth $h = 0.33H$.

Usually it takes about $8 \div 9$ hours to "boil" a stratification in the homogeneous liquid with the temperature $t = 10°C$ and $3 \div 4$ hours to restore it night later.

A sphere of diameter $D = 150\ mm$ was towed with constant velocities $U = 0.014 \div 0.09\ m/s$ at the depth of about the thermocline centre $h = 0.32\ m \cong 2D$, which excluded free surface effect. The Reynolds and Froude numbers varied in the ranges $1.6 * 10^3 \leq Re = \frac{U*D}{\nu} \leq 1.1 * 10^4$ and $0.3 \leq Fi = \frac{U}{N*D} \leq 2.0$ respectively. Here ν is the fresh water kinematic viscosity coefficient for the temperature 12°C (water temperature in the center of the thermocline), $N = N_{max}(z)$ is the maximum value of the Brunt–Vaisala frequency:

$$N(z) = \left(-\frac{g}{\rho_o}\frac{d\rho}{dz}\right)^{1/2} \tag{1}$$

where

g acceleration due to gravity;

ρ_o water density at the center of the thermocline;

$d\rho/dz$ density variation due to the temperature variation at the horizon.

During the experiment the maximum buoyancy frequency $N_{max}(z)$ was kept equal to $0.30 \pm 0.02\ s^{-1}$ at the depth $z = 0.31 \pm 0.01\ m$. The vertical temperature profile has been recorded before every towing motion and the Brunt–Vaisala frequency $N = f(z)$ was calculated .

The drag force Rx was measured using a towing dynamometer presented a two – armed lever with arms ratio $L_1 : L_2 = 20.9$. The longer arm is formed by a towing knife having a cross–section in the form of the wing profile. The rotation axis of the lever is attached fixedly to the towing carriage normally to the trajectory of the towed body motion. The drag force was transferred from the towed body to elastic element which deformation caused variations of electric signal value. A differential inductive sensor with fixed coils and a core connected to the elastic element, was used as an energy transducer.

3. Experimental results

The drag force versus the sphere motion velocity $Rx = f(U)$ (is plotted in Fig. 1) in the presence of the thermocline stratification yields appropriate values of the drag coefficient

$$Cx = \frac{2Rx}{\rho_o * U^2 * S} \tag{2}$$

where

Rx	the measured drag force;
ρ_o	the water density at the thermocline centre horizon;
U	the towing velocity;
$S = \pi D^2/4$	the body's cross–section.

$$\Delta Cx = Cx - Cx_o, \tag{3}$$

where Cx_o is the drag coefficient of a sphere in the homogeneous liquid.

Maximum (threefold) increase of the towing drag coefficient is observed at the Froude number $Fi = 0.58$ ($U = 0.026\ m/s$) (see Fig. 2).

The internal waves (IW) field parameters were recorded by vertical chains of sensors. Four sensors were arranged one below another in the thermocline zone with spacing $0.07\ m$ at a distance of $3D$ from the sphere's trajectory. IW modes are represented as eigenfunctions $q_i(z)$ of the Sturm–Liouville boundary–value problem

$$\frac{d^2q_n}{dz^2} + q_n k_n^2 (N^2/\omega^2 - 1) = 0 \tag{4}$$

$$q_n(0) = q_n(H) = 0$$

where

q_n	the n-th mode eigenfunction;
k_n	the n-th mode wavenumber;
ω	the IW frequency;
N	the Brunt–Vaisala frequency;
H	the tank depth.

The problem was solved under the condition of weak dispersion of IW modes ($\omega \ll N_{max}(z)$, $Cp_n = \omega_n/k_n = const$). By expanding the displacement of isotherms in n modes and by minimizing rms error of measured isotherm oscillations we can find the mode amplitudes.

Parameters of IW analyzed simultaneously with drag measurements evidence that while the velocity of body's motion increases in the range mentioned above, the number of modes excited by the body increases also. The drag coefficient increases with the number of modes and has a maximum value for $U = Cp_1$. Thus of appreciable importance is the first mode which is also confirmed by comparing data of IW mode analysis with the $\Delta Cx(Fi)$ dependence (see Fig. 2). Fig. 3 exhibits spectra of the first three modes at various velocities of sphere motion. It can be readily seen that as the velocity (or the Froude number) grows, the first mode becomes predominant.

The prevalent excitation of the first mode while velocity of the sphere motion increases is observed when the sphere moves below the thermocline ($z = 0.46\ m$). Oscillograms of modes for this case are shown in Fig. 4. The growth of the amplitude for $Fi \geq 1.0$ is due to IW generation by the wake and differes definitely from the case of IW generation by the pressure field of moving body (a phenomenon observed also by Hopfinger et al. (1991)). Experiments with a streamlined body (an ellipsoid of revolution) showed that

lee *IW* have maximum amplitude for the same body's velosity ($U = Cp_1$) without its grouth for higher values of U.

4. Comparison of the wave–drag coefficient versus the Froude number for different stratification profiles

The comparative analysis results of drag coefficient versus Froude number based on drag measurements of uniformly and horizontally driven models both for two – layered and continuously stratified liquid (exponential stratification and thermocline) in the range of small Froude numbers ($Fi \sim 1$) are also presented.

As a towed body for continuously stratified liquid a sphere was used. In the exponentially stratified fluid (Lofquist & Purtell 1984) the sphere of diameter $D = H/8$ was towed at the depth $H/2$ (H is the fluid depth). In the case of two – layered fluid (Nikitina 1959) the ship model with the draught $R = (0.54 \div 3.0)\,H_1$ (H_1 is the upper layer thickness) has been used.

Froude numbers were calculated in accordance with following eqations:

— for the two – layered model

$$Fi = U/Co \tag{5}$$

— for the continuous stratification

$$Fi = U/(N * 2R) \tag{6}$$

where

U	body's velocity;
Co	internal wave speed in the two – layered liquid of finite depth;
R	characteristic vertical body dimension ($= D/2$ for bodies of revolution);
N	the Brunt–Vaisala frequency ($N = N_{max}(z)$ for the thermocline).

Experimental results matching method was based on the dividing – streamline concept (Snyder et al. 1985; Hanazaki 1988) that all the kinetic energy of the stationary and potential (for $Fi \leq 0.5$) flow passing around submerged body in the hydrostatic limit is converted into potential energy of the vertically displaced fluid parcel.

Resulting formulas for the dividing streamline displacement $\Delta = R - z_s$ versus Froude number for the flow of uniform velocity are as follows

— for the two – layered fluid

$$\Delta = 1/2 * H_1 * Fi^2 \tag{7}$$

— for the fluid with constant density gradient and for the thermocline, presented by an exponentially stratified layer placed between two homogeneous layers

$$\Delta = R * 2Fi \tag{8}$$

For wave – drag coefficients versus Froude number following dependences were obtained:

$$\Delta C_{exp}(Fi) = K * \Delta C_{double}(Fi) \tag{9}$$

$$\Delta C_{exp}(Fi) = \Delta C_{therm}(Fi) \tag{10}$$

With

$$Fi^2_{double} = K_1 * Fi_{exp} \tag{11}$$

$$Fi_{therm} = K_2 * Fi_{exp} \tag{12}$$

where K, K_1, K_2 are coefficients depended on the body's geometry and stratification parameters in the certain experiment.

Explanation of the dependence (11) and the value of coefficient K_1 follows from the comparison of Eqs. (7), (8) and the condition of relative displacements Δ/R and Δ/H_1 equality:

$$\frac{\Delta}{R} = \frac{\Delta}{H_1} = 2\,Fi_{exp} = 1/2\,Fi^2_{double} \tag{13}$$

$$K_1 = Fi^2_{double}/\,Fi_{exp} = 4 \tag{14}$$

K_1 values obtained from an experimental data comparison are in the range $3.88 \div 4.16$.

Results of adaptation of initial curves $\Delta Cx\,(Fi)$ for the two – layered fluid in accordance with Eqs. (9), (11) are presented in Figs. 5 *a*, *b* (cases when the ship model's draught is more and less than the upper layer thickness respectively).

The coefficient K_2 value in Eq. (12) has been defined taking into account the fact of similarity of *IW* propagation in continuously stratified fluids and equality of equations describing wave processes in one – waveguide systems. In particular, dispersion dependence for fluid with N = const and for the thermocline, modelling by the exponentially stratified layer contained between two homogeneous layers,

$$\omega^2 = N^2 \frac{k_n^2}{k_n^2 + k_{zn}^2} \tag{15}$$

where

ω	*IW* frequency;
N	the Brunt – Vaisala frequency;
k_n	n-mode horizontal wave–number;
$k_{zn} = \pi n/h'$	n-mode vertical wave–number;
h'	characteristic vertical waveguide dimension.

From Eq. (15) it follows an equation for dimensionless k_n.

$$(k_n\,h')^2 = \frac{1}{Fi^2{}_h} + (\pi\,n)^2 \tag{16}$$

where $Fi_h = Cp_n\,/\,N\,h'$.

As Froude numbers $Fi_h = Fi * 2R/h'$ are of order 10^{-2} for $Fi \leq 0.5$ it follows from Eq. (16) that $k_1 >> k_{z1}$. Eqs. (15) and (16) may be rewritten now

$$Cp_{1\,exp} = \frac{\omega}{k_1} \cong \frac{N}{k_1} \tag{17}$$

$$k_1 = \frac{1}{Fi_h * h'} = \frac{1}{Fi * 2R} \tag{18}$$

It seems to be natural to assume *the phase speed equality* to be the similarity condition for continuously stratified fluids $Cp_{1\,exp} = Cp_{1\,therm}$. Under this condition the Brunt

– Vaisala frequency provided the similarity of $\Delta Cx(Fi)$ for continuously stratified fluids will be defined from Eqs. (17), (18) as follows

$$N_{exp} = Cp_{1\,therm}/(Fi_{exp} * 2R_{exp}) \tag{19}$$

In the comparison of experimentally obtained dependences $\Delta Cx(Fi)$ the particular value of N has been defined from Eq. (19) for the maximum values $\Delta Cx_{max}(Fi)$. The obtained value of $N_{exp} = 2.73\ s^{-1}$ allowed to count the similarity coefficient of Fi for two stratification profiles

$$K_{Fi} = \frac{K_{Cp}}{K_N * K_R} \tag{20}$$

where

K_{Fi} proportionality coefficient for Froude numbers;
$K_{Cp} = 1$ similarity coefficient for phase velocities;
K_N similarity coefficient for Brunt-Vaisala frequencies;
K_R geometric similarity coefficient.

The theoretically obtained value of $K_{Fi} = Fi_{therm}/Fi_{exp} = 3.73$ equals to the result of experimental data adaptation. Curves of $\Delta Cx(Fi)_{exp}$ and $\Delta Cx(Fi)_{therm}$ where Fi_{therm} is transformed in accordance with Eq. (20), are presented in Fig. 6.

To explain the presence and relative position of nonmonotonicity regions in both curves ($Fi_{exp} = 0.5, Fi_{therm} = 0.4$) we can use the diagram of wake regimes past a sphere moving in the exponentially stratified fluid (Lin et al. 1992) (Fig. 7) .

It's obvious that the region of lee IW existence is limited from above by the Froude number $Fi = 0.4$ (with the transitional zone at $Fi = 0.4 \div 0.5$) in the Reynolds number range $Re = 200 \div 2000$. This is the reason of the wave-drag coefficient insensitivity from Re for $Fi \leq 0.5$ ($Fi \leq 1.0$ in their definition) noted by Lofquist & Purtell (1984) (corresponding characteristics are shown in Fig. 7 by dashed lines).

Characteristic line for the Brunt–Vaisala frequency $N = 2.73\ s^{-1}$ obtained under the condition of similarity of $\Delta Cx(Fi)$ is shifted to the diagram region where position of lee waves upper boundary becomes sensitive to Re. Comparing the nonmonotonicity regions position (points no. $4 \div 6$ in Fig. 7) we can find that their presence and relative position are connected with the change of IW generation regime by the vortex production.

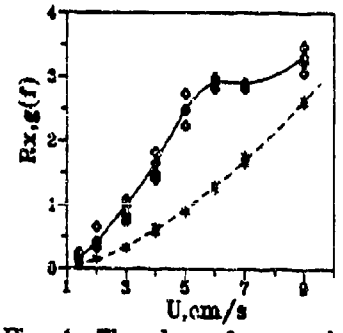


Fig. 1. The drag force value versus body's speed:
***** homogeneous fluid
***** stratified fluid:

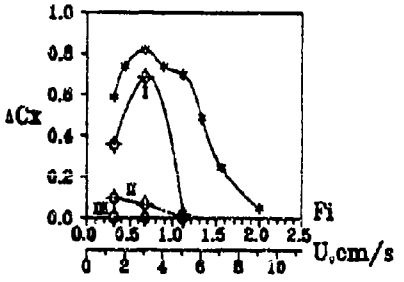


Fig. 2. The drag coefficient increment versus internal Froude number and the sphere's velocity:
***** the drag coefficient increment,
◇◇◇◇◇ wave-drag coefficient due to IW mode.

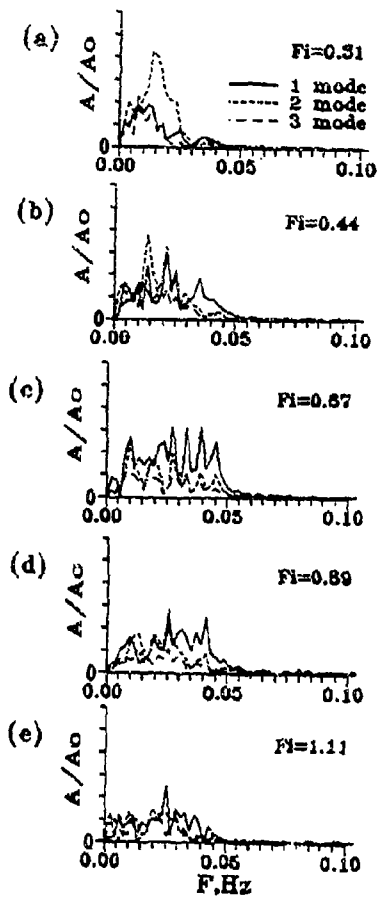


Fig. 3. IW modes spectra (sphere in the thermocline).

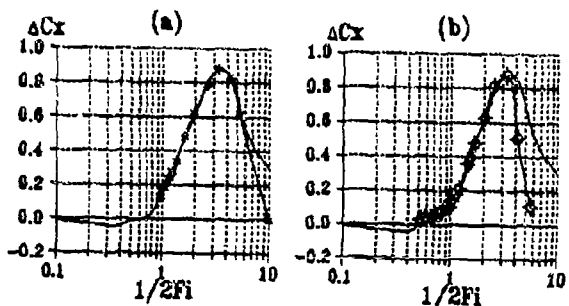


Fig. 5. The drag coefficient increment due to stratification versus inverse Froude number:
—— linear stratification Lofquist & Purtell (1984),
two-layered fluid Nikitina (1959):
***** (a) H1/R = 0.79,
◇◇◇◇◇ (b) H1/R = 1.32.

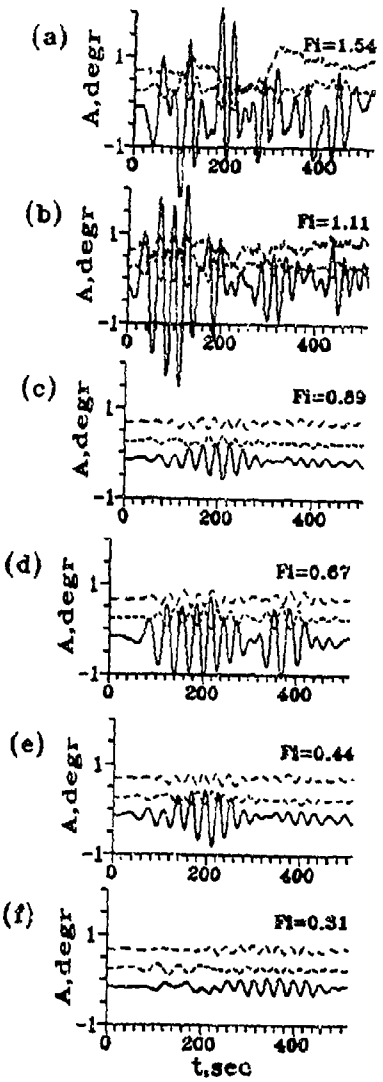


Fig. 4.
IW modes amplitudes (sphere under the thermocline).

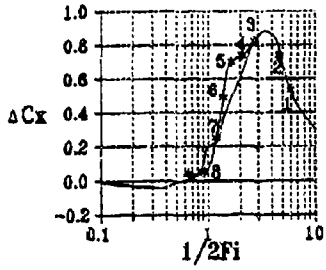


Fig. 6. The drag coefficient increment due to stratification versus inverse Froude number:
—— linear stratification Lofquist & Purtell (1984),
***** thermocline Bogatyrjov & Shishkina (1990).

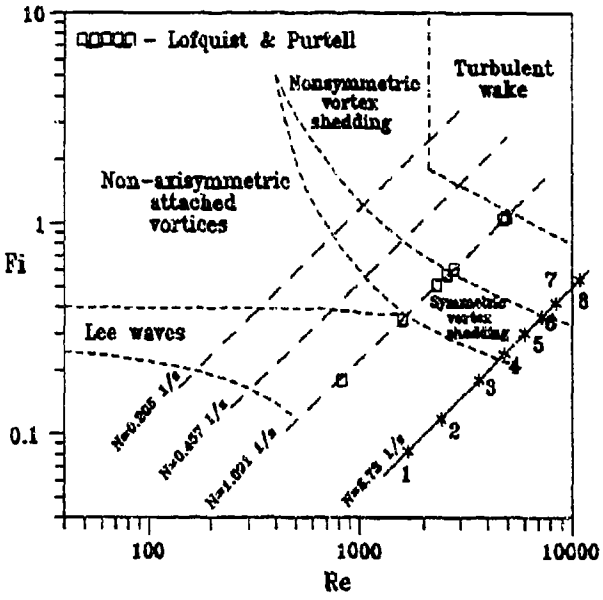


Fig. 7. The diagram of wake processes past a sphere in an exponentially stratified fluid [4].

6. References

1. Bogatyrjov S. D.; Shishkina O. D. 1990: An experimental study of induced internal waves parameters and there influence on hydrodynamic characteristics of a sphere in a stratified liquid. *Laboratory modelling of the dynamic processes in the ocean.* Novosibirsk, 81-84 (in Russian)
2. Hanazaki H. 1988: A numerical study of three – dimensional stratified flow past a sphere. *J. Fluid Mech.* 192, 393-419
3. Hopfinger E. J.; Flor J. B.; Chomas J. M.; Bonneton P. 1991: Internal waves generated by a moving sphere and its wake in a stratified fluid. *Exp. Fluids.* 11, 255-261
4. Lin Q.; Lindberg W.; Boyer D. L.; Fernando H. J. S. 1992: Stratified flow past a sphere. *J. Fluid Mech.* 240, 315-354
5. Lofquist K. E. B.; Purtell L. P. 1984: Drag on a sphere moving horizontally through a stratified liquid. *J. Fluid Mech.* 148, 271-284
6. Mason P. J. 1977: Forces on spheres moving horizontally in rotating stratified fluid. *Geophys. Astrophys. Fluid Dyn.* 8, 137-154
7. Nikitina H. A. 1959: Drag of the ships in a "dead water". *Izvestiya akademii nauk, OTN, Mechanika i machinostroyeniye.* 1, 188-192 (in Russian)
8. Snyder W. H.; Thompson R. S.; Eskridge R. E. 1985: The structure of strongly stratified flow over hills: dividing – streamline concept. *J. Fluid Mech.* 152, 249-288

SESSION B5

INVESTIGATION OF THE VERTICAL WATER EXCHANGE IN THE BALTIC SEA

R.V.OZMIDOV, A.V.OZMIDOVA

Institute of Oceanology, Russian Academy of Science, Moscow

Abstract

Estimates of exchange process intensities between the deep and surface waters in the deep basins of the Baltic Sea are obtained. For such estimations two methods - the integral (by general balance of salt content in the sea) and the differential one (by approximation of salinity vertical distribution curves with the diffusion equation solution) - were used. Both methods lead to values of the vertical salt diffusion coefficient close to 0.01 $cm^2 s^{-1}$ and to values of salt flux through the pycnocline of magnitude order 10^{-5}-10^{-6} $g\ cm^{-2} s^{-1}$.

In the deep basins of the Baltic Sea a sharp vertical water stratification is known to be observed /1, 2/ that is due to the presence of water with higher salinities and relatively high temperatures at the deep horizons of a basin, from one hand, and less saline water characterized of large seasonal temperature variations in the upper layers, from the other hand. The deep water has its origin in the North Sea water mass that intrudes at times into the Baltic through the shallow Danish sounds connecting the North and Baltic Seas. The surface waters are formed in the Baltic itself through the interaction of river discharge, precipitation, evaporation, the exchange with the deep waters, as well as the thermal processes in the water mass interior and at its boundaries.

The salinity in the bottom layers of the Southern Baltic can reach 15-20 °/₀₀ and in the northern regions it decreases to 7-10 °/₀₀. The underwater sills separating deep basins are the obstacles to the northward penetration of the saline water, so that the lower layers in some basins are often isolated from the saline water of adjacent basins. The water exchange between basins and the influx itself of the North Sea water that is rich in salt and oxygen into the Baltic Sea is not a regular process. It is of sporadic nature and occurs in the form of individual inflow spells of water mass that depend on a number of meteorological and hydrological factors both in the Danish sounds and in the North Atlantic. The frequency of the North Sea water inflow spells is not high. Thus some twenty spells were registered during 1950-1968, the spell of 1951 being an intensive one when about 200 km^3 of the North Sea water penetrated into the Baltic Sea / 1 /.

According to observations of this inflow spell the North Sea water reached the Gotland basin in 3 months, and the Landsort basin in 6 months after the passing through the Danish sounds. An intensive inflow spell was also observed in the winter 1975/1976, when the North Sea water spell reached the Gotland basin only in a year and increased the bottom water salinity from 12.5 to 13 °/₀₀ / 6 /. According to the data now available a very intensive inflow spell occured as well in January 1993. At the present time the information of the North Sea water movement over the Baltic is highly patchy and contradictory,but it is evident that this "new" water had not reached the Gotland basin by the vid of Aprill 1993.

There is a layer with high gradients of temperature, salinity and density between the upper brakish water layer and deep water mass in the deep basins of the Baltic. It lies at the depths down to 70-80 m depth in the central part of the sea. The water density jump in this layer in a number of casses attains to three and sometimes more conventional density units which hampers vertical exchange between the layers. When the inflow of a North Sea water new portion does not occur for a rather long time, the stagnation phenomena develop in the deep basins. The all oxygen brought in by the North Sea water is used up owing to oxidation of organic matter sinking from the upper layer and the hydrogen sulphide begin to store in the deep water. But the upper layer is well stirred due to wind action and vertical winter convection.

The upper water layers directly influenced by the atmosphere change rapidly their properties.With the beginning of the spring heating an upper warm water layer is formed separated from lower layers by a thermocline, the magnitude and the depth of which depend on heating duration, weather conditions and storm forcing. In the fall when the water is cooling the upper heated layer gradually vanishes and the conditions of convective mixing are established that expand down to the main pycnocline but do not destroy it.

Thus the deep water "ventilation" in the sea basins is mainly caused by the sporadic inflows of the North Sea water and by the rather impeded vertical exchange with the upper layers through the pycnocline.At the present time quantiative parameters of these processes are too porly known. The prediction of the North Sea water inflow spells into the Baltic is now impossible because of a great number of poorly known factors leading to such spells. And observation of the phenomenon requires a systematic monitoring not only in the Danish sounds but also in all the central Baltic. The aim of the monitoring should consist not only in the establishing the fact of water inflow spell but also in tracking the North Sea water subsequent expansion and its transformation during the movement. Organization of such a monitoring is to be a concern of all the Baltic states since a good prediction is of the paramount importance for planning fishery quotas and elaborating methods of the sea pollution control.

At the present time quantitative characteristics of the water exchange across the main thermohalocline in the deep basins are in fact unknown. Some authors (see, for example /2/) think that it is possibile to neglect such exchange and assume that the deep basin ventilation is realized only due

to the processes of horizontal advection. However it is avident that such a point of view is wrong, for all the sea salt brought through the Danish sounds by the North Sea water and then spread in bottom layers into the deep basins has (because of the mean steady-state hydrology of the sea) finaly to rise to the upper layers and be carried out by surface currents (in brakish form) through the sounds back into the North Sea. So in the deep basins of the Baltic the vertical salt transport through the thermohalocline must exist that tnsures such salt balance. Similar reasoning can naturally be repeated both for temperature and for example oxygen in the North Sea water. But for these properties such constructions become more complicated by the necessity to take into account possible sources and sinks in the water body owing to oxygen consumption by oxidation processes and heat generation in the this case as well as due to heat exchandge between the water mass and the bottom.

One can try to estimate the mean vertical transport of the salt (and thus water exchange) through the thermohalocline in the deep basins using the above reasoning if one knows the thermohalocline surface area and the mean intensity of the salt transport through the Danish sounds. If we assume according to / 1 / that the area of the thermohalocline is 80000 km^2 and take the above cited value 200 km^3 as a maximum unit inflow spell of the North Sea water with the salinity (when it passes over the sills Darsser and Drogden) close to 20 $^{o}/_{oo}$ / 1 /, then to estimate the mean vertical salt flux through the thermocline it would be necessary only to determine the duration of this saline water relaxation. Since such large inflow spells of the North Sea water occur rather rarely, we shall take 10 years as a rough estimate of the relaxation time. Under such assumptions we shall have the mean vertical specific salt flux through the thermohalocline in the deep basins:

$$Q = (200\ km^3 * 0.02\ g\ cm^{-3})/(80000\ km^2 * 10\ \text{years}) =$$

$$= (2 * 10^{17}\ cm^3 * 2 * 10^{-2}\ g\ cm^{-3})/(8 * 10^{14}\ cm^2 *$$

$$* 3.15 * 10^{8}\ s) = 1.58 * 10^{-8}\ g\ s^{-1}\ cm^{-2}.$$

This estimate is certainly very crude because of approximate values of the quantities used in the calculation. Besides, the vertical salt flux is naturally not uniform over the whole surface of the thermohalocline. It seems to be greater in the areas of the thermohalocline tapering at shallow water, where the phenomenon of internal surf with breaking of internal waves can exist, which has to lead to more intensive water mixing compared to the exchange rate in the regions remote from the shallow waters.

To clear some problems on water mixing processes in the Baltic sea the 29-th cruise of the r/v "Professor Shtockman"

was arranged and carried out in spring 1993. The information on the cruise route and the measurements realized during the cruise are given in / 3 /. The main work in the cruise was carried out in the Gotland basin and Slupsk trough, where 11 scanning sections of 427 n.m. full length and 2281 scannings were fulfilled using a towed STD-sound. As a result of the measurements detailed three-dimensional pictures of temperature, salinity and density fields as well as information of their variability in a wide range of spacial--temporal scales were obtained.

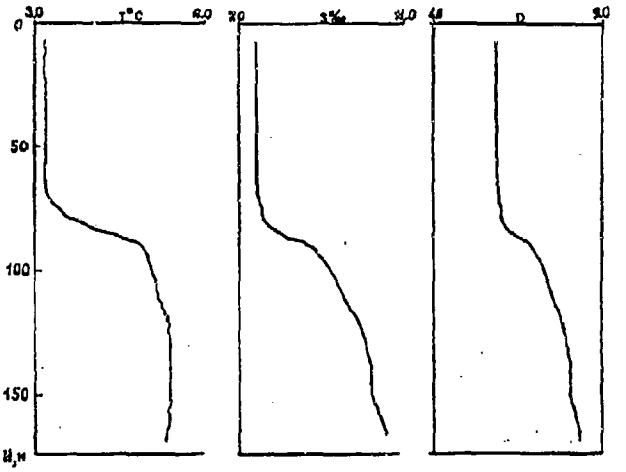


Fig. 1. Examples of typical vertical profiles of temperature T, salinity S and convectional density D of water in the Gotland Basin of the Baltic Sea after the measurements in April 1993 in the 29-th cruise of r/v "Professor Shtockman".

In fig.1 as an example typical vertical profiles of temperature, salinity and density at one of the stations in the Gotland basin are shown. A two-layered water structure is clearly seen with a layer of sharp gradients separating the upper water well-mixing by convection from the deep saltier and warmer water. We observe that the salinity plays here the main part in the increase of the bottom water density whereas the temperature contribution into the density variation does not exceed 3% of the salinity contribution. In this connection the following calculations will be done using the salinity profile data. In fig. 2 the vertical salinity profile S(z) of fig. 1 is shown in an enlarged form (curve 2). The curve appearance at the depth interval from about 87 down to 152 m suggests the approximation of it by the solution of the one-dimensional equation of vertical salt diffusion as follows:

$$dS(z,t)/dt = \varkappa\, d^2S(z,t,)/d^2z, \qquad (1)$$

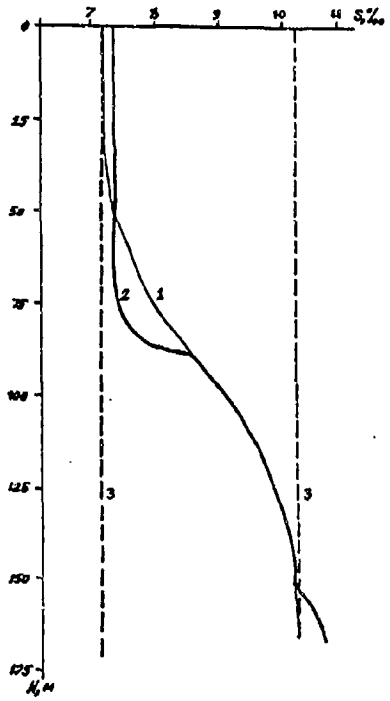


Fig.2. Approximation of a vertical salinity profile (curve 2) by the one-dimensional diffusion equation solution (curve 1). Straight lines 3 correspond to asymptotic values of the surface and deep water salinities.

where $S(z,t)$ - salinity as a function of the vertical coordinate z and time t, $\varkappa$ - the vertical salt exchange coefficient (diffusion coefficient) . If we place the coordinates origin in the mid of the halocline and direct the z-axis downward then we ca. obviously take the following boundary conditions for the equation (1):

$$S(z,t)\,|_{z=\infty} = S_1; \quad S(z,t)|_{z=-\infty} = S_2\,, \qquad (2)$$

where S_1 - salinity value at an infinite depth that is assumed close to the salinity value in the lower layer at a distance large enough from the halocline, S_2 - an asymptotic value of salinity in the upper water layer.

If then we assume that the interface between the upper and lower layers immediately after an inflow spell of the North Sea water ($t = 0$) is not yet eroded but has a stepwise form, the initial conditions for the equation (1) would be:

$$S(z, 0) = \begin{cases} S_1 & at \quad z <= 0 \\ \\ S_2 & \cdots \quad > 0 \end{cases} \qquad (3)$$

The solution of the equation (1) with the boundary conditions (2) and the initial conditions (3) would be /5/ :

$$S(z,t) = S_1 + \frac{1}{2\sqrt{\pi \varkappa t}} \int_0^{\infty} \exp\left[-\frac{(z-\xi)^2}{4\varkappa t}\right] \Delta S \, d\xi \qquad (4)$$

where $S = S_2 - S_1$, ξ - the integration variable.

The expression (4) by variable substitution $(z-\xi)/2\sqrt{\varkappa t} = \eta$ is reduced to:

$$S(z, t) = S_1 + \frac{\Delta S}{\sqrt{\pi}} \int_{-\infty}^{z/2\sqrt{\varkappa t}} \exp\left[-\eta^2\right] d\eta \qquad (5)$$

where η -a new integration variable.

In fig.2 a graph of the second item in the formula (5) is shown (curve 1). It is known as error integral and tabulated for example in /5/. The error integral attains the value of one fourth of the salinity difference ΔS at the distance of approximately 17 m from the inflexion point of the curve 1. But according to the tables the arror integral would take this value when $\eta = 0.48$. Then we have $0.48 = 1.7 * 10^3/2\sqrt{\varkappa t}$. To estimate the diffusion coefficient using this formula it is necessary to accept a value of diffusion duration t.Let us take it by analogy with the above reasoning to be equal to 10 years. Then the estimate of diffusion coefficient $\varkappa$ would be close to 0.01 $cm^2 s^{-1}$. This is a very small value but it is much more than the value of the molecular salt diffusion coefficient in the sea water that has the magnitude order of $10^{-5} cm^2 s^{-1}$ /4/. Thus the calculation made shows that the salt exchange (and therefore the water exchange as well) between the deep water and the surface water in the deep basins of the Baltic does exist and has a certain quantitative characteristic. Let us further estimate specific vertical salt flux Q that is deterrmined by the diffusion coefficient $\varkappa = 0.01$ $cm^2 s^{-1}$. As is known the flux Q is determined by the formula:

$$Q = -\varkappa \, (dS/dz), \qquad (6)$$

where dS/dz - the vertical salinity gradient at an

observation point.

Let us estimate the gradient dS/dz at the inflexion area of the curve 1 (fig. 2). Here the vertical salinity difference is clos to 1‰ per 25 m and consequently for the mean salt concentration gradient we have $dS/dz=4 * 10^{-7} g\ cm^{-2} s^{-1}$. This gradient value multiplied by the value of the diffusion coefficient, we have the specific wertical salt flux $Q=4*10^{-9} g\ cm^{-2} s^{-1}$, i.e. approximately four times less than the estimate of Q, mode above using integration method. Such a discrepancy between the Q estimates is quite explicable for using the integration method we estimated the salt flux under assumption of transport of all salt mass from the deep layer to the upper one whereas the Q estimation by differential method (by the formula (6)) we took into account only a partial transport of the salt stored in the lower layer to the upper one as it follows from fig.2. Besides, the calculation carried out does not take into account the boundary effects at the tapering thermocline in the shallow waters that can as was mentioned above be important for water exchange of the bottom water with the overlying fluid layers.

References

1. Gershanovich D.E. (ed.). Essays on the biologic productivity of the Baltic Sea. Vol.1 Coord.center of the states-members of Economic Mutual Aid Council on the problem "The World Ocean", Moscow,1984,390 pp.(in Russian)
2. Ozmodov R.V. (ed.) Research on the dynamics of the Baltic Sea waters. Coord. center of the states-members of EMAC on the problem "The World Ocean", Moscow, 1977, 306 pp. (in Russian).
3. Ozmidov R.V. Peculiarities of the mixing processes in the Baltic Sea (29th cruise of r/v "Professor Shtockman",March 25 - April 27, 1993) // Oceanology, Vol. 33, N5, p.788-791 (in Russian).
4. Popov N.I.,Fedorov K.N.,Orlov V.M. The sea water .Nauka, M. 1979, 328 pp. (in Russian).
5. Tikhonov A.N.,Samarsky A.A. Mathematical physics equations. State Publish. House of techn.-theoret literature ,M .-L. 1951, 660 pp. (in Russian).
6. Gerlach S.A. Nitrogen, phosphorus, plankton and oxygen deficiency in the German Bight and in Kiel Bay. Kieler Meeresforschungen, Solderheft Nr.7, 1990, 342 pp.

Turbulent Mixing in the Oceanic Boundary Layer Due to Internal Wave Reflection from Sloping Terrain

Donald N. Slinn and James J. Riley
University of Washington
Seattle, WA 98195

1. Introduction

An improved understanding of vertical mixing in the ocean is an important problem in physical oceanography. Large-scale dynamic models require accurate parameterizations for turbulent mixing to make realistic predictions for the transport of heat, salt, and chemical species. Other important processes also involve vertical mixing. For example, vertical mixing supplies the biological ecosystem with necessary ingredients, as heavy, nutrient rich bottom water is lifted to the surface to support plant and animal life. The ocean is stably stratified, which acts to inhibit vertical mixing. Munk (1966) has show that a basin-averaged vertical eddy diffusivity of roughly $\kappa = 10^{-4}$ m^2/s must exist to balance the effects of upwelling and downward diffusion. Field studies, however, have failed to observe such large vertical diffusivities in the ocean interior. Typical measured values for vertical diffusivity in the open ocean are in the range of $\kappa = 1.2 \times 10^{-5}$ m^2/s (Ledwell, 1993). The conclusion from the experiments is that 80-90% of the vertical mixing is not taking place in the ocean interior.

Instead the mixing is expected to occur at the boundaries, near continental slopes, islands, seamounts, and other topographic features. The idealized picture is one of active mixing in the benthic boundary layers with mixed fluid communicated to the interior along constant density surfaces. The exchange of mixed boundary fluid with interior stratified fluid provides a mechanism to weaken the interior density gradient, and continuously supply fresh stratified fluid to be mixed in the boundary layer. The overall process can work efficiently since horizontal advection is not inhibited by the surrounding stratification. Recent field experiments (Eriksen, 1985, 1994) have suggested that the oceanic internal wave field can provide a sufficient source of energy to activate strong mixing near sloping boundaries and account for a significant portion of the overall oceanic vertical mixing.

The angle of propagation of energy of an internal wave depends upon the wave frequency, ω, and the background density stratification according to the dispersion relation $\omega = N \sin\theta$, where N is the buoyancy frequency defined by $N^2 = (-g/\rho_o)(\partial\rho/\partial z)$, and θ is the angle between the group velocity vector and the horizontal. When an internal wave reflects from a larger-scale sloping boundary, its angle of propagation with respect to the horizontal is preserved. This can lead to an increase in the energy density of the reflected wave, as illustrated in Figure 1 for a linear internal wave ray tube, as the energy in the oncoming wave is concentrated into a more narrow ray tube upon reflection. Probably the most effective situation for boundary mixing arises when an oncoming wave reflects from a bottom slope which nearly matches the angle of wave propagation. In this case a small amplitude oncoming wave may be reflected with large amplitude and exhibit nonlinear behavior. The nonlinearity can cause the wave to transition to turbulence near the boundary and enhance mixing of the boundary layer fluid. The angle of wave propagation such that the wave reflects at the same angle as the bottom slope is called the critical angle. In this case linear wave theory predicts a reflected wave of infinite amplitude and infinitesimal wavelength and the trapping of the oncoming wave energy in the boundary region. In such a case linear theory is clearly inadequate to predict the flow behavior, as nonlinearities and turbulence come into play.

In this paper we present the results of numerical experiments simulating the reflection of internal wave trains from bottom terrain of various slopes. The numerical experiments comple-

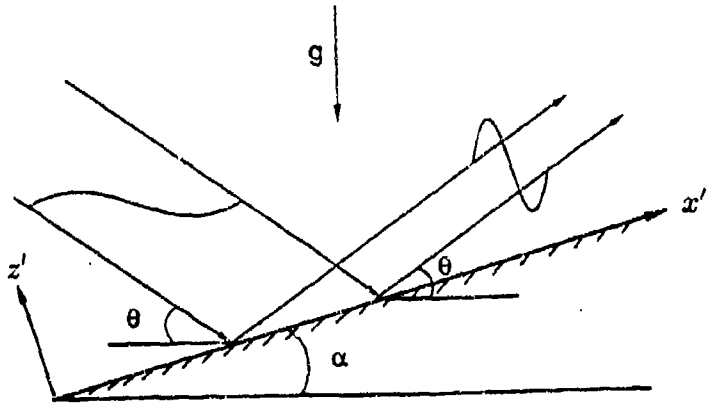


Figure 1: Ray tube diagram of internal gravity wave reflection from sloping terrain illustrating the basic geometry of the problem.

ment previous field and laboratory studies (Ivey, 1989; Taylor, 1993) with the ability to study the energetics and turbulence dynamics in detail. Additional strengths of the numerical approach include facilitating both flow visualization and parameter studies on the influence of key physical and nondimensional quantities. It offers the ability to simulate critical angle reflection down to slopes of about 3 degrees, which are typical of oceanic conditions (Thorpe, 1992).

2. Model Description

The model utilizes state-of-the-art numerical techniques to solve the three-dimensional, incompressible Navier-Stokes equations within the Boussinesq approximation. A detailed description of the physical and numerical model is to appear in a separate paper (Slinn and Riley, 1994). The problem of interest is to simulate the reflection of internal waves from the ocean floor. The buoyancy frequency N is taken to be constant, and a steady stream of oncoming waves is generated in a wave forcing region located away from the ocean floor. This is accomplished by adding localized forcing terms to the governing equations to produce a monochromatic train of waves with a specified wavelength and frequency. The waves propagate downward at a specified angle θ with respect to the horizontal, with group velocity $\vec{C}_g$, and wavenumber $\vec{k} = (k, l, m)$.

Figure 2 shows isopycnals taken at an intermediate time from a numerical experiment in which the internal wave train is propagating in a vertical plane (x', z') normal to the terrain surface. It represents a two-dimensional cross section of the density field of a three-dimensional simulation taken in the plane of the slope. The constant density contours indicate the amplitude of the oncoming wave train as well as show the development of a region of strong density gradient near the bottom boundary. The oncoming waves are of moderate amplitude and approach the wall in the plane of the slope. Here the bottom slope is 9.2 degrees and the fundamental frequency of the oncoming wave is chosen so that the propagation angle matches the bottom slope upon reflection, e.g. the wave is at the critical angle. The model is periodic in the x' and y directions and the bottom boundary conditions are no-slip for the velocity field and adiabatic (no source of heat or salt) for the density field.

The numerical scheme employs the pressure projection method, implemented with a variable time step third-order Adams-Bashforth scheme to achieve high temporal accuracy. Padé series expansions are used as the basis functions for spatial discretization. The method is formally fourth-order accurate in space and more accurately represents a wide range of wavenumbers than

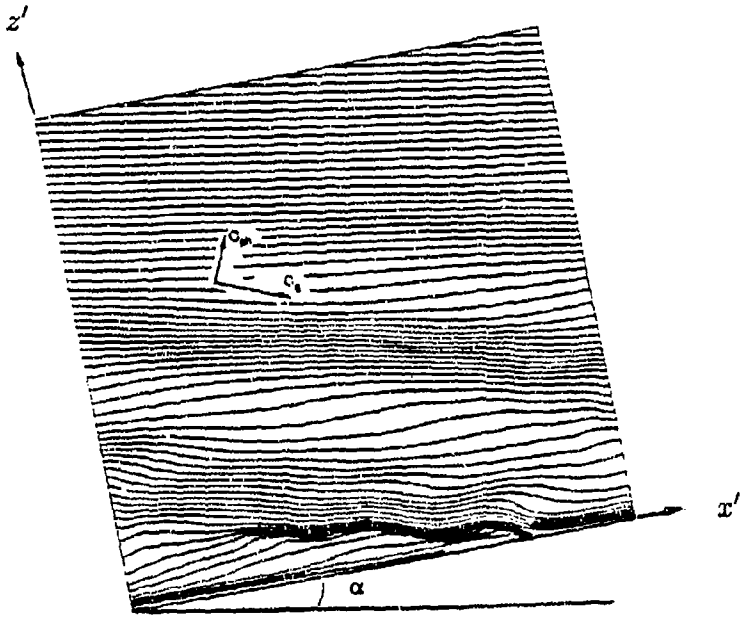


Figure 2: Density contours for an oncoming wave train generated in a forcing region above the bottom boundary propagating downward with phase and group velocities as indicated.

traditional difference schemes (Adam, 1977; Lele, 1993). The pressure field is determined by solving a Poisson equation using Fourier tranforms in the lateral directions and a fourth-order direct solution method in the vertical direction. A Rayleigh damping sponge layer is used at the top open boundary to mimic a radiation boundary condition. A variable grid in the vertical direction is used to achieve a higher density of computational nodes near the ocean floor in order to resolve the boundary layer. The computations were carried out on a numerical grid using 129 x 129 x 130 grid points. Care was taken so that the basic features of the flow are resolved throughout the simulations. The Reynolds numbers for the simulations, Re, based upon the current speed U and wavelength λ, are between 500 and 3500.

3. Results

Figure 3 shows a time series of the flow development throughout a period of wave breakdown visualized by constant density surfaces. The figures focus on the near wall region. The dimensions are one wavelength, λ, in the x' direction and one horizontal wavelength, $\lambda_z = 2\pi/k$, in x' direction. The figures are taken from a simulation with Re = 3500 for the critical angle case with a bottom slope of 9.2°, the same case as shown in Figure 2. Here time is nondimensionalized by the buoyancy frequency and the wave period is 39.2. At time t=70 the wave train has reached the wall and a steep gradient in density has formed in the x'-direction. This feature, called a thermal front by Thorpe (1992), moves upslope at the x' component of the phase speed of the oncoming wave. As time progresses wave overturning develops in the lee of the thermal front, and at time t=88, statically unstable fluid is apparent near the center of the domain. Another significant feature is also apparent at times t=88 and t=94. Near the wall a region of steep density gradient has developed in the z'-direction and across the entire breadth of the domain. As time continues the overturned regions break down into small scale turbulence and dissipate the wave energy in a three dimensional fashion. Also, the steep density gradient in the z'-direction is relieved so that by t=109 it is no longer a dominant feature of the flow.

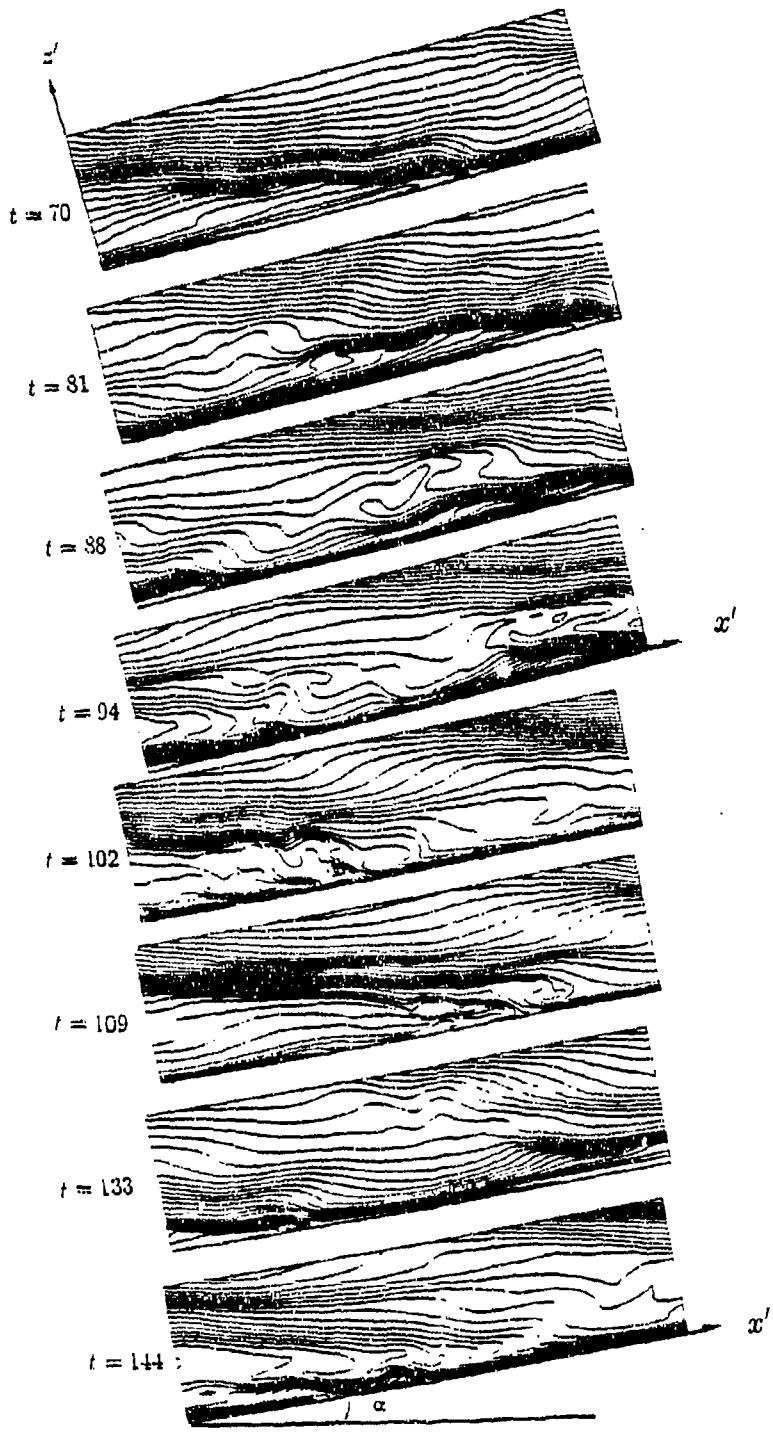


Figure 3: Time series of flow development in the near wall region.

Analysis of the velocity fields, not pictured here, indicates several small eddies of recirculating fluid. The eddies are associated with the regions of overturned fluid and are three-dimensional in character. When the strong density gradient in the z'-direction occurs, a strong region of downslope flow is produced near the wall similar to the backwash produced on a beach after a wave has broken on shore. During this phase the backwash creates a slippery boundary layer facilitating the breakdown of the oncoming wave further away from the wall.

Further analysis indicates that the flow is quasi-periodic, going through a cycle of strong mixing and small-scale dissipation, followed by a quieter period of relaminarization and weaker dissipation. The picture at time t=133 is similar in character to the flow at about t=81, and t=144 compares closely to the picture at t=94, showing that the flow is undergoing another mixing cycle. Some of the simulations have been run out for 10-20 wave cycles, and we conclude that the flows are quasi-steady although the background interior density stratification becomes gradually weakened throughout the process.

Statistical analysis of the overturned regions of fluid indicate that the static instabilities mainly occur within a distance of $\lambda/3$ of the wall, and are present in the boundary layer region about 50 percent of the time. This result is typical of critical angle cases for many different slopes when the Reynolds numbers are high enough for transition to turbulence to occur. Another measure of the local static instabilities is their frequency of occurrence at a fixed location. For a fixed location within the turbulent boundary layer the maximum frequency of static instability is about 15 % of the time, and it happens at a height of about $\lambda/8$.

A key issue related to the wave breakdown process is whether the turbulent boundary layer exchanges fluid with the interior domain or whether it predominantly continues to mix the same fluid. Two experiments were designed to study this issue. In the first the boundary layer fluid is "dyed" with a passive tracer after the flow has reached a quasi-steady state of mixing. Then after a couple of wave periods the flow is examined to determine if the dye is still predominantly located in the boundary layer region, or if it has moved off the wall to the interior stratified regions. For the case presented here a scalar field with an initial linear gradient in the z' (offwall)-direction was chosen and allowed to develop for two wave periods. The initial concentration, or magnitude of the scalar field, is highest at the wall, its value falling off with height. Any net transport of dye due to the wave shear is approximately eliminated by examining the results after an integral number of wave periods. The second approach is to track fluid particles which are released at various heights, and to determine if a statistically significant number of particles escape from the boundary mixed layer, or if particles initially outside the boundary layer are entrained into it.

Figures 4-7 illustrate the results of these experiments. Figure 4 shows the density field for the lowest vertical wavelength for critical angle reflection over a 20° bottom slope. The density field indicates that the mixed layer has a thickness of about .25 λ. These figures are taken at a time when the flow field is quasi-steady, and are representative of the initial and final states of the flow for the dye experiment. Figure 5 illustrates the velocity vectors in the same two-dimensional plane. Here the dominant feature is the shear of the oncoming wave, modified somewhat by recirculation and turbulence in the near wall regions. Figure 6 shows the difference in concentration of the scalar field between its initial and final states. The solid line contours indicate that the concentration of dye (scalar) is higher than in the initial state, indicating that fluid has migrated away from the wall in those regions. The dashed line contours indicate regions in which more dilute or lighter dyed fluid has moved downwards. It is evident that the boundary layer region contains predominantly lighter dyed fluid after two wave periods. The magnitudes of the highs and lows indicate the fraction of a wavelength in the vertical (offwall) direction that the scalar tracer has moved. For example, the high and low peaks at a height of about .4 λ are .268 and -.275 respectively. This indicates that the fluid has traveled over .25 λ in the

offwall direction, a distance greater than the nominal boundary layer thickness. By comparing the slope of the scalar transport contours with the slope of the isopycnals in Figure 4 it is evident that the advection process has favored transport along the constant density surfaces since the iso-scalar-transport and isopycnals are predominantly aligned with one another.

A significant feature of the boundary mixing process is that the internal wave field outside the boundary layer region plays a very active role. It serves to continuously pump fresh stratified fluid into the mixed layer, while simultaneously extracting the mixed fluid. This process is suggested by the strong internal wave shear seen in the velocity field in Figure 5. We refer to this exchange of boundary mixed and stratified fluid as internal wave pumping.

Figure 7 shows the traces in the x-z plane of the three dimensional trajectories of a set of 20 (out of a total of 400) fluid particles released at a height of .2 λ from the wall, well within the mixed layer. The particles are followed for one wave period. If the particles were released in a region of linear wave dynamics then, after one wave period, they would return to their initial locations. Here we see that several of the particles have escaped the boundary layer altogether, while many others have been more deeply entrained near the wall. After each additional wave period the particle dispersion has increased and appears to be more random.

In the analysis of the simulations, emphasis is given to the energetics of the flows. Table 1 presents the mixing efficiency for a series of simulations for a number of different critical slopes. The mixing efficiency is defined as the ratio of the total potential energy dissipation to the total work used to generate the oncoming wave train, and is a measure of the amount of wave energy converted into background potential energy through mixing. We find, for these critical angle simulations carried out for a wide range of bottom slopes and Reynolds numbers, that all the mixing efficiencies are near 35%. A typical energy budget for the oncoming waves is that about 35% of the wave energy goes into mixing the stratified fluid, 55% is dissipated as heat, and approximately 10% of the incident energy is reradiated away from the turbulent boundary layer by smaller scale gravity waves.

Table 1. Mixing Efficiency at Critical Angle

Slope	Reynolds No.	Mixing Efficiency
30°	3000	0.37
30°	800	0.37
20°	1800	0.36
20°	1100	0.35
9.2°	3540	0.35
9.2°	2680	0.37
9.2°	1950	0.36
9.2°	1210	0.38
7.7°	3000	0.35
7.7°	1500	0.33
7.7°	750	0.37
5°	3300	0.37
5°	2300	0.39
5°	1800	0.38
3.4°	2520	0.37
3.4°	1320	0.35

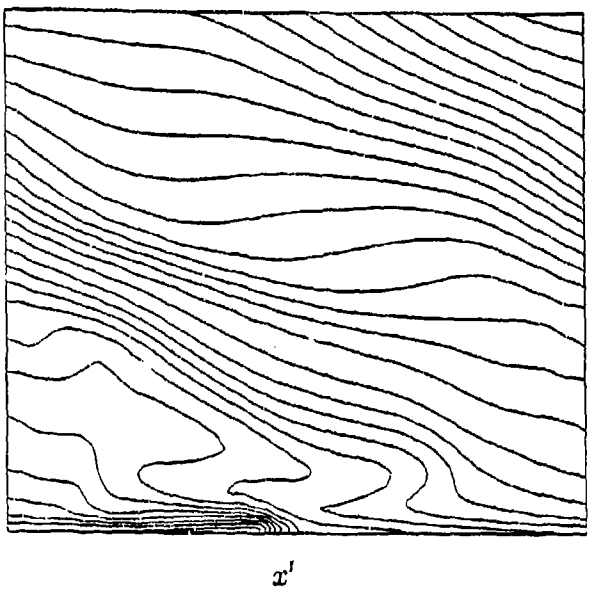


Figure 4: Density field at the end of the dye experiment.

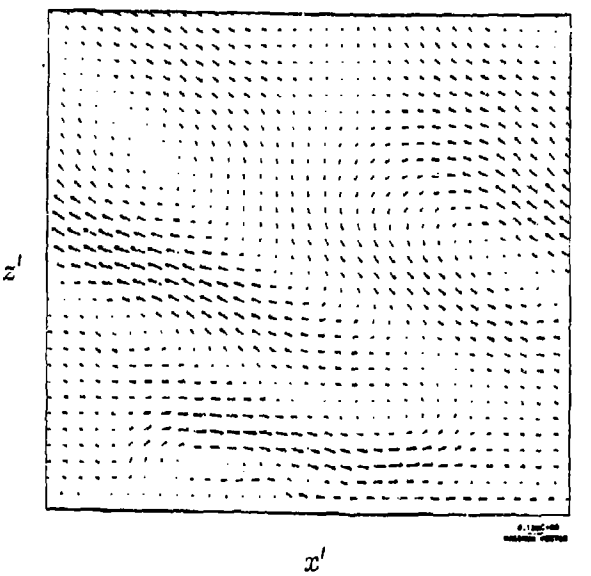
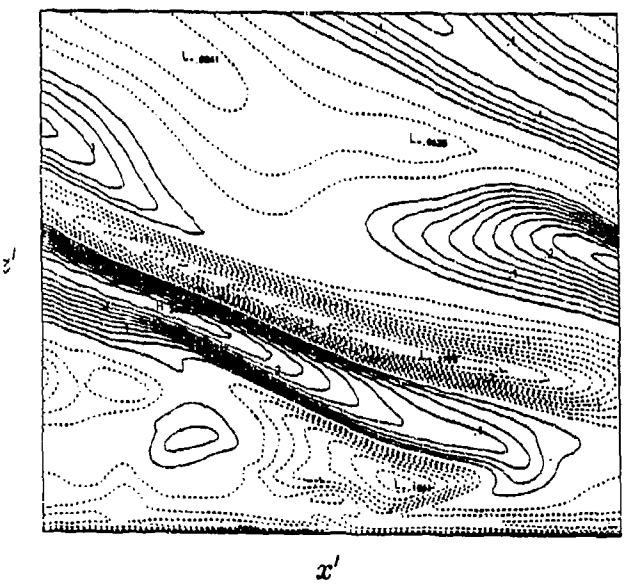


Figure 5: Velocity field at the end of the dye experiment



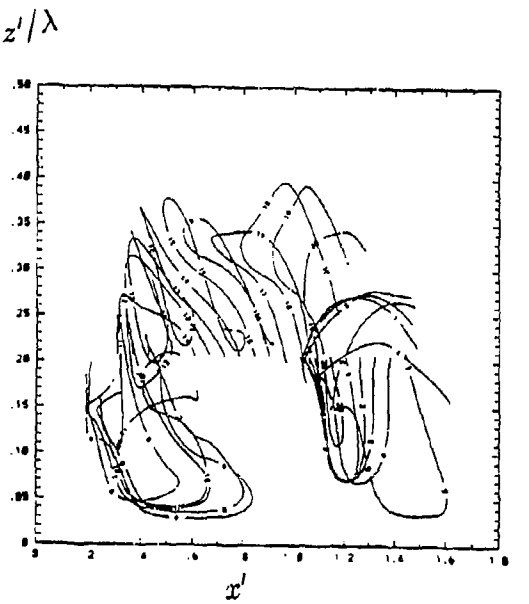


Figure 6: Scalar transport contours illustrating the distance dyed fluid has traveled in the offwall direction over the duration of two wave periods.

Figure 7: Particle trajectories over one wave period. The fluid particles were initially release at a heigh of $.20\lambda$ at a height within the turbulent boundary layer.

4. Conclusions

We have shown some of the details of a fluid mechanical process involving the frequent breaking of internal waves near sloping ocean boundaries, that likely makes a large contribution to the vertical mixing in the ocean. We find that linear oncoming gravity waves transition to turbulence when reflecting from a critical slope, and that the mixing efficiency of the process is about 35%. For steeper sloping terrain, the transition Reynolds numbers, based upon wave current speed and wavelength, for which vigorous three-dimensional mixing occurs in the boundary layers are approximately 1000. Somewhat higher Reynolds numbers are required for transition for the more shallow slopes. We find also that an intermittent turbulent boundary layer forms of approximate thickness $\lambda/3$ in which static instabilities are observed about 50% of the time.

One of the flow features most strongly evident is the existence of a thermal front which moves upslope at the phase speed of the oncoming wave. For steep slopes (greater than 20°) the thermal front resembles a turbulent bore exhibiting nearly continous localized mixing, whereas for shallower slopes (less than 10°) the mixing is observed across the breadth of the domain and is temporally periodic. For the small slopes the turbulence is forced by the oncoming waves and the cycles of strong mixing and dissipation are approximately equal to the wave period. The strong mixing occurs during the phase when the oncoming wave sets up a strong downslope flow at the bottom boundary similar to the backwash on a beach.

We find that the mixing process extends into the interior stratified fluid and is not restricted to a well-mixed boundary region. A key process in this interior communication is the internal wave pumping of mixed fluid into the interior and stratified fluid into the boundary layer. A net result of this process is a steady weakening of the interior stratification. Our results confirm those from field and laboratory studies that conclude that wave reflection from critically sloping terrain is a significant sink for internal wave energy.

5. Acknowledgements

This study was supported under U.S. Navy Office of Naval Research Contract N00014-90-J-1112. The simulations were conducted on the Cray-2 and CrayYMP computers at the National Center for Supercomputer Applications.

6. References

Adam, Y. 1977: "Highly accurate compact implicit methods and boundary conditions," *J. Comp. Physics*, 24, 10-22.

Eriksen, C. C. 1985: "Implications of ocean bottom reflection for internal wave spectra and mixing," *J. Phys. Ocean.*, **15**, 9, 1145-1156.

Eriksen, C. C. 1994: "Internal wave reflection and mixing at Fieberling Guyot," 1994 AGU Ocean Sciences Meeting, San Diego, CA.

Ledwell, J. R., Watson, A. J., Law, C. S. 1993: "Evidence for slow mixing across the pycnocline from an open-ocean tracer-release experiment," *Nature*, 364, 701-703.

Lele, S. K. 1992: "Compact finite difference schemes with spectral like resolution," *J. Comp. Phys.*, 103, 16-42.

Munk, W. H. 1966: "Abyssal recipes," *Deep-Sea Research*, 13, 707-730.

Slinn, D. N., Riley, J. J. 1994: "A model for the simulation of a turbulent boundary layer in a stratified fluid," in preparation.

Taylor, J. R., 1993: "Turbulence and mixing in the boundary layer generated by shoaling internal waves," *Dyn. Atmos. Oceans*, 19, 233-258. Thorpe, S. A., 1992: "Thermal fronts caused by internal gravity waves reflecting from a slope," *J. Phys. Ocean*, 22, 105-108.

Fourth International Symposium on Stratified Flows

INTERNAL TIDAL AMPHIDROMES IN VESTFJORDEN

J.H. Nilsen and T.A. McClimans
SINTEF NHL/The Norwegian Institute of Technology
N-7034 Trondheim, Norway

ABSTRACT

Vestfjorden is a very wide fjord to the east of the Lofoten archipelago at 67 - 68°N latitude. The region is know for its productive fishing grounds and sea bird communities. Plans for offshore oil exploration in this region require therefore a thorough evaluation of the environmental conditions in the sea. The tidal jets through the archipelago are important for propelling the ocean circulation and interfacial waves on the pycnocline between the coastal water and the underflowing Atlantic Water. In the present work, the focus is placed on internal tides which affect both underwater communication and surveillance.

Laboratory simulations using diurnal forcing in the 5 m diameter Coriolis basin at SINTEF NHL show internal tidal amphidromes with a separation of 25 - 30 km. The wave phases, obtained from photogrammetrical analysis of neutral buoys, imply a combined forcing from the tidal jets and flow over the main, deep sill at the entrance. Maximum amplitudes over 15 m are observed between these sources.

1. THE IMPORTANCE OF INTERNAL TIDES IN FJORDS

Underwater communication depends on reasonably homogeneous acoustic properties. The speed of sound is a function of temperature (T), salinity (S) and depth (-Z). The variations of S and especially T with depth and time complicate sound transmission in coastal and frontal regions where a variety of water masses collide and are pushed around by wind and tides. Stratified coastal waters are known to abound in internal waves.

Osborne et al. (1978) reported loss of contact with positioning hydrophones due to internal waves during drilling operations in the Andaman Sea. These waves originated in a narrow sound where tidal currents are strong.

Figure 1.1 shows the bathymetry of the Lofoten region for our study. Tides are expected to create internal waves at the sill to the SE of Røst and by the currents through the Lofoten archipelago.

Stratification, topography and the rotation of the earth are all important for steering (internal) interfacial waves along the pycnocline in a wide fjord like Vestfjorden. Relevant studies of interfacial tidal waves in Norwegian fjords include Stigebrandt (1976) and Moen (1989). Stigebrandt studied the propagation of internal waves from a sill to their shoaling along the sloping bottom. Moen studied the propagation of internal Kelvin waves into a wide fjord. For the present, very wide fjord, the effects of the earth's rotation are expected to be very important. A relevant study of internal tides in a wide basin open to the sea was made by Matsuyama and Ohwahi (1990). Their numerical model produced internal tidal amphidromes.

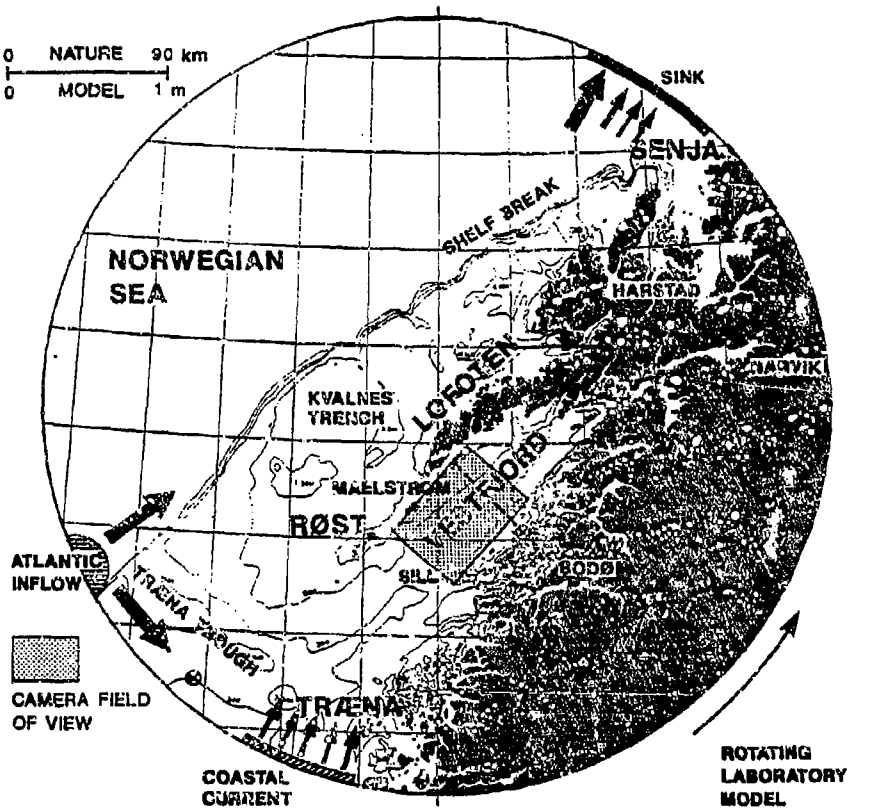


Figure 1.1 Places and isobaths within the geographical extent of the rotating laboratory model of the Lofoten region. Forced boundary conditions are noted (Nilsen, 1994)

2. LABORATORY MODEL OF THE LOFOTEN REGION

Internal waves in Vestfjorden were studied in a distorted stratified, rotating laboratory model. 3-D trajectories of neutral buoys embedded at various depths in the stratified flow were recorded by photogrammetric measurements and automatic particle tracking. The phase information derived from the particle motions was used to determine the direction of the interfacial waves.

The relevant parameters of the problem are the densimetric Froude number $F = U/(g'H)^{1/2}$ and the Rossby number $Ro = U/fL$, where H = vertical length, L = horizontal length, U = horizontal velocity, g' = reduced gravity and f is the Coriolis parameter. These give a consistent set of scaling laws for which the ratio of natural to model time scales is $T_r = L_r/(g_r'H_r)^{1/2}$.

Horizontal distances in nature are 90 000 times as large as model distances (horizontal length ratio L_r = 90 000). The vertical scale is exaggerated such that 900 m is half a meter in the model (height ratio H_r = 1 800), giving a distorted model. The density gradients ($\Delta\rho$) in the model are also exaggerated (by 84 %) (g_r' = 1/1.84). This is done to improve the accuracy of the salinity measurements and to provide a time scaling, according to the Froude model law, $T_r = L_r (H_r\ g_r')^{-1/2}$ = 2880. With this scaling, a day is simulated in 30 s and the regulations of the inflows are easy to follow on the laboratory clock. For the present study, however, the more appropriate time scale is the tidal forcing with a period of a pendulum day. This is due to the fact that the vertical axis is tilted slightly to simulate the tidal currents over the sill and through the Lofoten archipelago.

The model was used to simulate the transport of Atlantic and coastal waters through the fjord system (McClimans and Nilsen, 1991; McClimans and Myhr, 1992). Details of the model, scaling, and scale effects are given in Nilsen (1994).

3. MEASUREMENTS OF 3-D POSITIONS OF SUBMERGED, NEUTRAL BUOYS

Neutral buoys about 1 cm in diameter, embedded at various depths, were used to observe the flow field. In many laboratory experiments, three dimensional motions are obtained by taking orthogonal observations through side windows or through a side window and the surface. In cases with essentially 2-D topography, a 3-D picture of the motion can be constructed this way. However, with natural fjord topography it is necessary to use photogrammetric methods to construct a 3-D motion field from two or more oblique views through the water surface.

Photogrammetric techniques described by Nilsen and Hådem (1994) are used to calculate the three dimensional displacements of the neutral buoys. The buoys were situated both at the water surface and at different depths. Three video cameras monitored the area of interest in Vestfjorden between the Moskenes Sound and Landegode. Figure 3.1 shows a sketch of the camera set-up. The positions of the perspective centers of the three cameras are $(X_0,Y_0,Z_0)_1$, $(X_0,Y_0,Z_0)_2$ and $(X_0,Y_0,Z_0)_3$. Observed image coordinates for a certain particle in each of the three image coordinate systems, $(x_{im},y_{im},z_{im})_{1,2\ and\ 3}$, are also shown on the figure. At the surface, $(X_s,Y_s,Z_s)_{1,2\ and\ 3}$, the rays are exposed to refraction due to the different optical properties of air and water. The three rays all come from the buoy located inside the circle in Figure 3.1.

Seen from above, the three cameras are located in the corners of a wide triangle to achieve minimum uncertainty in the intersection point of the rays from the perspective centers through the image points. Details of the calibrations of the locations are given in Nilsen and Hådem (1994).

A unique problem for the present situation is the radial accelerations of the modeled flow. The position of the surface of the water in the basin was calculated from observations of particles moving on the surface. The surface of the rotating model was assumed to be an elliptic paraboloid of revolution and smooth (no capillary waves). At the intersection of the ray from the perspective center through the image point and the surface, a normal to the surface was calculated. The direction of the refracted ray was then determined, according to Snell's law of refraction.

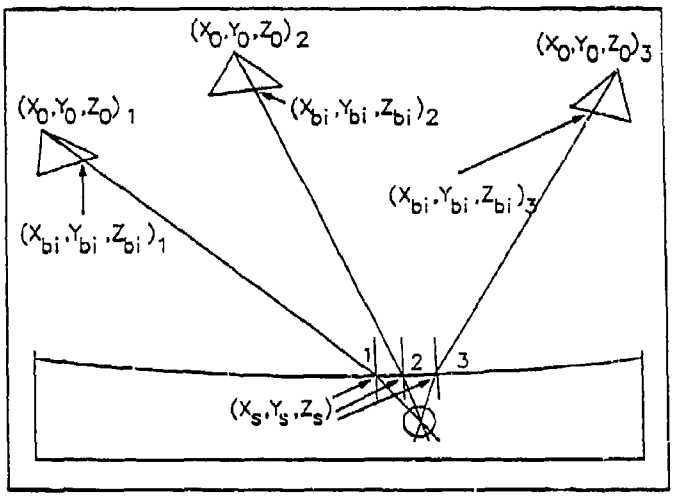


Figure 3.1 Sketch of the camera set-up

The point positions of the buoys were calculated using a method of least squares fit, such that the sum of the squares of the distances from these points to the three corresponding rays is minimum. The corresponding image coordinates of the buoys in each set of three images were found automatically by using a dynamic thresholding technique, center of gravity calculations and an epipolar approach to limit the search area within each image.

To follow a buoy through a series of time steps, a simple approach was used. Due to the relatively sparse coverage of buoys, small time steps and low velocity, it was possible to identify corresponding image points for the same buoy in image 1 at time t+dt, as those closest to these at time t. When the position of a certain particle at time t+dt was found by this method, the corresponding image coordinates in the two other images (at time t+dt), were found by searching through epipolar polygons in these two images for the candidate giving the minimum variance in the intersection point of the three rays and less than a certain value.

For well-defined points on the bottom of the rotating basin filled with water, the point repetition accuracy (RMSE) was 0.6 mm using 25 time steps. (RMSE = 0.15 mm in XY and 0.5 mm in Z (height) or ca 1/3000 of mean camera-to-object distance.)

The positions of the submerged buoys were somewhat more difficult to calculate. This was probably caused by changes in the backward light reflectance of the particles due to rotational motions and tipping, causing problems in the determination of the center of gravity.

Sometimes buoys were close enough to each other to cause more than one possibility of combining them photogrammetrically, and the image point in one image was related to two or more image points in one or both of the other two corresponding images. An algorithm for discriminating particles through different time steps is presented in Nilsen and Hådem (1994).

4. MODEL RESULTS

Figure 4.1 shows a graphic presentation of calculated positions of a submerged neutral buoy observed at 24 different times each ca 1.5 s apart. The left part of the figure shows the buoy positions seen from a perspective view in the model coordinate system. The trace to be considered is inside the circle in this part of the figure. On the right there are three coordinate systems. The uppermost shows the calculated vertical displacement of the buoy as a function of time. The two other coordinate systems show the buoy displacements projected on the x-z, and x-y planes. This motion gives the essential details for computing the local amplitude, phase and propagation direction of interfacial waves. The direction of wave travel, however, requires knowledge of the depth of the buoy relative to the depth of the pycnocline. For buoys in the lower (upper) layer, the wave propagates in the direction of travel at the crest (trough). It is therefore necessary to measure the density structure. This is done by salinity profiles.

Since the model was excited by a constant diurnal tidal forcing, buoy trajectories at quite different times and conditions are used by relating their phases to the time of current reversal to the NW in the Moskenes Sound (Maelstrom). The internal tidal map of Figure 4.2 was constructed from the general characteristics of the amplitude, phase and wave propagation directions of 40 neutral buoys.

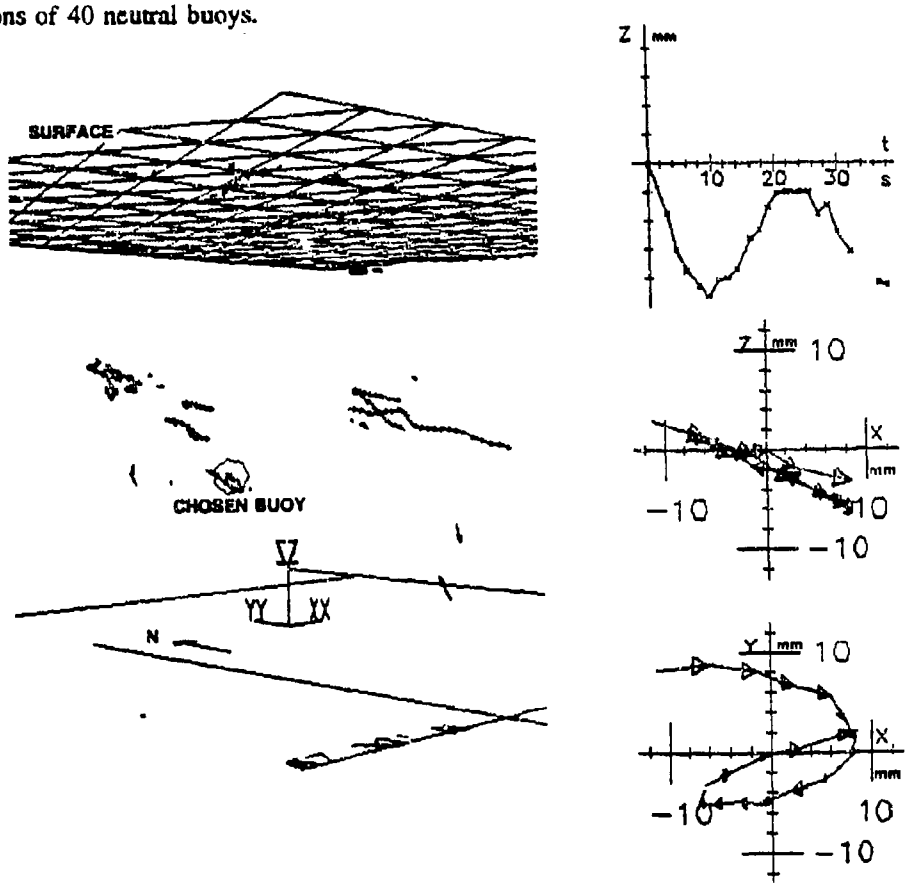


Figure 4.1 An example of the calculated traces of neutral buoy motions from the photogrammetric analysis. The X,Y,Z,t coordinates of the buoy trajectory encircled in the perspective view in model coordinates, are given on the right.

There appear to be three amphidromes in the field of view. This agrees well with the general knowledge of these phenomena; however, within the data set there were regions of consistent anomalies which are not yet fully understood. Details of these anomalies, as well as the residual flow field derived from the buoy trajectories, are given by Nilsen (1994).

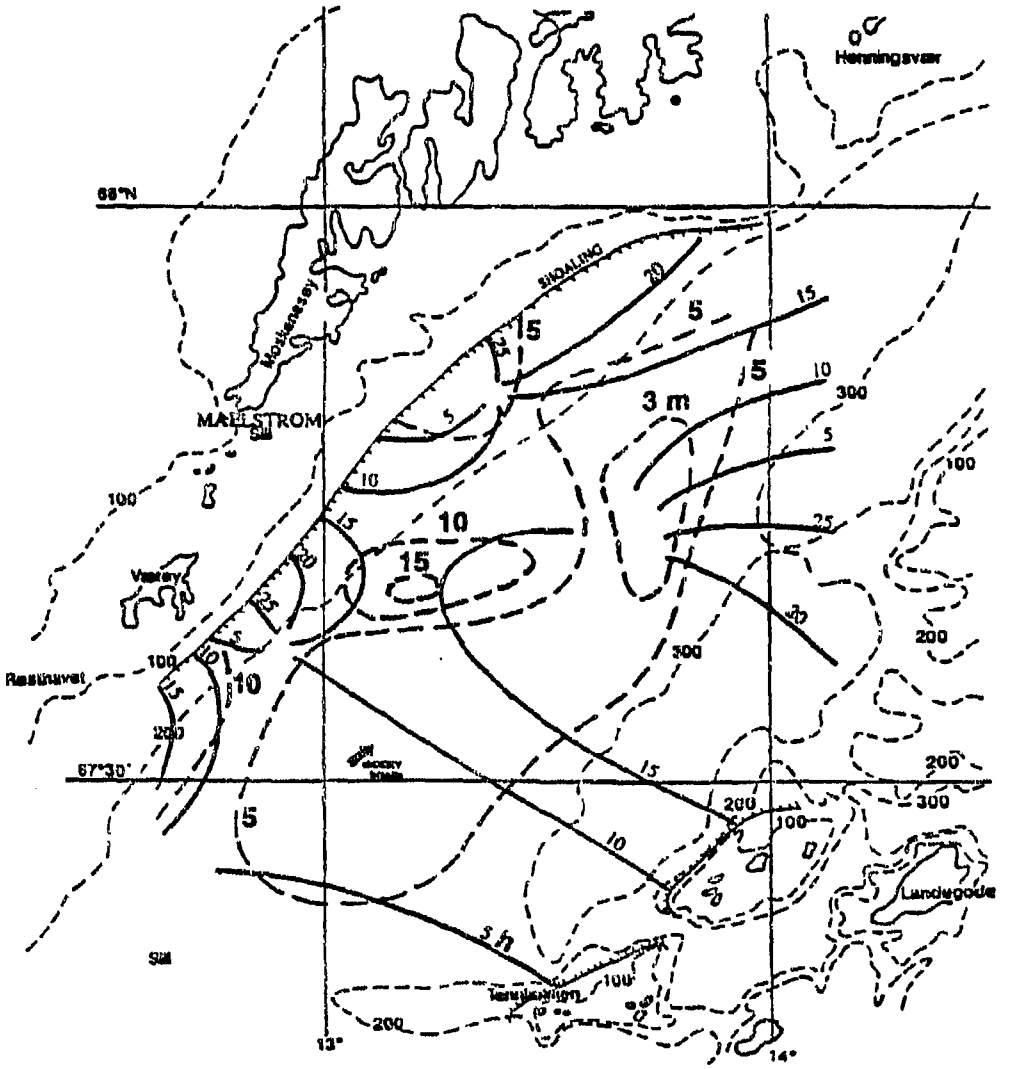


Figure 4.2 Internal tidal amphidromes in Vestfjorden derived from diurnal forcing of a stratified, rotating laboratory model; —— amplitude; -—— phase.

5. DISCUSSION

The present results of phase fields and amplitudes of internal tides in Vestfjorden are derived from a distorted, rotating laboratory model. Several comparisons with available sets of field measurements imply that the ocean circulation in the model is a good simulation of natural flows (McClimans and Nilsen, 1991; Furnes and Sundby, 1981).

Due to the distortion, only long-wave processes can be simulated within the framework of the Froude similitude. This includes internal tides. To our knowledge this is the first study of internal waves in Vestfjorden and it is therefore of interest to establish cause/effect relationships which may be tested/verified in future field measurement programs (or detailed analysis of existing, relevant data sets). Some very recent data, from a current meter array inside the sill, show interfacial waves propagating into the fjord (McClimans and Johannessen, 1994). The result (Rocky Road) is noted on the map in Fig 4.2.

Neutral buoys suspended in the moving density field were used to obtain three dimensional particle trajectories in the internal wave fields. High accuracy photogrammetrical methods gave sufficient information on interfacial waves using a sparce set of buoys. The buoy trajectories reveal first mode internal waves propagating from the Maelstrom and the sill. This general pattern does not seem to depend on the inflow conditions or the depth of the interface. There are, however, too few data available to give a statistically significant account of the effects of variable inflows.

The observed amphidromes indicate that the tidal jets through the Lofoten archipelago do indeed act as sources for internal tidal waves. This is more complicated than the situation modeled by Matsuyama and Ohwaki (1990). The largest amplitudes (> 15 m) appear along a ridge between the outer sill and the Maelstrom, and occur when the tidal currents change to the SE through the Lofoten archipelago.

At the present stage of development of our techniques it is time-consuming to construct an internal wave field. More automation is needed at the various stages of the analysis. A particularly critical phase is the selection/rejection of particles due to lost frames and interference in the sequences. A larger number of buoys increases the interference problem. More thought must be given to the systematic synthesis of these facts for automatic analyses.

The present analysis of the laboratory results raises many questions on the spatial distributions of internal wave phases and amplitudes forced by tides and steered by topography and the rotation of the earth. The result that the largest internal wave amplitudes are observed between the two main sources is reasonable; however, the phases and patterns of the amphidromes are expected to be quite different in nature, where the semi-diurnal tides dominate. More complete analyses of existing data and dedicated field measurement programs are needed to answer many of these questions. Alternatively, numerical models (e.g. Sveen and Martinsen, 1994) validated to these data, could provide many of the missing details and simulate local changes incurred by varying the inflows of Atlantic and coastal waters. Computer models can also provide more realistic tidal forcing than the constant diurnal forcing used in the laboratory model.

ACKNOWLEDGEMENTS

This work has benefitted from support by the Norwegian Defence Research Establishment in connection with the NATO collaboration "Rocky Road", the Office of Naval Research through Grants N00014-90-J-1882 and N00014-92-J-4016 and the Norwegian Research Council for Sciences and the Humanities. The model basin was constructed with additional support from the Institute of Marine Research and Operator Committee North. The authors would like to thank NDRE and John Scott, Defence Research Agency, Portland, UK for a fruitful collaboration on the Rocky Road project.

REFERENCES

Furnes, G.K. and Sundby, S. (1981): Upwelling and wind induced circulation in Vestfjorden. In The Norwegian Coastal Current. Eds. R. Sætre and M. Mork. Univ. of Bergen.

Matsuyama, M. and Ohwaki, A. (1990): Influence of internal tides on sea level variations at the Suruga Bay coast. La Mer 28:87-96.

McClimans, T.A. and Johannessen, B.O. (1994): Rocky Road field measurement analysis: Vol 1. The potential of a limited current meter array. SINTEF NHL Report STF60 F94050.

McClimans, T.A. and Myhr, B. (1992): Laboratory simulation of the ocean circulation around Lofoten. NHL Video.

McClimans, T.A. and Nilsen, J.H. (1991): Laboratory simulation of the ocean circulation around Lofoten from October 1982 to June 1984. SINTEF NHL Report STF60 A91027.

Moen, I. (1989): Studie av det dynamiske samspillet mellom fjord- og kystvann. Thesis in Oceanography, Univ. of Bergen.

Nilsen, J.H. (1994): An experimental study of internal tidal amphidromes in Vestfjorden. Ph.D. thesis, Dept of Civil Engineering, The Norwegian Institute of Technology.

Nilsen, J.H. and Hådem, I. (1993): Measurements of 3-D positions of submerged, neutral buoys. ISPRS Journal of Photogrammetry and Remote Sensing (submitted).

Osborne, A.R., Burch, T.L. and Scarlet, R.I. (1978): The influence of internal waves on deep-water drilling. J. Petroleum Tech. 30: 1497-1504.

Stigebrandt, A. (1976): Vertical diffusion driven by internal waves in a sill fjord. J. Phys. Oceanography 6: 486-495.

Sveen, V. and Martinsen, E.A. (1994): Operational use and some sensitivity tests with a 4 km high resolution ocean model in the Vestfjord area. DNMI T.R. No. 122.

Fourth International Symposium
on
STRATIFIED FLOWS

LEGI/Institut de Mécanique de Grenoble, CNRS - UJF - INPG
Grenoble, France, June 29 - July 2, 1994

Observations and Modelling of stratified Flow in the Sound between Denmark and Sweden

by

Jacob Steen Møller[1], Ph.D., Erland B. Rasmussen[1], M.Sc. and
Ann Christina Ellegaard[1], M.Sc.

ABSTRACT

A combined bridge and tunnel between Copenhagen (Denmark) and Malmö (Sweden) across the Sound (Øresund) has been planned according to an agreement between the Danish and Swedish Governments. The Sound is the second largest of the three straits connecting the Baltic Sea with the North Sea. The flow in the Sound is barotropically dominated, the meteorological forcing being the dominating mechanism governing the flow. The oscillating flow over the sill creates a highly stratified flow north of the sill with dense water plunging down the southern side of the sill during southward flow. Environmental concerns regarding the possible impact on the flow conditions from construction of the Link have constituted the basis for thorough hydrodynamic investigations comprising long term monitoring and detailed 3D modelling. The monitoring includes measurements of water levels, wind and air pressure, stratification and currents (measured from fixed stations as well as from vessels using shallow water Broad-Band Doppler techniques). The modelling includes 3D numerical modelling using the model SYSTEM 3 developed at the Danish Hydraulic Institute (DHI). Comparisons between measured and modelled flow are presented. In particular, the horizontal velocity distribution over complex topography (including headlands and islands) is investigated by means of direct comparison of ADCP (Acoustic Doppler Current Profiler) data with modelled results. In addition, the vertical velocity distribution is investigated using measurements from fixed stations. Finally, an account of the possible impact of the Link on the exchange flow is given.

1 INTRODUCTION - THE SOUND LINK

Denmark and Sweden are separated by the Sound, one of the three water ways that accounts for the exchange of water between the Baltic Sea and the North Sea. In 1990 the Governments of the two countries agreed on the construction of a fixed Link across the Sound. The Link consists of a submerged tunnel from the Danish island Amager under the Drogden channel leading to two artificial islands south of Saltholm connected by a low bridge, from the islands a bridge and a high bridge span the Flinten Channel to Sweden, Fig. 1. The Link has been designed in order to minimize the blocking of the flow through the Sound.

---

[1] Danish Hydraulic Institute, Agern Allé 5, DK-2970 Hørsholm, Denmark

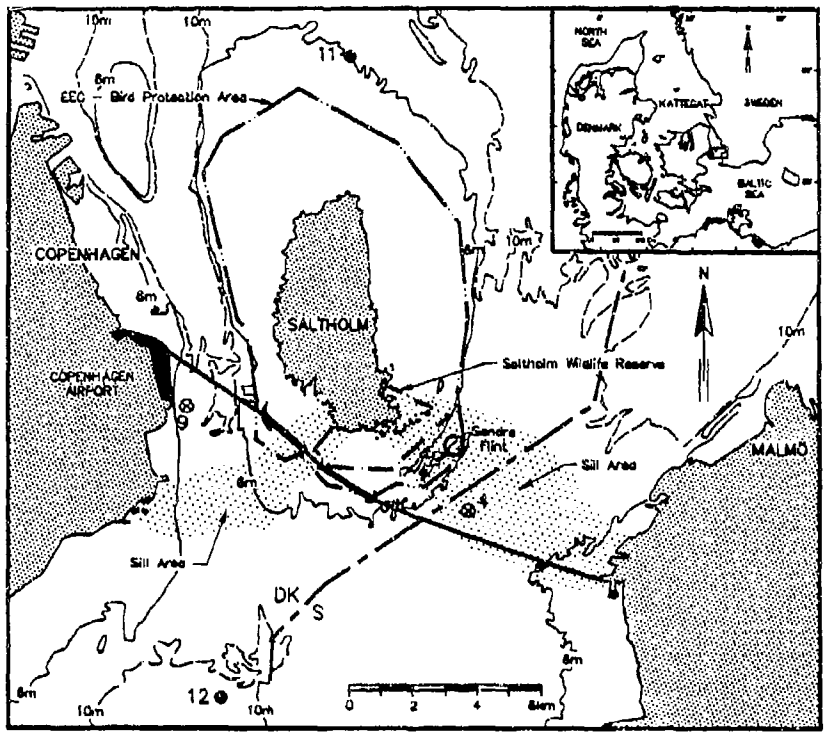


Figure 1 The planned fixed Link across the Sound connecting Denmark and Sweden. Illustration of relevant stations for monitoring currents and salinity (monitoring programme I).

The exchange of water between the Baltic Sea and the North Sea takes place through the Great Belt (Store Bælt) which is responsible for approximately 65% of the exchange, the Sound ~25% and the Little Belt (Lille Bælt) ~10% (Jacobsen, 1980). Changes in the flow conditions in the Sound, due to the Link, will influence the hydrography of the Baltic Sea. The aquatic environment of the Baltic Sea is a sensitive brackish ecosystem which is strongly dependent on the supply of oxygen rich, saline water from the North Sea through the Danish straits. Environmental concerns regarding the possible impact that the contruction of the Link may have on the flow conditions have constituted the basis for thorough hydrodynamic investigations comprising long term hydrographic monitoring and detailed 3D modelling.

2 GENERAL HYDRODYNAMICS OF THE SOUND

The fresh water surplus of the Baltic Sea forces a mean current from the Baltic of $1.4 \cdot 10^4$ m^3/s. The shifting weather conditions, dominated by low pressures travelling from the North Atlantic towards the east with time scales of 5 to 10 days, force the water to oscillate in and out of the Baltic Sea through the straits at irregular intervals.

The flow in the Sound is barotropically dominated. Hence, the meterological forcing, and the wind and water level differences between the Kattegat and the Baltic Sea are the dominating features governing the flow. The density difference between the north (typical salinity: 26 psu) and south (typical salinity: 8 psu) of the Sound is also of some importance for the flow. The flow is bottom friction dominated and the specific resistance depends on water level and stratification.

The flow of brackish water from the Baltic Sea and more saline water from the North Sea forms a stratified two or three layer system in the straits, Fig. 2. The Sound has a mean depth of 15-20 m

with a very shallow sill, at a depth of 7-8 m, across the Sound south of Saltholm, near the alignment of the Link. This Drogden sill separates the salt water in the Sound from the Baltic Sea and controls the southward flow through the Sound. The Drogden sill accounts for between 30 and 70% of the total flow resistance in the Sound, depending on water levels and stratification in the sill area.

During northward flow, Baltic water with a salinity of approximately 8 psu flows into the Sound thereby pushing Kattegat surface water, with a salinity of 20 psu, to the north. The mixing between the two layers is strong and increases the salinity of the upper layer to 12-15 psu. If the flow lasts for more than 3 days, a quasi-steady outflow situation is formed where the Helsingør-Helsingborg is the governing cross-section.

During southward flow, the surface layer with a salinity of 12-15 psu is forced to the south through the Sound across the sill. After some time, the interface to water with a salinity of 20 psu (Kattegat surface water) has risen to the level of the sill and starts flowing into the Baltic Sea. South of the sill the salt water plunges under the brackish Baltic water and forms a dense bottom current. At the sill the water is often totally mixed due to bottom generated turbulence. If the flow continues southward, water with a salinity up to 25 psu flows into the Baltic Sea.

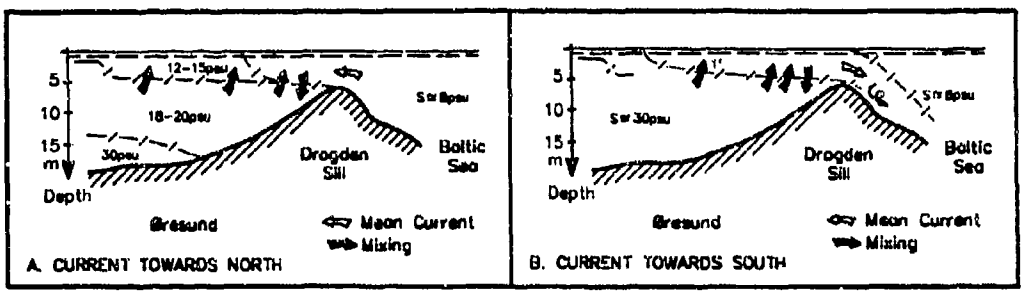
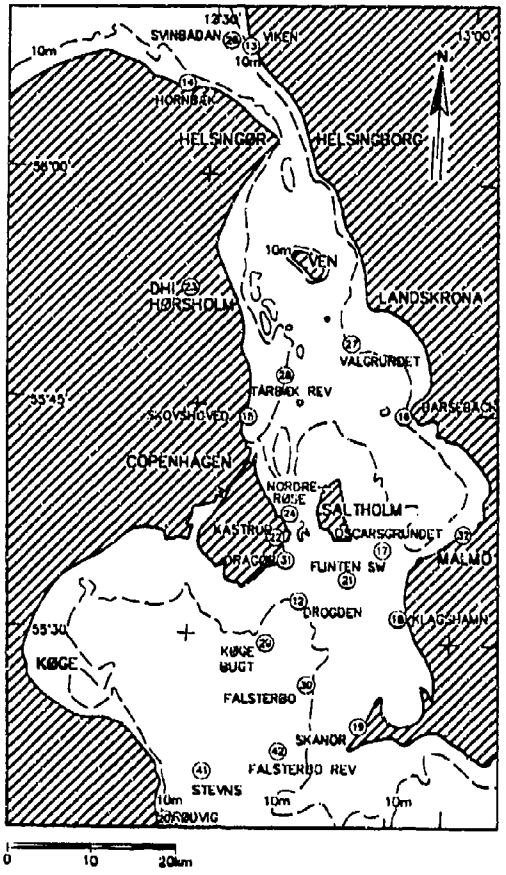


Figure 2 Section through the Sound describing the principles of (A) northward flow, (B) southward flow.

3 MONITORING

The first monitoring programme in connection with the Sound Link project was established in February 1992. Since then, the programme has been changed and extended to meet new requirements. The existing monitoring programme is customised to provide detailed information on the hydrodynamics of the strait and to provide data for set-up, and in depth calibration and validation of the 3D numerical model.

Wind and air pressure, water levels, currents and salinity are measured continuously at a number of fixed stations in the Sound, Fig. 3. Salinity and currents are measured at several depths at each station. The data are transmitted online to DHI. With regular time intervals, current and salinity profiles are measured from a survey vessel sailing along lines in areas of special interest. The current profiles are measured by shallow water Broad-Band Doppler techniques using an ADCP (Acoustic Doppler Current Profiler). In August and October 1993 and in January 1994, further intensive measuring campaigns were carried out. The vessel based measurements were intensified and supplemented with float tracking and an extended programme for current measurements at fixed stations close to the alignment of the Link.



ST.	LOCATION	WATER LEVEL	CURRENT	T/C PROFILE
12	DROGDEN	●		●
13	VIKEN	●		
14	HORNBÆK	●		
15	SKOVSHOVED	●		
16	BARSEBÄCK	●		
17	OSCARSGRUNDET	●		
18	KLAGSHAMN	●		
19	SKANÖR	●		
20	RØDVIG	●		
21	FLINTEN SW	●	●	●
22	KASTRUP			
24	NORDRE RØSE	●	●	●
26	SVINBADAN			●
27	VALGRUNDET			●
28	TÁRBÆK REV			●
29	KØGE BUGT			●
30	FALSTERBO			●
31	DRAGØR	●		
32	MALMÖ	●		
41	STEVNS			●
42	FALSTERBO REV			●

ST.	LOCATION	WAVES	WIND	TURBIDITY
12	DROGDEN	●		
13	VIKEN			
14	HORNBÆK			
15	SKOVSHOVED			
16	BARSEBÄCK			
17	OSCARSGRUNDET	●	●	
18	KLAGSHAMN			
19	SKANÖR			
20	RØDVIG			
21	FLINTEN SW	●		●
22	KASTRUP		●	
24	NORDRE RØSE			●
26	SVINBADAN			
27	VALGRUNDET			
28	TÁRBÆK REV			
29	KØGE BUGT			
30	FALSTERBO			
31	DRAGØR			
32	MALMÖ			
41	STEVNS			
42	FALSTERBO REV			

Figure 3 Fixed stations in the Sound. Hydrographic monitoring programme V.

4 STRATIFIED FLOW

The stratified flow through the Sound may be divided into three sections, ref. DHI/LIC/SMHI (1993):

North of the sill the water column is almost always stratified. When the current is northward the interface is pushed down and to the north, during southward current the interface is raised. The position of the interface varies 2-4 m between north- and southward flow, Fig. 4. The Coriolis force affects the flow through the Sound and tilts the interface in the east-westerly direction.

In the sill area the flow resistance is large during mixed conditions but reduced during situations where the water column is stratified. Measurements have shown that the flow across the sill is stratified during weak southward flow and when the flow direction is changing. The water column is stratified (salinity difference between surface and bottom > 1 psu) for 10% of the time when the flow is northward and 30% of the time with southward flow.

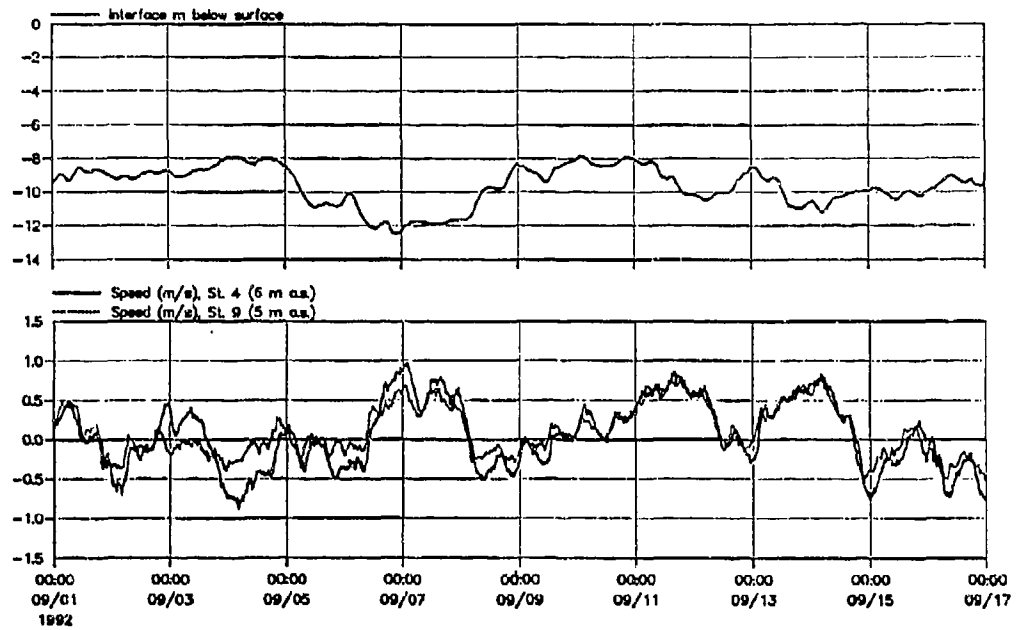


Figure 4 Calculated interface level at Station 11. Current measured at Stations 4 and 9. For station numbers see Fig. 1.

During northward flow the sill area is stratified until outflowing Baltic Sea water has flushed the sill, the flushing lasts approximately half a day. When the near bed velocity is small and the vertical density difference large, the stratification is stable and exists across the sill. When the velocity in the bottom layer increases, the interface breaks down due to bottom generated turbulence. Fig. 5 illustrates examples of measured flow conditions across the sill. An analytical calculation regarding the mixing between the two layers based on equations for entrainment into the lower and upper layers has been carried out. Below is shown the equation for the downwards entrainment.

The calculation of the mixing effect (entrainment) is based on the bulk flux Richardson's number theory, ref. Bo Pedersen (1986):

$$R_f^T = \frac{POT}{PROD} \tag{1}$$

where R_f^T (~4.5%) is a constant for sub-critical flows, called the bulk flux Richardson number, PROD is the integrated production of turbulent kinetic energy in a layer, and POT is the integrated increase in potential energy in a layer or the work performed by the turbulence, which can be written as follows:

$$POT_j = v_{E,0}\frac{1}{2}\delta\rho_R g h_j \tag{2}$$

$v_{E,0}$ is the entrainment into the bottom layer, h_0 is the thickness, g is the gravity, δ is the dimensionless reduced density and ρ_R is a reference density.

The production of turbulent kinetic energy in the lower layer ($PROD_0$) is determined by the following expression, ref. Bo Pedersen (1986):

$$PROD_0 = \tau_i(u_i - V_0) + \tau_b V_0 = \rho_R \frac{f_b}{2}\left(1 + \frac{f_i}{f_b}(3\frac{h_1}{h_0+h_1})^{3/2}\right)v_0^3 \qquad (3)$$

Based upon the Richardson bulk flux number theory, the downwards entrainment is then estimated to be:

$$v_{E,0} = \frac{R_f \frac{\tau f_b}{2}}{\frac{1}{2}g}\left(1 + \frac{f_i}{f_b}(3\frac{h_1}{h_0+h_1})^{3/2}\right)\frac{V_0^3}{\delta h_0} \approx 9{\cdot}10^{-5}\frac{V_0^3}{\delta h_0} \qquad (4)$$

In the following section, this expression is applied to observed conditions.

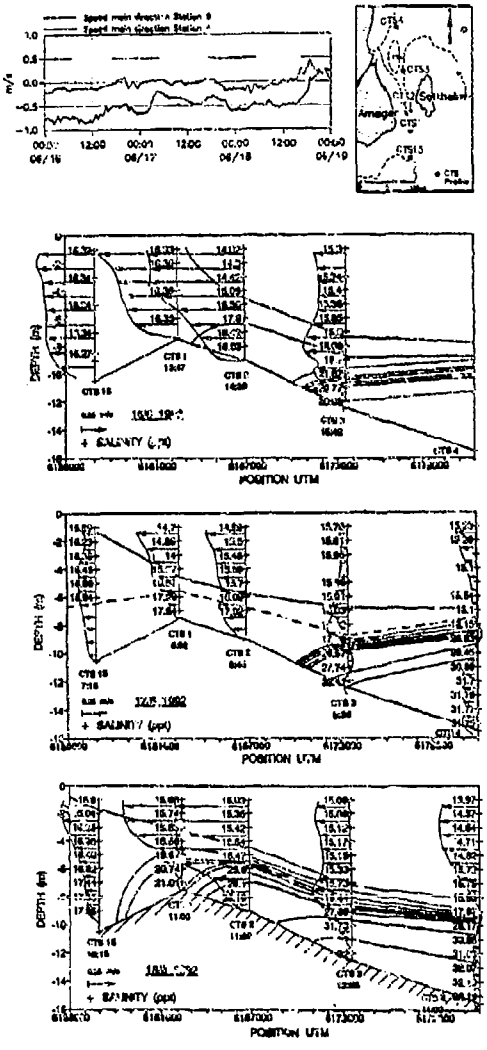


Figure 5 Profiles of salinity and currents measured along a N-S line in the Drogden channel.

On 16 June 1992, the salinity near the surface at Station CTS3 was 15.3 psu, at Station CTS2 14.3 psu, and at Station CTS1 16.3 psu. Surface water of increasing salinity flows towards the sill, which was why water of higher salinity was measured closer to the surface at Station CTS3 than at Station CTS2. The higher salinity near the surface at Station CTS1 than at Station CTS2 was due to mixing. The wind velocity (W) on 16 June 1992 was approximately 6 m/s. At Station CTS2 the upper layer thickness (h_1) was 5.5 m, the lower layer thickness (h_0) was 3.5 m, the lower layer velocity (V_0) was 0.5 m/s and the salinity difference between the layers 3 psu. Based upon these data the upwards entrainment at Station CTS2 is calculated to be $39 \cdot 10^{-5}$ m/s, and the downwards entrainment to be $134 \cdot 10^{-5}$ m/s. The distance between Station CTS2 and Station CTS1 is 5000 m giving a travelling time of approximately 2.8 hours. In 2.8 hours, a downwards entrainment velocity of $95 \cdot 10^{-5}$ m/s increases the lower layer thickness by approximately 10 m. This calculation indicates that the upper layer is mixing into the lower layer before Station CTS1, which is supported by the measurements.

On 17 June 1992, the salinity stratification was observed across the sill. The wind velocity (W) was approximately 4 m/s. At Station CTS1 the upper layer thickness (h_1) was 5.0 m, the lower layer thickness (h_0) was 3.0 m, the lower layer velocity (V_0) was 0.1 m/s, and the salinity difference between the layers 2.5 psu. The entrainment upwards at Station CTS1 is calculated to be $0.8 \cdot 10^{-5}$ m/s, and the entrainment downwards $1.5 \cdot 10^{-5}$ m/s. A change of the interface position of 1 m would take approximately 40 hours. According to this calculation, a stratified structure at the sill is not mixing into one homogenous layer, which is supported by the observations.

In situations where the current speed in the upper layer becomes very large the interface rises and the bottom layer is lifted over the sill due to low pressure generated by the rapidly flowing upper layer, the Bernoulli effect, Fig. 5.

South of the sill the inflowing salt water plunges under the light brackish Baltic water. The plunging line moves back and forth depending on density differences, and the flow velocity and time scale. When the flow direction changes to northward, the saline water, which passed the sill during southward flow, continues to flow to the south into the deeper parts of the Baltic Sea.

5 3D NUMERICAL MODELLING

The water and salt exchange through the Sound is modelled using the 3D model, SYSTEM 3 developed at the Danish Hydraulic Institute (DHI), ref. DHI (1990). The 3D model is fully three-dimensional and non-hydrostatic solving the momentum equation and continuity equations in the three cartesian directions. SYSTEM 3 simulates unsteady flow, taking into account density variations, bathymetry and external forcing such as meteorology, tidal elevations, currents and other hydrographical conditions. The model is composed of a hydrodynamic module, a turbulence module and an advection dispersion module. The flow is decomposed into mean quantities and turbulent fluctuations. The closure problem is solved through the Boussinesq eddy viscosity concept relating the Reynold stresses to the mean velocity field. To handle density variations, the equations for conservation of salinity and temperature are included. An equation of state constitutes the relation between the density and the variations in salinity and temperature.

The 3D model is used to simulate the water flow and salt flux through the Sound throughout a design period in the reference situation before the construction of the Link and after the construction by parameterisation of the Link elements. The Sound Link is calculated to block 0.5% of the exchange of water and salt to the Baltic Sea if no compensation dredging is performed. The salt water transported through the Sound into the Baltic Sea enters different levels of the Baltic Sea depending on the salinity. The bottom waters in the deep parts of the Baltic Sea are only occasionally exchanged with more oxygen rich water, when high saline water enters the Baltic Sea. It is, therefore, important for the environment, especially in the deeper parts of the Baltic Sea, that the transport of water with different salinities is unchanged after the construction of the fixed Link. In order to achieve this compensation, dredging is performed so that the combined effect of the dredging and the Link is nil regarding the discharge to and from the Baltic Sea.

6 COMPARISON BETWEEN OBSERVED AND MODELLED FLOW

The 3D model is calibrated against measured water levels and currents for the period 1-17 August 1993. The monitoring program for measuring salinity was not fully launched during this period and the calibration is, therefore, only preliminary. The calibration of the model against observations of water levels, salinity and currents for the period 18-31 October 1993 is ongoing.

Fig. 6 illustrates comparisons between modelled and observed (using vessel based ADCP) horizontal current profiles. Figs. 7 and 8 illustrates time series of modelled and observed current and salinity at the fixed stations near the alignment of the Link. Generally, there is satisfactory agreement between modelled and observed currents except in the middle of the Drogden channel during southward flow. This inconsistency is due to baroclinic effects. Just north of the sill the water column is mostly stratified during southward flow. If the stratification in this area is modelled inadequately, the flow resistance is exaggerated and thus the current speed underestimated.

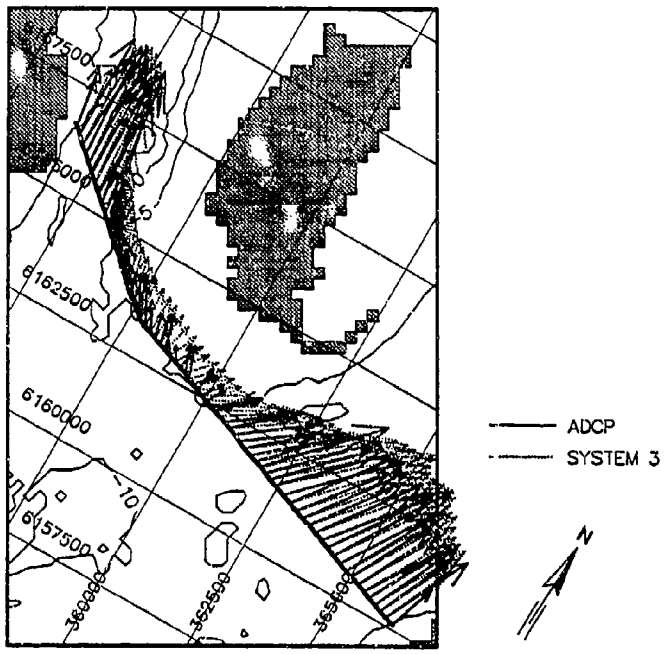


Figure 6 Modelled and observed horizontal current profiles on 15 August 1993 (measured using a vessel based ADCP).

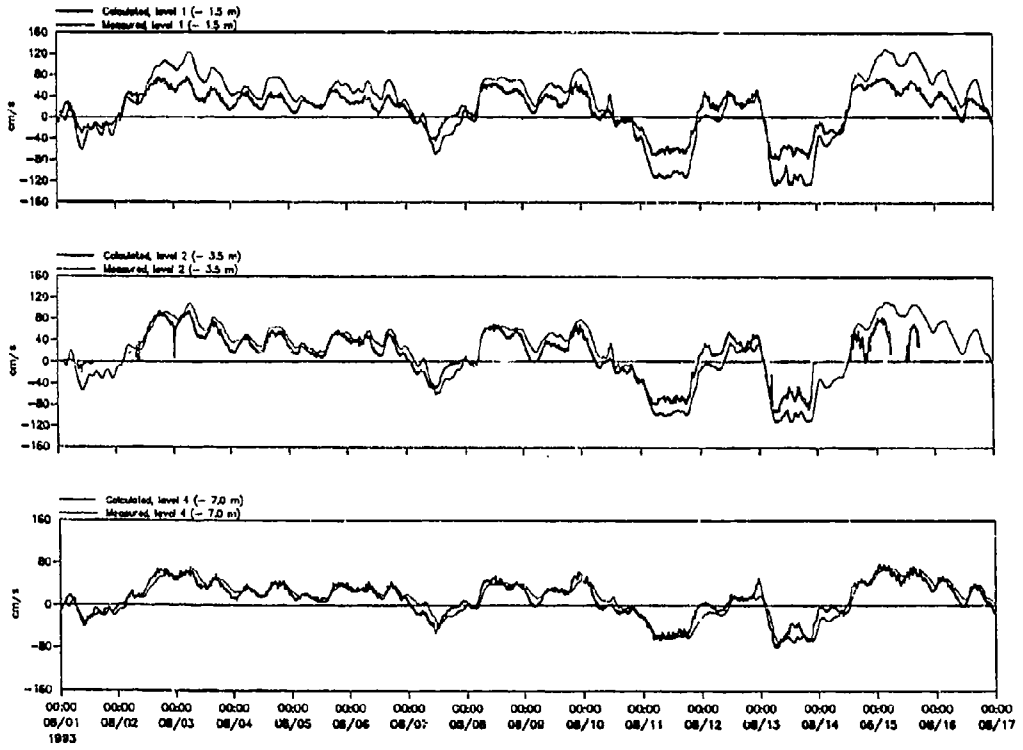


Figure 7 Time series of modelled and observed current at Station 4 (Fig. 1).

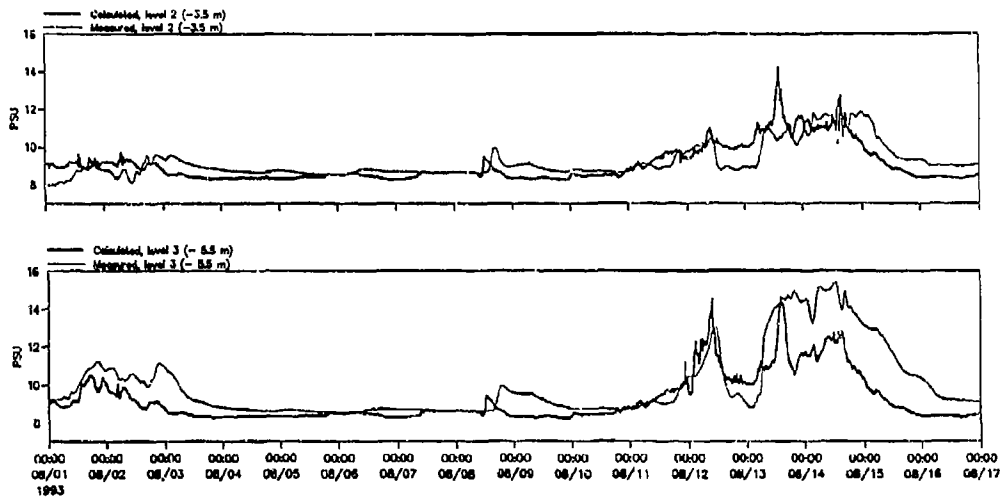


Figure 8 Time series of modelled and observed salinity at Station 4 (Fig. 1).

7 ACKNOWLEDGEMENT

Øresundskonsortiet consent to publish the results is highly acknowledged.

8 REFERENCES

Jacobsen (1980) Sea water exchange of the Baltic. Measurements and methods. The Belt Project.

DHI/LIC/SMHI (1993) The Øresund Link. Hydrographic investigations, Campaign I-IV. Øresundskonsortiet, November 1993.

Bo Pedersen (1986) Environmental Hydraulics: Stratified Flows. Lecture Notes on coastal and Estuarine Studies No. 18, Springer Verlag, September1986.

DHI (1990) SYSTEM 3, A three-dimensional hydrodynamic model. Technical reference. Danish Hydraulic Institute. May 1990.

The variability of vertical finescale temperature structures in Lake Geneva, Switzerland

S. M. Zhang, U. Lemmin
LRH-EPFL
CH-1015, Lausanne
Switzerland

E. H. Hopfinger
L.E.G./IGM
38041, Grenoble Cedex
France

Abstract

Based on a series of monthly temperature profiles taken in Lake Geneva since 1986, an analysis of stratification dynamics distinguishes two ranges in z-t space: a strongly stratified upper layer (seasonal variable) and a weakly or non stratified lower layer without time variation (Fig.1). Temperature spectra show the same pattern: strong seasonal variability in the energy level in the upper layer and no variability in the lower layer (Fig.3 and Fig.4). The Thorpe scale and the inversion percentage for each profile reveal slightly larger values in the lower layer (80-260m depth) and during the destratified period (Fig.5). A lognormal distribution of the Thorpe scale is comparable to the one found by Thorpe in Loch Ness (Fig.6). The vertical mixing coefficients calculated with the Thorpe scale and the buoyancy frequency are smaller than those calculated by the budget method for the upper layer during the heating season (Fig.7), and give values equivalent to those obtained in other lakes and in the interior of oceans in the lower layer (Fig.8). All three analyses show that in Lake Geneva there is a 200m thick intermediate layer that has the characteristics of the ocean interior.

1. Introduction

A series of water temperature profiles has been taken regularly (about once a month) at stations along the axis of Lake Geneva since 1986 with a temperature resolution of 0.001°C and a depth resolution of 20cm. They show frequent small steps and temperature inversions. Based on these high precision profiles, three aspects, i.e., the dynamical state, a length scale estimation and energy levels, are calculated and discussed. The dynamic analysis allows us to understand the status of stratification and the effects of the buoyancy force in Lake Geneva. The scale analysis will be useful to gauge inversion structures and to describe the instability of the water column. The energy analysis will reveal the origin of energy of turbulent stirring and present the turbulent energy distribution in space and time. The aim of this study is to understand and quantify vertical mixing processes.

In the present calculation, the influence of the near surface activities and the diurnal thermocline (0~20m) is excluded. In the case where the temperature has its maximum value at a depth below 20m, the region to be analyzed will begin at the depth ($z_{T\,max}$) where the maximum temperature occurs. Because turbidity and conductivity in the bottom boundary layer have strong gradients, the calculations are limited to the zone above 260m for stations S1, S2 and S3 which are situated on the central plateau of lake and have a depth of about 300m. We will only consider temperature fluctuations if the temperature in the observed profile differs from that in the stable profile by more than the noise level (0.001°C), i.e., $T' \geq 0.002$°C.

2. Analysis of stratification dynamics

Vertical mixing is often modified by the existence of a thermocline with a strong density stratification in lakes and reservoirs. The stratification expresses a vertical force that may change the structure of eddies, restrict the vertical motion, and is traditionally quantified by the buoyancy frequency, N, defined as $N^2 = -g\rho^{-1}\partial\rho/\partial z$. The distribution of N in both space and time is shown in Fig.1. There exist two different zones: a strongly stratified zone (A) and a weakly or non stratified zone (B). In zone A, which is situated in the upper layer and during the heating season, the values of N are generally much larger than that in zone B. Very large values (N>100 cph) are typically found at a depth above 40m. In zone B, the buoyancy decreases to a range of 0 to 10 cph. The depth where N reaches its maximum

decreases slightly with time after late summer. Penetrative convection is more active during this period, and it causes thermocline deepening. In the upper layer, the buoyancy frequency, N, arrives at a maximum value in autumn near the surface and has its lowest values in spring, comparable to levels in zone B. Inversely, the buoyancy frequency in the lower layer almost remains nearly constant during the whole year. As a consequence of the existence of this variation in stratification, the concepts or methods which have been developed for zone A cannot directly be applied to zone B. The turbulence in the stratified zone A is anisotropic, but it may be regarded as locally isotropic. Turbulence in non-stratified zone B seems to approach isotropy because the vertical density gradient is small.

3. Spectral analysis

Temperature fluctuations in time or in space can be caused by different processes: straining of a mean temperature profile by internal waves, overturning and mixing by turbulent eddies, as well as differential advection by density or turbidity intrusions in the horizontal to name a few. Each of these processes has different dynamics and is expected to show a different spectral form. In order to study these different mixing processes which cover a wide range of different time and length scales in the lake, calculations of spectra of temperature are carried out. To obtain the general spectral form, all temperature spectra of station S1 from 1986 to 1990 (60 profiles) are calculated. We found that the vertical energy spectra of temperature in Lake Geneva are characterized by two distinct bands. For smaller wave numbers, the spectra have a $\kappa^{-1.75}$ dependence, which is somewhat smaller than -2 obtained by Roden (1971), Hayes et al. (1975) and Gregg (1977). This corresponds to the internal wave band. For larger wave numbers the spectra have a $\kappa^{-2.65}$ dependence, which is consistent with the previous results of -2.5 ~-3.0 (Roden; Hayes et al.; Gregg; Joyce et al., 1978). This corresponds to the fine scale band. The break is situated near 0.1 cpm. The energy level of the vertical T' spectrum arrives at a maximum value in late autumn and falls to a minimum value in early spring (Fig.2). Energy levels vary with season, but the physical mechanisms, such as internal wave and turbulent eddies, keep the same combination, as indicated by an unchanged spectral slope, specially for the fine scale range. Since the absolute fluctuation value is related to the spectral function as $T'^2 \sim E_T$, the mean T' in autumn (typically September) is much greater than in spring (typically February).

In order to address and compare the different mixing processes between the epilimnion and the hypolimnion, the water column is cut into two parts as shown in Fig.1, i.e., an upper layer, the depth of which varies from 20 to 80 meters (epilimnion and thermocline), and a lower layer from 80 meters to the bottom about 260 meters (hypolimnion) for stations S1, S2 and S3. All spectra of temperature data from 1986 to 1991 are calculated and summarized for the epilimnion and the hypolimnion in Fig.3 and in Fig.4 respectively. The epilimnetic spectra (Fig.3) consist again of two bands and a break range. In the first band (wave numbers from 0.005 to 0.08 cpm), the ratio of upper-contour to lower-contour, i.e., the ratio of maximum and minimal energy level, is about 10^4, meaning $T'_{max} / T'_{min} \sim 10^2$. In the second band (wave number larger than 0.1 cpm), the ratio $E_{T\,max} / E_{T\,min}$ is about 10^3, i.e., $T'_{max} / T'_{min} \sim 33$.

The first band of hypolimnion spectrum (Fig.4) is very short and narrow (the wave numbers from 0.02 to 0.08 cpm), in which the ratio $E_{T\,max} / E_{T\,min} \sim 10^{1.3}$, thus, $T'_{max} / T'_{min} \sim 4.5$. In the second band $E_{T\,max} / E_{T\,min}$ is only $10^{0.4}$, i.e., $T'_{max} / T'_{min} \sim 1.5$. Therefore, the two terms, "steak" and "bone", are used to visualize the spectral patterns of the epilimnion and the hypolimnion respectively. In other words, the ratio of temperature variance has a large seasonal range in the epilimnion and in the thermocline. However, it has a very small seasonal range in the hypolimnion. Comparing the energy levels shown Fig.3 and Fig.4, the temperature fluctuation variation range in the epilimnion is much bigger than in the hypolimnion (mean value 10 times). That implies that in Lake Geneva, which is large and deep, internal waves affect mainly the upper layer and the influence on the lower layer may

be negligible in terms of energy level. In summary, epilimnetic temperature variations in the fine scale range depend strongly on atmospheric forcing and are greatly influenced by seasonal temperature changes. Hypolimnetic temperature variations in the fine scale range depend less strongly on atmospheric changes and are caused by internal waves which are slightly influenced by atmospheric changes.

4. Scale analysis

The estimation of the length scales of the observed vertical overturning structures, being potentially unstable, may help in understanding and quantifying vertical mixing in particular in the lower hypolimnion where the traditional heat budget method does not give any results (Michalski and Lemmin, 1992).

Turbulence mixing theories often depend on assumptions about the length scale of turbulent eddies, and early Prandtl mixing length theories explicitly used the size of turbulent eddies as a fundamental variable. Measurements of the length scales can provide evidence for the theory. Thorpe (1977) proposed an objective method of estimating a length scale (the 'Thorpe scale', L_T) associated with overturning events in a stratified fluid. The method of calculating L_T consists of ordering an observed potential density profile, which contains inversions, into a stable monotonic profile. When the flow is homogeneous in the horizontal and the density (temperature) inversions are the result of turbulent stirring, the Thorpe scale is strongly correlated with the Ozmidov scale L_O (Dillon, 1982; Ivey and Imberger, 1989).

The Thorpe displacement is a measure for the vertical displacements caused by the turbulent motions before significant molecular diffusion has occurred (Thorpe, 1977). It is also useful as a visual aid in defining the vertical extend of some mixing events. For the calculation of the Thorpe scale, the temperature profiles may be treated as density profiles because they are monotonic with depth provided T>4°C. A temperature inversion structure indicates that the corresponding density profile is gravitationally unstable.

In this study, the inversion percentage is defined as a ratio of the region occupied by temperature inversions to the whole range under consideration. It will be used to measure the percentage of the water column which is potentially unstable and contributes to mixing, and it indicates the development of turbulence in space.

If the averaging range covers the entire profile depth (between 20m or $z_{T_{max}}$ and 260m), the resultant Thorpe scale, named profile Thorpe scale, will be a measure of the typical inversion scale of the whole profile. Based on the data of station S1, S2 and S3 from 1988 to 1993, the profile Thorpe scales in different months can be determined by the following equation:

$$L_T(month) = \frac{1}{Ns\,(year_1 - year_0)} \sum_{station=1}^{Ns} \sum_{year=year_0}^{year_1} L_T(month, year, station) \qquad \text{(Eq.1)}$$

In the present study:

month = 1, 12 (*Jan. to Dec.*); *Ns* = 3 (*Station S1, S2, S3*); $year_0 = 1988$, $year_1 = 1992$.

Each L_T is an average over many profiles which are assumed to be statistically similar, and cover the same vertical range.

Profile Thorpe scales as function of month are shown in Fig.5. It follows that the profile Thorpe scale has an order of 2m with an average inversion percentage of 15%. The Thorpe scale during the cooling season is slightly larger than that during the heating season.

The probability of a certain Thorpe scale for a vertical region under consideration is given by

$$P(L_{T_i} + \Delta d/2) = n_{(L_{T_i}, L_{T_i}+\Delta d)} / N_{total}, \qquad \text{(Eq.2)}$$

where N_{total} is the total number of Thorpe scales observed and $n_{(d, d+\Delta d)}$ is the number of Thorpe scales which fall into a range specified between L_{T_i} and $L_{T_i}+\Delta d$. For each individual profile which contains inversions, Eq.2 can be used to obtain the empirical probability distribution. Based on the data from about 150 profiles, Fig.6a presents the cumulative curves

for stations S1, S2 and S3, giving probability distributions from 1988 to 1993. While there is some scatter as expected, the highest probability always occurs at the scale less than 1 meter, and the probability function is nearly flat at larger scales. There is little difference between the curves of the three stations for the small scale range. The regression curves of the empirical probability can be well approximated by a lognormal distribution (Fig.6b). The points in the figures which are the results of Thorpe (1977) agree well with the overall trend of Lake Geneva data. The probability in Lake Geneva is lower for the very small scales and slightly higher for the intermediate scales. This documents the effect of the microscales which have not been measured here.

For isotropic turbulence, we may assume that $u' \sim v' \sim w'$ and $u'/U \sim v'/V \sim 0.1$ in Lake Geneva. According to the currents listed in Table 1, w' will be an order of 1cm/s in the upper layer and 0.1cm/s in the lower layer, where the dynamics are controlled by very weak motions.

Table 1 Typical fluctuation of temperature in different layers (data from Couchy 8182 campaign)

	18m	75m	175m
T'_{max} (°C)	2.0	0.4	0.1
U (cm/s)	6.0	3.0	1.0
$N_{typical}$ (cps)	0.0222	0.0042	0.0028

Recently, Omstedt and Murthy (1993) found that Richardson numbers near the bottom of Lake Ontario are mainly below the critical value of 0.25, indicating that the current shear in this layer is strong enough to overcome stability and generate turbulence. In Lake Geneva, instability may frequently occur and the overturning process produces patches of turbulence and mixing in most of the range of the lower layer. In the epilimnion and thermocline region, the turbulence was mainly damped (Richardson number much larger than 1 by using the values in Table 1). That signifies stable conditions for the upper layer. However, some generation of turbulence is probably still taking place in the thermocline region, as indicated by a small inversion percentage in this layer.

5. Vertical mixing

Thorpe (1987) first proposed that a mixing coefficient can be determined by treating individual vertical profiles. Considering an unstable range occupied by an inversion structure (or eddy) of size L_T, where the buoyancy frequency is N, the eddy mixing coefficient will be

$$K_z = \gamma \varepsilon N^{-2}, \qquad \text{(Eq.3)}$$

where $\varepsilon \approx L_o^2 N^3$ and the constant γ is proposed by Ivey and Imberger (1989) as

$$\gamma = R_f/(1-R_f). \qquad \text{(Eq.4)}$$

R_f is the flux Richardson number, indicating the mixing efficiency. It depends on the magnitude of the ratio L_o/L_T, and is proposed to be 0.20 in the case of L_o/L_T=1, resulting in γ=0.25. This is close to the mean estimate (γ=0.24) obtained by Oakey (1985) and Gregg et al. (1986). Dillon (1982) found the ratio L_o/L_T=0.8 for oceans and lakes. Although doubt still exists about the appropriate value, we shall take those two constants (R_f=0.20 and L_o/L_T=0.8) for Lake Geneva as Thorpe (1987) did.

The mixing coefficients are calculated for different seasons and different depths, as shown in Fig.7 and Fig.8 for the heating season and the cooling season respectively. Fig.7 indicates that the mixing coefficient, as expected, increases with depth until a depth of about 100m, then keeps fluctuating down to the bottom. Inversely, K_z during the cooling season exhibits large scale fluctuations over the entire profile (Fig.8).

Using the heat flux gradient method (budget method), we estimated vertical mixing coefficients for Lake Geneva. Fig.8 shows that the coefficients calculated by the budget method are larger than those by Eq.3 in the upper layer during the heating season. This is most likely because the mean temporal and spatial temperature gradients used by the heat flux gradient method integrate over a large number of processes on different time and length

scales. In contrast, the coefficients, quantified by Eq.3 and shown in Fig.7 and Fig.8, are only the contribution to mixing due to the instantaneous inversion structures. For the lower layer, the vertical mixing coefficients give values comparable to those obtained by the heat flux gradient method falling into the range of 0.3 to $5\,cm^2/s$. The order of K_z shown in Fig.7 and Fig.8 corresponds to the results in the literature for the hypolimnion of other lakes (Hutter, 1983; Wuest, 1987), and observations in the interior of the ocean: about 0.3 cm^2/s (Ivey, 1987). If the coefficient is an indicator of the intensity of turbulent motions, we may conclude that the intensity of turbulence and the potential of mixing in the hypolimnion of Lake Geneva are comparable with that in other lakes and in the interior of oceans.

6. Conclusions

Temperature inversions indicative of vertical overturning structures were observed in all profiles at all depths. Dynamic analysis distinguishes two ranges in z-t space: zone A, i.e., a strongly stratified zone (upper 80m), and zone B, i.e., a weakly or non stratified zone (80m to 260m). While zone A shows strong seasonal variation, zone B remains constant.

Energy density spectra of the finescale temperature gradients show that in the range between 20m (just below the seasonal thermocline) and 80 m depth where mean temperature gradients display a strong seasonal variation, the energy level changes with season, being highest in August when stratification is strongest and lowest in February when the lake is near homothermal. The spectral slope remains constant at around 2.5. From 80m to 260m depth where seasonal variations are not evident, spectral energy is found to remain at the level of that of February in the above layer during all seasons.

Thorpe scales calculated from the temperature profiles show slightly larger values in the lower layer (80-260m depth) and during the destratified period. A lognormal distribution of the Thorpe scale can be established for all profiles, which is comparable to the one found by Thorpe in Loch Ness. The vertical mixing coefficients calculated by the Thorpe scale and the buoyancy frequency in this study are smaller than those calculated by the budget method for the upper layer during the heating season, and give values comparable to those obtained in other lakes and in interior of ocean in the lower layer. Imberger and Patterson (1989) had shown that in "typical" lakes the bottom boundary layer starts immediately below the stratified layer. All three analyses show that in Lake Geneva there is a 200m thick intermediate layer that has the characteristics of the ocean interior.

7. References

Dillon, T.M. (1982). Vertical overturns: a comparison of Thorpe and Ozmidov length scales. J. Geophy. Res., 87, pp9601-9613.

Gregg, M.C. (1977). A comparison of fine-structure spectra from the main thermocline. J. Phys. Oceanogr., 7, pp33-40.

Gregg, M.C., D'Asaro, E.A., Shay, T.J. and Larson, N. (1986). Observations of persistent mixing and near-inertial internal waves. J. Phys. Oceanogr., 16, pp856-885.

Hayes, S.P., Joyce, T.M. and Millard, J. (1975). Measurement of vertical fine structure in the Sargasso Sea. J. Geoph. Res., 80, pp314-319.

Hutter, K., (1983). Hydrodynamics of lakes. Springer, 341P.

Imberger, J. and Patterson, J.C. (1989). Physical limnology. Advances in applied mechanics; J.W. Hutchinson and T.Y. Wu, eds., 27, pp303-475.

Ivey, G.N. (1987). The role of boundary mixing in the deep ocean. J. Geoph. Res. 92, pp11873-11878.

Ivey, G.N. and Imberger, J. (1989). On the nature of turbulence in a stratified fluid part 1: the efficiency of mixing. J. Phys. Oceanogr., 21, pp649-658.

Joyce, T.M., Zenk, W. and Toole, J. M. (1978). The anatomy of the antarctic polar front in the Drake Passage. J. Geoph. Res., 83, pp6093-6114.

Michalski, J. and Lemmin, U. (1991). Dynamics of vertical mixing in the hypolimnion of Lake Geneva. Rapport annuel, LRH-EPFL.

Oakey, N.S. (1985). Statistics of mixing parameters in the upper ocean during JASIN Phase 2. J. Phys. Oceanogr., 15, pp1662-1675.
Omstedt, A. and Murthy, C. R. (1993). Currents and vertical mixing in Lake Ontario during summer stratification. Internal communication, CCIW.
Roden, G.I. (1971). Spectra of north pacific temperature and salinity perturbations in the depth domain. J. Phys. Oceanogr., 1, pp25-33.
Thorpe, S.A. (1977). Turbulence and mixing in a Scottish Loch. Phil. Trans. Roy. Soc., London, A286, pp125-181.
Thorpe, S. A. (1987). Current and temperature variability on the continental slope. Phil. Trans. Roy. Soc. London. A 323, pp471-517.
Wuest, A. (1987). Ursprung und Grösse von Mischungsprozessen im Hypolimnion natürlicher Seen. Dissertation ETH-Zürich, Nr. 8350. 114 p.

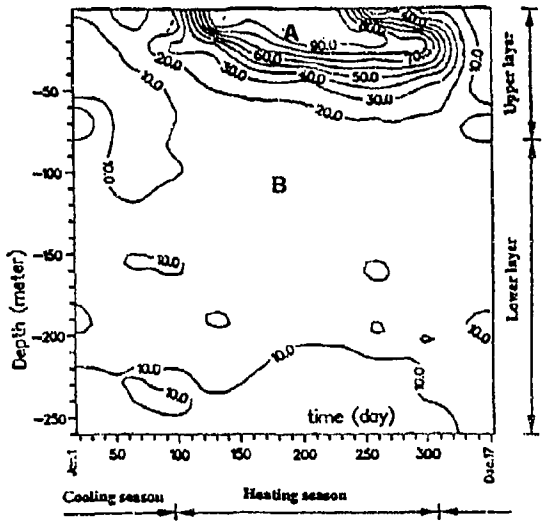


Fig.1 Buoyancy frequency, N (cph), in time and space field: zone A and zone B are marked (data from S1, 1990).

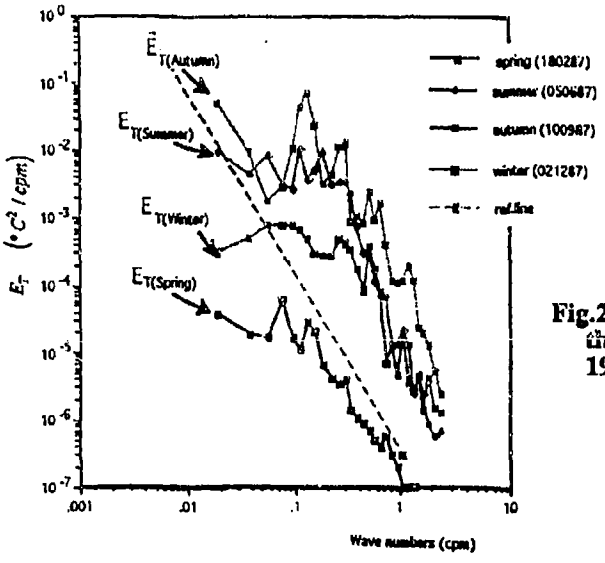


Fig.2 Typical temperature spectra for the four seasons (data from S1, 1987).

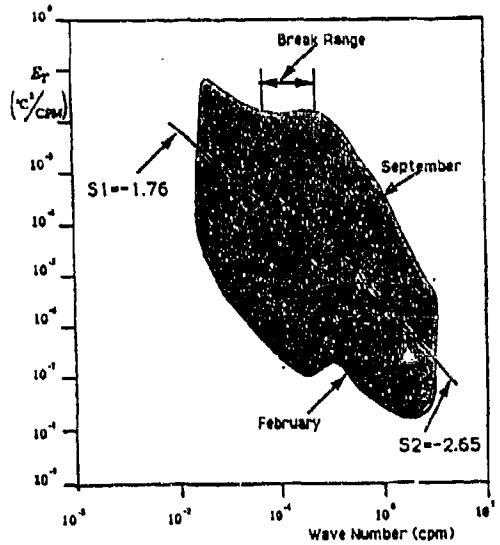


Fig.3 "steak" pattern of epilimnion spectrum (data from S1, 1986 to 1991, 60 profiles used)

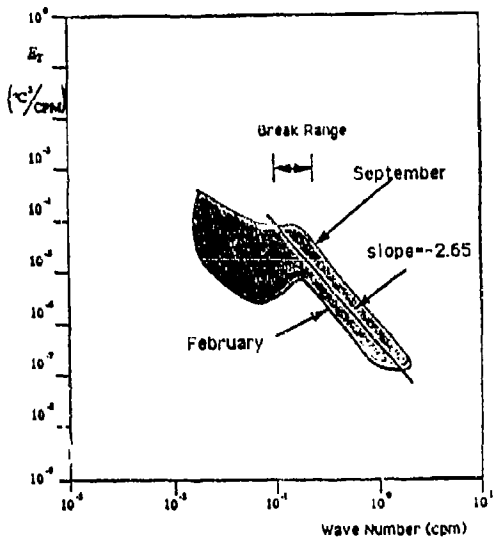


Fig.4 "bone" pattern of hypolimnion spectrum (data from S1, 1986 to 1991, 60 profiles used)

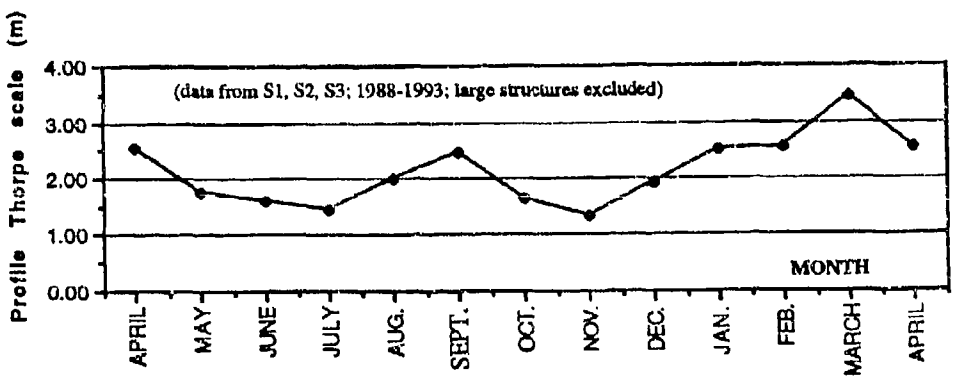


Fig.5 Profile Thorpe scale as a function of month (150 profiles used)

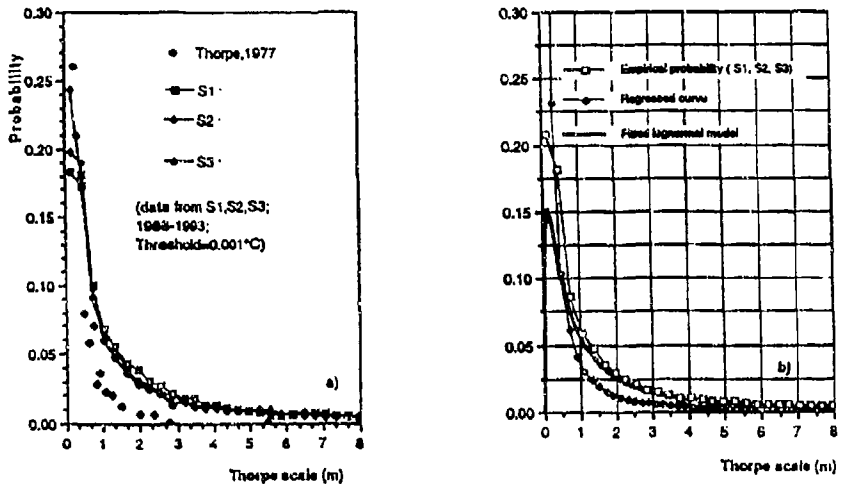


Fig.6 a) Empirical probabilities and results of Thorpe (1977), b) fitted lognormal model and regression curve

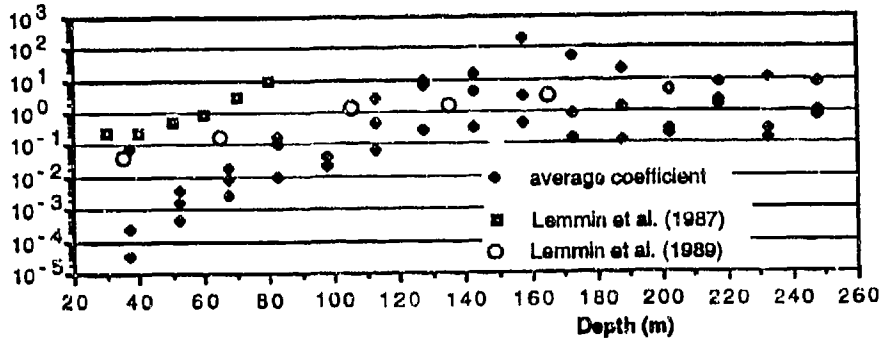


Fig.7 Mixing coefficients as a function of depth, compared with the results of the budget method calculated for the stratification period (data from S1, 1987-1992, heating season)

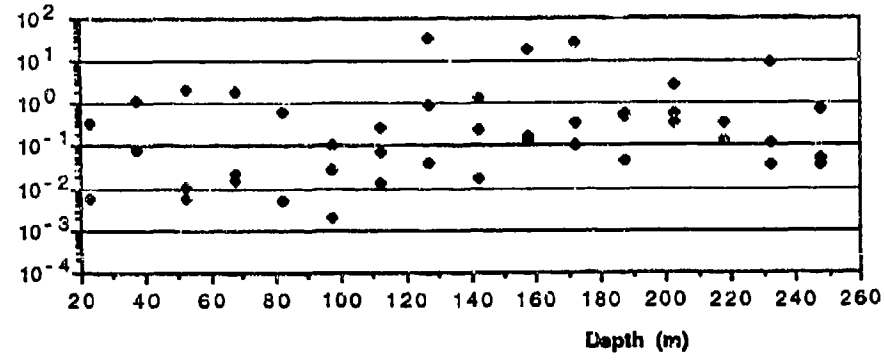


Fig.8 Typical mixing coefficients as a function of depth during the cooling season (data from S1, 1990-1991, cooling season)

The variability of vertical finescale temperature structures in Lake Geneva, Switzerland

S. M. Zhang, U. Lemmin
LRH-EPFL
CH-1015, Lausanne
Switzerland

E. H. Hopfinger
L.E.G./IGM
38041, Grenoble Cedex
France

Abstract

Based on a series of monthly temperature profiles taken in Lake Geneva since 1986, an analysis of stratification dynamics distinguishes two ranges in z-t space: a strongly stratified upper layer (seasonal variable) and a weakly or non stratified lower layer without time variation (Fig.1). Temperature spectra show the same pattern: strong seasonal variability in the energy level in the upper layer and no variability in the lower layer (Fig.3 and Fig.4). The Thorpe scale and the inversion percentage for each profile reveal slightly larger values in the lower layer (80-260m depth) and during the destratified period (Fig.5). A lognormal distribution of the Thorpe scale is comparable to the one found by Thorpe in Loch Ness (Fig.6). The vertical mixing coefficients calculated with the Thorpe scale and the buoyancy frequency are smaller than those calculated by the budget method for the upper layer during the heating season (Fig.7), and give values equivalent to those obtained in other lakes and in the interior of oceans in the lower layer (Fig.8). All three analyses show that in Lake Geneva there is a 200m thick intermediate layer that has the characteristics of the ocean interior.

1. Introduction

A series of water temperature profiles has been taken regularly (about once a month) at stations along the axis of Lake Geneva since 1986 with a temperature resolution of 0.001°C and a depth resolution of 20cm. They show frequent small steps and temperature inversions. Based on these high precision profiles, three aspects, i.e., the dynamical state, a length scale estimation and energy levels, are calculated and discussed. The dynamic analysis allows us to understand the status of stratification and the effects of the buoyancy force in Lake Geneva.

The scale analysis will be useful to gauge inversion structures and to describe the instability of the water column. The energy analysis will reveal the origin of energy of turbulent stirring and present the turbulent energy distribution in space and time. The aim of this study is to understand and quantify vertical mixing processes.

In the present calculation, the influence of the near surface activities and the diurnal thermocline (0~20m) is excluded. In the case where the temperature has its maximum value at a depth below 20m, the region to be analyzed will begin at the depth ($z_{T\max}$) where the maximum temperature occurs. Because turbidity and conductivity in the bottom boundary layer have strong gradients, the calculations are limited to the zone above 260m for stations S1, S2 and S3 which are situated on the central plateau of lake and have a depth of about 300m. We will only consider temperature fluctuations if the temperature in the observed profile differs from that in the stable profile by more than the noise level (0.001°C), i.e., T'≥0.002°C.

2. Analysis of stratification dynamics

Vertical mixing is often modified by the existence of a thermocline with a strong density stratification in lakes and reservoirs. The stratification expresses a vertical force that may change the structure of eddies, restrict the vertical motion, and is traditionally quantified by the buoyancy frequency, N, defined as $N^2 = -g\rho^{-1}\partial\rho/\partial z$. The distribution of N in both space and time is shown in Fig.1. There exist two different zones: a strongly stratified zone (A) and a weakly or non stratified zone (B). In zone A, which is situated in the upper layer and during the heating season, the values of N are generally much larger than that in zone B. Very large values (N>100 cph) are typically found at a depth above 40m. In zone B, the buoyancy decreases to a range of 0 to 10 cph. The depth where N reaches its maximum decreases slightly with time after late summer. Penetrative convection is more active during this period, and it causes thermocline deepening. In the upper layer, the buoyancy frequency, N, arrives at a maximum value in autumn near the surface and has its lowest values in spring, comparable to levels in zone B. Inversely, the buoyancy frequency in the lower layer almost

remains nearly constant during the whole year. As a consequence of the existence of this variation in stratification, the concepts or methods which have been developed for zone A cannot directly be applied to zone B. The turbulence in the stratified zone A is anisotropic, but it may be regarded as locally isotropic. Turbulence in non-stratified zone B seems to approach isotropy because the vertical density gradient is small.

3. Spectral analysis

Temperature fluctuations in time or in space can be caused by different processes: straining of a mean temperature profile by internal waves, overturning and mixing by turbulent eddies, as well as differential advection by density or turbidity intrusions in the horizontal to name a few. Each of these processes has different dynamics and is expected to show a different spectral form. In order to study these different mixing processes which cover a wide range of different time and length scales in the lake, calculations of spectra of temperature are carried out. To obtain the general spectral form, all temperature spectra of station S1 from 1986 to 1990 (60 profiles) are calculated. We found that the vertical energy spectra of temperature in Lake Geneva are characterized by two distinct bands. For smaller wave numbers the spectra have a $\kappa^{-1.75}$ dependence, which is somewhat smaller than -2 obtained by Roden (1971), Hayes et al. (1975) and Gregg (1977). This corresponds to the internal wave band. For larger wave numbers the spectra have a $\kappa^{-2.65}$ dependence, which is consistent with the previous results of -2.5 ~-3.0 (Roden; Hayes et al.; Gregg; Joyce et al., 1978). This corresponds to the fine scale band. The break is situated near 0.1 cpm. The energy level of the vertical T' spectrum arrives at a maximum value in late autumn and falls to a minimum value in early spring (Fig.2). Energy levels vary with season, but the physical mechanisms, such as internal wave and turbulent eddies, keep the same combination, as indicated by an unchanged spectral slope, specially for the fine scale range. Since the absolute fluctuation value is related to the spectral function as $T'^2 \sim E_T$, the mean T' in autumn (typically September) is much greater than in spring (typically February).

In order to address and compare the different mixing processes between the epilimnion and the hypolimnion, the water column is cut into two parts as shown in Fig.1, i.e., an upper layer, the depth of which varies from 20 to 80 meters (epilimnion and thermocline), and a lower layer from 80 meters to the bottom about 260 meters (hypolimnion) for stations S1, S2 and S3. All spectra of temperature data from 1986 to 1991 are calculated and summarized for the epilimnion and the hypolimnion in Fig.3 and in Fig.4 respectively. The epilimnetic spectra (Fig.3) consist again of two bands and a break range. In the first band (wave numbers from 0.005 to 0.08 cpm), the ratio of upper-contour to lower-contour, i.e., the ratio of maximum and minimal energy level, is about 10^4, meaning $T'_{max} / T'_{min} \sim 10^2$. In the second band (wave number larger than 0.1 cpm), the ratio $E_{T\max} / E_{T\min}$ is about 10^3, i.e., $T'_{max} / T'_{min} \sim 33$.

The first band of hypolimnion spectrum (Fig.4) is very short and narrow (the wave numbers from 0.02 to 0.08 cpm), in which the ratio $E_{T\max} / E_{T\min} \sim 10^{1.3}$, thus, $T'_{max} / T'_{min} \sim 4.5$. In the second band $E_{T\max} / E_{T\min}$ is only $10^{0.4}$, i.e., $T'_{max} / T'_{min} \sim 1.5$. Therefore, the two terms, "steak" and "bone", are used to visualize the spectral patterns of the epilimnion and the hypolimnion respectively. In other words, the ratio of temperature variance has a large seasonal range in the epilimnion and in the thermocline. However, it has a very small seasonal range in the hypolimnion. Comparing the energy levels shown Fig.3 and Fig.4, the temperature fluctuation variation range in the epilimnion is much bigger than in the hypolimnion (mean value 10 times). That implies that in Lake Geneva, which is large and deep, internal waves affect mainly the upper layer and the influence on the lower layer may be negligible in terms of energy level. In summary, epilimnetic temperature variations in the fine scale range depend strongly on atmospheric forcing and are greatly influenced by seasonal temperature changes. Hypolimnetic temperature variations in the fine scale range depend less strongly on atmospheric changes and are caused by internal waves which are slightly influenced by atmospheric changes.

4. Scale analysis

The estimation of the length scales of the observed vertical overturning structures, being potentially unstable, may help in understanding and quantifying vertical mixing in particular in the lower hypolimnion where the traditional heat budget method does not give any results (Michalski and Lemmin, 1992).

Turbulence mixing theories often depend on assumptions about the length scale of turbulent eddies, and early Prandtl mixing length theories explicitly used the size of turbulent eddies as a fundamental variable. Measurements of the length scales can provide evidence for the theory. Thorpe (1977) proposed an objective method of estimating a length scale (the 'Thorpe scale', L_T) associated with overturning events in a stratified fluid. The method of calculating L_T consists of ordering an observed potential density profile, which contains inversions, into a stable monotonic profile. When the flow is homogeneous in the horizontal and the density (temperature) inversions are the result of turbulent stirring, the Thorpe scale is strongly correlated with the Ozmidov scale L_O (Dillon, 1982; Ivey and Imberger, 1989).

The Thorpe displacement is a measure for the vertical displacements caused by the turbulent motions before significant molecular diffusion has occurred (Thorpe, 1977). It is also useful as a visual aid in defining the vertical extend of some mixing events. For the calculation of the Thorpe scale, the temperature profiles may be treated as density profiles because they are monotonic with depth provided T>4°C. A temperature inversion structure indicates that the corresponding density profile is gravitationally unstable.

In this study, the inversion percentage is defined as a ratio of the region occupied by temperature inversions to the whole range under consideration. It will be used to measure the percentage of the water column which is potentially unstable and contributes to mixing, and it indicates the development of turbulence in space.

If the averaging range covers the entire profile depth (between 20m or $z_{T\max}$ and 260m), the resultant Thorpe scale, named profile Thorpe scale, will be a measure of the typical inversion scale of the whole profile. Based on the data of station S1, S2 and S3 from 1988 to 1993, the profile Thorpe scales in different months can be determined by the following equation:

$$L_T(month) = \frac{1}{Ns}\frac{1}{(year_1 - year_0)}\sum_{Station=1}^{Ns}\sum_{year=year_0}^{year_1} L_T(month, year, station)$$

In the present study: (Eq.1)

$month = 1, 12$ (*Jan. to Dec.*); $Ns = 3$ (*Station S1, S2, S3*); $year_0 = 1988$, $year_1 = 1992$.

Each L_T is an average over many profiles which are assumed to be statistically similar, and cover the same vertical range.

Profile Thorpe scales as function of month are shown in Fig.5. It follows that the profile Thorpe scale has an order of 2m with an average inversion percentage of 15%. The Thorpe scale during the cooling season is slightly larger than that during the heating season.

The probability of a certain Thorpe scale for a vertical region under consideration is given by

$$P(L_{Ti} + \Delta d/2) = n_{(L_{Ti}, L_{Ti}+\Delta d)}/N_{total}, \quad \text{(Eq.2)}$$

where N_{total} is the total number of Thorpe scales observed and $n_{(d', d'+\Delta d)}$ is the number of Thorpe scales which fall into a range specified between L_{Ti} and L_{Ti}+Δd. For each individual profile which contains inversions, Eq.2 can be used to obtain the empirical probability distribution. Based on the data from about 150 profiles, Fig.6a presents the cumulative curves for stations S1, S2 and S3, giving probability distributions from 1988 to 1993. While there is some scatter as expected, the highest probability always occurs at the scale less than 1 meter, and the probability function is nearly flat at larger scales. There is little difference between the curves of the three stations for the small scale range. The regression curves of the empirical probability can be well approximated by a lognormal disturibution (Fig.6b). The points in the figures which are the results of Thorpe (1977) agree well with the overall trend of Lake Geneva data. The probability in Lake Geneva is lower for the very small scales and slightly higher for the intermediate scales. This documents the effect of the microscales which have not been measured here.

For isotropic turbulence, we may assume that $u' \sim v' \sim w'$ and $u'/U \sim v'/V \sim 0.1$ in Lake Geneva. According to the currents listed in Table 1, w' will be an order of 1cm/s in the upper

layer and 0.1cm/s in the lower layer, where the dynamics are controlled by very weak motions.

Table 1 Typical fluctuation of temperature in different layers

(data from Couchy 8182 campaign)

	18m	75m	175m
T'_{max} (°C)	2.0	0.4	0.1
U (cm/s)	6.0	3.0	1.0
$N_{typical}$ (cps)	0.0222	0.0042	0.0028

Recently, Omstedt and Murthy (1993) found that Richardson numbers near the bottom of Lake Ontario are mainly below the critical value of 0.25, indicating that the current shear in this layer is strong enough to overcome stability and generate turbulence. In Lake Geneva, instability may frequently occur and the overturning process produces patches of turbulence and mixing in most of the range of the lower layer. In the epilimnion and thermocline region, the turbulence was mainly damped (Richardson number much larger than 1 by using the values in Table 1). That signifies stable conditions for the upper layer. However, some generation of turbulence is probably still taking place in the thermocline region, as indicated by a small inversion percentage in this layer.

5. Vertical mixing

Thorpe (1987) first proposed that a mixing coefficient can be determined by treating individual vertical profiles. Considering an unstable range occupied by an inversion structure (or eddy) of size L_T, where the buoyancy frequency is N, the eddy mixing coefficient will be

$$K_z = \gamma \varepsilon N^{-2}, \qquad \text{(Eq.3)}$$

where $\varepsilon = L_o^2 N^3$ and the constant γ is proposed by Ivey and Imberger (1989) as

$$\gamma = R_f/(1-R_f). \qquad \text{(Eq.4)}$$

R_f is the flux Richardson number, indicating the mixing efficiency. It depends on the magnitude of the ratio L_o/L_T, and is proposed to be 0.20 in the case of L_o/L_T=1, resulting in

γ=0.25. This is close to the mean estimate (γ=0.24) obtained by Oakey (1985) and Gregg et al. (1986). Dillon (1982) found the ratio L_o/L_T=0.8 for oceans and lakes. Although doubt still exists about the appropriate value, we shall take those two constants (R_f=0.20 and L_o/L_T=0.8) for Lake Geneva as Thorpe (1987) did.

The mixing coefficients are calculated for different seasons and different depths, as shown in Fig.7 and Fig.8 for the heating season and the cooling season respectively. Fig.7 indicates that the mixing coefficient, as expected, increases with depth until a depth of about 100m, then keeps fluctuating down to the bottom. Inversely, K_z during the cooling season exhibits large scale fluctuations over the entire profile (Fig.8).

Using the heat flux gradient method (budget method), we estimated vertical mixing coefficients for Lake Geneva. Fig.8 shows that the coefficients calculated by the budget method are larger than those by Eq.3 in the upper layer during the heating season. This is most likely because the mean temporal and spatial temperature gradients used by the heat flux gradient method integrate over a large number of processes on different time and length scales. In contrast, the coefficients, quantified by Eq.3 and shown in Fig.7 and Fig.8, are only the contribution to mixing due to the instantaneous inversion structures. For the lower layer, the vertical mixing coefficients give values comparable to those obtained by the heat flux gradient method falling into the range of 0.3 to 5 cm^2/s. The order of K_z shown in Fig.7 and Fig.8 corresponds to the results in the literature for the hypolimnion of other lakes (Hutter, 1983; Wuest, 1987), and observations in the interior of the ocean: about 0.3 cm^2/s (Ivey, 1987). If the coefficient is an indicator of the intensity of turbulent motions, we may conclude that the intensity of turbulence and the potential of mixing in the hypolimnion of Lake Geneva are comparable with that in other lakes and in the interior of oceans.

6. Conclusions

Temperature inversions indicative of vertical overturning structures were observed in all profiles at all depths. Dynamic analysis distinguishes two ranges in z-t space: zone A, i.e.,

a strongly stratified zone (upper 80m), and zone B, i.e., a weakly or non stratified zone (80m to 260m). While zone A shows strong seasonal variation, zone B remains constant.

Energy density spectra of the finescale temperature gradients show that in the range between 20m (just below the seasonal thermocline) and 80 m depth where mean temperature gradients display a strong seasonal variation, the energy level changes with season, being highest in August when stratification is strongest and lowest in February when the lake is near homothermal. The spectral slope remains constant at around 2.5. From 80m to 260m depth where seasonal variations are not evident, spectral energy is found to remain at the level of that of February in the above layer during all seasons.

Thorpe scales calculated from the temperature profiles show slightly larger values in the lower layer (80-260m depth) and during the destratified period. A lognormal distribution of the Thorpe scale can be established for all profiles, which is comparable to the one found by Thorpe in Loch Ness. The vertical mixing coefficients calculated by the Thorpe scale and the buoyancy frequency in this study are smaller than those calculated by the budget method for the upper layer during the heating season, and give values comparable to those obtained in other lakes and in interior of ocean in the lower layer. Imberger and Patterson (1989) had shown that in "typical" lakes the bottom boundary layer starts immediately below the stratified layer. All three analyses show that in Lake Geneva there is a 200m thick intermediate layer that has the characteristics of the ocean interior.

7. References

Dillon, T.M. (1982). Vertical overturns: a comparison of Thorpe and Ozmidov length scales. J. Geophy. Res., 87, pp9601-9613.

Gregg, M.C. (1977). A comparison of fine-structure spectra from the main thermocline. J. Phys. Oceanogr., 7, pp33-40.

Gregg, M.C., D'Asaro, E.A., Shay, T.J. and Larson, N. (1986). Observations of persistent mixing and near-inertial internal waves. J. Phys. Oceanogr., 16, pp856-885.

Hayes, S.P., Joyce, T.M. and Millard, J. (1975). Measurement of vertical fine structure in the Sargasso Sea. J. Geoph. Res., 80, pp314-319.

Hutter, K., (1983). Hydrodynamics of lakes. Springer, 341P.

Imberger, J. and Patterson, J.C. (1989). Physical limnology. Advances in applied mechanics; J.W. Hutchinson and T.Y. Wu, eds., 27, pp303-475.

Ivey, G.N. (1987). The role of boundary mixing in the deep ocean. J. Geoph. Res. 92, pp11873-11878.

Ivey, G.N. and Imberger, J. (1989). On the nature of turbulence in a stratified fluid part 1: the efficiency of mixing. J. Phys. Oceanogr., 21, pp649-658.

Joyce, T.M., Zenk, W. and Toole, J. M. (1978). The anatomy of the antarctic polar front in the Drake Passage. J. Geoph. Res., 83, pp6093-6114.

Michalski, J. and Lemmin, U. (1991). Dynamics of vertical mixing in the hypolimnion of Lake Geneva. Rapport annuel, LRH-EPFL.

Oakey, N.S. (1985). Statistics of mixing parameters in the upper ocean during JASIN Phase 2. J. Phys. Oceanogr., 15, pp1662-1675.

Omstedt, A. and Murthy, C. R. (1993). Currents and vertical mixing in Lake Ontario during summer stratification. Internal communication, CCIW.

Roden, G.I. (1971). Spectra of north pacific temperature and salinity perturbations in the depth domain. J. Phys. Oceanogr., 1, pp25-33.

Thorpe, S.A. (1977). Turbulence and mixing in a Scottish Loch. Phil. Trans. Roy. Soc., London, A286, pp125-181.

Thorpe, S. A. (1987). Current and temperature variability on the continental slope. Phil. Trans. Roy. Soc. London. A 323, pp471-517.

Wuest, A. (1987). Ursprung und Grösse von Mischungsprozessen im Hypolimnion natürlicher Seen. Dissertation ETH-Zürich, Nr. 8350. 114 p.

Oakey, N.S. (1985). Statistics of mixing parameters in the upper ocean during JASIN Phase 2. J. Phys. Oceanogr., 15, pp1662-1675.
Omstedt, A. and Murthy, C. R. (1993). Currents and vertical mixing in Lake Ontario during summer stratification. Internal communication, CCIW.
Roden, G.I. (1971). Spectra of north pacific temperature and salinity perturbations in the depth domain. J. Phys. Oceanogr., 1, pp25-33.
Thorpe, S.A. (1977). Turbulence and mixing in a Scottish Loch. Phil. Trans. Roy. Soc., London, A286, pp125-181.
Thorpe, S. A. (1987). Current and temperature variability on the continental slope. Phil. Trans. Roy. Soc. London. A 323, pp471-517.
Wuest, A. (1987). Ursprung und Grösse von Mischungsprozessen im Hypolimnion natürlicher Seen. Dissertation ETH-Zürich, Nr. 8350. 114 p.

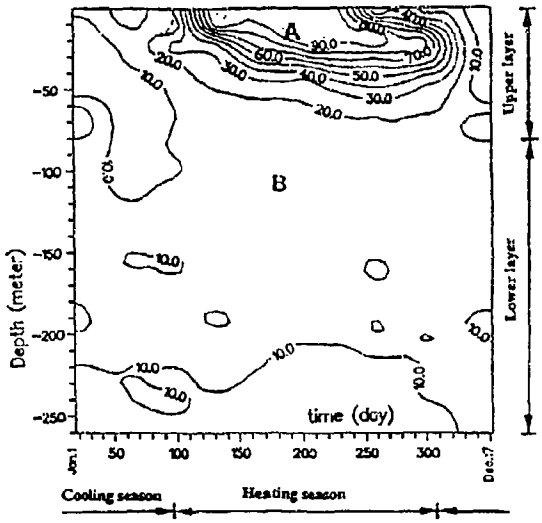


Fig.1 Buoyancy frequency, N (cph), in time and space field: zone A and zone B are marked (data from S1, 1990).

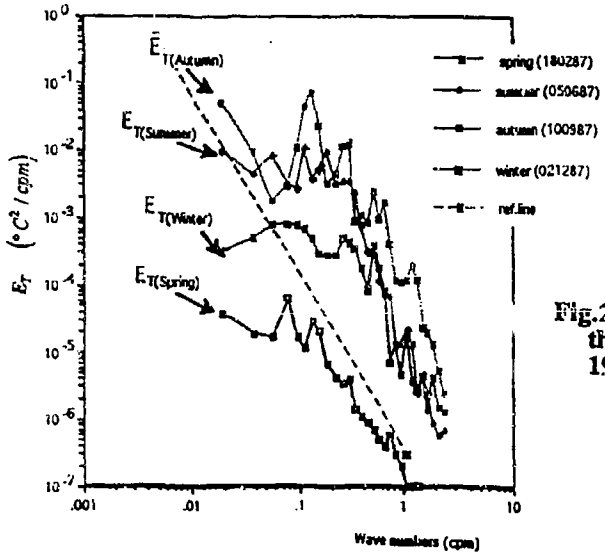


Fig.2 Typical temperature spectra for the four seasons (data from S1, 1987).

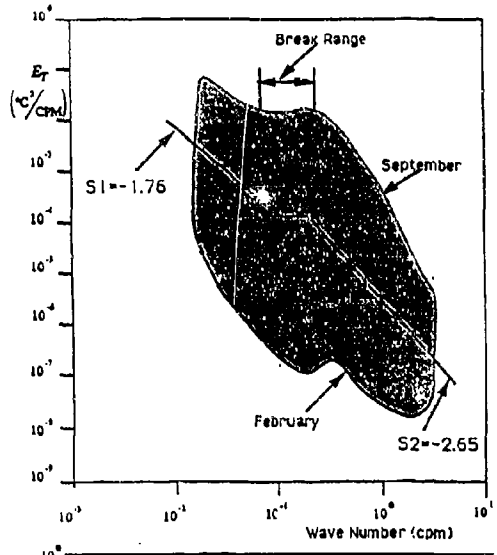


Fig.3 "steak" pattern of epilimnion spectrum (data from S1, 1986 to 1991, 60 profiles used)

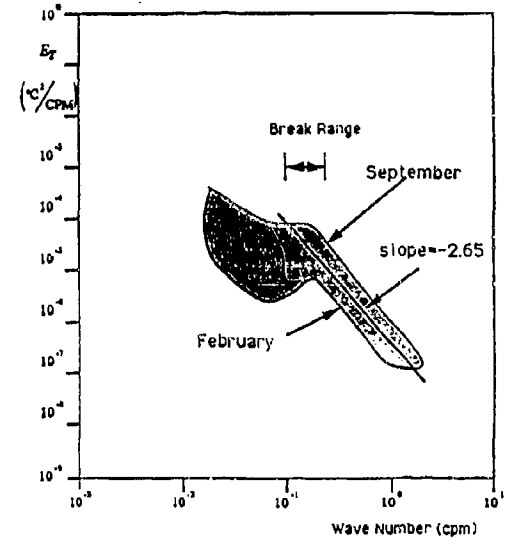


Fig.4 "bone" pattern of hypolimnion spectrum (data from S1, 1986 to 1991, 60 profiles used)

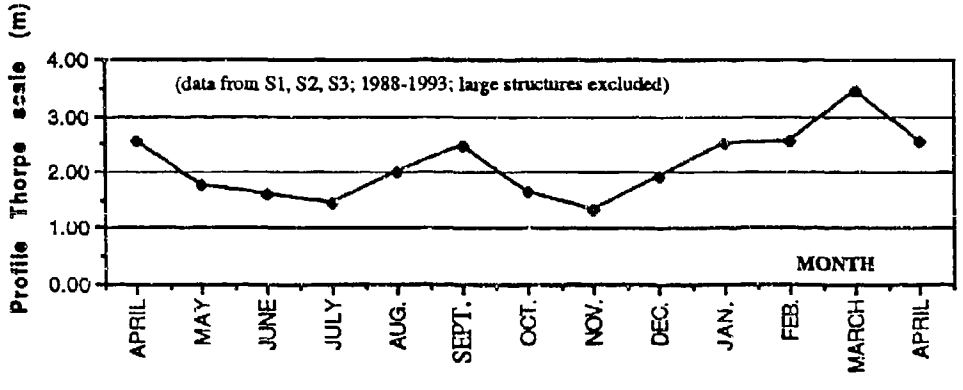


Fig.5 Profile Thorpe scale as a function of month (150 profiles used)

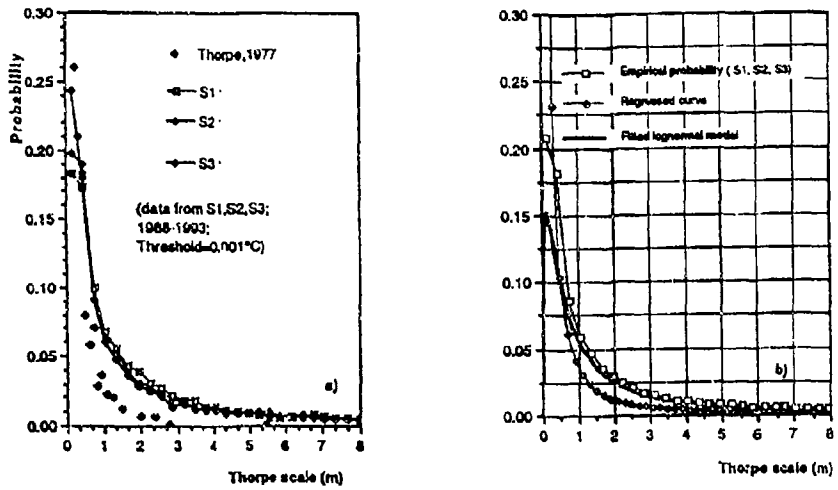


Fig.6 a) Empirical probabilities and results of Thorpe (1977), b) fitted lognormal model and regression curve

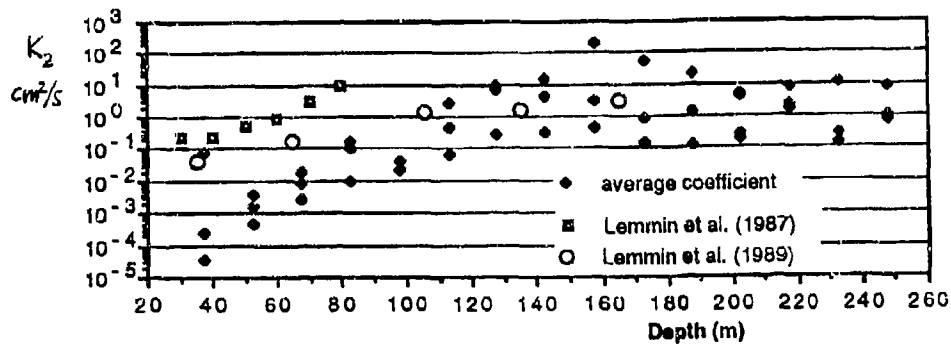


Fig.7 Mixing coefficients as a function of depth, compared with the results of the budget method calculated for the stratification period (data from S1, 1987-1992, heating season)

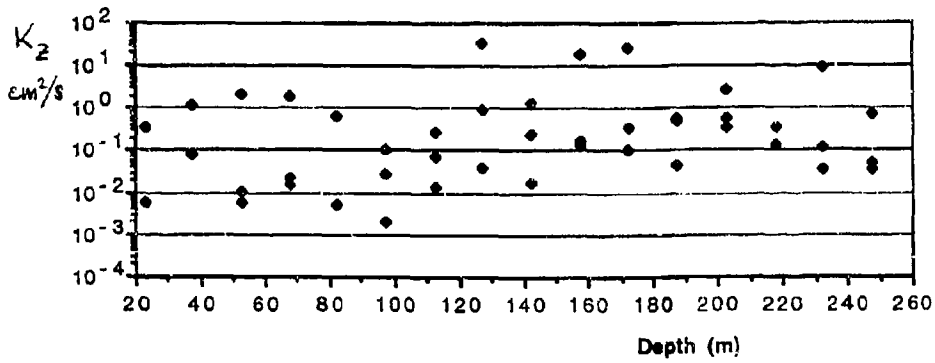


Fig.8 Typical mixing coefficients as a function of depth during the cooling season (data from S1, 1990-1991, cooling season)

A Numerical Investigation of Stratified Circulation over Abrupt Topography on the Norwegian Continental Shelf

W. P. Budgell
Nansen Environmental and Remote Sensing Center, Bergen, Norway

B. Hackett, L. P. Røed
Nansen Environmental and Remote Sensing Center, Oslo, Norway

P. E. Bjerke
Statoil, Stavanger, Norway

1 Introduction

In the region where the Norwegian Trench approaches the coast of Norway in the vicinity of the entrance to the Fensfjord (figure 1), strong bottom bottom currents (> 0.5 ms^{-1}) have been observed. As shown in figure 2, the outer Fensfjord bathymetry can

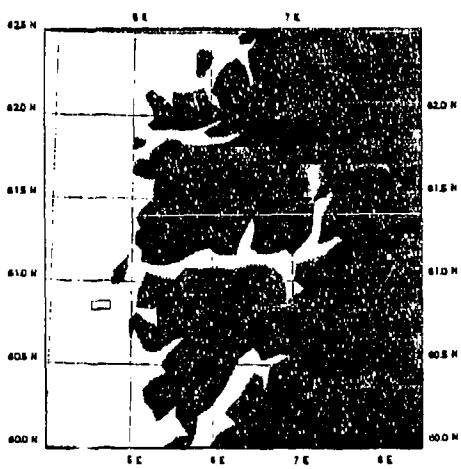


Figure 1: Location of the model domain

be characterized as an east-west trough superimposed on two sills then intersected by a north-south channel.

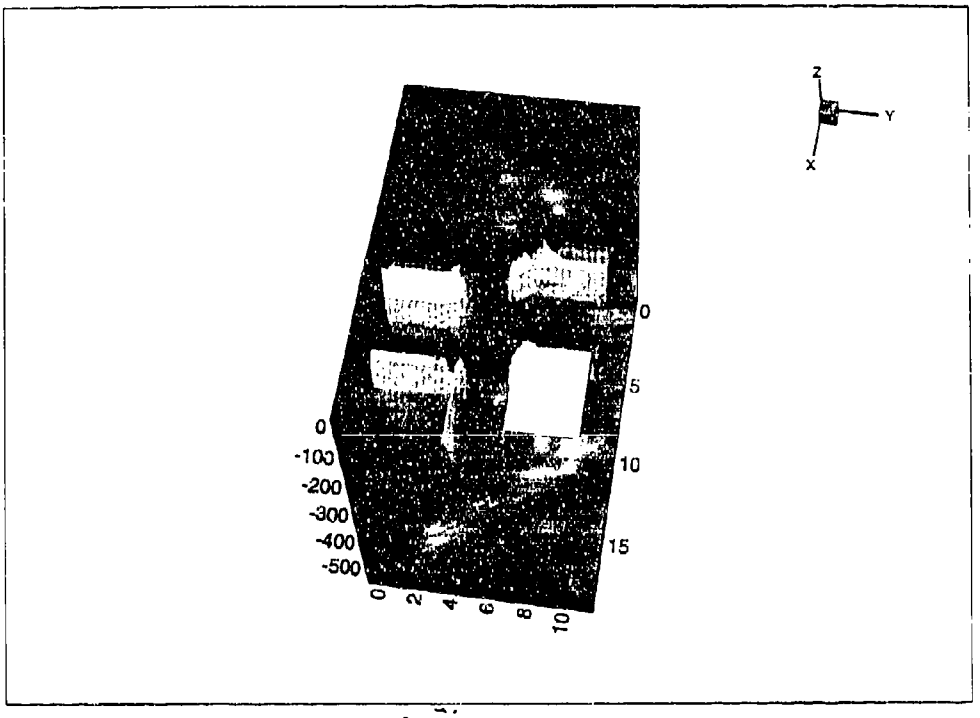


Figure 2: Fensfjord bathymetry as used in the model, viewed from the east

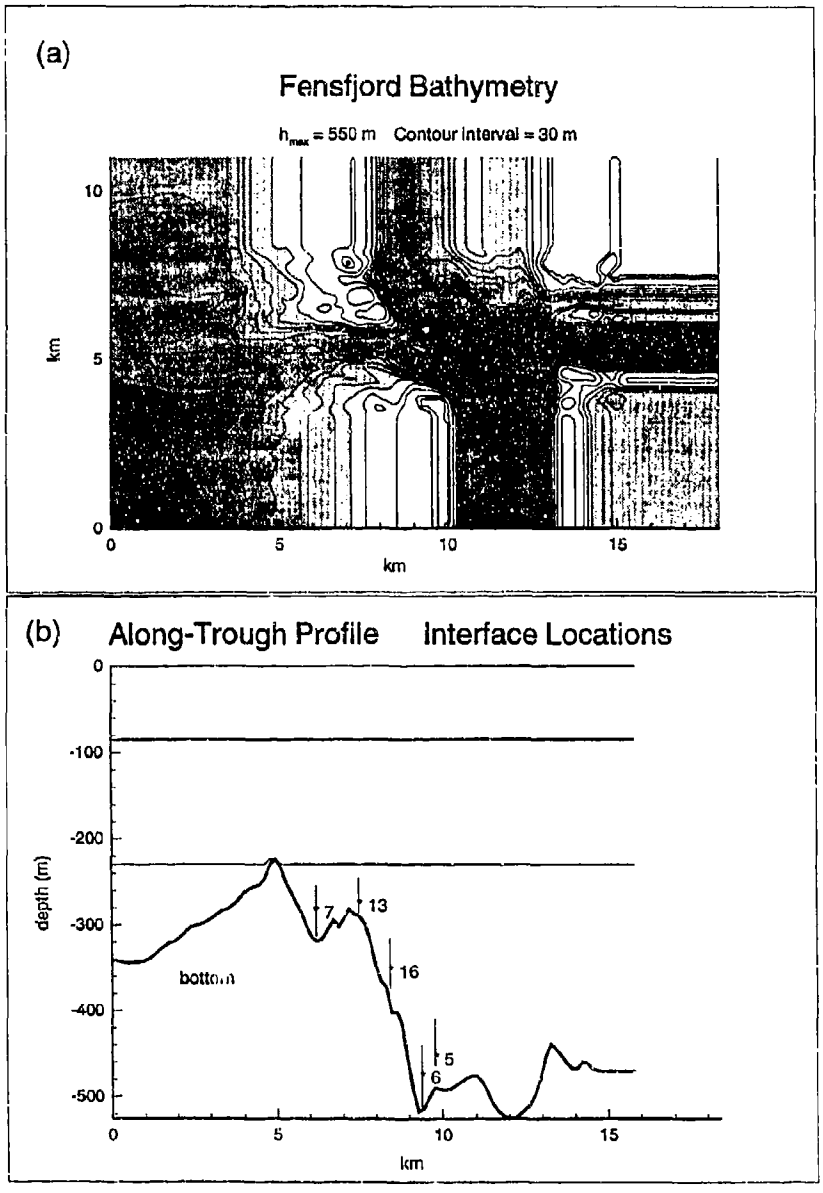


Figure 3: (a) Fensfjord model bathymetry. Note that isobaths have been artificially extended to the southern, northern and eastern boundaries in order to fill the rectangular model grid. (b) along-trough bathymetry profile (corresponding to dashed line in (a)) and initial interface locations. Current meter mooring locations are designated by (*)

It has been hypothesized (McClimans, 1993) that strong bottom currents in the Fensfjord region are caused by sill overflow events associated with eddies in the Norwegian Coastal Current and retroflected Atlantic Water in the Norwegian Trench. To examine the potential role of sill overflow dynamics in driving strong bottom currents, a numerical model was developed for the region.

The Miami Isopycnic Coordinate Ocean Model (MICOM) (Bleck *et al.*, 1992) was employed for this purpose. MICOM is a three-dimensional, primitive equation, general ocean circulation model in which the vertical structure is represented as a series of constant-density layers separated by isopycnic surfaces. Because positive-definite transport algorithms are employed within MICOM to compute layer thicknesses, disappearing layers (zero layer thickness) associated with isopycnal outcropping at the surface, intersection of isopycnals with the bottom and merging of internal isopycnic surfaces do not present any difficulties in the numerical computations. This property is extremely important in regions of abrupt topography, such as in the Fensfjord area.

2 Model Configuration

The model domain is as shown in figure 3a. The domain is 18 km long in the east-west (x) direction while it is 11 km wide in the north-south (y) direction. The east and west boundaries are open. Camerlengo and O'Brien (1980) radiation conditions are applied to the upper two layers of the western boundary and to all three layers on the eastern boundary. The lower layer on the western boundary is forced with a prescribed inflow velocity. Free-slip sidewalls are imposed on the north and south boundaries. The model's horizontal grid size is 200 m. Three isopycnic layers are employed in the model.

3 Baseline Experiment

A baseline experiment was conducted to examine the behaviour of the system under conditions representative of October 8–15, 1993. Low-pass filtered time series observations of along-trough lower layer currents at the 5 locations shown in figure 3b are displayed in figure 4. The low-pass filter has a half-power point at 31.5 hr. The strong bottom current event is characterized by a duration of nearly 4 days during which the along-trough velocities remain near the maximum values. Since the response to this event is quasi-steady, it was decided to perform a numerical experiment in which the lower layer inflow velocity along the western boundary was spun-up from rest to a steady value of 0.1 ms^{-1} over an interval of 2 days. The results are examined at day 10 of the simulation, by which time a steady circulation has developed.

Initially, the upper layer is 85 m thick and the middle layer is 145 m thick, as depicted in figure 3b. The equilibrium layer thicknesses and along-trough velocity components for the along-trough transect are shown in figure 5. The density difference across the upper two layers, $\Delta\rho_{12}$, is 1.1 kg/m^3, while the difference across the lower two layers $\Delta\rho_{23}$, is 0.2 kg/m^3, giving phase speeds of 0.81 ms^{-1} and 0.40 ms^{-1} for the first and second internal modes, respectively, at the mooring no. 7 location.

In this simulation, the lower interface rises to intersect the upper one, thus demonstrating the ability of MICOM to accommodate disappearing layers. The lower layer becomes supercritical at the second sill (km 7.5, figure 5). The maximum speed attained in the supercritical state is 0.8 ms^{-1}. The lower layer returns to a subcritical state after passing through an internal hydraulic jump at km 9. The equilibrium lower layer along-trough velocity components from this simulation are superimposed on the corresponding observed

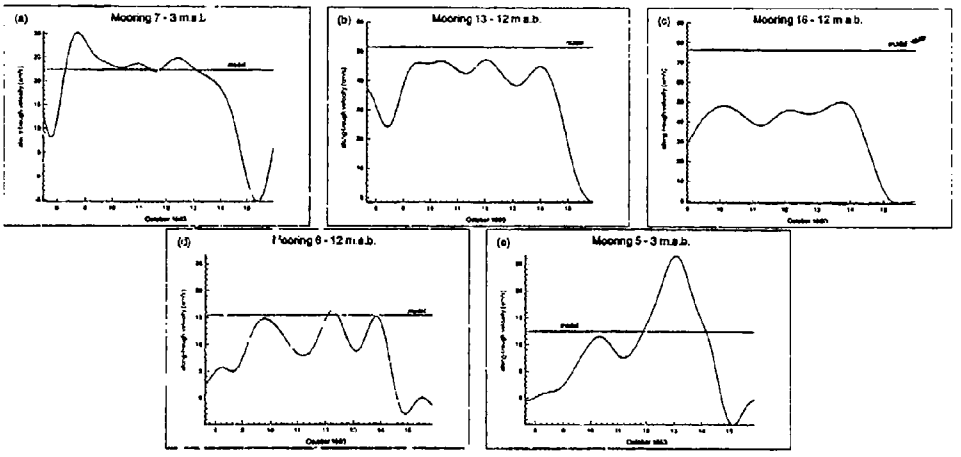


Figure 4: Low-pass filtered time series observations of along-trough velocity components and final equilibrium model values for(a) mooring 7 at 3 m above bottom (m.a.b.), (b) mooring 13 at 12 m.a.b., (c) mooring 16 at 12 m.a.b. (d) mooring 6 at 12 m.a.b. and (e) mooring 5 at 3 m.a.b.

current mooring time series observations in figure 4. While the agreement between the simulated and observed values is generally good, the model tends to overestimate the velocity by as much as 60% in the supercritical region of mooring 16. This is not surprising since neither layer entrainment nor interfacial shear stress has been applied in this simulation. The only dissipation mechanisms active during the simulation are quadratic bottom stress and a deformation-dependent horizontal viscosity. It is anticipated that interfacial mixing will be required to produce realistic velocities in the supercritical zone (Cristodoulou, 1986; Fernando, 1991).

The observed time series at mooring 5 (figure 4e) displays a surge in the current during the interval October 12–15 that is not evident at the other mooring locations. The current

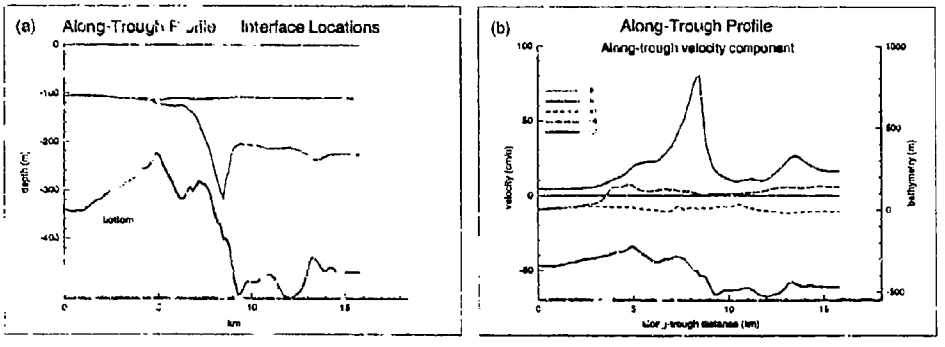


Figure 5: (a) Layer interface and (b) along-trough velocity component taken from a transect along the centre axis of the trough

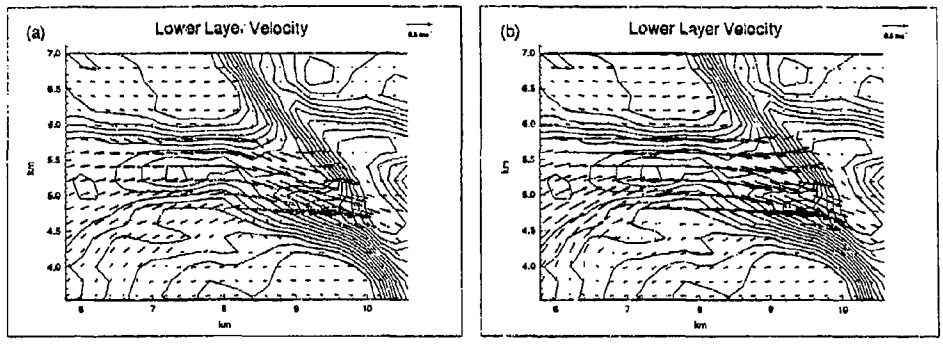


Figure 6: Lower layer velocity in the vicinity of the ravine (a) with Coriolis and (b) without Coriolis

speed associated the surge is significantly larger than the model equilibrium value. It is likely that exchange processes in the north-south channel account for this anomaly.

Although the trough is narrow ($\simeq$ [illegible] in the vicinity of the critical section (km 8–10) relative to the first and second in[illegible]ormation radius values of 6.4 km and 3.1 km, earth's rotation still has an influence, as can be seen from figure 6. The baseline simulation (figure 6a), in which Coriolis is included, shows a rightward deflection of the vectors relative to the non-rotating case shown in figure 6b. In addition, the high velocity region in the rotating case is focused over the ravine (km 9–10), whereas in the non-rotating case the velocities are high along a greater length of the trough (km 6–10). The maximum speed (0.8 ms^{-1}) is the same in both cases.

4 Sill Overflow Experiment

To examine the transient response of the system to a sill overflow event, an extreme case is considered. The Atlantic Water of the lower layer is initially taken to be entirely below and to the west of the first sill, as shown in figure 7a. An inflow is spun up in the lower layer on the western boundary, as described previously. A sequence depicting the evolution of the layer interfaces over the first 30 hours of the simulation is shown in figure 7 (a)–(f). Within the first hour, whole bottom layer propagates as a front past the first ridge. By hour 6, the flow has become supercritical over the whole length of the second sill and the ravine (km 8.5–9). As the inflow progresses downstream, an internal hydraulic jump forms at km 9, over the location of mooring 6. A second critical section forms east of the small sill at km 13.5. Depending upon the stage in the development of the overflow, the internal hydraulic jump can be to the east, to the west, or immediately over the mooring location 6 at the bottom of the main slope. Model lower layer velocities of 0.5–0.6 [illegible]$^{-1}$ for this case are consistent with observations at mooring 6, 12 m.a.b., of 0.4 ms^{-1} from March 29–April 1, 1993, during what appears to be an overflow event. As at mooring 16, model velocities would likely be reduced to more realistic values by inclusion of an appropriate entrainment parameterization for the lower layer.

5 Discussion

Although MICOM was designed for basin-scale and mesoscale general ocean circulation problems (Bleck *et al*, 1992), as opposed to the small-scale internal hydraulic pro-

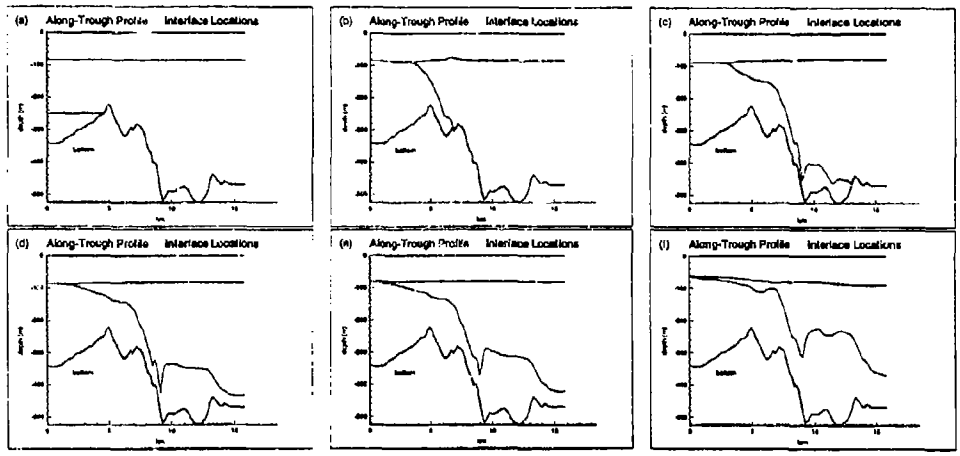


Figure 7: (a)–(f) Evolution of layer interfaces at times 0 hr, 1 hr, 6 hr, 12 hr, 18 hr, and 30 hr, respectively

cesses addressed here, it has proven to be a remarkably useful tool for these purposes. Supercritical flow, as well as internal hydraulic jumps, can be simulated with MICOM.

The model displays no numerical difficulties in the presence of even extremely abrupt topography. North of the ravine (x =8.5 km, y =6.5 km, on figure 3a) topographic slopes as great as 1.0 are present in the bathymetry. While it is likely that, in nature, processes in such regions are non-hydrostatic, it is encouraging that MICOM is robust enough to "filter" potentially troublesome large vertical accelerations.

The model is producing results which are, in a general sense, consistent with the observations. A more detailed model-data comparison, in which the dynamic response of the model is assessed, requires that a number of uncertainties be addressed. On such a small domain (18 × 11 km), the influence of open boundary conditions is paramount. Actual conditions at the upstream (western) and downstream (eastern) boundaries are unknown. They can only be inferred from information from the interior of the domain. Furthermore, boundary conditions on the north-south channel intersecting the domain are unknown. In the simulations discussed here, the north and south lateral boundaries are closed. However, in actuality, there is likely to be transport through this channel, as suggested by the observations at mooring 5 (figure 4e). Current development of the model entails the implementation of flow relaxation boundary conditions (Martinsen and Engedahl, 1987),

Further validation of the model will also require information on the vertical density structure at the same time that currents are measured during an overflow event. Vertical density profiles are required to assess the computed evolution of the layer structure.

In order to improve the description of supercritical flow regimes, the model requires a realistic representation of lower layer dissipation and entrainment.

References

Bleck, R., C. Rooth, D. Hu and L.T. Smith, 1992. Salinity-driven thermocline transients in a wind- and thermohaline-forced isopycnic coordinate model of the North Atlantic. *J. Geophys. Res.*, 22:, 1486–1505.

Camerlengo, A. L., and J. J. O'Brien, 1980. Open boundary conditions in rotating fluids. *J. Comput. Phys.*, 35: 12–35.

Christodoulou, G. C., 1986. Interfacial mixing in stratified flows. *J. Hydraul. Res.*, 24: 77–93.

Fernando, H. J. S., 1991. Turbulent mixing in stratified fluids. *Annu. Rev. Fluid Mech.*, 23: 455–493.

Martinsen, E. A. and H. Engedahl, 1987. Implementation and testing of a lateral boundary scheme as an open boundary condition for a barotropic model, *Coastal Eng.*, 11: 603–637.

McClimans, T. A., 1993. Large bottom currents near Holmengrå: their occurrence and causes, SINTEF NHL Report STF60 F93077.

Acknowledgements

This work has been supported in part by Den norske statsoljeselskap A.S (Statoil).

Diapycnal Diffusivity Measured by Microstructure and Tracer Techniques - A Comparison

A. Wüest[1], D.C. Van Senden[1], J. Imberger[2], G. Piepke[1] & M. Gloor[1]

(1) Swiss Federal Institute for Environmental Science and Technology (EAWAG) and Swiss Federal Institute of Technology (ETH) CH-8600 Dübendorf, Switzerland
(2) Centre for Water Research, University of Western Australia Nedlands, Perth, Western Australia 6009

Summary

Quantification of small-scale turbulent diapycnal diffusivity in the ocean thermocline still poses a problem. Values inferred from microstructure measurements are typically an order of magnitude smaller than values obtained with tracers. In order to evaluate this discrepancy, a comparison study was conducted in the hypolimnion of a lake over a period of one month. Diapycnal diffusivity was estimated by tracer (SF_6) spreading, and a high resolution temperature profiler was used to determine diapycnal diffusivities from dissipation rates inferred from temperature gradient spectra.

The comparison reveals that the benthic boundary is the most turbulent zone in the hypolimnion. Based on assumptions for the functional form of the buoyancy flux in the bottom boundary layer, microstructure and tracer diffusivities agree to within a factor 2. We conclude that the two techniques yield the same results as long as the mixing processes are adequately sampled. The results of this study support recent findings from the open ocean.

1. Introduction

Density structure and thermocline circulation in the oceans as well as the global geochemical fluxes are affected by turbulent fluxes across isopycnals. Despite extensive efforts by modelers and experimentalists over a long period, quantification of small-scale diapycnal diffusivity in the ocean thermocline still poses a problem. Values inferred from microstructure or dissipation measurements in the main pycnocline in the open ocean (Gregg, 1987) are typically an order of magnitude smaller than values found in tracer diffusion studies (Sarmiento et al., 1976; Ledwell et al., 1986), which are close to the canonical value of 1 cm^2s^{-1} (Munk, 1966).

This study attempts to explain this apparent important discrepancy observed between the two methods. In a naturally density-stratified lake, the diapycnal diffusivities were determined from the vertical spreading of deliberately injected sulfurhexafluoride (SF_6) and from temperature microstructure data taken during

the same period of one month. A lake was regarded as an ideal site as turbulent mixing in the pycnocline of lakes is generally shear-induced, as in the ocean, and lacustrine diapycnal diffusivities (Imberger and Patterson, 1989; Imboden and Wüest, 1994), which are usually determined by budget methods, show similar values as oceanic thermocline diffusivities.

Assuming horizontal homogeneity, we determined the diapycnal diffusivity K^t of the tracer by measuring the temporal rate of spread of the vertical tracer variance $\sigma^2(t)$ using the relation $K^t = 0.5 \cdot d\sigma^2 / dt$.

The dissipation method, a completely different approach, uses the balance equation for turbulent kinetic energy in density-stratified water. We assume stationary and homogeneous conditions, where the production of turbulent kinetic energy is equal to the loss by dissipation ε plus buoyancy flux J_b, which expresses the work against stratification. Buoyancy flux J_b is related to diffusivity K^ε and stability N^2 by $J_b = K^\varepsilon \cdot N^2$ (where $N^2 = - g \cdot \rho^{-1} \cdot \partial\rho/\partial z$; g = acceleration due to gravity; ρ = density and z = vertical coordinate, positive upward). Furthermore, one has to assume that the ratio of buoyancy flux J_b to dissipation ε can be expressed by an empirical function γ_{mix}. This leads to the relation $K^\varepsilon = \gamma_{mix} \cdot \varepsilon \cdot N^{-2}$ (Osborn, 1980). In this study, dissipation ε is determined by fitting the theoretical Batchelor shape to spectra of temperature fluctuations. For γ_{mix} we applied different parameterizations.

2. Experiment

The comparison study was conducted in July 1989 in Lake Alpnach (Fig.1) where local wind exposure leads to diapycnal diffusivities, comparable to ocean thermocline values. Lake Alpnach has a length ~5 km, a width ~1 km, and a maximum depth of 34 m (Fig. 1). In July, density stratification is strong (maximum stability N^2 ~$2.5 \cdot 10^{-3}$ s^{-2} at 7 m) and almost unaffected by dissolved solids (salinity ~ 0.3 ‰). Shear-induced mixing is caused by internal seiching driven by predominantly diel winds blowing parallel to the major axis (Münnich et al., 1992). Internal motions along the lake axis were monitored at 10 min intervals by three Aanderaa thermistor strings (Fig. 1), each consisting of eleven evenly-spaced sensors. For the tracer experiment, 52 g of SF_6 were released in two streaks over a total length of 6 km (Fig. 1) at a depth of ~17 m in Lake Alpnach. To minimize the initial diapycnal spread of SF_6, injection was adjusted to the isopycnal corresponding to the 8°C isotherm using a CTD. From the CTD record during injection, we calculated an initial variance of the vertical tracer distribution of $\sigma_o^2 \approx 4.4$ m^2 (Fig. 2). To determine the diapycnal spreading, 57 SF_6 profiles were collected over 8 days. SF_6 concentrations were measured using a gas chromatograph with an

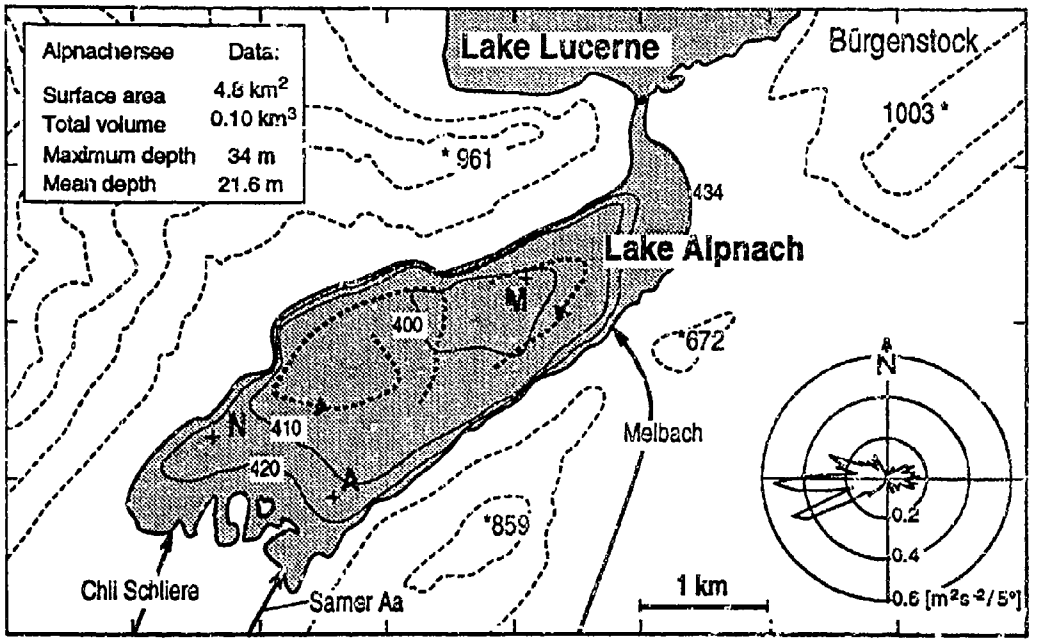


Fig.1: Map of Lake Alpnach (situated in central Switzerland): The locations of thermistor strings, labeled A (length: 20 m), M (30 m) and N (15 m), are marked by "+". A meteorological buoy was moored at M. Depth contours, lake surface elevation and heights of nearby mountains (asterisks) are given in m a.s.l. The outlet of Lake Alpnach is a passage 3 m deep connecting Lake Alpnach to Lake Lucerne.
Inset: Cumulative distribution of the square of the wind speed at mooring M (vectors shown in the direction of the wind). Adapted from Münnich et al. (1992).

electron-capture detector (Schlatter et al., 1990). Simultaneously, CTD profiles were collected to match the SF_6 sample depth with temperature (density).

On 9 days, 130 casts of temperature microstructure were collected with a self-contained profiler (Carter and Imberger, 1986), rising at about 0.1 m/s and collecting data at 100 Hz from a pair of FP07 thermistors. Data was filtered as required for response matching (Fozdar et al., 1985). To select those mixing events whose temperature fluctuations fulfill the criterion of stationary turbulence, a special algorithm was used (Imberger and Ivey, 1991). Power spectra were estimated from these segments, and dissipation ε was determined by a Batchelor fit (Gibson and Schwartz, 1962; Dillon and Caldwell, 1980). The quality of each fit was checked, and subsequent analyses were carried out using only the data from segments following the characteristic Batchelor spectrum.

For each of the 130 casts, bin-averaged dissipation estimates were obtained for two series of bins: "depth bins" beginning at the lake surface and extending downwards, and "height bins" beginning at the lake bottom and extending upwards. Averages were weighted with the segment length by assuming zero dis-

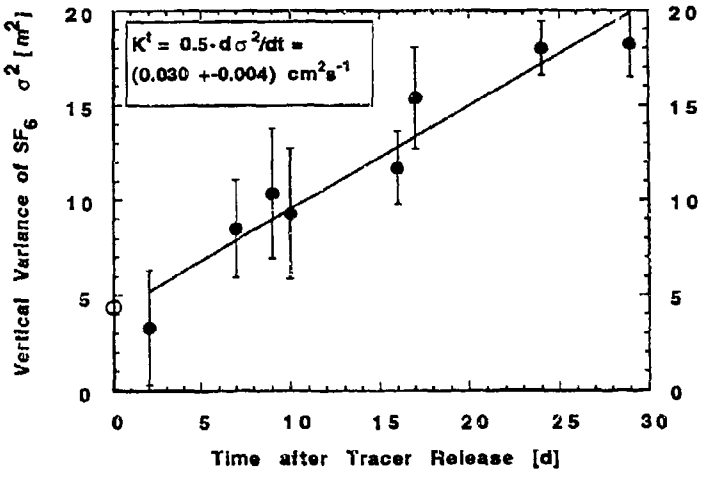


Fig. 2: Vertical variance σ^2 of the tracer SF_6 as a function of time after tracer release (June 26). $K^t = 0.5 \cdot d\sigma^2/dt$ was determined by linear regression. The fitted initial variance σ^2 (t=0) is close to the value determined by continuous CTD recording during tracer release (open symbol). The errors of the variances were determined by fitting a Gaussian distribution to the vertical profiles.

sipation outside turbulent segments. Since most of the observed hypolimnion is non-turbulent, the averages are clearly lower than the individual dissipation in the turbulent segments. The arithmetic mean, as well as the maximum likelihood estimate (Baker and Gibson, 1987) were both calculated.

3. Observations

Tracer SF_6 : Within the first 10 days after injection, SF_6 concentrations were highly variable due to input heterogeneities. Thereafter, horizontal mixing (Peeters, 1994) eliminated horizontal gradients. To achieve statistically representative vertical variances of the tracer distribution, we averaged the profiles to obtain daily means. To remove reversible displacements due to internal seiching, SF_6 profiles were averaged in bins of constant temperature and averages were retransfered to depth by using the daily mean temperature profiles. The increase of σ^2 (from 2.1 m to 4.3 m within the one month period) is plotted in Fig. 2 as a function of time after injection. The diapycnal diffusivity was calculated by linear regression and yielded $K^t = 0.5 \cdot \partial\sigma^2/\partial t = 0.030\ cm^2s^{-1}$ (Fig. 2).

Wind and Internal seiches: The diurnal wind (Fig. 1) excited internal seiching motion as exemplified in Fig. 3. Spectral analysis revealed two dominant periodicities that correspond to the first vertical first horizontal and second vertical first horizontal seiche modes (Münnich et al., 1992). A subsequent field campaign

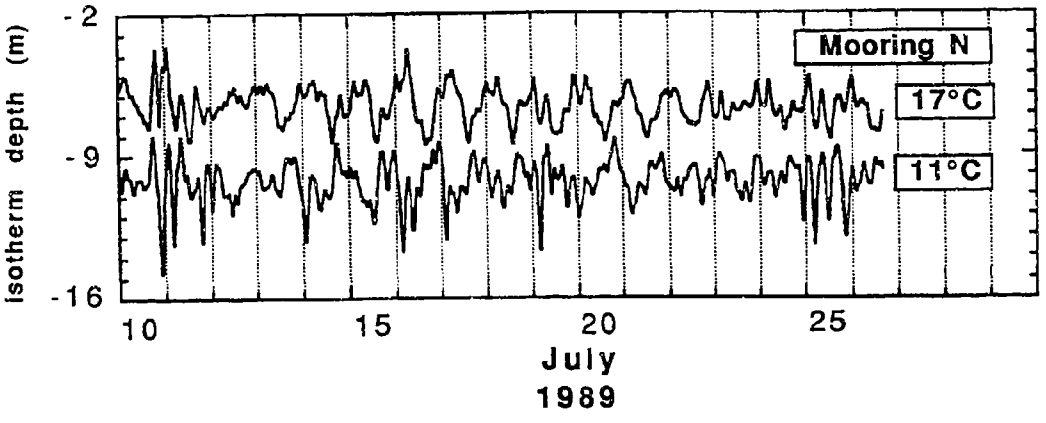


Fig. 3: Part of the time series (July 10 to 26 1989) of the depths of two selected isotherms calculated from thermistor chain data taken at mooring N. Data was low-pass filtered with a 2.5 h cutoff. Two peak periodicities of 24 h and 7.5 h are well developed. The shorter period (see e.g. July 11) represents the first vertical mode, and the 24 h seiching (e.g. July 14 to 20) the second mode (Münnich et al., 1992).

revealed that for both modes, bottom currents along the major axis of the lake correlate perfectly with the displacements of the hypolimnetic isotherms in Fig. 3 (Gloor et al., 1994). The corresponding phases reveal that the whole hypolimnetic water body is excited by modes of first horizontal structure. With this simple structure it was possible to determine the basin-wide hypolimnetic velocity field by a topography-dependent seiche model (Münnich, 1993). Thus we were able to identify the regions of high seiche-induced vertical shear, relevant to diapycnal mixing; i.e., the upper thermocline and the benthic boundary layer.

Dissipation: Arithmetic means of dissipation $\bar{\varepsilon}$, averaged in vertical "depth bins" (over the 130 casts), cannot directly be used to calculate diapycnal diffusivity since these horizontal averages do not necessarily yield a representative dissipation. Since most of the casts extended to depths between 20 and 32 m, the upper thermocline averages contain data mainly from the interior of the water body, whereas deep water averages are dominated by turbulence in the bottom boundary layer. In order to obtain adequate averages, we have divided the water column into two regions: "interior" (distance from bottom > 10 m) and "boundary layer".

Fig. 4 displays separate arithmetic averages for the two regions in "depth bins" (Fig. 4a) and in "height bins" (above sediment; Fig. 4b). Dissipation in the interior region decreases with depth, rapidly reaching its detection limit (Fig. 4a), whereas dissipation increases towards the bottom (Fig. 4b) and is approximately

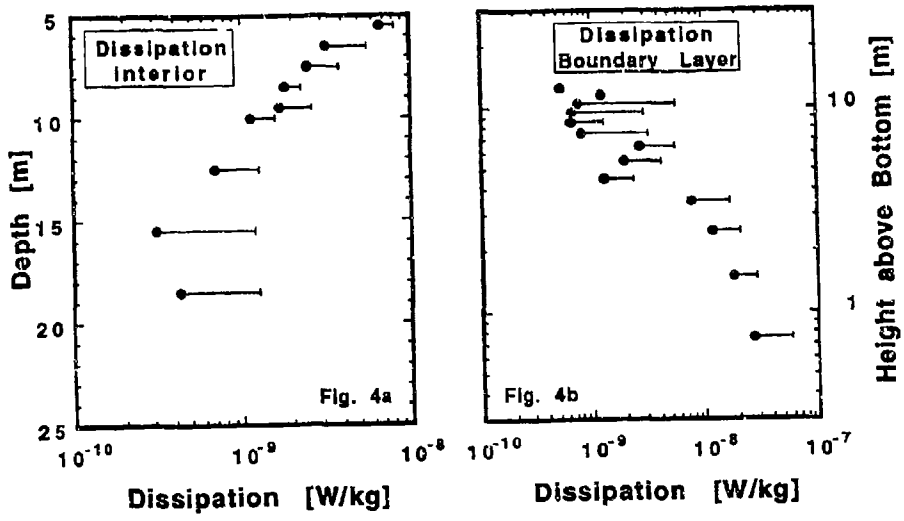


Fig. 4: Average dissipation of the 130 casts: a) Averaged in "depth bins"; b) In (bottom-parallel) "height bins". The single sided error bars are the variances of the maximum likelihood estimate. Within these error bars, dissipation follows a h^{-1} slope.

proportional to h^{-1} (h = distance to the local bottom), as predicted by the classical boundary layer theory. Within the vertical range of interest, i.e. between 12 and 20 m depth, where over 50% of SF_6 was located, dissipation is dominated by turbulence in the benthic boundary layer, as shown by a simple calculation based on the ratio of sediment surface A to water volume V.

4. Comparison of Diffusivities

Like dissipation, the average buoyancy flux in 12 to 20 m depth comprises contributions from the "interior" water body and from the "boundary layer". The results of the two different methods used to form volume averages are given in Table 1. For case (a) we assumed that the dissipation ε is proportional to $u_*^3\,(kh)^{-1}$ down to the boundary of the viscous layer (δ_v), and that the buoyancy flux is a constant fraction γ_{mix} of dissipation throughout the boundary layer. In case (b) we assumed the buoyancy flux to increase towards the sediment, as in (a), but to remain constant in the homogenized lower part of the bottom boundary layer δ_{mix}. Integration formula and parameter values are summarized in Table 1 and described in more detail elsewhere (Wüest et al., 1994).

Both results are compatible to within a factor 2 with the tracer diffusivity (Fig. 2, Table 1). A physical interpretation of the two cases reveals that (a) probably yields

Table 1: Comparison of diffusivities at 17 m depth

Method	Applied formula	K (cm^2/s)
Passive tracer (SF_6):	$\frac{1}{2}\frac{\partial \sigma^2}{\partial t}$	0.030 ± 0.004
Dissipation (Composition of "interior" and botton. "boundary layer"):		
a) Integration to δ_v (1)	$\frac{\gamma_{mix}}{N^2}\cdot[\varepsilon_I^{17m} + \frac{\partial A}{\partial V}\int_{\delta v}^{\delta_B} u_*^3 (kz)^{-1}\, dz]$	0.027 ± 0.004
b) Constant buoyancy flux (2)	$\frac{\gamma_{mix}}{N^2}\cdot[\varepsilon_I^{17m} + \frac{\partial A}{\partial V}\frac{u_*^3}{k}\{1+\ln\left(\frac{\delta_B}{\delta_{mix}}\right)\}$	0.017 ± 0.003

(1) Integration down to the viscous boundary layer of thickness δ_v; ε_I^{17m}: dissipation in the interior ; N^2: stability ; u_*: friction velocity; k: von Karman's constant; δ_B =10m (thickness of the Prandtl layer).

(2) Assumption of constant buoyancy flux in the homogenized boundary layer of thickness δ_{mix}.

an overestimate of the buoyancy flux (and consequently of the diffusivity), and that (b) is more a realistic assumption as mixing in a mixed layer (of thickness δ_{mix}) is less efficient. Taking into account that tracer undersampling generally over-estimates diffusivity, agreement is most probably even better than a factor 2.

5. Conclusion

This study, which compares diffusivity in the thermocline of a lake over a period of one month using tracer and temperature microstructure techniques, yielded two important results: (1) the main source of turbulent kinetic energy is the benthic boundary layer; (2) diapycnal diffusivity is due to a combination of buoyancy flux in the interior and at the boundary layer. If averaged adequately, the results obtained by the two methods show agreement to within less than a factor 2, which is less than the discrepancies found in the ocean. The results of this study support recent findings from the open ocean (Ledwell., 1993).

Acknowledgments

We are in debt to many people from the Environmental Physics Department at EAWAG for their generous support in the field: M. Hofer, D. Imboden, M. Münnich,

F. Peeters, J. Schlatter, M. Ulrich and especially to M. Schurter for his unfailing presence on the lake. This work was supported by Swiss National Science Foundation grants no. 20-27751.89 and 20-32700.91

References

Baker, M.A., and C.H. Gibson, Sampling Turbulence in the stratified Ocean: Statistical consequences of strong intermittency, *J. Phys. Oceanogr.*, *17*, 1817-1836, 1987.

Carter, G.D., and J. Imberger, Vertically rising microstructure profiler, *J. Atmos. Oceanic Technol.*, *3*, 462-471, 1986.

Dillon, T.M., and D.R. Caldwell, The Batchelor spectrum and dissipation in the upper ocean, *J. Geophys. Res.*, *85*, 1910-1916, 1980.

Fozdar, F.M., G.J. Parker, and J. Imberger, Matching temperature and conductivity sensor response characteristics, *J. Phys. Oceanogr.*, *15*, 1571-1588, 1985.

Gibson, C.H., and W.H. Schwartz, The universal equilibrium spectra of turbulent velocity and scalar fields, *J. Fluid Mech.*, *16*, 365-384, 1963.

Gloor M., A. Wüest, and M. Munnich, Benthic Boundary Mixing and Resuspension Induced by Internal Seiches, *Hydrobiologia* (in press), 1994.

Gregg, M.C., Diapycnal mixing in the thermocline: A review, *J. Geophys. Res.*, *92*, 5249-5286, 1987.

Imberger, J., and J.C. Patterson, Physical Limnology, *Advances in applied mechanics, Academic Press, Cambridge*, 303-475, 1989.

Imberger, J., and G.N. Ivey, On the nature of turbulence in a stratified fluid, part II: Application to lakes, *J. Phys. Oceanogr., 21*, 659-679, 1991.

Imboden, D.M., and A. Wüest, Mixing mechanisms in lakes in A. Lerman [Ed.] "Lakes: Chemistry, Geology, Physics", *Springer*, New York, (submitted), 1994.

Ledwell, J.R., A.J. Watson, and W.S. Broecker, A deliberate tracer experiment in Santa Monica Basin, *Nature, 323*, 322-324, 1986.

Ledwell, J.R., A.J. Watson, and C.S. Law, Evidence for slow mixing across the pycnocline from an open-ocean tracer-release experiment. *Nature. 364*, 701-703, 1993

Münnich, M., A. Wüest, and D.M. Imboden, Observations of the second vertical mode of the internal seiche in an alpine lake, *Limnol. Oceanogr., 37*, 1705-1719, 1992.

Münnich, M., On the influence of bottom topography on the vertical structure of internal seiches, Ph.D. diss. no. 10434, ETH-Zürich, 97 pp., 1993.

Munk, W.H., Abyssal recipes, *Deep Sea Res., 13*, 707-730, 1966.

Osborn, T.R., Estimates of the local rate of vertical diffusion from dissipation measurements, *J. Phys. Oceanogr., 10*, 83-89, 1980.

Peeters, F., Horizontale Mischung in Seen, Ph.D. diss. no. 10476, ETH, 147 pp., 1994.

Sarmiento, J.L., H.W. Freely, W.S. Moore, A.E. Bainbridge, and W.S. Broecker, The relationship between vertical eddy diffusion and buoyancy gradient in the deep sea. *Earth Planet. Sci. Lett., 32*, 357-370, 1976.

Schlatter, J., M. Hofer, and D.M. Imboden, Die Verwendung von Schwefelhexafluorid zum Studium von Transportprozessen in Seen, *Gas-Wasser-Abwasser 70(1)*, 36-42, 1990.

Wüest, A., D.C. van Senden, J. Imberger, and G. Piepke, Diapycnal diffusion in a small lake: A comparison between microstructure and tracer estimates (in prep.)

Observations of Mixing in a Stratified Lake

By P.F.Hamblin+, C.L.Stevens* and G.A. Lawrence*

+ National Water Research Institute, Burlington, Ontario L7R 4A6 Canada.

* Environmental Fluid Mechanics Group, Dept. Civil Engineering, University of British Columbia, Vancouver, B.C. V6T 1Z4 Canada

Abstract

Quantification of mixing in the surface layers of lakes is important for the understanding of various biological processes. Our study is a case in point where we attempted to obtain mixing rates of fertilizer added to the surface layers in order to enhance biological productivity. In this report we focus on the observations taken on June 8, 1992 in Kootenay Lake, British Columbia, during a period of strong near surface stratification and shear as well as indications of vigorous mixing at one of three moored temperature profilers. These observations were made near a constriction in the lake cross-sectional area. An acoustic doppler current profiler(ADCP), a conductivity-temperature-depth profiler(CTD), dye patch dispersion and meteorological data complemented the mooring data.

During the middle of that day strong winds (7 m/s) blew for 6 hours. Shortly before the start of the wind and after six hours of steady wind high frequency temperature fluctuations were observed at the thermistor chain located in the flow constriction. The two events appeared to be active at this location for over an hour and a half, with the region of greatest activity occurring from a depth of 10 m to around 20 m. At the beginning of the mixing period continuous temperature profiles recorded with the CTD were smooth, however, three hours later the temperature profiles had developed a step-like structure, indicating possible vertical mixing. At the same time current shear measured by the ADCP, when combined with the observed buoyancy frequency profile deduced from the temperature profiler, yielded gradient Richardson numbers in the range 0.25 to 0.6 over upper 20 m of the water column at locations several kilometres downstream in the direction of flow.

Additional evidence of vigorous vertical mixing was derived from concurrent observations of dye injected into the upper 10 m. From direct measurements of horizontal dye dispersion and dispersion theory (Fischer et al. 1979) it is possible to infer estimates of the rate of turbulent kinetic energy dissipation. Dissipation rates from the dye and scaling analysis of the high frequency temperature fluctuations are from ten to one hundred times larger in the mixing zone than those found in the ocean and in other lakes.

INTRODUCTION

The interaction between basin-scale motions in lakes and the

small scale physics thought to be responsible for mixing continues to be of great interest to limnologists. In the long but narrow lakes of concern in this study Hamblin (1977) observed high frequency internal waves in the vicinity of a large river inflow and at a mid-lake location during episodes of intense basin-scale internal seiche activity, Hamblin(1978). Farmer(1978) observed high frequency internal waves and evidence of mixing following the passage of internal surges in a long narrow lake. Such observations in lakes have rarely been accompanied by measurements of the background shear necessary to interpret the suspected mixing events unlike the case in the ocean where a large number of studies have concurrently observed both the large and small scale physics, for example, Carr et al.(1992), Marmarino and Trump(1992 & 1991) and Peters et al.(1991).

The desire to better understand mixing in stratified environmental flows as exemplified by our field observations of some small-scale events which possibly indicate mixing provides the focus for the present study. The emphasis here is on the links of the small-scale physics to the large-scale physical setting as determined by the meteorological forcing, lake basin-scale internal wave-induced shear and stratification.

EXPERIMENTAL DETAILS AND DATA ANALYSIS

During a 2-week long study of the mixing characteristics of the surface waters of Kootenay Lake, British Columbia for the purposes of optimizing the dispersal of nutrients added to the lake, we observed several small-scale events at one of three moored temperature profilers on June 8, 1992. The data discussed here were observed at a meteorological station, a thermistor chain and by two motor vessels whose tracks are shown in Figure 1. Moored temperature data were also collected at the meteorological station and at a another location about 9 km to the north of the station. The meteorological station consisted of a raft supporting wind speed and direction sensors, relative humidity and temperature of the air and incoming solar radiation. A solar-powered data logger recorded all variables every ten minutes. The position of the vessels was determined electronically by Miniranger fixes. At the thermistor chain temperatures were recorded at one-minute intervals over ten unevenly spaced depths from 1 m to 50 m. Aboard one vessel a yo-yoing CTD profiler recorded temperature, conductivity and Rhodamine dye fluoresence profiles while on the other a 1.2 MHz ADCP of RDI manufacture sampled flow over 1-m depth bins down to 25 m. The ADCP data were used to estimate average shear over 2-m depth ranges from five sequential velocity profiles selected for least variability in ship's speed and heading. The error in shear is estimated to be $0.006(s^{-1})$. Due to cross-bin averaging the narrow-band ADCP is known to underestimate shear. Thus, an experiment was conducted on another data set where ADCP and standard current meter measurements were observed concurrently. Based on the 70 individual comparisons of the 2-m shear between the two methods of current measurement there was no statistically significant difference in shear. At the approximately 2 m/s ship speed the shear would be averaged over a distance of 150 m. It was found that averaging over greater or smaller distances increased the variability of the shear. In order to calculate profiles of

Richardson number, Ri, associated with the shear, 30-min average profiles of stability or Brunt-Vaisala frequency, N, were formed.

$$Ri = \frac{N^2}{(\frac{du}{dz})^2 + (\frac{dv}{dz})^2}; \qquad N^2 = -\frac{g}{\rho}\frac{d\rho}{dz}$$

where ρ is the density ,g is the acceleration of gravity and u and v are the horizontal velocity components.

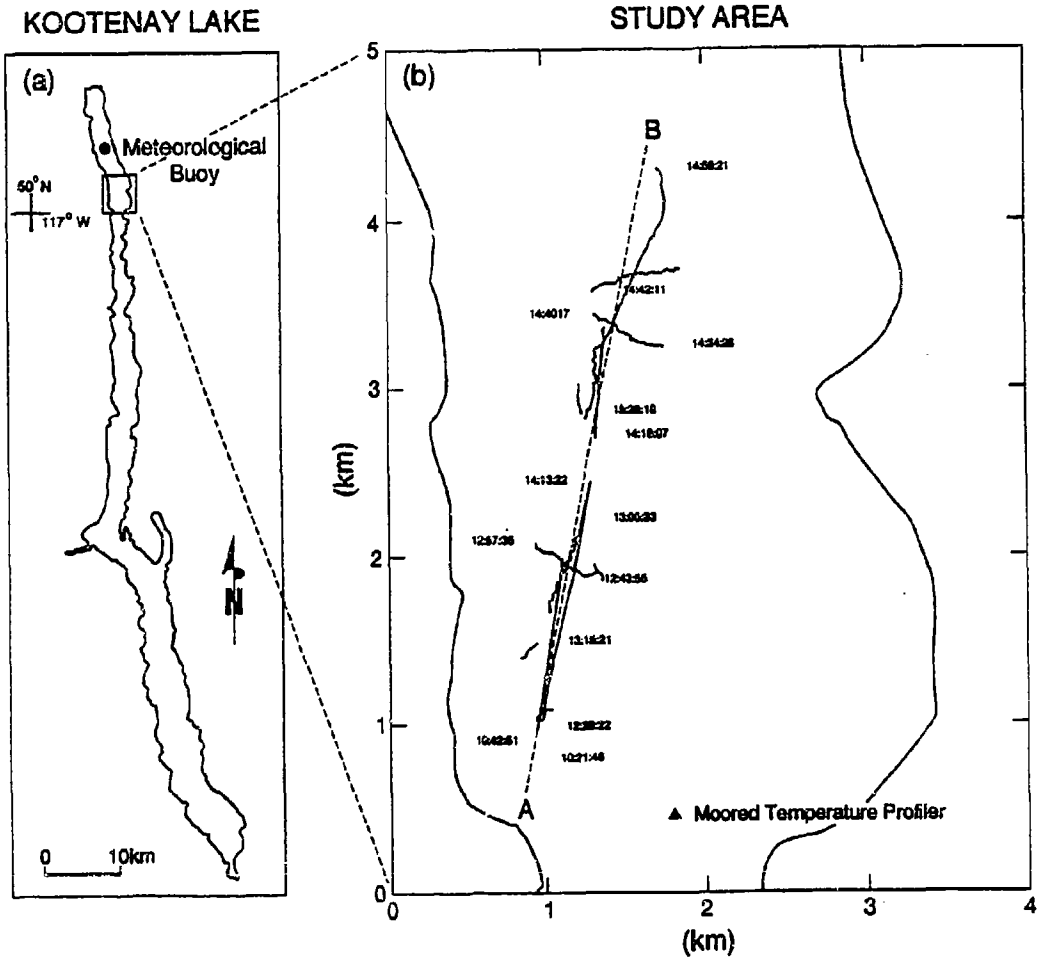


Figure 1. Study location,Kootenay Lake, and various station locations. Time is Pacific Daylight.

Air and water temperatures are displayed in the upper panel of Figure 2 for a 24-hr period covering the attended field activities. Similarly the wind speed and direction are shown below. Since the wind stress and the buoyancy flux are the major surface forcing terms for turbulent mixing, the lower two panel of Figure 2 present these quantities. Surface heat fluxes were calculated from standard bulk formulae(Fischer et al.,1979). Incoming longwave radiation was calculated from air temperature

and inferred cloud cover. In the bottom panel friction velocity, u*, is compared to a buoyancy velocity scale, w*, assuming the

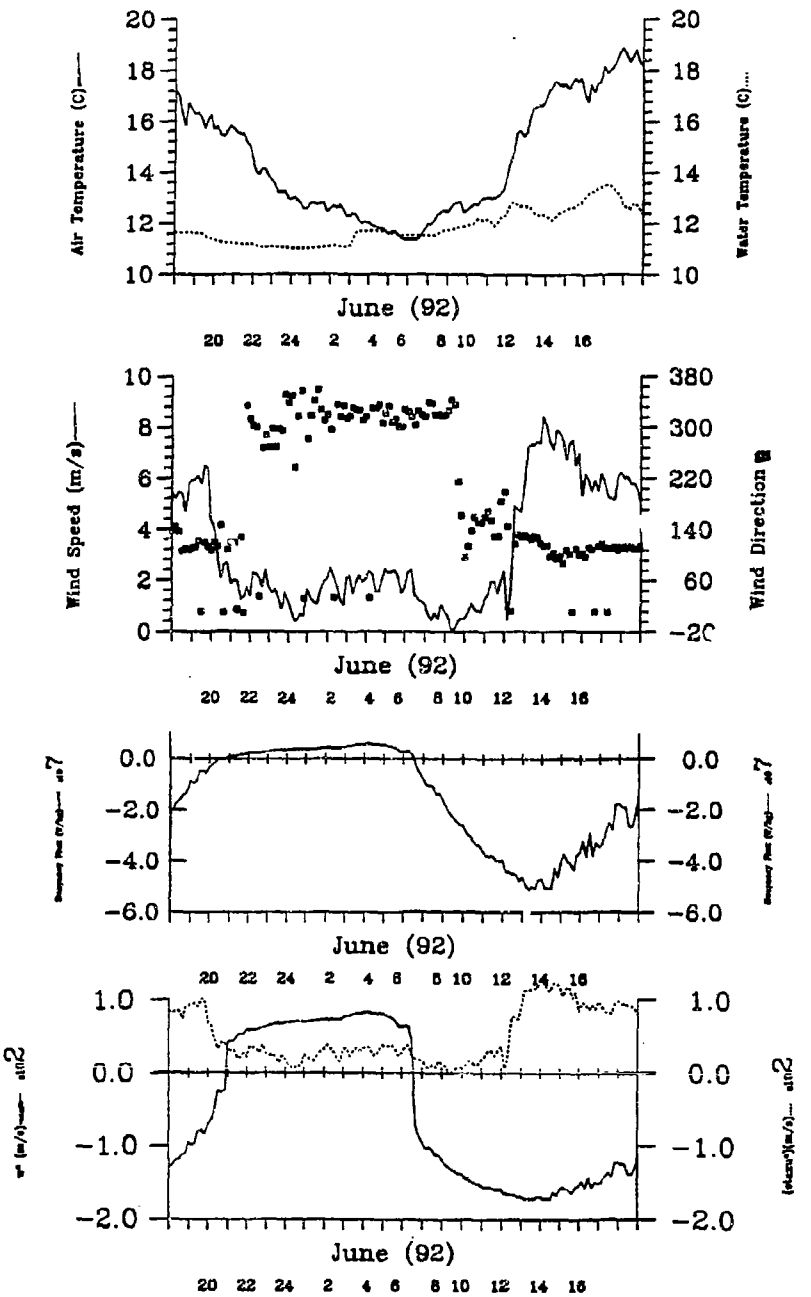


Figure 2. Selected ten-minute meteorological forc[illegible] from 18:00 June 7 to 18:00 June 8. Time is Pacific Daylight [illegible] mixing depth is on the order of 10 m, th[illegible]ch of the dye diffusion floor. For the sake of compari[illegible] u* has been

multiplied by the usual mixed layer efficiency factor of 1.23(Fischer et al.,1979).

Unfortunately, no direct measurements of turbulence such as the rate of turbulent kinetic energy dissipation were available. Instead, turbulent mixing was inferred in bulk from the horizontal and vertical spreading as determined by the shipboard profiler of a 8-Kg release of dye at the position marked 10:21:48 on Figure 1 over a 5-hr period. Secondly, small-scale temperature "activity" served as an indicator of turbulent mixing. This activity has been defined by Marmarino and Trump(1991) as the magnitude of the first difference of the 1-min temperatures at each thermistor normalized by the local vertical temperature difference. According to Marmarino and Trump this activity parameter serves as a qualitative measure of the likelihood that mixing has occurred.

DISCUSSION

During the present experiment stratification was developing rapidly. From an examination of the isotherm displacements at the other thermistor chains to the north it appeared that a first mode internal seiche was taking place with flow at the surface to the north until June 10. The drift of the dye as seen in Figure 1 and the ADCP data corroborate this with both indicating a northward flow of 25 to 30 cm/s at the surface decreasing to much lower flow at 25 m depth. Contours of vertical shear squared, stability frequency, and Richardson number are shown on Figure 3 as a function of depth and horizontal distance along the line A-B(Figure 1) from the dye release point. It is noteworthy that shear is strongest towards the southern end of the line which is closest to the narrows or constricted flow. A plot of the shear as a function of time(not shown) does not show a trend despite the onset of strong wind forcing at 11:30. This suggests that the northward trending flow as evidenced by the dye trajectory of Figure 1 and the ADCP data is associated partly with basin-scale internal waves and consequently should have existed before the period of data displayed in Figure 3. The likely southward intensification of the shear and continuity consideration suggest that at the thermistor chain the average shear could be up to twice as large as that measured by the ADCP in the more open portion of the lake to the north. A plot similar to Figure 3(also not shown) based on this assumption and the observed temperature data at the thermistor chain indicates Richardson numbers less than the critical value of 0.25 over the upper 6 m of the water column for the entire 3-hr period in contrast to a much more limited area of the plot shown in Figure 3. Either plot demonstrates that the stability frequency is relatively constant in the area of the dye release but that low Richardson numbers are due to intensified vertical shear as the surface is approached.

Mixing in the study area may be inferred indirectly by comparison of the CTD temperatures with those upstream at the mooring allowing for varying advection of fluid parcels at the appropriate depths. Stability frequencies at the mooring are, in general, twice as large as those downstream. As well, despite the surface heating due to penetrative shortwave radiation and buoyancy flux surface temperatures are 1.5 °C less in downstream zone, presumably due to vigorous mixing. Finally,the

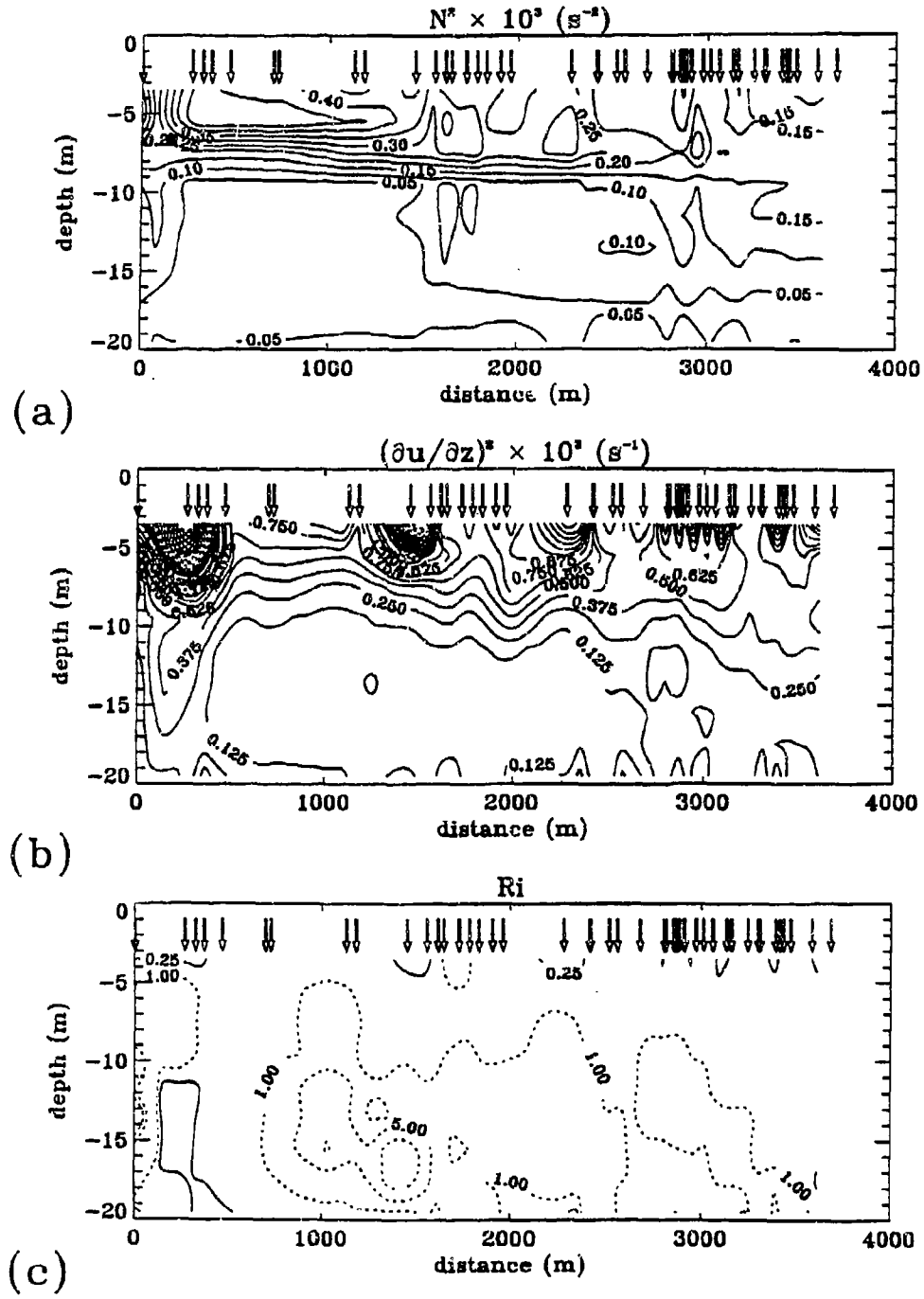


Figure 3. (a) average vertical shear squared (s^{-2}); (b) N^2 (s^{-2}); (c) Richardson number: note uneven contour intervals, Observation points are indicated by arrows. Distance from dye release. CTD profiles taken in the area of the dye tracking develop a step-like structure which may be an indicator of mixing.

While a surrogate for direct measurements of turbulent mixing, the temperature activity is a more direct indicator of turbulent mixing than the above considerations. The activity plot of Figure 4 suggests that turbulent events over depths from 10 to 20 m occur just before the wind increases at the meteorological buoy and also after the wind has been blowing strongly for 4 to 5 hours. It is evident from Figure 2 that during the wind event the wind stirring is about the same magnitude as the counteracting buoyancy flux. Thus, turbulent energy input from the wind and associated wave breaking may not be dampened and so diffuses downward. The question arises of why the first mixing event occurs apparently before the wind strength increases. This may be due to the direction of the wind disturbance travelling in the same direction as the wind. Since the wind was observed about 9 km north of the thermistor chain it may have taken an hour for the wind disturbance to reach the meteorological raft.

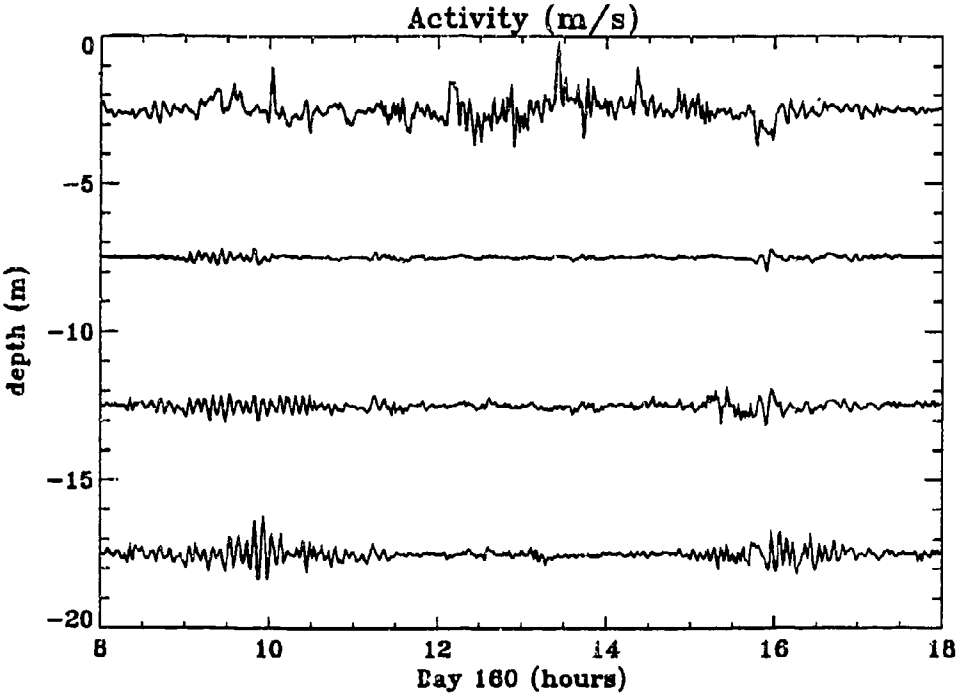


Figure 4 Four levels of temperature activity at the thermistor chain.

The temperature activity seen in Figure 4 is associated with vertical isotherm displacements of amplitudes of about 1 to 2 m and periods of 6 minutes. Since temperature activity was not observed during the period of nocturnal convective cooling, it is hypothesized that the activity is evidence of shear instabilities. If these displacements are associated with Kelvin-Helmholtz instabilities then the scale of the most energetic overturns, l_0, may be estimated as O(0.1 times the billow height or 10-20 cm)(Marmarino and Trump, 1991). A 10-cm overturning scale corresponds to an rate of turbulent kinetic energy dissipation of $(l_0/1.25)^2 N^3$ or $5.x10^{-4}$ cm^2/s^3. The dissipation downstream may be inferred from the dispersion of a patch of dye according to the

standard scaling arguments(Fischer et al., 1979). Measured horizontal dispersion coefficients of).095, 0.7 and 0.12 m^2/s and patch sizes of 95, 400 and 300 m respectively are consistent with a dissipation rate of 1 to $6x10^{-5}$ cm^2/s^3. These rates are from 10 to 60 times larger than oceanic values(Fischer et al.,1979) and those observed in other kes(Lawrence et al., 1994). As well as enhanced vertical mixing horizontal mixing may be accelerated by turbulent eddies shed by flow separation downstream of the flow constriction. We have mapped eddies during the ADCP surveys near promontories in Kootenay Lake. It is noteworthy that dissipation is possibly even larger in the restricted channel at the thermistor chain.

CONCLUSIONS

The ADCP measurements are a useful complement to the underway CTD profiles and permit Richardson numbers to be calculated and consequently zones of likely mixing to be identified. We conclude that vigorous mixing can occur even during periods of active development of stratification under certain conditions. Vertical shear associated with lake basin-scale internal waves which has been enhanced by coincident wind forcing of even short-term duration and focussed by basin geometry may increase to critical levels leading to mixing. Under these circumstances, despite the stabilizing effect of buoyancy flux, mixing rates as inferred from dye dispersion and fine-scale temperature activity are seen to be more intense than typical mixing rates found in the ocean and other lakes. Direct measurement of such turbulent quantities as the rate of dissipation would have been required in order to parameterize the mixing rates in terms of readily observable large-scale variables such as wind, shear and stability.

Acknowledgements: We are grateful to Cheng He for assistance in preparing this manuscript.

REFERENCE

Farmer,D.M. 1978. Observations of long nonlinear waves in a lake. J.Phys. Oceanogr. Vol.8, 63-78

Hamblin,P.F., 1977. Short-period internal waves in the vicinity of a river-induced shear zone in a fjord lake. J. Geophys. Res. 82(21): 3167-3174

Hamblin,P.F., 1978. Internal waves in a fjord lake. J. Geophys. Res. 85(C5):2409-2418

Lawrence, G.A, K.I.Ashley, N.Yonemitsu and J.R.Ellis, 1994 Natural dispersion and the fertilization of a small lake. Manuscript submitted for publication

Marmorino,G.O. and C.L.Trump, 1992 High-wavenumber shear and temperature structure during the patches experiment.J. Geophys. Res. 97(C2): 2309-2318

Marmorino,G.O. and C.L.Trump, 1991 "Turbulent mixing" induced by upgoing near inertial waves in the seasonal thermocline of the Norwegian Sea. J. Geophys. Res. 96(C4): 7137-7143

Peters, H.,M.C.Gregg and T.B.Sanford,1991. Equatorial and off-equatorial fine-scale and large-scale shear variability at 140W J. Geophys. Res. 96(C9):16,913-16,928

Wind Forcing of Internal Waves in Long Narrow Stratified Lakes

By Craig Stevens†, Gregory Lawrence†, Paul Hamblin‡ and Eddy Carmack*

† Environmental Fluid Mechanics Group, Dept. Civil Engineering, University of British Columbia, Vancouver, V6T 1Z4, BC, Canada.
‡ National Water Research Institute, Burlington, L7R 4A6, Ont., Canada.
* Ocean Physics, Institute of Ocean Sciences, Sidney, V8L 4B2, BC, Canada.

Abstract

An analysis of wind and thermistor chain data from a long, narrow, stratified lake is provided. It is apparent that the forcing is very sporadic relative to the likely response frequencies. A vertically integrated approach provides results that differ in some respects from inferences based on data from specific depths. This leads to the observation of horizontal mode two internal waves and in one instance, over a two month period, it is possible to infer potential energy losses of up to 60% from the energy observed in the first peak tilt after the wind event to the peak a single wave period later.

Introduction

Internal waves are a ubiquitous feature of stratified lakes and their description has received worthy attention in the literature (e.g. Hutter 1984). The elucidation of their behaviour is important for a number of environmental and social reasons. For example, salmon populations in British Columbia, Canada, are extremely sensitive to rapid temperature changes. Any responsible artificial modification of lake inflow and outflow must consider the internal dynamics.

Considerable advances have been made in correctly identifying the various modes of oscillation (Hutter 1984) and identifying the nature of waves (Thorpe 1974, Farmer 1978). In this paper we consider field data in the context of a simple lake model. The emphasis here is on the links between the wind, the internal wave response and subsequent amplitude decay in long narrow lakes where the periods of the fundamental waves are long and, because of width constraints, the effect of the earths rotation is secondary.

Analysis

The analysis is pursued by considering a depth averaged wave equation derived from the horizontal component of the equations of motion and continuity for an enclosed basin of fluid of length L, constant depth h and breadth with an overall density difference represented by a modified gravity g' and forcing f (see Fig.1). We arrive at the following equation

$$[u_{tt} - c_0^2 u_{xx}] + NL(u) = f_t + D(k,u) \qquad (1)$$

where u is the horizontal velocity, c_0 is the long-wave speed in the system given by

$$c_0 = \sqrt{g'h}$$

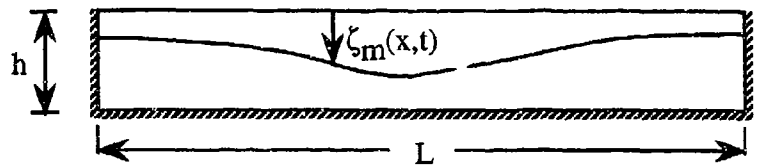


Figure 1. Schematic illustration

where g' is the modified gravitational acceleration and k is the eddy diffusivity. The t and x subscripts refer to partial differentiation with respect to the temporal and longitudinal dimensions respectively. Non-linear components of the equation of motion are compiled within $NL(u)$, the forcing term in the original equation of motion is given by f and the diffusive effects are contained within $D(u,k)$.

Forcing variations: The vertical integration has removed the depth dependence which negates any detailed vertical specification of the stress distribution. The forcing appears in the wave equation formulation of (1) only through its temporal derivative. Consequently in a linearised and non-diffusive system the phase difference generated by the duration of a wind event is fundamental in gauging the response. A change in the forcing initiates the wave response, which, in the absence of the D and NL terms, continues. If at some later time the forcing returns to its initial condition a negative wave emerges. In the unlikely event that the wind duration is some multiple of the fundamental wave period there would be zero resultant motion. However the inclusion of losses and dispersion in (1) removes this possibility.

Non-linearities and Diffusion: While the non-linear interactions are clearly important they are treated extensively elsewhere. For the time being we shall concentrate on identifying how energy gets from the wind field into the linear wave field. The coefficient of eddy diffusivity is a function of the flow, consequently, holding D constant is a weak assumption. Energy from the wind may be transferred to transverse motions, turbulence and higher vertical modes (Mortimer and Horn 1982, Münnich *et al.* 1992, Roget *et al.* 1993). Most of these "losses" involve transfer of energy to spatially and temporally varying processes. Thus, we can assume that the diffusive term in (1) is represented by

$$D(k,u) = \frac{\partial}{\partial t}\left(\frac{\partial}{\partial x}\left(k\frac{\partial u}{\partial x}\right)\right). \tag{2}$$

Observations

The wave equation (1) is discussed here in the context of the extensive data set described by Wiegand and Carmack (1986). The data we are concerned with here is that recorded by three thermistor chains placed at the North end (SC), middle (PB) and South end (TB) of Kootenay Lake in British Columbia, Canada (Fig. 2). The lake is 110 km long, 4 km wide on average and between 80 and 140 metres deep with a very steep shoreline. A pair of meteorological stations recorded radiative fluxes and wind forcing.

The data record lasts for almost three years and as such is one of the longer records available of these types of observations. This paper will cover only the middle Spring-Summer-Autumn period of 1977. The largest internal waves appear in the latter half

of this period from late-July through to the end of October; the enhanced activity in October observed by Thorpe (1974) and others is not evident in this data.

Wind data: A digital low-pass filter, using an 8 hour period for the cut-off, was used to remove the high frequency information in the wind speed data U_4, recorded at a height 4 m above the still-water surface (Fig. 3a). The modified data show peaks of 8 ms^{-1} and a 10 month average of around 3 ms^{-1}. Farmer (1978) and Stevens *et al.* (1993) illustrate the directional variability of the wind field over the surface of a lake, consequently, making general statements about the wind direction and strength based on point measurements from a few locations is ill-advised. Fig. 3b also includes the temporal derivative of the forcing term U_4^3 that indicates the spikiness of the energy put into the water column. Finally, as discussed below, differences in the centres of mass between locations are shown in Fig. 3c.

Two analyses are applied to the wind time series; firstly by including the direction to find some along-axis component and then defining starts and ends to wind "events" based on zero crossings it is possible to get an indication of the forcing. The average wind speed during this period is calculated and the compilation of total number of events over the full three year data set indicate that there are only about 5 to 10 events of sufficient duration to generate the steady state conditions described by Spigel and Imberger (1980). A scatter plot of "duration" and wind speed (Fig. 4) shows that low speed wind events generally last for a few hours but that some of the strongest wind events can last for many hours.

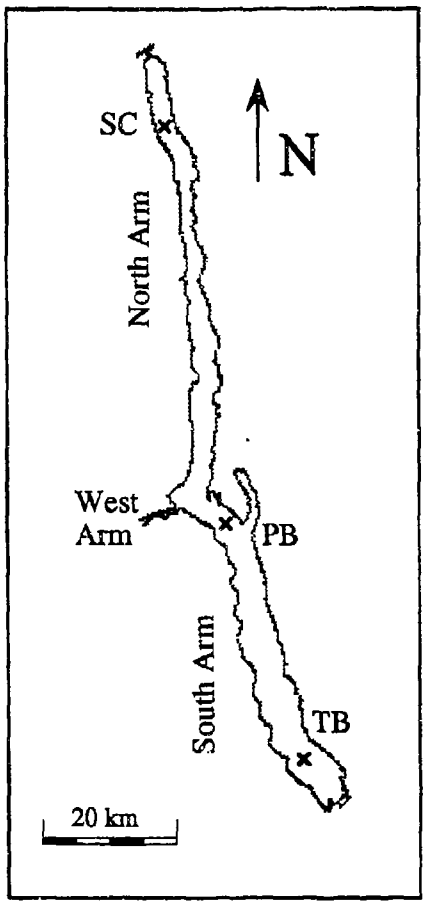


Figure 2. Kootenay Lake shoreline and station positions

Because the fundamental period varies between one and two weeks over the summer this makes for coarse results when examining the temporal distribution of the results of Fourier transforms of the wind data. An alternative analysis involves applying the wavelet transform to the data (Gao and Li 1993); this has improved temporal resolution at the expense of frequency response. Practically speaking the technique involves convolving a time series with a window (the kernel) that has temporal and frequency information. In a series of convolutions the kernel is allowed to spread (dilate) so that it identifies features of the same form as the kernel but with different basic frequency distributions.

Wavelet transforms of the absolute wind speed for the 1977 Spring-Summer-Autumn period have captured four distinct pulses of energy centered around a period of 7 days. This corresponds to the first mode period in the middle of Summer but is up to 50 % too rapid earlier and later in the season. The roughly weekly pulses of wind energy correspond presumably to a peak in the frequency distribution in the regional weather patterns.

Temperature data: In keeping with the vertically integrated wave equation the temperature data at various depths is converted to density and then such properties as the centre of mass and the average density are estimated from the discrete data. The centre of mass calculations are relative to the fluid of minimum density recorded in the time series.

Differences between the centres of mass ζ_m (Fig. 3c) at the three stations (SC-PB and PB-TB) exhibit quite different characteristics. The most apparent observation is that the bulk baroclinic slope is of opposite sign in the two ends of the basin; the centre of mass being highest at the PB station. In addition, the weaker Spring-early Summer stratification leads to markedly greater excursions in the centre of mass.

Discussion

Internal Waves: The lack of coherence between spectra of the depth of the 8°C isotherm at different locations led Wiegand and Carmack (1986) to conclude that they had captured observations of underdamped, free oscillating seiches. This means that observations at any time are an integrated response to *many* previous forcing events. However, a convolution of the baroclinic tilting based on differences in the ζ_m time series' at the stations with the wind speed record yields some coherency. The difference in the centre of mass position between Schroeder Creek and Pilot Bay yields an identifiable peak in the convolution suggesting a phase difference of approximately 2 days. This convolution has other peaks of comparable amplitude approximately 7 days apart; these are related to the cycle in the wind field. This coherence does not exist in the Pilot Bay-Twin Bays data.

Anecdotal evidence reported by Wiegand and Carmack (1986) suggests that storm driven wind events may move up the West Arm and diverge around Pilot Bay moving Northward in the North Arm and Southward in the South Arm. The obvious result from this is that horizontal mode two waves might be forced. These have periods of 3.5 days or greater and are thus much more likely to be forced to their maximum steady state amplitude. Figure 3c clearly shows the opposite sign of $\partial\zeta_m/\partial x$ in the North and South Arms. While this constant difference in sign can possibly be related to variations in local mixing, the transient response shows the slopes change in magnitude by similar amounts but in opposite directions.

Correlation coefficients, ρ, between the the filtered U_4^3 and the difference between ζ_m's at the various stations are shown in Fig. 5abc where each panel is based on a two month segment of data. The response time of the fluid is so slow relative to the wind event duration that there is no correlation between the ζ_m's and $\partial U_4^3/\partial t$. Representative periods of the first modes are 16, 7 and 10 days respectively. At most instances the full basin correlation lies between the coefficients for the two arms. The Spring record (Fig. 5a) has generally lower values of ρ than the two later records. The broad peaks and low values are in part due to the fundamental period changing by a factor of 2 during this time making correlations over useful times difficult to achieve. The SC-PB and PB-TB

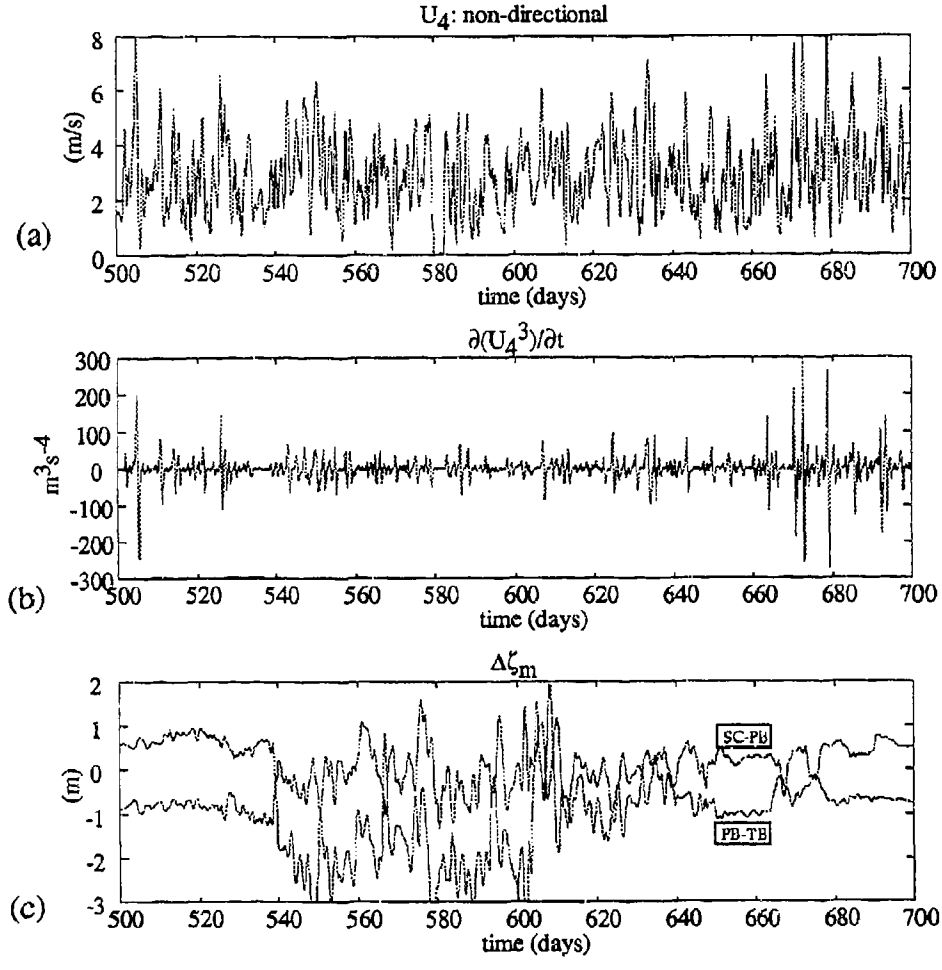


Figure 3. Time series' of (a) Wind Speed U_4, (b) $\partial U_4^3/\partial t$ and (c) differences in ζ_m between the stations. The ζ_m's are measured from the surface down.

having different signs indicating a possible horizontal mode two response although the setup occurs more quickly than basin scale periods indicate. The same-sign correlation at around 9 days is equivalent to the half period of the first horizontal mode.

The mid-Summer record of Fig. 5b is quite different in structure with obvious same-sign correlations at 3.5 and 8 days. The peaks at -7 days could be linked to the regional weather bringing in strong events on a roughly weekly cycle. The PB-TB record has $\rho = 0$ for up to two days before the correlation is apparent whilst the North Arm is tilting downward.

The final (Fig. 5c) late Summer-Autumn record clearly shows the opposing signs of ρ and if this indeed were the setup due to a horizontal mode two wave then we would expect the amplitude to peak at around 3.5 days if the wind were of sufficient duration

(2 days). As indicated by Fig. 4 this is unlikely so Fig. 5c shows the appearance of a partially developed mode two wave. This is followed by a weaker equivalent to that seen in the Summer record with a peak, most obvious in the South Arm, at around 5 days.

Damping: Based on one clear observation from Fig. 5c where, over one cycle of the second horizontal mode, we see the maximum local ρ decrease from 0.14 to 0.03 in the North Arm; a drop of 79%. The South Arm is significantly less dissipative with a decrease of only 45 %. As this quadratically represents the potential energy we may assume that this is equivalent to between 60% and 20% of the potential energy being lost in one wave cycle. Monismith (1985) furthers this avenue by considering the potential energy of a tilted baroclinic structure in a small lake and comparing this to energy lost through typical values of dissipation. He shows that it is possible to lose the potential energy to viscosity in a time comparable to the wave period. If we reverse this argument it is possible to show that a dissipation per unit mass of order of $10^{-9}\mathrm{m}^2\mathrm{s}^{-3}$ is required to provide the measured loss in energy. This is a relatively low value (Imberger and Ivey, 1991). However, observations have shown significant transverse motion introduced by the numerous variations in basin width (the bottom is relatively smooth) and we speculate that a portion of the energy will first be transferred to transverse motions generated by variations in channel width. The enhanced shearing associated with this will lead to higher levels of dissipation through (2).

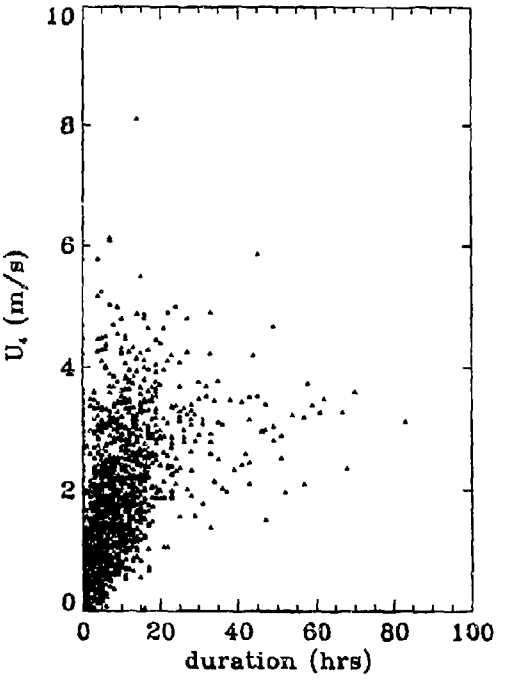


Figure 4; Averaged wind velocity as a function of duration

In this paper we have shown that (i) we can correlate the baroclinic response to the wind, (ii) horizontal mode 2 waves are may be generated and (iii) we can crudely estimate the loss of energy from the basin scale waves. We have demonstrated that integrated properties of the water column prove to be more informative with respect to longitudinal variations than information derived at a single depth. Furthermore, it is the energy applied to the fluid that generates the internal waves, so that comparison between forcing and response is better served by using the wind energy.

Acknowledgements: This work was supported by a Canadian NSERC Fellowship and a Bamfield Marine Station Research Associate Award.

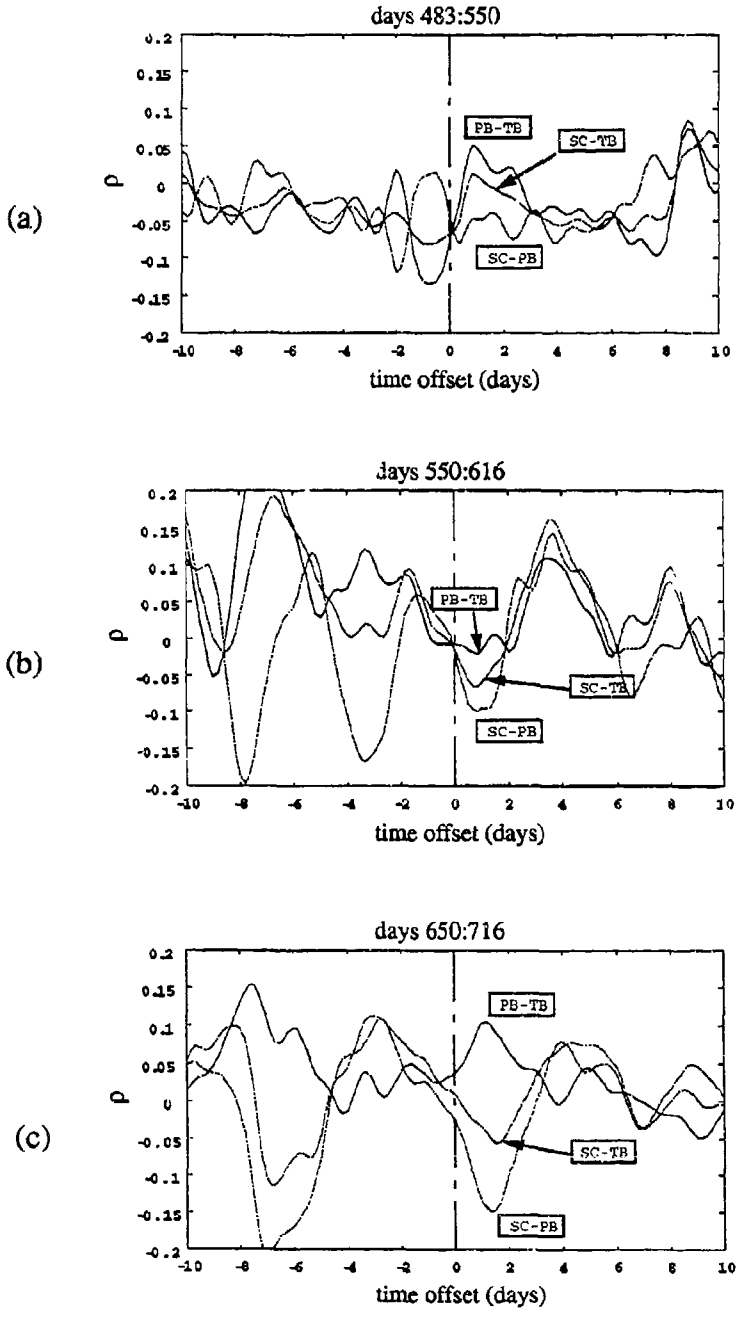


Figure 5: Cross-correlation coefficients between the filtered wind data and the ζ_m differences over 3 periods, each of 66 days duration, in (a) Spring, (b) Summer and (c) Autumn.

References

FARMER, D.M., 1978 Observations of long nonlinear waves in a lake. *J. Phys.Oceanogr.*, Vol. 8, 63-78.

GAO, W. AND B.L. LI, 1993 Wavelet analysis of coherent structures at the Atmosphere-Forest interface. *J. App. Meteor.*, Vol. 32, 1717-1725.

HUTTER, K., 1984 Hydrodynamics of Lakes. CISM no. 286, Springer-Verlag, 341pp.

IMBERGER, J. AND G.N. IVEY, 1991 On the nature of turbulence in a stratified fluid, part II: application to lakes. *J. Phys. Oceanogr.*, **21**, 659-680.

MONISMITH, S.G., 1985 Wind-forced motions in stratified lakes and their effect on mixed layer shear. *Limnol. Oceanogr.*, **30**(4), 771-783.

MORTIMER, C.H. AND W. HORN, 1982 Internal wave dynamics and their implications for plankton biology in the Lake of Zurich. *Vierteljahresschr. Naturforsch. Ges. Zürich*, **127(4)**, 299-318.

MÜNNICH, M., A. WÜEST AND D.M. IMBODEN, 1992 Observations of the second vertical mode of the internal seiche in an alpine lake. *Limnol. Oceanogr.*, **37**(8), 1705-1719.

ROGET, E., G. SALVADÉ, F. ZAMBONI AND J.E. LLEBOT, 1993 Internal waves in a small lake with a thick metalimnion. *Verh. Internat. Verein. Limnol.*, Vol. 25, 91-99.

SPIGEL, R.H. AND J. IMBERGER, 1980 The classification of mixed-layer dynamics in lakes of small to medium size. *J. Phys. Oceanogr.*, **10**, 1104-1121.

STEVENS, C.L., P.F. HAMBLIN, G.A. LAWRENCE AND F. BOYCE, 1993 River-induced Surface Transport in a British-Columbian Fjord-Lake. ASLO, 1993 Annual meeting, Edmonton, Canada.

THORPE, S.A., 1974 Near resonant forcing in a shallow two layered fluid: A model for the internal surge in Loch Ness. *J. Fluid Mech.*, 63, 509-527.

WIEGAND, R.C. AND E.C. CARMACK, 1986 The climatology of internal waves in a deep temperate lake. *J.Geophys.Res*, **91**(C3), 3951-3958.

STRATIFIED FLOW IN A LAGOON

P. PÉCHON, J-M. JANIN and F. LEPEINTRE

Electricité de France, Laboratoire National d'Hydraulique,
6, quai Watier, 78400 Chatou, France

ABSTRACT

The numerical model TELEMAC-3D simulates three-dimensional flows in rivers and in coastal zones. It is used to study for instance mixing of fresh and salted waters, thermal dilution, mixing of pollutant in ambient waters, suspended sediment transport.

The code is described and the simulation of the water flow and the salinity stratification in the lagoon of Berre (Mediterranean Sea) is presented. The numerical results are in good agreement with the available measurements.

1. INTRODUCTION

For about a decade three-dimensional models have been used in practical studies to compute free-surface flows in rivers or in coastal areas for problems related to pollution, thermal dilution or suspended sediment transport.

LNH had a code based on finite difference methods to solve 3D flows (Coëffé et al., 1982). However that code obviously could not include the "user friendly" possibilities allowed by recent developments in finite element methods, e.g. local refining of the mesh, without increasing dramatically the computation cost. Therefore, using the modern numerical techniques, a new model called TELEMAC-3D was developed inside the system TELEMAC which also include models for 2D horizontal flows, wave propagation, sediment transport and water quality processes.

The lagoon of Berre is a rather difficult case both for numerical and physical reasons. For numerical reasons because the simulated duration is quite long, of about height days, and a small numerical inaccuracy can amplify and can strongly affect the final result. The turbulence phenomena is also a difficult point because it is partly due to action of wind and induced waves which sometimes destroys the stratification. However for the tested conditions presented here the wind intensity is moderate and its effect on the mixing of momentum and salinity is not considered.

2. DESCRIPTION OF THE NUMERICAL MODEL TELEMAC-3D

2.1 THE EQUATIONS

The basic equations of the model are the Navier-Stokes equations and the pressure is assumed to be hydrostatic. The code also solves the advection-diffusion of the temperature, the salinity and any other needed variables. It includes physical phenomena which affect the flow and the simulated variables : variation of density, Coriolis force, turbulence mixing, wind stress at the surface, heat exchange with the atmosphere. Variations of the density are taken into account in the momentum equations via the Boussinesq's approximation.

So the equations to be solved are :

$$\frac{\partial u}{\partial t} + u\frac{\partial u}{\partial x} + v\frac{\partial u}{\partial y} + w\frac{\partial u}{\partial z} = -\frac{1}{\rho_o}\frac{\partial p}{\partial x} + \frac{\partial}{\partial x}\left(\nu_H \frac{\partial u}{\partial x}\right) + \frac{\partial}{\partial y}\left(\nu_H \frac{\partial u}{\partial y}\right) + \frac{\partial}{\partial z}\left(\nu_z \frac{\partial u}{\partial z}\right) + F_x$$

$$\frac{\partial v}{\partial t} + u\frac{\partial v}{\partial x} + v\frac{\partial v}{\partial y} + w\frac{\partial v}{\partial z} = -\frac{1}{\rho_o}\frac{\partial p}{\partial y} + \frac{\partial}{\partial x}\left(\nu_H \frac{\partial v}{\partial x}\right) + \frac{\partial}{\partial y}\left(\nu_H \frac{\partial v}{\partial y}\right) + \frac{\partial}{\partial z}\left(\nu_z \frac{\partial v}{\partial z}\right) + F_y$$

$$p = \rho_o g\,(S-z) + g\int_z^S \Delta\rho\; dz$$

$$\frac{\partial u}{\partial x} + \frac{\partial v}{\partial y} + \frac{\partial w}{\partial z} = 0$$

$$\frac{\partial s}{\partial t} + u\frac{\partial s}{\partial x} + v\frac{\partial s}{\partial y} + w\frac{\partial s}{\partial z} = \frac{\partial}{\partial x}\left(\nu_{Hs} \frac{\partial s}{\partial x}\right) + \frac{\partial}{\partial y}\left(\nu_{Hs} \frac{\partial s}{\partial y}\right) + \frac{\partial}{\partial z}\left(\nu_{zs} \frac{\partial s}{\partial z}\right) + Q$$

with

t,x,y,z	time and space coordinates	ν_H, ν_z	eddy viscosity tensor (spherical and anisotropic)
u,v,w	velocity components	κ_{Hs}, κ_{zs}	diffusivity tensor (spherical and anisotropic)
p	pressure	f_u, f_v, f_s	source terms for u, v and s (Coriolis force...).
S	free surface level	g	gravity
ρ_0	density of reference		
$\Delta\rho$	density variation		
s	salinity, temperature or any other variable		

2.2 THE TURBULENCE MODELLING

The turbulence mixing is simulated using an eddy viscosity either constant or computed by a mixing length model or a k-ε model.

In the the application presented here, a mixing length model is used. Since the turbulence is affected by density gradients, the mixing length depends on the Richardson number Ri:

$$Ri = -g\,\frac{1}{\rho}\frac{\partial \rho}{\partial z} \Big/ \left(\left(\frac{\partial u}{\partial z}\right)^2 + \left(\frac{\partial v}{\partial z}\right)^2\right)$$

The vertical viscosity and diffusivity read :

$$\begin{Bmatrix} \nu_z \\ \nu_{sz} \end{Bmatrix} = \begin{Bmatrix} f(Ri) \\ f_s(Ri) \end{Bmatrix} lm^2 \sqrt{\left(\frac{\partial u}{\partial z}\right)^2 + \left(\frac{\partial v}{\partial z}\right)^2}$$

lm : mixing length for constant density

If $z-z_b < 0.2d$ $\quad lm = \kappa\,(z - z_b)$

If $z-z_b \geq 0.2d$ $\quad lm = 0.2\,\kappa\,d$

$\kappa = 0.41$ Karman constant

z_b bottom level

d water depth

f and f_s are damping functions illustrated on figure 1 (derived from Soliva, 1982).

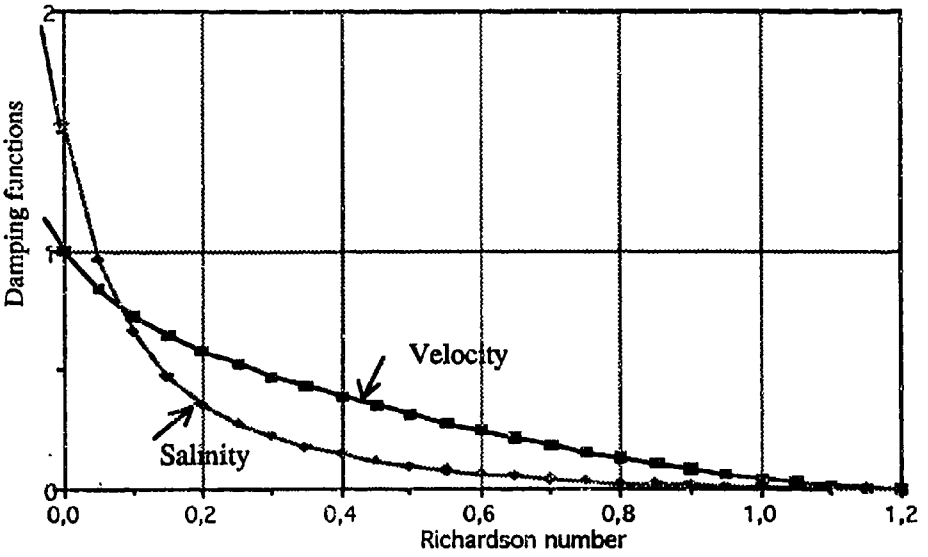


Fig. 1 Damping functions related to Richardson number

2.3 THE NUMERICAL SOLUTION

TELEMAC-3D uses recent developments in finite element techniques (Janin et al., 1992). So it allows local refining of the mesh in parts of interest. The adopted discretization is a finite element discretization in prisms with vertical quadrangular sides. That way the horizontal 2D projection of the mesh is made of triangles and the mesh grid can be derived from a two-dimensional one, easier to generate. Moreover it makes easier the integration of variables over the water depth required in the numerical method. The vertical coordinate of any point of the mesh depends in time on the motion of the free surface.

The equations are solved by means of a decomposition in fractional steps. Each numerical operator can this way be treated by an adequate method :

- The advection step. It is computed by means of a characteristics curve method with the classical change of variable called σ-transformation.

- The diffusion step. The two main points in that step are the computation of the matrices and the resolution of the matrix system. The diffusion and the mass matrices are stored element by element,.except for the diagonal which is assembled. On vectorial computers such a data structure allows the vectorisation of matrix vector product. The derived system is solved by means of a conjugate gradient algorithm, which is well suited to this type of matrix storage because it requires only matrix-vector products.

- The free surface-continuity-pressure step. By integrating the equations along the vertical without the advective and diffusive terms, the classical shallow water equations are obtained. The free surface level is calculated with the two-dimensional model TELEMAC-2D which also takes advantage of E.B.E. methods (Hervouet, 1992). The velocity components are then deduced.

3. STRATIFIED FLOW IN THE LAGOON OF BERRE

The lagoon of Berre is subjected to increasing environmental concern. A research programme is conducted in order to determine strategies of pollutant reduction. This presentation only focus on the modelling of currents and salinity distribution.

The lagoon extends approximately 13 km by 17 km and its depth increases regularly from about 2 m in the North to 9 m in the South. It is connected to the Mediterranean Sea through a channel in the South-West and it receives fresh water from the River Durance in the North (fig. 2).

The domain of computation includes the Gulf of Fos on the Mediterranean Sea in order to simplify the boundary counditions. The horizontal mesh grid has 3426 nodes and the size of the triangles varies from 27 m at the river outlet to 500 m in the Gulf of Fos. The vertical axis is discretized with 12 prisms. So the 3D mesh grid contains 44538 nodes.

The main phenomena which generate water circulations are the wind, the tidal range at the linking with the sea, and the discharge of the River Durance regulated by upstream power stations.

A typical situation was simulated, with a tidal range of 16.0 cm prescribed at the maritime boundary, a discharge of 190 m^3/s at the river outlet and a constant NNW wind of 8.0 m/s. The salinity of the inflowing waters at the maritime boundary was 38 g/l and it was 0 g/l at the river outlet. At the initial time still water was specified with a salinity distribution in the lake of 20 g/l above the level -7.0 m, of 38 g/l under -8.0 m and varying linearly between these two levels. In the Mediterranean Sea, the initial salinity was homogeneous and equal to 38 g/l. The velocity field and the salinity were computed for 16 tidal cycles.

At the latest simulated tidal cycle the flow pattern is stabilized. The current (fig. 3) is mainly driven by wind stress and river discharge whereas tidal movement have a rather local influence in the vicinity of the channel of Caronte.

At the surface the velocity vectors are orientated southwards and the intensities are of about 0.20 m/s. In the lower part of the water body the water flows northwards and the intensities at the top of the first prism (1/15th of the water depth) are of about 0.10 m/s.

The fresh water at the river outlet is driven towards the surface by buoyancy forces. It generates a large plume which extends southwards and goes out of the lagoon through the channel of Caronte (fig. 4). In the lower layer salted water is transfered from the Mediterranean Sea to the lagoon of Berre and a stratification takes place. The salted deepest water located in the center of the domain is advected northwards by currents and reaches the surface in the northern part.

These computed results agree with obrservations on the site (fig. 3). Accurate comparison with measurements are unfortunatly not possible because of lack of extensive data. However the results enable a good understanding of the circulations and are valuable for water quality studies.

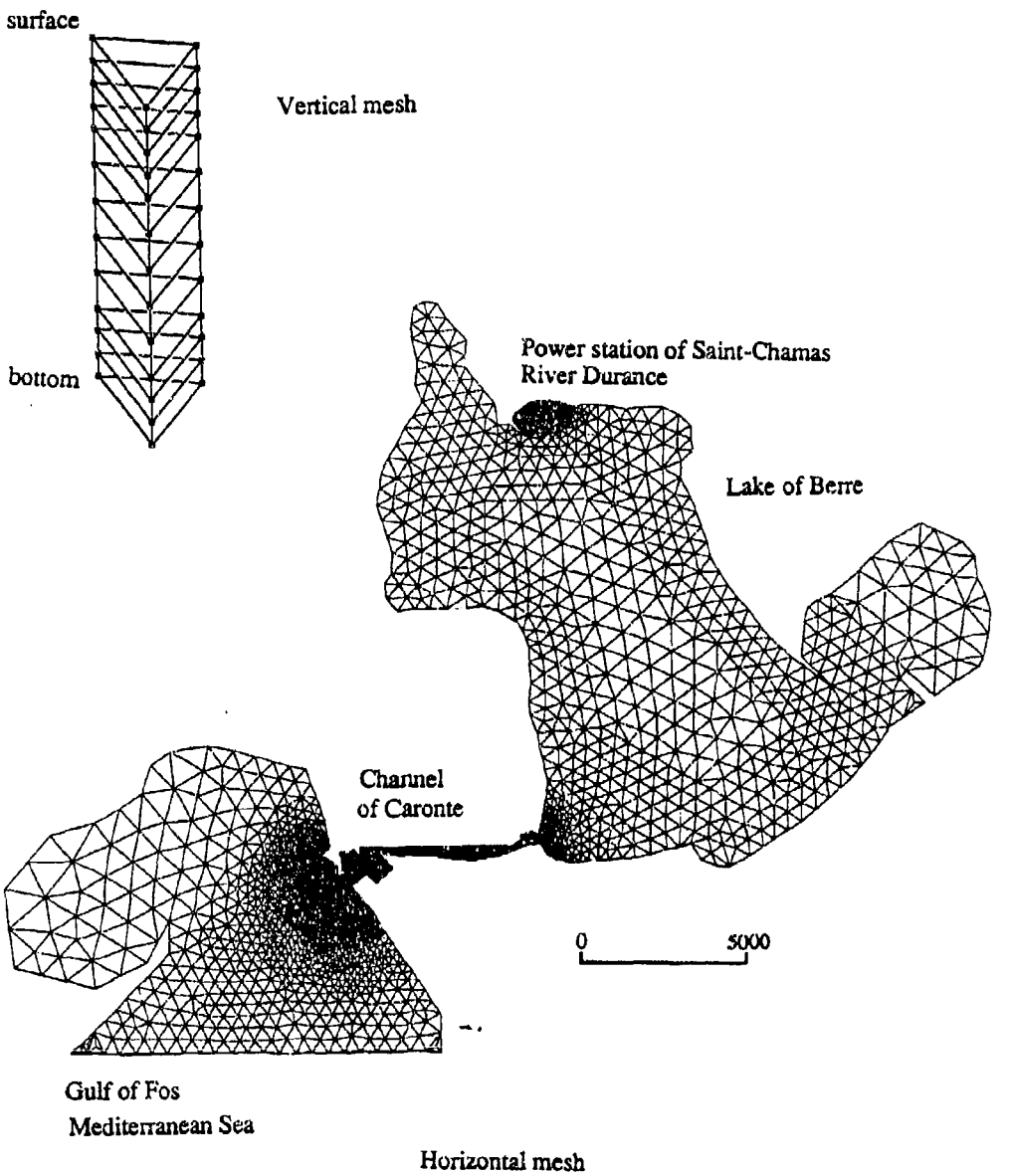


FIG. 2. THE DOMAIN OF COMPUTATION AND THE MESH GRID

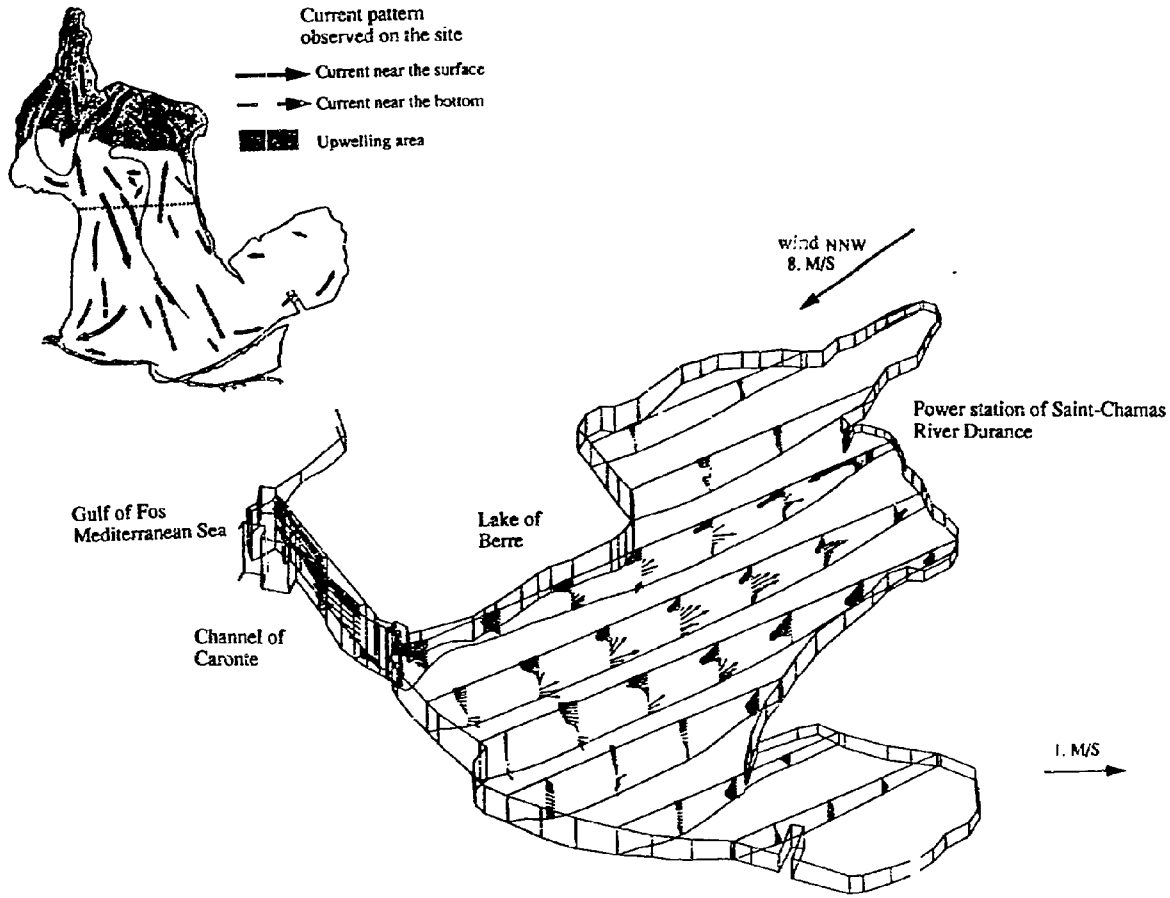


FIG. 3. VELOCITY VECTORS ALONG FEW VERTICAL LINES

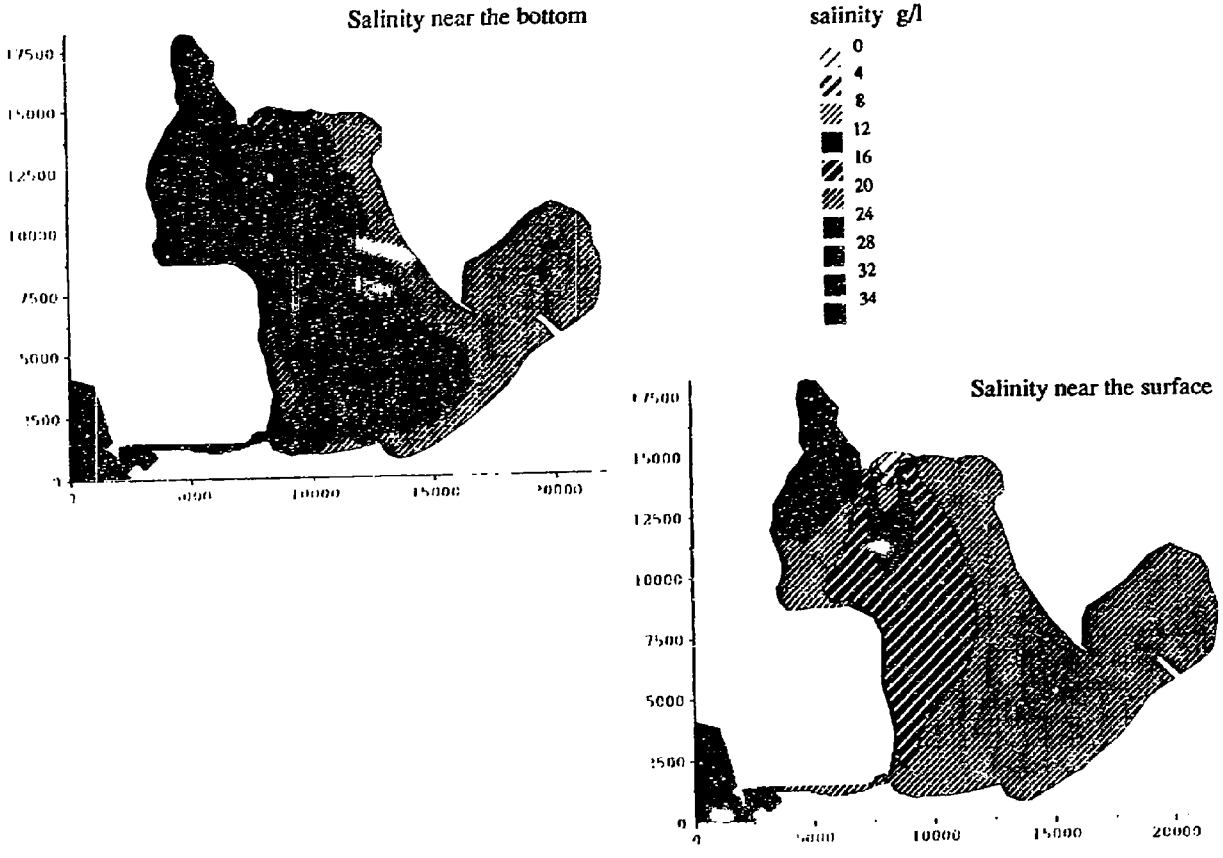


FIG. 4 SALINITY DISTRIBUTION NEAR THE SURFACE AND THE BOTTOM

4. CONLUSION

The progress of the numerical modelling allows engineers to use such tools in a wide range of problems. The accurate solution of the free-surface flow equations in a large domain with a very refined mesh grid in specific areas is now possible with TELEMAC-3D. This is shown here through the case of the stratified flow in the lagoon of Berre

Of course the numerical technics could be improved yet to have more and more efficient tools, but the efforts in the future will focus on the physics. Moreover it will be necessary to couple phenomena in connected domain such as hydrodynamics, sedimentology, biology, chemistry and water quality.

REFERENCES

COEFFE Y., WARLUZEL A. and BURG M.C. - Three-dimensional numerical model for tidal and wind generated flow. International Conference on Coastal Engineering. Cape Town, 1982.

JANIN J-M., LEPEINTRE F. and PECHON Ph. - TELEMAC-3D : a finite element code to 3D free surface flow problems.Computer Modelling of Seas and Coastal Regions. Southampton, April 1992. Report EDF HE-42/92.07

HERVOUET J-M - Element by Element methods for solving shallow water equations with F.E.M. IX International Conference on Computational Methods in Water Resources. Denver, Colorado.USA 9-12 June 1992.

SOLIVA J-C. - Modèle tridimensionel d'écoulements méso-météorologiques. Etude de la convection-diffusion d'un polluant passif à cette échelle. Thèse de l'Ecole Nationale des Ponts et Chaussées. Décembre 1992.

Vertical and horizontal structure of a density current in an small lake

E. Roget and J. Colomer
Institut d'Ecologia Aquatica and Environmetal Department (Physics). Universitat de Girona
E-17071 GIRONA (Spain)

1.- Introduction

The vertical structure of a gravity current induced by thermal differences between the two lobes of a small lake (**figure 1**) and the description of how this current spreads all over the bottom and embodies the bulk water is presented from temperature data. In Roget et al., 1993 it is discussed how the different heating between the two lobes is due to their different mean depth and to the higher underground warm inflow into one of them. Further, also in Roget et al., 1993, it is shown that at the end of Autumn and at the beginning of Winter, because of this gravity current, the water in the northern lobe is renovated about every 5 days (that is, every 5 days there is an overturn of the whole lake).

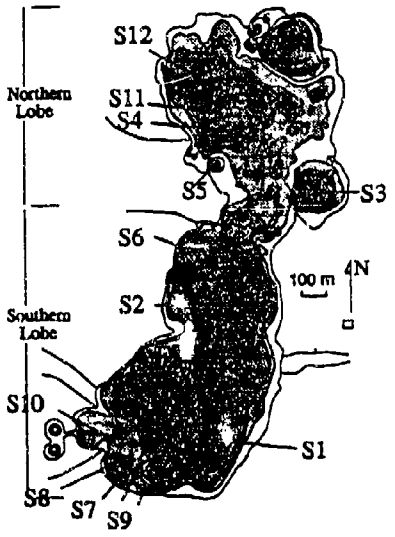


Fig. 1.- Bathymetric map of Lake Banyoles. (S1-S12) indicate underground springs. A, C1, C2, F and E are the locations of the different stations where data from figures 2, 5 and 7 have been recorded.

The effect of the wind over this current is discussed in Roget et al., 1991 and also in Roget et al., 1993, from real data. Summarising, when the wind blows from the south, the increase in pressure in the northern lobe intensifies the bottom gravity current which is already flowing from north to south. On the other hand, if the wind blows from the north so that a surface circulation from north to south appears, a deeper returning flow coming from the south appears and counteracts the bottom baroclinic current. These effects of the wind can also be observed from **figure 2(a)** where the vertical structure of the gravity current has been presented from temperature data measured at station C2 (see f g. 1) at 17, 16, 15, 14 13 and 8 m depth, during the 16th and 17th of Nov. 1991.

First, however, we will briefly comment how in **fig.2(a)** it is observed that the temperatures at 8 and 13 metres depth evolve analogously but this is not the case under 15 metres depth where there is the gravity current. This can be clearly seen, for instance, when after the 8th hour (day 16) and the 32nd hour (day 17) the more superficial layer begins to warm up, but the temperatures at 15, 16 and 17 m keep on decreasing due to colder water which is horizontally advected. So, in this case, it can be assumed that at station C2, the thickness of the bottom current layer is at least 3 metres.

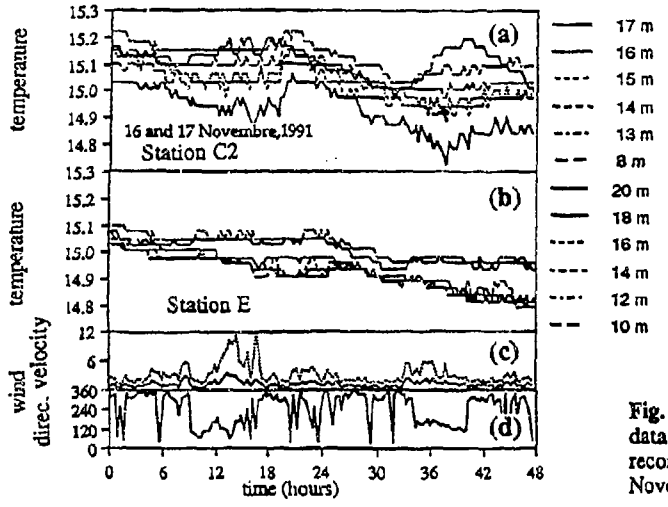


Fig. 2.- Wind and water temperature data at stations C2 and E (see fig.1) recorded during the 16th and the 17th of November 1991.

From fig.2(a) it can also be observed that during the afternoon of either the 16th or the 17th, the temperature of almost all the water column increases. This could be due to convective mixing because of the cooling of the more superficial layer but, if this was the only reason, the fact that this increase in temperature is observed to be higher in the deeper part of the water column could not be explained. However looking at **figures 2(c & d)** it is observed that during this time the wind blows from the north and so it forces a returning current over the bottom flowing to the north which is slightly colder (because it comes from the southern lobe). The interaction of this returning current and the gravity current already present explains the increase in temperature in **fig.2(a)**. In Roget et al., 1993, it is discussed that such events use to happen every afternoon due to the very regular wind pattern in the area during this time. The wind may alter the vertical structure of the current but usually does not stop the gravity current flowing towards the south, although its velocity is observed to decrease.

In **figure 2(b)** the thermal structure of the column at station E (see fig. 1) has also been represented so that differences between station C2 and E can be evaluated. In fig. 2(b) the temperature is represented every two metres because the thermal gradient at this station is smaller than at station C2. However the different thermal tendency between the upper and lower layers is also observed at station E. This is the case in the period between the 34th and the 40th hour (day 28) when up to 16 m the temperature is decreasing while at the upper layer it is not. Also, during the 27th, a different thermal evolution between the superficial and the deeper layer is found. Although the difference in temperature between the current and the rest of the column at station E is smaller than at station C2, the thickness of the current is greater. This fact indicates that this current embodies the quiescent and slighter warmer water immediately above. Then as it flows further south, not only the thickness of the gravity current increases but it flows slower and its temperature is becoming more similar to that of the rest of the water column in the southern lobe.

2.- Methods

In order to illustrate the spatial variability of this gravity current, some temperature data of an intensive campaign were taken under no relevant wind conditions. These temperature data, which are plotted in figures 4, 6 and 8, have been simultaneously recorded by two sensors with a sensivity of 0.05C, 10 consecutive times at an interval of 4 seconds. All the temperature values represented have been obtained at least 9 times out of 10. If this was not the case or if the different case was the last, there are no temperature data in the schemes represented in the

figures which have been mentioned above. However, no data can also mean that the temperature has not been measured.

In order to know the meteorological conditions during the campaign, data from a meteorological Aanderaa station placed at 200 m from the west shore of the lake were available. In **figure 3** the wind pattern during the campaign period is summarised. More precisely, the horizontal line under the x-axis indicates the period when the data presented in the following were taken. In day 6, for instance, measurements were made from 2 p.m. to 5.p.m., when the wind had a mainly southern component, and so it was favouring the baroclinic current. However, in this case, as in the other two cases the wind was very gentle.

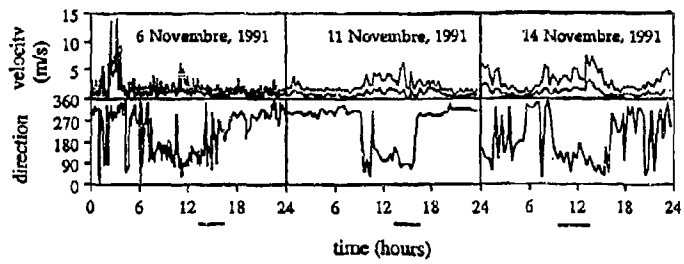


Fig. 3.- Wind conditions during the days that data represented in fig.4, 6 and 8 were recorded. More precisely, the horizontal lines under the x-axis indicates the period when these data were taken.

The location of the stations have been determined by the references of three different points in the shoreline together with an accurate bathymetric map of the lake (Moreno et al., 1989) and a Scubapro PDS depthmetre which has an accuracy of 0.5 m and a resolution of 0.1m.

Further, temperature data presented in this article different from those of figs.4, 6 and 8 have been recorded with Aanderaa TR7 thermistor chains which have an accuracy of 0.05C and a resolution of 0.03 Finally, an Aanderaa currentmeter RCM7 with a temperature sensor included was used. This currentmeter has a velocity threshold of 1.4 cm/s and a resolution of 0.1 cm/s. The characteristics of the temperature sensors are the same as those of the thermistor chains.

3.- Results

In **figures** 4 the different locations where temperature data have been taken during the 6th (**4(a)**), the 11th (**4(b)**) and the 14th (4(c)) of November are indicated. Further, around each location, there is a number of circles. These circles represent the number of times the thermistors resolution -0.05C- can be divided into the difference in temperature between one metre above the bottom at that station and the bulk temperature of the southern lobe (which is warmer). That is, the fact that around the letter D in fig. 4(b) there are 3 circles indicates that, at that location, the temperature of the water one meter above the bottom is 0.15C colder than the characteristic mean temperature of the southern lobe. At the F location, this difference is 0.25C and, at location L, only 0.05C. So, the representation drawn in these figures allows an idea of the space distribution of the gravity current. However for a better understanding of its distributions in the lake, the thermal vertical structure will also be represented for some cases.

From figures 4 and assuming that the number of circles around each station indicates the strength of the current in this location, it can be stated that the gravity current flows mainly along the west shore. However next to the east shore, just over the bottom, there is also water with a temperature corresponding to that of the gravity current. Further, in some locations in the middle of the plain in the bottom of the southern lobe, there is also colder water. This fact seems to indicate that although the current is deflected towards the west shore it is widely spread in the direction where the current is not confined by the shoreline.

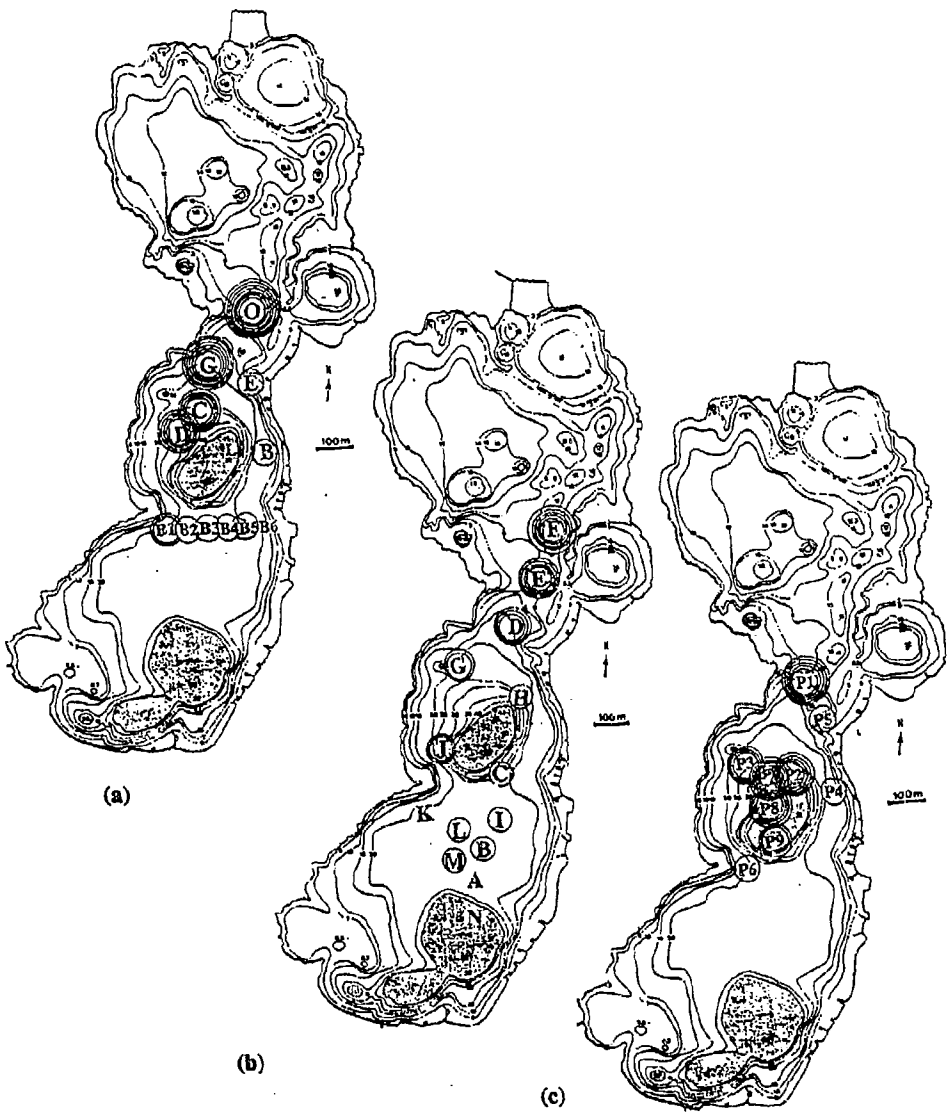


Fig. 4.- Different locations where temperature data have been taken during **(a)**: the 11th of Novembre 1991, from 1 p.m. to 5 p.m.; **(b)**:the 6th of Novembre, from 2 p.m. to 5 p.m.; **(c)**: the 14th of Novembre, from 10 a.m. to 1 p.m.

The existence of this slightly colder water just over the bottom is not due to a boundary layer effect independent of the gravity current. This can be deduced after finding that the temperature variations one meter above the bottom at station F (see fig. 1) is hardly correlated with the temperature variations of the upper layer but with a time shift. In **figure 5** (reproduced from Roget et al., 1993), a shift of about 10 hours can be observed on looking at the relative minima of the temperature data serie recorded at 5 m depth in the northern lobe (station A) and at 19 m depth in the main plain of the southern lobe (station F). From this figure, it is clear that the gravity current flows through station F: the daily variations observed in the temperature series are due to the day and night effect and, because at 14 m depth such variations are not observed, the thermal variations at 19 m depth can only be understood if there is water horizontal

advected from more superficial layers. From the time shift and taking into account the distance between stations A and F is 1300m a mean velocity of approximately 4 cm/s is deduced. This value agrees with current data recorded in the neck between the two lobes which will be presented later.

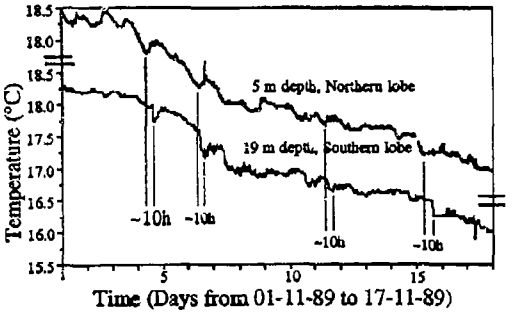


Fig. 5.- Thermal evolution of the lake at 5 m depth in the northern lobe (station A) and at 19 m depth in the southern lobe (station F).

In **figure 6** the isotherms in a vertical plane containing points F, E and D of fig. 4(b) have been drawn. Because stations F, E and D are located in a place where there is a narrow channel in the bottom (see fig. 4(b)), the assumption that the thermal profiles represented in fig.6 characterise the thermal structure of the transversal sections containing those points can be taken. If this is assumed, and considering that from a thermal point of view this current can be considered to be conservative -that is, diffusivity of heat being non relevant if related to entrainment- (Altinakar et al., 1990) the amount of entrained water can be calculated from a heat balance. In this case, from location F to location E it is found that the entrained water into the current is 20% of the current flow, while from E to D it is 70%. Such a high difference should be explained by the fact that the flow regime depends strongly on the bottom slope (Alavian, 1986)

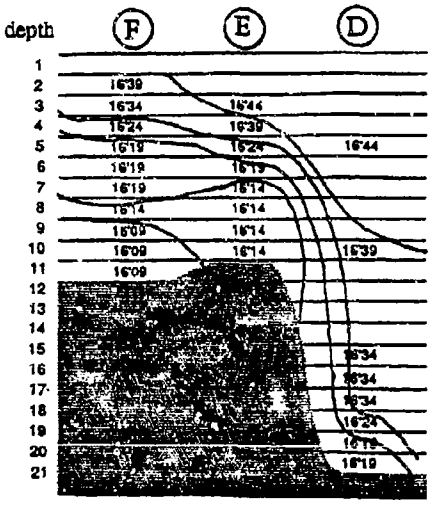


Fig. 6.- Scheme of the isotherms derived from the thermal profiles measured at the locations F, E and D indicated in fig. 4(a).

Considering that from continuity, the downstream divergence in mass flux should be equal to a entrainment constant ($dQ/dx=K_e$), the above percentages of entrained water correspond to $K_e=0.02$ m^2/s and $K_e=0.07$ m^2/s, respectively. These values are between one and two orders of magnitude less than the entrainment constants reported in Hamblin et al., 1978 for a volume flux which is also between 10 and 100 times that of the gravity current in Lake Banyoles.

However, usually, the entrainment is assumed not to be constant but to scale to the entrainment rate, E, in the way that $K_e=Eu$ where u is the velocity of the current along its path (Ellison et al., 1959). Then, if this is considered, the non-dimensional entrainment rate ($E_0=E(A)^{-1/2}$,

where A is the mean transversal area of the current) for the two cases here considered is found to be of 3 10^{-2} and 10^{-1}, respectively. These values are in accordance to the results summarised by Alavian, 1986 (fig. 10) when taken into account that the bulk Richardson number -which accounts the stability of the interface- for the cases considered in fig.6 is $R_i = g'\cos\theta/u^2 \sim 2$ (g' being the reduced gravity acceleration and θ the bottom slope). Also, Hamblin et al., 1987 find entrainment rates of the same order.

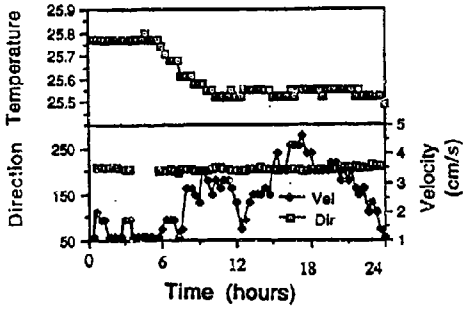


Fig. 7.- Characteristics of the current measured at stations C1 during the 6th of November, when data presented in the previous figure were taken.

The characteristics of the current measured at 1 metre above the bottom at location C1 (see fig. 1), during the day that data represented in fig. 6 were taken, are repre ted in **figure 7**. After 7 a. m. the current velocity, although very small, begins to increase t m/s coinciding with the rise of a wind with southern component (see fig.3). Later on, at about 11 p.m. a sporadic wind with a northern component causes the velocity to decrease again, but, very soon, the southern wind reappears and the current velocity increases up to 4 cm/s. In any case, however, the current is flowing south and has a direction of around 210 degrees which corresponds mainly with the direction of the bottom channel. This fact makes relevant that the morphometry of the bottom strongly influences the path of the current.

For the case of this gravity current and despite the small dimensions of the lake, the Rossby number is evaluated to range between 0.1 and 1. Further, assuming that the Coriolis force should compensate the centrifugal force, a radius of the orbit between 100 and 1000 m should be expected (Roget, 1992). These values may allow the Coriolis force to be relevant in addition to the confining effect of the bottom morphometry. Hamblin and Carmarck (1978) reach similar conclusions for the case of the incoming Thomson river in the Kamloops Lake (British Columbia,EUA). Alavian et al., (1992) refer to this case as an example of the importance of the Coriolis effect in large lakes (Kamloops Lake is 25 Km large and 2.1 Km narrow) however, looking at the magnitudes related to river Thomson it is found that its characteristic dimensions are of the same order of magnitude than those of the gravity current in the Lake Banyoles (Roget, 1992). That is: river Thomson enters the lake in an area of about 1200 m wide, has mean velocities of about 10 cm/s and flows towards its right so that after about 1500 m it reaches the shoreline. So, beside the effect of the bottom morphometry, the Coriolis effect may not be neglected in advance, although its importance is not demonstrate.

In **figure 8(a)** an schematic analogous to that of fig.6 is drawn from the thermal profiles measured at locations O, G and E of fig.4(a). Once more it can be observed that the gravity current deflects towards its right hand. For this case, values of K_e and E_o are respectively of 0.01 m^2/s and 0.01. These values have been calculated by linear interpolation in space between temperature data recorded at 0, G and E.

Another isotherm scheme, now of a transversal area located further south, is represented in **figure 8(b)**. In this case, at stations J and G, which are nearer the west shore (see fig.4(b)) the baroclinic current is observed at least from 15 m depth to the bottom which, at those locations, coincides with the main plain of the southern lobe (see fig.4(b)). At stations H and C, located nearer the eastern shore in an area deeper than the main plain of the southern lobe,

the current is also found over a warmer layer of 16.49C. The existence of this layer is due the underground water flowing into the source S2 (see fig.1 and fig.4(b)) which is located in this zone (Casamitjana and Roget, 1993). The fact that at location H the colder water is slightly warmer than the colder water at C should be explained if it is assumed that the underground water mixes with that of the gravity current and it is displaced towards the south. This will also accelerate the renovation time of the water in the hole where source S2 is located.

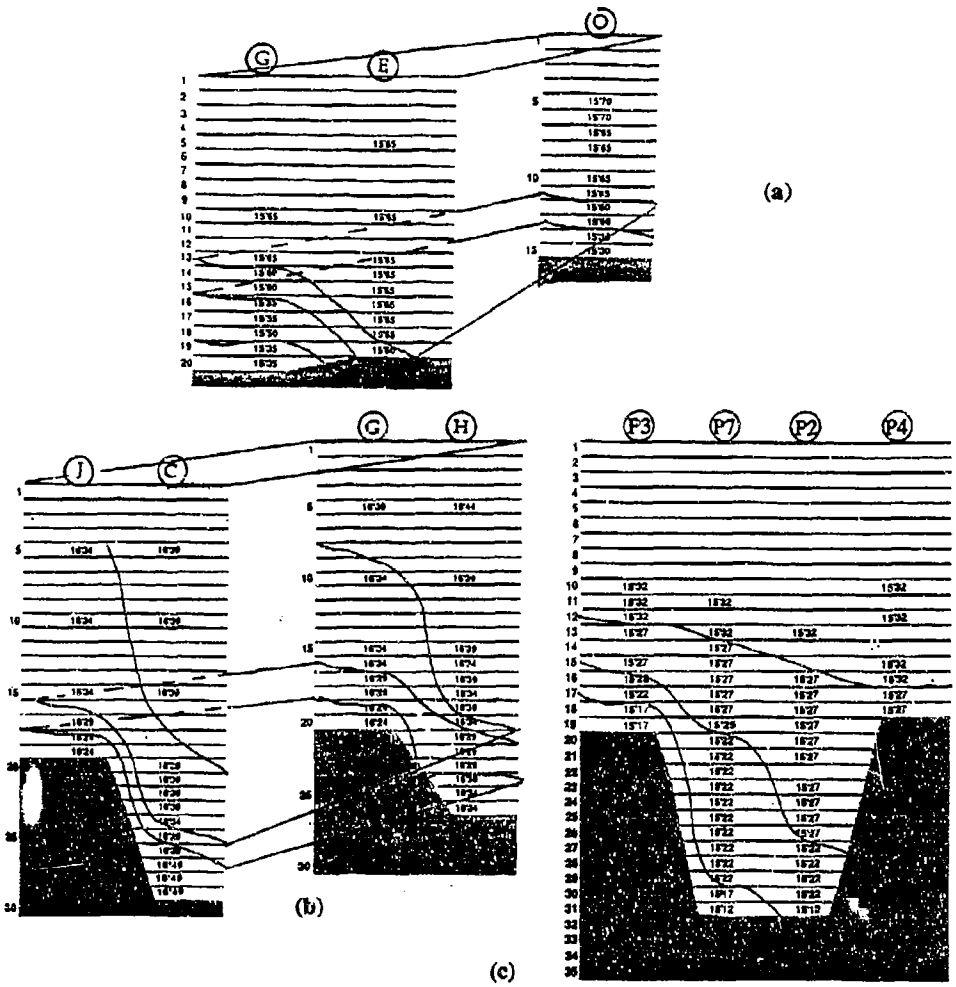


Fig. 8.- Representations, analogous to that of fig.6, of the thermal profiles at different locations indicated in (a): fig.4(a); (b): fig.4(b); (c): fig.4(c).

From **fig.8(b)** it is also observed that from 20 m up, the water column in J is colder than in C. This feature is found very often independent of the time of the day, that is, independent of the sun elevation and it should be explained either by penetrative convection (at this time of the year the mean daily surface heat flux is of about -100 W/m^2 and during day keeps often under negative values (Colomer et al., 1991)) or by wind stirring (Fischer et al., 1979). The fact that vertical mixing is only observed from temperature data along the west coast is due to the non simetric path of the density current: near the western shore the density current is strong enough

to affect the temperature of the whole column of water when it is mixed but near the eastern shore it is not.

The presence of the baroclinic current in the hole of source S2 can also be observed from **figure 8**(c) (see also fig. 4(c)). Data represented in this figure have been collected 8 days later than those in fig.8(b) , and then the warmer layer under the current is not observed anymore. In fig.8(c), as in fig.8(b), the fact that the baroclinic current is more important along the western shore than to the eastern is also observed. Further, from the inclination of the isotherms, a transverse advection from west to east can be deduced, if it is not counteracted by other factors.

4.- Conclusions

- Entrainment constants of order 10^{-2} m^2/s corresponding to volume fluxes of about 10 m^3/s and non-dimensional entrainment rates of order 10^{-2} have been found for a gravity current continuously fed by density differences due to differential heating (Ri~2).
- The slope of the bottom is found to greatly affect the entrainment so that a variation of the slope from 0 to 3% implies that the entrained water into the current varies from 20% to 70% of the current flow.
- The current is deflected towards its right-hand (being confined along the western shoreline) but it widely spreads in the opposite direction so that, although mean gradients of up to 2 10^{-4} degrees/m are found in the transverse area of the current, the gravity current can still be identified along the east coast from temperature data.
- The deflection of the current is obviously due to the effect of the bottom morphometry but Coriolis effect may not be neglected in advance, although its importance has not been demonstrate.
- As the density current is not homogenously distributed along the transverse area of the lake, vertical mixing will create horizontal gradients in the upper part of the water column and so transversal transport should be expected at any depth.
- The wind not only affects the distribution in the space of the current but it also modifies its vertical structure.

5.- References

Alavian, A., 1986. Behabiour of density currents on an incline. J. Hydr. Eng., 112/1:27-42.

Alavian, V., Jirka, G.H., Denton, R.A., Johnson, M.C. and H.G. Stefan, 1992. Density currents entering lakes and reservoirs. J. Hydr. Res., 118/11:1464-1489.

Altinakar, S., Graf, W.H. and E ` Hopfinger, 1990. Weakly depositing turbidity current on a small slope. J. Hydr. Res., 28/1:55-80.

Casamitjana, X. and E. Roget, 1993. Resuspension of sediment by focused groundwater in Lake Banyoles. Limnol. Oceanogr., 38/3: 643-656.

Colomer, J., and X. Casamitjana, 1991. Estimated heat fluxes at the interface of Lake Banyoles. VI AEL Congress. University of Granada. Spain.

Ellison, T.H., and J.S. Turner, 1959. Turbulent entrainment in stratified flows. J. Fluid Mech., 6, 423-448, 1959.

Fischer, H.B., List, E.J., Koh, R.C.Y., Imberger, J. and N.H. Brooks, 1979. Mixind in inland and coastal waters. Academic Press.483 p.

Hamblin,P.F., and Carmack, E.C., 1978. River-induced currents in a fjord lake. J. Geophys. Res., 83/C2:885-899.

Moreno et al., 1989. A new bathymetric map based on echosondation and morphometrical characterization of the Lake of Banyoles. Hydrobiologia, 185:83-90.

Roget, E., 1992. Internal seiches and baroclinic currents in Lake Bayoles. Ph.D.Dissertation. Autonomous Univ. of Barcelona. Bellaterra, Spain.

Roget, E. and J. Colomer, 1991. XXIV IAHR Congress proceedings (A), Madrid.

Roget, E., Colomer, J., Casamitjana, X. and J.E. Llebot, 1993. Bottom currents induced by baroclinic forcing ı Lake Banyoles (Spain). Aquatic Sciences, 55/3:1015-1621.

CONCLUSION

Turbulence and Mixing at Density Interfaces

H.J.S. Fernando
Environmental Fluid Dynamics Program
Department of Mechanical & Aerospace Engineering
Arizona State University, Tempe, AZ 85287-6106

Abstract

Density interfaces that coexist with contiguous turbulent layers are ubiquitous in nature, and turbulent mixing across them plays a major role in the dynamics of environmental flows. In nature, density interfaces are formed by the buoyancy forcing on turbulent fluids and they can be destroyed by turbulence itself when such forcing is absent. Mass and momentum transfer across stratified interfaces are much weaker, and often they control heat and mass balances in the atmosphere and oceans; here the rate limiting step is the rate of mixing across interfaces. In this paper, a brief review of turbulence and mixing in density stratified fluids is presented, paying particular attention to interfacial mixing. Some new results pertinent to turbulence and mixing in stratified fluids are also presented.

1. Introduction

Density stratification and turbulence are ubiquitous features in natural environments. Furthermore, they often exist together. Turbulent flows, while difficult to predict for homogeneous incompressible fluids, are vastly more complicated in the presence of stratification. Nevertheless, they must be dealt with in geophysical and industrial flow modeling. As a result, there is a continued interest in understanding and modeling of the interaction between stratification and turbulence. Some common examples of naturally occurring stratified turbulent flows are (i) the upper ocean mixed layer, which is located above the thermocline and driven by the wind stress (the atmospheric counterpart is the planetary boundary layer topped by the inversion layer), (ii) turbulence in the main oceanic thermocline, which is believed to be caused by mechanisms such as Kelvin Helmholtz instabilities, internal-wave breaking or critical-layer absorption, (iii) oceanic boundary turbulence induced by the tides or the reflection of internal/inertial waves at the continental margins, and (iv) the oceanic benthic boundary layer. These turbulent flows play a pivotal role in navigation, human and other biological activities, pollutant and nutrient distribution in the ocean, long-range aerosol and other green house-gas transport in the atmosphere and the evolution of climate systems.

One of the important practical applications of small-scale mixing parameterizations of stratified turbulent flows is the development of atmospheric and oceanic general circulation models (GCM's), including atmosphere-ocean coupling. State of the art oceanic GCM's have a resolution of a few tens of kilometers; scales that are smaller than this, which include turbulence, need to be parameterized properly based on the dynamics of stratified turbulence. Currently, to obtain realistic predictions, oceanic GCM's employ an eddy diffusivity of the order 1 cm^2s^{-1} (Bryan 1987) but the measurements of the microstructure community indicate a value of the order 0.1 cm^2s^{-1} (Ledwell 1994); the reason for this discrepancy is a subject that is in the heart of oceanic microstructure research. In current weather forecasting models (e.g., the European Center for Medium Range Weather Forecasting, ECMWF), the vertical resolution is of the order of a few hundred meters, and the mixing at the inversion layer is parameterized by assuming a uniform entrainment rate across the interface, irrespective of the local conditions (their earlier

models did not consider entrainment, and performed poorly!). Perhaps, an improved parameterization based on governing variables may improve the predictive capabilities.

This paper reviews some salient developments in stratified turbulence research, paying particular attention to interfacial phenomena such as mixing across density interfaces. Some new results pertinent to stratified turbulent flows will also be presented. Section 2 is devoted to the fundamentals of stratified turbulence and Section 3 deals with mixing across shear-free density interfaces. Sheared density interfaces are discussed in Section 4.

2. Turbulence in Stratified Fluids

Perhaps due to the difficulty of the subject matter, the number of studies reported in the open literature on the dynamics of stratified turbulent flows is much less than that for classical engineering turbulent flows. A key feature of stratified turbulence is the suppression of vertical diffusion beyond a limiting vertical length scale, at which buoyancy effects become important (Richardson 1920; Pearson et al. 1983). Beyond this scale, different scales of the flow evolve differently (Riley et al. 1981; Lienhard & Van Atta 1990; Holt et al. 1992). In the early days of turbulence research, the effects of stratification on turbulent motions have been studied by meteorologists such as Richardson (1920) and Taylor (1931), who also identified the key non-dimensional parameter, now known as the Richardson number, that governs stratified turbulence. Interest in this subject was renewed in the 1960's with the identification of a vertical length scale, beyond which the turbulent diffusion is inhibited; this scale was independently derived by Dougherty (1961) and Ozmidov (1965), in the atmospheric and oceanic context, respectively, as $L_R = (\varepsilon/N^3)^{1/2}$, where ε is the rate of dissipation of turbulent kinetic energy (TKE) and N is the background buoyancy frequency. With the rapid improvement of measurement techniques for turbulence, the necessity of presenting oceanic and atmospheric data on a solid theoretical framework was realized. To this end, Gibson (1980) proposed a theory based on scaling arguments to explain the evolution of oceanic turbulence; somewhat similar concepts were advanced earlier by Long (1978) in the context of turbulence in stratified fluids. Gibson (1980) assumed that oceanic turbulence is sporadically generated by powerful events (Caldwell (1983) referred to this as the Big-Bang hypothesis) as turbulent patches, which grow by entraining fluid from the surroundings. The total energy within the patch was assumed to be constant; from this assumption, the r.m.s. vertical velocity w was calculated. During the growth of the patches, the vertical inertial forces of the eddies w^2/L, where L is the integral length scale and w is the r.m.s vertical velocity of turbulence, decrease and the buoyancy forces against which the eddies must overturn N^2L increase. Since the patch cannot grow beyond a scale which is determined by a balance between these two forces, the limiting vertical lengthscale should be given by $L_b = w/N$. Thus the stratification begins to play a key role when the turbulent Froude number $Fr_t = u/NL$ is of order one, where u (~ w) is the r.m.s. horizontal velocity (Ivey & Imberger 1991; Taylor 1992). Assuming high Reynolds-number turbulence within the patch, which yields $\varepsilon = w^3/L$, L_b at this limiting height can be evaluated as $L_b \sim L_R = (\varepsilon/N^3)^{1/2}$, where L_R and L_b are called Ozmidov and buoyancy lengthscales, respectively. Thus, if the size of the turbulent patch is L_p (~ L), then, during the initial growth, $L_p << L_R$ or L_b, but as the turbulence evolves and buoyancy effects set in, all three length scales become of the same order.

Three more length scales are often used; they are the overturning length scale, defined as $L_O = b/N^2$, where b is the r.m.s. buoyancy fluctuation of turbulence, the Thorpe length scale L_T and the maximum Thorpe displacement L_{Tm}. The former was introduced by Ellison (1962), and was later modified by Stillinger et al. (1983) and Gargett et al. (1984) (so in some cases a numerical factor is used in front of it). The latter was introduced by Thorpe (1977) to facilitate the interpretation of oceanic microstructure data, which often consist of a single vertical cut of

temperature/salinity through the ocean. If turbulence is present (this is sometimes wrongfully inferred by the presence of inversions in the vertical profile), the individual density values of the profile are rearranged to obtain a stable density profile; the displacements required are called Thorpe displacements d_i, and both the maximum (L_{Tm}) and the r.m.s (L_T) values of d_i's are used as measures (Dillon 1982, 1984).

Using a laboratory experiment, Fernando (1988) investigated the growth of a continuously forced turbulent patch in a stratified fluid. It was found that the growth of the patch is inhibited at a critical vertical thickness after a time of $Nt_c \approx 4$. Thereafter, the formation of a strong density gradient layer, at the edges of the patch, which supported a field of internal gravity waves forced by the patch turbulence, was observed. Later studies (DeSilva & Fernando 1992) indicated that the destruction of the stratification within the patch is relatively slow, and is completed only after a time of the order $Nt \sim 100$; thereafter, the patch grows slowly (beyond the Ozmidov scale) due to the breaking of waves in the gradient layer at the edges.

Gibson (1980-1993), in a series of papers, extended the big-bang idea to interpret oceanic microstructure. His theory appears to be sound in a fluid dynamical sense, but its applicability to the ocean has been repeatedly questioned by the microstructure community. The theory assumes that, after the patch grows to L_R, eddies of the size of the integral scale cannot overturn against the stratification; turbulence is now said to be fossilized (following its first usage by Woods (1969)). The term "fossil turbulence" has also been used by Nasmyth (1970) to describe the temperature microstructure field that is left behind after the decay of oceanic turbulence, but the necessity of velocity fluctuations for the existence of temperature fluctuations is recognized in Gibson's theory. Eddies of size smaller than the integral scale can overturn and mix the fluid within the patches, with the largest overturn being of the order L_R. When L_R becomes of the same order as the Kolmogorov length scale L_K, the turbulence ceases to exist, and the flow is said to be completely fossilized; it was shown that this occurs when the parameter $G = \varepsilon/\nu N^2$, where ν is the kinematic viscosity, falls below a critical value G_{cr}. More precisely, Gibson's theory predicts that the scales larger than $1.2L_R$ are non turbulent, and the scales $1.2\,L_R > \ell > 15L_K$, are actively mixing. When $1.2\,L_R \approx 15\,L_K$, the turbulence is completely fossilized at all scales. Laboratory experiments show that G_{cr} can vary from about 8 to 25, with Gibson's (1980) prediction being 30. Further, this theory predicted the spectra for velocity and microstructure fields, based on the evolution of a single patch.

In oceanic measurements, only a single cut through a turbulent patch is possible and obtaining information on the state of the patch is an onerous task. Fossil turbulence theory assumes that the maximum Thorpe scale L_{Tm} represents the size of a growing patch, and if the patch is in the fossilization stage, L_{Tm} is a measure of the patch size at the onset of fossilization (i.e., maximum Thorpe scale does not collapse or change for long times). If so, the rate of dissipation at the onset of fossilization ε_o can be calculated using the measured L_{Tm} at any time as $\varepsilon_o \sim N^3 L_{Tm}^2$; if the dissipation at this time is ε, the state of the patch can be prescribed using the "turbulence activity parameter" $A = (\varepsilon/\varepsilon_o)^{1/2}$. By invoking experimental constants, A can also be written as $\varepsilon_o = 13DCoN^2 = 16.5\,N^3 L_T^2$, where D is the molecular diffusivity and Co is the Cox number. Based on such estimates, which can conveniently be depicted on so-called hydrodynamic phase diagrams, Gibson (1987, 1991) concluded that the oceanic microstructure is heavily undersampled, and at the time of the observations, most of the patches are in a fossilized state.

To investigate some of the modeling outlined above, a series of laboratory experiments was carried out at Arizona State University to study the evolution of stratified turbulence. The

experiments were performed in a 12.2m x 0.4m x 0.3m towing tank, with salt stratification. The towed bodies included monoplanar grids, spheres and cylinders; turbulence within the wakes of these bodies was investigated to identify the properties of stratified turbulence. Some salient results of these studies are summarized below.

Figure 1 shows the dispersion of a blob of passive scalar that was released in the wake of a grid; note the initial spreading of the blob in all directions, as in a homogeneous fluid, but its growth is arrested at a time $2 < Nt < 13$ (exactly at $Nt \sim 4$), whence the formation of a layered structure signified by horizontal intrusive motions can be seen. Particle-tracking velocimetry clearly indicated initial three-dimensional (3-D) motions and the formation of 2-D striations in the far wake representing the final stage of turbulence decay (Pearson & Linden 1983). Figure 2 shows a lengthscale diagram constructed using the measurements in a stratified cylinder wake; the scales were selected in concurrence with Gibson's model. Note the initial decay of L_R, the gradual growth of L_K, the onset of buoyancy effects when $1.2\,L_R \approx L_{Tm}$ at $Nt \sim 1.5$, and the complete fossilization when $1.2L_R \approx 15L_K$ at $Nt \sim 6$. The results clearly show that, if there is no external energy source, turbulence in stratified fluids is short lived and decays rapidly leaving behind internal wave motions; the persistence of L_b beyond $15L_K \approx 1.2\,L_R$ illustrates that, although turbulence is absent, internal wave motions can persist in the far wake (Figure 3).

Another important aspect is the decay of the Thorpe scale and the maximum Thorpe displacement; see Figure 4 pertinent to the wakes of spheres. For this case, L_T (and also L_{Tm}) cannot remain constant, and it decays because of the settling of heavy fluid elements that were displaced during the active phase of turbulence. When settling to their equilibrium positions, these particles tend to migrate under the inertia-viscous balance, while being affected by the molecular diffusion and exchanges with the environment. Sometimes, these settling motions can become turbulent, and the resulting flow is called "zombie turbulence." Gerz & Yamazaki (1993) argued that the migratory motion of buoyant particles, after the decay of turbulence, should be characterized by the stratification number $St = (L_{bo}/b'_o)/(db_R/dz)$, where b'_o and L_{bo} are the initial r.m.s. buoyancy fluctuation and the integral temperature lengthscale, respectively, and db_R/dz represents the background stratification. Turbulent motions are said to be initiated when $St < 1$, although one might expect that they should also be dependent on the molecular-diffusive parameters. In all, it appears that L_{Tm} may not be a good indicator of stratified turbulence at the onset of fossilization. According to C.H. Gibson (private communication), the relaxation time of L_{Tm} can be a function of the Reynolds number and in high Reynolds-number oceanic environments L_{Tm} may persist for long times; this assertion remains to be tested.

As mentioned, the microstructure community has taken a different view on oceanic turbulence. They assume that oceanic turbulence is more persistent than what Gibson's theory predicts (Caldwell (1983) refers to this as the "Continuous Creation" view point). The isolated turbulent regions in the ocean are thought to be in equilibrium with the "environmental" energy sources such as mean velocity shear (Dillon 1982; Caldwell 1983; Crawford 1986; Dillon et al. 1989) or the near-inertial wave shear (Gregg 1984, 1987), thus maintaining active turbulence; for example, an isolated patch that is in an active state has been recently detected by Hebert et al. (1992) during measurements in the Pacific Equatorial Undercurrent. Dillon (1982) reported that oceanic patches obey the empirical relationship $L_R = 0.8L_T$, except when they are in the surface mixed layer (according to Taylor (1992), this corresponds to $Fr_t = 0.86$). Gibson (1991) interpreted these patches as fossils, although others have argued to the contrary. Crawford (1986) and Imberger & Ivey (1991) have also reported cases for which the above correlation was satisfied. According to DeSilva & Fernando (1992), such a correlation is valid only when the patches are well mixed due to sustained agitation.

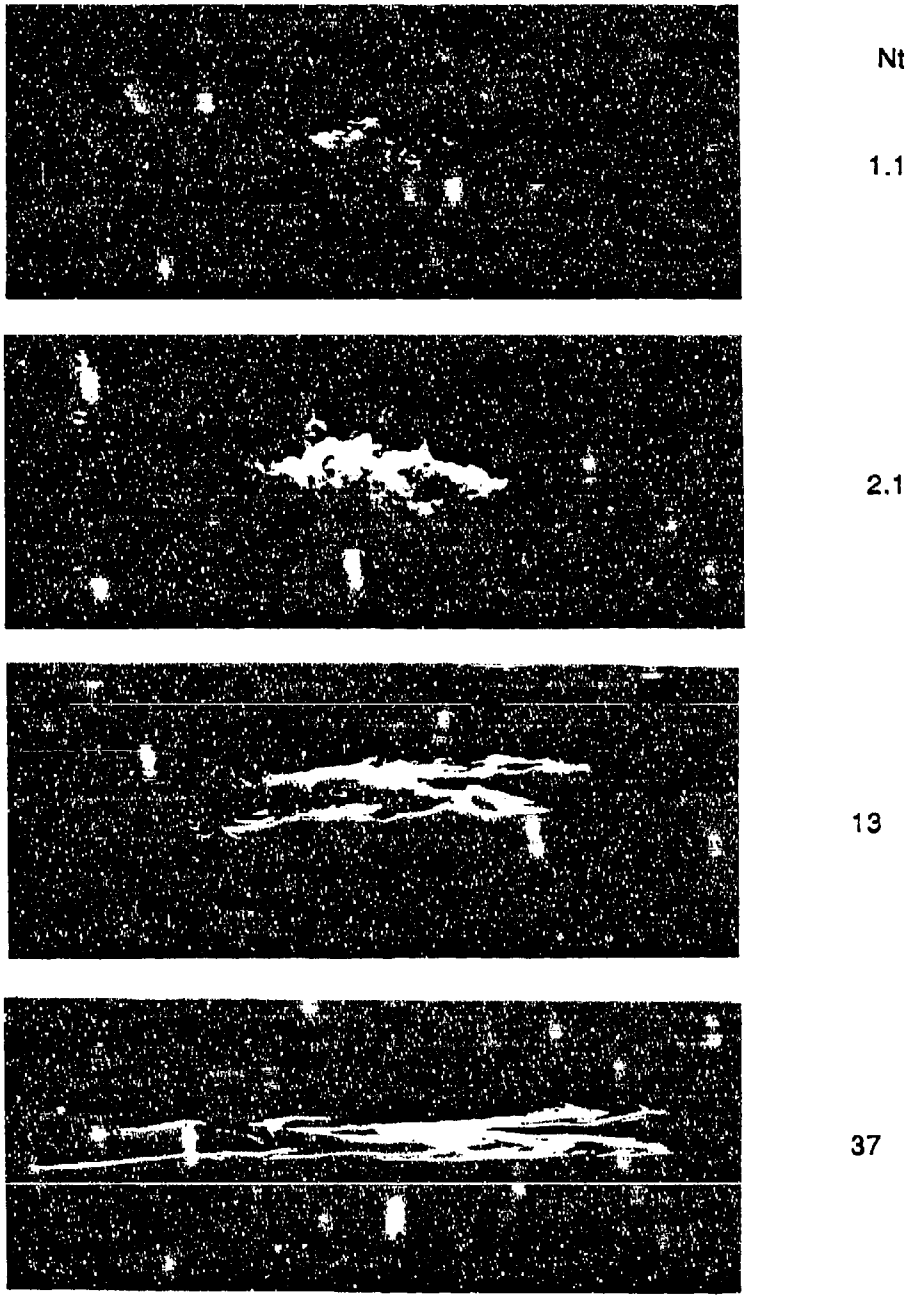


Figure 1. The dispersion of a passive scalar (a blob of dye) in the turbulent wake of a grid towed in a stratified fluid (grid speed U = 29 cm/s, N= 1.15 rad/s and mesh size M = 4.7 cm). The blob was injected horizontally with a very slow speed.

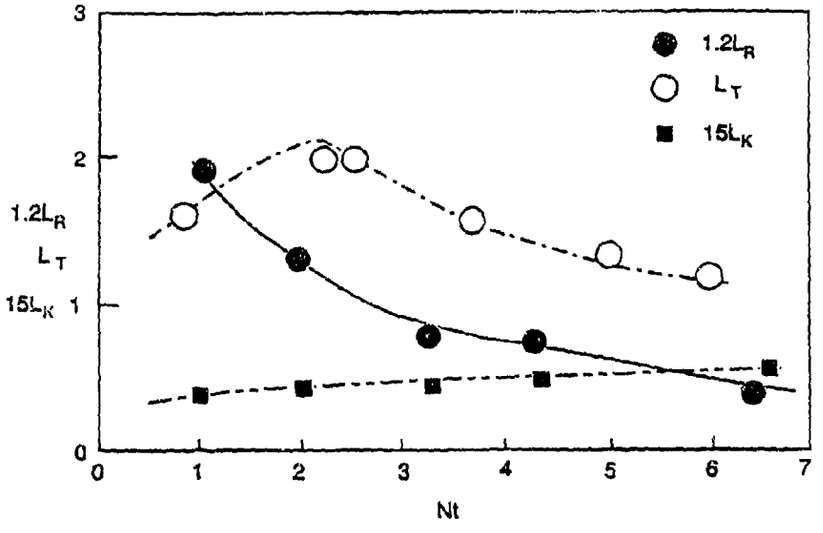


Figure 2: The evolution of Ozmidov (L_R), Kolmogorov (L_K) and Thorpe (L_T) scales in a stratified cylinder wake. The measurements were made at different downstream distances, which could be converted to non-dimensional evolution times Nt (Xu, 1994). The Reynolds and Froude numbers based on cylinder diameter are 4600 and 4.6, respectively.

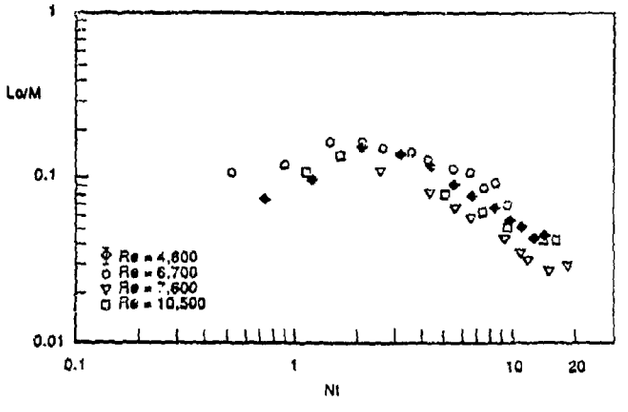


Figure 3: The evolution of the overturning lengthscale (normalized by the mesh size M) with the non-dimensional time in the wake behind a towed grid in a stratified fluid. The Reynolds number is defined as Re = UM/ν, where U is the tow velocity.

Vertical diffusion of fluid particles that are released from a steady source in a stably stratified fluid is also of interest (Csanady 1964). If the stratification is absent and the turbulence is homogeneous, then the particles will disperse according to the theory of Taylor (1921); i.e., the mean square displacement $\overline{\xi^2}$ after a time t from the release is given by (Pearson et al. 1983)

$$\overline{\xi^2} \sim 2\overline{W^2}\left[T_L t - \int_0^t \tau R_w(\tau)\,d\tau\right], \tag{1}$$

where $\left[T_L = \int_0^\infty R_w(\tau)\,d\tau\right]$ is the Lagrangian integral timescale, $\overline{W^2} = w^2$ is the mean square velocity and $R_W(\tau) = \overline{W(t)W(t+\tau)}$ is the Lagrangian autocorrelation function. As $t \to \infty$ and $T_L \neq 0$, (1) becomes $\overline{\xi^2} \sim \overline{W^2} T_L t$, as if it is governed by the diffusion equation with diffusivity $w^2 T_L$; for short time intervals, $\overline{\xi^2} \sim \left(\overline{w^2}\right)t^2$, and the r.m.s. displacement is expected to grow linearly with time. For stratified turbulence, (1) is valid only for short time periods, before the stable stratification comes into play. Figure 5 shows the r.m.s. particle displacement behind a towed grid, measured by tracking the displacement of neutrally buoyant particles. The r.m.s. displacement appears to follow $(\overline{\xi^2})^{1/2} \sim t$, until $Nt \sim 0(1)$, and then levels off because of the suppression of turbulence by the stratification.

Not many studies have been devoted to investigate the role of molecular-diffusive effects in stratified turbulent mixing. Previous wind and water tunnel experiments as well as direct numerical simulations show that such effects, signified by the Prandtl number Pr (or, more generally, Schmidt number Sc), play a role in the evolution of stratified turbulent flows because of their dominant role in small-scale mixing and homogenization (Lienhardt & Van Atta 1990; Holt et al. 1992). Consider a turbulent flow with r.m.s. velocity u and integral lengthscale L. A scalar inhomogeneity generated at the scale L will be broken down along the hierarchy of scales via non-linear processes, while ultimately reaching the molecular mixing stage. If $Sc > 1$, then the non-linear processes are terminated at the Kolmogorov scale $L_K = (\nu^3/\varepsilon)^{1/4}$, and thereafter the inhomogeneities are disintegrated by the straining motions of Kolmogorov eddies. The time scale t_k for the scalar to breakdown to L_K can be evaluated by noting that the transfer rate of scalar fluctuations at any wave number k in the inertial sub-range is given by (Broadwell & Breidenthal 1982)

$$\frac{dk}{dt} = f(\varepsilon, k) \sim \left(\varepsilon k^5\right)^{1/3} \tag{2}$$

or

$$\int_{2\pi/L}^{2\pi/L_k} dk / k^{5/3} \sim \varepsilon^{1/3} \int_0^{t_k} dt, \tag{3}$$

where f is a function. Thus $t_k \sim L/u$, indicating that the scalar flux reaches L_K in a time scale of the order of the eddy turn-over scale. Thereafter, the breakdown of inhomogeneities is performed by the straining motions of the Kolmogorov eddies, and the final homogenization takes place at the Batchelor scale $L_B = \left(D^2\nu/\varepsilon\right)^{1/4}$. The change of scales (wave numbers) by such straining motions can be written as (Townsend 1976)

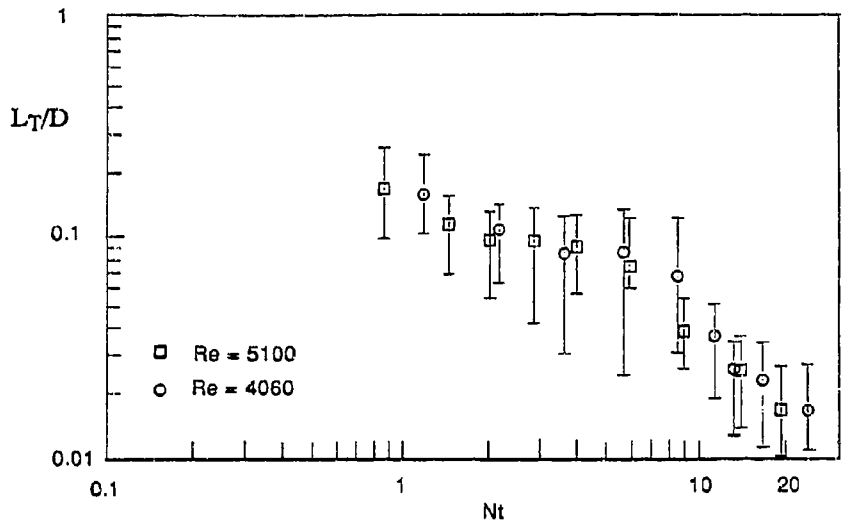


Figure 4: The time evolution of the Thorpe scale L_T, normalized by the diameter D, of a sphere wake.

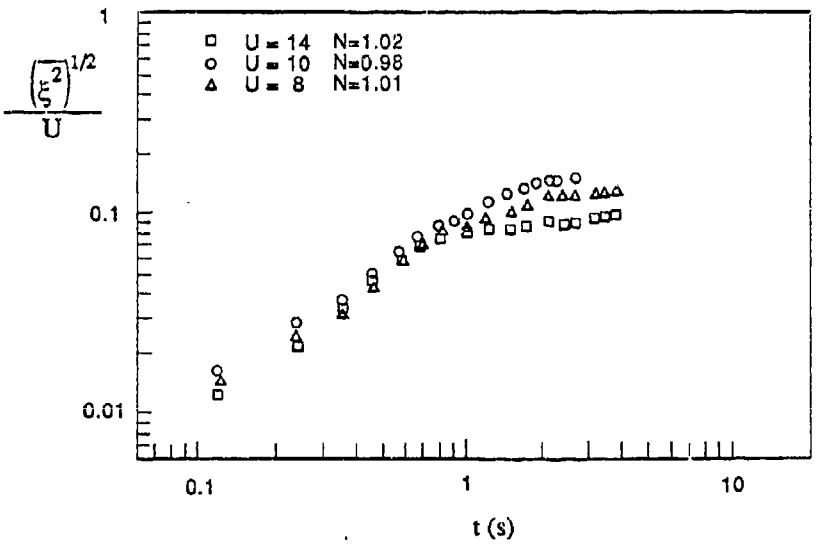


Figure 5: The r.m.s vertical particle displacement in the turbulent wake of a towed grid in a stratified fluid.

$$\frac{dk_i}{dt} = -\frac{\partial U_\ell}{\partial x_i} k_\ell, \tag{4}$$

where $\partial U_\ell/\partial x_i$ is the velocity gradient; for the case of wave-number distortions by simple elongational/compressional motions due to Kolmogorov eddies, (4) can be written as

$$\frac{dk}{dt} \sim \left(\frac{\varepsilon}{\nu}\right)^{1/2} k. \tag{5}$$

Thus, the scalar should break down form L_k to L_B during the time period

$$t_B \sim \left(\frac{\nu}{\varepsilon}\right)^{1/2} \ell n\left(Sc^{1/2}\right) \sim \left(\frac{\nu}{\varepsilon}\right)^{1/2} \ell n(Sc). \tag{6}$$

or

$$\frac{tu}{L} \sim Re^{-1/2}\, \ell n(Sc), \tag{7}$$

where $Re = uL/\nu$. The total time required to complete molecular-scale mixing can be written as

$$\frac{tu}{L} = \alpha_1 + \alpha_2\, Re^{-1/2}\, \ell n(Sc), \tag{8}$$

where α_1 and α_2 are constants. From (8), it is clear that the molecular-diffusive effects should play only a secondary role at high Re. In the case of low-Reynolds number flows, the Sc effects should come into play especially when Re drop to values of the order of $[\alpha_1/\alpha_2\, \ell n(Sc)]^{-2}$; such low Reynolds numbers are not uncommon in laboratory situations.

Because of the low mixing rates of large Sc flows at low Re, decaying turbulence in salt stratified fluids (Pr ~ 1000) may produce positive buoyancy fluxes. If turbulence is introduced to a stratified fluid, initially the flow behaves as if there is no stratification; the fossilization starts at the scale L_R, whence the turbulence begins to decay rapidly. If most of the molecular mixing has not taken place during the initial growth phase, the ensuing fossilized flow will contain unmixed fluid parcels, which may migrate to their equilibrium positions while producing "zombie turbulence" at times. It is interesting to note that laboratory wind tunnel experiments with heat stratification does not produce restratification, which can be attributed to the low Sc or Pr of air (~1).

3. Turbulent Mixing Across Shear Free Density Interfaces*

A large number of studies, both experimental and phenomenological modeling, have been carried out to investigate turbulent mixing across shear-free density interfaces, and a review of pertinent work is given in Fernando (1991). These studies have been motivated by geophysical applications such as the growth of atmospheric day-time convective boundary layer as well as oceanic nocturnal boundary layer in which turbulent motions are driven by buoyancy forcing. A typical configuration of interest is shown in Figure 6; here a thick three-layer fluid system with an inversion layer of thickness h is depicted, across which the density jump is $\Delta\rho$ (equivalent to a

* This work was performed in collaboration with Professor J.C.R. Hunt of the U.K. Meteorological Office.

buoyancy jump of Δb). The turbulence away from the interface has integral length and velocity scales of L_H and u_H, respectively. The configuration shown here is common in the atmosphere (when the diagram is read upside down!), where during the day-time evolution of the convective boundary layer a three layer system, with a bottom convective turbulent layer that is topped by a wave-bearing inversion layer in which the buoyancy frequency is N_2 is present; above that is a deep layer with a weaker stratification, for which the buoyancy frequency is N_3 ($<N_2$). Sometimes the stratification in the outer layer is absent and region (3) is either turbulent (double-sided stirring of the interface) or consists of irrotational motions (single-sided stirring). If h is considered as an independent variable, then the problem can be described by the following three parameters.

$$Ri = \frac{\Delta b L_H}{u_H^2} \text{ (Richardson number)}$$

$$Ri_{(I)} = \frac{\Delta b h}{u_H^2} = N_2^2 h^2 / u_H^2 \text{ (Internal Richardson number)} \qquad (9)$$

$$e = N_3 / N_2 \text{ (frequency ratio) or } Ri_{(3)} = N_3^2 L_H^2 / u_H^2$$

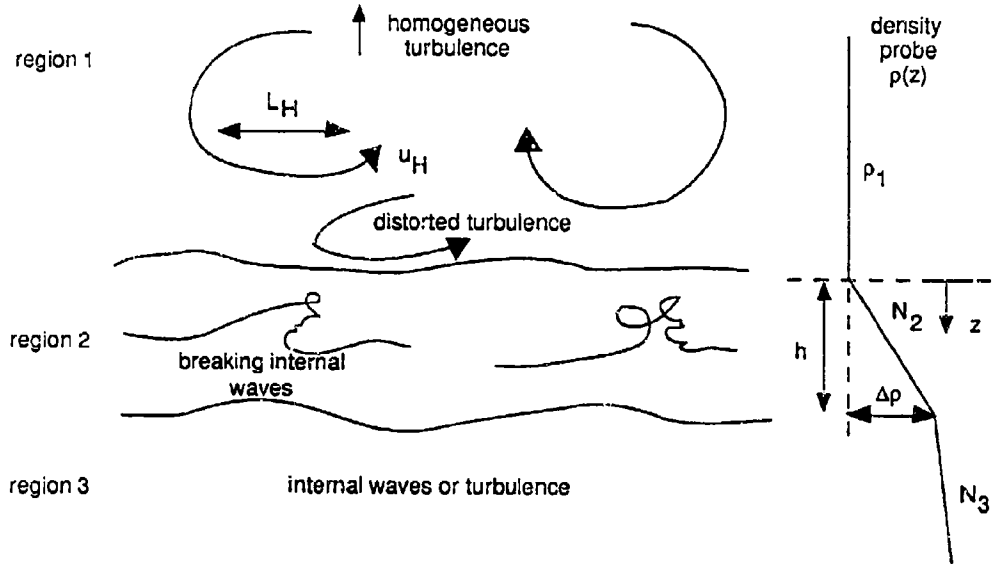


Figure 6. A schematic diagram of a density interface that coexists with an adjacent turbulent region (1) and a weekly stratified layer (region 3).

This flow configuration has been investigated by Carruthers & Hunt (1994) using a formal theoretical analysis. Accordingly, the nature of the interfacial motions are governed by the internal Richardson number $Ri_{(I)}$. If $Ri_{(I)} < \pi^2$, then the interfacial motions consist of the first mode of internal waves (called the flapping mode); this is typical of laboratory situations that have thin interfaces. For the case of $Ri_{(I)} > \pi 2$, many wave modes are possible and when $N_2 h/u_H < n\pi$, where n is an integer, there exist, at most n solutions, the number decreasing with increasing $N_3 (< N_2)$. Since the interfacial structure changes with the number of available internal wave modes, transitions between different entrainment regimes can be expected with the change of $Ri_{(I)}$.

A theoretical analysis can be performed to investigate the nature of the internal wave field of an interface, that is forced by a contiguous turbulent layer; this enables one to calculate the energy absorption into the interface from the turbulent layer. Such calculations are important, because the absorbed energy is key to the estimation of mixing rates. The technique devised by Hunt (1984) has been used by Carruthers & Hunt (1986, 1994) and Fernando & Hunt (1994) for the analysis of a wave field coexisting with a turbulent layer. In this approach, it is assumed that turbulence near an interface can be described by the superposition of a homogeneous turbulence field $\underline{u}^H$ and a distorted field $\underline{u}^D$. The homogeneous field is represented by four-dimensional Fourier transforms,

$$u_i^H(\underline{x},t) = \int_{-\infty}^{+\infty}\int\int\int S_i^H(\underline{k},\omega)\, e^{i(\underline{k}\cdot\underline{x} - \omega t)} dk d\omega \quad , \tag{10}$$

where $\underline{k} = (k_1, k_2, k_3)$ is the wave number, ω is the frequency, the Fourier coefficients satisfy the relation

$$\overline{S_i^{H*}(k_1,k_2,k_3,\omega)\, S_i^H(k_1,k_2,k_3',\omega)} = \chi_{ij}^H(k_1,k_2,k_3',\omega)\, \delta(k_3 - k_3'), \tag{11}$$

and χ_{ij}^H is the four-dimensional wave-number-frequency spectrum, i.e.,

$$\chi_{ij}^H(\underline{k},\omega) = \frac{1}{(2\pi)^4}\int_{-\infty}^{+\infty}\int\int\int \overline{u_i^H(\underline{x},t)\, u_j^H(\underline{x}+\underline{r},t+\tau)}\, e^{-i(\underline{k}\cdot\underline{r} - \omega\tau)} d\underline{r}\, d\tau. \tag{12}$$

The distorted field can be shown to be irrotational, and hence can be represented as $\underline{u}^D(\underline{x},t) = -\nabla\phi$, where ϕ is the velocity potential which is governed by $\nabla^2\phi = 0$; see Hunt (1984) for a justification of this assumption. The interfacial wave motions are assumed to be governed by the internal wave equations,

$$\frac{\partial^2}{\partial t^2}\left(\nabla^2 w\right) + N^2\left(\nabla_h^2 w\right) = 0 \tag{13}$$

and

$$\frac{\partial^2 w}{\partial t^2} + N^2 w = -\frac{1}{\rho_o}\frac{\partial^2 p}{\partial z \partial t}, \tag{14}$$

where $N = N_2$ for $0 < z < h$, $N = N_3$ for $h > z$, w and p are vertical velocity and pressure perturbation, respectively, and $\nabla_h^2 = \partial^2/\partial x^2 + \partial^2/\partial y^2$. Assuming that the turbulence and wave motions are statistically stationary and w and the other components of velocity (u_i) can be expressed as a Fourier transform in horizontal wave numbers and frequency as

$$w(x,y,z,t) = \iiint_{-\infty}^{+\infty} \hat{w}(k_1,k_2,z,\omega) e^{i(k_1 x + k_2 y - \omega t)} dk_1 dk_2 d\omega, \tag{15}$$

it is possible to write (13), for the region (2), as

$$\frac{d^2\hat{w}}{dz^2} + \frac{(N^2-\omega^2)}{\omega^2} k_{12}^2 \hat{w} = 0 , \tag{16}$$

where $k_{12}^2 = k_1^2 + k_2^2$.

The turbulent and wave fields are matched at the interfacial boundaries by using the kinematic condition and the continuity of pressure. The solutions of the resulting equations can be obtained in the form of

$$u_i(\underline{x},t) = \iiint_{-\infty}^{+\infty} \hat{u}_i(k_1,k_2,z,\omega)\, e^{i(k_1x+k_2y-\omega t)} dk_1 dk_2 d\omega, \tag{17a}$$

$$\phi(x,t) = \iiint_{-\infty}^{+\infty} \hat{\phi}(k_1,k_2,z,\omega)\, e^{i(k_1x+k_2y-\omega t)} dk_1 dk_2 d\omega, \tag{17b}$$

if the interfacial motions are stationary. If the flow is considered to be unsteady (e.g., in the presence of growing waves), (16) needs to be modified and solutions of the form

$$u_i(\underline{x},t) = \iint_{-\infty}^{+\infty} \hat{u}_i(k_1,k_2,z,t)\, e^{i(k_1x+k_2y)} dk_1 dk_2, \tag{18a}$$

$$\phi(\underline{x},t) = \iint_{-\infty}^{+\infty} \hat{\phi}(k_1,k_2,z,t)\, e^{i(k_1x+k_2y)} dk_1 dk_2, \tag{18b}$$

should be sought. Note that the steady solutions cannot extract energy, and hence unsteady solutions have to be used for energy calculations. To close the equations, an expression is required for the four-dimensional spectra, and it is usually modeled in the form (Carruthers & Hunt 1986)

$$\chi_{ij}^H(\underline{k},\omega) = \Phi_{ij}^H(\underline{k})\, \delta(|\omega| - |k|\, u_H), \tag{19}$$

where $\Phi_{ij}^H(\underline{k})$ is the three-dimensional spectral tensor, and it is assumed that the main cause of time variation of velocity at a given point in a frame of reference moving with the mean flow is the random advection of fluid elements by the energy containing eddies with velocity and length scales u_H and L_H, respectively. Thus this spectral form is valid only for frequencies $\omega > u_H/L_H$. A more exact model of the random advection changes this equation, but not significantly the results for waves at the interface.

The r.m.s. velocities and wave amplitude can be calculated using steady solutions and the unsteady solutions can be used to calculate the energy flux into the interface. Of course, certain problems arise in such calculations because of the presence of growing resonant wave modes within the interface. These waves grow, break, and dissipate energy - an aspect not readily amenable to theoretical treatment or direct numerical simulation. Some modeling ought to be invoked to circumvent this difficulty. For example, Carruthers & Hunt (1994) considered the case where the density interface is thick ($h \sim L_H$), and introduced Rayleigh friction to artificially remove energy from growing resonant modes; they adjusted the Rayleigh damping coefficient so that the r.m.s. wave slope is maintained at a threshold just enough to initiate breaking. Alternatively, Fernando & Hunt (1994) employed a simpler closure hypothesis, in which they assumed that breaking waves produce discontinuities in isopycnal contours; the mathematical requirement that contours with discontinuities should lead to k^{-2} spectrum in the wave number space and ω^{-2} in the frequency space renders the velocity spectrum flat in the wave-breaking regime. The vertical velocity spectrum of Fernando & Hunt (1994) consisted of a linear part, for which the solution is known, and a non-linear part, for which the spectrum is flat based on the above argument. The energy was assumed to be equi-partitioned among linear and non-linear regimes because an imbalance would cause the energy to redistribute either by growing waves or by non-linear transfer processes. A model based on above concepts was developed for the case $Ri < \pi^2$, and satisfactory predictions for the r.m.s. wave amplitude and velocity were obtained (Figure 7).

The unsteady calculations for the case where $Ri_{(1)} < \pi^2$, $Ri_{(3)} = 0$ and the bottom layer consists of irrotational motions, show that the flux of energy absorbed into the interface ($\mathcal{P}$) is given by

$$\mathcal{P} = gRi^{-n}, \text{ where } g = \sqrt{\frac{h}{L_H}}\frac{g_3\pi^2}{2^{4/3}}. \tag{20}$$

If it is assumed that the breaking of waves acts as a sink to this energy, so that a part of the energy is dissipated (with the rate of dissipation ε) and the rest is used to sustain the buoyancy flux (q), with a mixing efficiency of $q/(q+\varepsilon) = 0.25$ (McEwan 1983), then it is possible to estimate the entrainment rate E_b^* for the single-sided stirring case as

$$E_b = \frac{E_b^*}{u_H} = 0.19\, Ri^{-1.17}, \tag{21}$$

where E_b is the entrainment coefficient. This prediction is in good agreement with the measurements of Nokes (1988), who found that $E_b = 0.15\ Ri^{-1.21}$. It should be noted that the above entrainment law may not be valid for thick interfaces with $Ri_{(1)} > \pi^2$. In such cases the amount of energy absorbed into the interface as well as interfacial energetics are different; further, the resonant modes grow faster, thus allowing less time for mixing (Carruthers & Hunt 1994). Laboratory experiments performed with thick interfaces indeed show significantly lower entrainment rates than that of thin interfaces with same Ri (Figure 8); and a comprehensive theoretical treatment on this discrepancy is yet to be reported.

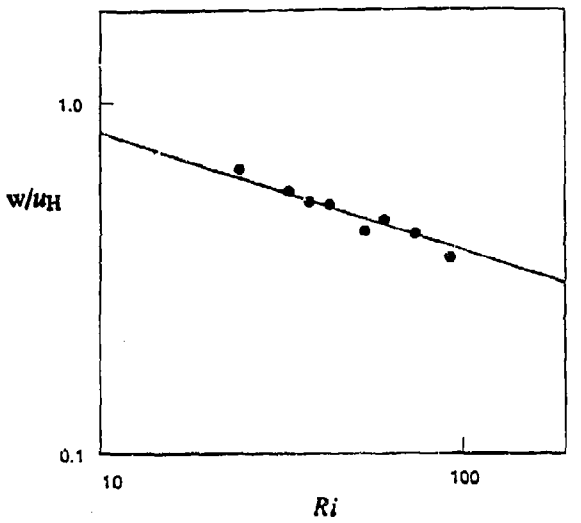


Figure 7: A comparison of the predicted (solid line) normalized r.m.s. vertical velocity w/u_H variation with Ri with the experimental results (solid symbols) of Hannoun & List (1988).

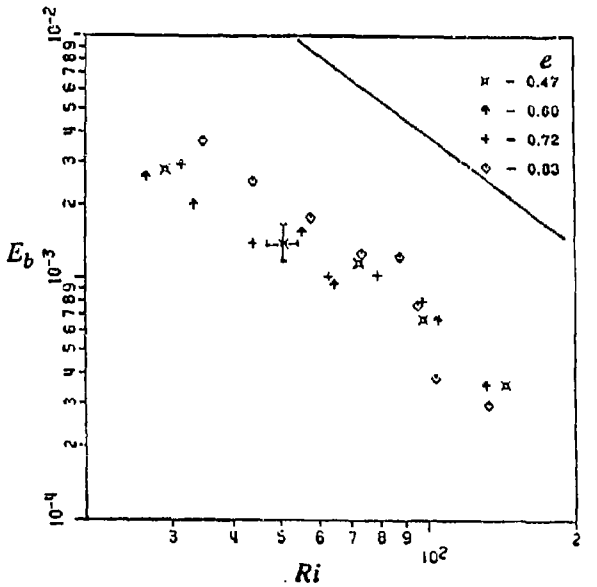


Figure 8: A comparison between the entrainment coefficient versus Ri data for the thin-interface case (solid line) with a thick-interface case (symbols); the results are from E & Hopfinger (1986) and Perera et al. (1994), respectively.

4. Mixing in Stratified Shear Flows

The flow configuration shown in Figure 6 does not incorporate velocity shear that may present across the interface, and hence it represents a simple flow configuration with somewhat limited applications. However, most of the natural density interfaces are subjected to velocity shear, and hence the class of problems that deal with sheared interfaces is of prime interest. A typical example is the upper ocean mixed layer, which is driven by wind forcing and generates strong velocity shear at the base of the mixed layer. The interface is now subjected to the turbulence of the mixed layer as well as to the turbulence that is generated locally by the shear instabilities of the stratified layer. Theory (e.g., Miles 1984), laboratory experiments (Rohr & Van Atta 1987) and field observations (Nieuwstadt 1984) show that the turbulence in the stratified layer is generated when the local gradient Richardson number $N^2/(d\overline{U}/dz)^2$, where $(d\overline{U}/dz)$ is the local mean velocity gradient, drops below a critical value of the order of 0.2 - 0.3. Thus the entrainment of non-turbulent fluid from the interface into the turbulent layer is expected to occur either by the engulfment of fluid by the mixed-layer eddies (this mechanism can also be present for the shear-free case) and by the shear instabilities of the interface. These two mechanisms are discussed below in detail.

(a) *Eddy engulfment mechanism*

Consider the flow configuration shown in Figure 9, where a turbulent mixed layer is driven over a stratified interface. Eddies of various space time scales slosh over the interface and may penetrate and scour non-turbulent dense fluid from it. If these eddies penetrate a distance δ and scour fluid particles of the same size, then the buoyancy associated with a lifted particle is

$$\Delta b_p \sim \frac{\Delta b}{h}\delta. \tag{22}$$

If the size of an inertial-subrange eddy involved in this process is ℓ, then its vertical velocity can be written in terms of the r.m.s. velocity and the integral lengthscale L_H as

$$w_\ell \sim u_H\left(\frac{\ell}{L_H}\right)^{1/3}. \tag{23}$$

If these eddies are capable of carrying scoured fluid particles into the mixed layer, then the resident time t_R of the fluid particles before they fall back on the interface can be evaluated as

$$t_R \sim \frac{w_\ell}{\Delta b_p}. \tag{24}$$

Further, it is possible to write

$$\frac{\delta^2}{L_H^2} \sim Ri^{-1}\left(\frac{\ell}{L_H}\right)^{2/3}\left(\frac{h}{L_H}\right). \tag{25}$$

Note that the maximum penetration and hence the entrainment, occurs due to the energy containing (integral-scale) eddies. Combining (23), (24) and (25), the resident time of scoured particles can be written as

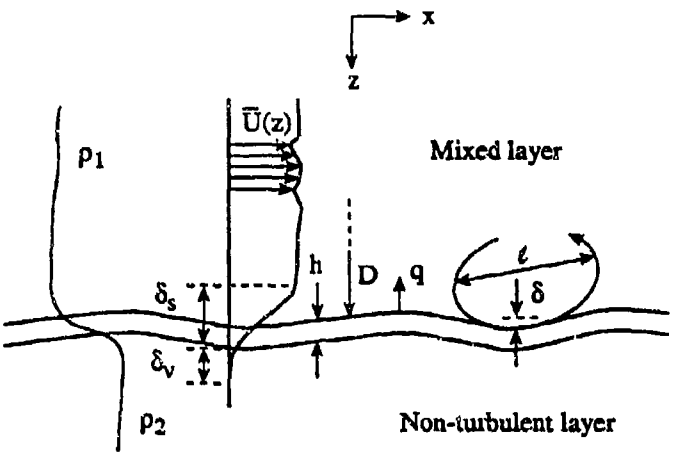


Figure 9: A simplified diagram of an entraining stratified fluid with interfacial shear, drawn on the basis of the experimental observations (Narimousa & Fernando 1987). The mixed layer is fully turbulent and the shear layer (thickness δ_s) extends above the entrainment interface. Beneath it is the viscous momentum diffusive layer (thickness δ_v) that usually extends below the density interfacial layer.

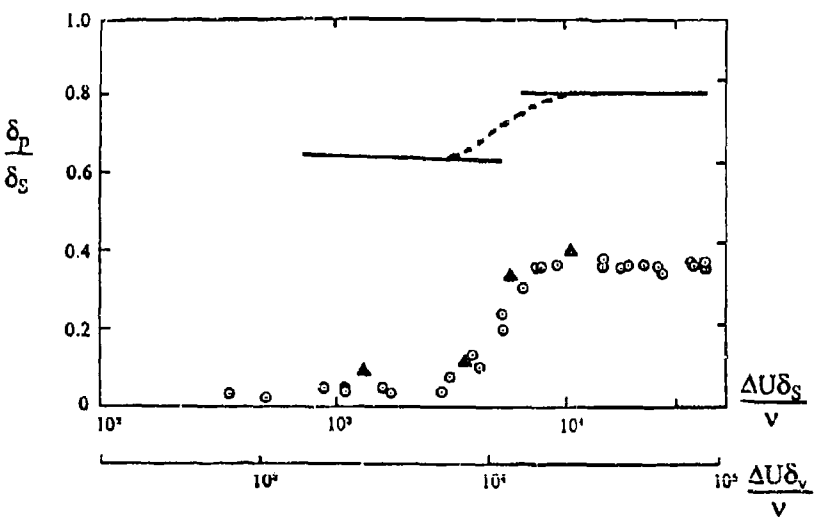


Figure 10: The dependence of the amount of molecular mixing in a shear layer on the Reynolds numbers based on the visual shear layer thickness (δ_s) and the vorticity thickness (δ_V). ΔU is the velocity jump across the layer, and δ_p is the product thickness defined in Koochesfahani & Dimotakis (1986) from which this figure is adopted. The solid line represents the gaseous mixing layer results of Konrad (1976). The measurements of Breidenthal (1981) are also shown by solid symbols.

$$t_R \sim \left(\frac{h}{\Delta b}\right)^{1/2}, \tag{26}$$

which is the buoyancy time scale of the interface. While heavy fluid particles are in the mixed layer, they are broken down by eddies of different sizes and may ultimately homogenize (or mixed) with the turbulent layer thus completing the entrainment process. Based on the arguments presented in Section 2, it is clear that this mixing is completed within a time scale of the order ℓ/w_ℓ; hence for the entrained fluid to mix molecularly before falling back on the interface, the following condition should be satisfied;

$$\left(\frac{h}{\Delta b}\right)^{1/2} > \frac{\ell}{w_\ell}, \tag{27}$$

$$\text{or } \frac{h}{L_H} > \left(\frac{\ell}{L_H}\right)^{4/3} Ri. \tag{28}$$

Since h/L_H is generally small (Stephenson & Fernando, 1991), it is clear that only small eddies can contribute to the scouring process (dense fluid particles associated with larger eddies simply fall back on the interface). However, the depths of fluid δ entrained by such eddies are negligible so as their entrainment abilities. Thus, much faster mechanisms such as resonant growth of waves and shear instabilities are expected to play the dominant role in mixing across interfaces, especially at high Richardson numbers.

(b) ***Shear Instabilities***

It appears that at moderate and high Richardson numbers interfacial mixing is caused by local shear instabilities. Depending on interfacial conditions, these instabilities may appear in different forms, for example, Kelvin-Helmholtz (K-H) billows, Holmboe instabilities and growing interfacial waves; see Fernando (1991). Shear-layer instabilities without stratification have been studied extensively, particularly by the Caltech Aeronautics group (e.g., Konrad 1976; Breidenthal 1981; Mungel & Dimotakis 1984; Koochesfahani & Dimotakis 1986). Their results have delineated very useful information on entrainment and molecular mixing that occur during the roll up of the shear layer.

Experiments on large Reynolds-number shear layers show that the mixing processes are dominated by the dynamics of large-scale vortical structures. Initial entrainment of one fluid to another leads to the appearance of markedly different concentrations in the center of the shear layer. Of course, such inhomogeneities should disappear as mixing proceeds, but the observations indicate that molecular-mixing time scales should be given due regard in entrainment studies. Another noteworthy observation is the existence of a mixing transition; i.e., the increase of molecularly-mixed products by a significant factor beyond a certain Reynolds number (Figure 10). The mixing rates thereafter do not seem to depend on the Reynolds number, and the tendency for molecular mixing in gases is clearly higher than that in liquids; the differences of Schmidt number have been attributed to this disparity. Does this mean, for example, that mixing characteristics in oceans differ from that of the atmosphere? Data from very high Reynolds number cases are required to address such questions. Preliminary studies indicate that gaseous and liquid mixing curves merge with each other at large Reynolds numbers

The nature of instabilities in stably stratified shear layers is different from nonstratified cases. In the former, the instabilities (usually the K-H type) are possible only when the local gradient Richardson number Ri_g drops below a critical value, and this local value can be much smaller than that is based on bulk parameters. For example, if the shear-layer thickness is δ_s and the interfacial-layer thickness is h, then, based on bulk parameters, $Ri_g \sim (\Delta b \delta_s/\Delta U^2)(\delta_s/h)$, where ΔU is the velocity jump across the shear layer; if $\delta_s \sim h$, $Ri_g \sim \Delta b \delta_s/\Delta U^2$. Although the bulk Ri_g is large in most practical situations, its local value often falls below the critical value of Ri_{gc} necessary for instabilities because of the straining of the interface by the internal wave field. The experimental results of DeSilva et al. (1994) clearly show the possibility of small local Ri_g values for high overall gradient Richardson number situations. Observations that have been made in lakes (Spigel et al. 1986), oceans (Hebert et al. 1992) and in the atmosphere (Nappo 1991) indicate that the appearances of K-H instabilities are rather sporadic and are possibly controlled by a critical Ri_g criterion. When δ_s is small, Ri_g tends to be small and K-H billows may appear; consequent mixing causes δ_s to increase while increasing Ri_g; mixing is ceased when Ri_g increases beyond a critical value (which is of the order of 0.3; see Thorpe (1987) for a review). If background turbulence is present, this thickened interface can be eroded thus decreasing δ_s again. By this way, recurrence of K-H instabilities is possible in natural shear layers.

By estimating the largest possible local velocity gradient in the base of a mixed layer, Fernando & Stephenson (1991) estimated the local Ri_g as

$$Ri_g \sim Ri\,Re^{-2}\left(\frac{D}{h}\right)\left(\frac{\Delta U}{u_H}\right)^4. \qquad (29)$$

This expression can be employed to calculate the *Ri* range required for the appearance of K-H instabilities by using the criterion $Ri_g < Ri_{gc}$, where $Ri_{gc} \approx 0.25$. Below a critical *Ri*, K-H instabilities are possible. Above this value, the flow is dominated by wave-like instabilities which grow and break sporadically (Narimousa & Fernando 1987). At very large *Ri*, the interface tends to be flat, non-entraining and dominated by molecular-diffusive effects. Estimates based on (29) were found to predict the transitions between different entrainment regimes of the laboratory experiments of Stephenson & Fernando (1991) satisfactorily.

Entrainment characteristics of sheared interfaces have been well studied, but unfortunately no unified consensus exists on the entrainment law; see Fernando (1991) for a review. In addition, there are some outstanding questions concerning the energy radiation past the interface into the stratified region, transitions between various entrainment regimes and wave-turbulence interactions at the interface. A rigorous theoretical analysis encompassing these issues is yet to be developed.

Acknowledgments

The author wishes to thank the financial support provided by the National Science Foundation, Office of Naval Research and the Environmental Protection Agency for his research work at Arizona State University. Discussions with Professors J.C.R. Hunt and E.J. List stimulated some of the thoughts presented in this paper, and their generosity is gratefully acknowledged.

References

Breidenthal, R. E., 1981. Structure in turbulent mixing layers and wakes using a chemical reaction. *J. Fluid Mech.*, **109**, 1-24.

Broadwell, J.E., and Breidenthal, R.E., 1982. A simple model of mixing chemical reaction in a turbulent shear layer. *J. Fluid Mech.*, **125**, 397-410.

Bryan, K., 1987. Parameter sensitivity of primitive equation ocean circulation models. *J. Phys. Oceanogr.*, **17**, 970-985.

Caldwell, D.R., 1983. Oceanic turbulence: Big bangs or continuous creation? *J. Geophys. Res.*, **88(12)**, 7543-7550.

Carruthers, D.J., and Hunt, J.C.R., 1986. Velocity fluctuations near an interface between a turbulent region and a stably stratified layer. *J. Fluid Mech.*, **165**, 475-501.

Carruthers, D.J., and Hunt, J.C.R., 1994. Waves, turbulence and entrainment near an inversion layer. *J. Fluid Mech.*, submitted.

Crawford, W.R., 1986. A Comparison of lengthscales and decay times of turbulence in stably stratified flows. *J. Phys. Oceanogr.*, **16(11)**, 1847-1854.

Csanady, G.T., 1964. Turbulent diffusion in a stratified fluid. *J. Atmos. Sci..*, **21**, 439-447.

De Silva, I.P.D., and Fernando, H.J.S., 1992. Some aspects on mixing in a stratified turbulent patch. *J. Fluid Mech.*, **240**, 601-625.

DeSilva, I.P.D., Fernando, H.J.S., Eaton, F., and Hebert, D., 1994. Kelvin-Helmholtz billows: When do they become turbulent?, submitted for publication.

Dillon, T.M., 1982. Vertical overturns; A comparison of Thorpe and Ozmidov lengthscales. *J. Geophys. Res.*, **87**, 9601-9613.

Dillon, T.M., 1984. The energetics of overturning structures: Implications for the theory of fossil turbulence. *J. Phys. Oceanogr.*, **14(3)**, 541-549.

Dillon, T.M., Moum, J.N., Chereskin, T.K., and Caldwell, D.R., 1989. Zonal momentum balance at the equator. *J. Phys. Oceanogr.*, **19(5)**, 561-570.

Dougherty, J.P., 1961. The anisotropy of turbulence at the meteor level. *J. Atmos. Terr. Phys.*, **21**, 210-213.

E, X., and Hopfinger, E. J., 1986. On mixing across an interface in stably stratified fluid. *J. Fluid Mech.*, **166**, 227-244.

Ellison, T.H., 1962. Laboratory measurements of turbulent diffusion in stratified flows. *J. Geophys. Res.*, **67(8)**, 3029-3031.

Fernando, H.J.S., 1991. Turbulent mixing in stratified fluids. *Ann. Rev. Fluid Mech.*, **23**, 455-493.

Fernando, H.J.S., 1988. Growth of a turbulent patch in a stratified fluid. *J. Fluid Mech.*, **190**, 55-70.

Fernando, H.J.S., and Hunt, J.C.R., 1994. Modeling of turbulent mixing at shear-free density interfaces. To be submitted to *J. Fluid Mech.*

Fernando, H.J.S., and Stephenson, P.H., 1991. Mixing across sheared stratified interfaces. Environmental Hydraulics (Ed., J.H.W. Lee and Y.K. Cheung), Balkema Publishing, 391-396.

Gargett, A.E., Osborn, T.R., and Nasmyth, P.W., 1984. Local isotropy and the decay of turbulence in a stratified fluid. *J. Fluid Mech.*, **144**, 231-280.

Gerz, T., and Yamazaki, H., 1993. Direct numerical simulation of buoyancy-driven turbulence in stably stratified fluid. *J. Fluid Mech.*, **249**, 415-440.

Gibson, C.H., 1980. Fossil turbulence, salinity and vorticity, turbulence in the ocean. *Marine Turbulence*, Elsevier Oceanographic Series, **16**, 221-257.

Gibson, C.H., 1987. Fossil turbulence and intermittency in sampling oceanic mixing processes. *J. Geophys. Res*, **92**, 5383 -5404.

Gibson, C.H., 1991. Laboratory, numerical, and oceanic fossil turbulence in rotating and stratified flows. *J. Geophys. Res.*, **96**, 12, 549-12, 566.

Gregg, M.C., 1984. Persistent turbulent mixing and near-inertial waves. *Internal Gravity waves and small scale turbulence, Aha Hulikoa Winter Hawaiian Workshop Proceedings* (Eds: P. Müller and R. Pujalet). 1-24.

Gregg, M.C., 1987. Diapycnal mixing in the thermocline: A review. *J. Geophys. Res.*, **92**, 5249-5286.

Hannoun, I. A., and List, E. J., 1988. Turbulent mixing at a shear free density interface. *J. Fluid Mech.*, **189**, 211-234.

Hebert, D., Moum, J.N., Paulson, C.A., and Caldwell, D.R., 1992. Turbulence and internal waves at the equator part II: Details of a single event. *J. Phys. Oceanogr.*, **22**, 1346-1356.

Holt, S.E., Koseff, J.R., and Ferziger, J.H., 1992. A numerical study of the evolution and structure of homogeneous stably stratified shear turbulence. *J. Fluid Mech.* **237**, 499-539.

Hunt, J. C. R., 1984. Turbulence structure in thermal convection and shear-free boundary layers. *J. Fluid Mech.*, **138**, 161-184.

Imberger, J., and Ivey, G.N., 1991. On the nature of turbulence in a stratified fluid. Part 2: application to lakes. *J. Phys. Ocean.*, **21**, 659-680.

Ivey, G.N., and Imberger, J., 1991. On the nature of turbulence in a stratified fluid. Part 1: The efficiency of mixing. *J. Phys. Oceanogr.*, **21(5)**, 650-658.

Konrad, J.H., 1976. An experimental investigation of mixing in two dimensional turbulent shear flows with applications to diffusion-limited chemical reactions. Ph.D. Thesis, Caltech.

Koochesfahani, M.M., and Dimotakis, P.E., 1986. Mixing and chemical reactions in a turbulent liquid mixing layer, *J. Fluid Mech.*, **170**, 83-112.

Ledwell, J.R., 1994. A tracer study of mixing in the oceanic pycnocline. Submitted to *Nature*.

Lienhard, J.H., and Van Atta, C.W., 1990. The decay of turbulence in thermally stratified flow. *J. Fluid Mech.*, **210**, 57-112.

Long, R. R., 1978. A theory of mixing in a stably stratified fluid. *J. Fluid Mech.*, **84**, 113-124.

McEwan, A. D., 1983. Internal mixing in stratified fluids. *J. Fluid Mech.*, **128**, 59-80.

Miles, J. W., 1984. Richardson number criterion for the stability of stratified shear flow. *Phys. Fluids*, **29(10)**, 3470-3471.

Mungel, M.G., and Dimotakis, P.E., 1984. Mixing and combustion with low heat release in a turbulent shear layer. *J. Fluid Mech.*, **148**, 349-382.

Nappo, C.J., 1991. Sporadic breakdowns of stability in the pbl over simple and complex terrain. *Boundary Layer Meteo.*, **54**, 69-87.

Narimousa, S., and Fernando, H.J.S., 1987. On the sheared density interface of an entraining stratified fluid. *J. Fluid Mech.*, **174**, 1-22.

Nasmyth, P.W., 1970. Oceanic turbulence. Ph.D. Dissertation, University of British Columbia.

Nieuwstadt, F. T. M., 1984. The turbulent structure of the stable, nocturnal boundary layer, *J. Atmos. Sci.*, **41**, 2202-2216.

Nokes, R. I., 1988. On the entrainment across a density interface. *J. Fluid Mech.*, **134**, 195-204.

Ozmidov, R.V., 1965 On the turbulent exchange in a stably stratified ocean. *Bull. Acad. Sci U.S.S.R. Atmos. and Oceanic Phys*, **1**, 493-497.

Pearson, H.J., and Linden, P.F., 1983. The final stage of decay of turbulence in stably stratified fluid. *J. Fluid Mech.*, **134**, 195-203.

Pearson, H.J., Puttock, J.S., and Hunt, J.C.R., 1983. A statistical model of fluid element motions and vertical diffusion in a homogeneous stratified turbulent flow. *J. Fluid Mech.*, **129**, 219-249.

Perera, M.A.J.M, Fernando, H.J.S., and Boyer, D.L., 1994. Turbulent mixing at an inversion layer, *J. Fluid Mech.*, **267**, 275-298.

Richardson, L.F., 1920. The supply of energy from and to atmospheric eddies. *Proc. Roy. Soc.* **97**, 354-373.

Riley, J.J., Metcalfe, R.W., and Weissman, M.W., 1981. Direct numerical simulations of homogeneous turbulence in density-stratified fluids. In Nonlinear Properties of Internal Waves (Ed: B.J. West), *AIP conf. Proc.*, **76**, 79-112.

Rohr, J.J., and Van Atta, C.W., 1987. Mixing efficiency in stably stratified growing turbulence. *J. Geophys. Res.*, **92**, 5481-5488.

Spigel, R.H., Imberger, J., and Rayner, K.N., 1986. Modeling the diurnal mixed layer. *Limnol. Oceanogr.*, **31(3)**, 533-556.

Stephenson, P.H., and Fernando, H.J.S., 1991. Turbulence and mixing in a stratified shear flow. *J. Geophys. Astrophys. Fluid Dyn.*, **59**, 147-164.

Stillinger, D.C., Helland, K.N., and Van Atta, C.W., 1983. Experiments on the transition of homogeneous turbulence to internal waves in a stratified fluid. *J. Fluid Mech.*, **131**, 91-122.

Taylor, G.I., 1921. Diffusion by continuous movements. *Proc. Lond. Math. Soc., ser. 2*, **20**, 196-212.

Taylor, G.I., 1931. Internal waves and turbulence in a fluid of variable density. *Conseil Perm. Int. pour. l'Expl. de la Mer., Rapp. et Procverb,*, **76**, 35-42.

Taylor, J.R., 1992. The energetics of breaking events in a resonantly forced internal wave field. *J. Fluid Mech.*, **239**, 309-340.

Thorpe, S.A., 1977. Turbulence and mixing in a Scottish loch. *Phil. Trans. Roy. Soc. Lond.*, **286**, 125-181.

Thorpe, S. A., 1987. Transitional phenomena and the development of turbulence in stratified fluids: A review. *J. Geophys. Res.*, **92(C5)**, 5231-5248.

Townsend, A.A., 1976. The Structure of Turbulent Shear Flows. Cambridge University Press.

Woods, J.D., 1969. On Richardson's number as a criterion for laminar-turbulent-laminar transition in the atmosphere and ocean. *Radio Science*, **4**, 1289-1298.

Xu, Yu, 1994. Wakes of cylindrical bodies in stratified flows, Ph.D. Thesis, Arizona State University, in Preparation.

PARTICLE-DRIVEN GRAVITY CURRENTS

Abstract for
4th International Stratified Flow Symposium

by
Herbert E. Huppert
Institute of Theoretical Geophysics, Department of Applied Mathematics and Theoretical Physics, University of Cambridge, Silver Street, Cambridge CB3 9EW, UK

Gravity currents occur whenever fluid of one density flows primarily horizontally into fluid of a different density. Inviscid currents in which the driving buoyancy is due to compositional differences were first considered quantitatively by von Karman (1940) and later by Benjamin (1968). This presentation will concentrate on currents which are driven by particles which gradually fall out as the current propagates. Examples of such flows include sediment-laden currents which flow over the sea floor (known as turbidites), avalanches, and ash-laden pyroclastic flows from volcanic eruptions.

After a few introductory remarks about gravity currents, a shallow-water model of a particle-laden current will be described for which the dynamics of the current are assumed to be dominated by a balance between the inertial and buoyancy forces. The local density of the gravity current, and the contribution this makes to the buoyancy, depends on the local concentration of particles. The transport equation for this particle concentration is based on the assumption that the particles are vertically well-mixed by the turbulence in the current, are advected by the mean flow and settle through a viscous sublayer at the bottom of the current. In addition, it is assumed that no entrainment of ambient fluid into the current takes place. The resulting equations describing the instantaneous release of a fixed volume of a suspension onto a horizontal floor have been solved numerically for various geometries (Bonnecaze, Huppert & Lister, 1993; Bonnecaze, Hallworth, Huppert & Lister, 1994). To test the validity of the theoretical model we have carried out a series of experiments using non-cohesive silicon carbide particles in water. In each experiment the length (or radius) of the current as a function of time and the resulting deposition pattern were measured. This data compared very well with the theoretical predictions, which involve no adjustable parameters. Guided by the theoretical results, we will then describe the interpretation of data obtained from naturally occurring deposits from the deep sea (Dade & Huppert, 1994).

We (Dade, Lister & Huppert, 1994) have also investigated the propagation of and deposition from a non-eroding gravity surge by a simple model for a two-dimensional, well-mixed buoyant cloud of suspended particles moving down an inclined surface. The model includes the effects of entrainment of ambient sea water, deposition of suspended sediment, sea floor friction and slope. Solutions have been obtained to the coupled equations that describe the conservation of momentum, total mass and particulate mass of the surge. The solutions are found to vary on two length scales: x_o, beyond which the behaviour of the surge is independent of the inertial momentum and shape; and x_r, over which the driving

buoyancy of the surge is lost due to particle settling.

The amount of entrainment of ambient fluid into the head of a gravity current propagating along a horizontal surface will be discussed, and illustrated using a novel experimental procedure. The technique relies on the neutralization of an alkaline current by entrainment of acidic ambient fluid, which is visualized by using a pH indicator. Dimensional analysis indicates that the proportion of ambient fluid entrained into the head of a gravity current depends only on the initial geometry of the current and distance from the release point, and is independent of the initial value of the density difference, a result which is confirmed by the experimental data. It will be shown that measured downstream dilution is in quantitative agreement with the prediction of the theoretical model (Hallworth *et al.*, 1993).

References

Benjamin, T.B. 1968 Gravity currents and related phenomena. J. Fluid Mech. **88**, 223-240.

Bonnecaze, R.T., Huppert, H.E. & Lister, J.R. 1993 Particle-driven gravity currents, J. Fluid Mech. **250**, 339-369.

Bonnecaze, R.T., Hallworth, M.A., Huppert, H.E. & Lister, J.R. 1994 Particle-driven gravity currents. Part 3: Axisymmetric flows, J. Fluid Mech. (in preparation).

Dade, W.B. & Huppert, H.E. 1994 Predicting the geometry of channelised deep-sea turbidites, Geology (in press).

Dade, W.B., Lister, J.R. & Huppert, H.E. Fine-sediment deposition from gravity surges on uniform slopes, J. Sed. Pet. (in press).

Hallworth, M.A., Phillips, J., Huppert, H.E. & Sparks, R.S.J. 1993 Entrainment in turbulent gravity currents, Nature **362**, 829-831.

von Kármán, T. 1940 The engineer grapples with nonlinear problems. Bull. Am. Math. Soc. **46**, 615-683.

EXPERIMENTAL STUDY OF REGULAR BACKGROUND AND SHIP INTERNAL WAVES INTERACTION IN THE THERMOCLINE

OLGA D. SHISHKINA

Institute of Applied Physics, Russian Academy of Sciences,
46 Ul'janov st., Nizhny Novgorod 603600, Russia [1]

ABSTRACT

Experimental results on ship internal waves propagation in a fluid with the thermocline – type stratification in presence of favorable regular plane internal waves of various frequencies are presented.

The spectrum analysis showed that in the case of low background wave frequency the interaction between two internal waves systems is absent, i.e. resulting internal wave spectrum is a superposition of the background and ship waves spectra. For higher background wave frequencies the initial spectrum transformed.

1. Introduction

The problem of internal waves interaction with submerged obstacles – hydrodynamics of submereged bodies as well as waves scattering at the obstacle – is one of important problems of the stratified fluid theory.

At the present time this question is widely examined for the homogeneous liquid and surfase waves presence. In the stratified fluid even for the linear assumption and regular internal waves in the ideal incompressible fluid the pointed problem's solution causes a lot of difficulties.

Theoretical investigations in the field of background waves influence on hydrodynamic characteristics of submerged bodies have been fufilled by Wu & Eatock Taylor (1987), Wu (1991) – for a submergrd body of the arbitrary form in a homogeneous liquid and by Sturova (1992, 1993) – the plane problem on the surface and internal waves generation and scattering by a cylinder disposed under the sharp density jump (two–layered and continuous) in the case of potential fluid movement.

The author is aware of a single experimental work in this field in the stratified liquid. But this way seems to be one of the perspective ways of hydrodynamic investigations which allows to avoid serious theoretical problems. In the work by Yermanyuk (1993) results of the power influence of plane regular internal waves in the two–layered liquid on a fixed submerged sphere versus amplitude and frequency of internal waves and the sphere's position relatively to the inner interface are presented.

The aim of the present series of experiments on background and ship internal waves interaction is a preliminary study of a phenomenon: reveal of resonant regimes and ship internal waves parameters transformation. An another destine is the experimental data use for the inverse hydrodynamics problem: calculation of the wave drag on a submerged body by internal waves parameters.

2. Experimenal equipment

[1]E-mail: olga@hydro.nnov.su

Experiments have been carried out in the thermostratified tank in the IAP RAS with the horizontally homogeneous thermocline – type stratification and overall dimensions $L*B*H = 5*1.6*1.2\ m^3$. The thermocline thickness was $d = 0.20\ m$ with its center's depth $h = 0.30\ m$. The upper and the lower layers densities were equal to the fresh water density for the temperature $t = 20^0$C and $t = 4^0$C respectively. Profiles of the temperature $t = f(z)$, the Brunt–Vaisala frequency $N = f(z)$ and the conventional density $\sigma = f(z)$ are shown in Fig. 1.

As the ship internal waves source a sphere of diameter $0.15\ m$ with its center position of $0.30\ m$ and $0.26\ m$ was used. In the first case several lower modes were excited, in the latter case the first mode prevailed.

The working velocity value $U = 0.03\ m/s$ was chosen because of maximum respective induced internal waves amplitude as the resonant case of the I-mode generation (with respect to the mode's phase velocity) occurs.

The Reynolds and the Froude numbers provided were $Re = 3614$ and $Fi = 0.67$ respectively.

$$Re = \frac{U * D}{\nu} \tag{1}$$

where

U sphere's velocity,

D diameter of the sphere,

ν the fresh water kinematic viscosity coefficient for the temperature 12°C (water temperature in the center of the thermocline).

$$Fi = \frac{U}{N_{max} * D} \tag{2}$$

$N_{max}(z)$ the maximum value of the Brunt–Vaisala frequency:

$$N(z) = \left(-\frac{g}{\rho_o}\frac{d\rho}{dz}\right)^{1/2} \tag{3}$$

where

g acceleration due to gravity;

ρ_o water density at the center of the thermocline;

$d\rho/dz$ density variation due to the temperature variation at the horizon.

The data recording and processing system is completely automated. Internal waves pattern was recorded by horizontal chains of thermistors placed at the thermocline center depth and at a distance of $2D$ from the sphere's trajectory. Digitized thermistors signals were visualized at the TV monitor.

Plane regular internal waves generation was provided by the horizontal circular hemicylinder of a diameter $0.10\ m$ installed at one of the butt–end walls of the basin at a depth of the thermocline's center. Wavemaker oscillation frequencies were $0.11\ s^{-1}$, $0.18\ s^{-1}$ and $0.26\ s^{-1}$ (are shown by dashed lines in Fig. 2) with the maximum Brunt–Vaisala frequency $N_{max} = 0.35\ s^{-1}$. The amplitude of wavemaker oscillations was equal to 2.5 cm with the background internal waves amplitude of about 0.5 cm which is of the same order with the ship internal waves induced by the sphere.

One of the serious problems for experiments on internal waves generation is wave damping. Wave's natural relaxation time is, as a rule, lost time. In the case of a two–layered liquid this problem may be solved by means similar to surface waves damping.

The case of continuous stratification is more complicated. In this experiment a rather simple device, made of a great number of hanging down across the thermocline narrow cellophane ribbons, fixed at a horizontal framework, was installed in the far end of the tank and reduced waiting time twice. The device consists of two side parts (on each side wall) with a centerplane space for a towed body and has a longitudinal dimension of a half of typical (for this tank) internal waves length ($\lambda \sim 1.40\,m$). The internal waves damping effects due to scattering of the running wave energy whilst the wave and damping ribbons interaction. So, the regime of running background internal waves was provided.

3. Experimental results

After stationary background internal waves recording the sphere was towed along the tank favourably to the background waves propagation and resulting internal waves profiles were fixed.

In the case of the sphere's depth $h = 0.30\,m$ and the sphere's velocity of $U = 0.03\,m/s$ the first and the second modes generation is provided. Corresponding ship internal waves frequencies are in the "middle" range – about half of the $N_{max}(z) = 0.35\,s^{-1}$ (see Figs. 2 and 3).

The ship internal waves transformation has been examined by the graphic subtraction of the background waves profile from the resulting data. The spectrum analysis of obtained profiles showed that in the mentioned case the background wave of high and low frequency ($0.11\,s^{-1}$ and $0.26\,s^{-1}$) interacts weakly with the ship internal waves system. I.e. resulting internal wave spectrum is a superposition of ship and background waves spectra. But middle frequency ($0.11\,s^{-1}$) seems to be resonant for those regimes (see Fig. 3).

In the case of the sphere's depth $h = 0.26\,m$ the first mode prevailes in the ship waves system and corresponding higher frequencies close to $N_{max}(z)$ are excited. As it is shown in Fig. 4 the low-frequency background wave didn't transform the ship internal waves system and presented a sharp line in the resulting spectrum. For higher background wave frequencies the initial spectrum transformed.

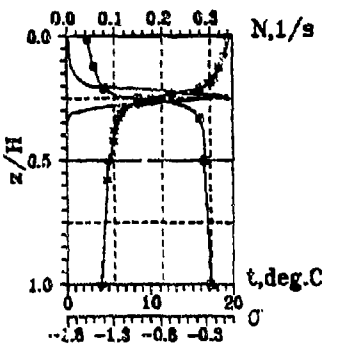


Fig. 1.
The Brunt-Vaisala frequency (——) the water temperature and (+++++) the conventional density (□□□□□) versus basin's depth.

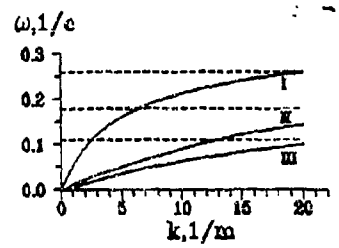


Fig. 2. Dispersion curves for three lower internal waves modes.

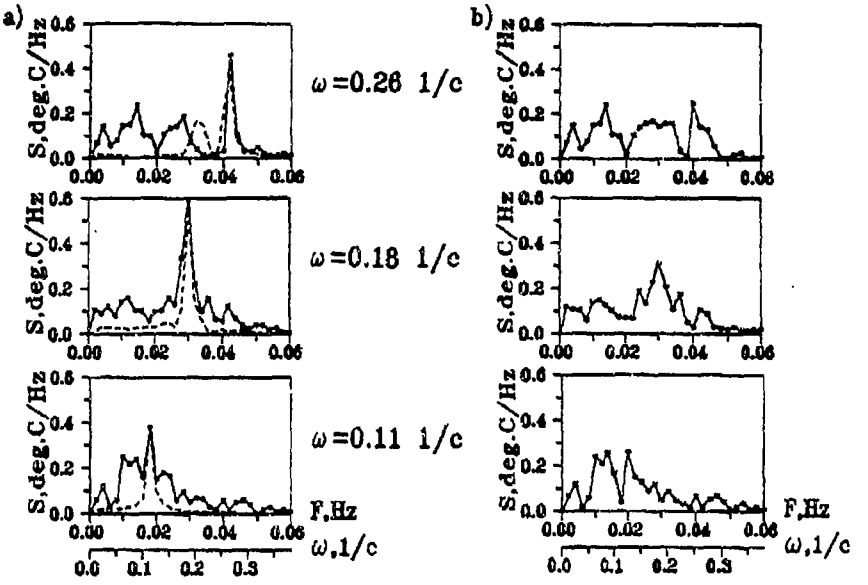


Fig. 3. IW spectra (sphere at the depth h = 0.3 m):
a) ship waves with background waves: b) ship waves only
——— ship and background waves,
------- background waves.

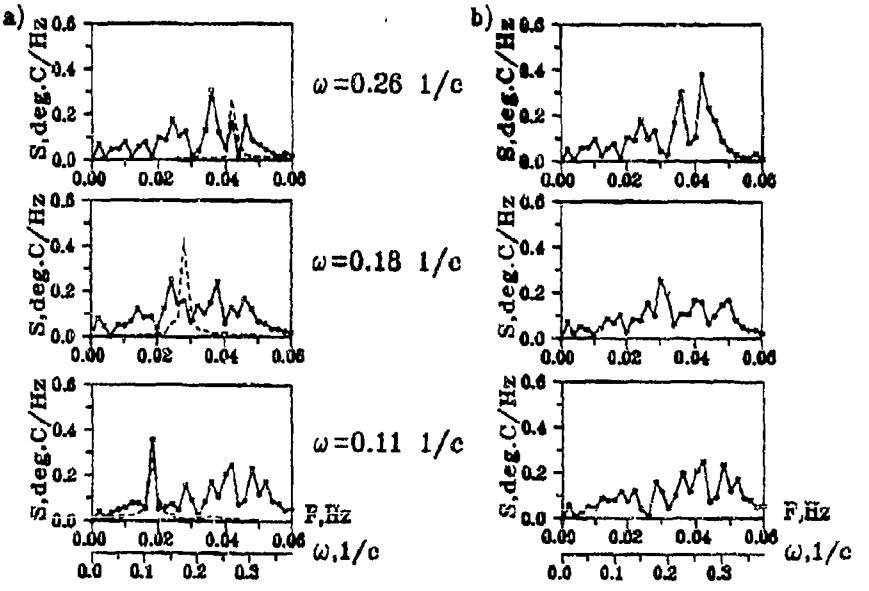


Fig. 4. IW spectra (sphere at the depth h = 0.26 m):
——— a) ship waves with background waves: b) ship waves only
------- ship and background waves,
background waves.

4. References

1. Sturova I. V. 1992: Generation and scattering of waves by a submerged body moving in the stratified liquid. *Proceedings of the 4th annual workshop "Laboratory modelling of dynamic processes in the ocean"*. Svetlogorsk. P.17 (in Russian)
2. Sturova I. V. 1993: Regular waves influence on the moving sumerged body in the stratified liquid. *Proceedings of the sci.–tecn. conference "Improvement problems of the forecasting complex methods of the ships and ocean treaty facilities navigational characteristics"*. St.–Petersburg. 149-151 (in Russian)
3. Wu G. X., Eatock Taylor R. 1987: Hydrodynamic forces on submerged cylinders at forward speed. *Proc. Roy. Soc. London*, A414, N. 1846, 149-170
4. Wu G. X. 1991: Hydrodynamic forces on a submerged cylinder advancing in water waves of finite depth. *J. Fluid Mech.*, 224, 645-659
5. Yermanyuk Ye. V. 1993: An experimental study of the power influence of internal waves on a fixed sphere. *Proceedings of the sci.–tecn. conference "Improvement problemsof the forecasting complex methods of the ships and ocean treaty facilities navigational characteristics"*. St.–Petersburg. 142-143 (in Russian)

EFFECT OF STRATIFICATION ON THE HYDRODYNAMIC LOADS ACTING ON A SUBMERGED CYLINDER ADVANCING IN WATER WAVES

I.V.Sturova

Lavrentyev Institute of Hydrodynamics
630090 Novosibirsk, Russia
E-mail: wave@hydro.nsk.su

The 2-D problem on radiation and scattering of the small- amplitude surface and internal waves by a horizontal cylinder moving at constant depth under a pycnocline is considered. The fluid is nonviscous and incompressible. The sharp and smooth pycnoclines are simulated by the two-layer fluid and the three-layer one , respectively. In the two-layer fluid, the upper layer can be both infinite and bounded by a rigid lid or a free surface. In the three-layer fluid, the upper layer is bounded by a rigid lid. In all the cases concerned, a submerged body is fully located in the lower layer of infinite depth.

Previously the problem of a submerged body advancing in regular water waves has been considered only for surface waves in homogeneous fluid. The most efficient method of its solution for bodies of complicated shape in a 2-D and 3-D flows is recognized the coupled finite element method (CFEM) [1, 2]. The velocity potential is represented by the finite element method in a narrow region surrounding a body and by the boundary integral equation in the outer region. This method may be also used in a stratified fluid if the density varies only on the depths above and below a submerged body.

This paper describes the author's results given in [3-7]. The case of the two-layer fluid under a lid involving a possible occurrence of the only free internal waves is most completely analyzed.

Let the fixed frame of reference be taken with the $\bar{x}$-axis directed along an equilibrium position of the interface, orthogonally with respect to a cylinder axis, and the y-axis pointed vertically upwards. In the undisturbed state, the upper layer with the thickness H and density ρ_1 occupies the domain $-\infty < \bar{x} < \infty$, $0 < y < H$, the lower one, with the density $\rho_2 = \rho_1(1+\varepsilon)$ $(\varepsilon > 0)$, occupies the domain $-\infty < \bar{x} < \infty$, $y < 0$. The fluid flow in each layer is irrotational.

In the fixed frame of reference the incident potential may be written as

$$\psi_0^{(s)} = \frac{i\omega_0}{k_0}\phi_0^{(s)} \exp[i(\omega_0 t \mp k_0 \bar{x})],\ \phi_0^{(1)} = -\frac{\cosh k_0(y-H)}{\sinh k_0 H},\ \phi_0^{(2)} = e^{k_0 y},$$

where the incident wave frequency ω_0 depends on the wave number k_0 according the dispersion relation,

$$\omega_0 = \Omega(k_0), \quad \Omega(k) = \sqrt{\varepsilon g k / B(k)}, \quad B(k) = 1 + \varepsilon + \coth kH,$$

signs '+' and '-' correspond to waves travelling from right and from left, respectively, superscript s is equal to 1 for the upper layer and 2 for the lower one, g is the gravitational acceleration.

In the moving reference frame $x = \bar{x} - Ut$ the total potential can be written as

$$\Phi^{(s)}(x,y,t) = -Ux + U\bar{\Phi}^{(s)}(x,y) + \ \mathrm{Re}\sum_{j=0}^{4} \eta_j \Phi_j^{(s)}(x,y)e^{i\omega t},$$

where $\bar{\Phi}^{(s)}$ is the steady potential due to the unit forward speed; the components $\Phi_j^{(s)}$ $(j = 1,2,3)$ are the radiation potentials due to motions of the cylinder with unit amplitude in each of three degrees of freedom; η_j are corresponding motion amplitudes; $\Phi_0^{(s)} = \phi_0^{(s)} \exp(\mp ik_0 x)$ and $\Phi_4^{(s)}$ are the potentials of the incident and diffracted waves, respectively; and $\eta_0 = \eta_4$ is the incoming wave amplitude. In the moving reference frame, the incident waves arrive with the encounter frequency $\omega = \omega_0 \mp k_0 U$.

Based on the assumptions of linear potential flow theory, we can write the following governing equations for the steady potential

$$\Delta\bar{\Phi}^{(1)} = 0 \quad (0 < y < H), \qquad \Delta\bar{\Phi}^{(2)} = 0 \quad (y < 0) \tag{1}$$

with boundary conditions

$$\partial\bar{\Phi}^{(1)}/\partial y = 0 \quad (y = H),$$

$$(1+\varepsilon)\frac{\partial^2\bar{\Phi}^{(2)}}{\partial x^2} - \frac{\partial^2\bar{\Phi}^{(1)}}{\partial x^2} + \frac{\varepsilon g}{U^2}\frac{\partial\bar{\Phi}^{(1)}}{\partial y} = 0, \ \frac{\partial\bar{\Phi}^{(1)}}{\partial y} = \frac{\partial\bar{\Phi}^{(2)}}{\partial y} \quad (y = 0),$$

$$\frac{\partial\bar{\Phi}^{(2)}}{\partial y} \to 0 \ (y \to -\infty), \frac{\partial\bar{\Phi}^{(s)}}{\partial x} \to 0 \ (x \to \infty), \left|\frac{\partial\bar{\Phi}^{(s)}}{\partial x}\right| < \infty \ (x \to -\infty).$$

The boundary condition for $\bar{\Phi}^{(2)}$ should be satisfied at a mean position of the body surface L: $\partial\bar{\Phi}^{(2)}/\partial n = n_x$ $(x, y \in L)$, where $\vec{n}$ is the inward normal of the cylinder surface and n_x is the component of $\vec{n}$ in the x-direction.

The radiation and diffraction components of potential satisfy the equations, similar to (1), with boundary conditions

$$\partial\Phi_j^{(1)}/\partial y = 0 \quad (y = H), \tag{2}$$

$$(1+\varepsilon)D\Phi_j^{(2)} - D\Phi_j^{(1)} + \varepsilon g\partial\Phi_j^{(1)}/\partial y = 0, \ \partial\Phi_j^{(1)}/\partial y = \partial\Phi_j^{(2)}/\partial y \quad (y = 0), \tag{3}$$

$$\partial\Phi_j^{(2)}/\partial y \to 0 \quad (y \to -\infty), \tag{4}$$

$$\partial\Phi_j^{(2)}/\partial n = i\omega n_j - Um_j \ (j = 1,2,3), \quad \partial\Phi_4^{(2)}/\partial n = -\partial\Phi_0^{(2)}/\partial n \quad (x, y \in L),$$

where

$$D \equiv (U\partial/\partial x - i\omega)^2, \ (n_1, n_2) = (n_x, n_y), \ n_3 = (y - y_0)n_x - (x - x_0)n_y,$$

$$(m_1, m_2, m_3) = \left\{\frac{\partial^2\bar{\Phi}^{(2)}}{\partial n\partial x}, \frac{\partial^2\bar{\Phi}^{(2)}}{\partial n\partial y}, \frac{\partial}{\partial n}\left[(y - y_0)\left(\frac{\partial\bar{\Phi}^{(2)}}{\partial x} - 1\right) - (x - x_0)\frac{\partial\bar{\Phi}^{(2)}}{\partial y}\right]\right\},$$

x_0 and y_0 are the coordinates of a point with respect to which the body oscillates rotationally.

The radiation condition for $\Phi_j^{(s)}$ $(j = 1, ..., 4)$ states that a wave travelling in the direction of the forward speed and with its group velocity larger than the forward speed is far in front of the body, and otherwise the waves propagate behind.

The moving body in waves is affected by the hydrodynamic force $\vec{F}$ and moment M determined by integrating the fluid pressure $p = -\rho_2(\partial\bar{\Phi}^{(2)}/\partial t + |\nabla\Phi^{(2)}|^2/2)$ over the cylinder surface L

$$\vec{F} = \int_L p\vec{n}dl, \quad M = \int_L pn_3 dl. \tag{5}$$

The representation $\vec{F} = (F_1, F_2)$, $M = F_3$ is commonly used and for the linearized problem Eq.(5) is substituted for the sum

$$F_j = F_{sj} + \mathrm{Re}(F_{nj} + F_{ej})e^{i\omega t}, \tag{6}$$

where the first term is due to an steady speed of the body and equals

$$F_{sj} = \rho_2 U^2 \int_L (\partial\ddot{\Phi}^{(2)}/\partial x - |\nabla\ddot{\Phi}^{(2)}|^2/2)n_j dl.$$

The second term in (6) is the contribution from the unsteady potentials $\Phi_j^{(2)}$ $(j = 1, 2, 3)$. Three components of the force and the moment are written in the matrix form

$$F_{nj} = \sum_{k=1}^{3} \eta_k \tau_{jk}, \quad \tau_{jk} = -\rho_2 \int_L (i\omega\Phi_k^{(2)} + \vec{V}\nabla\Phi_k^{(2)})n_j dl,$$

where $\vec{V} = U\nabla(\ddot{\Phi}^{(2)} - x)$ is the velocity vector of a steady flow in the lower layer relative to the moving reference frame. The radiation forces are represented in the form $\tau_{jk} = \omega^2\mu_{jk} - i\omega\lambda_{jk}$, where μ_{jk} and λ_{jk} are known as the added masses and damping coefficients, respectively.

The exciting forces are determined as follows

$$F_{ej} = -\rho_2\eta_0 \int_L [i\omega(\Phi_0^{(2)} + \Phi_4^{(2)}) + \vec{V}\nabla(\Phi_0^{(2)} + \Phi_4^{(2)})]n_j dl.$$

To use the coupled finite element method it is necessary to determine the Green function $G^{(s)}(x, y, \xi, \eta)$, satisfying the equations

$$\Delta G^{(1)} = 0 \quad (0 < y < H), \quad \Delta G^{(2)} = 2\pi\delta(x - \xi, y - \eta) \quad (y < 0)$$

and boundary conditions similar to (2)-(4). The solution of the problem for the Green function in the lower layer $G^{(2)}$ takes the form:

$$G^{(2)} = \ln(rr_1) + 2(1 + \varepsilon)\mathrm{pv}\int_0^\infty \frac{B(k)}{kP(k)} e^{k(y+\eta)} \times$$

$$\times \left\{ \left[(U^2k^2 - \omega^2)^2 - (U^2k^2 + \omega^2)\Omega^2(k) \right] \cos k(x - \xi) + 2i\omega kU\Omega^2(k) \sin k(x - \xi) \right\} dk +$$

$$+\pi\{\alpha_1 \exp[k_1(y + \eta - i(x - \xi))] - \alpha_2 \exp[k_2(y + \eta - i(x - \xi))] -$$

$$-\alpha_3 \exp[k_3(y + \eta + i(x - \xi))] + \alpha_4 \exp[k_4(y + \eta + i(x - \xi))]\},$$

where pv indicates the principal-value integration,

$$r^2 = (x - \xi)^2 + (y - \eta)^2, \; r_1^2 = (x - \xi)^2 + (y + \eta)^2,$$

$$P = \prod_{s=1}^{4} P_s, \; P_{1,2}(k) = Uk + \omega \mp \Omega(k), \; P_{3,4}(k) = Uk - \omega \mp \Omega(k),$$

$$\alpha_s = \frac{i(1 + \varepsilon)\Omega(k_s)B(k_s)}{2k_s[U - \gamma c_g(k_s)]} \; (\gamma = 1 \text{ at } s = 1, 2, 3 \text{ and } \gamma = -1 \text{ at } s = 4),$$

$c_g(k_s) = d\Omega/dk\ |_{k=k_s}$ is the group velocity of the wave k_s. The equation $P_1(k) = 0$ has two simple real solutions, k_1 and k_2, with $k_1 > k_2$, if only

$$U < U_c, \quad \omega < \omega_c, \tag{7}$$

where $U_c = \sqrt{\varepsilon g H}$ is the critical velocity for a steady problem in the two-layer fluid and $\omega_c = \Omega(k_c) - Uk_c$ is defined post-solving the equation $c_g(k_c) = U$. Solutions k_1 and k_2 coincide, if $\omega = \omega_c$, and are absent, if conditions (7) are not met. There are no real solutions for equation $P_2(k) = 0$. In contrast, the equations $P_3(k) = 0$ and $P_4(k) = 0$ always possess unique real solutions, such as k_3 and k_4, respectively, with $k_3 > k_4$.

With $H \to \infty$, the k_s solutions are equal to

$$k_{1,2} = \frac{\bar{g}}{2U^2}(1 - 2\tau \pm \sqrt{1 - 4\tau}), \quad k_{3,4} = \frac{\bar{g}}{2U^2}(1 + 2\tau \pm \sqrt{1 + 4\tau}),$$

where $\tau = \omega U/\bar{g}$, $\bar{g} = \varepsilon g/(2 + \varepsilon)$. In this case $\omega_c = \bar{g}/4U$. With $\varepsilon \to \infty$ one will obtain the known solution for a homogeneous fluid with a free surface [1].

The numerical calculations are performed for the elliptic cylinder

$$x^2/a^2 + (y + h)^2/b^2 = 1,$$

where a and b are the large and small half-axes of the ellipse, h is the depth of submergence of its center under the interface.

The steady loads (a wave resistance, a lift and a trim moment) has been studied extensively for the different types of the density stratification in [3]. The numerical calculations are compared with the approximate analytical solution based on the use of the Kochin function and suitable for a body deep-submerged under the interface.

For simplicity let us give the approximate solution for a wave resistance in the two-layer fluid under a lid :

$$F_x = -\frac{(1 + \varepsilon)\rho_2 \Omega(\lambda)}{2B(\lambda)[U - c_g(\lambda)]} K^2(\lambda).$$

Here λ is the root of an equation $\Omega(\lambda) = U\lambda$, which exists only at $U < U_c$ and K is the Kochin function for the elliptic cylinder

$$K(\lambda) = 2\pi U b \sqrt{\frac{a + b}{a - b}} J_1(\lambda\sqrt{a^2 - b^2}) e^{-\lambda h},$$

where J_1 is the Bessel function of the first order. For small values of the product $\lambda\sqrt{a^2 - b^2}$ the Kochin function may be presented $K(\lambda) \approx \pi U b \lambda (a + b) e^{-\lambda h}$. The wave resistance determined by this means is called the dipole solution.

The approximate solution for the wave resistance in two-layer fluid with a free surface presents a sum of surface and internal wave contributions.

A steady loads for the elliptic cylinder in the two-layer fluid with a free surface determined by CFEM with the element number $m = 18$ are shown in Fig. 1 for $a = h = 2b$, $\varepsilon = 0.03$, $H = b$, $x_0 = 0$, $y_0 = -h$ (solid lines). The following designations are used $(\bar{F}_x, \bar{F}_y) = (-F_x, F_y)/\rho_2 U^2 b$, $\bar{M} = -M/\rho_2 U^2 b^2$. The above values are compared with similar those for the two-layer fluid under a lid (dark points) over the range of the Froude number $0 < \mathrm{Fr} = U/\sqrt{gh} < 0.2$ and for a homogeneous fluid ($\varepsilon = 0$) (light points) over the rauge $0.2 < \mathrm{Fr} < 3$. In Fig. 1 are shown the approximate solution (dot-and-dash line) for a wave resistance and dipole solution (dash line). With small values

of the Froude number, the internal waves are principally excited and their characteristics agree practically with those of the two-layer fluid under a lid. Then with increasing Fr the generation of the internal waves ceases and the only surface waves are excited. The critical velocity of the body for internal waves shown with an arrow is $U_c/\sqrt{gh} = 0.1224$.

In the three-layer model ot a smooth pycnocline the fluid density distribution in the undisturbed state takes the form:

$$\rho(y) = \begin{cases} \rho_1 & (H_1 < y < H_1 + H_2), \\ \rho_1[1 + \varepsilon(1 - y/H_1)] & (0 < y < H_1), \\ \rho_2 = \rho_1(1 + \varepsilon) & (y < 0), \end{cases}$$

where H_1, H_2 are the depths of middle and upper layers, respectively. The fluid flow in the upper and lower layers is irrotational. The wave flow equation for the middle linearly stratified layer is used in the Boussinesq approximation.

The steady loads in the three-layer fluid are presented in Fig.2 at $\varepsilon = 0.03$, $H_1 = b$, $H_2 = 0.5b$, $a = 2b$, $h = 1.5b$. In Fig.2 are shown the results of CFEM (solid lines), the approximate solution for the wave resistance (dash-and-dot line) and dipole solution (dash line). The following critical velocities of generating appropriate modes of internal waves are depicted (arrows with numbers): $U/\sqrt{gh} = 0.1137$ ($n = 1$), 0.0336 ($n = 2$), 0.0186 ($n = 3$). For comparison with the two-layer fluid, the value $\bar{h} = h + H_1/2$ is entered, which defines the distance from the body centre to the pycnocline midline. Fig. 2 gives the only range of values $U/\sqrt{g\bar{h}} \geq 0.013$ wherein there are yet no more than three internal modes. From the comparison of Figs. 1 and 2 it is obvious that the internal wave in the two-layer fluid and the first wave mode in the three-layer one have a similar hydrodynamic effect.

The solution of radiation and diffraction problems at $U = 0$ are obtained for the two-layer fluid bounded both by a rigid lid and by a free surface [4,5]. In the diffraction problem, apart from exciting forces, also is determined the behavior of scattered waves in a far field. The reciprocity identities relating the solutions of radiation and diffraction problems are derived. The first diagonal term of the radiation load for the elliptic cylinder in the two-layer fluid with a free surface is demonstrated in Fig.3. The flow parameters coincide with those used in Fig.1. The coefficients μ_{11} and λ_{11} are compared with similar values for the two-layer fluid under a lid (dark points) and the homogeneous fluid (light points). For the damping coefficient λ_{11}, the approximate solution obtained by the Kochin function is shown with dash-and-dot line and the dipole solution is denoted with dash line. With small frequency of body oscillation, the internal waves are significantly excited and their characteristics agree practically with those of the two-layer fluid under a lid. As the frequency increases, the generation of internal waves is weaken and the surface waves whose characteristics are slightly affected by the density variation become dominant.

An interesting peculiarity of the diffraction problem for stratified fluid is that when the given mode wave incidents on a body it scatters not only into itself but also into all the other modes. This is one of the mechanisms of energy redistribution due to wave motions, in particular, that of the surface wave energy transfer to depth.

Based on the approximate solution for a deep submerged body, the influence of anomalous frequency dispersion of internal waves on the processes of scattering and generation is determined [6]. This internal waves are characterized by a nonmonotonic

behavior of their group velocities. One example of this fluid is a three-layer one involving linearly stratified upper and middle layers and a homogeneous lower one. In this case the mode 'leap-frog' is observed when the excitement of higher modes is more intensive then of lower ones.

For radiation and diffraction problems with forward speed all the components of loads are correlated for the cylinder moving under the free surface in a homogeneous fluid and under the interface in the unbounded and the bounded by lid two-layer fluid [7]. Contrary to the case without forward speed the added mass and damping coefficients have no longer the symmetry properties and there are some motion regimes where the damping coefficients take negative values. Starting from the assumption of a deep submersion of a body, the amplitudes of radiation and diffraction waves in the far field as well as the diagonal damping coefficients and exciting forces are calculated. The numerical calculations of μ_{jj} and λ_{jj} are shown in Fig.4 for the elliptic cylinder located under the free surface in the homogeneous fluid (a), under the interface in the two-layer unbounded fluid (b) and in the two-layer fluid with a bounded upper layer (c) given the same parameters as in Fig.3 and $U/\sqrt{\bar{g}b} = 0.4$. In Fig.4 are shown also the approximate values of λ_{jj} for the same three cases of the fluid density stratification. The following designations are used

$$M_{jj} = \mu_{jj}/\mu^*_{jj}, \quad \Lambda_{jj} = \pi b\omega\lambda_{jj}/\bar{g}\mu^*_{jj}, \ (\mu^*_{11}, \mu^*_{22}, \mu^*_{33}) = \pi\rho_2[b^2, a^2, (a^2-b^2)^2/8].$$

With forward speed the approximate solution is seen to provide a quite rough representation for damping coefficients, especially for λ_{33}. The values $\omega_c^2 b/\bar{g} = 0.3906$ (Figs. 4a,b) and 0.3642 (Fig. 4c) are indicated by arrows.

References

1. Wu G.X., Eatock Taylor R. Hydrodynamic forces on submerged oscillating cylinders at forward speed. Proc. Roy. Soc. London, 1987, v.A414, n.1846, pp.149-170.

2. Wu G.X., Eatock Taylor R. The numerical solution of the motions of a ship advancing in waves. Proc. 5th Int. Conf. on Num. Ship Hydrodynam., Hiroshima, pp.386-394.

3. Sturova I.V. Effect of internal waves on the hydrodynamical characteristics of a submerged body. Izv.RAN. Fiz.Atmos.i Okeana, 1993, v.29, n.6, pp.732-738 (in Russian).

4. Sturova I.V. Two-dimensional submerged body without forward speed in waves of two-layer fluid. Izv.RAN, Mekh.Zhidk.i Gaza (in Russian) (in press).

5. Sturova I.V. Scattering of surface and internal waves on submerged body. Computational Technology, Novosibirsk, 1993, v.2, n.4, pp.30-45 (in Russian).

6. Sturova I.V. Effect of anomalous dispersion dependence on scattering and generation of internal waves. Prikl.Mekh.Tekhn.Fiz. (in Russian) (in press).

7. Sturova I.V. Two-dimensional submerged body at forward speed in waves of two-layer fluid. Prikl.Mekh.Tekhn.Fiz. (in Russian)(in press).

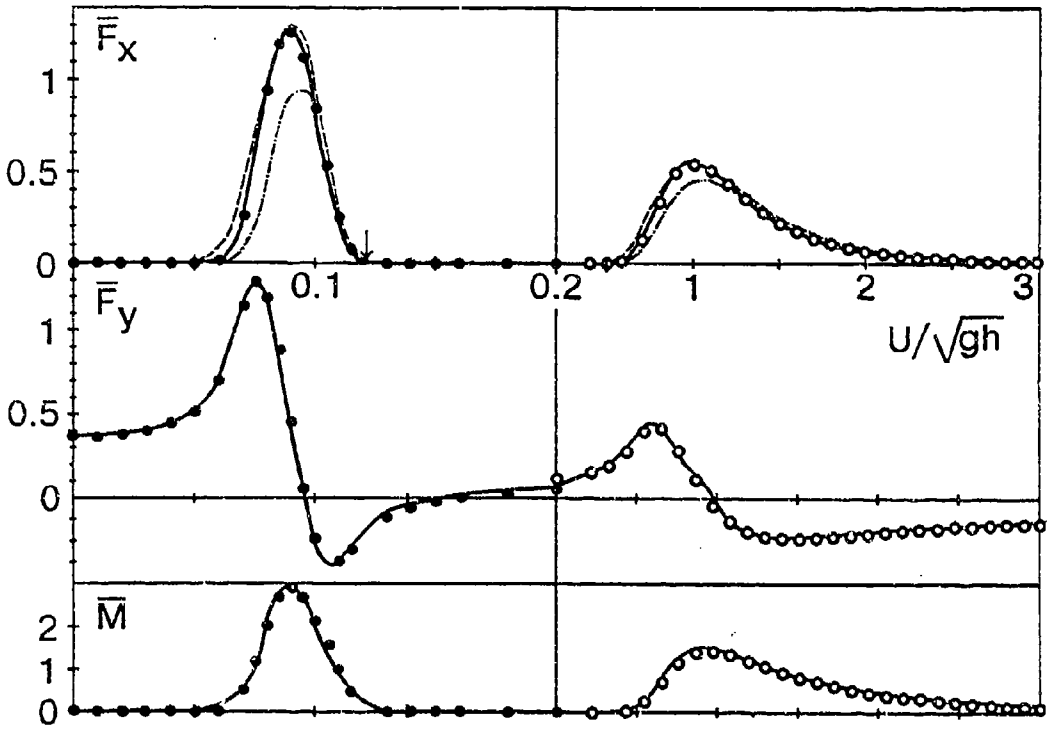

$\bar{F}_x$
1
0.5
0
0.1
0.2
1
2
3
$\bar{F}_y$
$U/\sqrt{gh}$
$\bar{M}$
2
1
0

Fig. 1

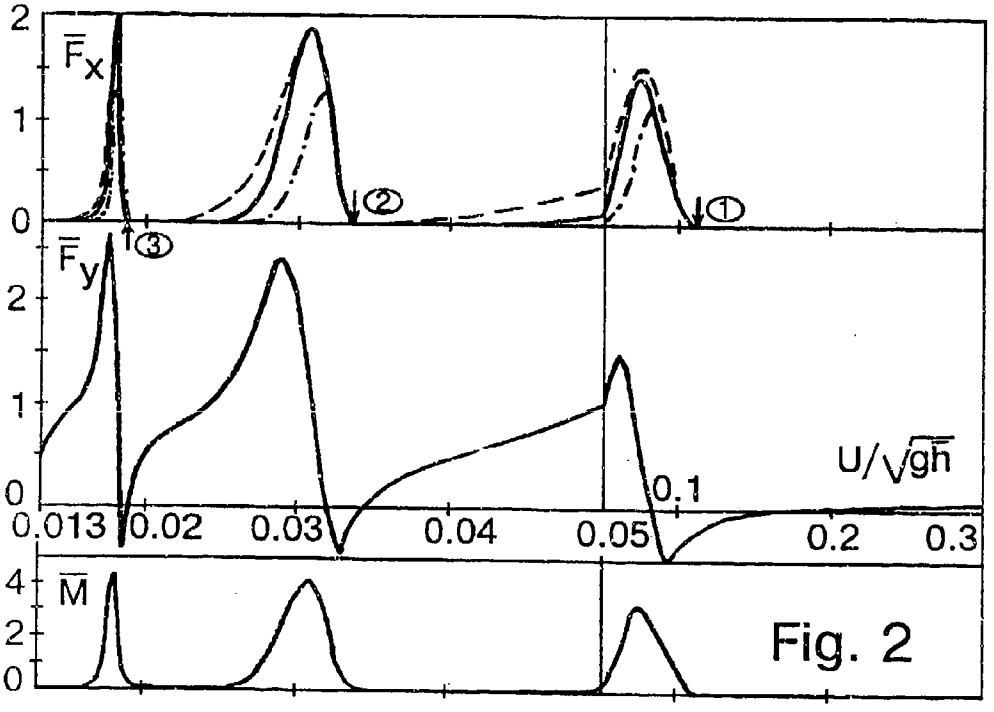

2
$\bar{F}_x$
1
0
②
①
③
$\bar{F}_y$
$U/\sqrt{gh}$
0.1
0.013
0.02
0.03
0.04
0.05
0.2
0.3
4
$\bar{M}$

Fig. 2

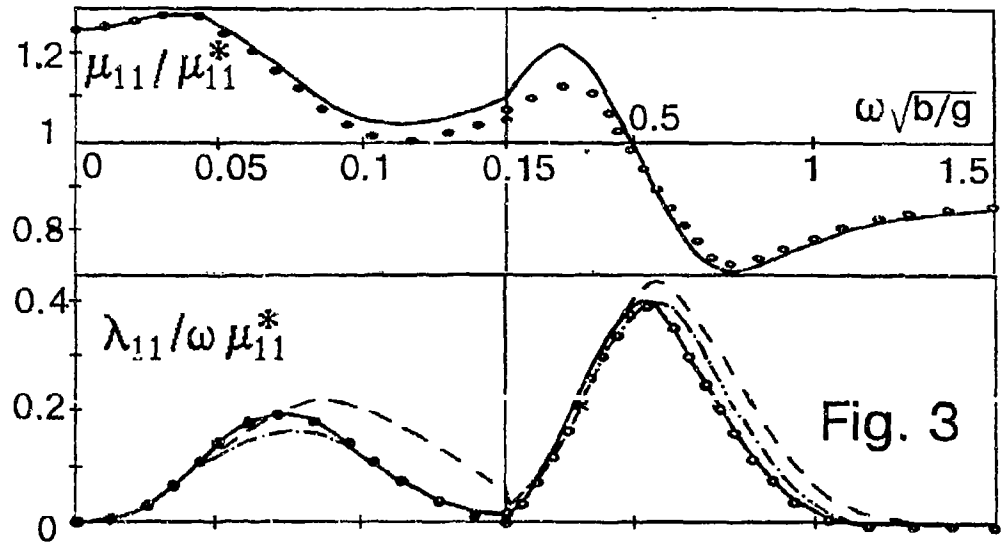

1.2
1
0.8
μ_{11}/μ_{11}^*
0
0.05
0.1
0.15
0.5
1
1.5
$\omega\sqrt{b/g}$
0.4
0.2
0
$\lambda_{11}/\omega\,\mu_{11}^*$

Fig. 3

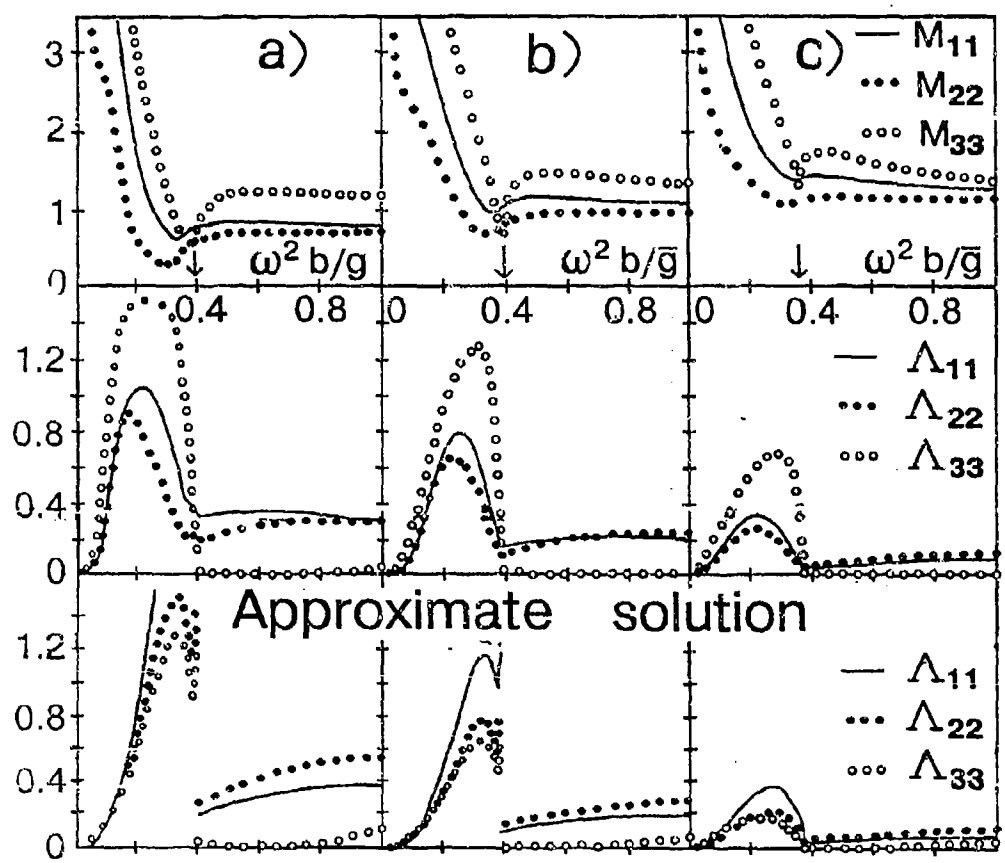

a)
b)
c)
M_{11}
M_{22}
M_{33}
$\omega^2\,b/g$
$\omega^2\,b/\bar{g}$
$\omega^2\,b/\bar{g}$
Λ_{11}
Λ_{22}
Λ_{33}
Approximate solution
Λ_{11}
Λ_{22}
Λ_{33}

Fig. 4

Lee waves and hydrodynamical loads due to the motion of a submerged horizontal circular cylinder in a three-layer fluid.

by Oivind A. Arntsen, Dr.ing.,
Department of Structural Engineering,
The Norwegian Institute of Technology.

Abstract: Laboratory experiments and analytical studies investigating the interaction of two-dimensional, uniform stratified flow with a submerged horizontal circular cylinder are presented. Measurements were made of the interfacial waves formed behind the cylinder towed horizontally at constant speeds, and of the drag and lift forces exerted on the cylinder. An analytical linear model that describes the wave field and the associated wave induced drag force is formulated. In this model, the water is modeled as a uniform flow of three layers of inviscid and immiscible fluids. A solution is found for the case of the cylinder located in the upper layer. The experiments showed that large amplitude first mode internal waves are generated when the cylinder is towed at about one half of the long wave celerity of first mode waves. The analytical results underestimate the wave-induced forces, but demonstrate the role of a finite stratified layer. The results are applied to the proposed tube bridge across Hoegsfjorden in Norway.

Introduction: Norwegian fjords often exhibits a distinct density variation in the upper water. Between the upper mixed layer and the salt water layer a transition zone exists (often called the pycnocline). This region of strongly variable density can act as a duct for low energy density waves that propagate on the pycnocline without significant interference with the free surface to the atmosphere. The free-surface vertical displacement due to these internal waves is much smaller, by a factor $\Delta\rho/\rho_3$, than that of the internal disturbance; and thus, for many practical applications, the free surface may be considered as a "rigid-lid".

Depending on the type of disturbance and the basin in question, different types of waves may occur, standing, propagating or combinations. For example, the disturbance of a slowly moving object on the surface of the water, may be an effective internal wave maker, while at the same time disturbances on the free surface is hardly seen. Similarly, a uniform flow over a submerged object such as an underwater sill can originate standing internal waves, known as lee-waves. These effects are closely related to the phenomenon called "dead-water". This effect, known for sailors for centuries, was studied for the first time by Ekman (1906). The advent of offshore activity has again led to slow tows, and a re-appearance of "dead-water" was documented by Arntsen (1986) during a towing of the large volume structure, Condeep Gullfaks A, off the Norwegian coast in August 1985. More recently, a renewed interest has evolved connected with the effort of analyzing the induced internal wave pattern produced by moving vessels using remote sensing means. The emphasis there is on determining the kinematic features of the internal wave-field, rather than the wave resistance.

In this paper I address a somewhat different, but related problem. During the last years a new type of structure has been proposed to be installed in Norwegian waters - the submerged tube bridge. This is a watertight hollow cylinder (proposed to be of circular crossection) with an inner diameter large enough for road traffic. It is located below the sea surface deep enough such that ships may pass over it. Carpenter and Keulegan (1960) present a series of experiments pertinent to the topic of this question. Submerged cylinders both circular and non-circular were towed at constant speed in water consisting of two layers of water with different salinity (density) and an extremely thin stratified interface layer. The

noncircular cylinders had a length to thickness ratio equal to three and were not very streamlined. They found that the main characteristics of the internal waves were independent of the shape of the cylinders. Carpenter and Keulegan give also a linear potential solution for the flow in two immiscible fluid layers and disturbed by a disturbance modeled as the flow around a circular cylinder in homogeneous water. Their model fails to estimate the observed wave heights, but it works well for wave lengths. In their experiments Carpenter and Keulegan did not include measurements of the hydrodynamic forces on the cylinder. They suggested that the total drag force on the cylinder can be estimated by adding the wave induced drag to the drag present in homogeneous water. The wave induced drag is to be calculated from the lee wave and stratification variables. However, it is not as obvious as for streamlined obstacles that the total drag force is given by this sum. The presence of stratification may move the point of separation and alter the form drag part of the force.

The investigation discussed in this paper resembles much that of Carpenter and Keulegan. The basic difference is the inclusion of force measurements in the experiments and that the stratified layer is of finite width rather than shallow. It is demonstrated that the dispersion effect of a finite width of the stratified layer down-shift the towing speed for maximum "dead-water" effect. The inclusion of a stratified layer in the theoretical framework of Carpenter and Keulegan shows improvement of describing the computed internal wave-field. In spite of this success, the observed maximum wave height is about two times the value of the theoretical, but an adjustment of a free parameter γ can correct this deficiency. The investigation provides a database for "dead-water" forces exerted on submerged cylinders in stratified uniform flows, and guidelines for applications in full scale are suggested.

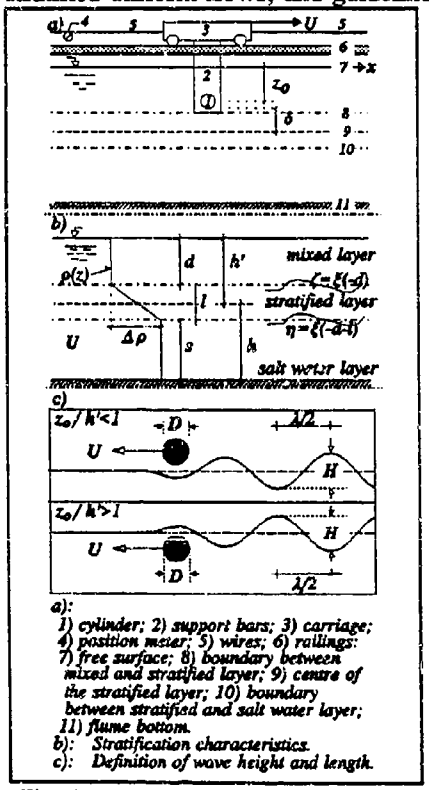


Fig. 1 Definition sketches of the setup.

Laboratory experiments: In the following, a brief description of the present experimental arrangement and techniques for the measurements of internal waves and hydrodynamic forces are given. Only some of the experimental results will be shown. A more detailed description and presentation is given in Arntsen (1994). The work presented covers two-dimensional model tests of a fixed submerged circular cylinder towed at constant speed in three-layer stratified water.Of a total of 350 tows, 225 were with stratification and 125 in homogeneous water. The runs were performed in a test channel which was a 6*m* long, 1*m* wide and 0.4*m* deep plywood tank. Over a distance 4*m*, parts of the side-walls were replaced by perspex facilitating optical recording. The salt water was mixed and dye was added such that the interface became distinctly visible. When the salt water was well mixed and came to rest, a layer of fresh water was carefully spread on the top of the salt water. During this process some mixing occurred on the interface and the stratified layer developed. This layer (approx. 4cm thick) was kept unchanged throughout the experiments, though its thickness and location changed slightly after each tow.

The machined circular cylinder of diameter 50*mm*

and spanning the width of the tank, was mounted under a carriage that was pulled vibrationless on a pair of tempered steel rods, one mounted on each flank of the tank. The towing speed was kept constant for each tow and the start and the stop was impulsive. The cylinder was kept in position at a chosen depth in a frame attached to the carriage. A definition sketch of the model is shown in Figure 1a and the stratified layers are as in Figure 1b. Before each tow, small particles were distributed in the tank approx. 10*cm* from the front wall. These particles of typical dimension 2*mm* and with densities less than the salt water but heavier than the fresh water, were excellent tracers of maximum vertical displacements of the stratified layer during tows. When the tank was illuminated from behind, the dye and the particles became sufficiently visible.

For the measurements of the forces a stiff, sensitive and accurate system was needed. The improvement of an existing shear force transducer that fulfilled these requirements was accomplished during this investigation. A pair of these transducers were connected to a 50*cm* long section of the cylinder in the middle of the tank, and provided simultaneous measurements of flow-induced in-line and transverse forces exerted upon it. The documentation of each tow consisted of time series recordings of cylinder position, lift and drag forces and photos and video recordings, and measurements of density profile.

The wave pattern obtained from tows like this is fundamentally the same as for the hydraulic problem of steady flow past a fixed cylinder. The difference is mainly a subtraction of the tow speed. A difference that may be of importance, but not considered here, is the turbulence level of the undisturbed flow. In these experiments it is approximately zero, while in a steady stream it can be considerable and with energy in a wide frequency band. Disregarding this effect and by correct scaling, the model data can be used to determine the "dead-water" loads on a tube bridge exposed to transverse stratified flow.

The flow around the cylinder perturbs the interface, and at lower speed tows a series of internal waves of the type sketched in Figure 1.c are formed behind the cylinder. The characteristics of these waves, the wave height H and wave length λ, are presented in Figure 2 and Figure 3 respectively. The wake behind the cylinder undergoes changes which is of importance concerning the wave resistance f_x (mean in-line force per unit cylinder axis length) and the lift force f_z (mean transversal force per unit cylinder axis length) on the cylinder. These results are summarized in Figure 4 and Figure 5 respectively. For the cases of uniform flow of homogeneous water past a cylinder and which external bounding surfaces are far from the cylinder, it is well understood that the flow character depends on a single dimensionless variable, the Reynolds number, $Re = UD/\nu$, in which ν is the kinematic viscosity coefficient of water. However, with the presence of a stratified water these data show that there is a flow regime where a densimetric Froude number

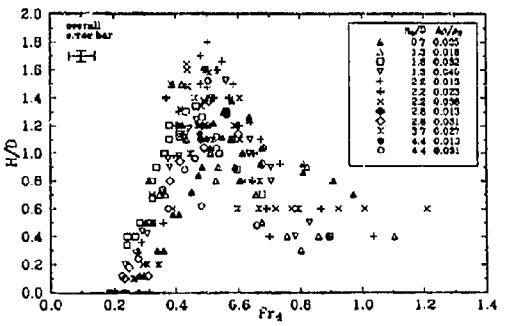


Fig. 2 Variation of wave heights.

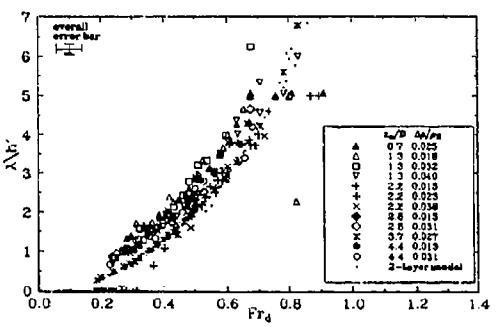


Fig. 3 Variation of wave lengths.

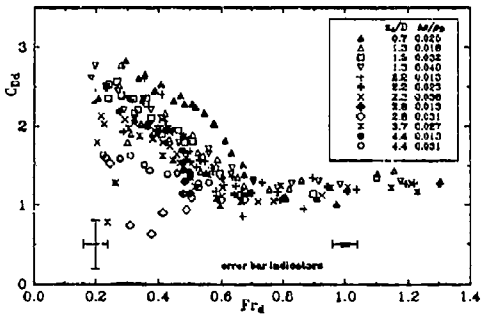


Fig. 4 Variation of in-line forces.

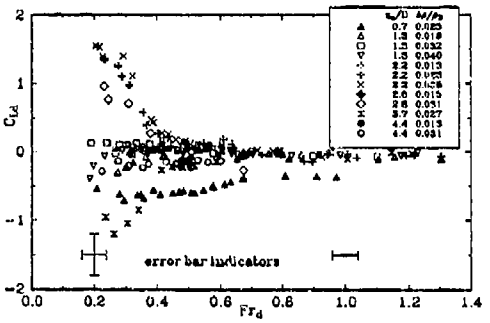


Fig. 5 Variation of transverse forces.

$$Fr_d = \frac{|U|}{c_i} , \qquad (1)$$

in which

$$c_i^2 = \frac{\Delta\rho}{\rho_3} g \frac{h'h}{h'+h} , \qquad (2)$$

is the proper dimensionless variable. The apparent spread of the data is mainly due to the geometric non-similarity between the tests. g is the acceleration of gravity (local value $=9.81 m/s^2$). The hydrodynamic coefficients in Figure 4 and Figure 5 are defined as

$$(C_{Dd}, C_{Ld}) = \frac{(f_x, f_z)}{0.5\,\rho\,D\,U^2} . \qquad (3)$$

The range of the experimental input variables during the experiments were:

$$0.2 < Fr_i < 1.4 ; \quad 0 < z_o/D < 4.5 ;$$
$$0.013 < \Delta\rho/\rho_3 < 0.039 ; \quad 0.7 < l/D < 1.0 ;$$
$$h'/D \simeq 3 , \quad h/D \simeq 5 ; \quad 1000 < Re < 10000 .$$

An internal wave version of the tow resistance formula given by Lamb (1932, art.:249) relates the far downstream waves to the wave induced tow resistance R_w:

$$R_w = E(1 - c_g/U) \simeq 0.125\Delta\rho g H^2 (1 - c_g/U), \qquad (4)$$

where E is the mean energy per unit horizontal area due to the presence of internal waves, and c_g is their associated group velocity. This expression has been compared to the difference of in-line forces measured in homogeneous and stratified water. For $0.4 < Fr_d < 0.6$ the present data show that R_w is a good estimate for the increased tow resistance, except for the case when the cylinder is located within the stratified layer. There, the in-line force does not increase but decreases in stratified water, although waves of appreciable heights were observed. Else, the diagram of Figure 6 can be used for calculation of the internal wave induced drag force. Let $Fr_{d,cr}$ define when the steady in-line force in stratified water drops below the similar homogeneous water value. Comparisons of the present results with those of Carpenter and Keulegan (1960) suggests an l/D dependency of $Fr_{d,cr}$. As mine experiments reveal maximum wave heights at $Fr_d \simeq 0.5$ and $Fr_{d,cr} \simeq 0.6$ and the previous had maximum waves at $Fr_d \simeq 0.8$, this suggests that $Fr_{d,cr} \simeq 0.9$ for those conditions. This presumption is used in the

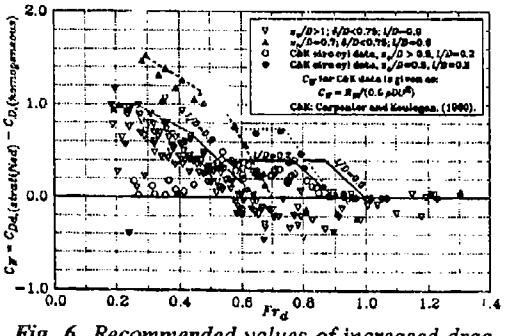


Fig. 6 Recommended values of increased drag coefficient for a horizontal cylinder exposed to stratified flows.

construction of Figure 6. The graph is valid if $0<\delta/D<0.75$, where δ is the distance from the nearest edge of the cylinder surface to the center of the undisturbed stratified layer, and it is divided into three ranges. The thick lines apply if $z_o/D>1.3$ where the l/D-dependency is included. The dashed line is for $z_o/D=0.7$. If the cylinder touches the surface the dotted line apply. If $\delta/D>1.5$ and $z_o/D>1.0$ there will be no influence on the drag force due to stratification. For values of δ/D between 0.75 and 1.5 linear interpolation of the forces seems appropriate, provided $z_o/D>1.0$. For $z_o/D<1.0$ and $\delta/D>1.5$ the presented data can not tell the effect of stratification. However, this situation fits the conditions of the theory presented below very well.

Theoretical development: These experiments showed that the largest internal waves occurred for densimetric Froude numbers somewhat below the value Carpenter and Keulegan found in their investigation. The major difference between my experiments and those of Carpenter and Keulegan lies in the width of the stratified layer. Their theoretical approach to the problem is therefore adopted to a *three layer fluid system*. Only the case when the cylinder is moving with constant horizontal velocity in the upper layer is considered. It is assumed that the surface of the cylinder is located far from the interface $z=-d$. A rigid lid boundary condition is applied at $z=0$ and the method of successive images, (see Carpenter,1958), is used to find flow potential Φ_1 in the upper layer (with velocity components $= -\nabla\Phi_1$):

$$\Phi_1 = -Ux + \frac{U(\gamma r)^2}{x^2+(z+z_o)^2} + \frac{U(\gamma r)^2}{x^2+(z+z_o)^2} + \phi_1 \ . \tag{5}$$

Here ϕ_1 represents the disturbance potential including the wave motion. γ is a factor accounting for an effective increase of the cylinder radius due to the image doublets. When the cylinder is far from the interface $z=-d$, γ is a function of z_o/r $(r=D/2)$, and is determined by the methods found in Carpenter (1958) and plotted in Figure 7. In the lower salt water layer the two middle terms can be disregarded and the flow can be modeled by the potential:

$$\Phi_3 = -Ux + \phi_3 \ . \tag{6}$$

Both potentials satisfy the Laplace equation:

$$\nabla^2\Phi_j = 0 \ , \quad j=1,3 \ . \tag{7}$$

In the stratified layer the motion will not be irrotational. Following Phillips (1977) and the assumptions of small disturbances and Boussinesq approximation, the equations of motion for the disturbance become:

$$\frac{\partial w_j}{\partial z} + \frac{\partial u_j}{\partial x} = 0 \ , \quad j=1,2,3 \ ; \tag{8}$$

$$U^2\frac{\partial^2}{\partial x^2}\left(\frac{\partial^2 w_j}{\partial z^2} + \frac{\partial^2 w_j}{\partial x^2}\right) + N^2\frac{\partial^2 w_j}{\partial x^2} = 0 \ , \quad j=1,2,3 \ . \tag{9}$$

Here, u_j and w_j are the perturbed horizontal and vertical particle velocities within each fluid layer j, and

$$N^2 = -\frac{g}{\rho}\frac{\partial\rho}{\partial z} = \begin{cases} 0 \ ; & -d < z < 0 \\ N_0^2 \ ; & -d-l < z < -d \\ 0 \ ; & -d-l-s < z < -d-l \end{cases} \ . \tag{10}$$

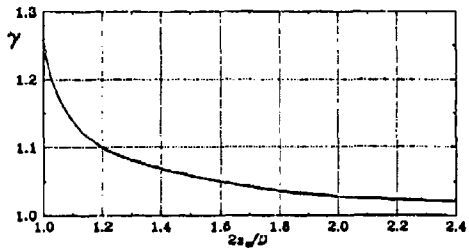


Fig. 7 Variation of radius factor with distance below the free surface (after Carpenter (1958)).

Combined with the proper set of boundary conditions, listed below, these equations determine the resulting non-viscous flow around the submerged cylinder.

location	kinematic	dynamic
$z = 0$	$w_1 = 0$	-
$z = -d$	$w_2 = w_1 = U\,\partial\zeta/\partial x$	$u_1 = u_2$
$z = -d-l$	$w_3 = w_2 = U\,\partial\eta/\partial x$	$u_2 = u_3$
$z = -d-l-s$	$w_3 = 0$	-

A horizontal Fourier-transform method is used to derive the solution of the problem. The transform pair used is shown in eq.'s (11 a,b). The inversion integral for vertical displacement ξ is found to be as in eq.(12),in which $\kappa^2 = (N_0/Uk)^2 - 1$.

$$\tilde{f}(k,z) = \int_{-\infty}^{\infty} f(x,z)\,\exp(-ikx)\,dx \;; \qquad f(x,z) = \frac{1}{2\pi}\int_{-\infty}^{\infty} \tilde{f}(k,z)\,\exp(ikx)\,dk \;. \tag{11a,b}$$

$$\xi(x,z) = \int_0^{\infty} \frac{\kappa}{\pi}\frac{S(k)\,G(k,z)}{Q(k)}\cos(kx)\,dk \quad ;$$

where

$$a): \quad S(k) = 2\,\pi\,U\,(\gamma r)^2\,e^{(-kd)}\cosh(kz_o) \;,$$

$$b): \quad G(k) = \frac{1}{U}\,\{\,[Q(k) + T(k)\sinh(kd)]\cos(\kappa\,k\,(z+d)) + \frac{1}{\kappa}\,[Q(k) - T(k)\cosh(kd)]\sin(\kappa\,k\,(z+d))\,\}\;, \tag{12}$$

$$c): \quad T(k) = \kappa\,tg(\kappa k l)\tanh(ks) + \frac{1}{\kappa}tg(\kappa k l) + \tanh(ks) - 1 \;,$$

$$d): \quad Q(k) = \cosh(kd)\,\{\kappa[\tanh(kd) + \tanh(ks)] - tg(\kappa k l)\,[\kappa^2\tanh(kd)\tanh(ks) - 1]\} = \cosh(kd)\,q(k) \;.$$

The value $\xi(x,z)$ is controlled by the behavior of the denominator, $Q(k)$, near its roots in *k-space*. $Q(k)=0$, with Uk in κ replaced by ω, is in fact the *dispersion relation* for waves freely propagating in the non-flowing three layer fluid system. For a given k, $Q=0$ as a function of κ has an infinity of solutions, κ_j, each representing a different wave mode. However, when N_0 and U are given, the number of solutions, J, is bounded by the requirement; $c_0^{(J+1)} < U < c_0^{(J)}$, where $c_0^{(J)}$ is the maximum wave celerity for wave mode no. J. First mode internal waves ($J=1$) are the most dominant observed behind the cylinder. It can be shown that $c_0^{(1)} = N_0 l/a_0$, where a_0 is the lowest valued nonvanishing root of $tg(a_0) = a_0(d+s)l/(a_0 ds - l^2)$. The Cauchy integral theorem and the principal value (CPV) give the wanted solution. Since our main interest is placed upon the condition at some distance downstream of the cylinder where only the oscillatory part of the CPV value is significant, the amplitude of the vertical displacement (in the stratified layer) is given by eq. (13),in which $q'(k_0) = (\partial q(k)/\partial k)\,|_{k=k_0}$, and k_0 is the lowest valued nonvanishing root of $q(k)=0$. The value $k_0 = 2\pi/\lambda$ is the wavenumber of the internal wave standing stationary behind the cylinder. Maximum vertical displacement occurs within the stratified layer for $z=z_m$ defined where $w_2(z)$ has its maximum. i.e. where $\partial\tilde{w}_2(k,z)/\partial z = 0$, which yields

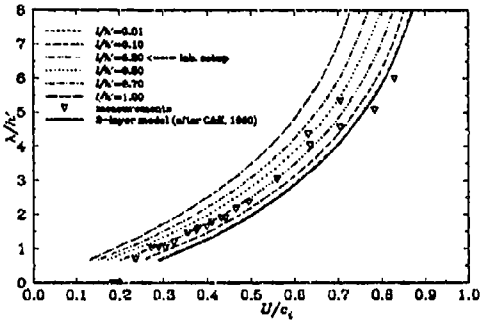


Fig. 8 Dispersion relation for different stratified layer thicknesses.

$$\xi_0(z) = \left| \frac{2\,\kappa_0\, S(k_0)\, G(k_0,z)}{\cosh(k_0 d)\; q'(k_0)} \right| \qquad (13)$$

$z_m = -d - \left| arctg(1/(\kappa \tanh(kd)) \right| / (\kappa k)$. In the derivations above it is assumed that no disturbancesare present far upstream. The experiments confirmed this assumption.

Recalling the assumptions of the theory, it can only apply to the observed waves of z_o/D equal 0.7 or 1.3. In Figure 8, theoretical and observed wave-lengths are compared for one set of data. The dispersion effect of the presence of a stratified layer is clearly seen. A very good agreement is achieved for $U/c_i < 0.6$. Similar results are obtained for other data sets. In Figure 9, theoretical curves for wave amplitude for different values of γ are shown together with one set, $z_o/D = 1.3$ of the observed values. According to the method of Carpenter (1958), the proper γ-*value* is 1.02. It is seen that the observed values for the smaller wave heights is better modeled by γ about 1.4. Better resemblance between theory and observations is achieved when $z_o/D = 0.7$, see Figure 10. This configuration is also in more accordance with the theoretical assumptions. In light of these findings, it is concluded that the theoretical formulation can be used to model the wave heights. But as the cylinder approaches the internal boundary, the γ-*value* needs to be increased. The present study, suggests $\gamma = 1.6$ as the conservative upper limit, and that the theory is valid up to the towing speed corresponding to the observed maximum wave heights.

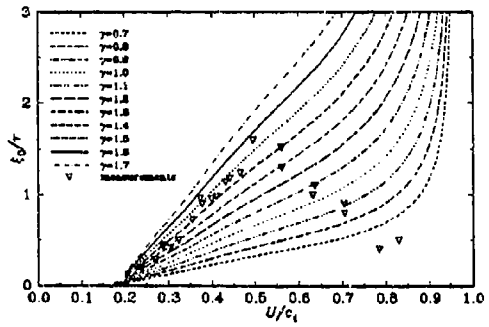


Fig. 9 Variation of wave height, comparison with theory. $z_o/D=1.3$, $l/h'=0.3$, $\Delta\rho/\rho_3=0.039$.

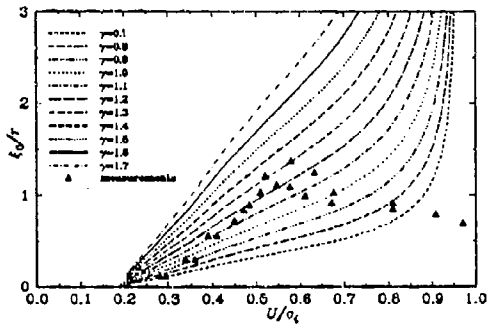


Fig. 10 Variation of wave height, comparison with theory; $z_o/D=0.7$, $l/h'=0.3$, $\Delta\rho/\rho_3=0.024$.

Application - Hoegsfjord tube bridge, Norway: The aims of the model tests and the theoretical approaches were fundamental, and do not directly apply to a scaled model of a particular bridge. However, the results agree fairly well, so together with realistic site specific hydrographic data and some simplifications, the major influence which stratification has on the hydrodynamic loads exerted upon the bridge can be derived. For all calculations, it is assumed that the bridge is a smooth circular cylinder of 10m diameter, lying horizontally with its axis at $z_o = -25m$. Based on site measurements, four extreme stratified conditions have been determined for the analysis of 'dead-water' effects, these are listed in Table 1. Eidnes & al. (1988) recommend design current speed $U_{100} = 90\,cm/s$ at $z = -5\,m$ and $60\,cm/s$

at $z=-20m$ and deeper. For depths in between, linear interpolation is used.

First, I consider steady in-line forces. An important parameter in the discussion of loads is $Fr_{d,dim}$, which is defined as the lowest possible Froude number at design current speed. If $Fr_{d,dim} > Fr_{d,cr}$, the design loads determined for homogeneous water need not be changed. If the conservative value of $Fr_{d,cr}=0.8$ is used, $Fr_{d,dim}$ is larger than $Fr_{d,cr}$ at $z=-5m$, but less for $z=-20m$. For the stratifications E10, E15 and E20 the design speed gives $Fr_{d,dim}=0.7$. Therefore, C_D should be increased. Referring to Figure 6, an increase of 0.4 is conservative with respect to the force value. This has the same effect as if the design current speed were increased from 0,6 to 0.8 m/s and without changing the C_D valid for homogeneous water.

Referring to Figure 4, maximum 'dead-water' effect occurs at $Fr_d \simeq 0.5$, and Figure 6 gives an increase of C_D by 0.4. For stratifications as in Table 1, this occurs at $U \simeq 0.45 m/s$. The appropriate drag coefficient in homogeneous water is 0.5. Thus at this speed the effect of stratification increases the in-line drag from 520 *N/m* to 940 *N/m* bridge length.

For densimetric Froude numbers below 0.45 and the tube located near the stratified layer ($\delta/D<1$), the laboratory experiments show the possibility of a mean lift force. Maximum lift occurs when the tube has a clearance to the center of the stratified layer equal of about $D/2$. The magnitude of the lift is independent of whether the tube is located above or below the stratified layer (but negative for tubes below the pycnocline). Referring to Figure 5, maximum lift occurs at $Fr_d=0.3$. When the model data are scaled to prototype values it is found that a steady flow induced lift force of 400 - 500 N/m length of the bridge may occur during moderate flows ($\simeq$0.3 m/s) and strong stratification (E15).

Table 1 Extreme stratification in Hoegsfjorden.

Stratification:	h' [m]	$\Delta\rho$[kg/m^3]	N_0 [rad./s]	l [m]	c_i [m/s]
E5	5	10	.16	3.8	0.70
E10	10	7	.13	4.0	0.82
E15	15	5	.10	4.8	0.85
E20	20	4	.10	3.9	0.88

References:

Arntsen, Ø., (1986): "Slepemotstand i lagdelt sjø." Division of Port and Ocean Engineering, The Norwegian Institute of Technology, Trondheim. Report No. R-6-86. (In Norwegian).

Arntsen, Ø.A.,(1994): "Disturbances, lift, and drag forces due to the translation of a horizontal circular cylinder in stratified water". Submitted to Experiments in Fluids.

Carpenter, L.H., (1958): "On the motion of two cylinders in an ideal fluid." Journal of Research of the National Bureau of Standards. Vol. 61, No.2, August 1958, pp 83-87.

Carpenter, L.H. and Keulegan, G.B., (1960): "Disturbances due to the motion of a cylinder on a two-layered liquid system." Journal of Research of the National Bureau of standards. Vol. 64C, No. 3, July-September 1960, pp 241-253.

Eidnes, G., Arntsen, Ø. and Lothe, A., (1988): "Rørbru over Høgsfjorden. Samlet Hydrofysisk vurdering." SINTEF Report STF60 F88098. (In Norwegian).

Ekman, V. W., (1906): "On dead-water.", in The Norwegian North-Pole Expedition, 1893-1896, Scientific results, ed. F. Nansen, Vol. 5(15) pp 1-152 (printed in 1904).

STRATIFIED FLOW OVER THREE-DIMENSIONAL TOPOGRAPHY

By Y.KADRI[1], P.BONNETON[2], J.M.CHOMAZ[3] and M.PERRIER[1]

[1]METEO-FRANCE, 42 avenue Coriolis, 31057 Toulouse, France
[2]IMFT, avenue du Prof.C.Soula, 31400 Toulouse, France
[3]LADHYX, Ecole Polythechnique, 91128 Palaiseau-Cedex, France

ABSTRACT : In order to investigate the flows over a topography in atmospheric context, we have experimentally studied the wake structure of axi-symmetric gaussian obstacles towed in a linearly stratified medium. Three dimensionless parameters govern the flow dynamics : F, the Froude number based on the topography height h ; Re, the Reynolds number based on the width 2L measured at the mid-height and the aspect ratio r=h/L. The main regimes determined for the sphere by Chomaz et al (1993) are retrieved. For F<0.7 the flow is observed to go around the obstacle and the wake consists mainly in a quasi-two-dimensional layer with vortical motions . This layer is topped by a region only affected by the lee wave whose amplitude is an increasing function of r and F. For 0.7<F<1/r the flow is entirely dominated by a lee wave of saturated amplitude which suppresses the detachment of the boundary layer from the obstacle. Above the critical value 1/r, the lee wave amplitude decreases with F and, a recirculation zone reappears behind the obstacle. Simultaneously, coherent large scale vortices start to be periodically shed from the wake at a Strouhal number that decreases as 1/F until its neutral value.

1. Introduction

Recently, a large research effort has been devoted to the study of geophysical flows over a topography. Such phenomena, are particularly important in meteorological context since the earth topographies generate internal gravity waves that transfer energy from the surface to the upper atmosphere. The processes induced by the propagation of internal waves are important and ought to be taken into account in weather forecasting models. New developments of non-hydrostatic models, requires precise laboratory experiments in order to document test cases. Brighton (1978) and Hunt and Snyder (1980), studying reliefs with aspect ratios (r=h/L) close to 1, have shown that such flows are mainly controlled by the Froude number F=U/Nh, where U designs the flow velocity and N the characteristic Brunt-Väissälä frequency of the medium. They demonstrated that for small values of F, the near wake is quasi-two-dimensional, and that for F≈1, the flow separation line is conditioned by the generated lee wave field. Chomaz et al (1993) and Bonneton et al (1993) have extended such an investigation by examining the dynamics of the stratified flow past a sphere for a large range of Froude number.
Theoretical analyses, of the stratified flow over an obstacle, have been elaborated by Smith (1980), in the hydrostatic frame work, and by Crapper (1959), Lighthill (1978) and Voisin (1992) for the non-hydrostatic approach. In this paper we describe the near wake structure of axi-symmetric gaussian obstacles towed uniformly in a linearly stratified fluid. We demonstrate the influence of both, the Froude number and the aspect ratio, on the flow structure. Experiments were performed in a water towing tank of size $0.5*0.5*4$ m^3. This tank was filled with a linear stratification using salt solutions, a wide range of N has been explored : N∈[0.67, 2 rad/s]. Four gaussian models : r=0.28, r=0.56, r=0.8 and r=1.12 were used in the experiments. The towing velocities were varied from 0.5 to 25 cm/s. when for a given stratification N and a given model r the velocity is varied, the two dimensionless numbers F and Re (Re=U(2L)/ν, where ν is the fluid kinematic viscosity), evolve proportionally in the form Re=Re(F=1)F, where Re(F=1)=2NrL^2/ν. In the present study, F was varied from 0.2 to 14 and Re from 800 to 25000.

Visualisation and measurement techniques applied in the experiments presented here have here have been described in detail in Chomaz et al (1993).

2. The lee wave dynamics

Particle streak photographs of the flow over two gaussian models r=0.28 (figures 1.a, 1.b, 1.c) and r=0.8 (figures 1.d, 1.e and 1.f) illustrate the evolution of the lee wave versus F. At large F (figures 1.a and 1.d) a three-dimensional (3D) recirculation zone is present behind the obstacles. Both the size and the unsteadiness of this zone increase with F, whereas the lee wave amplitude decreases. For F close to 1 (figures 1.b and 1.e) the flow is entirely dominated by a saturated lee wave (SLW regime). For F smaller than 0.7 (figures 1.c and 1.f), the lee wave amplitude decreases and a two-dimensional (2D) layer appears close to the ground. For r=0.28 (figure 1.c) the wave amplitude is much smaller than for r=0.8 (figure 1.f) and only the first crest is visible.

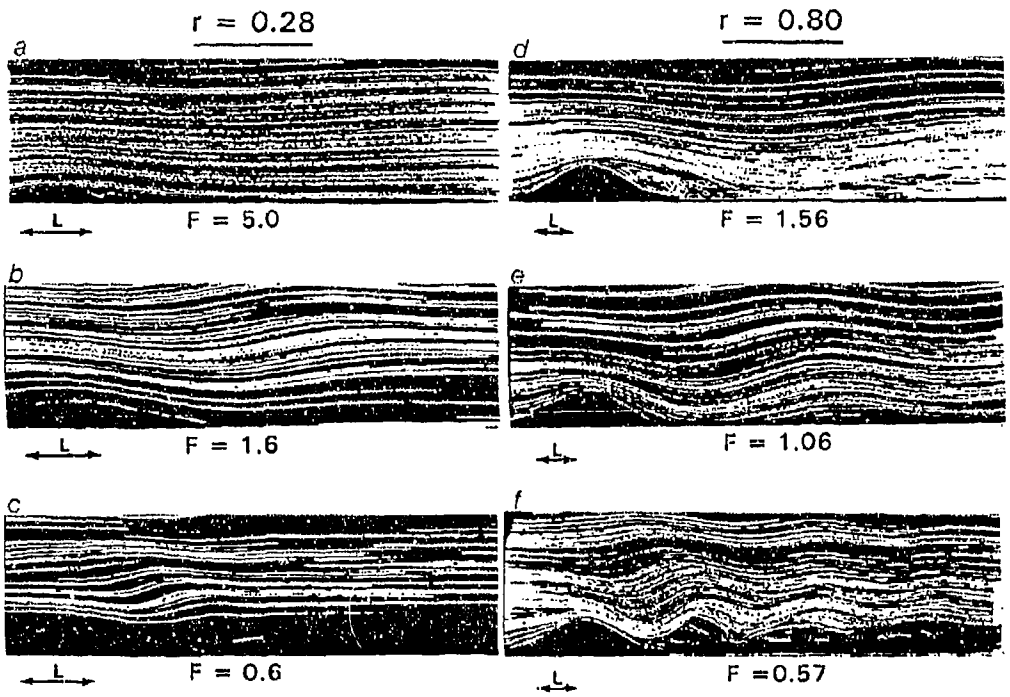


Figure 1 : Vertical particle streak photographs for r=0.28 (Re(1)=1600) and for r=0.8 (Re(1)=2100)

On figure 2, we have plotted measurements of the lee wave wavelength as obtained from the particle streak visualisations for three gaussian models (r=0.28, 0.8 and 1.12), we have also reported Hanazaki numerical results (dashed line) for a sphere, and the point source linear theory predictions (continuous line). We observe that measurements are in good agreement with the theoretical predictions without influence of the body shape detail. From such visualisations we have determined the spatial distribution of the vertical component of

the velocity field, which enables us, to deduce the correspondent distribution of the local amplitude of the lee wave. We have reported on figure 3, for r=0.28 and r=0.8, the angle θ between the horizontal and the direction where the local wave amplitude is maximum. We may see that for both models, θ decreases notably between F≈1.2 and 1.6. Even if, the precision is rather poor for r=0.28 when F is close to 0.4, because of the small amplitude of the lee wave, figure 3 clearly demonstrates that θ is much larger for r=0.28 than for r=0.8. For small r and small F, the measured angle θ is close to the value 90° given by the hydrostatic approach (Smith (1980)), whereas, for large r, the limit value of θ, as F goes to zero, is consistent with the point source linear theory prediction θ=45° (Lighthill (1978) and Voisin (1993)).

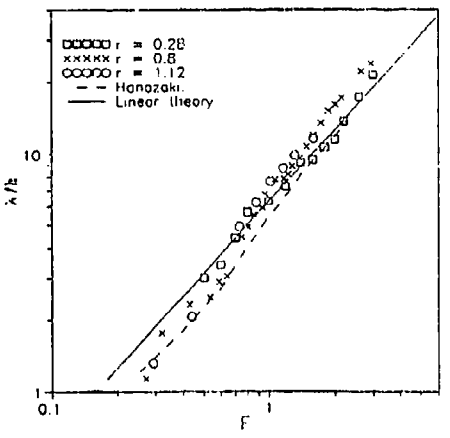


Figure 2
Evolution of the lee wave wavelength versus F for several models and several Re(F=1).

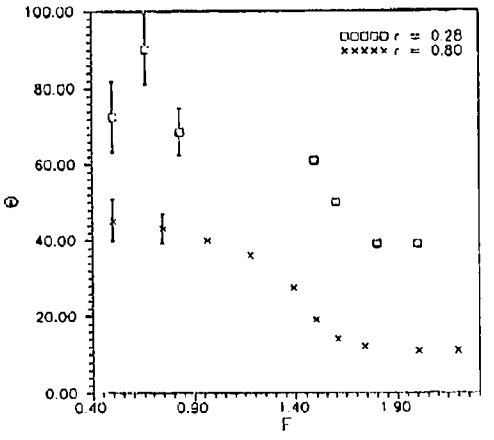


Figure 3
Evolution of the angle between the horizontal and the direction of maximum local amplitude versus F for r=0.28 (Re(1)=900) and for r=0.8 (Re(1)=2100).

Figure 4 presents the evolution of the maximum vertical displacement ζ of a fluid particle, due to the lee wave, as a function of F for r=0.28 and r=0.8. For both cases, we observe that the amplitude (ζ/h) increases up to F about 0.7 (2D regime). Then, it saturates around F≈1 (SLW regime) and finally, starts to decrease for F larger than 1/r. A similar behaviour is detected for the two other models r=0.56 and r=1.12. The initial increase of the amplitude with F may be explained by the energetic arguments of Sheppard which predicts : ζ/h = F. However, the theoretical predictions seem to overestimate the amplitude for the small aspect ratio (r=0.28) and underestimates it for large r (r=0.8). The transition in the lee wave amplitude at F≈1/r, has been theoretically predicted by Queney who showed that a resonant regime occurs when the effective wavelength of a mountain (2πL) equals the lee wave wavelength (2πU/N). For r =0.8, the decrease in amplitude, observed at large F, seems to agree with the point source theory which predicts : ζ/h =1/F.

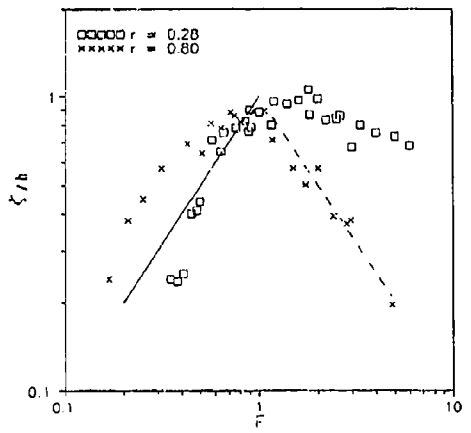


Figure 4 : Evolution of the wave amplitude versus F for r=0.28 (Re(1)=900, 1600 and 2400) and for r=0.8 (Re(1)=1300, 2100 and 2700).
————: Sheppard's theory ; ---------- : source point theory

3.The 3D regime (F≥1/r)

***Homogeneous wake* :**

In order to understand the stratification effects on the close wake, the knowledge of the wake in the homogeneous configuration is required. As well as for the sphere (Chomaz et al (1993), Kim and Durbin (1988)), we have observed that, for Reynolds numbers greater than a critical value Re_c, the wake is affected by two instability modes : a high frequency Kelvin-Helmholtz shear Instability (KH) of the separated layer and a low frequency mode (VS) associated with the shedding of large scale coherent vortices (figures 6.a and 6.d). For smaller Reynolds number values, only a single mode is present. Figure 5 shows for r=0.8, the evolution of the Strouhal numbers S (S=f(2L)/U where f is the emission frequency), as obtained either from fluorescent dye visualisations or from velocity measurements. Above Re_c=1300, the Strouhal number of the low frequency wake instability stabilises around S_{VS}=0.55 whereas the high frequency branch (KH mode) keeps increasing. A similar behaviour is observed for the different models tested, values of Re_c and S_{VS} function of r are reported in Table 1.

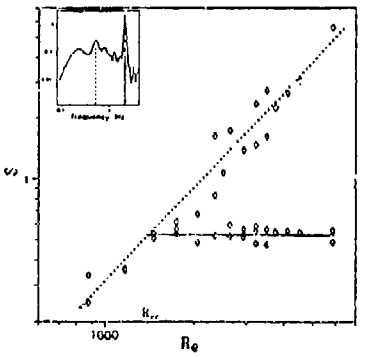


Figure 5 : Evolution of the Strouhal number S versus Re for r=0.8, in the homogeneous case.
The continuous line indicates the best power law to the data ($S \propto Re^{3/2}$), and the inclusion presents a typical velocity spectrum for Re=3750, the low and high frequency mode are indicated in.

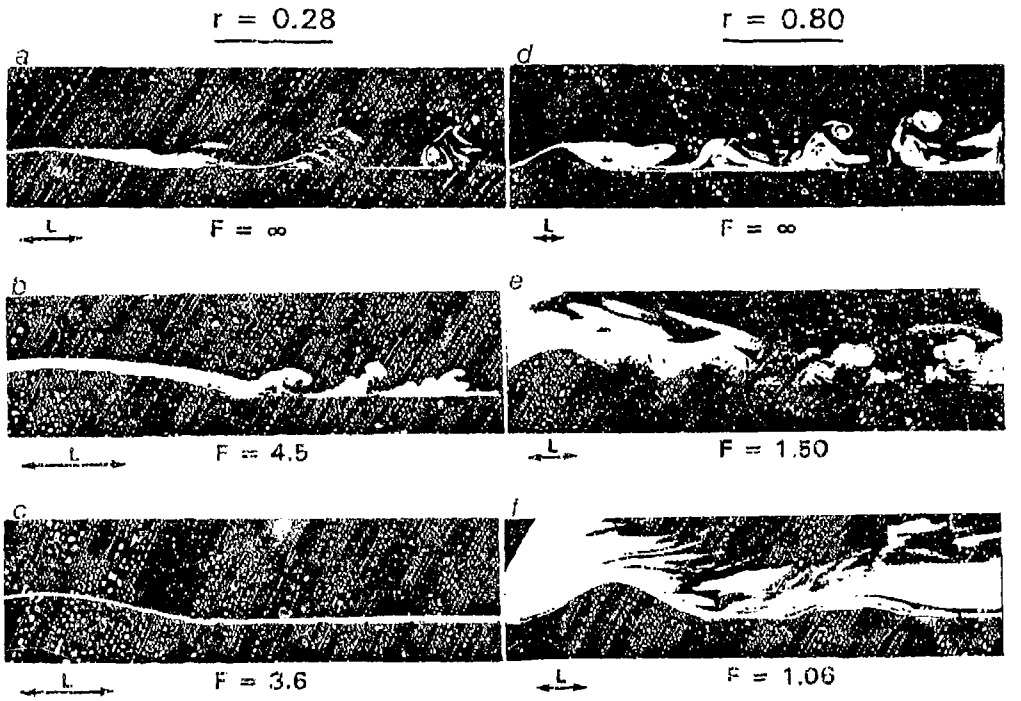


Figure 6 : Fluorescence induced by laser side views for r=0.28 (a : Re=2950, b : Re=4000, c: Re=3200) and for r=0.8 (d : Re=1500, e : Re=1800, f : Re=1400)

**** Stratified configuration :***

Figure 6 illustrates the progressive disparition of the shedding of large scale vortices as the stratification effects increase (F decreases). This disparition occurs at a critical Froude number F_c depending only on r as soon as $Re > Re_c$. For r=0.28 F_c is close to 4 (figures 6.b and 6.c) whereas it gets close to 1.2 for r=0.8 (figures 6.e and 6.f). On figure 7 we have reported the evolution of the Strouhal number S of the VS instability as a function of rF for several aspect ratios (r=0.28, 0.8 and 1.12). Values of S were obtained either from visualisations or from both conductivity probe and velocity measurements. In addition, for each aspect ratio r up to three sets corresponding to three different Re(F=1) have been collected. We note, from figure 7, that S decreases with F following an $1/rF$ law before stabilising at its neutral value. This result demonstrates that the VS mode frequency is controlled by stratification effects until it reaches its asymptotic value. We also see on figure 7 and table 1 that the critical value F_c equals $1/r$ and coincides with the limit of the saturated lee wave regime. The slight dispersion in the value of S, for given F and r, is partly due to variations in Reynolds number. This demonstrates the weak importance of Re as soon as the VS mode is established ($Re > Re_c$).

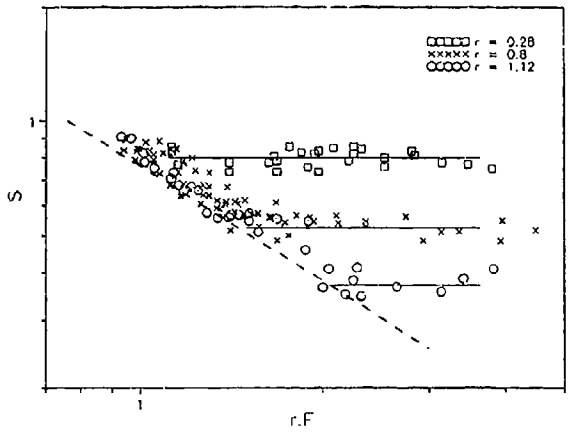


Figure 7 : Strouhal number S of the low frequency mode for r=0.28, 0.8 and 1.12

Type	r=0.28	r=0.56	r=0.8	r=1.12
R_{ec}	2000 ± 10%	1200 ± 10%	1300 ± 10%	1000 ± 10%
S_{vs}	0.85 ± 5%	0.55 ± 5%	0.55 ± 5%	0.4 ± 5%
F_c	4 ± 5%	2 ± 5%	1.2 ± 5%	0.8 ± 5%
rF_c	1.1 ± 5%	1.1 ± 5%	0.96 ± 5%	1.01 ± 5%

Table 1

4. The SLW regime :

For this regime the lee wave amplitude reaches its maximum and hence, the turbulent wake is suppressed as clearly demonstrated on figures 6.c and 6.f. For r=0.8 we note on figure 6.f, the generation of a three-dimensional steady isolated bubble under the first crest of the lee wave. For the gentle model (r=0.28) such a phenomenon is not observed because, may be, the wave energy propagates nearly vertically.

5. The 2D regime :

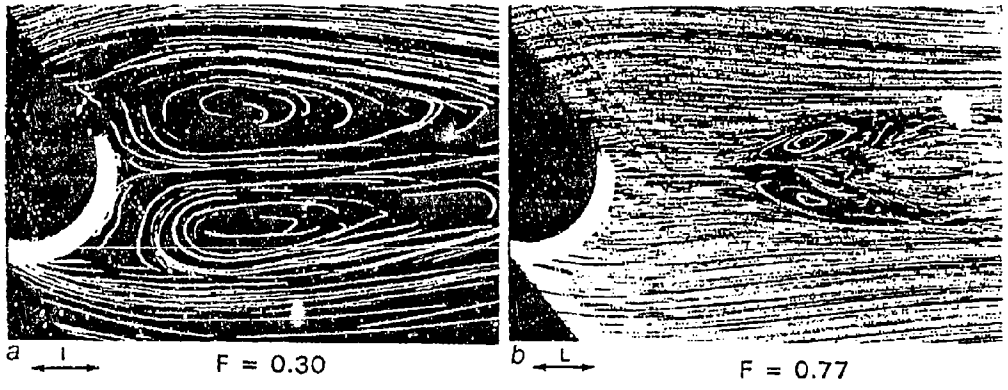


Figure 8 : Top view particle streak photographs for r=0.8 (Re(1)=1300)
(the flow is from left to right)

When F decreases below 0.7, the lee wave amplitude decreases and the fluid layer that goes around the obstacle, instead of passing over it, starts being animated by quasi-two dimensional motions. An attached pair of vortices appears in the lee side of the topography (figure 8.a). For the large aspect ratio model (r=0.8), this 2D layer is topped by a moustache-like shaped rollers visible on the top view 8.b. This complex structure, described by Sysoeva and Chashechkin (1986), lives under the first crest of the lee wave and therefore exhibits a similar shape as the isophase 2π. For the small aspect ratio model (r=0.28), rollers are no more present, probably on the account of the rapid drop in the lee wave amplitude and on the nearly vertical propagation of the wave energy observed in this case.

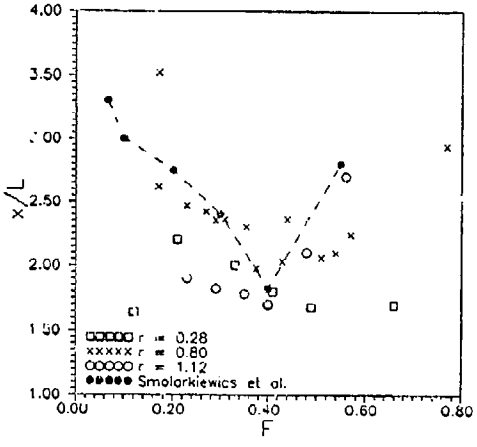


Figure 9 :
Evolution versus F of the nondimensional distance between the centre of vortices and the relief axis

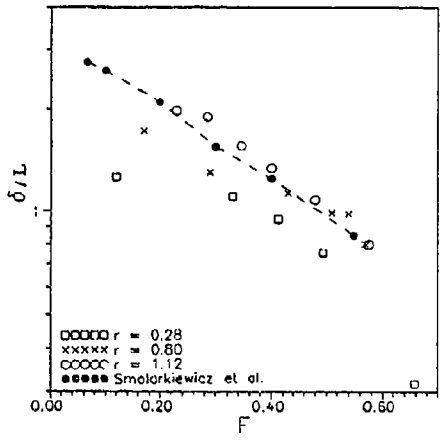


Figure 10 :
Evolution versus F of the nondimensional width between the centre of the lee vortices

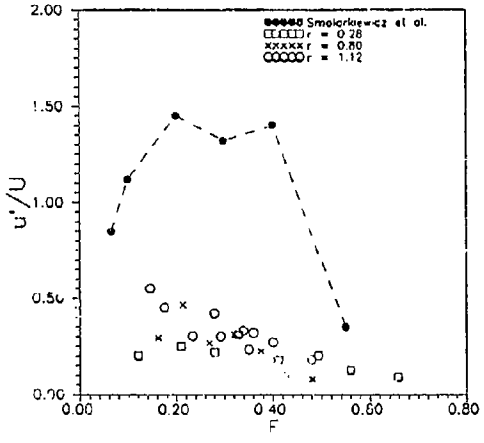


Figure 11 : Evolution of the nondimensional intensity of the vortices as measured by the maximum velocity in the adverse flow

Figure 9 (respectively 10 and 11) presents measurements of the distance x/L between the centre of the 2D vortex couple and the relief axis for r=1.12, r=0.8 and r=0.28 (respectively the width δ/L and the velocity u'/U of the associated adverse flow). For both the distance x/L and the width δ/L, results are in good agreement with the predictions of the inviscid numerical simulations of Smolarkiewicz and Rotunno (1989). On the contrary, the adverse flow amplitudes reported by Smolarkiewicz and Rotunno, are approximately five times greater than the experimental ones. This discrepancy is certainly due to the friction at the wall which is not taken into account in the inviscid numerical model. From the relative agreement between the simulations and the present experiments, one would be tempted to conclude that, the vorticity is mainly generated by the baroclinic mechanism introduced by Smolarkiewicz and Rotunno rather than by separation of the boundary layer on the topography. This issue deserve further investigations.

Acknowledgements---This work was supported by Météo-France. We are grateful to the team SPEA of the French Met Office and wish to thank for their co-operation and help during these experiments : B.Beaudoin, J.C.Boulay, A.Butet, C.Niclot, M.Niclot, S.Lassus-Pigat and H.Schaffner from Météo-France/CNRM/SPEA. We also wish to thank for his kind help and enthusiasm P.Dupont from IMFG/LEGI.

REFERENCES

Bonneton P., Chomaz J.M. and Hopfinger E.J. 1993 Internal waves produced by the turbulent wake of a sphere moving h ··tally in a stratified fluid. *J.F.M. vol 254.*
Brighton P.W.M. 1978 Strongly flow past three-dimensional obstacles. *Q.J.R.Met.Soc. vol 104.*
Chomaz J.M., Bonneton P. and Hopfinger E.J. 1993 The structure of the near wake of a sphere moving horizontally in a stratified fluid. *J.F.M. vol 254.*
Crapper G.D. 1959 A three dimensional solution for waves in the lee of mountains. *J.F.M. vol 6.*
Hanazaki H. 1988 A numerical study of three dimensional stratified flow past a sphere *J.F.M. vol 192.*
Hunt J.C.R. and Snyder W.H. 1980 Experiments on stably and neutrally stratified flow over a model three dimensional hill. *J.F.M. vol 96.*
Kim H.J. and Durbin P.A. 1988 Observations of the frequencies in a sphere wake and of drag increase by acoustic excitation. *Phys.Fluids vol 31.*
Lighthill M.J. 1978 Waves in fluids. *Cambridge University Press.*
Queney P. 1948 The problem of the airflow over mountains. A summery of theoretical studies. *Bull.Amer.Meteor.Soc. vol 109.*
Smith R.B. 1980 Linear theory of stratified hydrostatic flow past an isolated mountain. *Tellus vol 32.*
Smith R.B. 1989 Hydrostatic airflow over mountains. *Advances in Geophysics vol 31.*
Smolarkiewicz P.K. and Rotunno R. 1989 Low Froude number flow past three dimensional obstacles. Part I : Baroclinically generated lee vortices. *Jour.Atm.Sci. vol 46.*
Sysoeva E.Y. and Chashechkin Y.D. 1986 Vortex structure of a wake behind a sphere in a stratified fluid. *Jour.Appl.Mech. vol 152.*
Voisin B. 1993 Internal wave generation in uniformally stratified fluids. Part 1 : Green's function and point sources. *J.F.M. vol 231.*
Voisin B. 1993 Internal wave generation in uniformally stratified fluids. Part 2 : Moving point sources. *J.F.M. vol 231.*

ON THE AMPLIFICATION OF INTERNAL-WAVE SURFACE MANIFESTATIONS DUE TO SUBSURFACE SHEAR CURRENT

Victor I.Shrira *and* **Vyacheslav V.Voronovich**

P.P.Shirshov Institute of Oceanology Russian Academy of Sciences,
23 Krasikov str., 117218 Moscow, Russia

1.Introduction. Manifestations of internal waves on the sea surface were the subject of intensive studies in the last two decades reaching their peak in the mid of eighties. Until now internal waves remain the only "internal" process having numerous and well documented observations of its surface manifestations and, to our opinion, all the links between surface and interior merit primary attention. Despite great number of works the understanding of physics of these phenomena is still far from being complete. A good and still relevant overview of the situation in the field gives the book "*Effect of large-scale internal waves on the sea surface*". We summarize the present state of knowledge as briefly as possible, to reduce the conclusions relevant in our context to just the two points. First, we note that internal waves manifest themselves creating nonuniformity of some "end", i.e. directly observable, properties of the sea surface, which are, as a rule, specific for the situation and the way of observation. To give an idea we list just some of such "end" properties: albedo, colour, breaking wave probability, density of weeds or melting ice, temperature, scattering characteristics in different bands etc. As a rule these "end" properties are related through a cascade of different physical mechanisms with the "primary" distortions of the surface parameters created by internal wave. These mechanisms are numerous and the cascades could include many links, but, we would like to stress this point, most of the cascades are initiated by the nonuniformities of the horizontal velocity on the surface caused by internal waves as the main "primary" factor. The second major conclusion that can be derived basing on the accumulated experience of previous studies, being roughly formulated, is: if there is a strong "primary signal" due to internal wave in terms of horizontal velocity, then there are noticeable manifestations in various fields.

In this work we focus our attention on a mechanism providing amplification of the surface velocity variations. We shall take into account existence of mean shear current and its boundary-layer-type vertical structure. The currents of this type are caused by the wind and represent generic feature of the upper ocean. We shall show that the presence of subsurface shear currents often results in considerable amplification of surface manifestations.

2.Basic equations and preliminary assumptions. We shall study a linear internal wave dynamics in an inviscid, incompressible, horizontally homoge-neous, but vertically stratified fluid in presence of a steady parallel vertically sheared flow with basic velocity distribution $\mathbf{U} = \{U(z),0,0\}$. The x-axis of the chosen coordinate frame is oriented along the current while z-axis is directed vertically upward. The equilibrium fluid density $\rho_0(z)$ being an arbitrary function of z at the depth is supposed to be constant, say ρ_{00}, near the surface and to form so-called 'mixed' layer of the depth D. The mean current is assumed to be localized in the thin layer with typical thickness h near the surface and to be zero outside, h presumed to be smaller than D.

The set of nondimensional equations governing the linear evolution of small perturbations is standard: the Euler, mass conservation and incompressibility equations

$$(\partial_t + \mathbf{U}\cdot\nabla)\mathbf{u} + wU' + g\rho\mathbf{z} + \rho_0^{-1}\nabla p = 0 \qquad (2.1a)$$

$$\partial_t \rho + w\rho_0' = 0 \tag{2.1b}$$

$$\nabla \cdot \mathbf{u} = 0 \tag{2.1c}$$

where g is gravity acceleration, $\mathbf{z}$ is an unit vertical vector, prime denotes the derivative with respect to z and $\mathbf{u} = \{u,v,w\}$, p, ρ are the perturbation velocity, pressure and density correspondingly, their scales being characteristic speed U , typical wavelength L and the mixed layer fluid density ρ_{00}. Being interested in linear dynamics, we perform Fourier transform of the perturbation wave field components with respect to the homogeneous horizontal coordinates and time

$$f(x,y,z,t) = \iint_{-\infty}^{+\infty} \hat{f}(\omega,k,z)\, \exp\{i(\mathbf{k}\cdot\mathbf{r} - \omega t)\}\, dk d\omega \tag{2.2}$$

and study each Fourier-component separately. The elimination of pressure and density from (2.1) leads to the well-known Taylor-Goldstein equation (see e.g. (LeBlond & Mysak 1979) for the vertical velocity (the sign ^ is omitted hereinafter)

$$(\omega - \mathbf{U}\cdot\mathbf{k})^2 w'' + [(\omega - \mathbf{U}\cdot\mathbf{k})\mathbf{U}''\cdot\mathbf{k} + (N^2 - (\omega - \mathbf{U}\cdot\mathbf{k})^2)k^2]w = 0 \tag{2.3}$$

where $N^2(z) = -g\rho_0'\rho_0^{-1}$ is the square of Brunt-Väisälä frequency, and $k = |\mathbf{k}|$. The proper boundary conditions at the bottom $z = -H$ and at the surface are

$$w\big|_{z=-H} = 0\,, \qquad w\big|_{z=0} = 0, \tag{2.4}$$

the latter is so-called 'rigid lid' approximation.

We shall be interested in the evolution of internal waves long in comparison with the mean current typical thickness h, so that the quotient

$$\varepsilon = \frac{h}{L} \ll 1 \tag{2.5}$$

forms a small parameter. Obviously, dispersion and other essential characteristics of long internal waves weakly depend on the fine structure of subsurface current. So to facilitate our analysis we choose the simplest but still relevant form of the mean-current-velocity profile

$$U(z) = \begin{cases} 1 + \dfrac{z}{\varepsilon}\,, & -\varepsilon \le z \le 0 \\ 0\,, & z < -\varepsilon \end{cases} \tag{2.6}$$

3.Asymptotic analysis of mode distortion. The chosen model of the mean current characterized by a vorticity jump at $z = -\varepsilon$ implies that mode function $w(z)$ is to obey to special conditions at that level. These could be received by integrating (2.3) through the level $z = -\varepsilon$ in a standard fashion and represent in fact the conditions of continuity of a 'fluid line' displacement and pressure

$$\left.\frac{w}{\omega - \mathbf{U}\cdot\mathbf{k}}\right|_{z=-\varepsilon-0}^{z=-\varepsilon+0} = 0 \tag{3.1a}$$

$$(\omega - \mathbf{U}\cdot\mathbf{k})w' + \mathbf{U}'\cdot\mathbf{k}\; w\Big|_{z=-\varepsilon-0}^{z=-\varepsilon+0} = 0 \tag{3.1b}$$

where the notation $z = -\varepsilon \pm 0$ denotes the limits of the expressions while z tends to $-\varepsilon$ from above and from below correspondingly. Thus the ocean model to study consists of three different layers, and (2.3) should be solved in each of these independently and then the solutions are to be matched at the boundaries using (3.1) or similar conditions. The mean current being absent at the depth, (2.3) becomes the standard equation for internal wave mode function which can be solved by usual methods for any given stratification. We are not interesting in an analysis of particular models, we shall focus our attention on consideration of the general problem of perturbation of internal wave characteristics by a thin subsurface shear current.

Both in moving and resting parts of the mixed layer Brunt-Väisälä frequency $N(z)$ is assumed to be identically zero as well as the second derivative of the mean current velocity (2.6), (2.3) can be solved explicitly to yield the depth dependence of the mode function $w(z)$ depth dependence

$$w = A\ \mathrm{sh}\{kz\} \tag{3.2a}$$

in the subsurface layer and

$$w = B\ \mathrm{sh}\{kz\} + D\ \mathrm{ch}\{kz\} \tag{3.2b}$$

in the still part of the mixed layer. The solution (3.2a) is chosen to satisfy the boundary condition (2.4) at the surface. We note that coefficients B and D depend on the wave frequency ω and wave vector $\mathbf{k}$, the explicit form of the dependence is found by matching (3.2b) with the solution of (2.3) in the stratified layer.

Matching solutions in moving and resting parts of mixed layer by substituting (3.2a) and (3.2b) into (3.1) we receive the set of equations

$$A\ \mathrm{sh}\{\varepsilon k\} = B\ \mathrm{sh}\{\varepsilon k\} - D\ \mathrm{ch}\{\varepsilon k\} \tag{3.3a}$$

$$\left(\omega k\ \mathrm{ch}\{\varepsilon k\} - \frac{\mathbf{v}\cdot\mathbf{k}}{\varepsilon}\ \mathrm{sh}\{\varepsilon k\}\right) A = \omega k \left(B\ \mathrm{ch}\{\varepsilon k\} - D\ \mathrm{sh}\{\varepsilon k\}\right) \tag{3.3b}$$

which after elimination of A yields a required dispersion equation for the internal wave mode

$$\left(\omega - \mathbf{v}\cdot\mathbf{k}\ \frac{\mathrm{th}\{\varepsilon k\}}{\varepsilon k}\right)\left(B\ \mathrm{sh}\{\varepsilon k\} - D\ \mathrm{ch}\{\varepsilon k\}\right) = \omega\ \mathrm{sh}\{\varepsilon k\}\left(B - D\ \mathrm{th}\{\varepsilon k\}\right) \tag{3.4}$$

herein $\mathbf{v}$ is the mean flow nondimensional velocity at the surface $z = 0$, its absolute value being unity.

We now recall that nondimensional thickness ε of the mixed layer moving part was supposed to be much smaller than unity and use it as a small parameter while looking for solutions of (3.4) in the form of asymptotic series in powers of ε

$$\omega = \omega_0 + \varepsilon\omega_1 + \ldots \tag{3.5}$$

Being the functions of wave frequency ω the coefficients B and D should be expanded in corresponding Taylor power series as well as hyperbolic functions. Performing the necessary calculations we obtain in the main order in ε

$$(\omega_0 - \mathbf{v}\cdot\mathbf{k})\ D(\omega_0,\mathbf{k}) = 0 \tag{3.6}$$

Each multiplier in (3.6) taken to be zero represents a dispersion relation in itself. The roots ω_0^n of the equation

$$D(\omega_0^n,k) = 0 \tag{3.7}$$

correspond to the internal wave modes originating from the stratified thick layer and are not affected by the subsurface shear current. The additional eigenvalue

$$\omega_0^* = \mathbf{v}\cdot\mathbf{k} \tag{3.8}$$

corresponds to the pure vortical mode owing its existence to the jump in the background vorticity field supplied by the shear current. The celerity of that mode in this order of approximation equals to the projection of the mean current surface velocity on the direction of its propagation.

Effect of subsurface current on the internal wave modes first manifests in the next order in ε. Performing the necessary calculations and taking into account the results (3.7), (3.8) we receive the first-order correction to the internal wave frequency

$$\omega_1^n = - kB \left(\frac{\partial D}{\partial \omega}\right)^{-1}\Big|_{\omega=\omega_0^n} \frac{\mathbf{v}\cdot\mathbf{k}}{\omega_0^n - \mathbf{v}\cdot\mathbf{k}} \tag{3.9}$$

The mode function $w(z)$ in the moving part of mixed layer corresponding to the eigenfrequency ω^n is readily found to be (the main order in ε)

$$w = B(\omega_0^n,k) \frac{\omega_0^n}{\omega_0^n - \mathbf{v}\cdot\mathbf{k}} \operatorname{sh}\{kz\} \tag{3.10}$$

During deduction of the expressions (3.9), (3.10) we required implicitly that the characteristic frequencies of internal gravity and vortical modes be of the same order and not too close to each other, that is, their differences be of order of unity. The former requirement is valid only when nondimensional Brunt-Väisälä frequency is of order unity. This being the case, one can conclude that, though the influence of the subsurface shear current on the internal wave frequency is small (of order of ε) in comparison with its undisturbed value, the vertical velocity in the subsurface layer changes significantly. The analysis performed above is not valid when undisturbed frequency of vortical mode is too close to that of one of internal gravity waves. This phenomenon results in mode coalescence and therefore requires special consideration.

4.Resonant interaction between internal gravity and vortex mode. Whence the main-order eigenfrequency of vortex mode (3.8) coincides with that of some internal gravity mode the asymptotic expansion (3.5) is readily seen to become singular because of the first order eigenfrequency correction being singular. The phenomenon breaking the asymptotic scheme used above is the linear resonance of two eigenmodes of the boundary value problem (2.3), (2.4) occurring at some particular curve in wavevector space $\mathbf{k} = \mathbf{k}^n$, determined from the dispersion equation

$$D(\omega_0^+,\mathbf{k}^n) = D(\mathbf{v}\cdot\mathbf{k}^n,\mathbf{k}^n) = 0 \tag{4.1}$$

From the main-order analysis it follows that the dispersion surfaces $\omega^n = \omega^n(\mathbf{k})$ and $\omega = \mathbf{v}\cdot\mathbf{k}$ of internal gravity and vortex mode intersect at the curve $\mathbf{k} = \mathbf{k}^n$ and therefore the dispersion equation (3.6) has a double root. It is well-known that in reality the dispersion curves do not intersect but split and, either so-called 'change of identities' or linear instability takes

place; anyway, the dispersion in the vicinity of the curve of intersection is essentially enhanced (Craik 1985). To study the behaviour of dispersion surfaces in the small vicinity of the place of intersection one has to rescale wavevector

$$\mathbf{k} = \mathbf{k}^n + \varepsilon^{1/2}\mathbf{q} \tag{4.2}$$

and look for a solution of (3.4) in the form of series in powers of $\varepsilon^{1/2}$, rather than in powers of ε

$$\omega = \omega_0^n + \varepsilon^{1/2}\omega_* + \ldots \tag{4.3}$$

Substituting (4.2), (4.3) into dispersion equation (3.4) and performing the same operations as in the previous section we get once again (3.6) which was presumed to fulfill and an identity in the order of $O(\varepsilon^{1/2})$. But in the order of $O(\varepsilon)$ instead of (3.9) we now obtain

$$\left(\omega_* - \mathbf{v}\cdot\mathbf{q} \right)\left(\frac{\partial D^n}{\partial \omega}\,\omega_* + \frac{\partial D^n}{\partial \mathbf{k}}\,\mathbf{q} \right) = -\,\omega_0^n\, k^n B^n \tag{4.4}$$

where

$$\frac{\partial D^n}{\partial \omega} = \left.\frac{\partial D}{\partial \omega}\right|_{\omega=\omega_0^n,\mathbf{k}=\mathbf{k}^n}, \quad \frac{\partial D^n}{\partial \mathbf{k}} = \left.\frac{\partial D}{\partial \mathbf{k}}\right|_{\omega=\omega_0^n,\mathbf{k}=\mathbf{k}^n}, \quad B^n = B(\omega_0^n,\mathbf{k}^n) \tag{4.5}$$

As eigenfrequency ω can be considered as a function of wavevector $\mathbf{k}$ we are able to modify the second expression in (4.5) as follows (Whitham 1974)

$$\frac{\partial D^n}{\partial \mathbf{k}} = \frac{\partial D^n}{\partial \omega}\,\frac{\partial \omega}{\partial \mathbf{k}} = \frac{\partial D^n}{\partial \omega}\,\mathbf{c}_g \tag{4.6}$$

where $\mathbf{c}_g$ is the group velocity of the internal wave at the curve of intersection. After modification (4.6) the expression (4.4) can be reduced to a quadratic equation for the correction to the internal wave frequency owing to the resonant interaction with the vortex mode

$$\omega_*^2 - \omega_*(\mathbf{v} - \mathbf{c}_g)\cdot\mathbf{q} + \omega_0^n\, k^n \frac{B^n}{\partial D^n/\partial\omega} - (\mathbf{v}\cdot\mathbf{q})(\mathbf{c}_g\cdot\mathbf{q}) = 0 \tag{4.7}$$

Its solutions describing the splitting of intersecting dispersion surfaces are easily found to be

$$\omega_*^{\pm} = \frac{1}{2}\left\{ (\mathbf{v} - \mathbf{c}_g)\cdot\mathbf{q} \pm \left[\left((\mathbf{v} + \mathbf{c}_g)\cdot\mathbf{q} \right)^2 - 4\omega_0^n\, k^n \frac{B^n}{\partial D^n/\partial\omega} \right]^{1/2} \right\} \tag{4.8}$$

Whether the resonant interaction leads to linear instability or not is completely determined by the sign of the value

$$J = \omega_0^n \frac{B^n}{\partial D^n/\partial\omega} \tag{4.9}$$

independent of the shear flow features. The function $J(\omega,\mathbf{k})$ is completely determined by the internal wave inner characteristics and plays the role of adiabatic invariant related to the particular wave mode and determining the sign of wave energy. The linear mode coalescence is unstable when the coupling modes have different signs of energy and stable otherwise (Cairns 1979). In our case the instability occurs if only (4.9) has positive sign at the

resonant curve.

The distortion of mode function $w(z)$ in case of internal wave resonance with the vortex mode is much stronger than in nonresonant case. To illustrate the statement we use (4.8) and (3.3) and easily obtain in the main order in ε the vertical velocity mode function in the subsurface layer ($-\varepsilon < z < 0$)

$$w(z) = - \varepsilon^{-1/2}(k^n)^{-1}\frac{\partial D^n}{\partial \omega}(\omega_* + c_g \cdot q)\ \mathrm{sh}\{k^n z\} \qquad (4.10)$$

The negative power of the small parameter does not mean that vertical velocity becomes asymptotically large because the value of hyperbolic function in the upper layer is of order of ε. Meanwhile the resonance greatly amplifies vertical motion in the upper subsurface layer even in case of stable mode interaction while its influence on the mode function at the depth is still asymptotically small.

5.Surface manifestations of internal waves. We have already specified in the introduction that saying 'surface manifestations' we mean horizontal velocity perturbations at the sea surface. Though amplified in presence of shear current vertical velocity is still small and almost undetectable in the subsurface layer, as follows from (3.10), (4.10), becoming zero at the surface because of the boundary condition (2.4). So we shall analyze the effect of the mean current on horizontal velocity perturbations caused by the waves. In the linear approximation the horizontal components can be easily expressed through the already found vertical velocity by using (2.1). Obviously we are interested in their values at the surface $z = 0$. In absence of internal wave - vortex mode resonance we easily get from (2.1), (3.10) for the desired components of the perturbation wave field

$$u_h^n = i\,\frac{k}{k}\,\frac{\omega_0^n}{\omega_0^n - v\cdot k}\,B^n \qquad (5.1)$$

where expression (5.1) describes perturbation horizontal velocity field at the surface while corresponding to the n-th mode of internal waves. In case of resonance the perturbations of horizontal velocity are amplified significantly due to linear interaction of modes, the correspondent explicit expressions derived from (2.1), (4.10) being

$$u_h^n = - i\varepsilon^{-1/2}\frac{\partial D^n}{\partial \omega}(\omega_* + c_g \cdot q)\,\frac{k^n}{(k^n)^2} \qquad (5.2)$$

Both in (5.1) and in (5.2) we used the notations defined in paragraphs 3, 4. To judge the enhancement of horizontal motion in the subsurface layer produced by shear current one should compare (5.1), (5.2) with its analogs in absence of any mean current. If there were no current, the surface perturbations of horizontal velocity would be

$$u_h^n = i\,\frac{k}{k}\,B^n \qquad (5.3)$$

For comparison we choose the internal wave mode corresponding to the same unperturbed eigenfrequency ω^n and similarly normalized.

One can readily see from (5.1) - (5.3) that nonuniform horizontal velocity field created by internal waves are enhanced in a large extent if subsurface mean current is present, its order of magnitude increasing under resonant conditions reaching $O(\varepsilon^{-1/2})$ in compare with no current case. Henceforth, the effect of the thin subsurface current on the internal wave surface manifestations is significant, being the most intense in case of resonance

between internal wave modes and vortex mode appearing due to current presence.

6.Discussion. The analysis performed above shows that a subsurface shear current even being localized in the narrow sublayer within the 'mixed' layer strongly affects internal waves surface manifestations by amplifying greatly horizontal wave velocities and through them all the "end" observable characteristics. As such currents are almost always present in the real ocean environment their influence is one of the most important factors governing the internal wave manifestations.

We note also that in case we are interested in the manifestations of a stochastic internal field, we can expect that the resonant harmonics, i.e those Fourier-components whose celerity equals the flow surface velocity projection on the direction of wave propagation and thus are in resonance with the specific vortex mode generated by the mean current shear, will dominate in the manifestations of the stochastic internal wave field at the surface.

We note that the hypothesis about the key role of vorticity waves as well as vorticity waves themselves in the context of upper ocean dynamics were first discussed in *(Shrira 1989)*, but the hypothesis has not been elaborated.

The mechanisms of internal wave amplification considered above do not exhaust the problem, one of the most interesting in this context questions remaining open is: whether there is a place for an instability of this shear current. One might expect existence of internal waves with sign of energy different from that of vortex mode. They would have positive adiabatic invariant (4.10) and their linear interaction with the latter would lead to an instability, while even more intense process of explosive nonlinear interaction between internal gravity and vortex waves would likely to be possible. More specifically the question can be formulated as whether there are exist some stratification profiles possessing the necessary properties and, on the other hand, generic enough to merit special study. The only work the authors are aware of which tracts similar problem is that of Reutov (1990), where within the simplest two-layer model no unstable linear interaction was found. The authors own analysis of some simple models, both of three-layer fluid and of fluid with constant Brunt-Väisälä frequency, does not reveal any instability. Thus this question is still open.

REFERENCES

Cairns R.A. 1979 The role of negative energy waves in some instabilities of parallel flows. *J. Fluid Mech.*, **92**, 1 - 14.

Craik A.D.D. 1985 *Wave interactions and fluid flows.* Cambridge University Press.

LeBlond P.H. & Mysek L.A. 1979 *Waves in the ocean.* Elsevier.

Whitham G.B. 1974 *Linear and nonlinear waves.* John Wiley & Sons.

Reutov V.P. 1990 The internal wave instability in the stratified fluid with a near-surface flow. *Izv. AN SSSR Fizika atm. i okeana*, **26**, 871 - 877.

Shrira V.I. 1989 On the 'subsurface' waves in the oceanic upper mixed layer. *Doklady AN*, **308**, p.732-736.

"Effect of large-scale internal waves on the sea surface" (ed. **Pelinovsky E.N**), Institute of Appl. Physics Publishers, Gorky, 1982, 251pp (in Russian).

Interaction and Generation of Waves in a Two-Layer Fluid Flowing over Uneven Bottom

Mitsuaki FUNAKOSHI
Research Institute for Applied Mechanics, Kyushu University,
Kasuga, Fukuoka, 816, Japan

Abstract. In a two-layer flow over uneven bottom, both wave generation by the bottom topography and the resonant interaction between two wave modes are examined simultaneously. An evolution equation is derived which describes not only the resonant interaction between long internal mode and the wave packet of short surface mode, but also the generation of long internal mode due to the resonant motion of the fluid relative to the bottom unevenness. The interactions between the waves trapped by the localized bottom unevenness and steady progressive waves coming to it are examined numerically on the basis of this equation.

§1. Forced Long-Short Interaction Equation

When a two-layer fluid flows over a localized bottom unevenness of large horizontal scale at the velocity V which is close to the phase speed c_p of the internal mode in the long-wave limit, long internal-mode waves are generated resonantly (similarly to the cases of single-layer fluid[1,2] and continuously stratified fluid[3]). Furthermore, if we assume the existence of the surface mode whose group velocity is close to c_p, the resonant interaction between the long internal mode and the packet of the short surface mode is possible[4]. Aiming at examining the system with not only the resonant interaction but also the resonant generation, we derive, through a reductive perturbation method, the following 'forced long-short interaction equation' from the basic equations for irrotational motion of the inviscid fluid, under a few assumptions :

$$iS_T - i\lambda S_X - S_{XX} + SL = 0, \quad L_T - \lambda L_X - (|S|^2)_X + H_X = 0, \qquad (1a,b)$$

where L is proportional to the interface displacement of the long internal mode, whereas S to the complex amplitude of the short surface-mode wave packet. Also $H(X)$ expresses the bottom unevenness, and λ a small difference of V from c_p. X is a horizontal coordinate in which the fluid flows from the positive X direction, and T is the time. The details of the derivation of eq.(1) are shown in Ref.5.

§2. Steady Trapped Waves

Equation (1) has solutions corresponding to steady waves trapped by the localized bottom unevenness. The trapped waves are composed of trapped long waves (called TLW from now on) given by

$$S = 0, \quad L = \frac{1}{\lambda} H(X), \qquad (2)$$

and trapped coupled waves - called TCW from now on - expressed by

$$\zeta = \eta(X)\exp\{i(\lambda X - \Omega T)\} + (\text{complex conjugate}), \qquad (3)$$

where f, η and g are real functions satisfying

$$f(X) \to 0, \quad \eta(X) \to 0, \quad g(X) \to 0 \quad \text{as} \quad |X| \to \infty, \qquad (4)$$

and Ω is a real constant. Substituting eq.(3) into eq.(2), we have

$$g = \frac{1}{2}(\lambda - \lambda_0)f + \frac{1}{2}f'' + Hf, \qquad (5)$$

$$\eta'' - \frac{1}{2}f^2\eta - (\lambda - \lambda_0)H\eta - \frac{1}{4}(\lambda - \lambda_0)^2\eta - \Omega\eta = 0 \qquad (6)$$

where λ_0 is a constant and primes denote differentiation with respect to X. Boundary condition (4) and eq.(6) produce an eigenvalue problem with eigenvalue Ω for specified function H and value λ. Eigenfunction $f(X)$ and Ω can be computed using a kind of shooting method[5]. Then $g(X)$ is computed from eq.(5). It should be noted that there are generally many TCW's (with different Ω) for each function H and value λ.

In the computation of TCW for the symmetric mountain of the shape

$$H = \mathrm{sech}^2 X. \qquad (7)$$

in addition to symmetric waves with one or two peaks in $f(X)$, a variety of waves with many peaks, antisymmetric waves, and asymmetric (neither symmetric nor antisymmetric) waves were found (see Ref.5 for the details). Figures 1 and 2 show examples of the TCW for $\lambda < 0$ and $\lambda > 0$, respectively. There is also an analytic solution expressed by

$$S = \sqrt{1+2\lambda}\,\mathrm{sech}X\exp\{i[-\frac{1}{2}\lambda X - (1+\frac{1}{4}\lambda^2)T]\}, \quad L = -2\mathrm{sech}^2 X, \qquad (8)$$

if $\lambda > -1/2$. This is one of the symmetric TCW.

§3. Steady Progressive Waves over Even Bottom

Equation (1) has two kinds of steady progressive waves if the bottom is even ($H = 0$). The first wave is a soliton expressed by

$$\begin{cases} S = \sqrt{2(\lambda+\tilde{p})}\,\tilde{q}\,\mathrm{sech}[\tilde{q}(X-\tilde{p}T-X_0)]\exp\{i[-\frac{1}{2}(\lambda+\tilde{p})X - \hat{\Omega}T + \psi_0]\}, \\ L = -2\tilde{q}^2\mathrm{sech}^2[\tilde{q}(X-\tilde{p}T-X_0)], \end{cases} \qquad (9)$$

where $\tilde{p}$, $\tilde{q}$, X_0, and ψ_0 are arbitrary real constants and $\hat{\Omega} = \tilde{q}^2 - \tilde{p}^2/4 + \lambda^2/4$. This soliton is a coupled wave which propagates at the velocity $\tilde{p}$ and whose horizontal scale is characterized by $\tilde{q}^{-1}$.

The second wave is a free long wave (called FLW from now on) expressed by

$$S = 0, \quad L = \psi(X + \lambda T), \tag{10}$$

where ψ is an arbitrary function. This FLW propagates at the velocity $-\lambda$.

§4. Interactions between Trapped Waves and Progressive Waves

The interactions between the steady progressive waves coming to the localized bottom unevenness and the steady trapped waves are examined for the mountain given by eq.(7) by solving eq.(1) numerically with a finite-difference method. In discretizing eq.(1), central difference was used both for time evolution and for spatial variation. The computational domain was usually $-75 \leq X \leq 75$ with a periodic boundary condition. The spatial spacing $\Delta X = 0.05$ and the time increment $\Delta T = 0.0005$ were usually used. The accuracy of the computation was checked by comparing the results with those for smaller ΔX and ΔT and by calculating the conservative quantities of eq.(1).

One important point of view in considering the behaviour of waves is the effect of long waves on the short-wave packet. If we consider the equation $iS_T = -SL$, obtained from eq.(1a) by neglecting the second and third terms, and substitute $S = |S|\exp(i\hat{\theta})$ [$\hat{\theta}$ is a real function] into this equation, we obtain $\hat{\theta}_{XT} = L_X$. Its left-hand side expresses the time evolution of the wavenumber of the short wave. Thus, this wavenumber increases in the X region where $L_X > 0$. This results in the decrease in the group velocity because of the convex shape of the dispersion curve of the surface mode. Therefore, the movement of the short-wave packet to the $-X$ direction is expected. Opposite effect is expected in the X region where $L_X < 0$. Therefore, the positive part of L tends to repel the short-wave packet, whereas the negative part tends to attract it.

Another important point of view is the effect of the mountain on the long wave. If we consider equation $L_T = -H_X + \lambda L_X$, obtained from eq.(1b) by neglecting the third term, its general solution is $L = H(X)/\lambda + \hat{\psi}(X + \lambda T)$, where $\hat{\psi}$ is an arbitrary function expressing the FLW. Therefore, it is expected that in the absence of the short wave if $\lambda > 0 (\lambda < 0)$ then positive (negative) L is finally generated near the mountain,

Figure 3 shows the evolution of waves in the interaction between the TLW and a soliton ($\tilde{p} = \tilde{q} = 1.0$) for $\lambda = -0.5$. Here solid lines denote $|S|$, and broken lines L. The lowest solid line in each figure expresses $H(X)$, and the right-hand side of the mountain ($X > 0$) is the upstream side. The disruption of the incident soliton into two solitons and a positive FLW is found. Near the mountain, a symmetric TCW is generated after a part of short-wave component of the incident soliton is captured by the negative part of L through the mechanism described above.

Figure 4 shows the interaction between the symmetric TCW given by eq.(8) and the FLW expressed by $L = -2.5\mathrm{sech}^2(X - 10)$ for $\lambda = 1.0$. In this case, all the short wave is pushed away from the mountain, and the TLW is the final state near the mountain.

can be explained that the positive part of L generated by the moutain pushes the short wave away. This repelled short wave couples with the negative part of L and forms 2 or 3 solitons. Figure 5 shows the interaction between the TLW and a soliton ($\tilde{p} = \tilde{q} = 1.0$) for $\lambda = 1.0$. Near the mountain, short wave is pushed away and the TLW is the final state, as in Fig.4. The incident soliton is reflected at the mountain, and its amplitude becomes much larger.

Next, in order to examine the dependence of the final state on the initaial state quantitatively, a few series of computations were carried out. At first, in the initial condition similar to that for Fig.5, only $\tilde{q}_0$ ($\tilde{q}$ of the incident soliton) was changed within the range from 0.8 to 1.2. Although one soliton always exists in the final state of this case, its behaviour is classified into two quite different ones. That is, for $\tilde{q}_0 \leq 1.02$, the reflection and amplification of the soliton are observed as in Fig.5, whereas the incident soliton passes through the mountain with little deformation for $\tilde{q}_0 \geq 1.04$, as shown in Fig.6. Figure 7 shows the parameters $\tilde{p}$ and $\tilde{q}$ of the final soliton as the functions of $\tilde{q}_0$. We clearly see the abrupt change of the behaviour when $\tilde{q}_0$ crosses 1.03.

In the next series, for $\lambda = -0.3$, the interactions between the TLW and a soliton ($\tilde{p} = 1.0$, $\tilde{q} = \tilde{q}_0$) were examined for a variety of $\tilde{q}_0$ values. The TCW's for this λ value are composed of the symmetric mode (expressed by a solid line in Fig.8) and the antisymmetric mode (a broken line). In the numerical computations, we find the final state consisting of two solitons and a TCW for almost all the $\tilde{q}_0$ values within the range $0.4 \leq \tilde{q}_0 \leq 1.7$. This final TCW is antisymmetric for $\tilde{q}_0 \leq 0.8$, whereas symmetric for $\tilde{q}_0 \geq 0.9$ (an example of the former case is shown in Fig.9). Figure 10 shows the parameters $\tilde{p}$ and $\tilde{q}$ of the two final solitons and $f(0)$ (for symmtric mode) or $f'(0)$ (for antisymmetric mode) of the final TCW as functions of $\tilde{q}_0$. Although the dependence of these values on $\tilde{q}_0$ is mild for relatively small $\tilde{q}_0$, complicated dependence is found for $\tilde{q}_0 \geq 1.3$. Another example of such a complicated dependence on the initial condition is shown in Fig.11. Here $f(0)$ of the symmetric TCW generated by the interaction between a soliton ($\tilde{p} = 1.0$, $\tilde{q} = \tilde{q}_0$, $0.68 \leq \tilde{q}_0 \leq 1.39$) and TCW given by eq.(8) is shown as a function of $\tilde{q}_0$ for $\lambda = -0.3$. The value of $f(0)$ depends on $\tilde{q}_0$ in a complicated way. Moreover, for special values of $\tilde{q}_0$ such as 0.89 and 1.20, $f(0)$ is almost zero, implying the generation of the TLW.

§5. Conclusions

The interactions between the waves trapped by the localized bottom unevenness (TCW and TLW) and the steady progressive waves (soliton and FLW) coming to it are examined numerically on the basis of eq.(1). The results are summarized as :

(i) Near the moutain, the TLW is the final state for $\lambda > 0$, whereas a TCW is the final state for $\lambda < 0$ (except for the case of no short wave in the initial state).

(ii) The amplification, reflection, and disruption of the incident soliton occur in the in-

teraction.

(iii) The complicated dependence of the final state on the initial state, and the abrupt change of the final state associated with a small change of the initial state can be observed.

References

1) Wu, T. Y.: *Generation of upstream advancing solitons by moving disturbances*, J. Fluid Mech. **184** (1987) 75-99.

2) Lee, S., Yates, G. T. and Wu, T. Y.: *Experiments and analyses of upstream-advancing solitary waves generated by moving disturbances*, J. Fluid Mech. **199** (1989) 569-593.

3) Grimshaw, R. H. J. and Smyth, N.: *Resonant flow of a stratified fluid over topography*, J. Fluid Mech. **169** (1986) 429-464.

4) Funakoshi, M. and Oikawa, M.: *The resonant interaction between a long internal gravity wave and a surface gravity wave packet*, J. Phys. Soc. Jpn. **52** (1983) 1982-1995.

5) Funakoshi, M.: *Steady trapped solutions to forced long-short interaction equation*, J. Phys. Soc. Jpn. **62**(1993) 1993-2006.

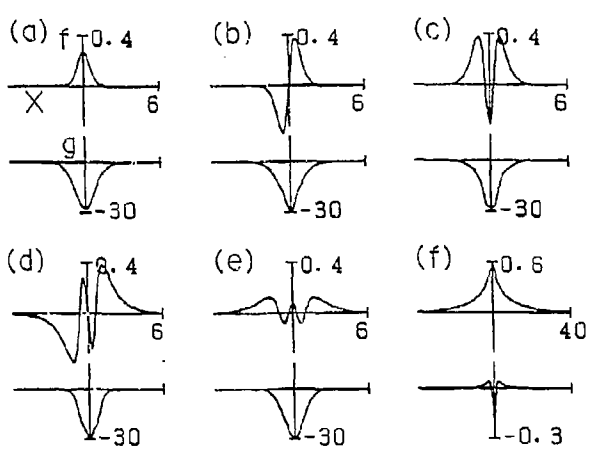


Fig.1 Examples of the TCW for $\lambda < 0$. (a) $\lambda = -1/30$, $\Omega = 23.5$, (b) $\lambda = -1/30$, $\Omega = 13$, (c) $\lambda = -1/30$, $\Omega = 6$, (d) $\lambda = -1/30$, $\Omega = 1$, (e) $\lambda = -1/30$, $\Omega = 0.7$, (f) $\lambda = -3$, $\Omega = 2.2583$.

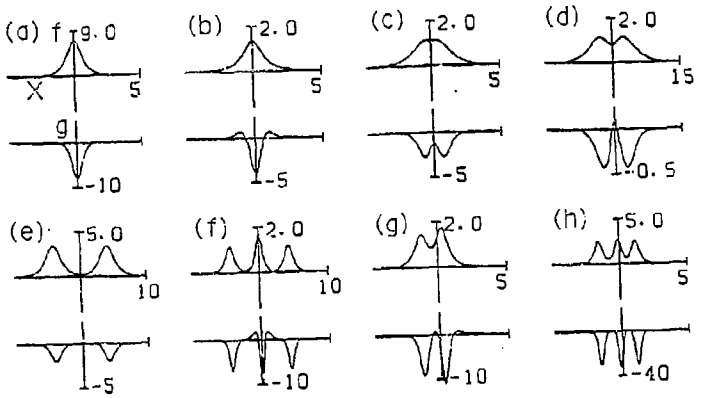


Fig.2 Examples of the TCW for $\lambda > 0$. (a) $\lambda = 6$, $\Omega = 13$, (b) $\lambda = 0.2$, $\Omega = 1$, (c) $\lambda = 0.2$, $\Omega = 1.6$, (d) $\lambda = 3$, $\Omega = 2.465$, (e) $\lambda = 6$, $\Omega = 10$, (f) $\lambda = 0.2$, $\Omega = 3.4$, (g) $\lambda = 0.2$, $\Omega = 4.6$, (h) $\lambda = 0.2$, $\Omega = 15.1$. (g) and (h) are asymmetric TCW.

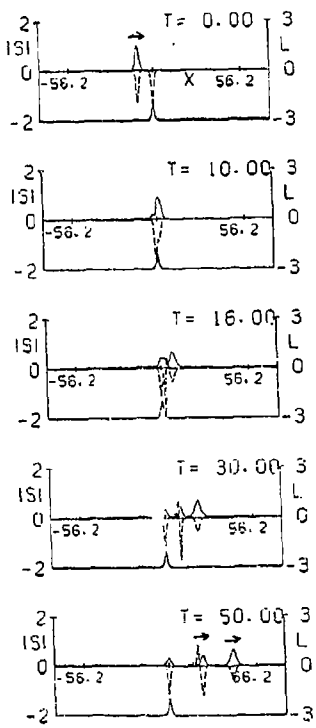


Fig.3 Interaction between the TLW and a soliton ($\tilde{p} = \tilde{q} = 1.0$). $\lambda = -0.5$. Solid lines denote $|S|$, broken lines denote L.

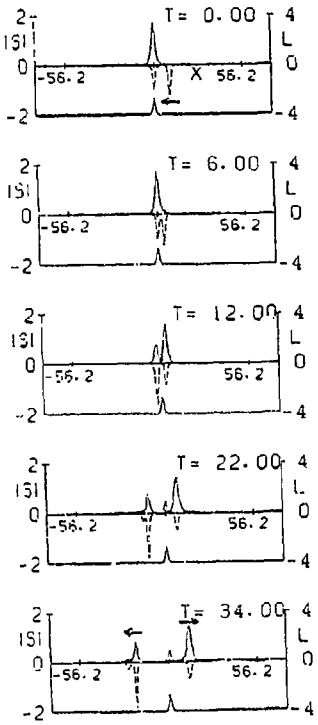


Fig.4 Interaction between the symmetric TCW given by eq.(8) and a FLW. $\lambda = 1.0$.

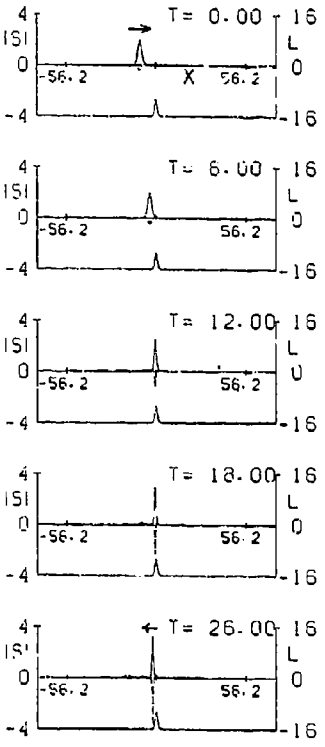


Fig.5 Interaction between the TLW and a soliton ($\tilde{p} = \tilde{q} = 1.0$). $\lambda = 1.0$.

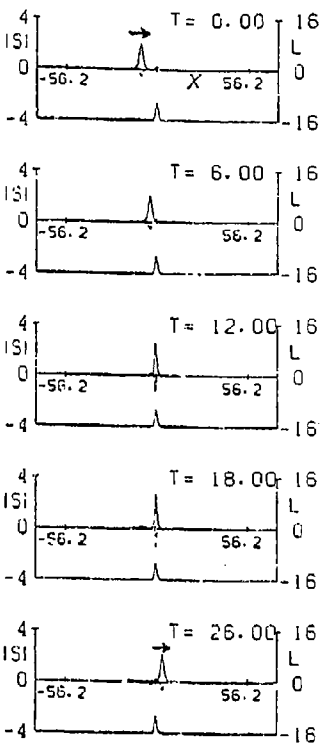


Fig.6 Interaction between the TLW and a soliton ($\tilde{p} = 1.0, \tilde{q} = 1.04$). $\lambda = 1.0$.

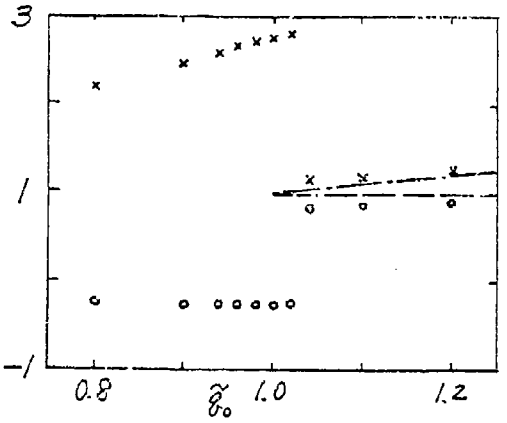


Fig.7 Parameters $\tilde{p}$ (o) and $\tilde{q}$ (×) of the soliton generated by the interaction between the TLW and a soliton ($\tilde{p} = 1.0$, $\tilde{q} = \tilde{q}_0$). $\lambda = 1.0$. Broken line is $\tilde{p}(= 1.0)$ of the incident soliton, dotted-broken line is $\tilde{q}(= \tilde{q}_0)$ of the incident soliton.

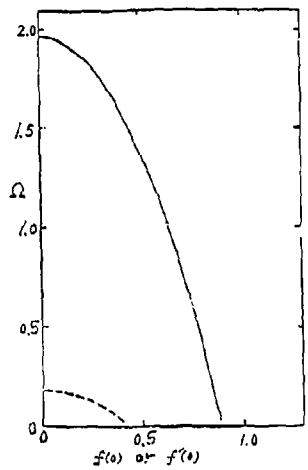


Fig.8 TCW's for $\lambda = -0.3$. Horizontal axis is $f(0)$ for symmetric mode (solid line), and $f'(0)$ for antisymmetric mode (broken line). Vertical axis is Ω in eq.(3).

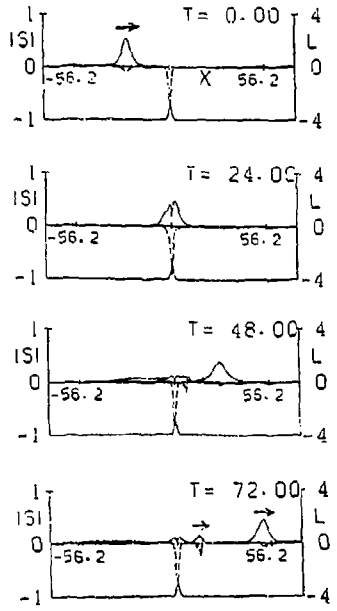


Fig.9 Interaction between the TLW and a soliton ($\tilde{p} = 1.0, \tilde{q} = 0.45$). $\lambda = -0.3$.

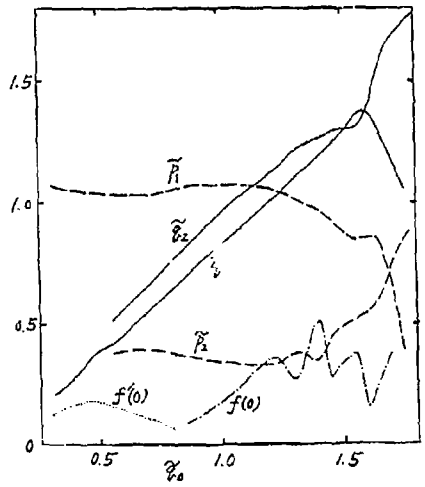


Fig.10 Dependence of the final state on $\tilde{q}_0$ in the interaction between the TLW and a soliton ($\tilde{p} = 1.0, \tilde{q} = \tilde{q}_0$). $\lambda = -0.3$. ($\tilde{p}_1$, $\tilde{q}_1$) and ($\tilde{p}_2, \tilde{q}_2$) are parameters of the two final solitons. Dotted line is $f'(0)$ of the final antisymmetric TCW, dotted-broken line is $f(0)$ of the final symmetric TCW.

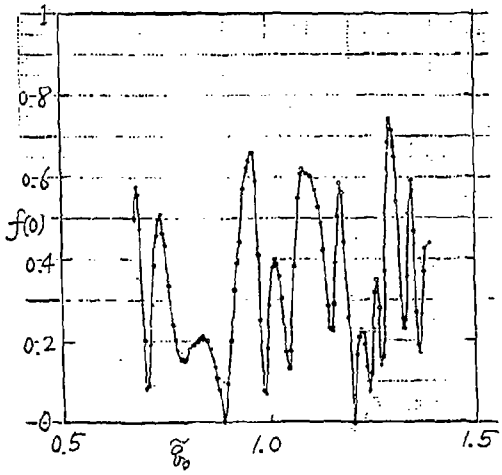


Fig.11 $f(0)$ of the symmetric TCW generated by the interaction between the symmetric TCW given by eq.(8) and a soliton ($\tilde{p} = 1.0$, $\tilde{q} = \tilde{q}_0$) . $\lambda = -0.3$.

STEEPENING OF THE LEADING AND BACK FACES OF SOLITARY INTERNAL WAVE-DEPRESSIONS AND ITS CONNECTION WITH TIDAL CURRENTS

A.N.SEREBRYANY

N.N.Andreev Acoustics Institute, Moscow 117036, Russia

1. Abstract

During internal wave investigation in summer season on the Pacific shelf of Kamchatka, internal waves depressions were recorded as having either steepened forward face or a steepened back face. It was established that these changes in profile are correlated with tidal phase. The waves with steepened leading face were most common during flood tide and the waves with steepened back face dominated during ebb. Significant properties of observed internal waves are revealed: the higher amplitude of the waves, the smaller steepening of face;the wave spreading during ebb are higher than w ives in flood tide.

2. Introduction

Large-amplitude internal waves observed in the sea often show two types of profile asymmetry which may be called vertical (crest-trough) and horizontal (due to difference in the slope of the leading and following edges) asymmetry [1]. The first type of asymmetry is attributed to the pycnocline being close to the sea surface or bottom. The second one is

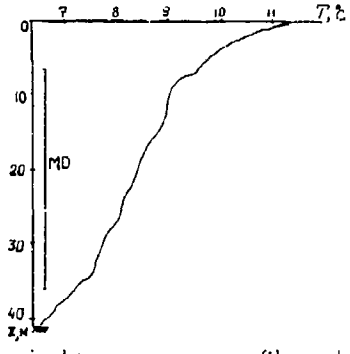


Figure 1: Typical temperature profile and position of the meter of vertical displacements.

typical for strong nonlinear waves and often precedes the wave breaking. The effect of horizontal asymmetry in field observations for solitary internal wave elevations manifests in a unique manner of leading wave face steepening while for wave depressions a definite pattern has not been detected [1,2]. At the same time the laboratory experiments demonstrate that a shoaling wave depression has only a steepened back face [3,4]. Of importance of current on the shape of internal waves was demonstrated in the works [5,6] on the basis of laboratory experiment and theoretical study. However field investigations on this question are practically absent. In this paper we present the results of field observations of internal wave-depressions in the coastal waters where either steepened forward face or a steepened back face were recorded. Some interesting features of observed waves including correlations of that profile changes and tidal phase were revealed.

3. Observations

The observations were made on the Pacific shelf of Kamchatka in front of one of the bays from anchored research vessel. A distance to the nearest shore was nearly 2 km and depth of the sea in the place of observation - 40 m. There is a relatively narrow continental shelf with cross size of 20 km and mean slope of 0.013. The measurements of internal waves were carried out during 34 hours, the August 20-21, 1988.

Internal waves were measured by means of meter for vertical displacements [7]. This meter consists of two identical distributed temperature sensors each 25 m long, shifted vertically by 5 m, relative to each other. The meter is deployed vertically in the layer with thermocline and continuously measures mean temperature and vertical gradient in the layer and so permits us to obtain the data on vertical displacements of the interfaces. Position of the lower end of the meter was monitored by means of pressure sensor. There was a calm weather during the observations and pressure sensor's readings showed an absence of any displacements or pollutant oscillations of the meter.

To provide information on currents two current meters with 5- minutes sampling interval were deployed on horizons 15 m and 30 m. Temperature distribution with depth and its variability was measured by means of CTD probe sampling. Vertical temperature profile in the place of observation was characterized with nearly uniform decay of temperature with depth (mean vertical gradient was 0.1 (°/m) except for upper 10 meter

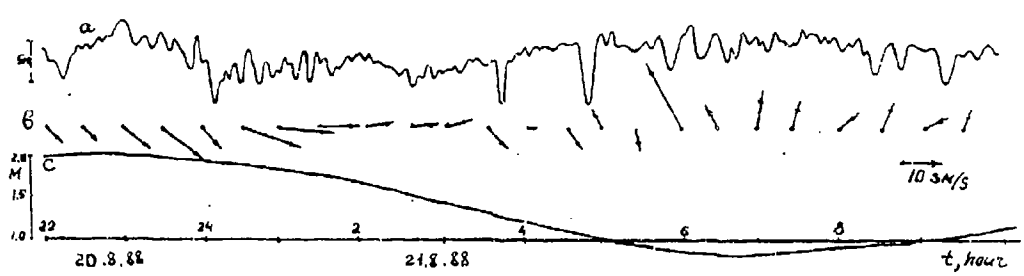


Figure 2: Part of records of the data: (a) vertical displacements; (b) currents on horizon 30 m; (c) sea surface.

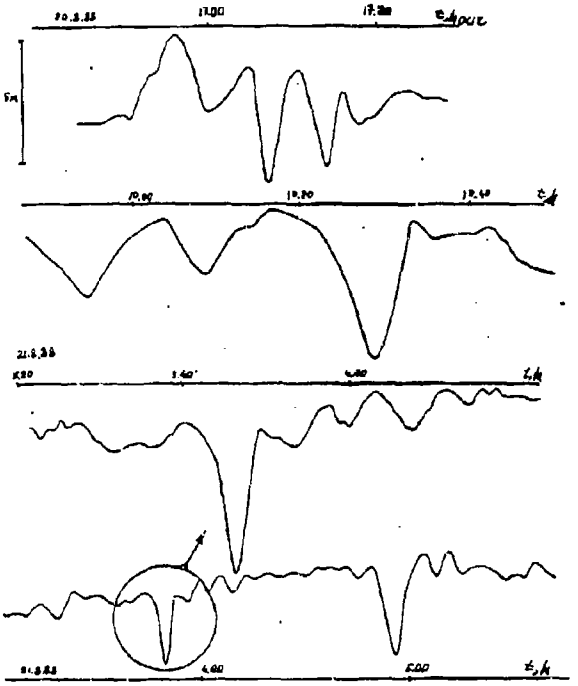


Figure 3: Examples of the waves of large amplitude.

subsurface layer with more sharp thermocline difference (see Fig. 1). The surface temperature was 11.5 C and near bottom temperature was 6.5-7 C. Density stratification was similar to the temperature distribution with depth.

4. Steepening of front and back faces of internal waves

Fig. 2 shows part of the record of thermocline vertical displacements together with current's data for horizon of 30 m. On this record we can see that there exist often short period waves the amplitudes of which is sometimes of significant value. At the same time long period oscillations of thermocline (tidal periodicity), despite the strong barotropic tide, appear only slightly on the record.

Common notion about the observed short-period internal wave field makes it possible to calculate the spectrum basing of the record. The spectrum has well pronounced picks in the ranges near 8 c/h and 2-3 c/h the decay law being close to power "minus two".

During the diurnal observations current direction significantly varied in time. First north-west currents have dominated. Then west, south-east and south currents have taken place. The data show that the ellipse of tidal currents in this place is very distorted. Currents are as high 0.25 m/s (mean value of 0.10 - 0.15 m/s).

Short period waves often emerging on thermocline resulted in its vertical displacements up to 5-8 m. The waves observed have both trains from several waves and solitary. Some

of the examples of observed waves are shown on Fig.3. Calculating number of intense waves on the diurnal record was done and their parameters – heights and periods were obtained and summarized in the table. Periods of the waves load between 5 and 23 minutes,heights are in the range from 2.3 to 8.3 meters. Because the measurements were done in one "point" we do not have data on the length of waves and the directions of their propagation. However, on the assumption of well known properties of internal waves on a shelf we can suppose with much probability that observed internal waves being travelling towards the shore. Indirect evidence of this circumstance, through visual observation of the sea surface with appropriately oriented slick stripes, were obtained.

Table 1. Parameters of internal waves. * — steepness is given in relative units:

N	*Time, hour*	*Period, min*	*Height, m*	*Front's* steepness*	*Back's* steepness*	*Relative steepness*
1	11.30	23	4.0	0.2	0.23	0.87
2	13.10	10	2.8	0.43	0.25	1.72
2′	13.21	13	3.3	0.35	0.25	1.40
3	17.00	8.5	3.0	0.45	0.28	1.61
3′	17.07	5.5	4.8	1.38	1.10	1.25
4	19.55	14.5	3.3	0.44	0.33	1.33
5	22.16	13	3.5	0.18	0.47	0.38
6	23.27	9	2.3	0.21	0.41	0.51
6′	23.13	14	2.3	0.23	0.15	1.53
7	23.54	10	5.0	0.63	0.43	1.47
8	0.30	10	4.7	0.31	0.53	0.58
9	1.16	8.5	4.0	0.37	0.56	0.66
9′	1.25	8.5	4.5	0.61	0.82	0.74
10	3.48	5.0	5.8	0.83	0.83	1.00
11	4.55	14	8.3	0.64	0.71	0.90
12	5.58	14	4.2	0.31	0.20	1.55
13	10.28	13	5.2	0.51	0.66	0.77
14	12.42	11	6.3	0.84	0.67	1.25
15	13.03	9	7.5	0.71	1.21	0.59

Of interest are two solitary waves separated by one hour interval (their heights are 5.8 m and 8.3 m, and periods are 5 and 14 minutes, respectively). There is a most striking characteristic shape of depressions,peculiar practically to all observed waves with higher above the mean value of amplitude. This is the well known nonlinearity effect of internal waves which takes place when wave guide is being close to the sea surface. In this case internal waves have shape with sharp narrow troughs and flattened crests. The observed stratification of environment has resulted in the manifestation of its nonlinearity effect.

Besides the vertical asymmetry, clear manifestation of horizontal asymmetry of internal wave profiles was revealed when slopes of front and back faces are different (See Fig. 4). As a measure of horizontal asymmetry of a wave we will take the relation of the front's slope to the back's slope, designate it as γ. Thus, for wave with symmetrical profile this parameter equal to 1. At more steep front slope, γ is larger then 1, and at more flattened one, γ is smaller then 1. Data on the steepness for 19 individual waves observed during diurnal period are summarized in the table. From this data we notice that the parameter

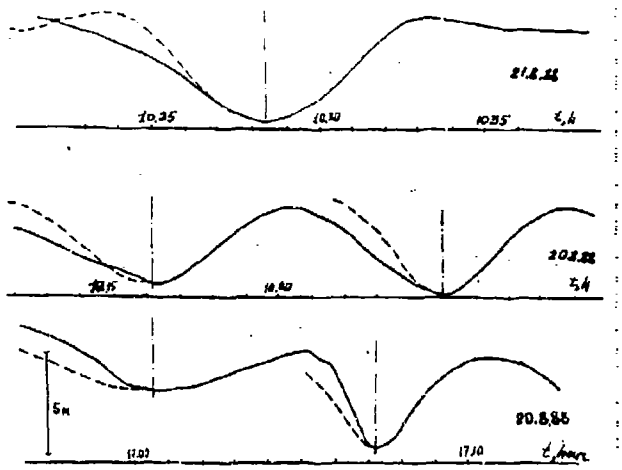


Figure 4: Effect of horizontal asymmetry in internal waves. Mirror mappings of the back faces of a wave, relative to vertical axis, passing through deepest point of the troughs , are shown (dotted line) to produce a clearer illustration of the effect.

of relative steepening γ is lying in the range from 0.38 to 1.64. Among the total of 19 waves only one wave has symmetrical profile, a number of the waves with steepened front and back faces is nearly equal (9 and 10 waves, respectively). It is interesting to note that the horizontal asymmetry, as a rule, is retained for all waves comprising the trains.

5. Correlation between heights and horizontal asymmetry of the waves

Let us compare the parameters of observed waves with their parameters of relative steepening. First we will test the dependence between period and asymmetry of the waves. Fig. 5a shows the appropriate results. From this figure it is evident that horizontal asymmetry is inherent practically for the waves of all considered periods. When we compare the heights of observed waves with parameter of horizontal asymmetry, we find an interesting tendency. This tendency is as follows: the waves of largest heights have more symmetrical profile while the lowest waves have more horizontal asymmetrical profiles (See Fig. 5b). This law takes place for both waves with steepened front and waves with flattened one. On the basis of the data observed the linear regression lines are plotted. They are as follows: $A = 1.85 + 4.46\gamma$ (for $\gamma > 1$) and $A = 12.75 - 6.08\gamma$ (for $\gamma < 1$). The appropriate correlation coefficients are $r_{A\gamma} = -0.84$ and $r_{A\gamma} = 0.48$. From whence one can see that for the case of "steep back slope" the correlation between heights and asymmetry is better than for the case of "steep front slope". To summarize, the effect of horizontal asymmetry takes place to a grater extent for the waves of relative low heights.

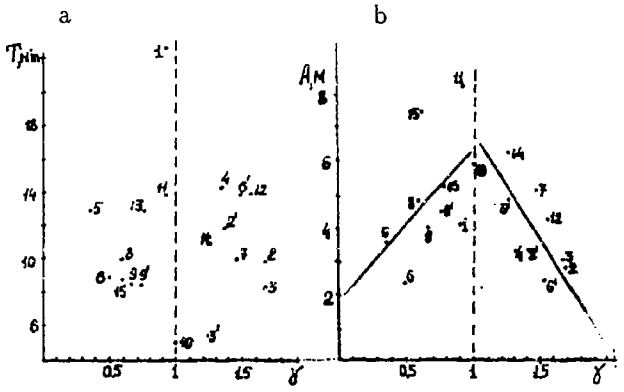


Figure 5: Data on periods (T) and heights (A) of the internal waves as function of relative steepness of waves (γ).

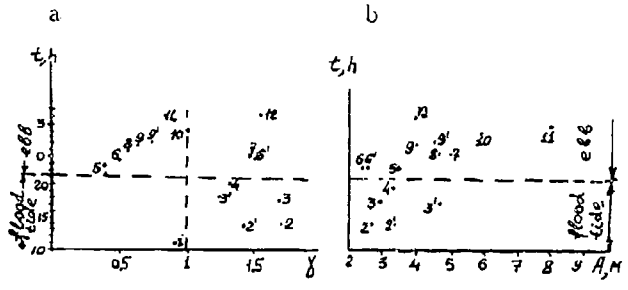


Figure 6: The distributions of γ and A in time.

6. Connection of effect of horizontal asymmetry with tidal phase

It is interesting to follow how effect of horizontal asymmetry is varied in time and whether there is correlations between it and tidal phase. To clear up this questions, we have plotted the graphical representation in which on the one axis we laid off time and on the other axis – relative steepening of the wave. From Fig. 6a it is seen that with the increasing of water level (during flood tide), up to high water time, the waves with steepened front are observed. During period of high water the waves of both type asymmetry were marked. During ebb phase after midnight the waves with steepened back faces dominated. Thus we can see the correlation between horizontal asymmetry of the waves and tidal phase. In this connection it is interesting to test whether there is also any dependence between heights of the waves and tidal phase as well. From data of Fig. 6b it is seen that internal waves during ebb are higher by amplitude then during flood tide. Thus we can see the tendency for waves with opposite to current direction to have higher amplitudes. This feature resembles the situation with short- period internal waves in the open ocean where the similar dependence often is manifested [8].

7. Discussion and conclusions

So, the scenario observed is roughly as follows. Against the background of hydrology with relatively weak vertical temperature and density gradients, short-period internal waves are moving from open sea towards the shore. Due to picnocline being closed to surface the travelling internal waves have form of depressions. The most striking shape of wave-depressions is manifested for waves with largest amplitudes. Propagation of internal waves is taking place against the background of alternative current (tidal) which for some time is co-directional with waves and for some time is opposite to them. As our observations show, there is an apparent effect of horizontal asymmetry of the wave profile which is correlated with tidal phase and consequently with directions of the tidal currents.

It is known that without background current when internal wave is moving to inclined bottom the internal wave profile is distorted so that back face of the wave becomes steeper. Accordingly the front of the wave becomes milder and becomes roughly parallel to the inclined bottom [3,4]. This specific changing of wave profile is due to the fact that during the shoaling of the wave the reverse flow in the lower layer is accelerating so as to conserve mass [4]. Besides the laboratory experiments this effect was found in the field observations of tidal internal waves on shelf [9].

Perhaps in our case the effect connected with the influence of inclined bottom play a certain role as well. but the effect due to strong shear tidal current seems to shadow it. Stable connection between steepening of front and back faces of the waves and ebb or flood tide, as well as near equal number of observed waves with steepening front and back faces, pointed to the effect of alternative tidal current is being dominated.

It is well known (see for example comprehensive observations[10]) that tidal currents are mostly the shear currents, having a maximum magnitude in near-surface layer and periodically changing of its cross-shore component from on-shore to off-shore direction. For short-period internal waves there occurs their own system of orbital wave currents (shear current). Background tidal current interacting with orbital currents may result in a reducing the reversal current of the wave in bottom layer (during flood tide) or its strengthening in ebb. It results in the profile of the wave being deformed so that in the first case front edge of the wave will be steeper, and in the second case the back edge will be steeper. The fact that waves of higher amplitudes are less prone to nonlinear profile distortions is indirect evidence of the connections between effect of horizontal asymmetry and alternative background currents. Since orbital currents of internal waves are proportional to their amplitude, in case off larger waves, background current plays a smaller role than in case of lower waves. Thus we can explain the fact that the biggest of the waves observed had nearly symmetrical profile.

The main purpose of our paper was to establish the factual data on the horizontal asymmetry effect of internal waves and give some preliminary speculations on its origin. We have plan to do more deep interpretation in the close future.

References

[1] Serebryany A.N. (1990) Nonlinearity effects in internal waves on a shelf. Izv. Acad. Nauk SSSR. Fiz. Atmos. Okeana. **26**. 285- 293.

[2] Serebryany A.N. (1985) Internal waves in the coastal zone of a tidal sea. Okeanologiya. **25**, 744-751.

[3] Helfrich K.R. (1992) Internal solitary wave breaking and run- up on a uniform slope. J. Fluid Mech.. **243**, 133-154.

[4] Kao T.W., Pan F.Sh and D. Renouard (1985) Internal solitons on the pycnocline: generation, propagation, and shoaling and breaking over a slope. J.Fluid Mech., **159**, 19-53.

[5] Thorpe S.A. (1978) On the shape and breaking of finite amplitude internal gravity waves in a shear flow. J. Fluid Mech., **85**, 7-31.

[6] Thorpe S.A. (1978) On internal gravity waves in an accelerating shear flow. J. Fluid Mech., **88**, 623-639.

[7] Konyaev K.V. and A.N. Serebryany (1991) Meter of vertical displacement for stratified bodies of water (in Russian). Inventor's certificate USSR N 16888875, 01 K 13/00. Bulletin of inventions N 29.

[8] Sabinin K.D.,Nazarov A.A. and A.N. Serebryany (1990) Short period internal waves and current in the ocean. Izv. Acad. Nauk SSSR. Fiz. Atmos. Okeana. **26**, 847-853.

[9] Pingree R.D., Griffits D.K. and G.T. Mardell (1983) The structure of the internal tide at the Celtic Sea shelf break. J. Mar. Biol. Ass. U.K., **64**, 99-113.

[10] Loder J.W., Buckman D. and E.P.W. Horne (1992) Detailed structure of currents and hydrography on the northern side of Georges Bank. J. Geophys. Res.. **97**, 14331-14351.

Capillary–gravity interfacial waves

F. Dias
Institut Non-Linéaire de Nice
UMR 129 - CNRS & UNSA
1361 route des Lucioles
F-06560 Valbonne

Abstract

This paper deals with capillary–gravity waves at the interface between two fluids of differing densities. Several types of waves are considered: space- and time-periodic waves and travelling waves. For space- and time-periodic waves, a weakly nonlinear analysis to third order provides the normal form that relates the wave frequency with the amplitude. The special case of internal resonance between the fundamental and its second harmonic is also considered. It is shown that an unusual type of periodic waves, which are neither travelling nor standing waves, may exist. For travelling waves, an analysis based on a formulation of the problem as a dynamical system in space shows that there is a critical density ratio which strongly affects the branching behavior of periodic waves and which determines the type of solitary waves which bifurcate at the minimum of the dispersion curve.

1 Introduction

The problem of interfacial waves has not been studied as much as the problem of water waves. Although many results on water waves can be extended to interfacial waves without leading to significant qualitative differences, there are some wave phenomena for which the density ratio can play an important role. In particular, it is shown that certain types of solitary waves ("dark" solitons), which are not possible in the context of water waves, are possible in the context of interfacial waves. Following a brief review of the formulation of the problem of interfacial waves, the paper is then divided into two main parts. The first part is devoted to the study of space- and time-periodic waves. The analysis makes use of the temporal Hamiltonian structure of the problem. The second part is devoted to the study of travelling waves. The analysis is based on a formulation of the problem as a dynamical system in space. Bifurcations of solitary waves are studied.

2 The physical problem

The propagation of capillarity–gravity waves at the interface between two horizontal layers of perfect fluids with constant densities ρ and ρ' is considered. The layers are two-dimensional and semi-infinite in the vertical direction. The flow is supposed to be irrotational in each layer. The physical quantities relative to the upper layer are denoted with the symbol '. The coordinates are x in the horizontal direction and y along the vertical direction, with $y = 0$ representing the interface at rest. The interface is described by $y = \eta(x,t)$. The acceleration due to gravity is g and the interfacial tension coefficient is T. The velocity components are u and v. Velocity potentials ϕ and ϕ' are introduced in each fluid. The governing equations are given by

$$\nabla^2\phi = 0, \qquad \nabla^2\phi' = 0, \tag{2.1}$$

subject to the conditions

$$\lim_{y\to-\infty}|\nabla\phi|=0\,,\qquad \lim_{y\to+\infty}|\nabla\phi'|=0\,. \tag{2.2}$$

At the interface $y=\eta(x,t)$, the kinematic condition is given by

$$\eta_t=\Phi_{(y)}-\eta_x\Phi_{(x)}=\Phi'_{(y)}-\eta_x\Phi_{(x)}\,, \tag{2.3}$$

and the dynamic condition by

$$\rho\left(\Phi_{(t)}+\tfrac{1}{2}(\mathrm{u}^2+\mathrm{v}^2)\right)-\rho'\left(\Phi'_{(t)}+\tfrac{1}{2}(\mathrm{u}'^2+\mathrm{v}'^2)\right)+g(\rho-\rho')\eta-T\frac{\eta_{xx}}{(1+\eta_x^2)^{\frac{3}{2}}}=0\,, \tag{2.4}$$

where $\Phi_{(*)}=\phi_{(*)}(x,\eta,t)$, $\mathrm{u}=u(x,\eta,t)$, $\mathrm{v}=v(x,\eta,t)$.

So far, no assumption has been made on the type of solutions we are looking for. The problem depends of course on the horizontal variable x and on time t. It is a nonlinear problem, the nonlinearities being present not in the governing equations but in the boundary conditions at the interface. Existence theorems are extremely difficult to obtain. The analysis of the problem is simpler if one considers solutions in the form of travelling waves, the "trick" being that such solutions are steady solutions in a frame of reference moving with the wave. Another simplification of the general time-dependent problem consists in looking for solutions which are periodic (in space or in time or in both) or for solutions which are slow modulations (in space or in time or in both) of the previous solutions. In the sequel, different formulations will be used to study different types of wave phenomena: a temporal Hamiltonian formulation and a dynamical system formulation.

The following dimensionless numbers will be used in the analysis:

$$\alpha=\frac{gT}{\rho c^4}\,,\qquad \tau=\frac{Tk^2}{(\rho-\rho')g}\,,\qquad R=\frac{\rho'}{\rho}\,,\qquad \varrho=\frac{\rho-\rho'}{\rho+\rho'}\,, \tag{2.5}$$

where k is the wave number and c the wave speed.

3 Temporal Hamiltonian formulation

The problem (2.1)–(2.4) has a temporal Hamiltonian formulation given by

$$\eta_t=\frac{\delta H(\zeta,\eta)}{\delta\zeta}\,,\qquad \zeta_t=-\frac{\delta H(\zeta,\eta)}{\delta\eta}\,, \tag{3.1}$$

with the derivatives δ as variational derivatives. The canonical variable ζ in (3.1) is equal to $\rho\Phi-\rho'\Phi'$. The Hamiltonian H is the sum of kinetic energy K and potential energy V, which are given by

$$K(\phi,\phi',\eta)=\int\left[\int_{-\infty}^{\eta}\tfrac{1}{2}\rho|\nabla\phi|^2\,\mathrm{d}y+\int_{\eta}^{+\infty}\tfrac{1}{2}\rho'|\nabla\phi'|^2\,\mathrm{d}y\right]\mathrm{d}x\,, \tag{3.2}$$

and

$$V(\eta)=\int\left[\tfrac{1}{2}(\rho-\rho')g\eta^2+T\left(\sqrt{1+\eta_x^2}-1\right)\right]\mathrm{d}x\,. \tag{3.3}$$

If spatial periodicity with wave length L and wave number $k = 2\pi/L$ is assumed in the x-direction, the integrals over x are from 0 to L. If solitary waves are considered, the integrals over x are from $-\infty$ to $+\infty$. In (3.2), the kinetic energy is given as a function of ϕ and ϕ'. To prove that ϕ and ϕ' only appear in the combination ζ can be done by using the calculus of variations. That is, $K(\zeta,\eta)$ is obtained as the minimum of $K(\phi,\phi',\eta)$ with η fixed on the constant set $\rho\Phi - \rho'\Phi' = \zeta$.

The above Hamiltonian formulation has an equivalent Lagrangian formulation: the set of equations (3.1) can be recovered from setting the first variation of

$$\mathcal{L} = \int_{t_1}^{t_2} \left(K(\eta_t,\eta) - V(\eta)\right)\,\mathrm{d}t \tag{3.4}$$

equal to zero. The link between η_t and ζ is provided by

$$\eta_t = \frac{\delta K(\zeta,\eta)}{\delta\zeta}. \tag{3.5}$$

With the restriction to space- and time-periodic functions, the canonical variables $\eta(x,t)$ and $\zeta(x,t)$ can be formally identified with a double Fourier series expansion in x and in t. For computational purposes, the Fourier series are restricted to N terms. In the nonresonant case, the linearization of the problem gives profiles of the type

$$\eta = \mathrm{Re}\left[A_1 \mathrm{e}^{-i(\omega t - kx)} + B_1 \mathrm{e}^{-i(\omega t + kx)}\right], \tag{3.6}$$

where ω is the frequency of the wave. The dimensionless average $\mathcal{H}$ of H over a time period is

$$\mathcal{H} = 2\varrho(1+\tau)E_1 + \varrho\left[\alpha E_1^2 + \beta M_1^2\right] + \cdots, \tag{3.7}$$

where

$$E_1 = |A_1|^2 + |B_1|^2, \quad M_1 = |B_1|^2 - |A_1|^2,$$

and where α and β depend on the parameters τ and ϱ. The normal form, truncated at order three, is

$$\begin{aligned} \left(\omega^2 - \varrho(1+\tau)\right)A_1 - (\alpha E_1 - \beta M_1)A_1 &= 0, \\ \left(\omega^2 - \varrho(1+\tau)\right)B_1 - (\alpha E_1 + \beta M_1)B_1 &= 0. \end{aligned} \tag{3.8}$$

In the case of the 1:2 resonance, which occurs when τ is close to $1/2$, the linearisation of the problem gives a profile of the type

$$\eta = \mathrm{Re}\left[A_1 \mathrm{e}^{-i(\omega t - kx)} + B_1 \mathrm{e}^{-i(\omega t + kx)} + A_2 \mathrm{e}^{-i(2\omega t - 2kx)} + B_2 \mathrm{e}^{-i(2\omega t + 2kx)}\right]. \tag{3.9}$$

The dimensionless average $\mathcal{H}$ of H over a period is

$$\begin{aligned} \mathcal{H} &= 2\varrho(1+\tau)E_1 + 2\varrho(1+4\tau)E_2 + \tfrac{1}{4}\varrho\omega^2 S \\ &+ \varrho\left[\alpha_{11}E_1^2 + \beta_{11}M_1^2 + \alpha_{22}E_2^2 + \beta_{22}M_2^2 + 2\alpha_{12}E_1E_2 + 2\beta_{12}M_1M_2\right] + \cdots, \end{aligned} \tag{3.10}$$

where

$$E_2 = |A_2|^2 + |B_2|^2, \quad M_2 = |B_2|^2 - |A_2|^2,$$
$$S = A_1^2\overline{A_2} + \overline{A_1}^2 A_2 + B_1^2\overline{B_2} + \overline{B_1}^2 B_2,$$

and where α_{ij} and β_{ij} depend on the parameters τ and ϱ. The normal form, truncated at order three, is

$$\begin{aligned}
\left(\omega^2 - \varrho(1+\tau)\right) A_1 - \varrho\omega^2 \overline{A_1} A_2 - 2\varrho A_1 (\alpha_{11}E_1 - \beta_{11}M_1 + \alpha_{12}E_2 - \beta_{12}M_2) &= 0, \\
\left(\omega^2 - \varrho(1+\tau)\right) B_1 - \varrho\omega^2 \overline{B_1} B_2 - 2\varrho B_1 (\alpha_{11}E_1 + \beta_{11}M_1 + \alpha_{12}E_2 + \beta_{12}M_2) &= 0, \\
\left(2\omega^2 - \varrho(1+4\tau)\right) A_2 - \tfrac{1}{2}\varrho\omega^2 A_1^2 - 2\varrho A_2 (\alpha_{12}E_1 - \beta_{12}M_1 + \alpha_{22}E_2 - \beta_{22}M_2) &= 0, \\
\left(2\omega^2 - \varrho(1+4\tau)\right) B_2 - \tfrac{1}{2}\varrho\omega^2 B_1^2 - 2\varrho B_2 (\alpha_{12}E_1 + \beta_{12}M_1 + \alpha_{22}E_2 + \beta_{22}M_2) &= 0.
\end{aligned} \tag{3.11}$$

The symmetries of the normal forms (3.8) and (3.11) are natural consequences of the symmetries of the full problem.

The solutions of (3.8) are of two types: progressive waves (one of the amplitudes A_1 or B_1 is zero) or standing waves (the amplitudes A_1 and B_1 are equal in magnitude). The solutions of (3.11) are of five types: pure progressive waves (both amplitudes A_1 and B_1 are zero, and one of the amplitudes A_2 or B_2 is zero), pure standing waves (both amplitudes A_1 and B_1 are zero, and the amplitudes A_2 and B_2 are equal in magnitude), travelling Wilton ripples (both amplitudes A_1 and A_2 or B_1 and B_2 are zero), standing Wilton ripples (the amplitudes A_1 and B_1 as well as A_2 and B_2 are equal in magnitude), mixed waves (one of the amplitudes A_1 or B_1 is zero). The profile of the mixed waves is for example

$$\eta = \mathrm{Re}\left[A_1 \mathrm{e}^{-\mathrm{i}(\omega t - kx)} + A_2 \mathrm{e}^{-\mathrm{i}(2\omega t - 2kx)} + B_2 \mathrm{e}^{-\mathrm{i}(2\omega t + 2kx)}\right]. \tag{3.12}$$

So far, three-mode mixed waves have been studied only theoretically. Such waves are generic in the presence of a two-mode interaction and they persist at any order of the normal-form truncation. A proof of existence of such waves for the full problem remains an open problem (like the proof of existence of standing waves for that matter!). Numerical solutions for such waves would be a first step towards a better description of their nature. What the weakly analysis suggests is that three-mode mixed waves arise from the superposition of a travelling Wilton ripple in one direction and of a pure travelling wave in the opposite direction. One may alternatively view such waves as travelling waves in which the fundamental excites not only the second harmonic in the same direction (as in the classical 1:2 resonance for travelling waves) but also the second harmonic in the opposite direction. Branches of three-mode mixed waves connect branches of travelling waves with branches of standing waves. For more details, see the papers Christodoulides & Dias (1994) and Dias & Bridges (1994).

4 Dynamical system formulation

The above analysis dealt with waves which are periodic in time and in space. The analysis below is restricted to waves travelling uniformly with a constant speed c. Mielke (1991) proposed a dynamical system formulation of the problem (2.1)–(2.4) in a frame of reference moving with the wave with x and the streamfunction ψ as independent variables. With such a formulation, the center manifold theorem can be used to reduce the problem to a set of ordinary differential equations. We use $T/\rho c^2$ as unit length and c as unit velocity.

The dispersion relation for linearized waves is given by

$$k^2 - (1+R)k + \alpha(1-R) = 0, \tag{4.1}$$

where k is the dimensionless wavenumber. For given values of R between 0 and 1 and of c larger than 0, equation (4.1) can have zero, one, or two real roots. We concentrate here on the case where equation (4.1) has a double root in k, that is to say when

$$\alpha = \alpha_c = \frac{(1+R)^2}{4(1-R)}, \quad k = k_c = \frac{1+R}{2}.$$

For α below α_c, (4.1) has two real roots k_1 and k_2 and there are two branches of periodic waves bifurcating from the trivial solution. For α above α_c, (4.1) has two complex roots. When α is equal to α_c, branches of solitary waves bifurcate from the trivial solution.

From the dynamical system formulation due to Mielke, one can use the center manifold theorem (which is essentially a separation of variables) to show that all bounded solutions in a neighborhood of the 1:1 resonance (α near α_c) can be written as

$$\mathrm{w}(x) = A(x)\varphi_0^+ + B(x)\varphi_1^+ + \overline{A(x)}\varphi_0^- + \overline{B(x)}\varphi_1^- + \text{higher order terms}, \tag{4.2}$$

where

$$\mathbf{w} = \left[\tfrac{1}{2}(u^2+v^2-1), \frac{v}{u}, \tfrac{1}{2}(u'^2+v'^2-1), \frac{v'}{u'}, \eta_x\right]^T \tag{4.3}$$

and where φ_0^+ (resp. φ_1^+) is an eigenvector (resp. a generalized eigenvector) corresponding to the double root k_c of (4.1). The bifurcation parameter μ is equal to $\alpha_c - \alpha$. The amplitudes A and B, which only depend on the spatial variable x, are complex. One easily finds that

$$\begin{aligned}
\varphi_0^+ &= \left[-\mathrm{e}^{(1+R)\psi/2}, \mathrm{i}\,\mathrm{e}^{(1+R)\psi/2}, \mathrm{e}^{-(1+R)\psi/2}, \mathrm{i}\,\mathrm{e}^{-(1+R)\psi/2}, \mathrm{i}\right]^T, \\
\varphi_1^+ &= \left[\mathrm{i}\,\psi\mathrm{e}^{(1+R)\psi/2}, \psi\mathrm{e}^{(1+R)\psi/2}, \mathrm{i}\,\psi\mathrm{e}^{-(1+R)\psi/2}, -\psi\mathrm{e}^{-(1+R)\psi/2}, 0\right]^T.
\end{aligned}$$

The normal form of the dynamical system, which allows to express the higher order terms in (4.2) in a rather simple form, is

$$\begin{aligned}
A_x &= \mathrm{i}k_c A + B + \mathrm{i}AP\left(\mu; |A|^2, \tfrac{1}{2}\mathrm{i}(A\overline{B} - \overline{A}B)\right), \\
B_x &= \mathrm{i}k_c B + \mathrm{i}BP\left(\mu; |A|^2, \tfrac{1}{2}\mathrm{i}(A\overline{B} - \overline{A}B)\right) + AQ\left(\mu; |A|^2, \tfrac{1}{2}\mathrm{i}(A\overline{B} - \overline{A}B)\right),
\end{aligned} \tag{4.4}$$

where P and Q are real polynomials

$$\begin{aligned}
P(\mu; U, V) &= -p_1\mu + p_2 U + p_3 V + O(|\mu| + |U| + |V|)^2, \\
Q(\mu; U, V) &= -q_1\mu + q_2 U + q_3 V + O(|\mu| + |U| + |V|)^2.
\end{aligned} \tag{4.5}$$

The coefficients p_1 and q_1, which can be easily computed from (4.1), are found to be $p_1 = 0$ and $q_1 = 1 - R$. The other coefficients (see details in Dias & Iooss (1993) on how to compute them) require more work. The expression for q_2 is

$$q_2 = -\frac{11 - 42R + 11R^2}{8(1+R)^2}. \tag{4.6}$$

There is a critical value $R = R_c = (21 - 8\sqrt{5})/11$ of the density ratio for which the coefficient q_2 is zero. A precise study of the solutions in a neighborhood of that critical value requires the computation of higher order terms and will be the subject of future work. Here we consider the cases $R > R_c$ and $R < R_c$, with R not too close to R_c.

The next step is to find the solutions of the normal form. The analysis is greatly simplified by using the fact that system (4.4) is integrable, with integrals

$$K = \tfrac{1}{2}\,\mathrm{i}\,(A\overline{B} - \overline{A}B) \quad \text{and} \quad H = |B|^2 - \int_0^{|A|^2} Q(\mu; s, K)\,\mathrm{d}s\,. \tag{4.7}$$

Bridges et al. (1994) showed that these integral are closely related to the energy flux and the momentum flux of the waves. A complete analysis of (4.4) was provided by Iooss & Pérouème (1993). The sign of the coefficient q_2 turns out to play a key role in the structure of the solutions.

Small density ratio

This case corresponds to $R < R_c$ (that is to say $q_2 < 0$). When $\mu > 0$, the solutions are periodic or quasi-periodic. When $\mu < 0$, the solutions are periodic, quasi-periodic or homoclinic. The homoclinic solutions correspond to solitary waves of the type shown in figure 1. They look like wave packets.

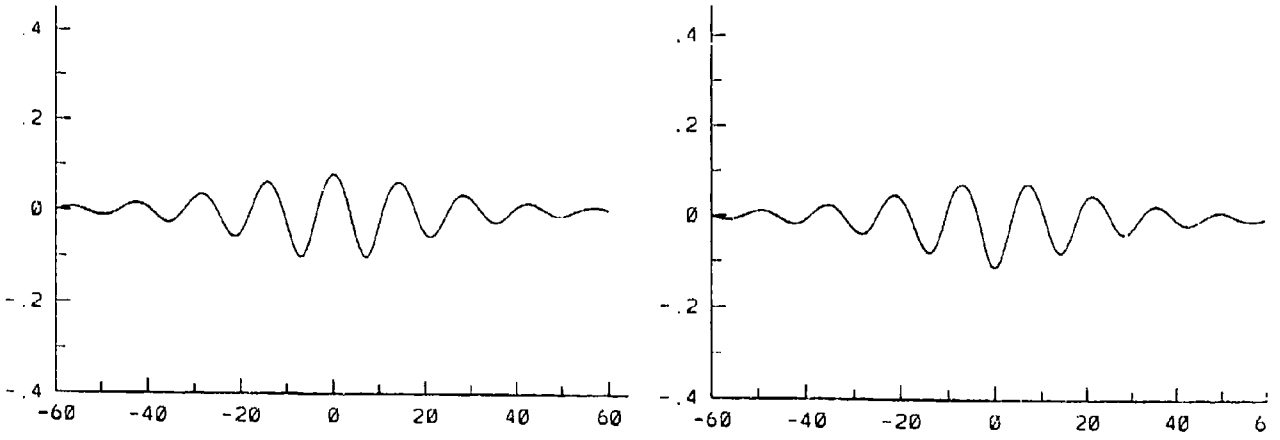


Figure 1: Two solitary waves bifurcating at the minimum of the dispersion curve when the density ratio is small

Density ratio close to one

This case corresponds to $R > R_c$ (that is to say $q_2 > 0$). When $\mu > 0$, the solutions are periodic, quasi-periodic or homoclinic. The homoclinc solutions correspond to solitary waves of the type shown in figure 2. They look like dark solitons. They are connected to the same periodic wave at plus and minus infinity, with a phase shift. In the central part, the amplitude is small.

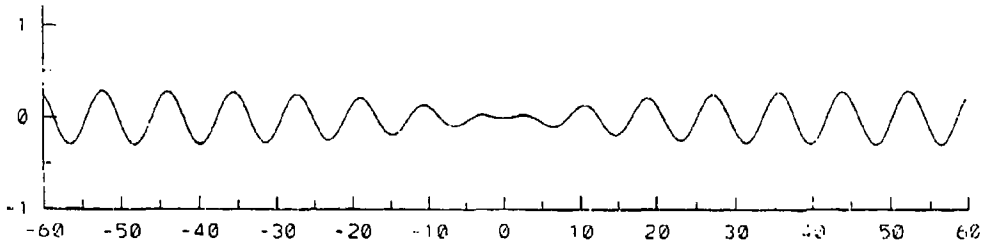


Figure 2: Solitary wave bifurcating at the minimum of the dispersion curve when the density ratio is close to one

REFERENCES

- Bridges, T. J., Christodoulides, P. & Dias F. 1994 Spatial bifurcations of interfacial capillary–gravity waves when the phase and group velocities are nearly equal. Université de Nice, preprint.
- Christodoulides, P. & Dias, F. 1994 Resonant capillary–gravity interfacial waves. *J. Fluid Mech.* **265**, 303–343.
- Dias, F. & Bridges, T. J. 1994 Geometric aspects of spatially periodic interfacial waves. *Stud. Appl. Math.*, to appear.
- Dias, F. & Iooss, G. 1993 Capillary–gravity solitary waves with damped oscillations. *Physica D* **65**,399–423.
- Dias, F. & Iooss, G. 1994 Ondes solitaires "noires" à l'interface entre deux fluides en présence de tension superficielle. *C. R. Acad. Sci. Paris*, to appear.
- Iooss, G. & Pérouème, M.-C. 1993 Perturbed homoclinic solutions in reversible 1:1 resonance vector fields. *J. Diff. Eq.* **102**, 62–88.
- Mielke, A. 1991 Homoclinic and heteroclinic solutions in two-phase flow. Universität Stuttgart, preprint.

TURBULENT MECHANISMS IN STRATIFIED FLUIDS

J. M. REDONDO, M.A. SANCHEZ & I.R. CANTALAPIEDRA
Dept. Física Aplicada. Universitat Politécnica de Catalunya,
J. Girona 31, B5 Campus Nord, Barcelona 08034, Spain.

Abstract. Probability distribution of basic instabilities appearing in stratified flows and point density fluctuations have been studied. Different parameters of the mixing process have been changed in the experiments in order to investigate mixing. Detailed flow visualisation as well as point density measurements are used in zero-mean-flow laboratory experiments such as: Grid-stirred turbulent mixing across a density interface and bubble induced mixing. The overall mixing efficiency of the processes depends on the local Richardson as well as on the local vorticity. Parameter distributions of low and high mixedness corresponding to different instabilities are presented, showing that dipolar vortices, penetrating the interface are the most efficient mixing instabilities.

Keywords: Stratified flows – Zero-mean-flows – Turbulent mixing

1. Introduction

The range of mixing efficiencies and the related turbulent diffussion coeficients is very large and its proper parametrization in geophysical flows is important to model correctly mesoscale flows. See Hopfinger(1987) and Fernando (1991) for discussions on mixing efficiency in stratified flows. We present some results on two series of experiments on the mixing across a density stratified interface when the turbulence is produced by a distribution of air bubbles or by grid stirred turbulence.

2. Description of the experiments

Grid generated turbulence

An experimental apparatus similar to the one described by Turner(1973) was used, a perspex box of 25.4 × 25.4 in base and 42 cm high with a metal grid made of square bars of section 1 cm^2 and a mesh of 5 cm was driven in an oscillatory motion by a motor coupled to a gear.

Several authors have used this configuration, and the turbulence produced by the grid depends on the distance from it in the following way, see Fernando(1991) for further references,

$u' = C(M,a)\omega\ z^{-1}$ and $\ell = \beta(M,a)\ z$ where ω is frecuency of oscillation of the grid, z the distance to the grid centerplane, a the amplitude of oscillation, ℓ, the integral lengthscale of the turbulence and u' the r.m.s. turbulent velocity, C and β are functions of the grid characteristics, which were kept constant in the experiments, ($M = 5cm, a = 1cm$). An interface, produced by overlaying a fresh layer on a layer of brine of fixed density $\rho + \Delta\rho$, where the grid was located. The density interface was placed at diferent distances from the grid, and its evolution

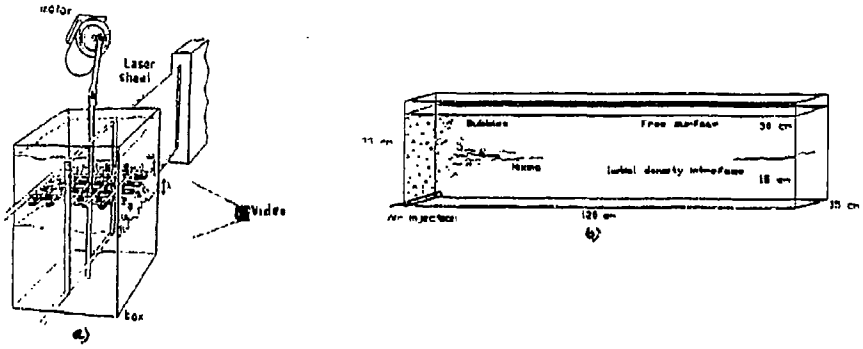


Fig. 1. Experimental configurations a) Oscillating grid and tank. b) Bubble generated turbulence on one side of the tank

(entrainment, $E = Ve/u'$) measured, conductivity probes and video recordings were used to investigate mixing across the interface.

Air bubble generated turbulence

A box made of 1 cm perspex plate, 120 × 15 cm in base and 35 cm in height was used. The turbulence was produced by means of bubbles generated by a line source. The bubble generator used in this experiment consisted of a plastic tube with holes 1 cm apart drilled on one side placed in the bottom corner of the tank and spanning the width of the base. A sharp density interface between brine and fresh water was placed in the center of the fluid column 30 cm deep. The experiment started injecting air, which formed the line of bubbles rising at their terminal speed and began to mix the two layers from the side. See Redondo and Cantalapiedra (1993) for further details

3. Definition of experimental parameters

The density interface and the turbulence producing the mixing in the experiments described here are characterized by means of a local Richardson number $Ri = \frac{g\Delta\rho\ell}{\rho u'^2}$, where g is gravity, $\Delta\rho$ the density step, ρ the reference density, ℓ, the integral lengthscale of the turbulence and u' the r.m.s. turbulent velocity, which can be related to the air flow or to the oscillating grid characteristics. In both experiments the mixing could be measured as an entrainment velocity Ve or as a total mixing time, T_m when the fluid was homogeneous, as the initial density interface was placed in the center of the tank of height H, we can relate both measurements as $T_m = \frac{H}{2Ve}$

Density fluctuations and mixing

Density fluctuations were measured and analized. Probability distributions of the signals were calculated, $P(\rho)$, and from them moments of the distribution, M_i were computed $M_i = \int_0^\infty P(\rho)\ \rho^i\ d\rho$, $i = 1, 2$.

The mean and variance were also calculated as: $\overline{\rho} = \frac{1}{n}\sum_0^n \rho(t)$, and $M_2 = (\frac{1}{n})\sum_0^n(\rho - \overline{\rho})^2$. being the standard deviation $\rho' = (M_2)^{1/2}$. The Skewness $S = \frac{M_3}{(\rho')^3}$, and the Kurtosis : $K = \frac{M_4}{(\rho')^4}$, were computed for the grid stirred experiments but not for the non-homogeneous bubble induced mixing ones, due to the shorter records available.

From the transport equations for velocity and density fluctuations in homogenous turbulence for a zero mean flow we can deduce , using the definition of the scales $L_o = (\epsilon/N^2)^{1/2}$, as the Ozmidov scale , $L_b = w'/N$, the buoyancy scale, in terms of the Brunt-Vaisalla frequency $N^2 = -\frac{g}{\rho}\frac{\partial \rho}{\partial z}$ and L_t, defined below, the relation

$$\frac{w'}{\epsilon}\frac{\partial u'^2/2}{\partial z} = -\frac{1}{L_o^2}L_b L_t \frac{\overline{\rho' w'}}{\rho'\ w'} - 1 \ ,$$

The interaction between these three scales for different types of instabilties at different ranges of the Richardson number will control the amount of turbulent energy that produces mixing. $\frac{\overline{L_b\ L_t}}{L_o^2}$, can be considered as a flux Richardson number or a mixing efficiency $Rf = \frac{g}{\rho}\frac{\overline{w'\rho'}}{\epsilon}$

Itswiere et.al.(1986) used the definition of the largest turbulent scale of the flow, in a statistical sense as: $L_t = \frac{\rho'}{\frac{\partial \rho}{\partial z}}$ which represents a typical vertical distance travelled by fluid particles before either returning to their equilibrium level or mixing, we have $\frac{L_t}{h} = \frac{\rho'}{\Delta\rho}$ and L_t reaches a maximum value at a maximum Richardson number.

The term mixedness, M(z), was used by Koop & Browand(1979) among other authors and is defined as

$$\mathrm{M}(z) = \frac{2}{\Delta\rho T}\int_0^T (\rho_b - \rho)H(\rho - \overline{\rho(z)}) + (\rho - \rho_t)H(\overline{\rho(z)} - \rho)\ dt \ .$$

where $H()$ indicates the Heavyside or step function, $\overline{\rho(z)}$ is the average density at height z and t and b indicate top and bottom density values.

An interpretation of this quantity is that near the centre of the interface, at the average density level ($\rho = \overline{\rho}$), M(z) measures the degree to which the density of entrained fluid has been altered by molecular processes. Clearly, if the density fluctuations consist of random step functions, then M(z)=0. On the other hand, if there are little fluctuations of the density around $\rho = \overline{\rho}$, then M(z)$\approx$ 1. At vertical locations other than the centre of the interface M(z) is not bounded by unity.

The mixedness can also be calculated from the probability distribution functions $P(\rho)$. For a density sample consisting of N data points, we can express M(z) as

$$\mathrm{M}(z) = \frac{2}{(\rho_t - \rho_b)N} \sum_{i=1}^{N} [(\rho_b - \rho(i))H(\rho(i) - \overline{\rho(z)})P(\rho(i)) + (\rho(i) - \rho_t)H(\overline{\rho(z)} - \rho(i))P(\rho(i)]d\rho \ .$$

where $\rho(i) = \rho_b + \left(\frac{i-1}{N-1}\right)(\rho_t - \rho_b)$, and $d\rho$ is the width of the window used. M(z) and $\frac{\rho'}{\Delta\rho}$ are inversely related, in fact at the centre of the interface $\frac{\rho'}{\Delta\rho} = \frac{1-M(z)}{2}$.

The mixedness has been used to characterize the local instabilities, as well as the video recordings of the interface, describing the dominant instability type observed for different parameter ranges.

4. Experimental results

We will only present results for the mixing box experiments, described by several authors, Turner(1973), Linden(1975), Hopfinger and Linden (1982), E and Hopfinger(1986), Fernando(1991) and references therein, The advance of the interface follows an entrainment law of the type $E = aRi^{-n}$ with n between 1 and 7/4, and most of the times $n = 3/2$, We varied the distance between the interface and the grid and found large differences in entrainment for the same Richardson number and diferent distance.

The appearence of the interface showed that larger, less intense vortices, mixed relatively less than smaller ones inpinging on the interface, In figure 2 two different shapes of the interface are shown for low and medium local Ri. For large Ri the appearence of the interface was almost flat, until a inpinging eddy produced small scale mixing.

The conductivity probe measurements shown here were taken at the centre of the interface, this is not easy to define, even if the probe was also videotaped as the interface advanced, as an example of the convolutions of the interface, shown in figure 3 for different Ri , both the thickness and the position vary in time.

In figure 4 the position of the interface vs. non dimensional time, $t\omega^3 N^{-2}$ is shown for different experiments with different initial grid-interface distances, D_g. This non-dimensional time was used by Linden(1975) and shows the entrainment produced by different vorticities eroding the interface. Note that the average vorticity at the interface may be expressed as $\frac{u'}{\ell} \propto z^{-2}$.

We show the effect of dipolar vortices that inping across the interface, thereby causing substantial local mixing. In figure 5, point density measurements for two different Ri show that for low Ri it is common to find sharp variations of density at the center of the interface, but not for the large Ri indicating that the Mixedness is high at high Ri, and fluid from the lower layer mixes before reaching the center of the interface. In figure 6 the values of density r.m.s. fluctuations taken at the center of the interface (or near the centre, for low Ri) are shown versus Ri in a) and the values of the Kurthosis are shown in b), for these experiments, $z/\ell \approx 10$.

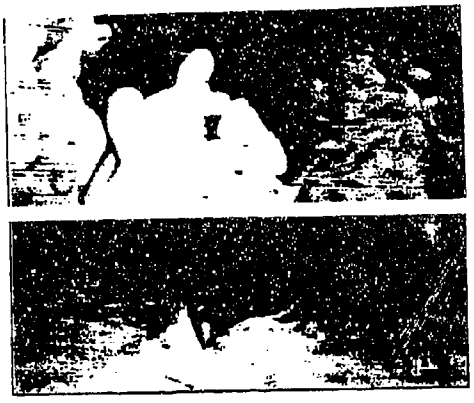


Fig. 2. Images of the small scale turbulence at the interface produced by the grid stirred turbulence a) shows a medium - high Ri experiment and b) a low Ri experiment

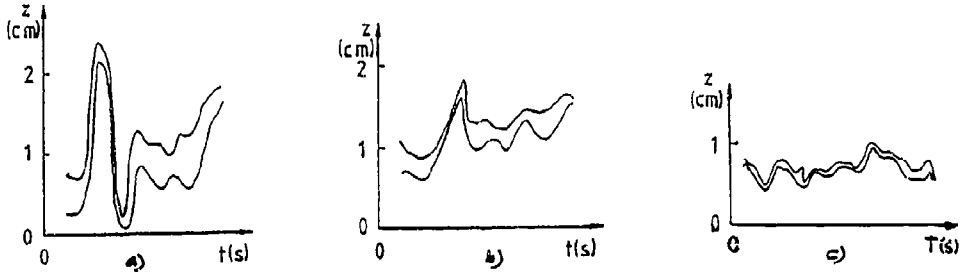


Fig. 5. Digitised lines marking a 5% and 95 % light intensity values in time, for three experiments a) Low Ri, b) Medium Ri, c) High Ri.

For low Richardson numbers a typical fluctuation (r.m.s.) is a tenth of the maximum possible fluctuation, for intermediate Richardson numbers the values of non-dimensional standard deviation of density, $\frac{\rho'}{\Delta\rho}$, are as high as 0.5, showing that there is probably direct contact and mixing between fluid from both layers. The relationship between r.m.s density values and local mixing can be interpreted as follows. If the value of the non-dimensional r.m.s. density is 0.5 , successive particles of fluid from the upper and lower layers arrive to the center of the interface without mixing and there will be direct contact between fresh and salty fluids.

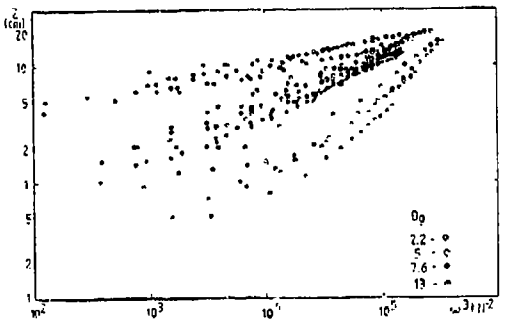


Fig. 4. Position of the interface vs. non dimensional time, $t\omega^3 N^{-2}$ different simbols indicate experiments with different initial grid-interface distances, D_g.

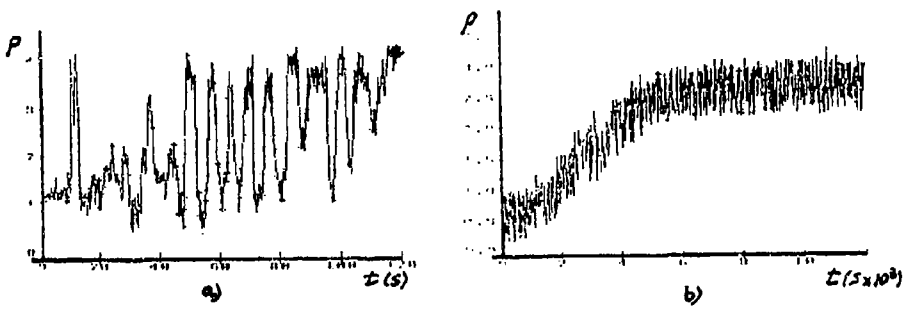


Fig. 5. Point density measurements vs. time, for experiments with different Ri a) indicates a low Ri experiment b) a medium Ri.

For higher Richardson numbers, $\rho'/\Delta\rho$ is reduced substantially, indicating than it is rare to have direct entrainment between the two layers. The Kurthosis for high Ri shows that most of the times the interface center has a well mixed inner layer and only seldom an energetic instability or eddy can bring in outer unmixed fluid.

In figure the value of the Mixedness is plotted against Ri and the nondimensional distance to the grid, low Mixedness values indicate that there is energetic transport across the interface, we indicate with crosses the experiments in which dipolar vortices were observed penetrating across the interface more than 25 /agreement with the parameter areas of low mixedness. The diferent initial distances used were $D_g = 2.2cm, 5cm, 7.6cm$ and $13cm$

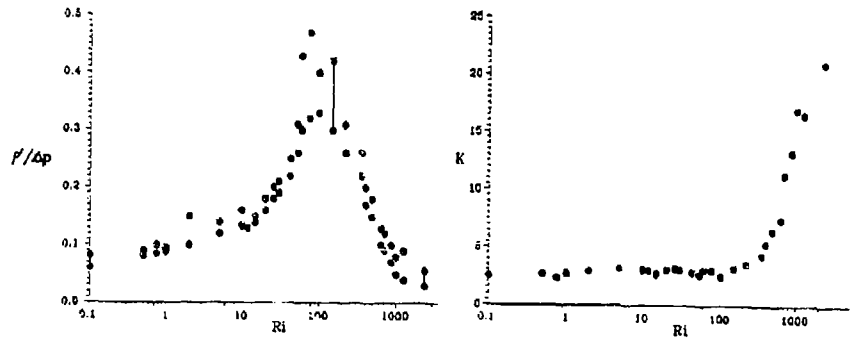


Fig. 6. Moments of the density fluctuations vs. Ri, a) nondimensionalized r.m.s. b) Kurthosis.

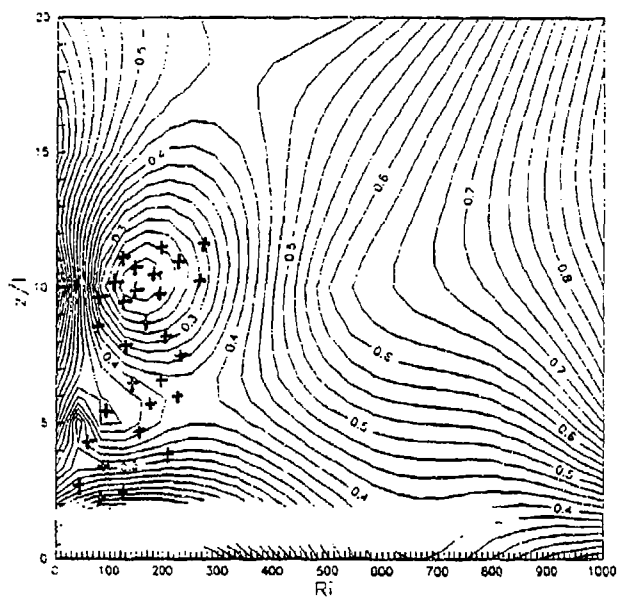


Fig. 7. Parameter map describing the Mixedness as a function of Ri and non dimensional distance from the grid z/ℓ.

5. Discussion and conclusions

From the density fluctuation measurements, or conversely from the mixedness values in the oscillating grid experiments we see that a region of intermediate Ri allows higher direct transport of unmixed fluid across the interface, this mechanism

should provide higher mixing efficiencies at intermediate Ri showing consistency with Linden(1979,1980), Rohr et.al (1986) and Redondo(1987), on the other hand the experiments with bubble generated mixing show mixing efficiencies in agreement with McEwan(1983a,b) and Britter et. al.(1984,1986). Only for very strong density interfaces a decrease in mixing efficiency with Ri can be appreciated. We argue that for very high Ri, there is more time where the interface can support internal waves of higher buoyancy frequency, thus dissipate more energy which otherwise could produce mixing, This excess energy is disipated away from the source and subsequently contributes to mixing in the hetereogeneous experiment, but for the grid-stirred experiments the wave energy excess does not produce significant mixing as the energy distribution everywhere at the interface is similar. The Mixedness values are of help in analizing different parameter ranges, and it has been shown that the vorticity at the interface contributes significantly to local mixing. The dipolar vortex mechanism seems an efficient one that could produce the high mixing efficiencies at intermediate Richardson numbers.

References

[1] Linden, P.F. (1980),"Mixing across a density interface produced by grid turbulence ". J.Fluid Mech. **100**, 3-29.

[2] Redondo J.M. (1987) "Difusion turbulenta en fluidos estratificados" Ph.D. Thesis. Univ. Barcelona.

[3] Britter R.E. (1984) "Diffusion and decay in stably-stratified turbulent flows" in "Turbulence and Diffusion in Stable Environments" 13-24 Ed by IMA, Ed. J.C.R. Hunt. Clarendon, Oxford.

[4] McEwan A.D.(1983b) "Internal mixing in stratified fluids " J. Fluid Mech. **128**, 59-80.

[5] McEwan A.D.(1983b) " The kinematics of stratified mixing through internal wave breaking " J. Fluid Mech. **128**, 47-58.

[6] Hopfinger, E.J. (1987) "Turbulence in stratified fluids, a review" J. Geophys Research. **92** 5287-5302.

[7] Fernando, H.J.S.(1991) "Turbulent mixing in stratified fluids" Annu. Rev. Fluid Mech. **23**, 455-493.

[8] Koop,C.G. & Browand F.K. (1979) "Instability and turbulence in a stratified fluid with shear" J.Fluid Mech.**135**,135-147.

[9] Rohr,J.J. Itsweire, E.C. & Van Atta, C.W. (1984) " Mixing efficiency in stably stratified decaying turbulence " Geophys. Astrophys. Fluid Dyn. **29**, 221-226.

[10] Itsweire, E.C, Helland, K.N. & Van Atta, C.W. (1986) " The evolution of grid-generated turbulence in a stably stratified fluid " J. Fluid Mech. **162**, 299-338.

[11] Turner S.T. (1973), "Buoyancy effects in fluids" Cambridge University Press.

[12] Linden, P.F. (1975) " The deepening of a mixed layer in a stratified fluid". J. Fluid Mech. **71**, 385-405.

[13] Redondo J.M. and Cantalapiedra I.R. (1993) "Mixing in horisontally heterogeneous flows" Applied Scientific Res. **51**, 217-222.

INTERFACIAL RESISTANCE AND MIXING IN STRATIFIED CHANNEL FLOWS

P. Prinos and V. Dermissis
Hydraulics Lab., Dept. of Civil Eng.
Univ. of Thessaloniki, Thessaloniki, Greece

The interfacial resistance and rates of entrainment are significant factors in two-layered stratified open channel or duct flows. In some problems (i.e. fresh-salt water in estuaries) the mixing should be kept as low as possible and hence appropriate conditions should be established for doing so. A key factor is the interfacial friction and the associated interfacial friction coefficient. The theoretical analysis of such problems is based on the one-dimensional energy equation, applied in both layers of the stratified channel flow, first developed by Schiff and Schoenfeld (1953). Such an analysis provides an average interfacial friction coefficient over the effective length of the interface and does not give any indication about its variation along the interface. This variation may be significant in certain regions of the stratified system and may enhance or depress local mixing in the area.

Based on such an analysis Dermissis and Partheniades (1984) found that the average interfacial friction coefficient is best correlated with the parameter $ReFr^2$ (where Re is the Reynolds number of the fresh water layer and Fr is the regular (nondensimetric) Froude number) and the realtive density difference $\Delta\rho/\rho$. The results were given as a family of curves with $ReFr^2$ as an abscissa while $\Delta\rho/\rho$ was an independent parameter. A minimal scattering of the data points was observed about each curve.

In an another category of problems instability of the interface results on the onset of the interfacial mixing and hence the rates of eutainment or turbulent diffusion mixing must be computed based on some geometric and hydraulic characteristics of the stratified system. Also in this case the theoretical analysis is based on the some equations as before with the difference that the interfacial mixing velocity q directed from the less to the more turbulent layer is included in the equations. Various interfacial mixing equations have been developed by several investigators (Grubert, 1989) relating the interfacial mixing with the bulk Richardson number and the interfacial and boundary friction factors.

Grubert (1989), based on his experimental results, developed three different equations for interfacial mixing. The first relates the interfacial velocity to a shear velocity, a shear Richardson number and a densimetric Reynolds number. The second takes into acount a total shear velocity and a boundary shear Richardson number. Finally the third is expressed

in terms of a Richardson number and the ratio of the boundary to the interfacial friction factor. The latter was calculated from the relationships developedd by Dermissis and Partheniades (1984).

The above analysis provides some useful equations about the rates of mixing but does not give an insight of the mechanisms related to mixing which should be underestood well in certain geophysical problems before any management strategies take place. For example understanding the mechanism of purging of density stabilized ponds by a lighter overflow is an important factor in the development of a river management strategy. Armfield and Debler (1993) have investigated experimentally and numerically the purging of density stabilized basins. In the experimental program the channel fresh flow over the stagnant salt water cavity was turbulent while the numerical model, based on the Navier-Stokes, was suitable for laminar flows. Hence comparison of small scale phenomena between the experimental and computational study was inappropriate.

A more generalized approach is required, able to take into account all the phenomena described before which fall into the general category of stratified flows. Such an approach is described in the following paragraphs which is based on the unsteady Reynolds - averaged Navier-Stokes equations accounting for both laminar and turbulent flow regimes. For the latter a turbulence model of the k-ε is also included for calculating the Reynolds stresses appearing in the Reynolds equations.

The numerical model solves the two-dimensioal, unsteady, Reynolds - averaged Navier-Stokes equations together with the solute transport equation using a finite-volume method described by Patankar (1980). For the turbulent regime a turbulence model of the low-Re k-ε type, acounting for buoyancy forces, is incorporated into the numerical procedure, as described by Launder and Sharma (1974), since in some regions the fluid remains stagnant, turbulence is suppressed and laminar phenomena dominate.

The main characteristics of the finite-volume method used for solving the set of the differential equations are the following:

(a) The QUICK scheme is used for discretizing the convection terms of the momentum equations while the PLDS scheme is used for the rest (solute, turbulence kinetic energy and its dissipation). A first order implicit Euler scheme is used for the unsteady terms.

(b) The continuity equation is transformed to a Poisson-type equation using the SIMPLE method.

(c) The system of the resulting algebraic equations is solved using the TDM Algorithm.

Appropriate boundary and initial conditions are specified for solving the equations, depending of the problem considered. For the problem of purging of salt-water cavities the

equations are solved in an unsteady manner with the fluid being at rest initially everywhere with non-dimensional solute concentration of 1 in the cavity and of 0 in the channel. At the inlet a fully developed velocity profile is applied (together with profiles of the turbulence characteristics) which is allowed to develop in the flow field. At the exit aud the walls usual boundary conditions are applied with no specific treatment.

Initial results are encuraging, indicating the large scale features of the flow observed in the experimental program of Armfield and Debler (1993) such as the initial development of a splash resulting from the impulsive start-up and also the development of a recirculation in the upper part of the cavity which transports the fresh water in the lower portion of the cavity and hence purging is satisfactory.

REFERENCES

Armfield S.W., and Debler W. (1993). Purging of density stabilized basins. Int. J. of Heat, Mass Transfer, vol. 36, no 2, pp. 519-530.

Dermissis, V. and Partheniades, E. (1983). Interfacial resistance in stratified flows. J. of Waterway, Port, Coastal and Ocean Eng. vol. 110, no 2, pp. 231-250.

Grubert, J.P. (1989). Interfacial mixing in stratified channel flows. J. of Hydraulic Eng., vol. 1, pp. 131-138.115, no 7, pp. 887-905.

Launder, B.E. and Sharma, B.I. (1974). Application of the energy-dissipation model of turbulence to the calculation of flow near a spinning disc. Letters of Heat and Mass Transfer, 1,pp. 131-138.

Patankar, S.V. (1980). Numerical Heat Transfer and Fluid flow. Hemisphere Pub. Co.

Schijf, J.B. and Schoenfeld, J.C. (1953). Theoretical considerations on the motion of Salt and Fresh water. Proc. of Int. Hydraulics Conv., pp. 321-332

SEA-STRAIT TYPE FLOWS AND BREAKING UP PHENOMENA OF INTERFACE BY VERTICAL JETS

Tülay T.NUMAN
Bs.Ms,Ph.D in C.E.
M.E.T.U.

ABSTRACT

In this study behaviour of vertical jets discharging into sea-strait type flows are investigated. A special reference is given to the problem of the breaking-up phenomena. Due to the complexity of the problem, experimental approach is preferred. To explore the behaviour of jets discharged into stratified flow, a special rectangular channel was constructed so that cold water flowing in the lower part and hot water in the upper part. Inter-layer characteristic were determined by temperature measurements. Jet flows are discharged from the bottom, at the mid-section of the channel.

As a result of experimental findings, intially, the variation of intermediate layer thickness (h_i) due to Richarson number (Ri_i) was determined. For breaking-up conditions of the interlayer by jets, evaluations of the findings showed that, jet Froude number-Richardson number relation takes an important role in the explanation of the phenomena. For weak stratification conditions, Fr_j-Ri_i relation is linear, but for moderate Ri_i numbers there is a transition zone; for highly stable stratification conditions, breaking up velocity of jet (hence Fr_j) is independent of Ri_i number.

1. INTRODUCTION

In the field of hydraulics and environmental engineering several vital stratified flow problems arise. Most geophysical flows in nature are stratified, such as atmospheric currents, ocean currents, sea-strait flows and estuaries. On the other hand, during the discharge of pollutants from urban regions, industrial sources, thermal centers and power plants, turbulent buoyant jet flows appear. Since discharge of pollutants is generally a continious phenomenon, it carries the risk of environmental pollution. These problems become more complex in the case of sea-straits.

The purpose of this study is to investigate the behaviour of jets discharging into two layered, two directional flows. Special reference is given to the problem of breaking-up phenomena. In two-layered systems, if the effluent arrives at the intermediate layer, the jet flow behaves as a drilling factor on the interface; so in the limit case breaking-up

phenomenon takes place at the interface by the effect of the jet. This can be applied to hydraulics and environmental problems since they become more severe and vital at sea-straits. Due to complexity of the phenomenon, in order to develop a comprehensive understanding, researches are based on experimental investigations.

2. GENERAL

There has been considerable attention focused on two-layered flows and jet flows during last fourty years. Starting with Harleman's review, continuing with the studies of Parker, Krenkel and Turner, first symposium of IAHR on stratified flow held in U.S.S.R. and second in Trondheim, Norway (1980). Maxwell, Holley and Tekeli [1] gave the explicit study on equations of motions for two layered flow in rectangular channels, including the result of integrations. Mikio Hino et al, Abraham (1979) [2], Sümer and Bakioğlu(1981) [3] are among the ones who worked on interfacial shear stress. Recently, starting from 1986, Armi [4] and Baines (1988) have been working on depth change, side and upstream effect in stratified flows. On jet flow, there have been many experimental and theoretical studies starting with Albertson. Studies on jets in cross-flows intially were collected and published by Chan and Kennedy [5], Later, Jirka (1975), Rajaratnam (1976), Fisher (1979), Chen and Rodi (1980) and Ger, M (1979) [6] worked on jets. These are summarized in Numan's study [7]. Discharge of thermal jets into the fresh environment indicated by Tatom (1985), later investigated by Baddour R. and Jones D. (1991) [8]. They concluded that the density buoyant jets does not adequately predict the thermal buoyant jets. Yannopoulos and Noutsopoulues (1990) also worked on equations of motion of jets with some simplifications.

There are no mathematical models which predict the behaviour of jets in two-layered flow and breaking-up condition of interlayer. Analytical study in this step seems impossible; therefore an experimental approach to the problem is preferred. Due to the complicated character of the problem, many parameters take part in the phenomena, a group of them being related to stratified flows others to jet flows. Some of the parameters are depicted in Fig.1. These parameters are grouped and Buckigham's π theorem is applied and second order of magnitude terms are neglected [7]. Considering the intermediate layer stability, shear stress denotes "how stable the interface is". It is essential in the breaking-up (drilling) of the interface by the jet action. τ_i being a function of Reynolds and Richardson numbers,

$$\tau_i = \rho . k_i \ldots (\Delta U)^2 \quad ; \quad k_i = f(Re_i, Ri_i) \tag{1}$$

after Vreughenhil (1971). Here, k_i is the friction coefficient, ΔU is the relative velocity of two layers ($|U1| + |U2|$)in sea-straits. Due to researches between 1971-1979, τ_i may be xpressed as a function of Ri_i, for high Re numbers. When Re_i attaints a value of about 10^4, k_i is independent of Re [2]. Then, to represent the parameters which are in primary importance in the breaking-up phenomena

$$U_{jL}/U_2 = f(Fr_j, Fr_{dj}, Ri_i, \theta, \frac{h_2}{D_j}, \frac{h_1}{D_j}, \frac{U_{jL}}{U_1}) \tag{2}$$

might be given, U_{jL} beign the limit jet velocity. Important parameters appear as a result of experiments. Experimental procedure is arranged in the light of these discussions.

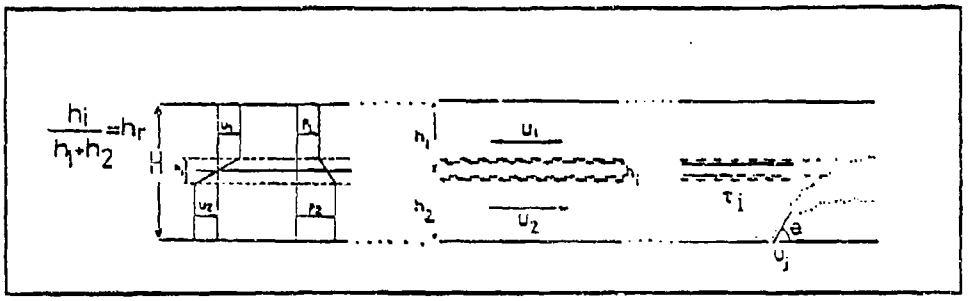


Figure 1. Sketch for two layered flow and jet discharge

3. EXPERIMENTAL MEASUREMENTS

In order to explore the behaviour of jets in two-layered flow, a special rectangular channel of 10 m in length with horizontal bottom was constructed. Special inlet and outlet sections were constructed, since cold water would flow in the lower portion of the channel and hot water in the upper part. As a control section in the hot water outlet, a sliding spillway gate was designed. The jet discharge system was mounted into the bottom of the channel at the mid-section. Here, for the inspection of the flow, the mid 4 m section of the channel was installed from plexiglass walls. This part was supportened by steel frames and provided the support system for the traversing cart where thermal probes and levelling systems were placed.

For temperature measurements a thermistor probe was used so that water temperature of 12 °C - 65 °C could be measured rather accurately. Hot water supplied from the boiler and cold water was mixed in a cylindirical tank so that water supply of the desired temperature was obtained. On hot water, cold water and jet circuits, vanes and orificemeters connected to manometers were placed. Following the outflux of the cold water and the hot water, a V-shaped weir was placed for the control of discharge rates on each discharge open channel. For jet flow, an open constant head tank was designed and connected to the mid-section of the channel where jet nozzles were located. For visual inspections, the tracer injection, buretta-pipetta system was connected into the constant-head tank. A jet discharge nozzle section was designed so that it was possible to change the nozzle diameters and angles of attack. The grid system was mounted in front of the plexiglass inspection window so that, when tracer was used, all details of jet and breaking-up of interface could be recorded by photographical technique. Fig.2 shows the general system.

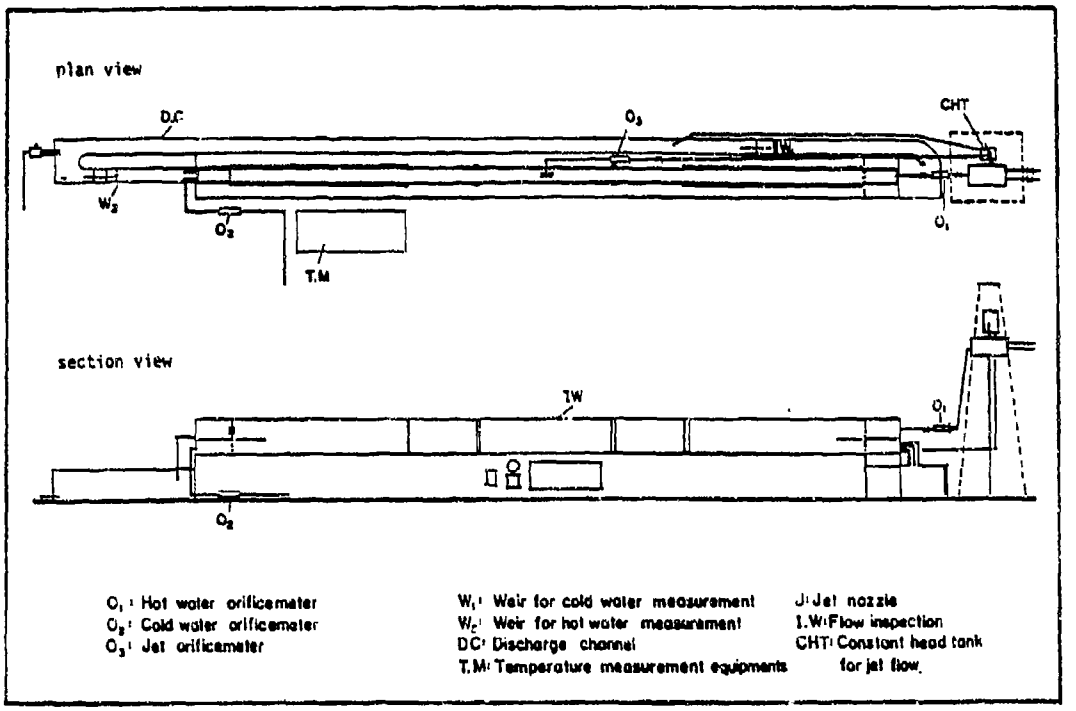


Figure 2. Plan and section wiev of the general experimental system

For each set of experiments, initially a steady-state two-layered flow was established in the channel. After collecting the data for stratification and inter-layer characteristics, a jet was discharged into the system. The lower depth and discharge was kept constant (0.20 m and 2 lt/sec). Also the temperature variation of cold water was negligible (12° - 16 °C). Upper layer thickness (0.15; 0.175 and 0.20 m), discharge (1.; 1.5 lt/sec) and temperature (22° - 61 °C) were the variables. For each flow condition, intermediate layer thickness h_i and Ri_i were defined before the jet measurements. In these experiments Ri_i interval was found as $0.2<Ri_i<1.1$ so that $0.0016 < \Delta\rho/\rho < 0.0167$. Variation of hi/H (ratio of interlayer thickness to total layer depth) was found in conformity with the explanation given in literature as $0.1 < hi/H < 0.25$; [7]. Secondly, vertical jets were discharged from the mid-section of the channel, to investigate the tearing effect of jet on intermediate layer. The jet discharge was changed carefully and limit jet velocity (U_{jL} denoting the breaking-up of interface) was detected visually and instantly by orificemeter reading.

In the first set of experiments, D_j was selected as constant. Effective and important parameters were defined through these tests. In the light of outputs and initial evaluations, new experimental programmes were prepared for different nozzle diameters, D_j=3 mm and D_j=7 mm respectively. In these programmes h_1 and h_2 were kept constant ($h_1 = h_2 = 0.20$ m) since the effect of h_1/h_2 was eliminated. Furthermore jet was discharged only in three different temperatures (cold, medium and max temperatures (55-60 °C)). Acoording to the findings, attained jet velocities were quite large ($U_j/U_2 > 24$ for $D_j = 3$ mm; $U_j/U_2 > 8$ for $D_j = 7$ mm) buoyant jet effect were somehow suppressed.

Parameters which were found in primary importance in the representation of jet flow behaviour on breaking-up phenomena are namely Fr_j, D_j/h_2, U_j/U_2 (jet angle of attack was kept constant as $\Theta=\pi/2$ for vertical jets). Parameters related to Re did not take part since Re is held constant and variation in Re was very small. U_j/U_2 did not appear since U_2 is kept constant through the investigations. During the initial studies Fr_{dj} was also considered for the evaluation of the data. But it was clearly seen that on the penetration of the jet into the interlayer, the momentum effect is much greater as compared to density variation effect. Fr_{dj} > 35; in many cases values over 80, 100 was attained. In literature, buoyant jet effect is considered important if Fr_{dj} values are smaller than 20. For the represantation of the interlayer characteristics, Ri_i was found as the basic parameter.

4. EVALUATION OF THE RESULTS

Investigations with different h_2/D_j ratios show that for low Ri_i numbers, penetration of jet into interface, hence, breaking-up phenomenon is easier and the limit jet velocities are lower. As it is seen in Fig.3, for small Ri_i values, Fr_j-Ri_i relation is linear:

$$Fr_j = A.Ri_i+B \qquad (0.2<Ri_i<0.45) \tag{3}$$

$$Ri_i = (g.h_i.\Delta\rho/\rho)/(\Delta U)^2 , \qquad \Delta U = |U_1| + |U_2| \tag{4}$$

A and B being determined from experimental findings.

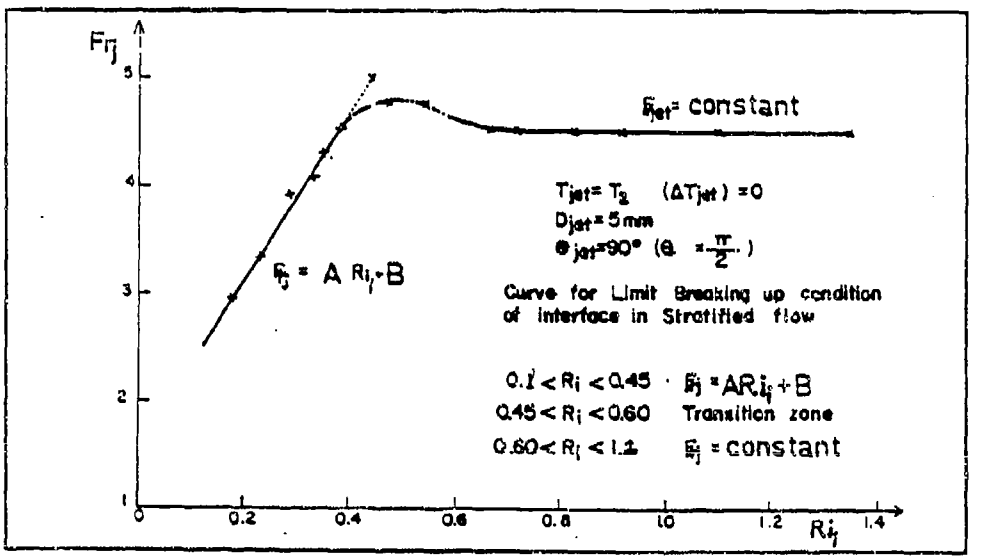
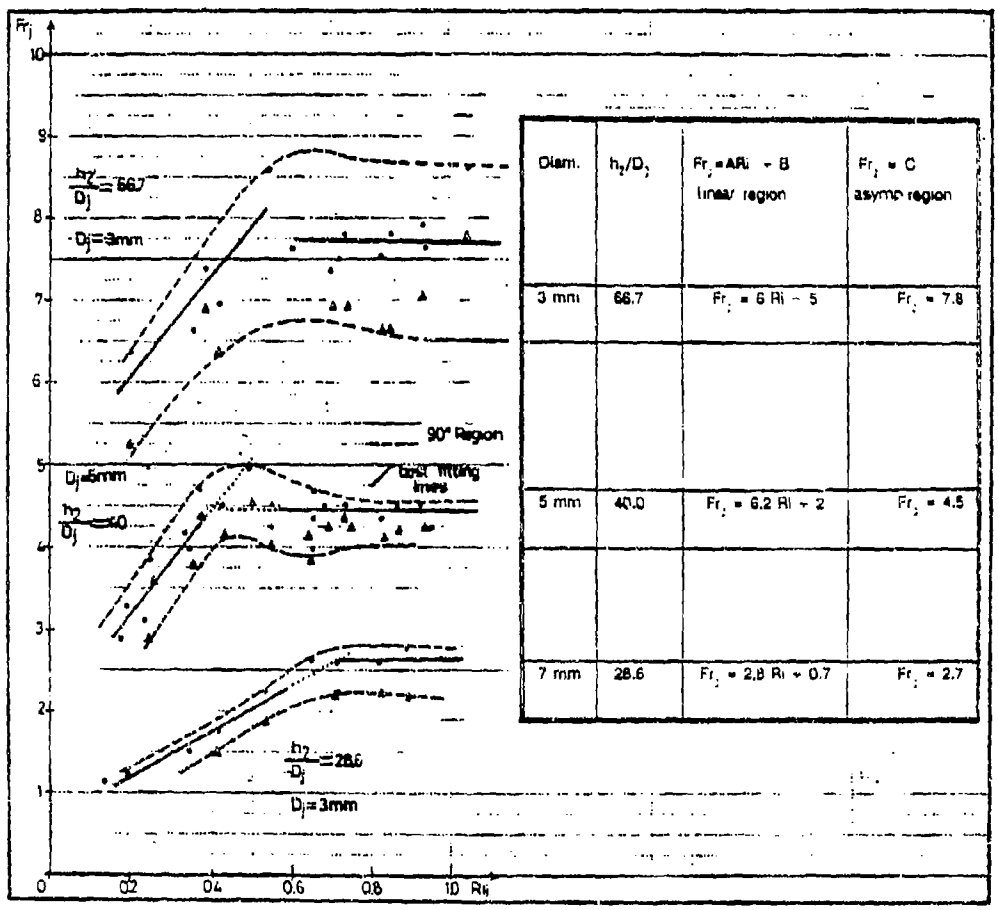


Figure 3. Evaluation of the results for $\Theta=90^{\circ}(h_2/D_j=40)$

Fig.3 is obtained by depicting the experimental result for $h_2/D_j=40$ on the graph. Here, the limit jet velocities responsible from the breaking-up of interface, appear in Limit Froude numbers. Abscissa shows the Ri_i values as an indicator of stratified flow. Also experimental findings for $h_2/D_j=66.7$ and $h_2/D_j=28.7$ verified the conformity of the above-mentioned

representation for low Ri_1 values. Following a transition zone ($0.45 < Ri_1 - 0.60$), stable interface region is achieved. The case of $Ri_1 > 0.6$ produces a highly stabilizing effect so that limit jet velocity does not vary with the variation in the stratification conditions. It is shown that working with a constant nozzle diameter, if $0.6 < Ri_1 < 1.1$ is attained, jet velocity, hence Fr number is constant ($Fr_j = C$). Surely for each nozzle diameter this costant changes and is determined from the experimental findings. It is observed Fr_j is a stong function of h_2/D_j.

Using the values obtained from experiments, best fitting lines for $Ri_1 < 0.5$ region are found out, by the least squares method. Also for asymptotic region ($Ri_1 > 0.6$) average values are calculated and standard deviations are found out. Standard deviations were found quite small and in acceptable range. A,B,C coefficients given in Fig. 4 were found for momentum jets. It can be deduced that asymptotic value ($Fr_j = C$) increases with an increase in h_2/D_j, hence a decrease in nozzle diameter.



Diam.	h_2/D_j	$Fr_j = ARi + B$ linear region	$Fr_j = C$ asymp region
3 mm	66.7	$Fr_j = 6\,Ri - 5$	$Fr_j = 7.8$
5 mm	40.0	$Fr_j = 6.2\,Ri + 2$	$Fr_j = 4.5$
7 mm	28.6	$Fr_j = 2.8\,Ri + 0.7$	$Fr_j = 2.7$

Figure 4. Fr_j-Ri_1 relations for different jet diameters

This is in conformity with the physical interpretation, since higher momentum flux is carried out with larger diameter hence the lower limit velocity will give rise to the breaking-up phenomena.

Straight lines in Fig.4 are the results of mean values for momentum jets. Momentum jet effect appears to be in primary importance since the variation in limit jet velocity due to temperature changes is always below 20% and in many cases in the order of 5% or less. By the analysis of experimental results, an approximation for $Fr_{j\,T}$ is found and expressed, but not given here. Lower (dashed) lines in Fig.4 indicate the result obtained for hot jets where $Fr_{j\,T}$ values are found for $T_j = T_{max}$. On these graps (Δ) triangles indicate outputs for hot jets for ($20\ ^{\circ}C < T_j < 60\ ^{\circ}C$) interval.

In conformity with the phenomenological discussions, we tried to express the breaking-up condition of interface by a unique parameter which includes the effect of other parameters in it. Starting from the idea of momentum ratio for jets in pipes, definition of momentum ratio ($Mr_L = M_{jy}/M_2$) to represent the limit jet condition for breaking-up of interface in two layered flow is found quite suitable and comprehensive. Since research on Mr is the subject of another study [9], further discussion on this matter is avoided here.

5. CONCLUSIONS

As a result of the experimental findings, following conclusions can be given;

1. Breaking-up condition of interface by jets may be explained by Fr_j-Ri_i relations, for low Ri_i numbers ($Ri_i < 0.6$); but it is independent of Ri_i for high Ri_i numbers ($0.6 < Ri_i < 1.1$). For lower Ri_i numbers, Fr_j-Ri_i relations are linear ($0.20 < Ri_i < 0.45$). For the transition region ($0.45 < Ri_i < 0.60$) it is not easy to given a definite relation. For highly stabilized region ($Ri_i > 0.6$), limit jet velocity, hence Fr_j is independent of Ri_i for a given jet diameter. For the first and third regions, semi-ampirical relations are found for various jet diameters.

2. Since breaking-up of interface occurs at quite high velocities ($U_j/U_2 >> 20$), momentum jet effect predominetes and temperature dependence is in second order of magnitude. Also properties of upper layer have influences on limit jet velocity indirectly, by its effect on inter-layer; hence h_1/h_2 does not given an effect on the breaking-up condition.

3. Variation in jet diameter affects the breaking-up condition as follows: For small jet diameters, higher limit jet velocities (hence large Fr_j) are attained for the limit case,but for large nozzle diameters, tearing of interface occurs at lower velocities.

4. Breaking-up of interface in sea-straits depends on momentum ratio (Mr_L) which is defined as the ratio of vertical momentum component related to limit jet velocity (M_{jy}) to the representative momentum (M_2) of the lower layer. For the experiments performed, $Mr_L = k(1 \pm 0.20)$ is defined and proposed for practical purposed.

The result found could be applicable to practical cases such as discharge of effluent into Bosphorous in various conditions.

REFERENCES

1. Maxwell, J.H., Holley, E.R. Lin, C. Tekeli, S., "Study of Stratified Overflow and Underflows", Rep. No. 98, Dept. of Civ. Eng., Univ. of Illinois, 1975.
2. Abraham, G.(1969), "Round Buoyant, Jet in Crossflow", Delft Hyd. Lab. Pub., no.514, p.26.
3. Sümer, M. and Bakioğlu,M, "Sea-Strait Flow With Special Reference to Bosphorous", İ.T.Ü. İnş. Fak. İst. 1981.
4. Armi, L., "The Hydraulics of Flowing Layers With Different Densities", J. of Fluid Mech., V.163, pp.27-58, 1986.
5. Chan, T.L. ve Kennedy, J.F., "Turbulent Nonbuoyant or Buoyant Jets Discharged into Flowing or Ouiscent Fluids", Iowa Inst. of Hyd. Res., Rep. No.140, Univ. of IOWA, 1972.
6. Ger, A.M., "Behaviour of Buoayant Submerged Jets in Stratified and Unstratified Media", Thesis for Assoc. Proffessorship. M.E.T.U., Ankara, 1979.
7. Numan, T.T., Breaking Up Phenomenon of Interface by Jets in Two Layered Flows, Ph.D. Thesis, M.E.T.U.,Ankara 1982.
8. Baddour, R. and Jones D.G., "Vertical Thermal Buoyant Jets", J. of Hyd. Res., V.29, No.5, pp.601-613, 1991.
9. Numan, T.T. " Breaking-up of Interface by Jets in Sea-Strait Type Flows and Momentum Ratio, Cyprus, Lefkosa, Turkish Dev. Ar. 1.I.P.I.S. Conference, June 22-24, 1992.

NOMENCLATURE

A,B,C: Experimental consants appearing in equations denoting limit jet constant
D_j : Jet diameter
Fr : Froude number
Fr_j : Jet Froude number
Fr_d : Densimetric Froude Number
$Fr_{j\,T}$: Fr_j values for hot jet experiments
M_j : Momentum of jet
M_2 : Momentum of cross flows
Mr_L : Limit momentum ratio (M_{jy}/M_2)
Q : Volumetric flow rate
Ri_1 : Richardson number of interlayer $(\delta\rho/\rho_0)g.hi/(\Delta U)^2$
Re : Reynolds number
T : Temperature
U_1 : Mean flow speed of upper layer
U_2 : Mean flow speed of lower layer
U_j : Jet outlet velocity
g : Acceleration of gravity
h_1 : Depth of upper layer
h_2 : Depth of lower layer
h_i : Intermediate layer thickness
k_i : Friction coefficient $\tau_i/\rho.(U)^2$
x,y : Distances in horizondal and vertical directions of the mean flow
θ : Angle of attack of the jet at the nozzle
ν : Kinematic viscosity
ρ : Fluid density
τ_i : Shear stress at the interface
Δ : Difference

A Numerical Study of the Breaking of an Internal Soliton and its Interaction with a Slope

By Kamal Saffarinia[1] and Timothy W. Kao[2]

ABSTRACT

The full Navier-Stokes and diffusion equations are applied to study real fluid effects on generation, propagation, and shoaling of solitary wave on the pycnocline in a two-layer system. First, these equations are solved numerically to study the limiting height and breaking of the soliton in the case of constant total depth. Breaking occurs when the particle velocity in a region of flow field exceeds the wave celerity. This results in a gravitational instability with the patch of dense water into the upper layer in the lee of the wave. The numerically determined breaking criterion is supported by an estimate using the first order KdV theory. Then, the model is used to examine the interaction of the soliton with a slope-shelf topography and a uniform slope. In both cases, the relative depths of the layers change at the turning point along the slope. Mechanisms of the wave breaking and the wave propagation process for both cases are described. Scaled bottom stresses and total wave run-up on the slope are also presented.

1. INTRODUCTION

Internal solitary waves have been observed in many coastal area through satellite pictures and field observation. Osborne and Burch(1) documented waves with very large amplitude in the Andaman sea. Other investigaters observed these waves in different locations in the world such as Apel(2) in Sulu sea and Haury, Briscoe, and Orr(3) in Massachusetts Bay. It is very well known that these waves are propagated shoreward and dissipated in-shore. The dissipation of internal solitary waves may occur through boundary-layer viscosity, scattering by bottom roughness, and wave breaking. The two-layer model that supports an internal solitary wave has been studied extensively beginning by Keulegan(4). Other investigators used a more realistic continuously stratified fluid model which supports an infinite set of internal waves. Kao et al (5) and Helfrich and Melville (6) have studied both models for the investigation of shoaling internal solitons through laboratory experiments under the KdV model. In this study, we solve the full Navier-Stoke and diffusion equations numerically for a two-layer model under a scheme that reduces the truncation errors to zero. Results of these experiments are compared with existing laboratory results.

2. GOVERNING EQUATIONS

Figure 1 illustrates the initial configuration for the slope-shelf topography. It shows a discrete two-layer system stratified fluid with a free surface in a channel of depth d and length L with a slope-shelf. The upper layer of depth h_1 has density ρ_1 and the lower layer of h_2 has density ρ_2 with $\rho_2>\rho_1$. The depth h_1 is selected so that $h_1>h_2$ on the shelf. The density differences represented by γ, which is density anomaly, was defined as $(\rho-\rho_0)/\rho_0$, ρ is the local density and ρ_0 is the reference density and is set equal to ρ_2. The shaded region of depth Δh and length ΔL represents the initial step-pool of fluid with density ρ_1.

---

[1]Post-Doctoral Research Fellow, Office of Research and Development, FHWA, McLean,VA 22101, USA.
[2]Dept. of Civil Engineering, The Catholic Univ. of America, Washington, D.C. 20064, USA.

The step-pool provides the initial potential energy for the generation of solitary wave. The location of the turning point which $h_1=h_2$ is denoted by Lsc. The governing equations for an incompressible, diffusive, two dimensional, viscous, and Boussinesq fluid are given as:

$$\frac{\partial \gamma}{\partial t}+\frac{1}{Q}\frac{\partial}{\partial x}(\gamma u)+\frac{\partial}{\partial z}(\gamma w)=\frac{1}{ReSc}\nabla^2\gamma \tag{1}$$

$$\frac{\partial \xi}{\partial t}+\frac{1}{Q}\frac{\partial}{\partial x}(\xi u)+\frac{\partial}{\partial z}(\xi w)=\frac{Q}{F^2}\frac{\partial \gamma}{\partial x}+\frac{1}{Re}\nabla^2\xi \tag{2}$$

$$\nabla^2\psi=\xi, \tag{3}$$

where the vorticity ξ is defined as:

$$\xi=Q^2\frac{\partial u}{\partial z}-Q\frac{\partial w}{\partial x}$$

and stream function ψ:

$$u=\frac{\partial \psi}{\partial z}, \qquad w=-\frac{1}{Q}\frac{\partial \psi}{\partial x},$$

where u and w are the horizontal and vertical velocities in x and z directions respectively. The dimensionless coordinates and velocities can be written respectively as $x=x^*/L$, $z=z^*/d$, and $u=u^*/C_o$, $w=w^*/C_o$, where the asterisk denotes the dimensional quantity. The aspect ratio of L/d is defined by Q. The non-dimensional time, t is defined by $t=t^*C_o/d$, where the reference velocity C_o is defined by:

$$\left[\frac{g(\rho_1-\rho_2)}{\rho_2}\frac{h_1h_2}{h_1+h_2}\right]^{1/2}.$$

The Laplacian is given by

$$\nabla^2=\frac{1}{Q^2}\frac{\partial^2}{\partial x^2}+\frac{\partial^2}{\partial z^2}$$

The dimensionless parameters are defined as the Reynolds number, $Re=C_od/\nu$, where ν is the kinematic viscosity, the Froude number, $F=C_o/(gd)^{1/2}$, where g is the gravitational acceleration, and the Schmidt number, $Sc=\nu/D$, in which D is the diffusivity of density anomaly. Equations (1) through (3) are solved subject to the following boundary conditions:

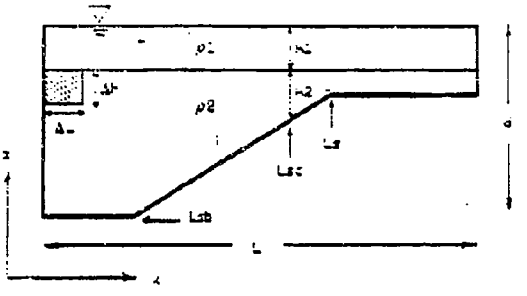


Figure 1

(i) for $z=1$, $0<x<1$; $\psi=0$, $\partial\gamma/\partial z=0$, $\xi=0$
(ii) for $0<z<1$, $x=0$; $\psi=0$, $\partial\gamma/\partial x=0$, $\xi=\partial^2\psi/\partial x^2$

(iii) for $0<z<Hs$, $Lsb<x<Ls$; $\psi=0$, $\gamma=0$, $\xi=Q^2\,\partial^2\psi/\partial z^2$
(iv) for $z=Hs$, $Ls<x<1$; $\psi=0$, $\gamma=0$, $\xi=Q^2\,\partial^2\psi/\partial z^2$
(v) for $z=0$, $0<x<Lsb$; $\psi=0$, $\gamma=0$, $\xi=Q^2\,\partial^2\psi/\partial z^2$
(vi) for $Hs<z<1$, $x=1$; $\psi=0$, $\partial\gamma/\partial x=0$, $\xi=\partial^2\psi/\partial x^2$,
where Lsb denote the x coordinate of the beginning of the slope and is at x=0.10, Lsc at 0.39, and Hs is the shelf length and is at z=0.78.

The boundary condition for density on the free surface, solid walls, and bottoms are no flux condition. No-slip condition is imposed for the velocity field along the boundaries setting u and w equal to zero. Pure-slip condition is imposed at the free surface (z=1) with velocities specified as $u=\partial\psi/\partial z$ and $w=0$. The initial condition for the density anomaly, γ, is set to be -0.01 for the upper layer and the step pool fluid and $\gamma=0.0$ for heavier fluid at the lower layer. The stream-function ψ is zero everywhere for fluid at rest(t=0.0).

3. NUMERICAL METHOD AND EXPERIMENTS

The governing equations are solved by the method described in Roache(8). This one-step explicit finite difference method uses central differencing in space and forward differencing in time for the linear terms of the governing equations. ETUDE, a special explicit up-wind scheme introduced by Valentine(9), was used for the non linear terms to reduce the truncation errors to zero. Values for Re, F, and Sc are 10000, 0.0257, and 833 respectively. The size of the step-pool is selected to generate only one soliton.

3.1 Limiting Height and Breaking of Soliton

We first consider the case of constant depth in order to examine the limiting height of solitons and the mechanism of wave breaking of large amplitude waves. A series of numerical experiments were undertaken with $\Delta L/d=0.40$ and $\Delta h/d=3/40$, 6/40, 15/40, 21/40 for Q=5 and Q=10 with $\Delta x=0.02$, $\Delta x=0.01$, and $\Delta z=0.025$. Results given in Figure 2 indicate that wave amplitude, a/d,approaches asymptotically towards a limiting height. we found that the limiting height of the solitary wave is at $a/d=0.20$ or $a/h_1=2.65$. All the runs are made for duration less than t=5.0 since only the establishment of the wave was sought. However, for $\Delta h/d=21/40$ the equilibrium was not achieved at t= 4.5 as seen in Figure 3.

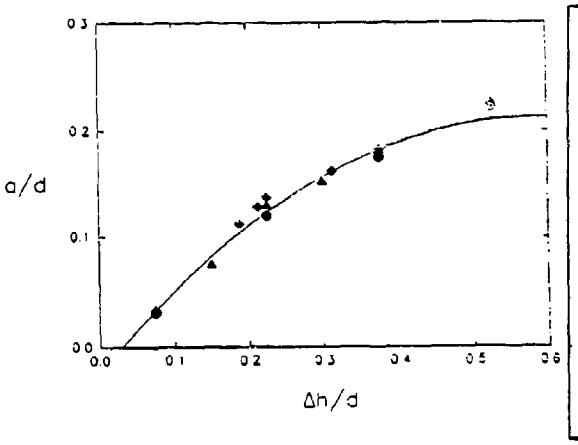


Figure 2

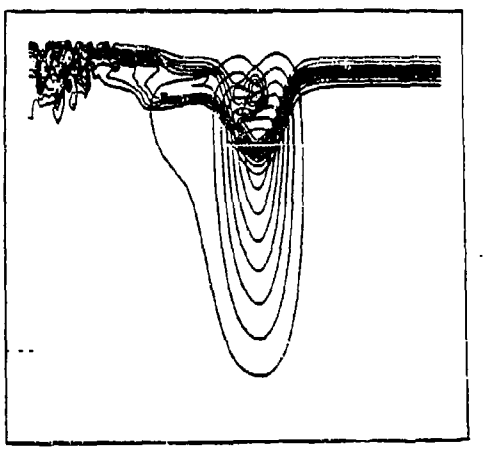


Figure 3

The main mechanism that limits the wave amplitude is the wave instability. For wave generated with initial step-pool depth $\Delta h/d$=3/40, 6/40, and 9/40 equilibrium was established at t=1.5 or earlier. The height of the soliton is always less than the depth of the step-pool due to breaking and energy dissipation. The local Richardson number, $J_z=-(1/F^2)\partial\gamma/\partial z/(\partial u/\partial z)^2$, was determined at the crest(or trough) of the wave and it was found that the Richardson number is decreasing rapidly as the wave amplitude increased. The maximum particle velocity in the wave was less than the wave speed. At $\Delta h/d$=9/40, local small pockets of closed isopycnals representing very weak gravitationally unstable regions appeared near the wave crest, signifying that gravitational instability was incipient. No gravitational instability had occurred at this stage. At $\Delta h/d$=21/40 large scale gravitational instability extended over a large region in the back of the wave. This is shown in Figure 3 with the streamlines superposed on the isopycnals. The isopycnals show an overturning event in the lee. There is entrainment of dense water into the wave during the overturning process. Local Richardson number at the crest decreased to near the critical value so that shear instability was also incipient. However a search of Richardson number over the entire field indicates that the local Richardson number falls below the critical only at the border of the gravitationally unstable region where the Richardson number becomes negative. This breaking process occurred over an extended period of time with the wave gradually decreasing its amplitude. In the present run, the numerical experiment was terminated before equilibrium was established. It can be concluded that breaking occurs when the wave amplitude is large enough so that the particle velocity in the wave exceeds the wave speed. For the present case, the variation of wave speed C with the non-dimensional amplitude a/h_1, and the variation of maximum particle velocity in the wave u_{max} with a/h_1 are plotted in Figure 4. The intersection of the two curves determines the limiting height from the breaking criterion just mentioned above.

An approximate estimate for breaking of internal solitary wave in a fluid of constant total depth due to gravitational instability can be found based on the KdV theory (To be sure the first KdV theory can not predict breaking). According to the first-order KdV theory, the wave speed for the internal solitary wave is given by $C/C_o = 1 + 2/3\ |r|\ a/d$. The value of r have been computed by Kao, et al (5). For example, using h_1/d=0.075, $|r|$=6.70 for αd=28. The criterion for overturning instability is $u_{max}/C_o > C/C_o$, where u_{max} is the maximum particle velocity in the wave. In the KdV theory $u_{max}=u_1$, where u_1 is the particle velocity in the upper layer at the wave trough(crest). Also from the first order KdV theory $u_{max}/C_o=a/h_1$. Therefore, it can be shown that the criterion for gravitational instability is $a/d_1>d/h_1/(d/h_1-2/3\,|r|)$. For αd=28, h_1/d=3/40, and r=6.70, we get $a/h_1>2.01$.

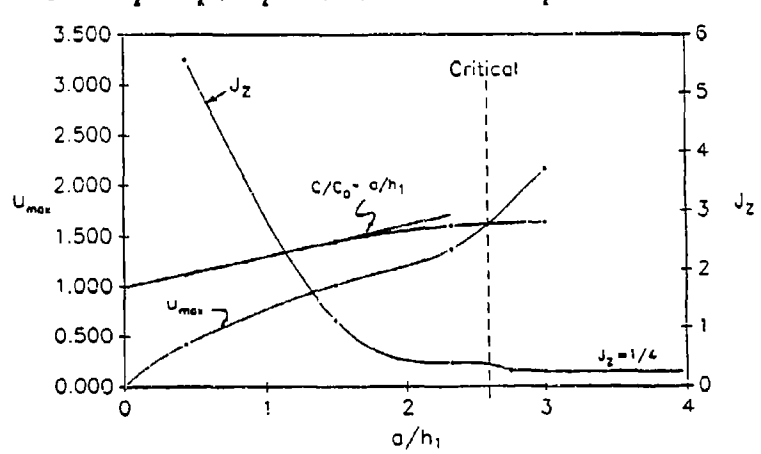


Figure 4

The first order KdV theory gives a linear variation of C/C_o and u_{max}/C_o with the dimensionless amplitude a/h_1, and therefore at least gives a lower bound estimate to the amplitude for breaking. If higher order terms are included in the KdV theory, the dimensionless amplitude a/h_1 for breaking will be larger. The present numerical experiment indicates that breaking occurs when $a/h_1>2.60$.

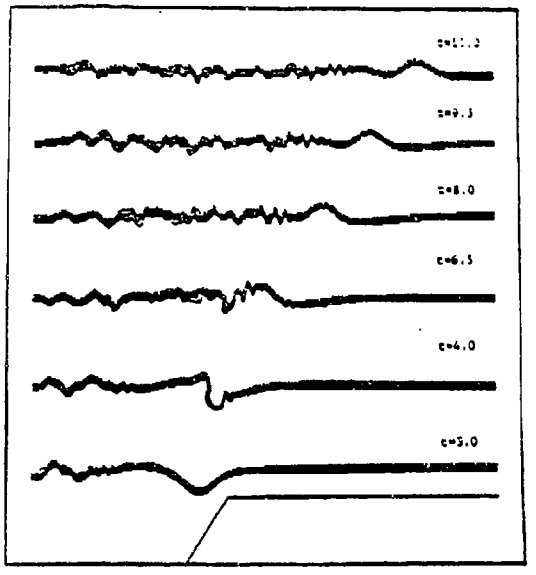


Figure 5

3.2 Interaction With Slope-shelf Topography

Several numerical experiments for interaction of a solitary wave with a slope-shelf topography are undertaken for which reversal of polarity is possible. Solitary wave reverse its polarity as they travel through a region (turning point), where h_1-h_2 changes sign. If the shoaling water is such that the depth of the pycnocline exceeds half the total water depth on the shelf then only wave of elevation is possible on the shelf water. We present results for a case with slope at 1:8. In this experiment h_1/d was set to be 2/14. Experiment started at t=0.0 and continued until t=11.0. A weakly non-linear solitary wave is generated. Figure 5 shows sequences of the solitary wave propagation over a slope which is represented by three mid-pycnocline isopycnal lines at various time, t. The wave reaches to the neighborhood of the turning point, Lsc, the dense water begins to build up at the back of the wave. This phenomenon resembles the creation of the "shelf" in the wake of the solitary wave proposed theoretically by Knickerbocker and Newell (10) for a model KdV equation in which the

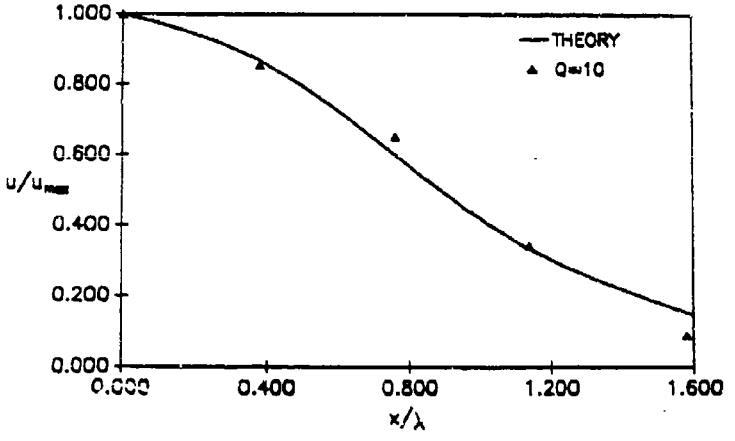


Figure 6

coefficient of the quadratic term varies linearly over the slope. The build-up is shown at time t=4.0. When the build-up reaches its maximum strength, it breaks up into a scattered oscillatory wave train as shown at time t=6.5. The scattered waves travel into a region with $h_1>h_2$, where the leading wave starts to separate and form a wave of elevation in what appears to be an emerging train of waves of elevation (t=8.0, 9.5, and 11.0). The vestiges of the original wave of depression persist in a weakened and distorted form ahead of the wave train for some distance as shown in the Figure 5. The prominent wave in the region where $h_1>h_2$, is clearly a wave of elevation. Therefore, it suggests that the mass and energy transports of the original soliton of depression are impeded as it shoals through the critical point and are redistributed to generate a new wave train compatible with the depths of the two layers on the shelf. It can be seen that no reflected waves evolved. The plot of the reversed wave profile based on horizontal velocity u/u_{max} is shown in Figure 6. This plot shows only the forward portion of the wave when the wave is fully reversed from both the space records and the temporal records for two times. The results show excellent agreement with the $sech^2$ profile, confirming that the wave is indeed a KdV solitary wave.

3.3 Interaction with Uniform Slope Topography

Results from the numerical experiments on the interaction of an internal solitary wave with a uniform slope and subsequent wave run-up over slopes with different inclinations(1:20, 1:40, 1:80) are discussed. For the present study, we chose the ratio of upper-layer depth to the total depth, h_1/d, to be 1/4 so that the interface-slope interaction is at x=z=0.75 on the slope (note that the total depth, d is deepest section of the channel). All experiments started at t=0.0 then continued until the wave is reached to its maximum run-up over the slope. Value for a/d was measured to be 0.080 at the beginning of the slope for all cases. Figure 7 is for the case with slope at 1:40. It shows the sequences of the wave breaking on the slope at different time interval. The wave is passed through the location L_s, which is the turning point ($h_1=h_2$) and changing its polarity. The rear face of the wave steepened so that the wave reaches to its maximum height, breaking at the interface-slope intersection region on the slope, resulting in the creation of a train of scattered waves with the leading wave propagating over the slope. The leading wave is indeed a soliton and propagating over the slope during the run-up process. As the leading wave advances over the slope, its height decreases and the front face of the wave was gradually become parallel to the slope. The wave moves up until it dissipated. The backflow contains a patch of light

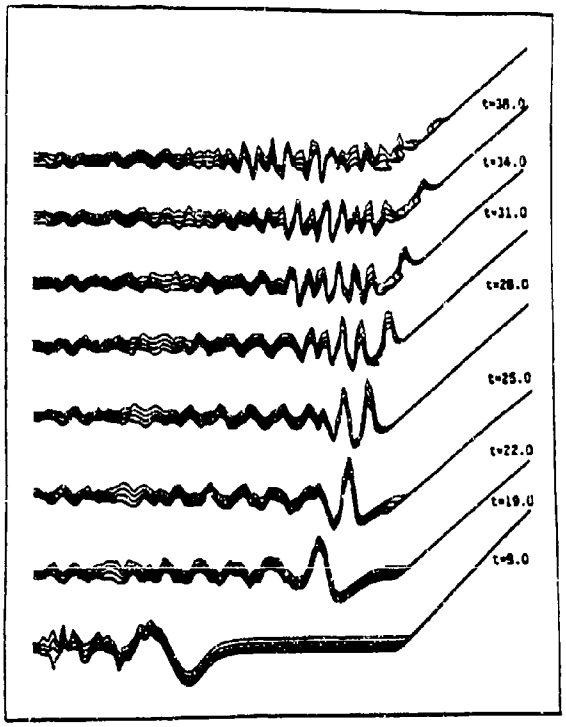


Figure 7

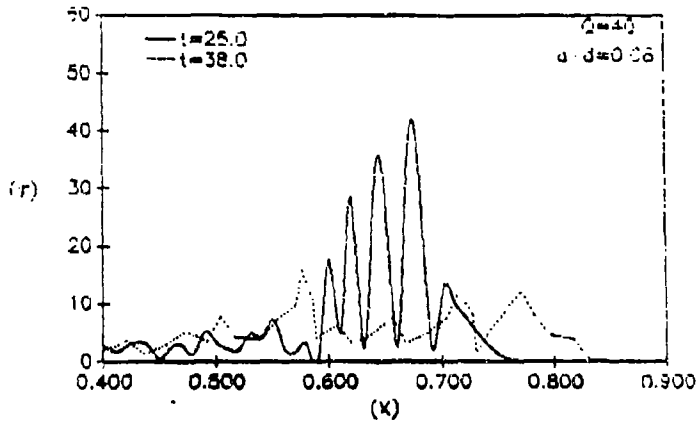


Figure 8

and heavy fluid which is carried-up by the second approaching wave. Results obtained from these numerical experiments are found to have the same breaking mechanisms as those found from laboratory experiments by Helfrich(7), in which slopes at 1:15, 1:20, and 1:30 were used. His experiments led to the production of multiple bolus type of waves during the shoaling process. In our study, no solitary wave of second mode was obtained during the run-up process. Similar results were also found for different slopes with smaller wave amplitude (a/d=0.055, 0.04, and 0.025).

Values for shear stress (τ) at a relatively small distance Δn away from the slope boundary was calculated from $\tau = \Delta u/\Delta n$, where $u=(u^2+w^2)^{1/2}$ and $\Delta n=\Delta x \cos(\tan^{-1}(1/Q))$. Figure 8 shows two plots of the shear stress distributions over the slope at two different times. The maximum shear stress had occurred when the wave was at the early stage of the run-up process. The values for τ is decreasing as the slope inclination and wave amplitude decrease. The dimensional value for shear stress with the dynamic viscosity of ocean water $\mu=10^3$kg sec/m^{-2}, is 0.066 dyne, while considering an eddy viscosity value of 10^{-1}m^2/s for ocean water.

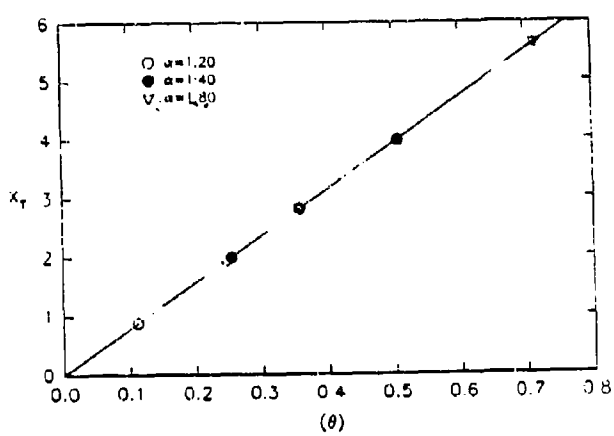


Figure 9

The total distance for the wave run-up, X_T, for different slope inclinations can be determined from $X_T = 7.87(\theta)$, where $\theta = \alpha^{-0.5}(a/d)$, with α=1/20, 1/40, 1/80, and a/d is the non-dimensional wave amplitude. This distance was measured from interface-slope intersection to the point that the wave reaches its highest run-up. Figure 9 shows the total wave run-up over the slope with θ is plotted versus the total wave run-up, X_T. The value for the total wave run-up in dimensional form for a wave with an amplitude of 2.85 cm, is 100 cm (for α=1/20). Similarly, the total run-up for cases with α=1/40 and α=1/80 at the same wave amplitude (a/d=0.08) are 160.93 cm and 201 cm, respectively. These results are found to be in good agreement with those reported by Helfrich(7).

4. CONCLUSIONS

A breaking criterion for the breaking of solitary wave was found. It was shown that the breaking occurs when the particle velocity exceeds the wave celerity in the flow field region. For the wave interaction with slope-shelf and uniform slope, the results conclude that a solitary wave of depression travelling from the region of $h_1<h_2$ into the region of $h_1>h_2$ gives rise to one or more solitary wave of elevation. In fact the original wave of depression is gradually dissipating through transfer of energy to build up mass at the back of the wave and through viscous dissipation. The build-up then collapses to give rise to solitons compatible with the geometry of the shelf region. For the slope-shelf case, the results show that at least one solitary wave emerges with its polarity reversed. For the uniform slope case, a packet of oscillatory standing waves exists in the breaking region. This packet generates a successive train of solitons of reversed polarity onto the slope. The successive passage of internal solitary wave over gentle slopes contribute to the transformation of high nutrient fluid from the off-shore region onto the coastal area when the total run-up of solitons is significant. Also, the internal wave run-up on the slope may have significant effects for the particle and sediment transport.

REFERENCES

(1) Osborne, A.R. and Burch, T.L., (1980) "Internal Solitons in the Andaman Sea," Science, 208, 451-460.

(2) Apel, J.R., (1981) "Update: Internal Waves in the Sulu Sea," Bull. Am. Meteor. Soc. 62, 1061-1062.

(3) Haury, J.M., Briscoe, M.G., and Orr, M.H. (1979) "Tidally Generated Internal Wave Packets in the Massachusetts Bay," Nature 278, 312-317.

(4) Keulegan, G.H., (1953) "Characteristics of Internal Solitary Waves," J. Res. Natl Bur. Stand. 51, 133-140.

(5) Kao, T.W., Pan, F.S. & Renouard, D., (1985) "Internal Solitons on the Pycnocline Generation, Propagation, Shoaling and Breaking over a Slope," J. Fluid Mech. 159,19-53.

(6) Helfrich, K.R., Melville, W.K., (1985) "On Long Nonlinear Internal Waves over Slope-Shelf topography," J. Fluid Mech. 167, 285-308.

(7) Helfrich, K.R., (1992) "Internal Solitary Wave Breaking and Run-up on a Uniform Slope," J.Fluid Mech., 243, 133-154.

(8) Roache, P. J., (1972) "Computational Fluid Dynamics", Hermosa Publishers, N. M.

(9) Valentine, D. T., (1987) "Comparison of Finite Differences Methods to Predict Passive Contaminant Transport," Computers in Eng., ASME, 263-269.

(10) Knickerbocker, C. J. and Newell, A. C., (1980)"Internal Solitary Waves near a Turning point," Physics letters 75A, 326-330.

Decay of Internal Solitary Waves and A Comparison of Timescales of Dissipation and Dispersion

H. Sandstrom and N.S. Oakey

Physical and Chemical Sciences, Department of Fisheries and Oceans, Bedford Institute of Oceanography, Dartmouth, Nova Scotia, B2Y 4A2.

Abstract. Solitons have been observed and studied on the Scotian Shelf using the vertical microstructure profiler EPSONDE. During one tidal cycle a packet of solitary waves has been sampled four times as it propagated onto the shelf to examine its evolution and decay. Enhanced turbulence and mixing were observed to occur in the strongest shear region of the wave packet as expected. About 20% of the energy lost as the solitary wave packet decayed can be attributed to turbulent dissipation. The effects of non-linearity, dissipation and dispersion are explored in terms of the Korteweg-de-Vries-Burgers (KdvB) equation. The dispersive timescale is always much shorter than dissipative timescale and both decrease as the soliton moves on-shelf. The mean dissipation time scale of 12 hours compared to the dispersion timescale of approximately 1 hour suggests that the waves are consistent with the KdVB description. Calculated vertical diffusivities are in the range of 10^{-5} to $10^{-4} m^2 s^{-1}$.

1. Introduction

The study of oceanic tides in the continental shelf areas reveals that as the tide is modified, an energy cascade from very large to very small scales takes place. The interaction of the surface tide with topography, such as the continental shelf edge, in the presence of stratification, generates an internal tide. In the process the surface tide loses a small amount of energy, insignificant for the surface tide, but appreciable with the relatively shorter scales of the internal tide. Although short in comparison with the surface tide, the wavelength of the internal tide is still long compared to the depth of water in which it travels. The internal tide therefore is influenced by both non-linear and dispersive effects and, given enough time, evolves into shorter undulations. These may be in the form of undular internal bores, internal solitary waves or "solitons". A very large, if not the major, fraction of the energy in the internal tide is then found in the short waves. This energy, due to the waves being short but highly intense, is more readily available to ocean mixing.

2. Dissipation of internal solitary waves, ocean mixing

In the transformation of internal tide into solitary waves the energy is repackaged or "quantized" into compact and isolated units. We also know that eventually the solitary waves disappear and that their energy is released to the ocean. The evolution of waves can be explored in terms of, for example, the Korteweg-de Vries (KdV) equation, but there is no comparable *a priori* framework for discussion of dissipation mechanisms and how the released energy is redistributed. Sandstrom and Elliott (1984) suggested, based on their observations on the Scotian Shelf, that most of the energy was dissipated in a narrow zone near the shelf edge, and that the average rate of dissipation there was $5 \times 10^{-2} W m^{-2}$. Assuming that mixing occurred in a 50 m-deep mixing layer, they obtained an average dissipation rate of $\epsilon = 1 \times 10^{-7} W kg^{-1}$. This value would increase five-fold if mixing occurred in a 10 m-deep layer, a scale more representative of the pycnocline scale. Shear instability and boundary layer friction, both interfacial and bottom, were put forth as mechanisms contributing to the dissipative process. Subsequent airborne

radar observations showed that at least some of the solitary waves travelled further inshore and survived longer than Sandstrom and Elliott's estimates, suggesting a revision of the dissipation estimate downward by a factor of 2. Sandstrom *et al* (1989) compared acoustic backscatter and temperature fine-structure from a towed CTD prior to and during the passage of a group of large-amplitude internal waves on the continental shelf off Nova Scotia. They concluded that both acoustic backscatter and temperature fine-structure could be associated with active turbulence generated by the internal waves. All of these increased significantly in well-defined layers of approximately 5 - 15 m thickness. They also found that the local Richardson number was small in the same layers, whence shear instability was expected to occur. Their estimated dissipation rate in the turbulent patches was $\epsilon = 10^{-5} W kg^{-1}$. Taking patchiness of turbulence into account, the average dissipation rate in a 10 m thick layer was approximately $2 \times 10^{-7} W kg^{-1}$, a figure similar to their earlier estimate (Sandstrom and Elliott, 1984).

Liu *et al* (1985) in their study of Sulu Sea solitons included an eddy viscosity coefficient in a parametric form in the numerical simulation of wave evolution. A typical value of the coefficient used was 10 - 30 $m^2 s^{-1}$, which translates into a dissipative time scale of approximately 1 - 3 days. In that time the average dissipation rate of a 50 m amplitude soliton, travelling at 2 ms^{-1}, is about $3 \times 10^{-3}\ Wm^{-2}$. The Sulu Sea solitons travel in relatively deep water and hence survive longer than solitary waves on shallow shelves. Liu *et al* do not specify the dissipation mechanisms explicitly. Their eddy viscosity coefficient is based on the assumption that the small-scale processes in a turbulent layer embedded in a thin pycnocline can be parameterized in this way. The eddy coefficient may vary with water depth, i.e. mixing in shallow water due to shoaling effects is deemed to increase the local value of eddy viscosity. The direct effect of bottom friction on soliton dissipation is small.

3. Dissipation: The Field Experiment

In order to further clarify and quantify the relationships between internal solitary waves, turbulence and acoustic backscatter in the water column, a field experiment was conducted at the same site where previous work by Sandstrom *et al* (1989) had shown vigorous internal wave activity to exist. The observations were made on the Scotian Shelf, over the corner of Banquereau Bank east of the Gully, in September of 1987, and the study was focused on the packets of solitary waves.

The observational strategy was to set up the sampling equipment on the ship ahead of the expected arrival of a wave packet, which we tracked by observing bands of increased sea surface roughness on ship's radar. The impending arrival of the first wave in the packet was the signal to start sampling. A microstructure profiler, EPSONDE (Oakey, 1988), was profiled to a depth of about 50 meters approximately every three minutes. Vertical profiles of temperature, temperature microstructure and velocity microstructure were obtained. This sampling continued with the ship drifting in the wave packet for a maximum of about two hours. The ship then repositioned itself again ahead of the packet for a second and subsequent series of profiles through the solitary wave packet as it evolved and propagated towards shallow water. A particularly interesting set of observations was obtained on September 8, 1987. The same wave packet was sampled during four different sampling periods over a total time span of about 8 hours, during which the waves propagated a distance of nearly 20 km. Each sampling period contained from 20 to 36 EPSONDE profiles. Figure 1 shows the extent of the sampling area. The heavy arrows indicate ship drift during stations 74, 76, 78 and 80. The start and end times at each station are in GMT.

The wave packet was first observed in 105 metres of water. During the first station, lasting one hour, the ship drifted over a small distance, essentially parallel to the wave crests. At the later stations the ship apparently drifted with the phase speed of the waves, and was in effect *surfing* on internal solitary waves.

To estimate the part of the energy that was dissipated, each vertical profile from EPSONDE was analyzed to obtain the average dissipation in successive 2 second segments of the vertical profile corresponding to approximately 1.8 metres in the vertical. The predominant dissipation occurred in a layer about 10 metres thick, similar to the pycnocline thickness and tracking it in its vertical excursions. The dissipation estimates were therefore averaged over 10 metres vertically at the depth of maximum dissipation to obtain the mean dissipation for each profile. These were averaged in turn to obtain the mean dissipation for the whole sampling period (station). Values at each station are shown in Table 1. The tabulated values

are estimated to be accurate to within a factor of 2 (Oakey, 1982). At each station the measured power loss is referred to a mean location and time, where the location is relative to that of the initial station. The Power Loss per meter of crest length for each station is estimated by assuming that the dissipation occurs in a 10 metre thick layer, and that the length of the wave packet is 3 km. The latter assumption is somewhat arbitrary, but is taken to represent the distance that includes the most energetic waves and hence a large ($\approx$ 90%) fraction of the total energy in the packet. At the initial station almost all of the wave packet passed under the ship. At other stations a packet length estimate is obtained from radar observations of number of bands of surface roughness and their separation (typically 6-7 bands separated by 400-500 metres). The Power Losses at each station are tabulated in Table 1. These multiplied by the time at the station yield Energy Losses per unit crest length at each station. Energy Losses between stations are calculated similarly by using the average of Power Losses at the two adjacent stations. A sum of all Energy Losses gives the total turbulent energy dissipation in the 10 metre thick layer over the eight hour sampling period as $4.5 \times 10^5 Jm^{-1}$.

In addition to the microstructure data, the EPSONDE profiles yield the temperature "macrostructure", from which the isopycnal displacements can be extracted. The changes of potential energy due to the internal waves can be estimated, and assuming equipartition of energy, the total baroclinic energy is obtained. Thus at station 74, where the wave heights are typically 20 m, the estimated energy in the 3 km long wave packet is $5 \times 10^6\ Jm^{-1}$ of crest length. At station 80 the displacements are reduced to about 15 m, and the energy has decreased by about 50 percent.

3.1 Discussion of Experimental Results

Repeated sampling of an internal wave packet has produced the first direct measurements of turbulent dissipation due to the waves in a part of the water column that includes the pycnocline. The wave packet travels from deeper (105 metres at station 74) into shallow (60 metres at station 80) water. The crests of waves, as seen by radar, are aligned with isobaths. Thus propagation direction is transverse to bathymetry. In addition to the radar observations of the sea surface, acoustic backscatter data of the water column provides supporting information on the wave packet. However, explicit discussion of the acoustic data is beyond the scope of this paper. Density data used in this discussion was obtained from CTD measurements preceding and following this particular 8 hour observation period.

The total baroclinic energy at station 74 is $5 \times 10^6 Jm^{-1}$. At station 80 half of this remains. Of the $2.5 \times 10^6 Jm^{-1}$ energy lost, about 20 percent ($0.45 \times 10^6 Jm^{-1}$) is accounted for by turbulent dissipation in the pycnocline. Turbulent dissipation outside the pycnocline is small in comparison. If the 20 percent of bulk dissipation goes into turbulent dissipation, and hence into mixing the water column, then the fractional mixing efficiency is 1/4. This ratio was suggested by Gregg and Briscoe (1979), albeit without observational support, and used by Sandstrom *et al* (1989). Of the remaining 80 percent of bulk dissipation, we estimate that approximately 1/4 to 1/3 is lost by bottom friction and the remainder is fed into

Table 1. Dissipation, Energy and Power Loss in Soliton Transit

Site	Samples	Time	Distance	Dissipation	Power Loss	Energy Loss
			Kilometers	Watts/m	$Watts/m^3$	Joules/m
74	20	17.38	0.00	1.41×10^{-4}	4.23	0.15×10^5
						(0.16×10^5)
76	27	19.07	4.49	4.15×10^{-4}	12.5	0.59×10^5
						(1.04×10^5)
78	29	22.38	11.87	4.88×10^{-4}	14.6	0.55×10^5
						(0.44×10^5)
80	36	24.11	17.23	1.07×10^{-3}	32.1	1.60×10^5

other scales of motion and/or radiated away. The mean dissipation rate over 8 hours is $5.3 \times 10^{-7} Wkg^{-1}$, corresponding to a vertical diffusivity of $5 \times 10^{-5} m^2 s^{-1}$. The values range over about an order of magnitude, from $1.3 \times 10^{-5} m^2 s^{-1}$ at station 74 to $1.0 \times 10^{-4} m^2 s^{-1}$ at station 80. The diffusivities are calculated using $\kappa_\rho = \Gamma \epsilon N^{-2}$, where $\Gamma = 0.25$ is typical (Oakey, 1985). The values are not large, with strong stratification offsetting large dissipation.

The reduction of wave energy by 50 percent in 8 hours translates into an energy dissipation timescale of about 12 hours or one semi-diurnal tidal cycle. The timescale of amplitude dissipation is about twice as long. However, the dissipative timescales vary by over an order of magnitude as the wave packet moves into shallow water, from approximately 70 hours at station 74 to 5 hours at station 80 for energy dissipation, and about twice as long for amplitude dissipation. The dissipative timescale is always much longer than the dispersive timescale, which is approximately one hour. Figure 2 shows the 20 km long section with the sketch of bathymetry and the calculated values of energy dissipation and the two time scales. The solitary waves can be expected to behave locally as solitary waves, for which the KdVB equation applies.

4. Shear-generated Turbulence, a Dissipation Model

The basis of the following model is the observation (Sandstrom *et al*, 1989) that in large-amplitude waves the vertical current shear can cause the local Richardson number to be small enough for the flow to be unstable. They found that $R_i < 1/4$ in a layer near the N maximum and associated this layer with the observed enhanced turbulence. They also suggested that in a wave packet, each successive wave could reinforce the turbulence in the already existing layer and implied that active turbulence could persist at somewhat higher value of Ri than 1/4.

The local Richardson number is (Sandstrom et al, 1989):

$$R_i = \frac{N^2}{(\partial u/\partial z)^2} = \frac{{c_o}^4}{N^2(z_o)\phi^2(z_o)} \times \frac{1}{U^2 a^2(x,t)} \qquad (4.1)$$

separated into a depth-dependent part and a part varying in time and in propagation direction. $a(x,t)$ is the wave amplitude and U and c_o are the propagation speeds of the solitary wave and the linear speed respectively. ϕ is the eigenfunction of vertical displacement. The depth-dependent part is calculated directly from density data and remains invariant as long as stratification is the same. The Richardson number thus varies inversely with $U^2 a^2$, the square of flux of a. Solitary wave troughs are therefore most likely sites of turbulent layers, although once initiated, the layers may persist for smaller than critical amplitudes.

We consider a solitary wave of amplitude a_o. The criterion for onset of turbulence, leading to loss of energy from the wave is $a_o > a_c$, where a_c is the critical amplitude defined as the amplitude at which $R_i = 1/4$. If the critical amplitude is not exceeded anywhere on the wave, dissipation is assumed not to occur. If the criterion for onset of turbulence is satisfied, we assume that the solitary wave loses energy, until the wave amplitude decreases to the critical value. This does not occur instantaneously, but gradually over a longer *dissipative time scale*. The wave meanwhile has to adjust its shape to the new energy environment. This adjustment takes place over the *dispersive time scale*, which, given the wave parameters, can be easily calculated. The usual assumption in connection with the KdVB equation is that the dissipative time scale is much longer than the dispersive time scale. Usually this cannot be assumed *a priori*, but we have shown it to hold at least during the 8 hours that a wave packet was followed.

4.1 Observations *vis-a-vis* the model

Using the appropriate water depths at stations 74, 76, 78 and 80, the corresponding critical wave amplitudes for $R_i = 1/4$ are calculated as 20.5, 19, 17 and 17 metres respectively. A slight change of critical Richardson number to 1/3 alters the critical amplitudes by a factor of $\sqrt{3/4}$, ranging now from 18 to 15 metres. The observed reduction of wave amplitudes from about 20 to 15 metres is therefore quite consistent with the criterion of onset of turbulence and the subsequent loss of energy from the waves. Only a fraction of the energy loss goes into mixing of the water column in the form of the measured ϵ.

5. Summary

For moderately non-linear motion, the Korteweg -deVries-Burgers (KdVB) equation describes the evolution of the internal tide and the solitary waves that the internal tide is transformed into. The non-linear and dispersive coefficients in the KdVB equation are derived from the internal wave eigen-functions, based on measured density data. The eddy viscosity coefficient is not a property of the fluid and a much more elusive quantity to determine. The decay of internal wave motion is due to different causes. In this paper we have focused on determining the attenuation due to turbulent layers and microstructure with shear instability as the probable cause.

By direct measurement of turbulent dissipation within a well-defined packet of internal solitary waves we can account for about 20 percent of total energy loss this way, arriving at a fractional mixing efficiency of 1/4. A simple dissipation model, based on the critical Richardson number criterion for onset of turbulence and loss of energy from the waves, is consistent with observations. The calculated vertical and horizontal diffusivities range from 10^{-5} to $10^{-4} m^2 s^{-1}$ and from 0.1 to $1 m^2 s^{-1}$ respectively, the latter being based on a typical horizontal scale for solitary waves of O(100) metres.

Acknowledgments. This research was supported in part by the Small-Scale Physical Oceanography Program of the Office of Naval Research under grant No. N00014-90-1887.

References

Gregg, M.C. and M.G. Briscoe, Internal waves, finestructure, microstructure and mixing in the ocean, Rev. Geophys. Space Phys., *17*, 1524-1548, 1979.

Liu, A. K., J. R. Holbrook and J. R. Apel, Nonlinear Internal Wave Evolution in the Sulu Sea, *J. Phys. Oceanogr.*, *15*, 1613-1624, 1985.

Oakey, N. S., Determination of the Rate of Dissipation of Turbulent Energy from Simultaneous Temperature and Velocity Shear Microstructure Measurements, *J. Phys. Oceanogr.*, *12*, 256-271, 1982.

Oakey, N. S., Statistics of Mixing Parameters in the Upper Ocean During JASIN Phase 2, *J. Phys. Oceanogr.*, *12*, 1662-1675, 1985.

Oakey, N. S., EPSONDE: An Instrument to Measure Turbulence in the Deep Ocean, IEEE J. of Oceanic Eng., *13*, 124-128, 1988.

Sandstrom, H. and J. A. Elliott, Internal Tide and Solitons on the Scotian Shelf: A Nutrient Pump at Work, *J. Geophys. Res.*, *89*, 6415-6426, 1984.

Sandstrom, H., J. A. Elliott and N. A. Cochrane, Observing Groups of Solitary Internal Waves and Turbulence with BATFISH and Echo-Sounder, *J. Geophys. Res.*,*19*, 987-997, 1989.

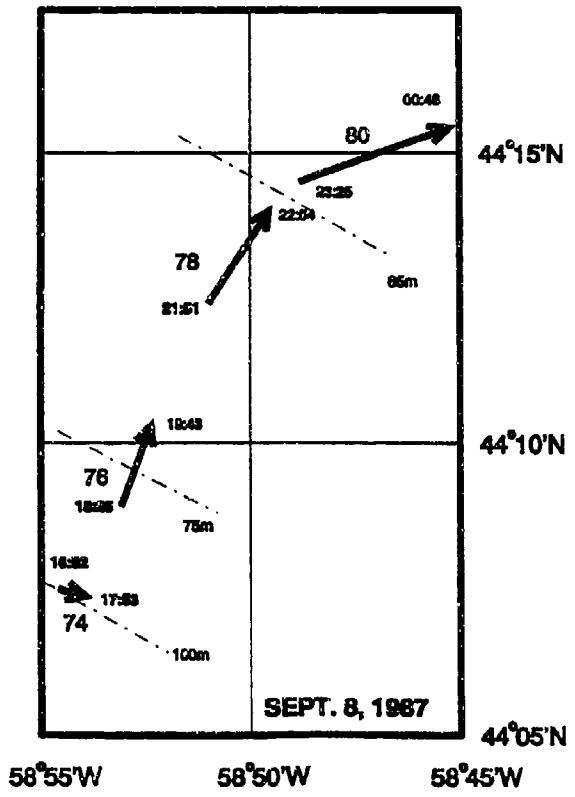
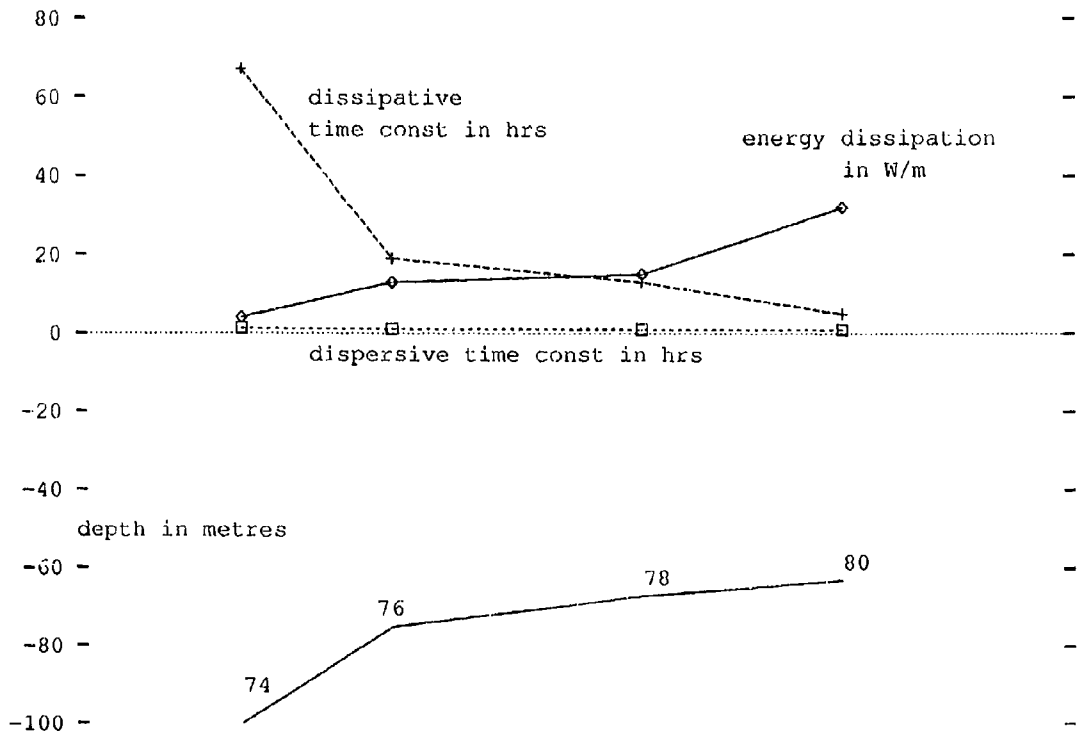


Figure 1. The sites of successive sampling of a packet of solitary waves, September 8, 1987. The arrows indicate the direction and distance of ship drift during sampling periods. Start and end times are in GMT; depth contours are dashed lines with depths in metres.

Figure 2. Sectional representation of the water depth in the sampling area with the mean position of the stations. In the upper half of the figure the measured energy dissipation at each station and the calculated time scales of dissipation and dispersion are shown.



Vertical mixing of passive scalars due to breaking gravity waves.

V. Schilling and D. Etling

Institut für Meteorologie und Klimatologie
Universität Hannover
Herrenhäuser Str. 2
30419 Hannover
Germany

1 Introduction

Large parts of geophysical flow systems like atmosphere and ocean are stably stratified with moderate or weak turbulent activities. Mixing of passive scalars (e.g. air pollutants) is rather slow under these circumstances except for some singular events like Kelvin-Helmholtz-instabilities or breaking gravity waves.

This is especially true for the lower Stratosphere, where there is little or no turbulance under usual circumstances. Concerning the problem of vertical diffusion of passive scalars this has become of some concern because of the possible influence of high altitude aircraft traffic on climate, e.g. green house effect or Ozon hole. Because pollutants from aircraft emissions are set free in a form of rather narrow line sources (few meters wide) it is of interest for modelling chemical reactions in global climate models, how fast these trace substances are distributed vertically. On the smallest scales this process is usually due to small-scale turbulence in the atmosphere. But as the lower Stratosphere is very stably stratified, no detectable permanent turbulence level is found in these regions. It has therefore long been suggested, that turbulence is created by shear-instabilities (Kelvin-Helmholtz-instabilities) or breaking gravity waves (e.g. Fritts and Rastogi, 1985) within limited local and spatial scales. The question then arises, what net effect can be gained from these events concerning dispersion of passive scalars, if averaged over space and time as suitable for large scale numerical models of atmospheric chemistry (e.g. Crutzen and Brühl, 1990).

In this paper we describe some numerical simulations on the dispersion of passive scalars due to breaking gravity waves. This extends earlier work on the mixing of air pollutants by Kelvin-Helmholtz-instabilities (Schilling and Janssen, 1992).

2 The Flow Model

Numerical simulations of gravity waves were performed with a two-dimensional model based on the anelastic version of the Boussinesq-approximation subject to usual Reynolds-averaging. Equations of motion, continuity equation and heat transfer equation can be written as:

$$\frac{\partial \overline{u}_i}{\partial t} + \overline{u}_k \frac{\partial u_i}{\partial x_k} = -\frac{1}{\varrho_0}\frac{\partial \overline{p}}{\partial x_i} + g\frac{\overline{\Theta}}{\overline{\Theta}_0}\delta_{i3} + \frac{\partial}{\partial x_k} K_m \frac{\partial \overline{u}_i}{\partial x_k} \quad , \tag{1}$$

$$\frac{\partial \overline{u}_i \overline{\varrho}}{\partial x_i} = 0 \quad , \tag{2}$$

$$\frac{\partial \overline{\Theta}}{\partial t} + \overline{u}_k \frac{\partial \overline{\Theta}}{\partial x_k} = \frac{\partial}{\partial x_k} K_h \frac{\partial \overline{\Theta}}{\partial x_k} \quad . \tag{3}$$

In (1)-(3) $\overline{u_i}$ is the mean velocity vector, $\overline{\Theta}$ the potential temperature and $\overline{p}$ pressure. K_m and K_h are the eddy viscosity and eddy heat diffusivity, respectively. Both are related via a Prandtl number by $K_h = K_m/Pr$.

The eddy viscosity is obtained from the Prandtl-Komogorov relation

$$K_m = c_1 \ell E^{1/2} \quad , \tag{4}$$

where $E = \overline{u_i'^2}/2$ is the turbulent kinetic energy and ℓ a mixing length. The latter is related to the grid size $\Delta = (\Delta x \cdot \Delta z)^{1/2}$ by

$$\begin{aligned} \ell = &\ min(\Delta, 0.76 N^{-1} E^{1/2}) \quad , N^2 > 0 \\ \ell = &\ \Delta \qquad\qquad\qquad\qquad\ \ , N^2 \leq 0 \quad . \end{aligned} \tag{5}$$

The turbulent kinetic energy is obtained from the usual equation

$$\frac{\partial E}{\partial t} + \overline{u}_k \frac{\partial E}{\partial x_k} = K_m \left(\frac{\partial \overline{u}_i}{\partial x_k} + \frac{\partial \overline{u}_k}{\partial x_i} \right) \frac{\partial \overline{u}_i}{\partial x_k} - K_h N^2 + \frac{\partial}{\partial x_i} K_m \frac{\partial E}{\partial x_i} + c_\varepsilon \frac{E^{3/2}}{\ell} \quad . \tag{6}$$

In (4) and (5) N is the local Brunt-Vaisala frequency

$$N = \left(\frac{g}{\Theta_0} \frac{\partial \overline{\Theta}}{\partial z} \right)^{1/2} \quad . \tag{7}$$

Equations (1), (3), (5) have been solved numerically and finite difference grid. The details on the numerical methods can be found in Schilling and Janssen (1992). The boundary and initial conditions will be given in section 4.

3 The Dispersion Model

Dispersion of a passive scalar within gravity waves due to mean flow and turbulence is simulated by means of a Lagrangian particle model (e.g. Legg and Raupach, 1982). Several thousands of weightless particles are set free in the source and their trajectories are followed by:

$$x_i(t + \Delta t) = x_i(t) + (\overline{u}_i(t) + u_i'(t))\Delta t \quad . \tag{8}$$

The turbulent velocity fluctuations u_i' are obtained from

$$u_i'(t) = R_L u_i'(t - \Delta t) + u_i^*(t) \quad , \tag{9}$$

where R_L is the Lagrangian autocorrelation given by

$$R_L = exp(-\Delta t/\tau_L) \quad . \tag{10}$$

u_i^* is a random velocity, which can be obtained from a stochastic process via the Monte-Carlo method:

$$\begin{aligned} u^* &= (1 - R_L^2)^{1/2}\sigma_u X + (1 - R_L)\tau_L \frac{\partial \sigma_u^2}{\partial x} \, , \\ w^* &= (1 - R_L^2)^{1/2}\sigma_w X + (1 - R_L)\tau_L \frac{\partial \sigma_w^2}{\partial z} \, . \end{aligned} \tag{11}$$

In (10) X is random number with normal distribution and σ_u and σ_w are the velocity variances. These are obtained from the turbulent kinetic energy by

$$\sigma_u = 1.0E^{1/2} \quad , \quad \sigma_w = 0.4E^{1/2} \quad . \tag{12}$$

The Lagrangian time scale τ_L needed in (9) and (10) is given by

$$\tau_L = K_m/E^{1/2} \quad . \tag{13}$$

By solving Equations (1) through (12) numerically it is possible, to obtain particle positions for every timestep Δt of the flow development. Concentrations can then be obtained by counting the number of particles contained in a box of the numerical grid.

4 Simulation of breaking gravity waves

The aim of our study was to investigate the mixing of passive scalars due to breaking gravity waves within the lower Stratosphere. As initial condition we choose a stably stratified shear flow with stratification $N = 8 \cdot 10^{-3} s^{-1}$ = constant and mean velocity $\overline{u}_0$ according to

$$\overline{u}_0(z) = -\Delta U \tanh[(z - z_c)/H] \quad , \tag{14}$$

with $H = 1000$m, $z_c = 25$km (critical level), $\Delta U = +20 ms^{-1}$. The computational domain was taken between 10km and 30km height in the vertical and 8km in the horizontal direction. The gravity waves were initiated at the lower domain level (z=10km). This simplifies the physical observation that gravity waves in the stratosphere are excitated by gravity waves starting in the troposphere. Following Fritts (1985), a single wave was prescribed at the lower boundary by a vertical velocity

$$w(x,t) = w_0[\sin k(x - ct)]g(t) \quad , \tag{15}$$

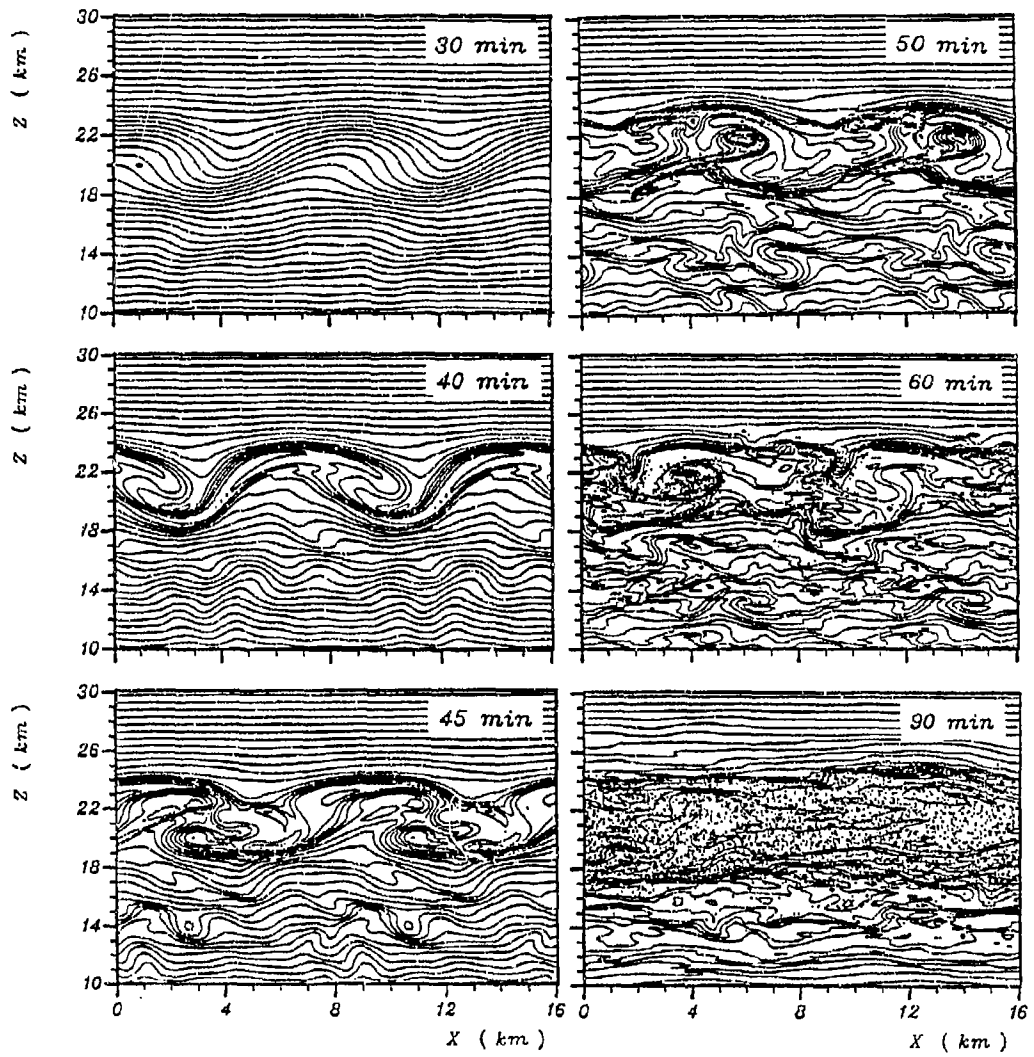


Figure 1: Structure of a gravity wave with $L = 8$ km and $c = 0$ ms^{-1} for different times after excitation at the lower boundary ($z = 10$ km). Shown are lines of constant potential temperature $\overline{\Theta}$ and cloud of particles set free at t=30 min.

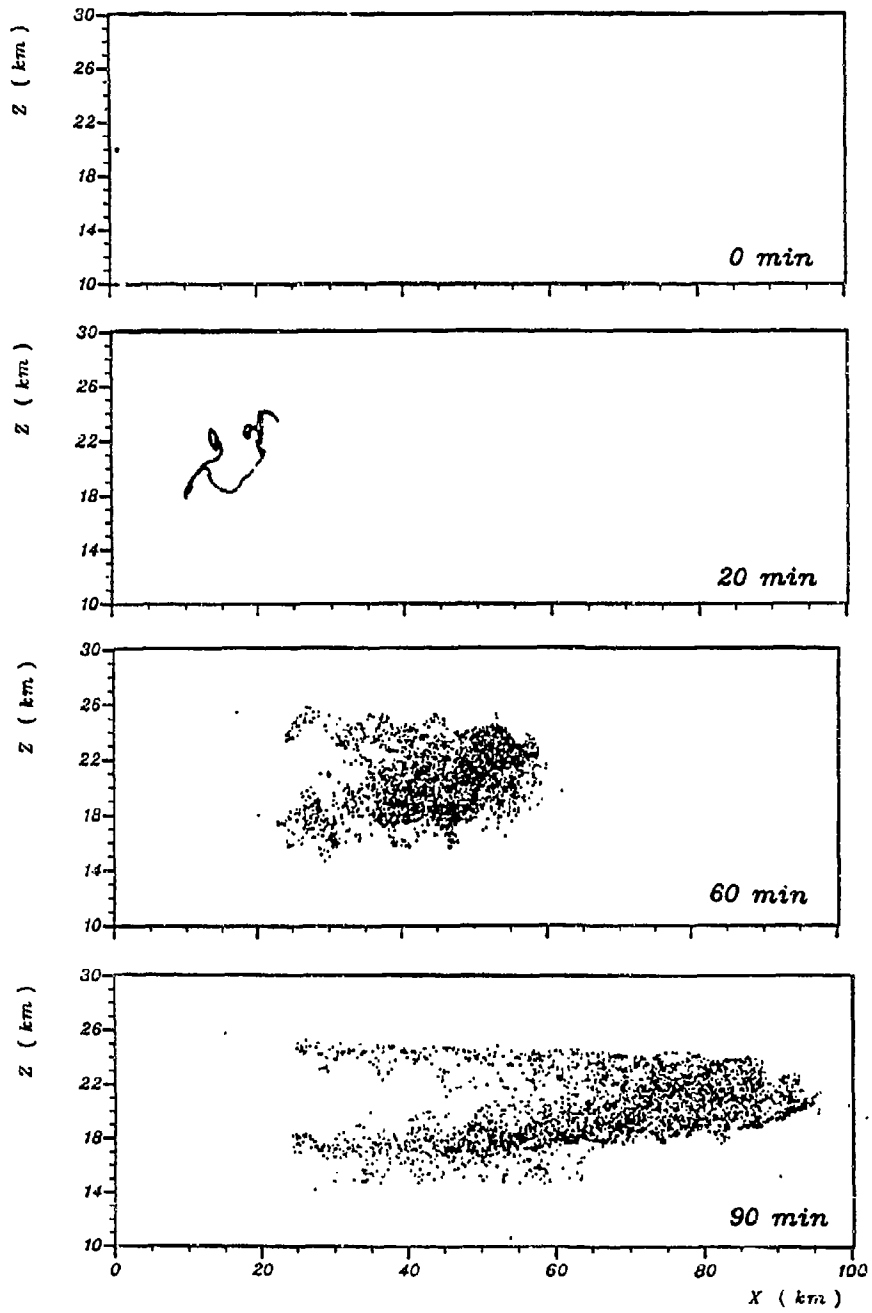


Figure 2: Dispersion of tracer particles within the breaking gravity wave shown in Fig. 1. Time after emission of a small particle cloud at x = 2 km and z = 20 km is given.

where $g(t)$ is an initialization function

$$\begin{aligned} g(t) &= \sin^2(2\pi t/T)\; t \le T \\ g(t) &= 1 \qquad\qquad\quad t > T \quad . \end{aligned}$$

The wave amplitude was increased in time according to (14) until $t = T$ (usually $T =$ 300s) and was then kept to constant at its final value $w_o = 1ms^{-1}$. Wave length $L = k/2\pi$ was varied between 2 km and 8 km and phase speed c between 0 ms^{-1} and 16.7 ms^{-1}.

An example of numerical simulations for the case L = 8km and $c = 0$ ms^{-1} is given in Fig. 1. About 30 minutes after the wave was excitated at the lower boundary (at $z = 10$km), a large amplitude wave can be seen at midlevel (about 22km) which breaks subsequently (t = 40 min - t = 1h). One should note, that wave breaking occurs already at z $\approx$ 20 km, which is below the critical level at z = 25km. Hence in this case, wave breaking is not due to wave-critical level interaction but due to self-induction of a local critical level by tilting of phase lines due to wind shear (Koop, 1981; Weinstock, 1982).

The wave breaking event has a dramatic effect on the dispersion of a cloud of passive scalar, which is injected into the gravity wave at time t=30 min at z=19km. Although the wave is starting to break at time 40 min, the particle cloud is stretched initially more or less in the horizontal direction due to shear effects. But after t=50 min, vertical transport starts to be very fast and the particle cloud is distributed vertically over about 6km within a few minutes. This behaviour is presented more clearly in Fig. 2, where the cloud development without gravity wave contours is shown (time is now counted from the start of injection of particle cloud).

5 Effective Diffusivity in Breaking Gravity Waves

The vertical mixing of passive scalars due to breaking gravity waves (Fig. 1,2) can not be regarded as turbulent diffusion in the usual sense, because mixing is due to the special event of wave breaking. But for large scale models of the stratosphere it is necessary, to parameterize diffusion by an effective subgrid diffusion coefficient. Hence it may be useful, to define a diffusion coefficient for the total event of a breaking gravity wave. This is of course not an easy task and it is not clear from the outset, which method will provide reasonable estimates.

For the case of mixing in Kelvin-Helmholtz waves, several methods of evaluating an effective diffusion coefficient have been tested (Schilling and Janssen, 1992). The estimate from a diffusion equation averaged over horizontal planes seemed to yield the most plausible results. If we denote mean concentration by $\overline{c}$, the one-dimensional diffusion equation can be written as

$$\frac{\partial \overline{c}}{\partial t} = \frac{\partial}{\partial z} K_c \frac{\partial \overline{c}}{\partial z} \quad . \tag{16}$$

Here $K_c(z)$ is an eddy diffusivity which can be evaluated from (14) by inserting concentrations $\overline{c}(z,t)$ as obtained from simulations with the Lagrangian model. For the case shown in Fig. 1,2, the temporal development for the vertical mean of $K_c(z)$ is shown in Fig. 3. Vertical mixing seems to be most effective in the first half an hour of the breaking gravity event. If we take the mean over the whole event of say 90 minute duration, we

get for the vertically and temporal averaged effective diffusivity $K_{eff} \simeq 0.7 m^2 s^{-1}$. This would be the average value for a breaking gravity wave over a vertical volume depth of 10km and time scale about 90 minutes. This value is comparable with estimated of K_{eff} given from other authors (e.g. Woodman and Rastogi, 1984).

More examples of breaking gravity waves for other combinations of wave length and phase speed and the dispersion of passive scalars within those wave events are given in Schilling (1993).

The final stage of breaking gravity wave will lead to layers of small-scale turbulence as is often observed in the lower Stratosphere. This is clearly a three-dimensional process which cannot be handled properly with a two-dimensional model as presented here. But with regard to dispersion of trace substances our results indicate (see e.g. Fig. 3), that vertical mixing is most effective within the early stages of wave breaking. As this part of the whole process can be still regarded as dominated by two-dimensional motions, the use of a two-dimensional numerical model seems to be justified for the purpose of this study.

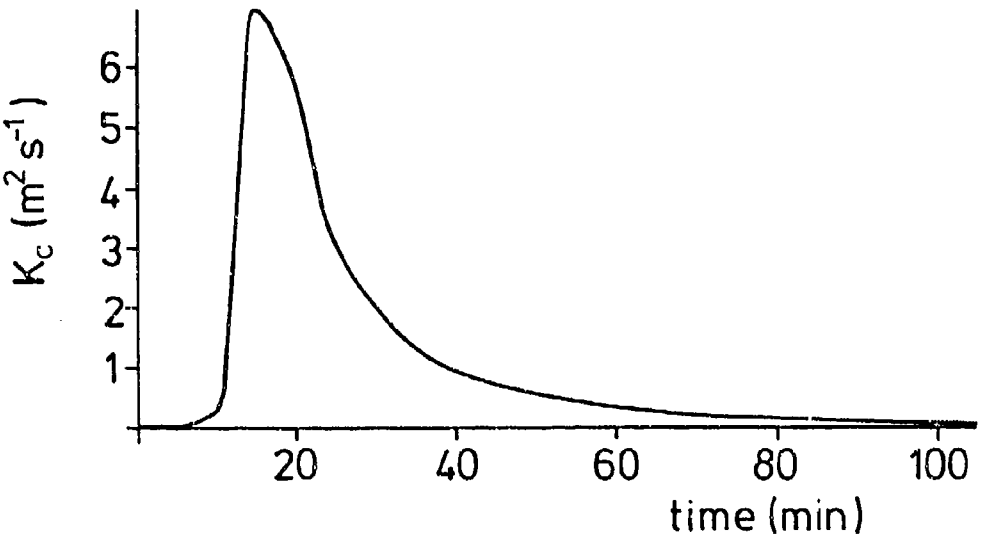


Figure 3: Temporal development of the spatial averaged effective vertical diffusivity K_{eff} for the case of breaking gravity wave in Fig. 1.2.

6 References:

Crutzen, P.J. und C. Brühl, 1990: The atmospheric chemical effects of aircraft operations. In: Air Traffic and the Environment (U. Schumann, ed.), Springer-Verlag, 96–106.

Fritts, D.C., 1990: A numerical study of gravity wave saturation: Nonlinear and multiple wave effects. J. Atmos. Sci., **42**, 2043–2058.

Fritts, D.C., und P.K. Rastogi, 1985: Convective and dynamical instabilities due to gravity motions in the lower and middle atmosphere: Theory and observations. Radio Sci., **20**, 1247–1277.

Koop, C.G., 1981: A preliminary investigation of the interaction of internal gravity waves with a steady shearing motion. J. Fluid Mech., **113**, 347–386.

Legg, B.J. und M.R. Raupach, 1982: Markov-chain simulation of particle dispersion in inhomogeneous flows: the main drift velocity induced by a gradient in Eulerian velocity variance. Boundary Layer Meteorol., **24**, 3–13.

Schilling, V.K., 1993: Effektive Diffusion von Luftbeimengungen in der Stratosphäre verursacht durch Kelvin-Helmholtz Instabilitäten und brechende Schwerewellen. Berichte Inst. Meteorol. Klimatol. Univ. Hannover, **44**, pp. 146.

Schilling, V.K., und U. Janssen, 1992: Particle dispersion due to dynamical instabilities in the lower stratosphere. Beitr. Phys. Atmosph., **65**, 259–273.

Weinstock, J., 1982: Nonlinear theory of gravity waves: Momentum deposition, generalized Rayleigh friction, and diffusion. J. Atmos. Sci., **39**, 1698–1710.

Woodman, R.F., und P.K. Rastogi, 1984: Evaluation of effective eddy diffusive coefficients using Radar observations of turbulence in the stratosphere. Radio Sci., **19**, 243–246.

A Numerical Study Of Wave-Breaking In Stratified Flow Over Obstacles

MF Paisley
School of Computing, Staffordshire University, Stafford, UK. ST18 0AD
and IP Castro
Department of Mechanical Engineering, University of Surrey, Guildford, UK. GU2 5XH

Abstract
This paper describes results of numerical computations of stratified flow of finite depth D over a variety of obstacles using the time-dependent Navier Stokes equations with stability-dependent eddy viscosity turbulence models. Most computations were performed with the Froude number F_h in the range $0.5 \le F_h \le 2$ and the parameter $K=D/(\pi h F_h)$ in the range $1 \le K \le 10$. Here $F_h = U/Nh$, where U is the free stream velocity, N is the buoyancy frequency and h is the height of the body. The domain and boundary conditions correspond to those of a towing tank experiment, and the initial conditions were 'impulsive start'. Critical Froude numbers for wave-breaking over two-dimensional obstacles are compared with theoretical predictions and experimental results. Preliminary results suggest that while a mixing length turbulence model may be adequate for two-dimensional flows, accurate representation of flows containing breaking waves in three-dimensions requires at least a one-equation model. The occurrence of 'merged flow', in which the breaking region joins with the secondary separation zone, and which has been seen in experiments, is found in the computations in three dimensions, but not those in two.

1. Introduction

It is well known that stationary lee waves can form in the flow of a density-stratified fluid over an obstacle. Under the right conditions, streamlines may steepen sufficiently that overturning occurs and the wave breaks. The phenomenon has been studied in a variety of ways, ranging from theoretical work to more recent experimental and numerical studies, usually in the simplifying context of uniform upstream flow and linear stratification. Miles & Huppert's (1969) analysis with Long's model for two-dimensional flow of infinite depth showed that the critical Froude number (the Froude number at which breaking first occurs) increases with body length, and values for different body shapes were predicted. Clark & Peltier's (1977) numerical simulations first revealed the profound effects of wave breaking on the surrounding flow in the atmosphere. Implications for gravity wave parametrisation schemes for atmospheric models and the prediction of transport rates of atmospheric constituents, for example, have motivated interest in detailed delineation of wave-breaking regimes.

Recent towing tank experiments (Rottman & Smith, 1989 and Castro & Snyder, 1993) have provided critical Froude numbers for a variety of three-dimensional hill shapes. To date, however, there has been little corresponding numerical work. The numerical work that has been done tends to falls into two categories. Firstly, inviscid atmospheric simulations (for example Clark & Peltier, 1977, Scinocca & Peltier, 1989 and Smolarkiewicz & Rotunno, 1989), and secondly, smaller scale computations (for example Hanazaki, 1989 and Lamb, 1994), used largely to provide comparison with theoretical models.

The numerical computations described here are part of a program of linked experimental and computational work designed to explore the phenomena associated with stratified flow over obstacles. Results for laminar flow over a two-

dimensional vertical barrier are summarised in Castro (1993) and Paisley et al (1994), for weak and strong stratification respectively. The latter results indicated significant unsteadiness, in keeping with that found experimentally for obstacles wide in the spanwise direction (Castro et al, 1990). Subsequent computations have included a boundary conforming transformation and simple turbulence models, allowing simulation of flows over smooth obstacles at realistic Reynolds numbers. The results described here are believed to be the first viscous predictions of critical Froude numbers for particular obstacle shapes.

Although most computations so far have been two-dimensional, we describe the results of some three-dimensional computations using the SWIFT code (Stratified Wind Flow over Topography, Apsley, 1993). A striking feature of recent towing tank experiments has been the occurrence of 'merged flow' (Castro & Snyder, 1993), or a 'hydraulic jump' (Hunt & Snyder, 1980). Under these conditions the breaking wave is observed to merge with the zone of separated flow in the wake to give a deep region of well-mixed flow extending downsteam. Although not seen in the two-dimensional computations, qualitative behaviour such as this has been seen in the three-dimensional computations.

2. Numerical Method

2.1 Discretisation and solution procedure

The nondimensional equations of motion for turbulent stratified flow in two or three dimensions are

$$\frac{Du_i}{Dt} = -\frac{\partial p}{\partial x_i} - \frac{1}{F_h^2}\theta\hat{z} + \frac{\partial}{\partial x_j}\left\{\frac{1}{Re}\frac{\partial u_i}{\partial x_j} + \tau_{ij}\right\}$$

$$\frac{D\theta}{Dt} = \frac{\partial}{\partial x_j}\left\{\frac{1}{Re.Sc}\frac{\partial \theta}{\partial x_j} + H_j\right\}$$

$$\frac{\partial u_i}{\partial x_i} = 0.$$

The equations have been non-dimensionalised by the freestream velocity U, the reference density ρ_0 and the height of the obstacle h. The equations are recast using a boundary-conforming transformation, and are discretised using a finite volume method with standard techniques for the diffusive terms and a flux-limited treatment for the advective terms. The solution procedure is implicit, employing Backward Euler time-stepping and an outer pressure-correction iteration. All the resulting discrete equations form diagonally dominant sets and are solved using a standard tridiagonal matrix method.

2.2 Turbulence parametrisation

In the eddy viscosity approach adopted, a mixing length model and a one-equation model have been used. The components of the Reynolds stress tensor and the turbulent contribution in the diffusive term in the transport equations are

$$\tau_{ij} = \nu_t\left\{\frac{\partial u_i}{\partial x_j} + \frac{\partial u_j}{\partial x_i}\right\}, \qquad H_j = (\nu_t/Pr)\frac{\partial \theta}{\partial x_j},$$

where Pr is the turbulent Prandlt number (=0.9). In the mixing length model the eddy viscosity is determined as $\nu_t = l^2 S$, where the strain rate S is given by

$$S^2 = \frac{1}{2}\left\{\frac{\partial u_i}{\partial x_j} + \frac{\partial u_j}{\partial x_i}\right\}^2.$$

and the mixing length l is given by $1/l = 1/l_o + 1/\kappa z$. Here κ is von Karman's constant, z is the distance from nearest solid surface and l_o is a constant.

In the one-equation model, a transport equation of the form

$$\frac{Dk}{Dt} = \frac{\partial}{\partial x_j}\left\{ \left(\nu + \frac{\nu_t}{\sigma}\right) \frac{\partial k}{\partial x_j} \right\} + P_k - \varepsilon + G_k$$

is solved for the turbulent kinetic energy, k, where P_k, G_k and ε are terms representing shear production, bouyancy production and dissipation rate. The eddy viscosity is now $\nu_t = C_\mu k^{1/2} l$ where C_μ is a standard constant.

In stratified flow the eddy viscosity is modified according to the local conditions of stability. Defining the value of the local gradient Richardson number as

$$R_i = \frac{1}{F_h^2} \frac{\partial\theta/\partial z}{S^2}$$

and setting a value for the critical value R_{ic} (say 0.25), the eddy viscosity is now:

Stable ($R_i > 0$): $\begin{cases} \nu_t(1-R_i/R_{ic})^2 & , \ 0 \le R_i \le R_{ic} \\ 0 & , \ R_{ic} \le R_i \end{cases}$

Unstable ($R_i < 0$): $\nu_t(1-R_i)^{1/2}$.

Details of the numerical method and procedure can be found in Paisley (1993).

3. Results and Discussion

3.1 Two-dimensional computations

Results have been obtained for two-dimensional flows over a vertical barrier and two cosine hills of the form $h(x)=0.5(1+\cos(\pi x/L))$. The axial aspect ratios of the hills are L/h=8.0 and L/h=1.8, giving slopes of 11° and 40° respectively. A typical computational domain is shown in figure 1, with associated boundary conditions. In all computations h/D=0.1 and initial conditions correspond to an 'impulsive start'. 76 cells were used in the vertical direction, with the smallest vertical cell dimension being 0.025 for the hills (at the surface) and 0.1 for the fence (at the tip). Although the upstream extent of the grids varied, there were around 200 points covering $-100h \le x \le 100h$, with the smallest horizontal grid dimension being 0.1. Most computations have been performed with $Re=10^4$ and the mixing length turbulence model, with selected cases being repeated with the k-l model.

Fig 2 shows typical streamlines for the long cosine hill, fence and short cosine hill at the approximate Froude number at which streamline overturning first occurs. In each case the discrete structure imposed on the flow by the presence of the upper lid can be clearly seen, with 2, 3 and 5 wave modes present respectively. Upstream influence is marked, as expected in two-dimensional finite depth flows, with blocking and upstream separation known to occur.

Data relating to the breaking waves in two dimensions is summarised in figs 3 and 4. Fig 3 shows the variation of the critical Froude number with the axial length of the three obstacles. The value of F_{crit} for the short cosine hill agrees well with Baines' (1977) experimental results for a similarly short Agnesi hill. The cosine hills follow the trend of Miles & Huppert's (1969) result for infinite depth in that F_{crit} increases with obstacle length. It is likely, however that F_{crit} for the long cosine hill is not independent of finite depth effects, since K is only just greater than 2, while K is between 4 and 5 for the short hill. The value of F_{crit} for the

fence is believed to be independent of such effects, for there was no change in F_{crit} when the computation was repeated with h/D=0.05. The value of F_{crit} for the fence is significantly greater than the Miles & Huppert prediction for a zero width body, and is closer to the value obtained experimentally for narrow triangular obstacles (Castro, 1987). It would appear that the separated wake gives the bluff body an apparent length, with the value of F_{crit} correspondingly higher.

Fig 4 shows the non-dimensional time to the first occurrence of streamline overturning for each obstacle. In each case there is a monotonic decrease as the Froude number decreases and wave speeds increase. The waves over the long hill break before those over the fence, presumably because the longer obstacle generates waves of greater amplitude. When waves over the short hill break however, they break sooner than those over either of the other two obstacles, probably a consequence of the matching of the shortest lee waves ($\lambda/h \approx 3.8$ when $F_h=0.6$) and the length of the topography ($2L/h=3.6$).

The computations with the short cosine hill were performed to provide a comparison with Castro & Snyder's (1993) recent experiments with three-dimensional hills of this cross-section. Fig 5 shows streamlines at Ut/h=20 (approximately one quarter of the total tow-time in the experiments) for the computations of the flow over the short cosine hill at $F_h=0.8$, 0.7 and 0.6. The breaking region, when it occurs, is quite distinct from the secondary separation zone, with no sign of merging at all. The influence of the turbulence model on these results was assessed by repeating the computation at $F_h=0.6$ with the k-l model, with little qualitative change.

As found in experiments with bodies which are wide in the spanwise direction, some of the two-dimensional flows computed here exhibit significant unsteadiness. Fig 6 shows drag histories for the three cases just described, in which pronounced oscillatory behaviour is observed. A fuller account of the data relating to unsteady behaviour is given in Paisley & Castro (1994).

3.2 Three-dimensional computations

The geometry for the three-dimensional cases corresponds to the COS3 hill used in the experimental study of Castro & Snyder (1993), the cross-section of which is the short cosine hill descibed above, and the end-section of which is generated by rotating the cross-section through 180°. As the hill is symmetric about its centre plane, only the flow in one half of the domain has been computed. The geometry corresponds to a rectangular cube of dimension $-25 \le x/h \le 100$, $0 \le y/h \le 12$ and $0 \le z/h \le 10$. Boundary conditions were as in the two-dimensional case with an additional symmetry boundary condition on the centre plane and wall boundary conditions at the far side. Two grids have been used, of sizes 64×24×32 and 96×32×48. The grid spacings near the hill are approximately four times and two times greater respectively than those in the corresponding two-dimensional grid.

The three-dimensional flows are qualitatively close to those found experimentally, although they are more sensitive to the numerical procedures than the corresponding two-dimensional flows. Because of the long computing times, so far only coarse grid computations with the mixing length turbulence model have been run on for long times. As expected, the drag histories (fig 7) for $F_h=0.8$, 0.7 and 0.6 indicate less variation than those of the two-dimensional cases (fig 6).

Velocity vectors in the centre plane at Ut/h=20 for these three cases are shown in fig 8. Although the flows at $F_h=0.8$ and 0.7 are qualitatively very similar to the

two-dimensional results of Fig 5, the flow at F_h=0.6 is quite different. Streamline overturning occurs at low level in the three-dimensional flow, with the breaking region and the separation zone merging, in a manner very similar to the observed experimental behaviour at this Froude number.

An attempt was made to verify these results with the mixing length model on the finer grid, but without success. Although the flow without breaking waves, F_h=0.8, was similar to the flow obtained on the coarse grid, streamline overturning did not occur in the other cases, either aloft at F_h=0.7 or at low level at F_h=0.6. In each case, surface separation is very much more pronounced. The mixing length model would appear to overpredict surface separation to such an extent that overturning aloft never occurs on the finer grid. The fact that the flows obtained on the coarse grid were qualitatively close to the those obtained experimentally appears to be fortuitous, and a result of the effect of poor grid resolution in predicting separation. Although the mixing-length model was found to be adequate for predicting wave-breaking in two dimensions it would appear to be just too crude (perhaps unsurprisingly) for more complex three-dimensional flows.

A third set of results was obtained with the k-l model on the coarse grid. These were qualitatively similar to the results with the mixing length model on the coarse grid (fig 8), with clear merging flow again apparent at F_h=0.6. These computations were repeated on the finer grid, fig 9, with better success than with the mixing length model. Streamline overturning and wave breaking is predicted, with evidence of merged flow at F_h=0.6. Although the qualitative features agree well with the experiments, the differences between the results on the two grids indicate that computations on finer grids are necessary to eliminate grid effects.

The fact that merging flow was not seen in two dimensions clearly points to the mechanism responsible being linked to flow in the third dimension. Indeed, examination of the flow in the lee of the hill shows that the flow remains largely two-dimensional in the non-merging cases. In the merging case, however, there is a large low-level cross-flow vortex (fig 10), the effect of which is seen in the strongly reversed flow in the centre-plane downstream of the obstacle (figs 8(c), 9(c)). This evidently contributes to the early separation and subsequent overturning of the low-level jet of fluid passing down the lee slope.

4. Conclusions

Computations of finite depth stratified flows over two- and three-dimensional obstacles have been performed with eddy viscosity turbulence models. The critical Froude numbers obtained for the two-dimensional obstacles are in good agreement with experimental data, and for the smooth obstacles follow the general trend of Huppert & Miles' (1969) result. For the fence, the computed F_{crit} is higher than the theoretical result, which is consistent with the separated wake giving the body an apparent length. In cases where breaking occurred, the breaking region was always distinct from the separation zone, and we conclude that merging flow does not occur in two dimensions. The precise nature of the turbulence model for these two-dimensional flows containing breaking waves does not seem to be important. Selected three-dimensional cases have been performed and the results compared to those of recent experiments. They indicate that a mixing length model is unable to adequately predict three-dimensional flows with breaking waves of the kind considered here, and that a one-equation model is the minimum required. The qualitative features of merging flow have been obtained for a particular case, in which a strong cross-flow vortex in the wake seems to be characteristic.

5. Acknowledgements

We would like to thank Mr D Apsley for his work in developing the codes used in the work described here. We also acknowledge the help of the support staff at the Rutherford Appleton Laboratories in the use of the CRAY YMP-8 for some of the runs. The first author acknowledges financial support from NERC, UK.

6. References

Apsley DD 1993 SWIFT user guide version 1.0. *Surrey Univ Rpt ME-FD/93.09.*

Baines PG 1977 Upstream influence and Long's model in stratified flows. *J.Fluid Mech.* **82**, 147-159.

Castro IP 1987 A note on lee wave structure in stratified flow over three-dimensional obstacles. *Tellus* **39A**, 72-81.

Castro IP 1993 Effects of stratification on separated wakes. Part I: Weak static stability. In *Waves & Turbulence in Stably Stratified Flows*, eds SD Mobbs & JC King, OUP.

Castro IP & Snyder WH 1993 Experiments on wavebreaking in stratified flow over obstacles. *J.Fluid Mech.* **255**, 195-211.

Castro IP, Snyder WH & Baines PG 1990 Obstacle drag in stratified flow. *Proc.R.Soc.Lond.* **A429**, 119-140.

Clark TL & Peltier WR 1977 On the evolution and stability of finite amplitude mountain waves. *J.Atmos.Sci.* **34**, 1715-1730.

Hanazaki H 1989 Upstream advancing columner disturbances in two-dimensional stratified flow of finite depth. *Phys.Fl.A1* **12**, 1976-1987.

Hunt JCR & Snyder WH 1980 Experiments on stably and neutrally stratified flow over a model three-dimensional hill. *J.Fluid Mech.* **96**, 671-704.

Lamb KG 1994 Numerical simulations of stratified inviscid flow over a smooth obstacle. To appear in *J.Fluid Mech.*.

Miles JW & Huppert HE 1969 Lee waves in a stratified flow. Part IV: Perturbation approximations. *J.Fluid Mech.* **35**, 497-525.

Paisley MF 1993 Stratified airflow over mountains. *Surrey Uni Rpt ME-FD/93.13.*

Paisley MF & Castro IP 1994 Unsteadiness in stratified over two-dimensional obstacle: a numerical study. In preparation.

Paisley MF, Castro IP & Rockliff NJ 1993 Steady and unsteady computations of strongly stratified flow over a vertical barrier. To appear in *Stably Stratified Flows IV*, eds IP Castro & NJ Rockliff, OUP.

Rottman JW & Smith RB 1989 A laboratory model of severe downslope winds. *Tellus* **41A**, 401-415.

Scinocca R & Peltier WR 1989 Pulsating downslope windstorms. *J. Atm. Sci.* **46**, 1154-1164.

Smolarkiewicz PK & Rotunno R 1990 Low Froude number flow past a three-dimensional obstacle. Part II: Upwind flow reversal zone. *J. Atm. Sci.* **47**, 1498-1511.

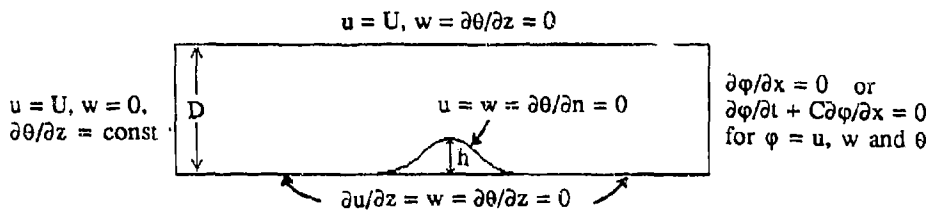


Figure 1. Typical domain and boundary conditions for computation of flow over smooth topography.

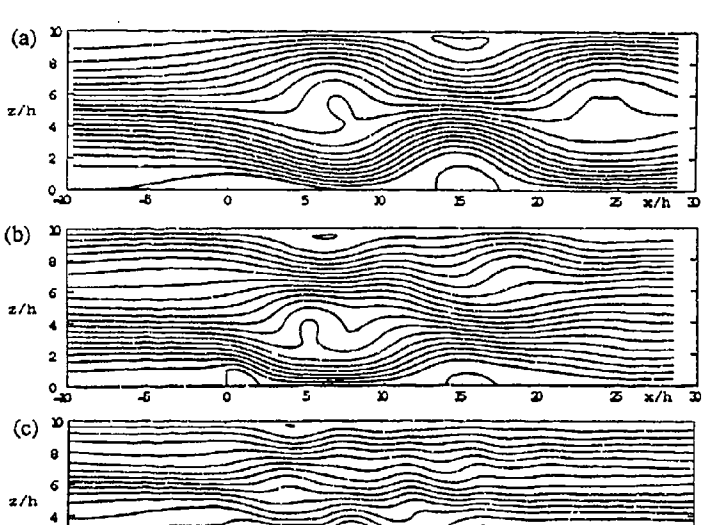


Figure 2. Flow over two-dimensional obstacles with Froude number just below its respective critical value. (a) Long cosine hill, F_h=1.4 (K=2.27), (b) Vertical barrier, F_h=1.0 (K=3.18), (c) Short cosine hill, F_h=0.6 (K=5.31).

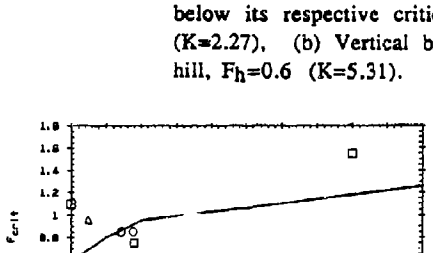


Figure 3. Variation of critical Froude number with axial aspect ratio for two-dimensional bodies.
□ present computations; ——Huppert & Miles (1969); △ experiments (triangular hills, Castro, 1987); ○ experiments (Agnesi hills, Baines, 1977).

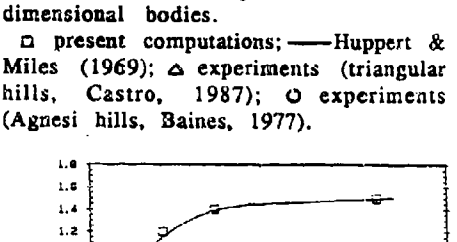


Figure 4. Time to wave overturning.
□ long cosine hill ; ○ fence; △ short cosine hill.

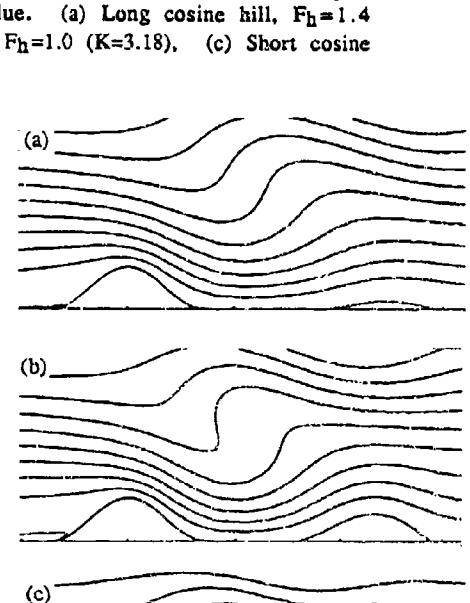


Figure 5. Streamlines for two-dimensional flow over short cosine hill, Ut/h=20. (a) F_h=0.8 (K=3.98), (b) F_h=0.7 (K=4.54), (c) F_h=0.6 (K=5.31).

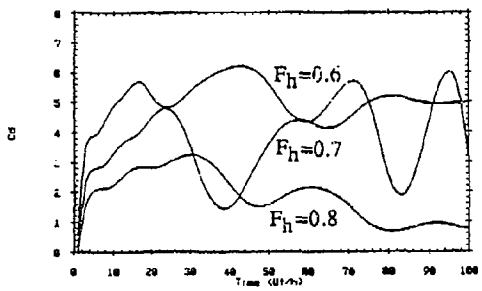


Figure 6. Time variation of the drag for flow over the two-dimensional short cosine hill.

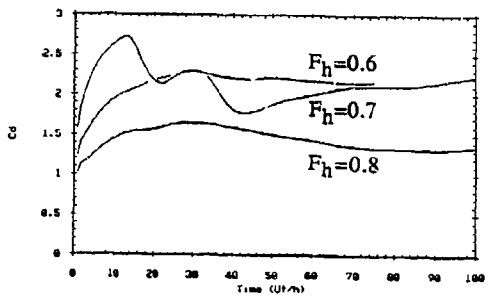


Figure 7. Time variation of the drag for flow over the three-dimensional COS3 hill.

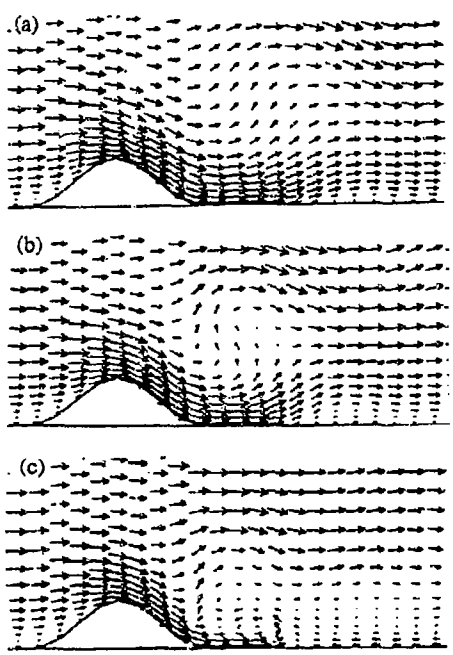


Figure 8. Velocity vectors in the centre plane for three-dimensional flow over COS3 hill. Coarse grid, 0-equation eddy viscosity, Ut/h=20. (a) F_h=0.8 (K=3.98), (b) F_h=0.7 (K=4.54), (c) F_h=0.6 (K=5.31).

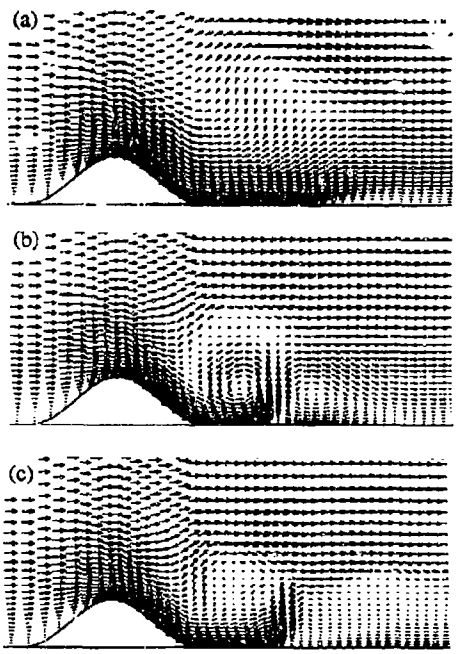


Figure 9. Velocity vectors in the centre plane for three-dimensional flow over COS3 hill. Fine grid, 1-equation eddy viscosity, Ut/h=20. (a) F_h=0.8 (K=3.98), (b) F_h=0.7 (K=4.54), (c) F_h=0.6 (K=5.31).

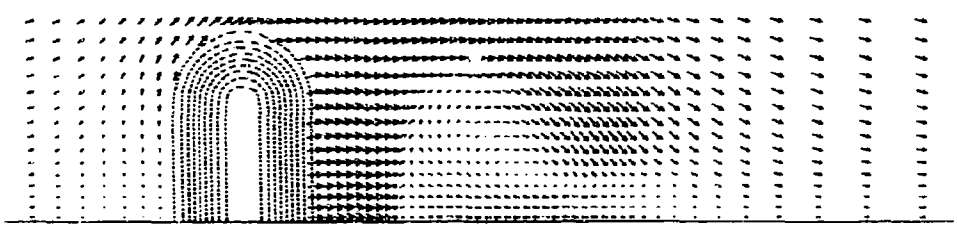


Figure 10. Cross-flow velocity vectors, z/h=0.1. Fine grid, 1-equation eddy viscosity, Ut/h=20, F_h=0.6 (K=5.31).

The dynamics of internal waves produced by parametric instability: an experimental study

D. Bénielli and J. Sommeria

Laboratoire de Physique
Ecole Normale Supérieure de Lyon (URA 1325 CNRS)
46, Allée d'Italie 69364 Lyon Cedex 07 France

May 10, 1994

Abstract

Standing internal waves are studied in a tank where a stable density stratification has been initially introduced by a gradient of salt concentration. A primary wave grows by parametric instability: a periodic modulation of the apparent gravity is produced by a vertical oscillation of the tank. Two aspects of the dynamics are studied
-The mechanism of breaking that leads to turbulence
-A kind of developed turbulence forced by wave breaking in the permanent regime.
A succession of instabilities leading to wave breaking has been clearly identified: the primary wave first excites a secondary wave at half its frequency by a mechanism of parametric instability. The density isolines associated with this secondary wave then locally overhang, and breaking occurs through a convective instability. In the turbulent regime, a specific inertial range with k^{-3} density spectra is measured.

1 Introduction

We study the complex dynamics of internal waves, by laboratory experiments performed in relation with numerical simulations[1][2]. The aim is to generate something equivalent to homogeneous turbulence, but in a strongly stratified situation: a wave field whose statistical properties would be a genuine feature of the dynamics, independently from the details of the forcing mechanism. In theoretical or numerical studies, some white noise forcing is often introduced for this purpose. However this may violate the "natural" dynamics in some way, and it is desirable to seek a more realistic mechanism of generation. The collapse of a strong turbulence in a stratified medium is a possibility, but the resulting dynamics seems to be somewhat different than in the regime of internal waves. Excitation by a wave maker selects

a particular structure associated with the driving mechanism. The parametric instability that we use here seems to produce instead a more random field. Also this mechanism of instability is interesting in itself, and it naturally occurs as a process of transfer from large scales to smaller ones, for instance in the Oceans. Parametrically generated internal waves in a continuously stratified fluid has been already realized by Mc Ewan [3] with similar motivations, but in a more qualitative way, and in a somewhat different system. Our first step is to study the parametrically instability itself in next section. Then the secondary instabilities leading to wave breaking will be described in section 3. Finally, an inertial range of turbulence is characterized, and related to atmospheric studies.

2 Apparatus and Experimental Procedure

The continuous stratification is produced by salt concentration in a water tank with rectangular cross section. This tank is oscillating with a motion of vertical translation, so that the apparent gravity and the Brunt Vaisala frequency are modulated around their value at rest. Dye is periodically injected at the tank bottom with the filling brine in order to mark fluid parcels with successive densities. The resulting fluorescent dye strips are visualized by a vertical laser sheet as they are deformed from their initial horizontal position. A conductivity probe can be positioned at different depths, to get time series of the local density.

3 The primary parametric instability

The free modes of standing internal waves have a simple sine structure, and are labelled by the numbers of half wave-lengths in each direction (nx, ny, nz). We consider here only modes with a purely vertical structure (ny=0) as visualized in Fig.1. Each mode can be considered as an oscillator with a natural frequency $\omega = N cos\theta$, where N is the Brunt Vaisala frequency and θ the angle of the wave-vector with the horizontal. An oscillator is parametrically excited when its natural frequency is in a "tongue" around half the exciting frequency. Therefore all the modes with the same θ, the same ratio of vertical to horizontal wave numbers, are in principle excited together. This is the case of the different modes of Fig.1, and the complex imbrication of the instability tongues is represented in Fig.2. This contrasts with the case of surface waves or interfacial waves[4][5], for which the different modes are well separated in frequency. The instability theory has been applied also to the case of a continuous stratification[6], but the actual dynamics involves wave breaking and is much more complicated, as discussed next.

4 Secondary instabilities leading to breaking

Indeed these primary modes are always unstable, and a well organized internal wave packet develops: this secondary wave, with frequency half the main mode, grows also by a para-

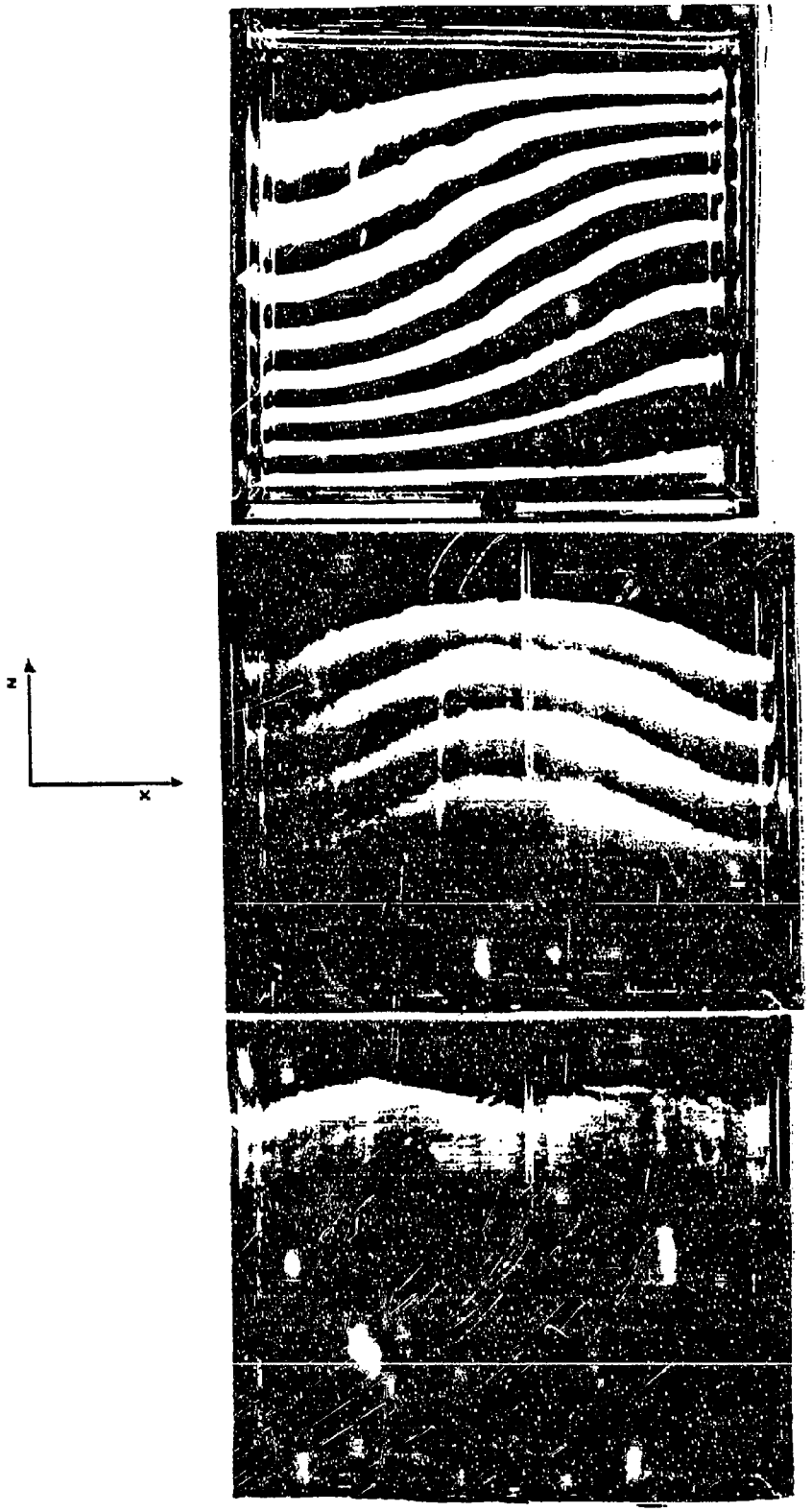
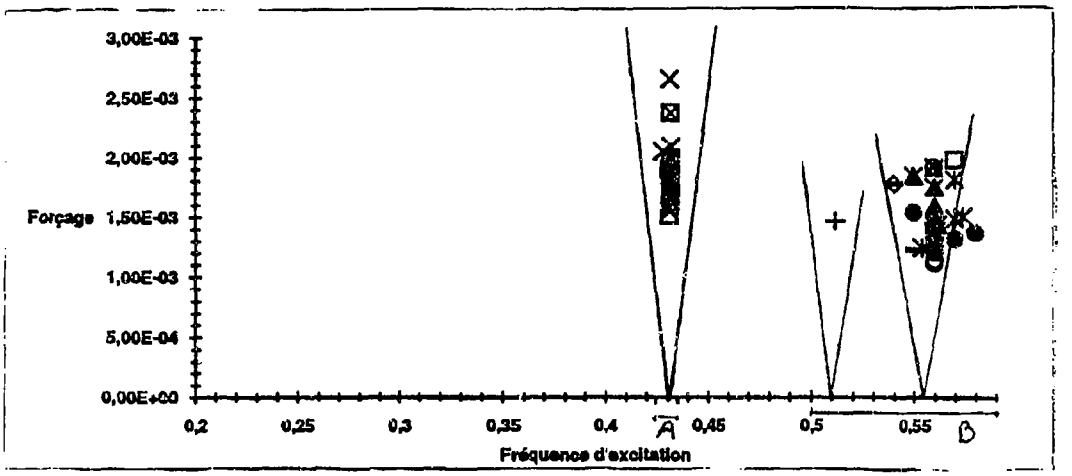
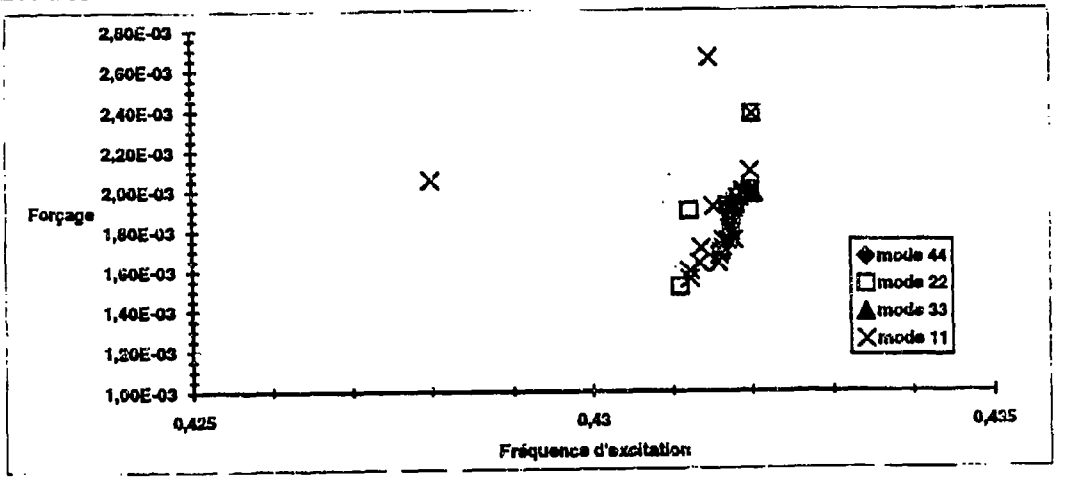


Figure 1: Examples of pure modes (two-dimensional in the vertical plane) in the phase of linear growth, obtained with very close experimental conditions (visualization of the deformed isodensity lines by dye strips) a) Mode (1, 0, 1), b) Mode (2, 0, 1), c) Mode (4, 0, 2)



Zoom A :



Zoom B :

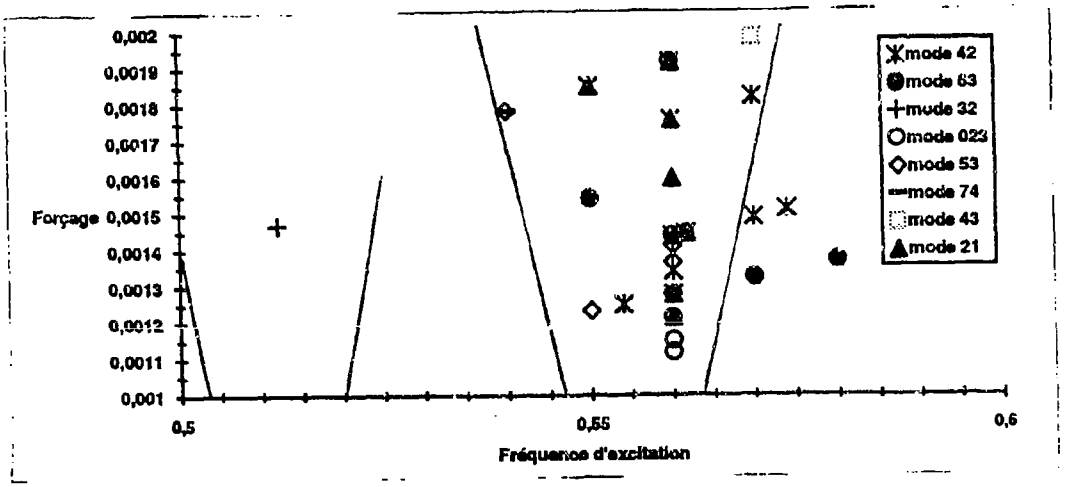


Figure 2: Diagram of unstable modes represented versus excitation frequency (in Hertz), and forcing amplitude (in relative variation of the apparent gravity). We observe that the tongues corresponding to the different modes with close natural frequencies are strongly imbricated.

metric instability. The excitation is now due to an oscillating tilt of the wave-packet, and a corresponding modulation of natural frequency, entrained by the primary wave oscillation (Fig.3). This wave packet quickly grows until local overturning of the density occurs. The locally unstable stratification then rapidly leads to convection and turbulence. The convective rolls are mainly aligned with axis transverse to the vertical plane of the main wave (Fig.3). This process of wave breaking contributes to the saturation of the primary wave instability. Near the instability threshold, an intermittent behavior results from successive periods of instability growth and decay. This dynamics is governed by weak wave interactions, and is strongly dependent on particular resonant interactions, which are very sensitive to the experimental conditions.

5 A turbulent inertial range associated with wave breaking

We observe that turbulent time spectra measured by the conductivity probe contain a well defined range with k^{-3} density spectra (Fig.4). We interpret the measured time series in terms of spatial fluctuations along the vertical direction by using a Taylor hypothesis, although the probe has no motion. We argue indeed that the fine scale structures, which are mostly horizontally stratified, are transported by the vertical motion of the main waves. By contrast with the spectral behavior at moderate frequency, the slope and level of this k^{-3} range depends only very little on the experimental conditions: this seems to be a quite general feature of the turbulence resulting from wave breaking. Beyond the viscous dissipation wave number, an advective sub-range with k^{-1} spectrum is expected, since the Prandtl number is very high. This may be observed in our experiments, but it is strongly perturbed by effects of mechanical vibrations.
A simple interpretation of such $k-3$ spectra is that the non-linear effects have the same strength at all scales:i.e. the Froude number is of order unity at each scale. Similar energy spectra are observed in the "buoyancy subrange" of the atmosphere [7], and has been explained by turbulent models [8]. However the interpretation of these atmospheric measurements is still controversial, and our experimental results, together with associated numerical computations [2] could new insight in this problem.

References

[1] Bouruet-Aubertot P., Sommeria J. & Staquet C.,1994 B.Submitted to J. Fluid Mech.

[2] Bouruet-Aubertot P., Sommeria J. & Staquet C, 1994, joint communication.

[3] A.D. Mc Ewan & R. M. Robinson 1975 , J. Fluid Mech. 67 (4), p667-687.

[4] V.A. Kalinichenko (1986), Izvestiya Atmospheric and Oceanic Physics 22 (2), p155-158.

[5] Ya. Sekerzh-Zen'kovich 1983, Dokl. Acad.Nauk SSSR 272 (5), p1083-1086.

[6] S. Ya. Sekerzh-Zen'kovich 1983, Sov. Phys. Dokl. 28 (6), p445-446.

[7] Sidi C. & Dalaudier F. (1989) Pageoph 130, 2/3.

[8] Lumley J.L. (1964) J. Atm. Sci. 21, 99-102.

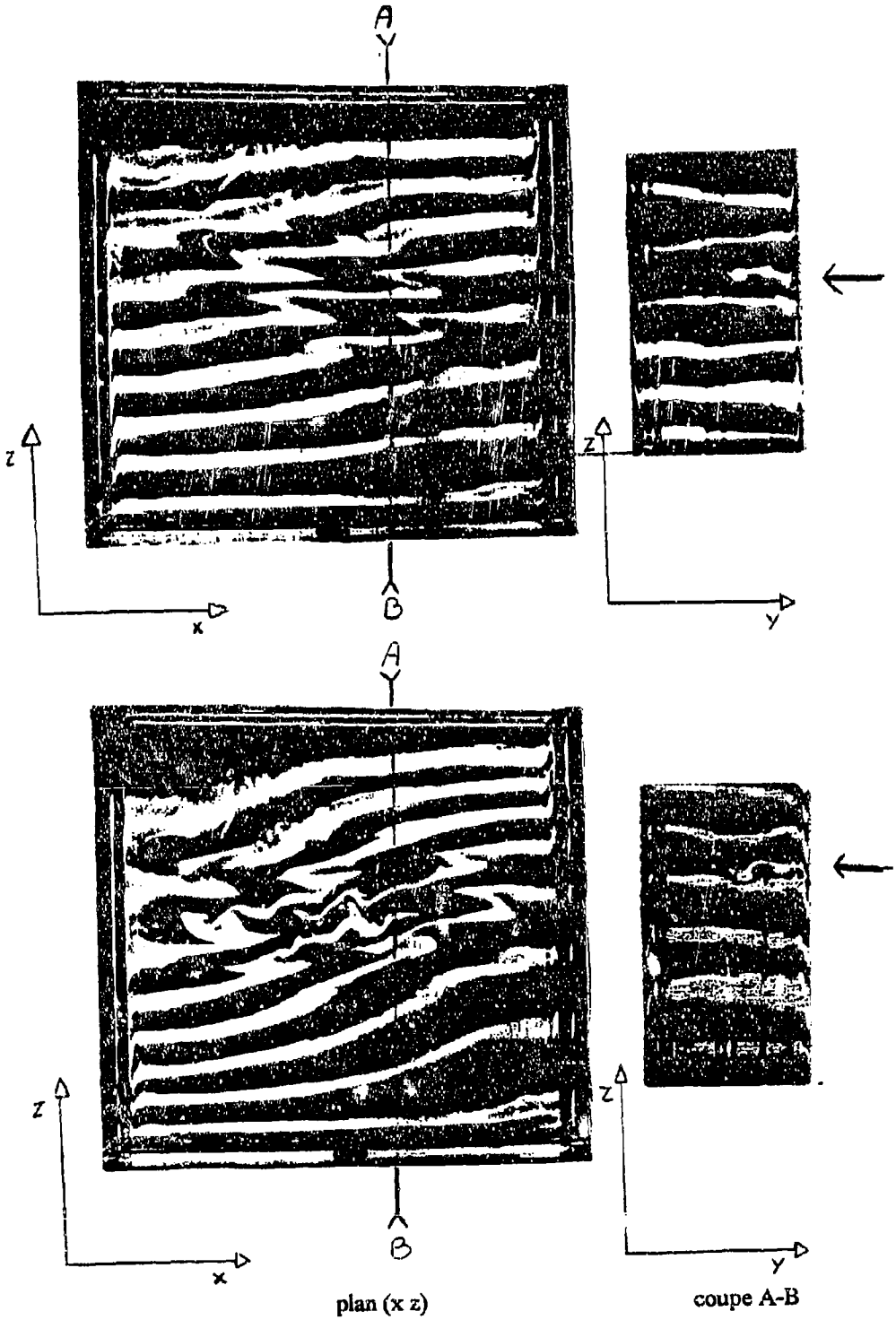


Figure 3: Visualization of internal wave breaking. Top photos: A secondary wave packet is growing by parametric instability. In the lateral view (right), the same dye strip is doubled by the overturning process, and a convective instability begins to grow in the region of overturning (arrow). Bottom: one second later, the wave has broken into small scale instability, and the developement of convective mushrooms is visible on the lateral view (right)

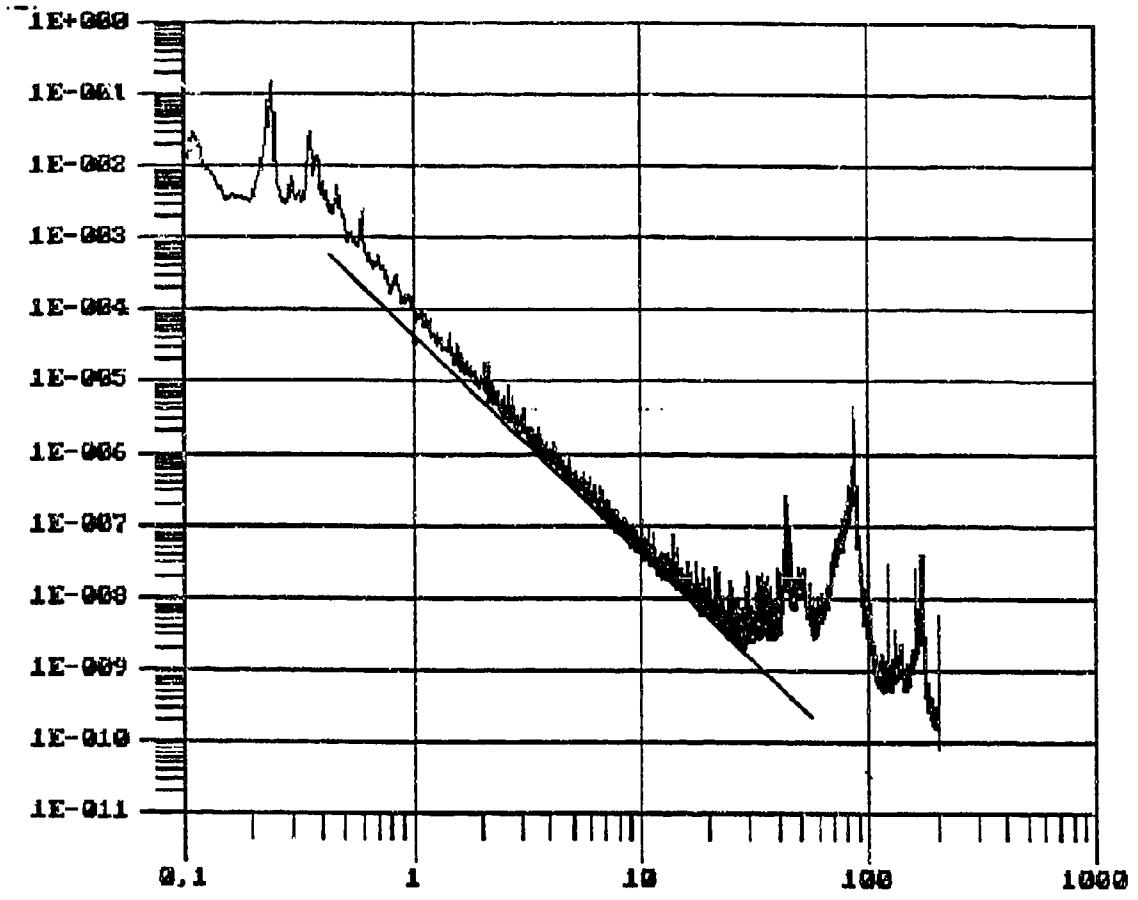


Figure 4: Concentration spectra measured from the conductivity probe (in Logarithmic coordinates). The frequency is expressed in Hz, and the spectrum is normalized by the density variance. The peak at 0.3 Hz corresponds to the primary excited wave (half the excitation frequency), while the main peak is excited by resonant interaction, as well as a continuum of low frequencies. The $k-3$ slope in the "inertial range"is indicated. High frequency peaks are due to spurious vibrations.

STRATIFIED TURBULENCE PRODUCED BY INTERNAL WAVE BREAKING

P. Bouruet-Aubertot, J. Sommeria and C. Staquet

Ecole Normale Supérieure de Lyon (URA 1325 CNRS)

46 allée d'Italie 69364 Lyon Cedex 07 France

e-mail: pbaubert@physique.ens-lyon.fr

1 Introduction

Wavebreaking is characterized by the onset of turbulence which leads to the decrease of the wave energy, either dissipated or irreversibly transformed.Indeed in the case of internal gravity waves, breaking also results in irreversible vertical mixing of matter. This is therefore an important mechanism of vertical heat transfers and chemical transport in stably stratified media like the oceans or the atmosphere (e.g. Muller et al. 1986).

The occurence of breaking is not limited to internal waves with very steep initial isodensity lines. For internal gravity waves of moderate amplitude, the breaking event itself is preceded by a slower phase of wave steepening. For instance, a propagating wave in a medium with non-uniform properties progressively steepens and breaks near critical layers, where the propagating velocity with respect to the medium vanishes (e.g. Winters & D'Asaro 1989, Winters & Riley 1992). For standing waves considered here, this process cannot occur, but a mechanism of resonant interaction between different modes can transfer energy to smaller wavelengths. It results in a progressive increase of the local slope of the isodensity lines, eventually leading to breaking. Such standing waves correspond to the case of a confined domain, e.g. laboratory tanks. A periodic primary wave is then forced by a paddle (McEwan 1971, Orlanski 1972) or by parametric instability (Mc Ewan & Robinson 1975, Thorpe 1994c, Benielli & Sommeria 1994). Breaking is indeed commonly observed in such experiments. In some other experimental conditions, with lower forcing amplitude, the secondary wave is stabilized by viscous effects, so that the non-linear transfers between a limited set of modes can be studied in isolation, and found in good agreement with weakly non-linear expansions (McEwan et al. 1972). However, the succession of events leading to the wave breaking itself are difficult to analyse precisely in laboratory experiments. Therefore direct numerical simulations can be very useful to analyse these mechanisms and compare them with theoretical models. Previous studies (Orlanski & Ross, 1973) showed a good agreement during the initial stage (i.e.: before wavebreaking) between experiments,

numerical results and analytic solution (up to second order in amplitude). However the mechanisms of wave breaking itself were not analysed because of a low resolution. This is the aim of the present paper: we start with a simple standing wave and study the succession of instabilities that lead to wave breaking and the properties of the turbulence next induced.

We briefly present the numerical model in next section. In section 3, we explain the presence of perturbations by the structure of the standing wave. The loss of coherence is described in the next section. The transition to turbulence is then analysed in the last section.

2 Numerical Model

We solve the two-dimensional Navier-Stokes equations in the Boussinesq approximation, using a pseudo-spectral method (Orszag 1971). The domain is a square in a vertical plane; in order to model the boundary conditions of laboratory experiments, normal velocities at the walls are set to zero. This is compatible with a pseudo-spectral method if symmetry boundary conditions are introduced. These symmetry properties allow use of Fourier transforms, involving only sines or cosines, to compute spatial derivatives (e.g. Brachet et al.1988). Integration in time is performed using an explicit third order Adams-Bashforth scheme and the diffusion terms are calculated explicitly. Resolution is 129^2, with a few test runs at 257^2 . We use Cartesian coordinates (x, y), with vertical coordinate y directed upwards. A vertically displaced fluid particle oscillates with the buoyancy (Brunt-Väisälä) frequency N, defined by $N^2 = -\frac{g}{\rho_0}\frac{d\bar{\rho}}{dy}$, where g is the acceleration of gravity, and $\bar{\rho}$ the basic density profile. We assume that N is constant, so that $\bar{\rho}$ is linearly decreasing with the vertical coordinate y. In the Boussinesq approximation, this basic density profile, as well as the superimposed density fluctuations $\rho*$, stay close to the mean density ρ_0. The condition of incompressibility is then assumed, and taken into account by introducing a stream function ψ, related to the two velocity components u_x and u_y by $u_x = \partial_y\psi, u_y = -\partial_x\psi$. We solve the Boussinesq equations in terms of the vorticity $-\Delta\psi$ and the reduced density fluctuations $\rho' = (g/\rho_0)\rho*$

$$(1) \quad \partial_t\Delta\psi + J(\Delta\psi,\psi) = \partial_x\rho' + \nu(-1)^{n+1}\Delta^{n+1}\psi$$

$$(2) \quad \partial_t\rho' + J(\rho',\psi) = -N^2\partial_x\psi + \frac{\nu}{Pr}(-1)^{n+1}\Delta^n\rho'$$

where the non linear advective terms are written by means of the Jacobian J, and the Prandtl number Pr is taken equal to unity unless otherwise specified. The numerical computations are performed in a square of side π, with a Brunt-Väisälä frequency $N = 1$, but the times will be often represented in units of the Brunt-Väisälä period $T_{BV} = 2\pi/N$. Any corresponding physical situation can be represented by these calculations with appropriate choices of length and time units. Dissipation is modelled either as an ordinary diffusion, using a Laplacian term (n=1) or by a bilaplacian (n=2), which better restricts the dissipation to the highest wave vectors. Before each run, the viscosity is adjusted to get its minimum possible value for a given spatial resolution.

3 A nearly periodic oscillation

The aim of this study is to observe the evolution of a simple standing wave, until breaking occurs. It is therefore natural to choose an initial condition with an unperturbed density field, and the velocity field of a linear standing wave (normal mode), with stream function, $\psi(x,y) = a\,sin(k_x\,x)sin(k_y\,y)$ and density, $\rho'(x,y) = 0$ represented in Fig. 1 for different choices of k_x, k_y. This velocity field will displace the iso-density lines, and the buoyancy restoring force will then reverse the velocity field, leading to periodic oscillations. The linear solution for this standing wave is

$$\begin{aligned} \psi(x,y,t) &= a\,sin(k_x\,x)sin(k_y\,y)cos(\omega t) \\ (3)\quad \rho'(x,y,t) &= -a\,\frac{k_x N^2}{\omega}cos(k_x\,x)sin(k_y\,y)sin(\omega t) \end{aligned}$$

The frequency ω is given by the linear dispersion relationship $\omega = N\,|cos\theta| = N\,|k_x/k|$ where θ is the angle of the wave-vector with the horizontal direction. This standing wave can be seen as the superposition of four pairs of plane waves with frequencies $+\omega$ and $-\omega$, and wave vectors $(k_x,k_y),(-k_x,k_y),(k_x,-k_y),(-k_x,-k_y)$. For simplicity, we will refer to this solution as the mode $\vec{k} = (k_x,k_y)$. While a single plane wave is an exact solution of the non-linear equations (1-2) (in an unbounded domain), the standing wave (3) is only a solution of the linearized equations (the Jacobian vanishes in the hydrodynamic equation (1) but not in the density equation (2)). Therefore, the evolution of the initial condition involves non-linear interactions, and the actual solution will progressively departs from the linear approximation.

4 The growth of a primary instability

A remarkably organized perturbation is progressively developing upon the standing wave, and its structure is best represented by the vorticity field (Fig.2). It is a straight diagonal band centered at the extremum in stream function of the primary wave. The perturbation is advected by the primary wave into a rocking motion (see Fig.2.c). In the same time, the perturbation is itself a wave, which happens to have the frequency half the primary wave frequency: we see indeed in Fig.2a and c that after two periods of the primary wave, the initial structure is restored (although it is somewhat distorted by the interaction with another unstable mode). In fact these distorsions result from a local parametric instability instability induced by the local rocking motion of the primary wave. The mechanism it self has been previously described by McEwan& Robinson (1975). However our simulations revealed the spatial structure of the instability. Furthermore we expleined this structure in terms of a wave packet of small wavelength oscillating with half the primary wave frequency, which correspond in fact to the parametric asymptotic branches obtained from the resonant interaction theory. We found a good agreement between this theoretical approach which predicts the dominance of parametric instability for a high frequency primary wave and our numerical results (Bouruet-Aubertot et al, 1994).

5 Transition to turbulence

The amplitude of this perturbation grows exponentially until the density field overturns (Fig.2d), producing small regions of static instability. This configuration appears not to

be immediately dynamically unstable, and the breaking seems rather to be initiated by the instability of the shear associated with the perturbation (Fig.2e). Note that at this final stage, high frequency components (much higher than the Brunt Väisälä) develop and burst at the time of breaking which must be attributed to a form of turbulence, or possibly rapidly advected waves. Visualizations of internal wave breaking in a laboratory experiment (Bénielli & Sommeria 1994) give evidence of the remarkable similarity, which indicates that our two-dimensional computations already capture some essential aspects of the dynamics. These successive instabilities lead to the developpment of the wavenumber energy spectrum (fig.3). Moreover our results suggest that a universal behaviour is obtained during the turbulent stage where the slope is approximately equal to -3 whatever the wave amplitude. Note that such a slope is predicted by the theory of Shur (1962) further developped by Lumley (1964) for stratified turbulence (i.e.: in the buoyancy subrange). Furthermore these results can be corrrelated with atmospheric spectra which also exhibit a k_z^{-3} dependency.

The wave breaking is associated with a decrease of the total energy, as shown in Fig.4. The energy decay is remarkably independent of viscosity, so that the dynamics are indeed controlled by inertial effects, although energy is dissipated by viscosity and diffusion (as in the cascade of homogeneous turbulence). A similar behavior is observed whatever the amplitude of the primary wave, but the perturbation has a different wave-length. This scenario for wave breaking is quite general for modes with fairly high frequencies, for instance (5,1). By contrast, modes with low frequency, for instance (1,5) with period $\sqrt{26}T_{BV}$, evolve quite differently. In that case, wave breaking also eventually occurs, but density overturning seems rather to be initiated by perturbations at frequencies higher than the primary wave. This difference of behavior can be related to the linear stability diagrams of the primary wave, obtained from the resonant interaction theory.

6 Conclusion

The evolution of an internal gravity wave has been investigated by direct numerical computations. We considered the case of a standing wave confined in a bounded (square) domain, a case which can be directly compared with laboratory experiments. We observe that breaking eventually occurs, whatever the wave amplitude: the energy begins to decrease after a given time because of irreversible transfers of energy towards the dissipative scales. The wave breaking itself is preceded by a slow transfer of energy to secondary waves by a mechanism of resonant interaction. The nature of the events leading to wave breaking depends on the wave frequency (i.e. on the direction of the wave-vector); most of the analysis is restricted to the case of fairly high frequencies. The maximum growth rate of the inviscid wave instability then occurs in the limit of high wave numbers. We observe that a well organized secondary plane wave packet is then excited. Its frequency is half the frequency of the primary wave, corresponding to an excitation by a parametric instability. Once this secondary wave packet has reached a high amplitude, density over-turning occurs, as well as unstable shear layers. A mechanism of shear instability then leads to a rapid transfer of energy towards dissipative scales. The possibility of applying these results to the breaking in more general internal wave fields deserves further investigations. The presence of a periodic primary wave, rather than a more complex wave field, is probably essential to feed the secondary wave packet by parametric instability. Propagating waves in an infinite domain, or in a horizontal channel (with vertical confinement) could probably

display similar properties. Since periodic internal waves are produced by the interaction of oceanic currents with bottom topography, such a formation of bands may lead to observable features in the density field and positions of mixing events. Applications to other waves with similar dispersive properties, in particular inertial waves of rotating fluids should also be considered.

This work has been supported by D.R.E.T. (Contrat no 90/1650/A000). P. Bouruet-Aubertot currently benefits from a financial support by D.R.E.T.. Part of the calculations have been performed on the Cray 2 of CCVR, thanks to computing time allocated by C.N.R.S. (Dept of Physical and Mathematical Sciences) and by Ministry of Education (D.R.E.D. Matter Science Dept). Finally we thanks S.A. Thorpe for pertinent comments on this work.

References

Benielli D. & Sommeria J., 1994. In preparation.
Bouruet-Aubertot P., Sommeria J.& Staquet C.1994. Submitted to the J. Fluid Mech.
Lumley J.L., 1964. J. Atmos. Sci., 21, pp.99-102.
McEwan A.D., 1971. J. Fluid Mech.50, pp.431-448.
McEwan A.D., Mander D.W. & Smith R.K. 1972. J. Fluid Mech. 55, pp.589-608.
Mc Ewan A.D.& Robinson R.M., 1975. J. Fluid Mech. 67, pp. 667-687.
Muller P., Holloway G., Henyey F. & Pomphrey N., 1986. Rev. of Geophys. 24, 493-536.
Orlanski I., 1972. J. Fluid Mech. 54, pp.577-598.
Orlanski I., Ross B.B., 1973. J. Geophys. Res. 78, pp.8808-8826.
Orszag S.A. 1971 J.Fluid Mech. 50, pp.75-112.
Sidi C., Dalaudier F., 1989. Pure and Applied Geophysics, 130, pp.547-569.
Shur G.N., 1962. report T-63-55 Aerospace Information Division, Library of Congress.
Thorpe S.A., 1994. J. Fluid Mech. 261, pp.33-45.
Winters K.B. & D'Asaro E.A., 1989. Dyn. Atmos. Oceans, 94, pp.1207-1219.
Winters K.B., Riley J.J., 1992. Dyn. Atmos. Oceans 16, pp.249-278

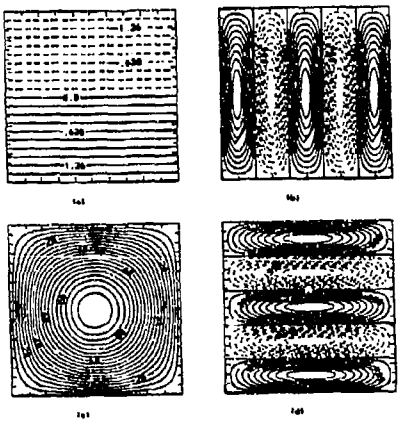
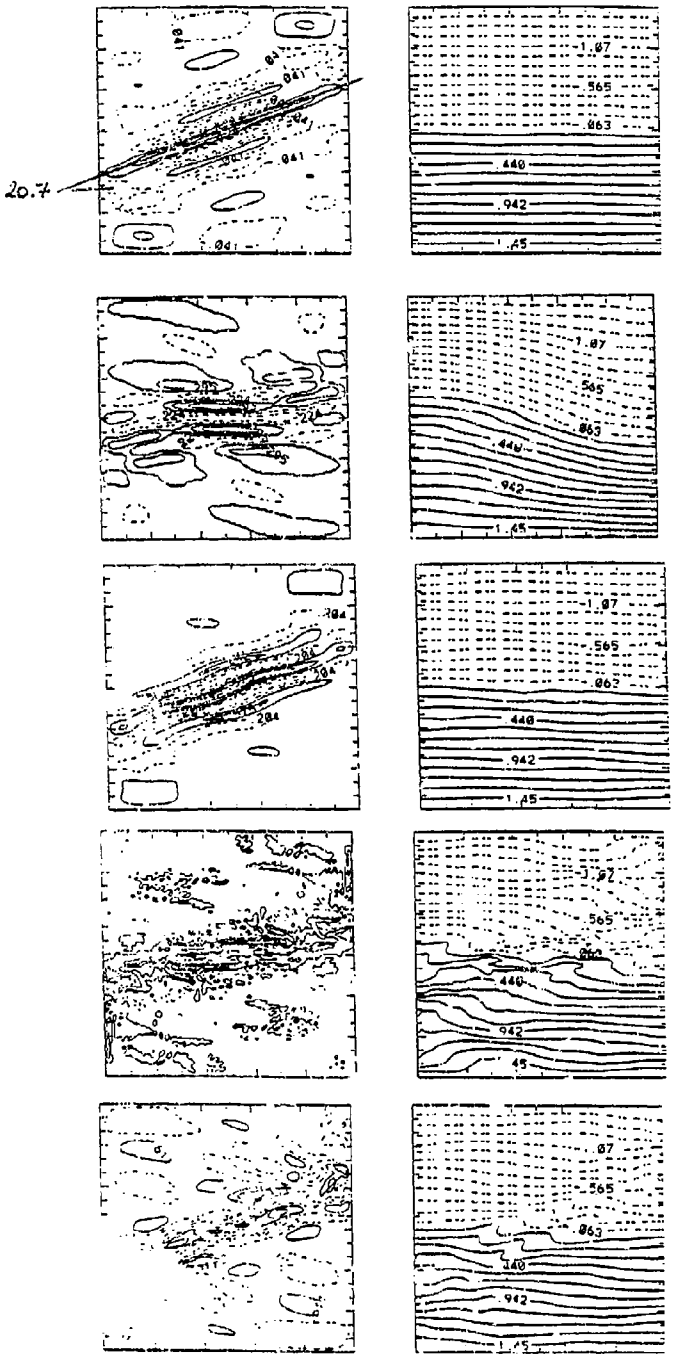


Figure 1: Different initial conditions for a standing wave. (a) total density field, (b)-(d) vorticity field, (b) $\vec{k} = (5,1)$, (c) $\vec{k} = (1,1)$, (d) $\vec{k} = (1,5)$



t_o

$t_o + \frac{5T}{4}$

$t_o + 2T$

$t_o + 6.5\ T$

$t_o + 9.5\ T$

Figure 2: Development of the secondary instability in the form of a plane wave packet (initial condition (5) with $\vec{k} = (1,1)$ and $a = 0.256$): successive snap shots of the vorticity field (1st column) and the total density field (2nd column). For the vorticity fields, the contribution in the Fourier mode (1,1) has been removed in order to better visualize the perturbation itself (and the represented iso-values depend on the extrema, with solid lines for positive values and dashed lines for negative values). In the last column, the corresponding position of an analogous pendulum is indicated for comparison:it is parametrically excited by the vertical oscillation of its support. (a) t=60.4 T_{BV}(42.5 periods of the main wave have occurred since t=0); (vorticity range [−.20; .36]). The deformation vanishes while the velocity (and vorticity) is extremal. The predicted inclination (25) of the perturbation wave crests $\theta_1 = 20.7^0$ is indicated. (b) t=62.1 T_{BV}, 1/4 period later, the pattern has been rocked by the main wave and reaches its minimum slope. (vorticity range:[−.30; .32]). The analogous pendulum rises with its support at the upper position (its rising motion then benefits from a low apparent gravity). (c) t=63.2 T_{BV}, the structure of (a) is recovered (with the development of a secondary perturbation) (vorticity range [−.39; .54]) (d) t=69.5 T_{BV} (49 periods of the main wave have occurred since t=0) The density is extremal and iso-lines first overhang, while vorticity perturbation is weak (e) t=73.7 T_{BV} The secondary wave is now strongly disrupted.

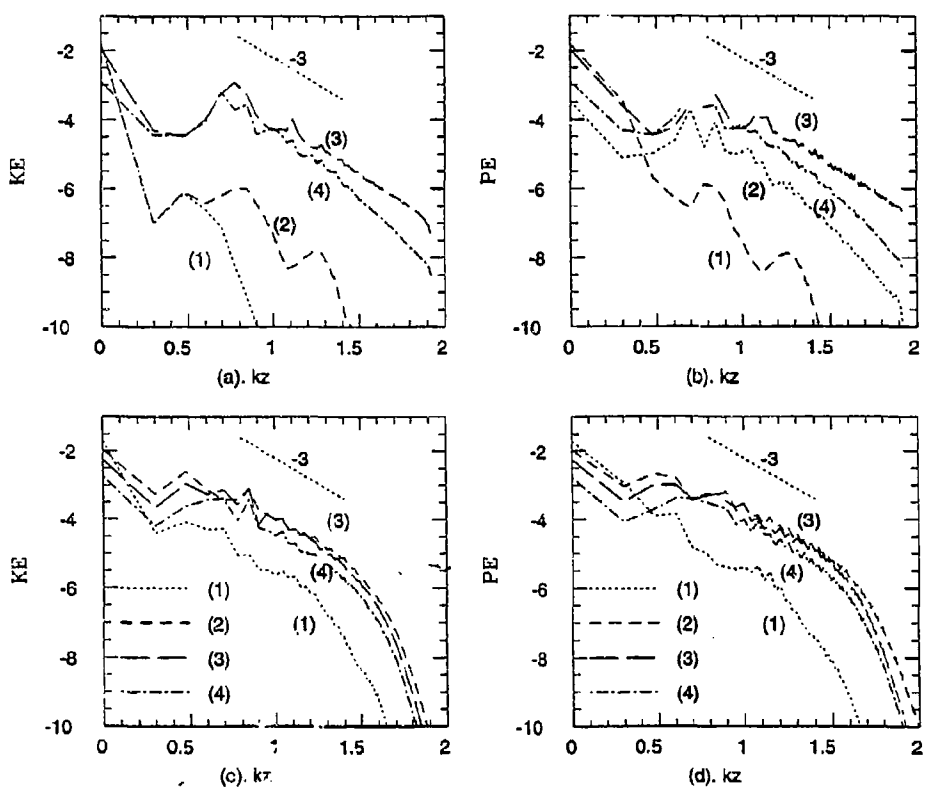


Figure 3: Density energy spectra versus vertical wavenumber obtained for the primary wave $\vec{k} = (1,1)$, (a)-(b) amplitude of the wave .256, (c)-(d) $a = .4$, (a)-(c): kinetic energy, (b)-(d): potential energy, density energy spectra averaged over 10 periods of the primary wave are represented at 4 differents stages: (1)-(2) during the growth of the instability, (3) during wavebreaking, (4) during the very last stage, when the energy has steeply decreased.

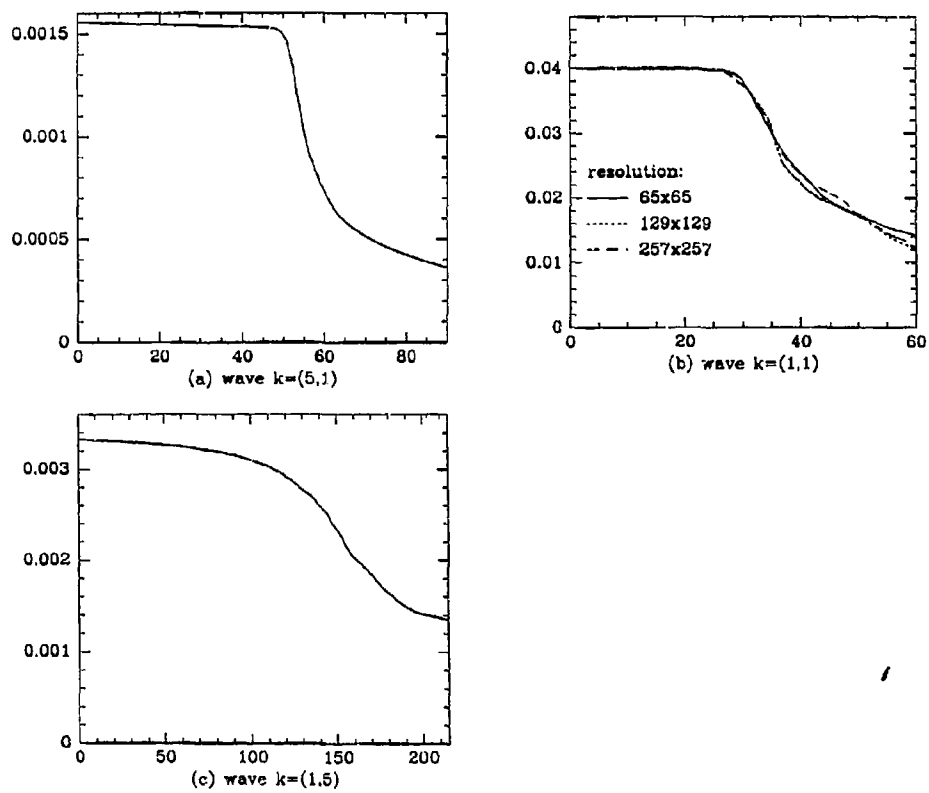


Figure 4: Decay of the total energy versus time (expressed in T_{BV} periods) for a standing wave with initial condition (Fig.1) (a) primary wave $\vec{k} = (5,1)$, $a = 0.0219$ (b) primary wave $\vec{k} = (1,1)$, $a = 0.40$, three computations, with different resolutions $65^2, 129^2, 257^2$ and corresponding coefficients of biharmonic dissipation ($\nu = 8.10^{-7}$, 4.10^{-7}, 2.10^{-7}), give very similar results. (c) primary wave $\vec{k} = (1,5)$, $a = 0.032$

INTERNAL WAVE BREAKING AND THE NONLINEAR CRITICAL LAYER

N.G.Potylitsine and W.R.Peltier

Department of Physics, University of Toronto
Toronto, Ontario, Canada M5S 1A7

1. ABSTRACT

In *Potylitsine and Peltier (1993)* we began an examination of the nonlinear excitation of outgoing radiation, in the form of vertically propagating internal waves, induced by critical layer breaking. On the basis of 2-D numerical simulations, it was demonstrated that the most efficient mechanism for the excitation of secondary radiation is through the direct stimulation of a shear layer from below with an incident internal wave. By employing a sufficiently high level of resolution in our numerical simulations we were able to trace the process of internal wave breaking in the critical level through a KH-billow intermediate state into a regime in which the wave dynamics is dominated by the transition from "trapped" KH-instabilities to propagating waves. Both observational and experimental evidence, however, suggests that KH-billows commonly collapse into turbulence long before they reach the stage in their evolution when outgoing radiation is predicted by the 2-D simulations. In the present paper we test the 2-D nonlinear "forced" KH-wave states against fully three-dimensional infinitesimal perturbations. By restricting our analysis to disturbances which grow quickly compared to the temporal variation in the background KH-wave we are able to reduce our problem to standard eigenvalue form.

2. THE MODEL

In this section we will briefly discuss the model used to examine gravity wave breaking processes in the vicinity of a stratified shear layer with the initial profile of horizontal velocity specified by:

$$U(z) = \frac{1}{2} U_0 \tanh\left(\frac{z}{z_0}\right) \tag{1}$$

where $U_0 = 10\ ms^{-1}$ and $z_0 = 200\ m$. We choose a constant background stratification with

$$N^2 = g\frac{d}{dz}\left[\ln(\Theta(z,0))\right] = \frac{g}{\Theta_{00}}\frac{\Theta_0}{H_\Theta} = constant \tag{2}$$

with a reference potential temperature $\Theta_{00} = 300^o K$ and a gravitational constant $g = 10\ ms^{-2}$. Parameter H_Θ can be interpreted as the potential temperature scale height $H_\Theta = g/N^2$. Thus the initial nondimensional potential temperature profile is:

$$\Theta(z,0) = 1 + \frac{\Theta_0}{\Theta_{00}}\frac{z}{H_\Theta} = 1 + \frac{J}{4G}\frac{z}{z_0} \tag{3}$$

where J is the minimum mean state Richardson number:

$$J = Ri_0 = \frac{N^2}{U_z^2} = 4G\frac{\Theta_0}{\Theta_{00}}\frac{z_0}{H_\Theta} \tag{4}$$

and G is the nondimensional gravitational constant $G = gz_0/U_0^2$. With the above choices for U_0 and z_0, $G = 20$.

In this study we assume that motion is two-dimensional, viscous and heat-conducting and that the Boussinesq approximation is valid. Adopting a streamfunction ψ and vorticity ω representation of the Navier-Stokes equations and using potential temperature θ instead of density, the equations of motion take the form, e.g. *Smyth and Peltier (1991)* :

$$\frac{\partial \omega}{\partial t} = J(\omega, \psi) + Ri\frac{\partial \theta}{\partial x} + Re^{-1}\Delta\omega \tag{5}$$

$$\frac{\partial \theta}{\partial t} = J(\theta, \psi) + (RePr)^{-1}\Delta\omega \tag{6}$$

$$\omega = \Delta\psi \tag{7}$$

where $J(f, g)$ is the Jacobian operator:

$$J(f, g) = \frac{\partial f}{\partial x}\frac{\partial g}{\partial z} - \frac{\partial g}{\partial x}\frac{\partial f}{\partial z} \tag{8}$$

This system has been nondimensionalized in a manner consistent with (1) and (2). Nondimensional parameters appearing in the model equations are the Reynolds number $Re = z_0U_0/\nu$, the Prandtl number $Pr = \nu/k$ and the bulk Richardson number $Ri = gz_0\Theta_0/\Theta_{00}U_0^2 = H_\Theta J/4z_0$, where ν is the molecular viscosity and k is the thermal diffusivity. By choosing $H_\Theta = 4z_0$ we obtain $J = Ri$ for this model. We seek solutions of $(5) - (7)$ which are periodic in the horizontal direction with fundamental wavelength L which is the horizontal length of the computational domain and fundamental wavenumber $\alpha = 2\pi/L$. Accordingly we assume that the dependent fields may be written as truncated Fourier series:

$$f(x, z, t) = \sum_{n=-N}^{N} F_n(z, t)\exp^{(in\alpha x)} \tag{9}$$

in which f may represent ω, ψ or θ. At the upper and lower boundaries ($z = 0$ and $z = H$) of the computational domain, we impose no-slip, isothermal boundary conditions, namely:

$$\omega = \psi = 0; \qquad \frac{\partial \theta}{\partial t} = 0 \tag{10}$$

The model is forced by specifying a vertical velocity perturbation on the lower boundary ($z = 0$). For convenience, we assume that the perturbation consists only of the fundamental ($N = 1$) mode. This velocity perturbation may be written:

$$w(x, 0) = W_0\cos(\alpha x) \tag{11}$$

This perturbation may be thought of as the perturbation arising from the flow of a fluid at speed U_0 over an infinite corrugated lower boundary:

$$h(x) \approx \frac{W_0}{\alpha U_0}sin(\alpha x) \tag{12}$$

3. MAIN RESULTS FROM THE 2-D SIMULATIONS

We have performed a sequence of numerical simulations using the model described above in order to investigate internal wave "breaking" process near the critical level. In this set of 2-D calculations we forced an initially stable ($J > 0.25$) critical layer from below by

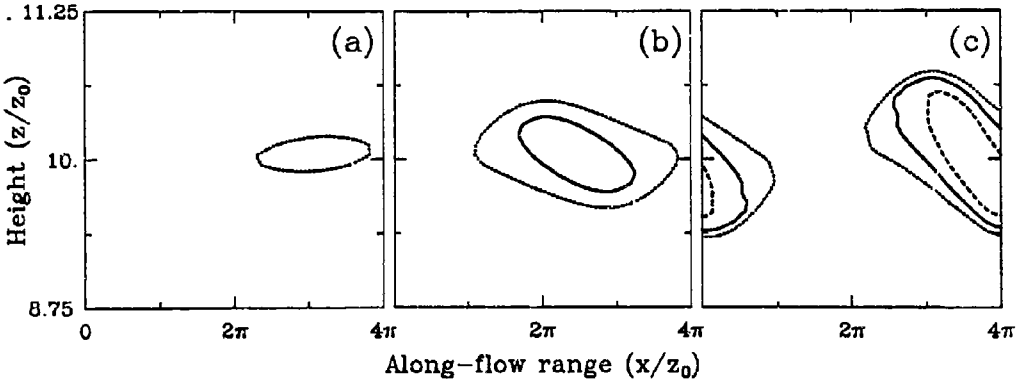


Fig.1 Unstable region developed by the nonlinear GW-CL interaction for times of (a) 7.96; (b) 10.35 and (c) 11.14 wave periods. The model parameters are: $J = 0.5$; $Ri = 0.5$; $Re = 4000$; $Pr = 1$; $\alpha = 0.5$. *Dashed, solid and dotted lines show areas with* $Ri < 0$; 0.25 *and* 0.5, *respectively.*

an incident internal wave and observed the evolution of the flow, associated with the gravity wave critical level (GW-CL) interaction. As we expected, the deposition of momentum into the mean flow caused by gravity wave "breaking" near the critical level changes the stability of the mean state mainly by increasing the velocity shear below the critical level that, in turn, decreases the mean state Richardson number. If the momentum absorbed by the mean flow is large, the mean state Richardson number below the critical level may become small enough ($Ri_0 \rightarrow J < 0.25$) to destabilize the GW-CL interaction. In other words the nonlinear GW-CL interaction can develop an unstable region in the vicinity of the critical level (Fig.1) with subsequent generation of Kelvin-Helmholtz (KH) instabilities (Fig.2).

4. A THEORY FOR THE STABILITY OF KELVIN-HELMHOLTZ WAVES.

In this section we outline the method developed initially by *Klaassen and Peltier (1985)* for analyzing the stability of two-dimensional finite-amplitude KH-waves against fully three-dimensional infinitesimal perturbations. As the flows being considered are no longer 2-D, we must abandon the vorticity-streamfunction formulation and use the full system of Navier-Stokes equations in terms of velocity $\vec{u}$, pressure p and potential temperature θ fields (Boussinesq approximation):

$$\frac{\partial \vec{u}}{\partial t} + (\vec{u} \cdot \nabla)\vec{u} = -\nabla p + Ri\theta + Re^{-1}\Delta\vec{u} \qquad (13)$$

$$\nabla \cdot \vec{u} = 0 \qquad (14)$$

$$\frac{\partial \theta}{\partial t} + (\vec{u} \cdot \nabla)\theta = (RePr)^{-1}\Delta\theta \qquad (15)$$

The nondimensional parameters Re, Pr and Ri appearing in (13)-(15) have been defined previously in (5)-(7). In the present analysis we will consider only those disturbances that have the same streamwise periodicity as the basic state wave. Furthermore, we assume

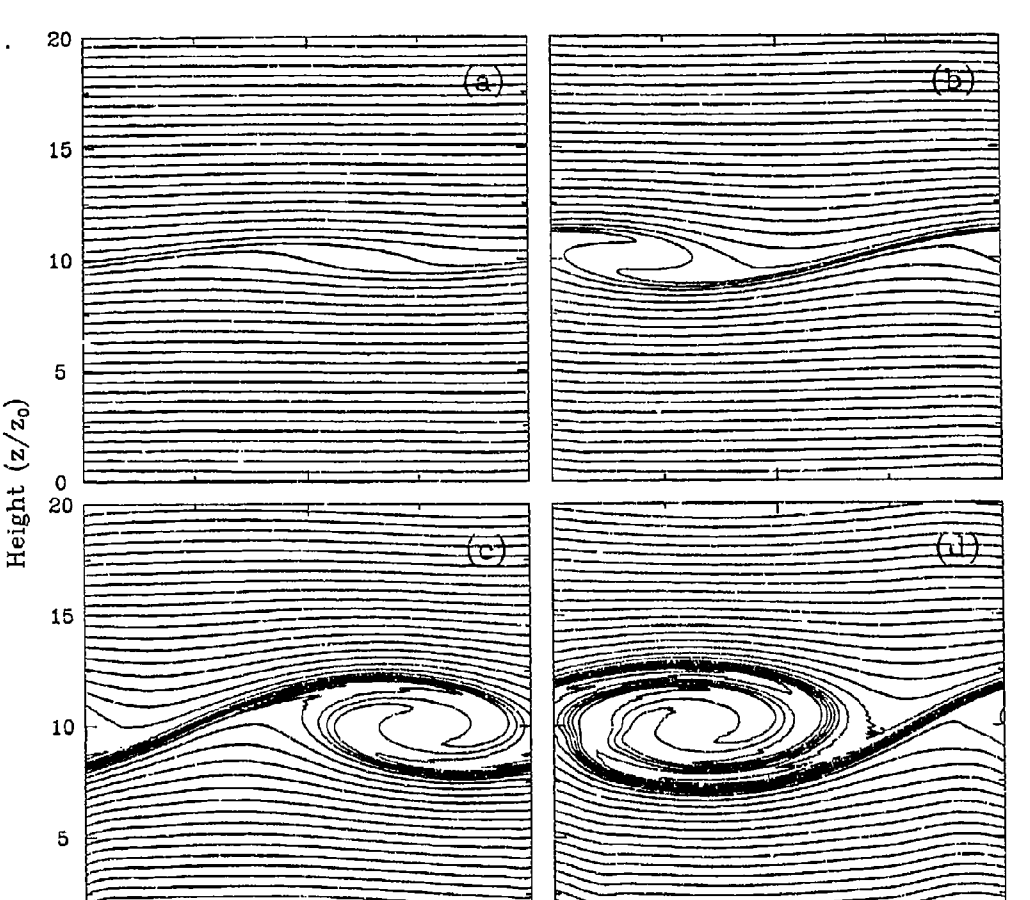


Fig.2 Potential temperature field at (a) 10.35; (b) 11.94; (c) 13.53 and (d) 15.12 wave periods illustrating the KH-billows growth in the initially stable shear layer forced from below by the single harmonic of an internal wave whose horizontal wavelength corresponds to the length of our domain L. The model parameters are: $J = 0.5$; $Ri = 0.5$; $Re = 4000$; $Pr = 1$; $\alpha = 0.5$.

that the superimposed 3-D perturbations evolve on a faster time scale than does the 2-D nonlinear wave, so that the time dependence in the latter may be neglected. These assumptions imply that the velocity, potential temperature and pressure fields in 3-D flow have the Floquet form:

$$f(x,y,z,t) = \tilde{F}(x,z) + \varepsilon \hat{f}(x,z) \cdot e^{i(bx+dy)} e^{\sigma t} \tag{16}$$

where $\tilde{F}(x,z)$ describes the 2-D "background state" and $\hat{f}(x,z)$ is periodic in x with period $2\pi/\alpha$; σ, b and d are the complex growth rate and real streamwise and spanwise wavenumbers of the disturbance, respectively, and ε is an ordering parameter. We are

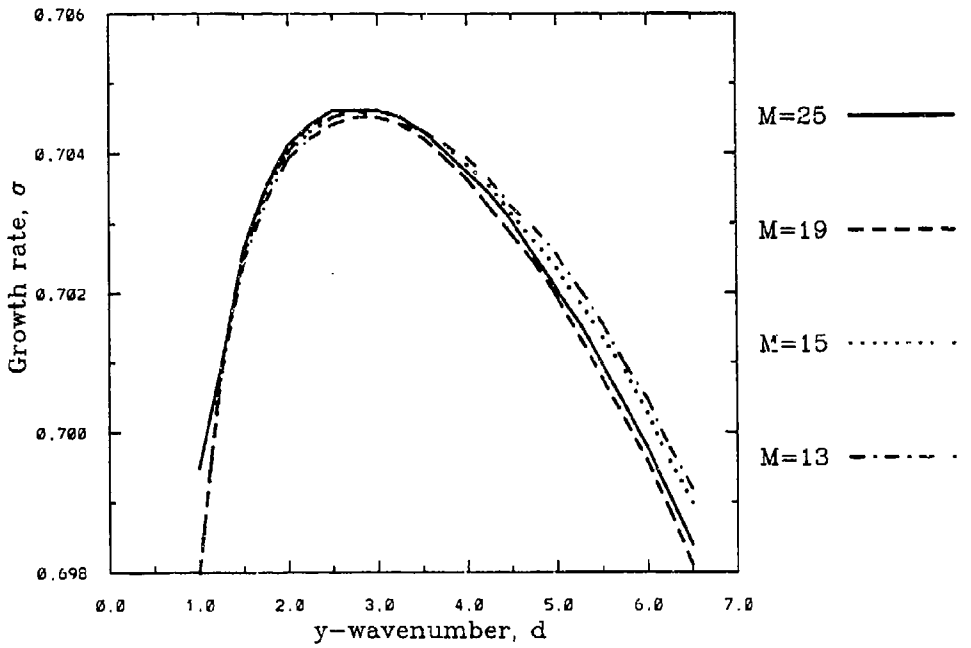


Fig.3 Convergence of the growth rates σ for the most unstable longitudinal mode of the $Re = 4000$, $Pr = 1$, $Ri = 0.5$, $\alpha = 0.5$ *KH-wave at the time equal to* 11.94 *wave periods. The numbers M refer to the truncation level where* $2|\lambda| + \nu \leq M$.

going to investigate here only the longitudinally symmetric disturbances with $b = 0$. Substituting (16) into the Boussinesq equations (13) – (15) we obtain, at order ϵ:

$$\sigma\hat{u} = -\tilde{U}\hat{u}_x - \widetilde{W}\hat{u}_z - (\tilde{U}\hat{u})_x - \tilde{U}_z\hat{w} - \hat{p}_x + Re^{-1}\Delta\hat{u} \tag{17}$$

$$\sigma\hat{v} = -\tilde{U}\hat{v}_x - \widetilde{W}\hat{v}_z - id\hat{p} + Re^{-1}\Delta\hat{v} \tag{18}$$

$$\sigma\hat{w} = -\tilde{U}\hat{w}_x - \widetilde{W}\hat{w}_z - (\widetilde{W}\hat{u})_x - \widetilde{W}_z\hat{w} - \hat{p}_z + Ri\hat{\theta} + Re^{-1}\Delta\hat{w} \tag{19}$$

$$\sigma\hat{\theta} = -\tilde{U}\hat{\theta}_x - \widetilde{W}\hat{\theta}_z - (\tilde{\Theta}\hat{u})_x - \tilde{\Theta}_z\hat{w} + (RePr)^{-1}\Delta\hat{\theta} \tag{20}$$

$$0 = \hat{u}_x + id\hat{v} + \hat{w}_z \tag{21}$$

in which $\hat{u}$, $\hat{v}$, $\hat{w}$, $\hat{\theta}$ and $\hat{p}$ are the (x,z)-dependent parts of the streamwise, spanwise and vertical velocity, potential temperature and pressure perturbations, respectively. A diagnostic equation for pressure is obtained by combining (17), (19) and the continuity equation (21):

$$\Delta\hat{p} = Ri\hat{\theta}_x - 2\tilde{U}_x\hat{u}_x + \widetilde{W}_z\hat{w}_z + \widetilde{W}_x\hat{u}_z + \tilde{U}_z\hat{w}_x \tag{22}$$

We replace (21) with (22) and find as a result that (18) decouples from the remainder of the system. We are thus left with four equations (17), (19), (20) and (22) for the dependent fields $\hat{u}$, $\hat{w}$, $\hat{\theta}$ and $\hat{p}$. The boundary conditions at $z = 0$ and $z = H$ are:

$$\hat{w} = 0; \quad \frac{\partial\hat{u}}{\partial z} = \frac{\partial\hat{v}}{\partial z} = 0; \quad \hat{\theta} = 0; \quad \frac{\partial\hat{p}}{\partial z} = Re^{-1}\frac{\partial^2\hat{w}}{\partial z^2} \tag{23}$$

In order to convert the described above system into an eigenproblem, we must discretize the (x,z)-dependence of the solution fields. This is accomplished via the Galerkin method,

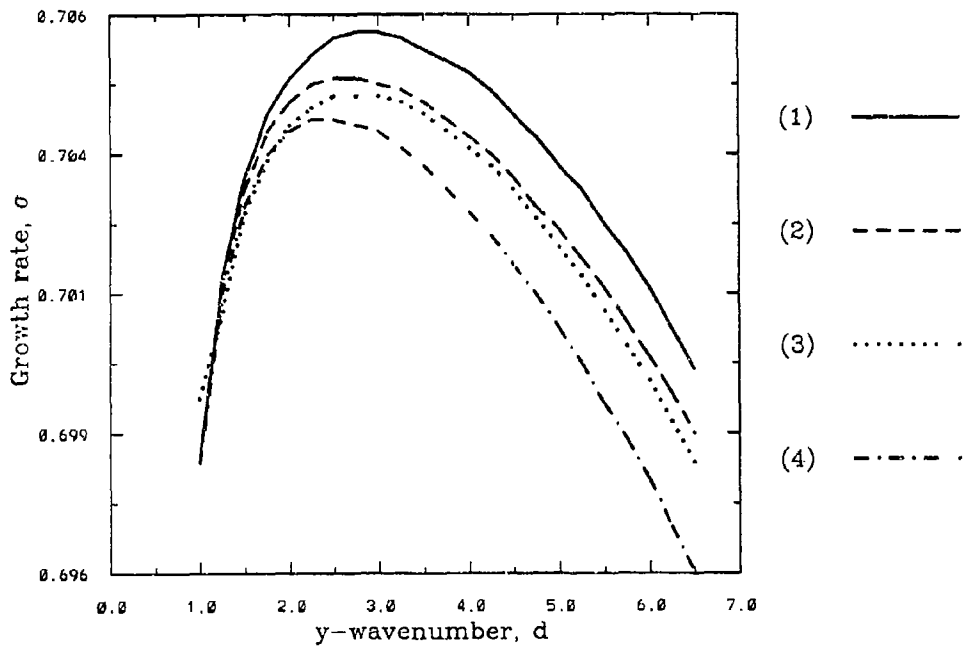


Fig.4 A comparison of the wavenumber dependence of the growth rates σ for the most unstable longitudinal mode at various times in the evolution of the $Re = 4000$, $Pr = 1$, $Ri = 0.5$, $\alpha = 0.5$ KH-wave. Labels (1), (2), (3) *and* (4) *correspond to* 13.53, 15.12, 11.94 *and* 10.35 *wave periods respectively.*

using the expansions:

$$\hat{u} = \sum_{\lambda=-L}^{L} \sum_{\nu=0}^{M} u_{\lambda\nu} F_{\lambda\nu}; \quad \hat{w} = \sum_{\lambda=-L}^{L} \sum_{\nu=0}^{M} w_{\lambda\nu} G_{\lambda\nu} \tag{24}$$

$$\hat{\theta} = \sum_{\lambda=-L}^{L} \sum_{\nu=0}^{M} \theta_{\lambda\nu} G_{\lambda\nu}; \quad \hat{p} = \sum_{\lambda=-L}^{L} \sum_{\nu=0}^{M} p_{\lambda\nu} F_{\lambda\nu} \tag{25}$$

in which

$$F_{\lambda\nu} = e^{i\lambda\alpha x} cos\left(\frac{\nu\pi z}{H}\right); \quad G_{\lambda\nu} = e^{i\lambda\alpha x} sin\left(\frac{\nu\pi z}{H}\right) \tag{26}$$

Following *Klaassen and Peltier (1985)*, we employ the truncation scheme:

$$L(\nu) = \left[\frac{M-\nu}{2}\right] \tag{27}$$

where M is the "truncation parameter". If we substitute (24) – (25) into the perturbation equations (17), (19), (20) and (22) and eliminate $p_{\lambda\nu}$ using (17), (19) and (22), we transform the system consisting of (17), (19), (20) and (23) into the following set of linear algebraic equations for the coefficients $u_{\lambda\nu}$, $w_{\lambda\nu}$ and $\theta_{\lambda\nu}$:

$$\sigma u_{k\mu} = \langle UU \rangle_{k\mu}^{\lambda\nu} \cdot u_{\lambda\nu} + \langle UW \rangle_{k\mu}^{\lambda\nu} \cdot w_{\lambda\nu} + \langle UT \rangle_{k\mu}^{\lambda\nu} \cdot \theta_{\lambda\nu} \tag{28}$$

$$\sigma w_{k\mu} = \langle WU \rangle_{k\mu}^{\lambda\nu} \cdot u_{\lambda\nu} + \langle WW \rangle_{k\mu}^{\lambda\nu} \cdot w_{\lambda\nu} + \langle WT \rangle_{k\mu}^{\lambda\nu} \cdot \theta_{\lambda\nu} \tag{29}$$

$$\sigma \theta_{k\mu} = \langle TU \rangle_{k\mu}^{\lambda\nu} \cdot u_{\lambda\nu} + \langle TW \rangle_{k\mu}^{\lambda\nu} \cdot w_{\lambda\nu} + \langle TT \rangle_{k\mu}^{\lambda\nu} \cdot \theta_{\lambda\nu} \tag{30}$$

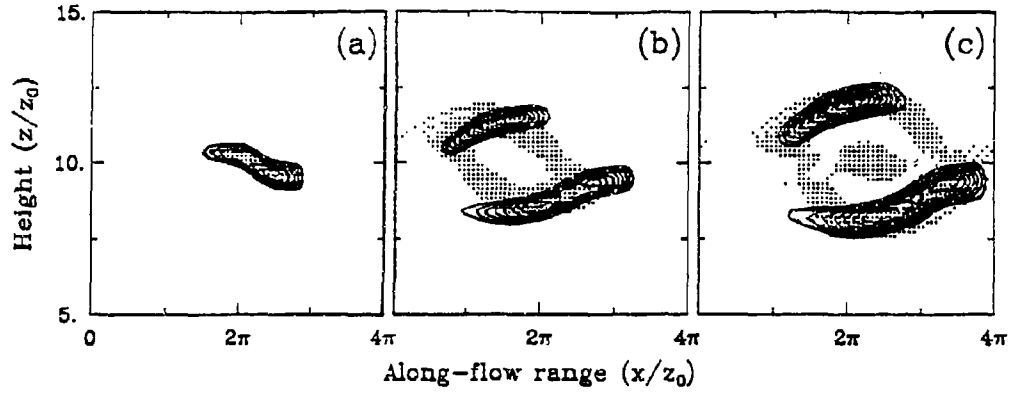


Fig.5 Evolution of the vertical heat flux correlations $\overline{\theta w}^y$ for the most unstable longitudinal mode of the $Re = 4000$, $Pr = 1$, $Ri = 0.5$, $\alpha = 0.5$ KH-wave. Vertical heat flux correlations are shown for 11.94 (a); 13.53 (b) and 15.12 (c) wave periods. The spanwise wavenumber $d = 3.5$ was chosen to be near that of the fastest growing 3-D mode. Note the correlation of the convective activity (positive heat flux) with the primary portion of the super adiabatic region (shaded area) where $N^2 < 0$.

Explicit expressions for the four-dimensional coefficient arrays $\langle UU \rangle$, $\langle UW \rangle$, etc. may be found in *Smyth and Peltier (1991)*. The system (28) – (30) may be written in the form:

$$\sigma \Phi_i = A_{ij} \Phi_j \tag{31}$$

in which A is a constant matrix and Φ is the concatenation of $(u_{\lambda\nu}, w_{\lambda\nu}, \theta_{\lambda\nu})$. Eigenvalues and selected eigenvectors of A are computed using subroutines from the IMSL library. Once the KH-wave state whose stability is to be tasted has been chosen and the horizontal longitudinal wavenumber d and the truncation level M have been specified, the matrix A may be computed and the eigensystem (31) solved.

5. THREE-DIMENSIONAL STABILITY ANALYSIS: RESULTS.

All results of the stability analysis presented here have been calculated with the truncation level $M = 25$ appeared to be the most efficient one for our simulations. In order to justify our choice we present the dependence of the eigen value curves upon the truncation level M (Fig.3). In Fig.4 we show the growth rates σ of the dominant longitudinal modes as a function of the spanwise wavenumber d at selected times during the simulation described in section 3. As in previous studies of a similar nature (*Klaassen and Peltier (1985)*, $\sigma(d)$ exhibits a strong local maximum in the vicinity of $d = 3$. This indicates a secondary instability with a well-defined spanwise wavelength which could lead the flow into a complex, but nevertheless laminar, three-dimensional state.

Fig.5 shows the contours of vertical heat-flux correlations $\overline{\theta w}^y$ for the most unstable longitudinal mode superimposed on the shaded superadiabatic regions (SAR) where $N^2 < 0$. It can be seen that the most unstable longitudinal mode is associated with convective activity (positive heat-flux) in the evolving statically unstable regions that develop above and below the core of the vortex.

6. CONCLUSIONS.

The deposition of momentum into the mean flow due to internal wave "breaking" near the initially stable critical layer ($J > 0.25$) can lead to the development of a dynamically unstable region with subsequent generation of growing Kelvin-Helmholtz (KH) instabilities. By performing appropriate 3-D linear stability analysis we have tested these "forced" 2-D KH-waves for stability against 3-D infinitesimal disturbances and have found that they are most unstable against longitudinal modes, which are confined to the local statically unstable regions induced by the roll-up of the nonlinear wave. We have shown that these longitudinal modes achieve their largest growth rates approximately at the same time as KH-billows attain their maximum amplitude but the growth of these 3-D instabilities is initiated earlier in the KH-wave's evolution. Our conclusions concerning the localized origin and intrinsic three-dimensionality of the unstable longitudinal modes are consistent with the theoretical results derived in *Klaassen and Peltier (1985)* for "pure" KH-billows. Since our analysis revealed that "forced" KH-billows are highly unstable against 3-D infinitesimal disturbances we expect that the momentum deposition into the critical level caused by the "breaking" of the incident internal wave will more likely engender a cascade of energy into small-scale turbulent mixing than lead to reradiation from the shear layer of outgoing internal waves. Although it is clear from our discussion that the instability we have described here is strongly related to the transition to turbulence in "forced" KH-waves, the precise way in which this transition proceeds remains unclear. We are in the process of investigating this question by performing three dimensional fully nonlinear simulations of gravity wave "breaking" near the critical level.

7. REFERENCES:

Klaassen G.P., Peltier W.R., 1985: The onset of turbulence in finite-amplitude Kelvin-Helmholtz billows. *J. Fluid Mech.*, **155**, 1-35.

Potylitsine N.G., Peltier W.R., 1993: Internal wave-vortex interaction: stimulated emission from stratified shear layers. *Preprints of the 9-th Conference on Atmospheric and Oceanic waves and stability*, AMS, 167-170.

Smyth W.D., Peltier W.R., 1991: Instability and transition in finite-amplitude Kelvin-Helmholtz and Holmboe waves. *J. Fluid Mech.*, **228**, 387-415.

On the breakdown into turbulence of propagating internal waves.

Peter A. Gallaire and James J. Riley.
University of Washington
Seattle, Washington 98195 USA

1 Introduction

The propagation of internal waves is an important feature of the small scale dynamics of the atmosphere and oceans. Internal waves can provide significant momentum and energy flux, and can also be an important source of turbulence and mixing (Gregg, 1987). Internal wave breakdown into turbulence can be due to a number of effects. For example, in the atmosphere, upward-propagating internal waves experience continual increase in amplitude due to the decrease in density with height. It is thought that this ultimately results in wave breakdown (Hines, 1960). Propagating internal waves in the ocean often experience critical levels (Henyey, et al., 1986), which can lead to wave breakdown, possibly in the form of streamwise vortices (Winters and Riley, 1992). And nonlinear wave-wave interactions can lead to wave breakdown, as demonstrated, e.g., in the laboratory experiments of McEwan (1983).

Using linear stability analysis, Drazin (1977) and Mied (1976) have shown that an internal wave of any amplitude, propagating in a uniform environment with no ambient current shear, is unstable to two-dimensional disturbances. Hence a propagating wave may break down on its own, independent of the mechanisms mentioned above. In the work presented in this paper, we examine the breakdown of a freely propagating internal wave in a uniform, nonrotating, nonshearing environment. It is thought that a better understanding of this breakdown process can be used as a basis for understanding the possibly more complex situations discussed above. To do this we first extend the stability analysis of Drazin and Mied to consider three-dimensional perturbations. The results of Winters and Riley for instability of a wave approaching a critical layer suggest the importance of three-dimensional perturbations. We then perform direct numerical simulations of this three-dimensional, unsteady breakdown process. Of particular interest is how breakdown occurs, e.g., it is initially two- or three-dimensional? Does it occur due to wave overturning or shear instability? Due to turbulent mixing, how much wave energy is ultimately deposited in the background density field as potential energy?

2 Stability analysis

We consider a fluid satisfying the Navier-Stokes equations subject to the Boussinesq approximation. The ambient conditions consist of a fluid at rest with a uniform, stable density gradient, characterized by the buoyancy frequency N, defined by

$$N^2 = -\frac{g}{\rho_o}\frac{d\overline{\rho}}{dz} > 0\,. \tag{1}$$

Here g is the acceleration of gravity, ρ_o a reference density, and $\overline{\rho}(z)$ the ambient density, assumed to depend only on the vertical coordinate z. An internal wave is assumed to be propagating through this fluid in the x-z plane, with vertical velocity given by

$$\tilde{w}(x,z,t) = -\frac{A\omega}{m}\cos(kx + mz - \omega t)\,. \tag{2}$$

Similar expressions exist for other flow variables. Here $\mathcal{A}$ is the wave amplitude, (k, m) is the wave number vector, and ω is the wave frequency, which must satisfy the dispersion relation

$$\omega = \pm N \frac{k}{\sqrt{k^2 + m^2}}. \tag{3}$$

Note that, neglecting viscous and diffusive effects, this single wave is an exact solution to the equations of motion for any amplitude $\mathcal{A}$, as the nonlinear terms are identically zero.

We consider a small perturbation to this base wave, e.g., writing the total vertical velocity as

$$w = \bar{w} + w'. \tag{4}$$

A new coordinate system is defined to move with the wave, and is rotated such that x' is in the direction of the wave current, and z' is in the direction of the wavenumber vector. Plugging this assumed form into the original equations, the resulting equations are linearized in terms of the perturbation amplitude. Furthermore, only normal mode solutions are sought, hence neglecting the contribution to the solution from the continuous spectrum. These assumptions can be ultimately tested by comparing the predictions of stability theory with the results from the direct numerical simulations.

The resulting stability problem is quite different from that for a stratified shear flow, i.e., the Taylor-Goldstein problem (Drazin and Reid, 1981). Squire's theorem does not apply. Furthermore, because of the periodic nature of the problem in the z'-direction, Floquet theory (Bender and Orszag, 1978) is needed to simplify the form of the resulting equations. The application of Floquet theory gives an eigenvalue problem in $\phi = z' - \omega t$ for the eigenvalue σ, the complex growth rate. The problem is defined in terms of the parameters describing the base wave, i.e., the nondimensional wave amplitude and wavenumber vector direction, and the wave number (α, β) of the disturbance, corresponding to the (x', y) directions. The Floquet parameter is chosen in order to examine perturbations which are periodic over the same wavelength as the base wave, or a rational fraction of this wavelength. The resulting eigenvalue problem is solved by Fourier expansion, taking full advantage of the symmetry properties of this problem.

The stability problem is solved for several different wave propagation angles, namely 30°, 45°, 60°, 80°, 85°, and 90° to the horizontal. Furthermore calculations are performed for various wave amplitudes, nondimensionalized by the amplitude of a wave at incipient overturning, ranging from 0.1 to 1.1. The Prandtl number is taken to be 1, and the Reynolds number, based upon the wavelength and maximum wave velocity, ranges from about 300, for comparison with direct numerical simulations, to up to about 10^6, an approximately inviscid, nondiffusive case.

Typical results are presented in Figure 1, which gives contours of maximum growth rate in the (α, β) plane for waves propagating at 45° to the horizontal, with nondimensional amplitudes ranging from 0.1 to 1.1, and a Reynolds number of the order of 10^6. For the smaller-amplitude cases, the maximum growth rates are for two-dimensional perturbations ($\beta = 0$). As suggested by Mied, the instability for small amplitudes can be shown to be a resonant interaction, the different resonant curves producing the rib-like structure seen in the curves. As the amplitude of the wave is increased, other instability modes appear, especially ones which are three-dimensional ($\beta \neq 0$). For the largest amplitude case, the growth rates of the three-dimensional modes are comparable to the two-dimensional ones, suggesting a fairly complex breakdown process.

3 Numerical simulations

In order to numerically simulate internal wave breakdown, we solve the initial value problem consisting of a freely-propagating internal wave train with an initial perturbation superimposed. We assume that the flow satisfies the Navier-Stokes equations subject to the Boussinesq approximation. Periodic boundary conditions are employed in all three spatial directions. The

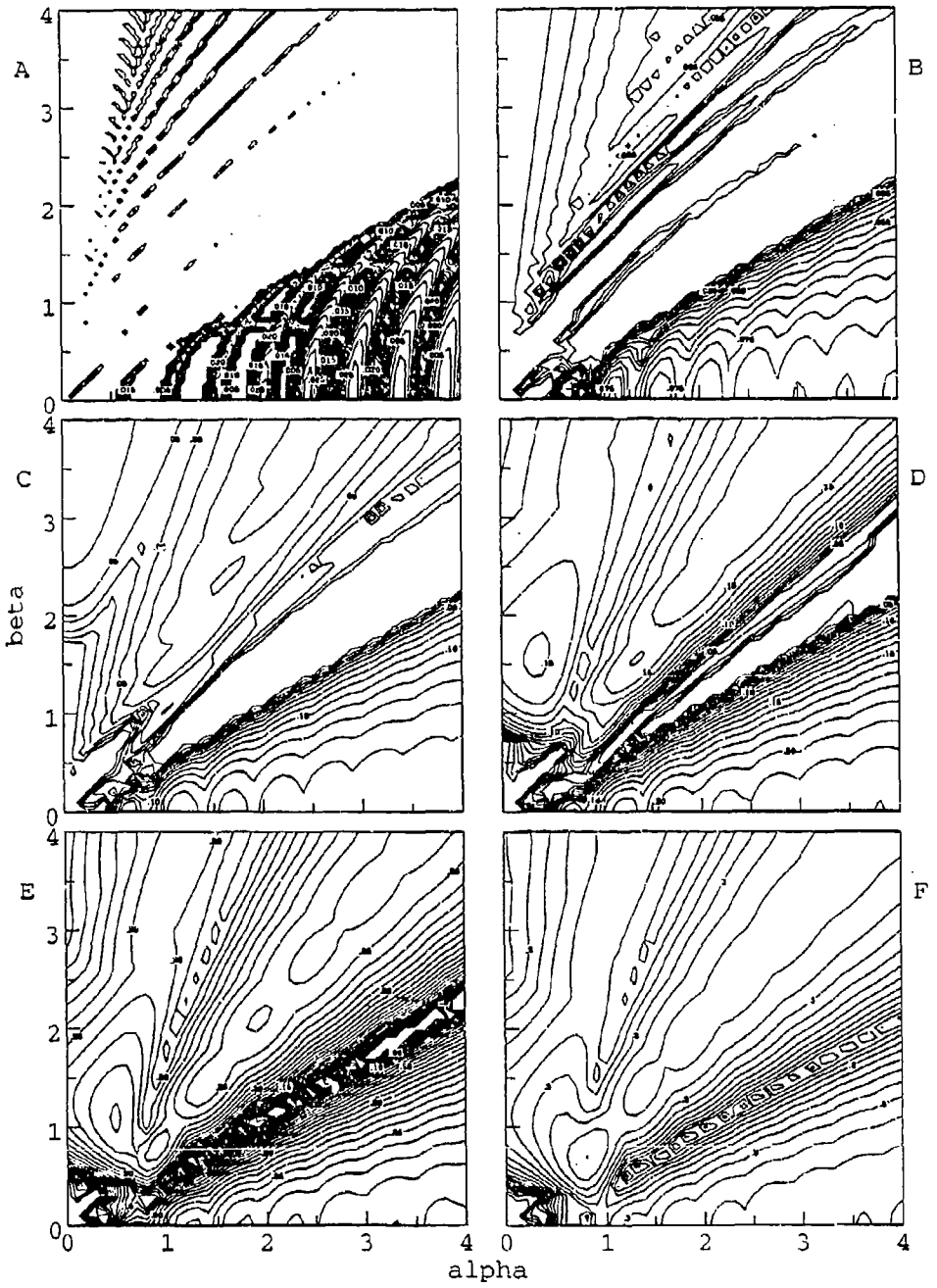


Figure 1: Growth rates for $\delta = 45°$: amplitude 0.1 (top left), 0.3 (top right), 0.5 (middle left), 0.7 (middle right), 0.9 (bottom left), and 1.1 (bottom right). The Reynolds number is of order 10^6.

periodicity length in any direction is taken to be an integer multiple of the periodicity length of the base wave in that direction, and depends on the specific problem considered. For initial conditions, we superimposed the base wave and a low-level perturbation. The perturbations considered are of two types:

i) low-level, broad-banded noise;

ii) low-level, broad-banded noise plus an eigenfunction taken from linear stability theory.

The first type (i) is meant to simulate background noise. In the second type (ii), the eigenfunction is generally taken as the most unstable one predicted by linear stability theory. Initialization with (ii) allows a more careful investigation of a particular instability than for (i), since in the latter case several competing modes of similar growth rates can be excited.

In order to solve the equations numerically, the nonlinear terms are advanced in time using a second-order Adams-Bashforth method. The viscous and diffusion terms are treated exactly using an integrating factor, while the pressure term is computed by the projection method. Fourier Galerkin methods are employed to approximate spatial derivatives, with an ellipsoidal wavenumber truncation at two-thirds of the maximum wave number in order to eliminate aliasing errors (Canuto et al., 1988). Simulations were performed on up to $128\times64\times128$-point computational grids in the x-, y-, and z-directions, respectively. The simulations were usually started on a smaller grid, e.g., with $32\times32\times32$ grid points, and then regridded to a finer mesh as the wavenumber spectrum broadened.

A number of simulations have been performed at different base wave amplitudes and propagation angles [Lombard (1994)]. We present here a particular case that has many of the characteristics of the other simulations. In this case the base wave is propagating at 45° to the horizontal, and has a nondimensional amplitude of 0.5. The Reynolds number, based on the wavelength and maximum velocity of the base wave, is 311, and the Prandtl number is set to 1. The linear stability theory results for this case are similar to those given in Figure 1c. (Note that the Reynolds number for Figure 1c is 10^6. The principal effect on linear instability of lowering the Reynolds number is to greatly reduce the growth rates for larger values of α and β. In the stability calculation for the Reynolds number of 311, no unstable modes are observed for α greater than about 6 or β greater than about 5.) For this case, the fastest growing instability is two-dimensional, although the instability is fairly broad-banded with significant regions off the α-axis. The computational domain in Fourier space is adjusted so that approximately the fastest growing mode is excited, as well as a number of its harmonics and a fast-growing oblique instability. Low-level, broad-banded noise is employed for excitation.

Initially, after some adjustment, the perturbation energy begins to grow at an approximately exponential rate for several decades. Here the growth rate is 0.099, close to the value of 0.108 predicted from linear stability theory for the most unstable mode, and indicating that this mode is a main participant in the instability process. This exponential growth proceeds until the base wave begins to lose a significant amount of its energy.

In order to understand the breakdown process, it is useful to first visualize the flow. Figure 2 contains a sequence of plots depicting the evolution of the wave at six different times, where time has been nondimensionalized by $1/N$, and lengths have been nondimensionalized by the wavelength of the base wave. The plots are two-dimensional slices of the flow field in the x-z plane (the plane of the base wave). The velocity field is indicated by vectors, the density field by contour lines, and shading is used to indicate regions of density overturning (i.e., where $d\rho/dz > 0$). Note that the wave period is 8.89 time units, while the domain size is 8.89 units along both the x- and z-axes. The wave has a phase speed in the direction of propagation of 0.707. In the frame of reference moving with the base wave, the principal instability has a phase speed of 1.68 along the wave front (from upper left to lower right). Thus in a fixed frame of

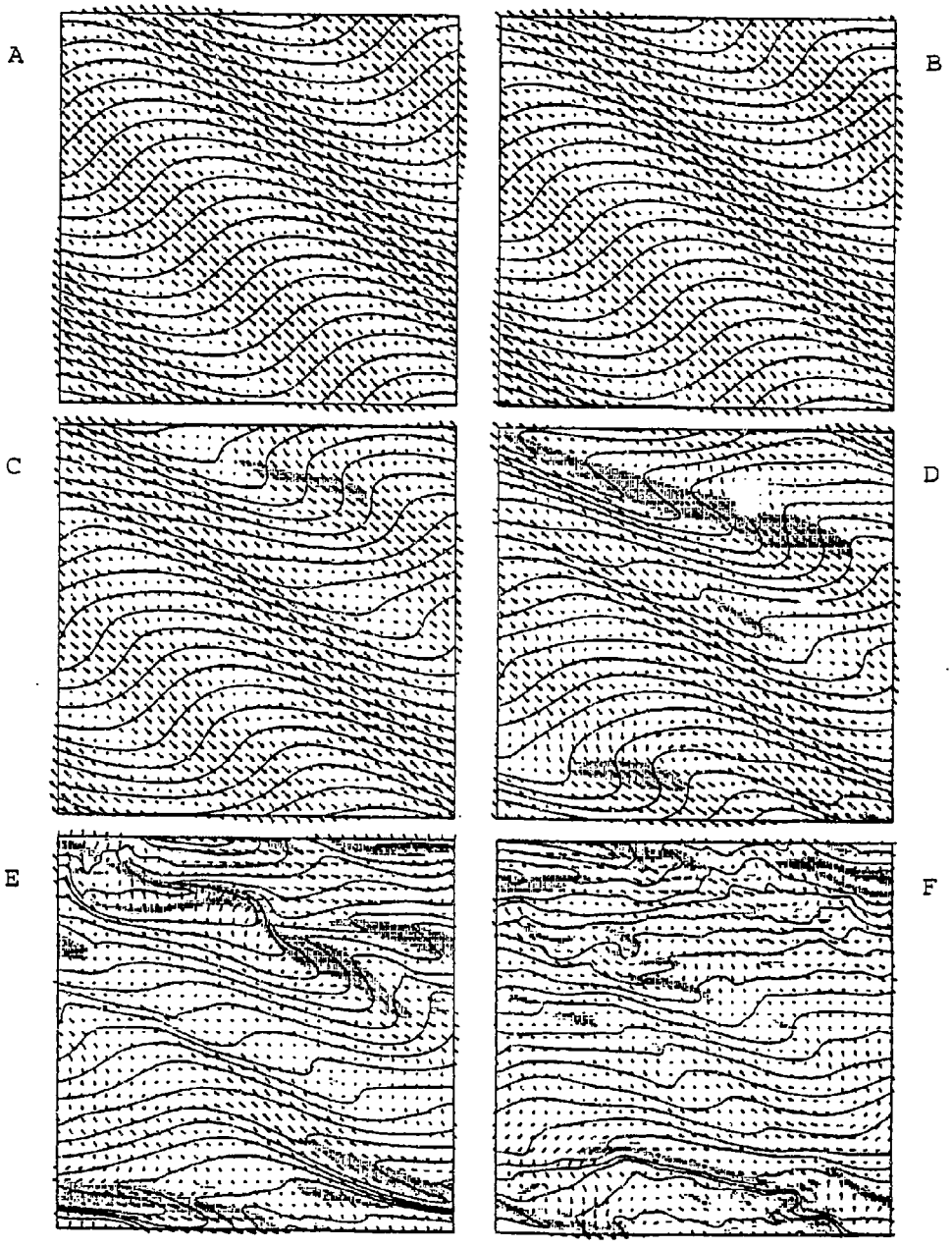


Figure 2: Velocity vectors and density contours in the x-z plane ... indicates regions of density overturning. Times are, from left to right, starting at the ... 68, 76, 84, 92, 100.

reference the instability has a phase speed of 1.69 in the x-direction and -0.69 in the z-direction. The instability, which has been growing for some time, is first readily visible as an isolated patch of statically unstable fluid (Figure 2c), although by this time significant steepening of the wave in other regions, as well as curvature of the flow direction, is observable. Initially this statically unstable region is somewhat two-dimensional, as the principal instabilities are two-dimensional. In Figure 2d another patch of statically unstable fluid has emerged as well. By this time the flow has become very three-dimensional (see below). The breakdown process is very complex, and at the time of the last image (Figure 2f), little vestige of the original wave is apparent (about 18% of its energy still remains).

More understanding of this breakdown process can be obtained by examining the flow energetics. It is convenient here to split the velocity field into three parts: (i) the base wave; (ii) the velocity in the vertical plane of the principal instability (in this case the x-z plane); and (iii) the remainder (in this case the three-dimensional part of the flow). Figure 3 contains plots of these three energy components as functions of time, along with various terms in the energy balance for each component. One observes the importance of the three-dimensional component of the instability, as it ultimately has more energy than that of the base wave. During the time period shown in this figure, the base wave loses kinetic energy by shear interactions to both the two- and three-dimensional components, and to potential energy through the buoyancy flux. The three-dimensional component gains kinetic energy from the base wave by shear interactions, and also from potential energy through the buoyancy flux, while losing energy to the two-dimensional component through shear interactions. The two-dimensional component loses kinetic energy to potential energy through the buoyancy flux, while gaining energy from the base wave and the three-dimensional component through shear interactions. From these results it is seen that it is not possible to classify the breakdown process as either shear-driven or convectively-driven. Both means of energy transfer are at work, removing energy from the base wave, ultimately leading to both the dissipation of kinetic energy into heat and also the mixing of the background density field.

A number of other aspects of this breakdown process have been examined. Of particular interest is this mixing of the background density field, in which the energy of the internal wave is converted into background potential energy. Defining the mixing efficiency to be the ratio of the potential energy dissipation to the kinetic energy dissipation, it was found to be approximately 0.85, considerably larger that the typical value measured in the ocean of about 0.3 (Gregg, 1987), but consistent with other results from numerical simulations (Winters and D'Asaro, 1994). This difference in mixing efficiencies is probably affected most by the difference in the Prandtl numbers, being 1 in the simulations compared to about 700 in the ocean. Furthermore, this single wave breakdown event may be a more efficient means of mixing in comparison to the far more random nature of the ocean.

4 Conclusions

From the stability analysis and direct numerical simulations, a number of conclusions can be drawn regarding the breakdown process for a propagating internal wave. For smaller-amplitude waves, a portion of the instability can be associated with resonant interactions (Mied, 1976), although other types of instabilities are present. For larger amplitude waves the resonance interpretation is not of use; the instabilities can be rather broad-banded and three-dimensional, and their specific character depends on the wave amplitude and propagation direction (in additional to the Reynolds and Prandtl numbers).

The breakdown process itself is due to the inherent instability of the wave. As the wave propagates, disturbances continually grow, drawing energy from the wave itself. As suggested by the stability theory, these growing disturbances can be rather broad-banded and three-dimensional.

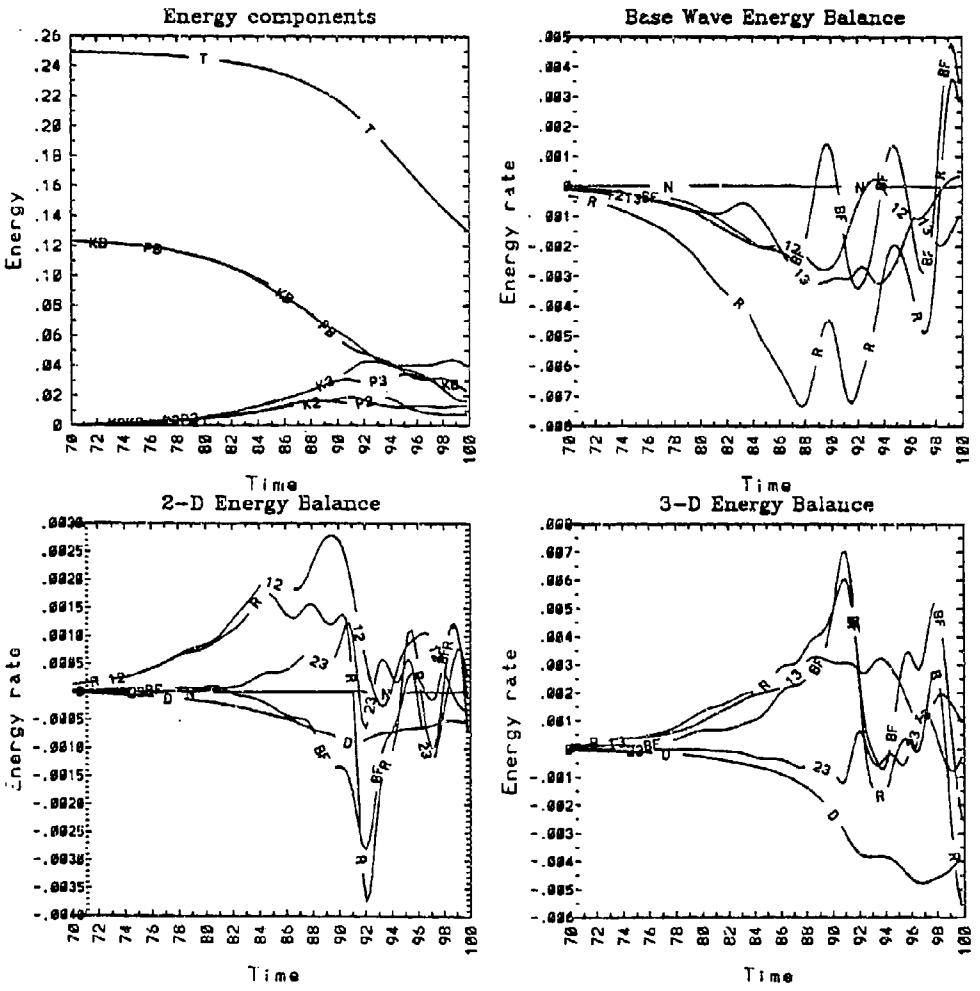


Figure 3: Base wave (B), two-dimensional component (2), and three-dimensional (3) kinetic (K) and potential (P) energy components and alsc the energy balances for the three. In the balance plots, R is the time rate of change, BF is the buoyancy flux, and D the dissipation. The energy transfer terms (12), (13),and (23) are the corresponding Reynolds stress terms. The net value (N) indicates any error in the energy balance.

As the perturbations reach finite amplitude, localized patches of hydrostatically unstable fluid are formed, breaking down in a complex, three-dimensional manner and leading to turbulence. The final result is that much of the wave energy is lost through mixing of the ambient density field as well as dissipation into heat, the ratio of these two effects being about 0.85. Thus the breakdown process cannot be classified as simply shear-driven or convectively-driven, but is a combination of the two. Moreover, overturning is not necessarily a cause of wave breakdown, but more an indication of the growing instability. And finally, the wave does not break down by one large-scale overturning, as with a "plunger-breaker" surface wave, but through several localized regions.

Acknowledgment. This research was supported by the U. S. Office of Naval Research (N00014-86-K-0690 and N00014-90-J-1112).

References

[1] Bender, C. M., and S. A. Orszag. *Advanced Mathematical Methods for Scientists and Engineers*, McGraw-Hill (1978).

[2] Canuto, C., M. Y. Hussaini, A. Quarteroni, and T. A. Zang. *Spectral Methods in Fluid Dynamics*, Springer-Verlag (1988).

[3] Drazin, P. G. "On the instability of an internal gravity wave", *Proc. Roy. Soc. Lond.*, **356**, 411-432 (1977).

[4] Drazin, P. G., and W. H. Reid. *Hydrodynamic Stability*, Cambridge University Press (1981).

[5] Gregg, M. G. "Diapycnal mixing in the thermocline: a review", *J. Geophys. Res.*, **92**(C5), 5249-86 (1987).

[6] Henyey, F. S., J. Wright, and S. M. Flatté. "Energy and action flow through the internal wave field: an eikonal approach", *J. Geophys. Res.*, **91**, 8487-8495 (1986).

[7] Hines, C. O. "Internal gravity waves at ionospheric heights", *Can. J. Phys.*, **38**, 1441 (1960).

[8] Lombard, P. N. *The Stability of Finite-Amplitude, Internal Gravity Waves*, Ph.D. Thesis, University of Washington (1994).

[9] McEwan, A. D. "The kinematics of stratified mixing through internal wave breaking", *J. Fluid Mech.*, **128**, 47-57 (1983).

[10] Mied, R. R. "The occurrence of parametric instabilities in finite-amplitude internal gravity waves", *J. Fluid Mech.*, **78**(4), 763-84 (1976).

[11] Winters, K. B., and J. J. Riley. "Instability of internal waves near a critical level", *Dyn. Atmos. Oceans*, **16**, 249-278 (1992).

[12] Winters, K. B., and E. A. D'Asaro. "Three-dimensional wave instability near a critical level", accept for publication by *J. Fluid Mech.* (1994).

The Dynamics of Sedimenting Surface-Gravity-Currents

T. MAXWORTHY
Departments of Aerospace and Mechanical Engineering
University of Southern California
Los Angeles, CA 90089-1191
and
Institute for Theoretical Geophysics
DAMTP
Cambridge University

Introduction:

We have performed a series of experiments on the dynamics of sedimenting surface-gravity-currents. The physical situation concerns a current with a total density (ρ_c) which is less than that of (ρ_a) the main body of fluid with which it interacts. In turn ρ_c is made up of interstitial fluid of density ρ_I and particles with a volume concentration c and density ρ_p. Of additional importance is the density deficit ratio (R_ρ) between the current and its surroundings. We use $R_\rho = \frac{\rho_a - \rho_I}{\rho_c - \rho_I}$ as a measure of the relative instability of the current and it will be noted that it is equivalent to the similarly defined quantity, $\beta\Delta S/\alpha\Delta T$, used in the study of double-diffusive convection. Thus when $R_\rho \gg 1$ the interface between current and ambient is very stable and it takes a large local particle concentration to generate a sufficiently large local density to penetrate the interface. On the other hand when $R_\rho \rightarrow 1$ the whole layer can penetrate the interface and substantial mixing can occur. It is this latter mixing process that is the key to a basic understanding of the dynamics of such currents and we present new measurements of the magnitude of this effect. That this is the case has become obvious during a number of experiments that explored the temporal evolution of particle-laden currents released at one end of a long, deep tank. In what follows we will present details of the experiments and the outline of a theory that appears to explain, in a general way, the results of those experiments.

Apparatus:

The main piece of equipment that evolved during the course of this investigation is shown in figure 1. It consists of a rectangular tank 2 m long and 0.65 m deep. In its original form it was 8 cms wide but it became clear after a number of initial experiment that this tank was too narrow. The results clearly showed the effects of viscous stresses at the side walls. Thus the tank was modified and its width increased to 16 cms. New experiments had a behaviour that were consistent with a negligible level of lateral viscous forces. The current itself was generated in two ways. In the first a well mixed and fixed volume of particle-laden fresh water was contained behind a barrier. At the start of the experiment the barrier was

removed and the gravity current allowed to evolve down the tank. In the second method a large container of particle-water mixture was suspended above the tank. The mixture was released at a constant flow-rate through 1 cm deep manifold spanning the width of the tank. Again the evolution of the current was followed and recorded on video-tape for later analysis.

When it became obvious that mixing generated by the instability of the interface was of crucial importance to our understanding of the dynamics of the current, the apparatus was modified further as shown in figure 1b. Here a partial barrier was placed approximately 65 cms from the upstream barrier. A gravity current was released but when it hit the second barrier it was stopped and a uniform, almost-stationary layer of mixture was generated. This then became unstable in a quasi-one-dimensional fashion. As discussed later, by taking fluid samples and measuring their density it is possible to infer the *total* amount of mixing that has taken place.

Results:

In what follows we will concentrate on details of the lock-exchange flow realizing that similar results hold for the constant flow-rate case as well. The lock exchange flow is characterised by a number of primary variables, ρ_a, ρ_I the particle volume concentration (c)[1] and the geometry (length and height) of the dammed volume. From these we extract or directly measure the initial current density (ρ_c)

$$\frac{1}{\rho_c} = \frac{c}{\rho_p} + \frac{(1-c)}{\rho_I}$$

and the density deficit ratio:

$$R_\rho = \frac{\rho_a - \rho_I}{\rho_c - \rho_I}$$

a) Gravity current evolution:

A sequence of photographs of a typical evolution is shown in figure 2. From photographs such as this and video recordings of the evolution of the gravity current it is possible to determine the time dependence of front location. Typical examples, chosen from the approximately 40 experiments that were run, are shown in figure 3 for the case of a constant volume release and in figure 4 for a release with almost constant flow rate. In both cases the critical power-law behaviours are noted. In particular we note that for the constant volume (V) release the flow starts out as a conventional gravity current with a more-or-less constant velocity and apparently undergoes a transition to a buoyancy-inertia balance after approximatley 20 secs. It then asymptotes a constant value of x rather than undergoing a transition to a viscous-buoyancy balance as would have happened had this been a particle-free current. Similarly

[1]Of course the characteristics of particles are important. Of primary interest is the particle density ρ_p. However the size distribution is also critical. These can be combined also into the distribution of particle fall velocity. In what follows we use, mainly, one grade of carborundum powder (the 1000 grade) with the size distribution shown in figure 1c.

for the case of constant inflow (Q) the current starts out in a conventional fashion with $x \sim t$, but then undergoes a transition to a power law considerably less steep, at $n = 2/3$, than that of a current under a viscous buoyancy balance ($n = 4/5$) These manifestations of particle settling across the interface between current and ambient fluid can be explained, partially, by invoking a particle induced stress at that interface (see the section on theory which follows for specific details). This stress is due to the fact that the particles, as they settle through the interface, drag with them fluid of density ρ_I. This fluid mixes with the lower layer fluid essentially to the bottom of the tank. Its major effect can be seen in the last photograph (j) of figure 2 where we note that a gravity current made up of particles and fluid of density intermediate between ρ_I and ρ_a runs along the bottom of the tank. As particles continue to settle out of this current the light fluid is released and rises, to eventually form a continuous density distribution beneath the surface. This latter case has been considered separately by Huppert, Kerr, Lister and Turner (JFM 226, pp. 349–369) and Sparks, et al. (Earth and Planetary Sci. Lett. 114, 243–257) for example. Its major effect is to generate a flow in the layer between the two gravity currents that opposes the motion of the one of interest, i.e., the surface current. Thus the interfacial stress is due to the fact that particles and interstitial fluid (ρ_I) carry their momentum with them as they pass through the interface. If we assign a vertical velocity (v) to this transfer process then the stress is given by $\rho v U$, where U is a measure of the horizontal velocity in the current. Thus v becomes a crucial characteristic of the system. It can easily be seen that in the present cases where c, the particle concentration is small ($c \approx 0.01$), the major effect concerns the amount of interstitial fluid that is dragged across the interface and requires an independent measurement.

b) Measurement of interface flux due to sedimentation:

A limited number of experiments on the mixing due to sedimentation were carried out in a modified version of the tank (fig. 1b). A barrier was placed 65 cms from the tank end and the initial, constant-volume gravity-current allowed to contact it after a short time. Only a few moments were necessary to generate a horizontally uniform layer of particles and interstitial fluid. Sedimentation began and when the density at the interface exceeded the density of the lower fluid convection commenced. The system was allowed to run until all the particle had settled to the bottom. As before, a gravity current of particles and mixed fluid moved along the bottom of the tank and into the right hand compartment where the mixed fluid was released away from the original layer. Samples were taken from various depths of this layer using a specially designed nozzle that reduced contamination from fluid at other levels. The sample densities were measured to 5 decimal places using a specific gravity bottle. A typical result is shown in figure 5. From these data the density deficit could be found and compared to the initial deficit. The difference divided by the initial density difference ($\rho_a - \rho_I$) is a measure of the depth (δ) of interstitial fluid lost to the lower fluid.

$$\text{i.e.} \quad \delta = \Delta - \int_0^\infty \frac{\rho_a - \rho(y)}{(\rho_a - \rho_I)} \cdot dy$$

A number of experiments with different values of R_ρ and initial fluid depths were carried out.

The results are summarised on figure 6 for the limited number of experiments performed. As expected the loss of interstitial fluid is greater as $R_\rho \to 1$ and clearly there is an optimum value of the fluid depth between $h = 3.4$ and 6.7 cms. Unfortunately such measurements only give the overall mixing due to sedimentation and not the mixing rate. We have plans to extend the measurements to not only measure the final state but intermediate states as well. In this way we hope to be able to estimate the necessary fluxes.

Theory:

The similarity solutions of Huppert (JFM 121, 43–58) and Maxworthy (JFM 128, 283–322) can easily be extended to the present case. For an intrusion the volume of which varies with time as:

$$Lh \sim \tilde{q} t^{\alpha}$$

Where L is the intrusion length and h its height. Then a balance between buoyancy and the interfacial stress $\rho U v$ results in a spreading law:

$$L \sim \left(\frac{g' \tilde{q}^2}{v} \right)^{1/4} t^{\frac{(2\alpha+1)}{4}}$$

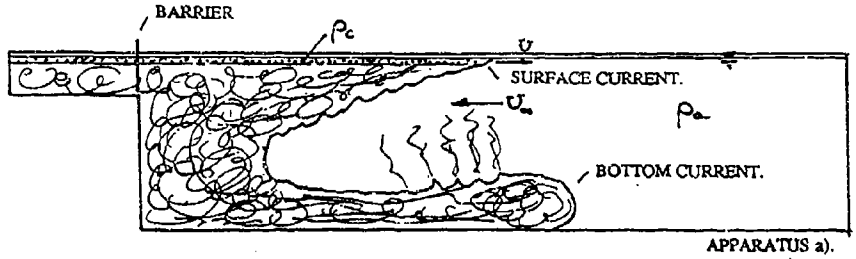
if there is no velocity in the outer flow. Here $g' = g(\rho_a - \rho_c)/\rho_a$. On the other hand if external forces (e.g., those due to the bottom boundary current) generate a flow (U_∞) to oppose the surface current then:

$$L \sim \left(\frac{g' \tilde{q}^2}{U_\infty v} \right)^{1/3} t^{2\alpha/3}$$

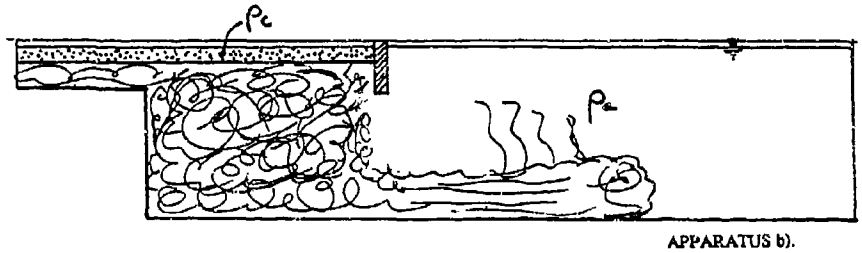
We note that for the case of a constant volume release, i.e., $\alpha = 0$, L tends to a constant value as has been found in the present experiments (figure 3). For a constant inflow, i.e., $\alpha = 1$, the similarity solution gives $L \sim t^{2/3}$. While such a result has been found in some cases, e.g., figure 4, often the slope is less steep than this suggesting that any of the quantities g', $\tilde{q}$ or U_∞ may perhaps have a power law behaviour in time as well due to the unsteady nature of the flow. There is, also, considerable merit to the idea of generating a more detailed computer model, but this reserved for the extended project.

Acknowledgements:

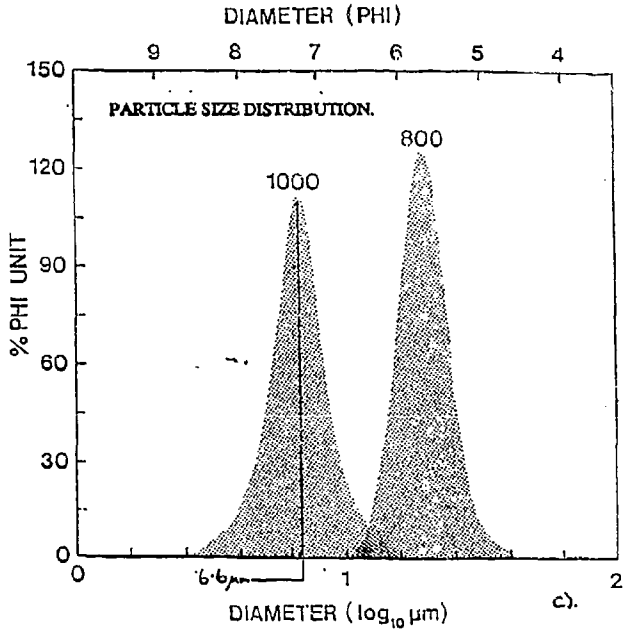
The work was performed while the author was visiting Professor H. E. Huppert, head of the Institute for Theoretical Geophysics at the DAMTP, Cambridge University. I extend my grateful thanks to him for arranging this visit, through a NERC grant, and for many useful and illuminating discussions. I thank, also, Mr. Mark Hallworth for taking time from his busy schedule to run the experiments that led to figure 1c. The invaluable design and construction skills of Mr. David Cheesley produced an apparatus that performed beyond my greatest hopes.



APPARATUS a).

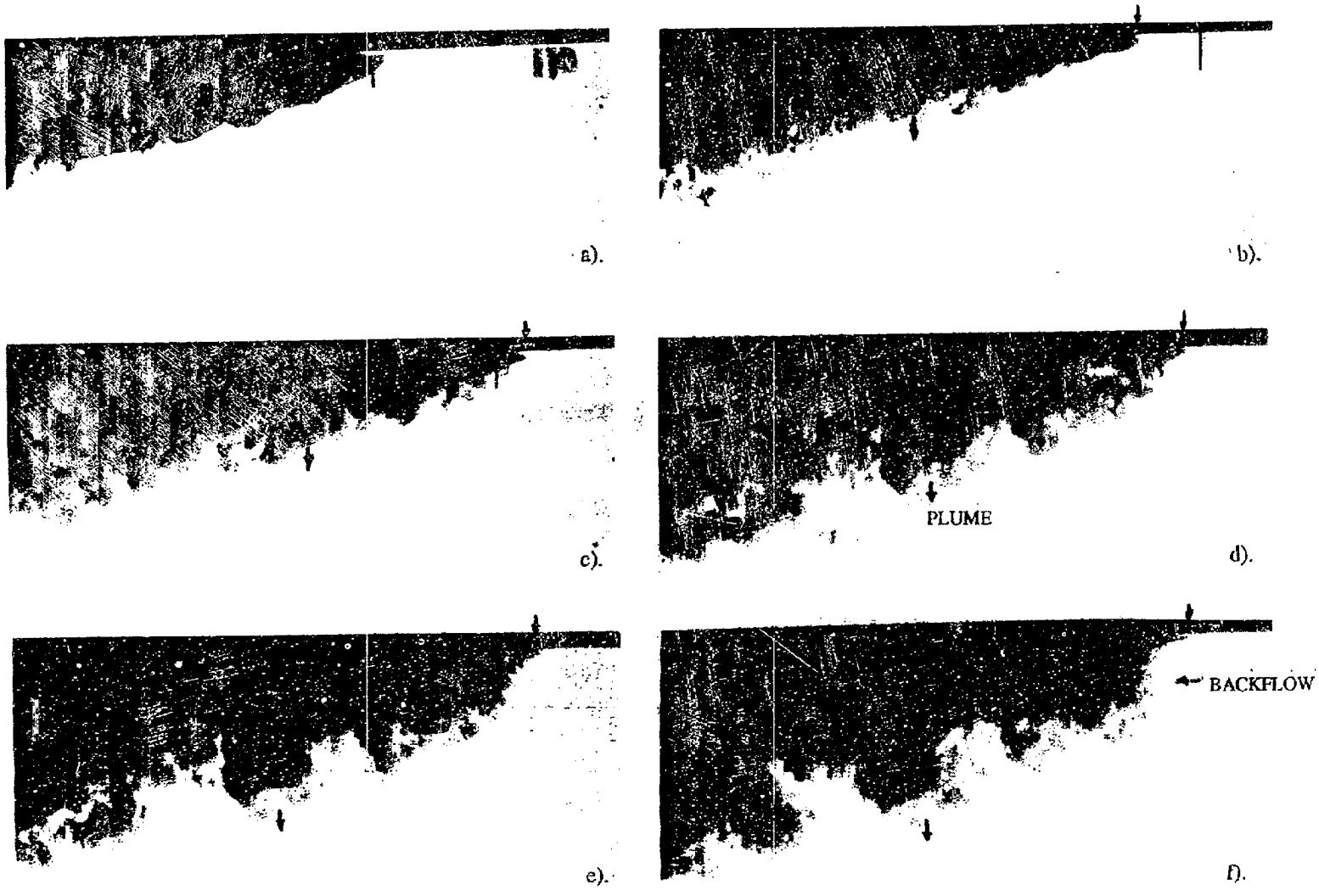


APPARATUS b).



c).

FIGURE 1.

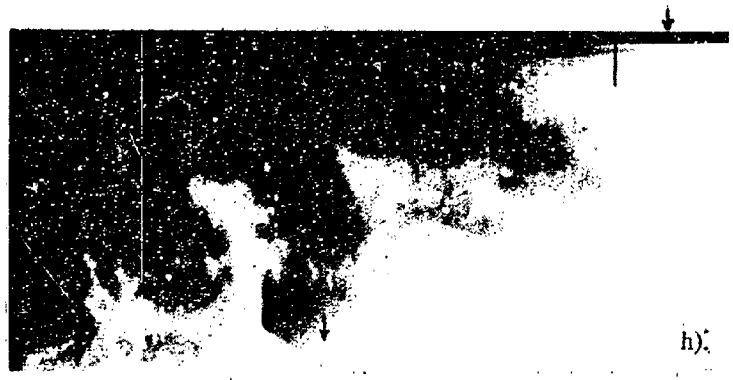


TEMPORAL EVOLUTION OF THE SURFACE CURRENT.

FIGURE 2.



g).



h).



i).

SURFACE CURRENT.



j).

BOTTOM CURRENT.

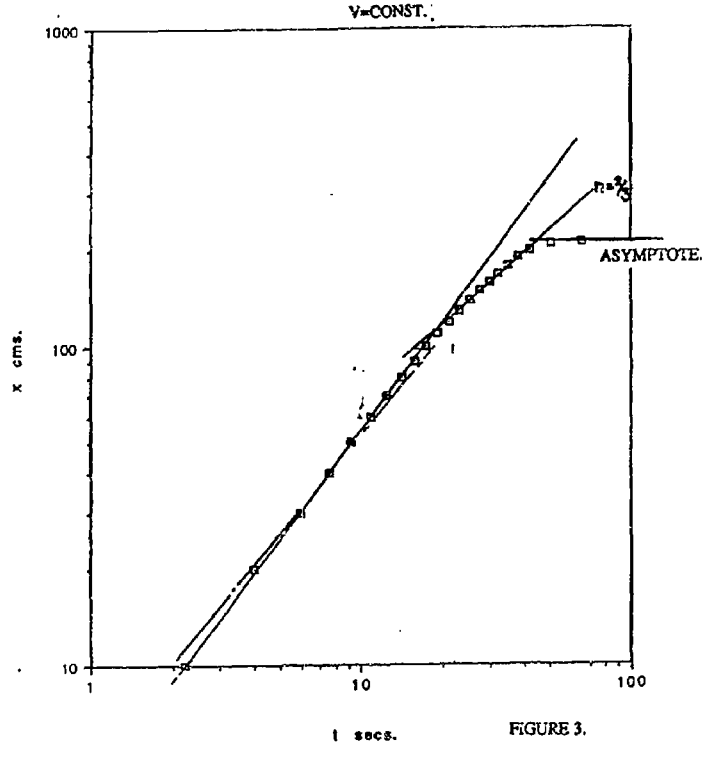


FIGURE 3.

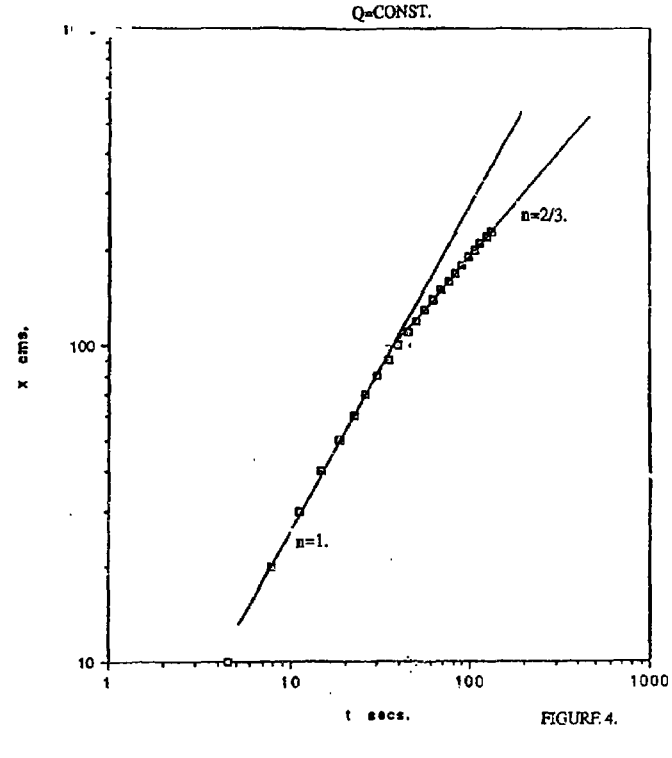


FIGURE 4.

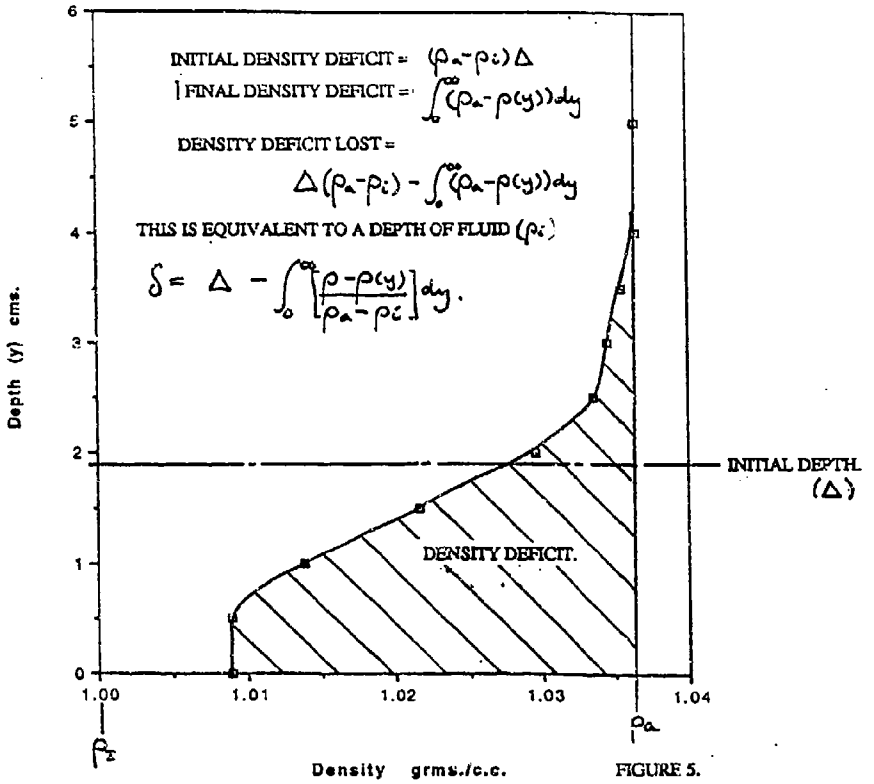


FIGURE 5.

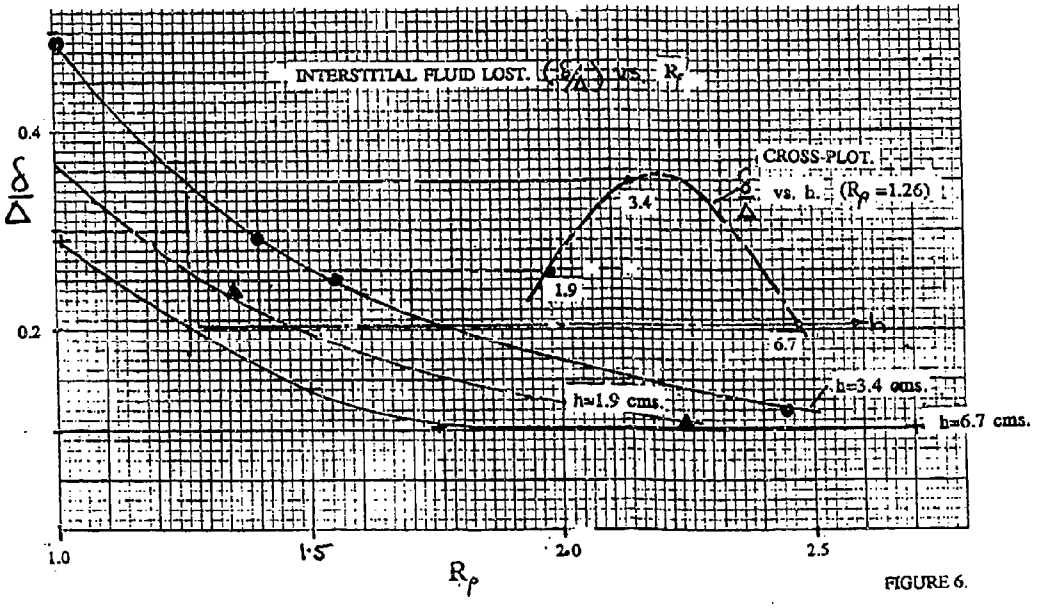


FIGURE 6.

The internal slab-collapse problem

J. Bühler*, S.J.Wright†, T.Dreier*

Abstract

A simple surface wave develops, for example, after a dam break in a reservoir. The wave lengthens as its upper edge travels into the reservoir, and the surface slopes gradually decrease. Steep slopes are maintained, however, in a region near the leading edge of the wave. This region is called a bore when the contents of the reservoir spill into a preexisting tailwater downstream of the dam, and a front when they spill onto a dry bed. The focus of the present contribution is on the corresponding two-layer flow, i.e. on the collapse of a fluid slab in another fluid of only slightly different density and of finite depth. Use is made of the fact that the interface along a simple internal wave advances with the local long wave speed, and of flow continuity. A general analytical solution for the shape of simple waves in inviscid Boussinesq flows is presented. Also, limits are outlined at which the interface of a simple wave becomes unstable. Experiments on the collapse of a slender slab of fresh water along the surface of a body of salt water were carried out, and the results for the shape of the collapse region are compared with the predictions.

Introduction

Simple waves and bores occur on the interface between warm surface water and cold bottom water in stratified reservoirs when the inflow rate suddenly increases or decreases (Fig. 1). Reasons for such a change of the inflow rate include emergency releases from an upstream reservoir or sudden floods, and the resulting interface level changes may affect the water quality at submerged intakes located along the reservoir.

While an increase of the inflow rate produces a bore which travels along the free surface of the reservoir, the corresponding internal wave may either steepen to form a bore as well, or it may gradually lengthen in time and propagate as a simple wave. Simple waves are also called rarefactions or negative waves, whereas bores are moving hydraulic jumps associated with energy dissipation.

Numerical solutions for the shape of simple internal waves in flows with small density differences (Boussinesq flows) were presented by Rottman and Simpson (1983) in their analysis of the lateral collapse of a slab of salt water beneath a body of fresh water, and by Kranenburg (1993) for intrusions of one fluid into another. A similar analysis is the one by Keller and Chyou (1991) for lock - exchange flows in ducts. Rottman

*Institute of Hydromechanics and Water Resources Management, ETH Hönggerberg, CH-8093, Zurich, Switzerland

†Dept. of Civil Engrg., The University of Michigan, Ann Arbor, MI. 48109

and Simpson (1983) also showed that an the interface becomes unstable when the slab thickness exceeds one-half of the water depth, and that this instability leads to the formation of a bore. Among the more recent concepts for the description of bores are those offered by Denton (1990), and by Keller and Chyou (1991). Other types of instabilities occur when the velocity difference between the two layers exceeds a limit depending on the flow depth (Long, 1956) or on the thickness of the more slender layer (Ellison and Turner, 1959). In this study an analytical solution for the shape of simple internal waves is derived. Experiments on the collapse of a slender slab of fresh water along the suerface of a body of saltwater are described, and the shapes measured shapes of the resulting simple internal waves are compared with predictions. The slabs extended over less than one-half of the water depth, in which case no bores develop.

Critical flow and simple waves

The present analysis is carried out for two-layer flows in a duct, as shown in Fig. 2, and the positive direction is towards the right. Ducted flows often involve considerable temperature and density differences, and the density terms will be retained in most of the results. In the Boussinesq limit the results will also be valid for flows with a free surface. Properties of the flow in the upper layer will be denoted by the index $i = 1$, and those in the lower layer by $i = 2$. Provided that the interfacial shear and the entrainment of fluid from one layer into the other can be neglected, the flow in each layer is then described by the fluid density ρ_i, as well as by the values of the layer thickness h_i and the velocity u_i at a given distance x along the duct and at time t. The corresponding discharge rate is $q_i = h_i u_i$. The throughflow rate $q = q_1 + q_2$ and the flow depth $h = h_1 + h_2$ are taken to be invariant along the duct and in time. The effective gravitational acceleration acting on the fluid is $g' = (1 - r)g$, where $r = \rho_1/\rho_2$.

It is convenient to examine gradually varying flows by using the fact that small disturbances on an interface travel at the phase speed λ of long interfacial waves of limiting amplitude. The flow in the frame of reference of such a disturbance is called critical, and the composite Froude number G^2 of the flow is equal to one. According to Armi (1986) and other authors the corresponding relation for a ducted flow is

$$\frac{r u_1^{*2}}{g' h_1} + \frac{u_2^{*2}}{g' h_2} = G^2 = 1 \tag{1}$$

The asterisk is used to denote quantities in the moving frame of reference, in particular, $u_i^* = u_i - \lambda$. In the special case that the density of the upper fluid can be neglected ($r \to 0, g' \to g$) the first term of the above equation vanishes, and the composite Froude number becomes equal to the square of the conventional Froude number for open channel flows. By solving the remaining statement for the phase speed of a disturbance on the free surface one obtains the familiar relation

$$\lambda = u_2 \pm \sqrt{g h_2} \tag{2}$$

where the upper sign applies to the leading wave field travelling at a speed λ^+ in the positive direction, and the negative sign to the trailing field moving at a lesser speed λ^-. A slightly different procedure can be used to solve the general form of (1) for the wave speeds. By noting that the throughflow velocity q/h is constant along the duct,

one may introduce $\lambda - q/h$ as a scale for the wave speed. Similarly, one may make use of the velocity difference $u = u_2 - u_1$ which is independent of the frame of reference ($u = u_2^* - u_1^*$). In dimensionless form, the resulting expression for the wave speeds is then

$$\Lambda - Q = \frac{U[(1-\xi)^2 - r\xi^2] \pm \sqrt{\xi(1-\xi)(\alpha - rU^2)}}{\alpha} \tag{3}$$

Here, $\xi = h_2/h$, $U = u/(g'h)^{1/2}$, $\Lambda = \lambda/(g'h)^{1/2}$, $Q = q/(g'h^3)^{1/2}$, and $\alpha = 1 - \xi(1-r)$. This result for ducted two-layer flows with small or large density differences was derived independently by Keller and Chyou (1991) and by Bühler et al. (1992).

For the further analysis of unsteady flows it is useful to consider a (moving) characteristic point defined by the intersection of the interface with a line at height h_2 above the floor, as the one marked by a filled circle in Fig. 2. An important feature of simple waves is that this point moves along the duct at the long wave speed λ, and that the flow through a cross-section moving with it remains time invariant. As a consequence, the velocity λ of the characteristic point is also a function of h_2 only, and not of time. In order to determine the variation of the velocity difference u between the two layers along a simple wave one may examine the change of the flowrate in the upper layer through adjacent characteristic cross sections. The flowrate in this layer through a characteristic cross-section moving at a velocity λ is $q_1^* = (u_1 - \lambda)h_1$. This flowrate exeeds that through an adjacent characteristic cross- section, which moves at a speed $\lambda + d\lambda$, by an increment which is equal to the rate $h_1 d\lambda$ at which light fluid is stored between the two cross-sections, and hence

$$\frac{d[(u_1 - \lambda)h_1]}{dh_2} = -h_1 \frac{d\lambda}{dh_2} \tag{4}$$

where both sides have been divided by the change dh_2 in the interface level from the first to the second cross-section. Similarly, one obtains

$$\frac{d[(u_2 - \lambda)h_2]}{dh_2} = -h_2 \frac{d\lambda}{dh_2} \tag{5}$$

for the lower layer.

The classical solution for the dam-break problem ($r = 0$) can be retrieved from (5) by eliminating u_2^* by means of (2), and by integrating the resulting expression. This leads to

$$\lambda - \lambda_0 = \pm 3g^{1/2}(h_2^{1/2} - h_{20}^{1/2}) \tag{6}$$

and a parabolic shape of the free surface. Here, h_{20} is the initial thickness of the slab. When the slab collapses towards the right and is initially at rest, u_2 is positive and $\lambda_0^- = -(gh_{20})^{1/2}$ is the wave speed on its upper surface.

Returning to two-layer flows, the variation of the velocity difference $u = u_2 - u_1$ along a simple wave can be derived from (4) and (5) as

$$\frac{du}{dh_2} = \frac{\lambda h - q + u(h_2 - h_1)}{h_1 h_2} \tag{7}$$

By nondimensionalizing this expression and using (3) one obtains

$$\frac{dU}{d\xi} = \frac{1}{\alpha}\left(\pm\sqrt{\frac{\alpha - rU^2}{\xi(1-\xi)}} + U(1-r)\right) \tag{8}$$

Rottman and Simpson (1983), Kranenburg (1993), as well as Keller and Chyou (1991) derived their relations for the change of the flow along simple interfacial waves from the inviscid shallow water equations. Keller and Chyou's relations are for ducted non-Boussinesq flows and can be shown equivalent to (8). There are a number of substitutions that convert (8) into standard forms of the Abelian differential equation of the first kind, but no general analytical solution was found. For the special case of Boussinesq flows, i.e. when r and α both approach a value of one, the variables can be separated. By substituting $U = sin(\phi)$ and $\xi = [1 + sin(\theta)]/2$, (8) can then be written as

$$d\phi = \pm d\theta \tag{9}$$

where the upper sign still applies for the leading wave system and the negative sign to the trailing system. After integrating from starting points ϕ_0 and θ_0, we obtain in terms of the original variables

$$U = sin\{arcsin(U_0) \pm [arcsin(2\xi - 1) - arcsin(2\xi_0 - 1)]\} \tag{10}$$

where the sign convention is the same as for (9). Fig. 3 represents two solutions generated from (10) for simple waves which are due to the collapse of slender slabs of fluid along the surface of a body of somewhat denser fluid (solid curves). To facilitate the physical interpretation of the curves the vertical axis is the one representing the interface level, i.e. the independent variable. The direction of the collapse is towards the left and associated with the leading wave, such that the velocity difference u across the interface is positive and the positive sign in (10) applies. Curves are drawn for two slabs of different thickness $1 - \xi_0$. The slab interfaces are initially at $\xi_0 = .5$ and $\xi_0 = .75$, and all fluid is initially at rest ($U_0 = 0$). These initial conditions are marked by solid circles in Fig. 3. For the thicker one of the two slabs (10) degenerates, and the corresponding curve is a straight line. The speed λ at which a characteristic point moves along the duct can now be obtained by setting $r \to 1$ in (3) and by combining the result with (10), or by evaluating the corresponding expressions in ϕ and θ. Results for zero throughflow ($Q = 0$) are shown in Fig. 4. Again, the same two starting points ξ_0 with $U_0 = 0$ are chosen as in Fig. 3, and marked by filled circles. The curves for Λ^+ starting at these points also reflect the shape of the simple wave since the distance x which a characteristic point has travelled along the duct in a time t after release is λt, and thus proportional to the interface velocity Λ at any height ξ. To emphasize the fact that the left end of the slabs collapses, a small part of the remaining horizontal slab surface is shown just to the right of the starting point. It should be mentioned here that the shape of the interface near the point where it meets the free surface is not realistic. The reason is that the shallow water equations do not account for a stagnation point which is present at the tip of the collapsing region. This stagnation point produces a blunt front, which was considered by Kranenburg (1993) and other investigators of simple waves (see also Fig. 5).

Finally, the interface curves for slender dense slabs collapsing to the along the bottom, as the one shown in Fig. 2, are symmetrical to those shown here about the horizontal axis at $\xi = 0.5$.

Instabilities

Rottman and Simpson (1985) noted that for slabs thicker than one-half the water depth the maximum of the interface speed does not occur at one of the end points of the corresponding simple wave, but somewhere along it. This leads to the formation of a bore, a region of rapidly varying flow which is associated with energy dissipation. Stable simple waves are thus only possible over parts of these curves which do not include a minimum. The value of U at the maxima of the interface curves, for ducted flows was derived by Bühler (1994), and for Boussinesq flows it is

$$U = \mp(2\xi - 1) \tag{11}$$

where the negative sign applies for the leading wave field. The corresponding relation does not intersect with the two curves in Fig. 3, so that no bores are expexted on the interface, and the only point which is included in (11) is the lower one of the filled circles in Fig. 3. Long (1956) showed that a second type of instability arises when the long wave speeds become imaginary, i.e. when the expression in the root of (3) becomes negative. For Boussinesq flows this occurs when $U > 1$. Fig. 3 shows that this instability is not relevant for the flows under consideration. Interfacial instability is also possible at shorter wavelengths and entails local mixing of the two fluids near the interface. Ellison and Turner (1959) suggested that mixing is largely absent when the bulk Richardson number of a gravity current is less than about 0.8. For the case considered here this means that no mixing is expected when

$$U^2 < 1.25(1 - \xi) \tag{12}$$

This limit is also shown in Figs. 3 and, by making use of (3), in Fig. 4.

Experiments

The solutions (3) and (10) are based on the inviscid shallow water equations, and it is of interest how much the interface is changed by mixing and other real fluid effects. To provide a basis for such comparisons, two experiments were carried out for slender slabs extending over less than one half the water depth. The fluid was contained in a glass-walled tank $3m$ long, $0.25m$ wide, and $0.55m$ deep. A removable vertical gate was installed at $1.76m$ from the right end of the tank. A gap was left between the lower end of the gate and the bottom of the tank. To run an experiment the tank was filled with slightly salty water to a depth of $0.336m$. For the first experiment the density of the salt water was $\rho_2 = 1006.1kg/m^3$, for the second one $1005.1kg/m^3$. Fresh water ($\rho_1 = 999.75kg/m^3$) containing some dye was carefully and slowly released onto the water surface on the right side of the gate until the total water depth was $0.48m$. In the absence of mixing this procedure would have led to a sharp interface at $\xi_0 = 0.54$. Finally, some detergent was released on the surface to the right of the gate to reduce the surface tension and the height of the frontal region of the collapsing slab. The gate was then removed to start the flow. Still pictures of the advancing wave were taken at intervals of $1.5s$ until the front was reflected at the wall, and started interfering with the flow in the region of interest. Fig. 5 is a picture of the flow in experiment 2, and at $t = 17.5s$ after the release. It was taken against a semitransparent paper illuminated from behind, and shows the remaining part of the initial slab interface on the right at

a level of $\xi_0 = 0.52$. The simple wave starts further to the left, and ends in a front. The initial location of the retaining gate at $x = 0$ is marked by a vertical arrow. The results for both experiments, and at 20.5s after the release are shown in Fig. 4. One rather striking result is the hump just to the left of Ellison and Turner's limit (12). The hump is also visible in Fig. 5, and appears to be a remnant of large structures near the lower fringes of the frontal region, which is gradually left behind and grows in size. An influence of standing surface waves on the evolution of the hump is unlikely as the time scales of the two motions are quite different. Another noteworthy feature of the results is the slope of the interface near the point $0.5, 0, 5$. At this point a maximum of the interface speed is reached according to (11), and the interface slope should be infinite, while the experimental data suggest a moderate slope. This discrepancy reflects the weakness of the shallow water concept in locations where the flow is, or should be, rapidly varying.

Conclusions

An analytical solution for the shape of simple waves in two-layer flows is presented. Solutions for the shape of these waves are based on the inviscid shallow water equations, and experiments were carried out to determine errors caused by the underlying simplifying assumptions. The results for the collapse of a slender slab of fresh water along the surface of a body of salt water (Fig. 5) agree reasonably well with predictions (Fig. 4), except that the real interface does not show abrupt changes in slope, and that a growing disturbance was observed in a region where interfacial mixing can be expected.

References

Armi, L., 1986 The hydraulics of two flowing layers with different densities. J. Fluid Mech., Vol. 163, pp. 27 - 58.

Bühler, J., Wright, S.J., Kim, Y., 1992 Source control of intrusions along horizontal boundary. Jour. Hyd. Eng. Vol. 118, No. 3, pp.442 - 459.

Bühler, J. 1994 Simple internal waves and bores. Jour. Hyd Eng., Vol. 120, No. 5.

Denton, R. A. 1990. Accounting for density front energy losses. Jour. Hyd. Eng., Vol. 116, No.2, 270-275.

Ellison, T.H., Turner, J.S. 1959 Turbulent entrainment in stratified flows. J. Fluid Mech. Vol. 6, 423 - 448.

Keller, J.J., Chyou, Y.-P. 1991 On the hydraulic lock - exchange problem. Zeitschrift f. angew. Math. und Physik, (ZAMP). Vol. 42, No. 6, pp. 874-910.

Kranenburg, C. 1993 Unsteady gravity currents advancing along a horizontal surface. Jour. Hyd. Research, Vol. 31, No. 1, pp. 49 - 60.

Long, R.R. 1956 Long waves in a two fluid system. Jour. Metereology, Vol. 13, 70 - 74.

Rottman, J.W., Simpson, J.E., 1983 Gravity currents produced by instantaneous releases of a heavy fluid in a rectangular channel. J. Fluid Mech. Vol. 135, pp. 95 - 110.

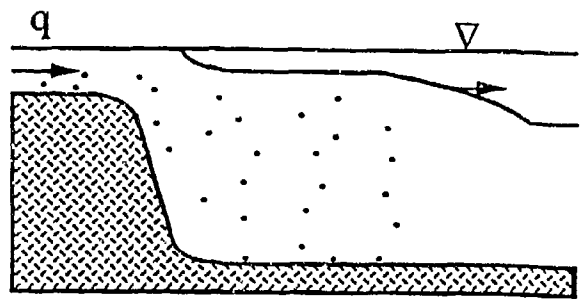


Fig. 1 Simple internal wave due to a sudden inflow into a reservoir

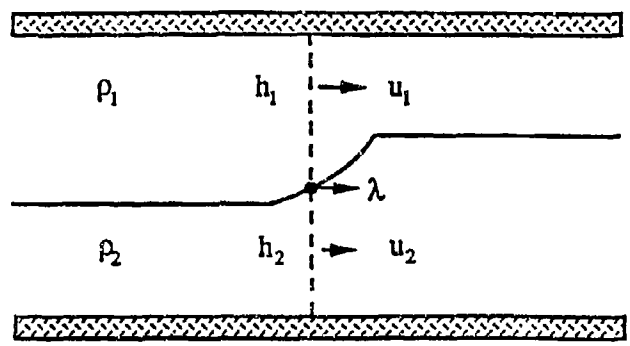


Fig. 2 Unsteady two - layer flow in a duct

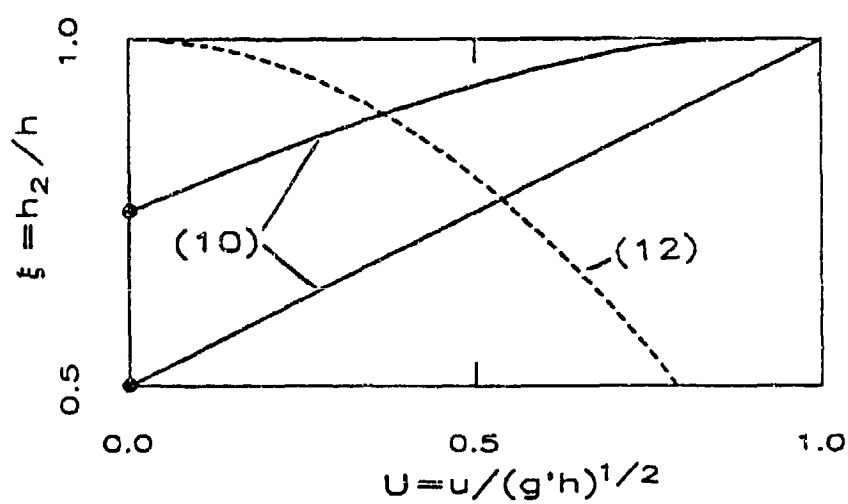


Fig. 3 Velocity difference u across the interface of two slender fluid slabs collapsing along a free water surface. Filled circles represent the initial conditions.

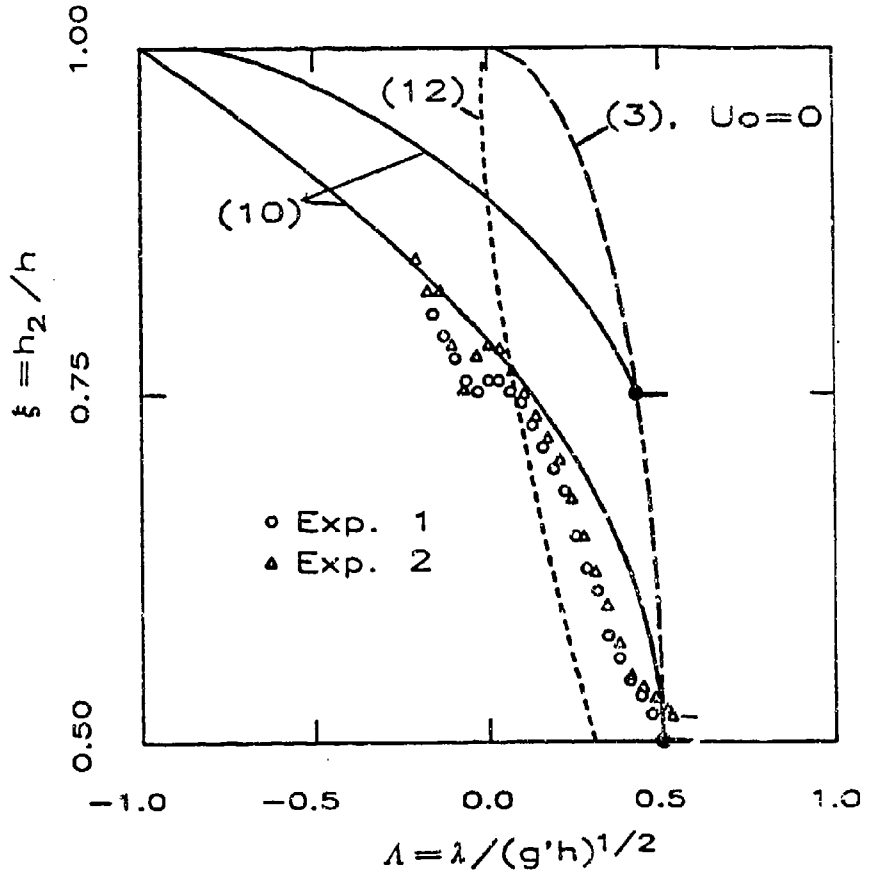


Fig. 4 Velocity λ of the interface, reflecting the shape of the collapse region

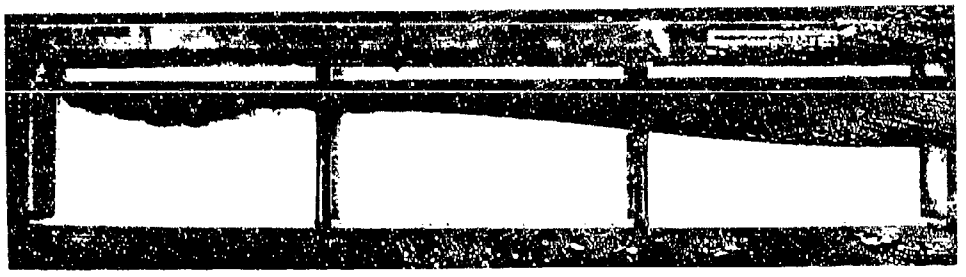


Fig. 5 Collapse of a slender slab of freshwater in a body of saltwater. The arrow marks the position of the retaining wall before its removal.

EXPERIMENTS ON 3-D TURBULENT DENSITY CURRENTS

G.C. Christodoulou and F.E. Tzachou
Department of Civil Engineering
National Technical University of Athens, Greece

Abstract

Experimental results from an on-going research program on 3-D density currents are presented. The experiments were conducted in a large laboratory basin so as to achieve rather large Reynolds numbers and avoid interference with side or end walls. Results from visual observations obtained via photographic records for four different bottom slopes between 5° and 15° are presented in non-dimensional form and discussed in comparison to earlier investigations. It is found that in most cases the current attains a nearly constant width, with minimal further growth. This width is proportional to a length scale expressed in terms of the initial buoyancy flux and density difference, with no influence of the initial width, the coefficient of proportionality being dependent on the bottom slope.

1. Introduction

The behaviour of 3-D steady density currents on a sloping bottom has been little studied so far, despite considerable work on 2-D currents. In a recent review, Alavian et al [2] state that 3-D currents attain an equilibrium condition given by linear increase of depth and lateral width, and a constant normal Richardson number. Yet, experimental evidence from available previous studies yields widely different estimates of the rate of spread of such currents, ranging from nearly 0° to nearly 90°.

Fietz and Wood [5] were the first to conduct an experimental study of 3-D currents: they used a small tank 1.2x0.9 m and placed the dense inflow near the wall, therefore they recorded the development of half of the current field. They observed that turbulent currents spread almost linearly, at angles ranging between 30° and 84°, depending on the initial Richardson number, and always considerably larger than respective laminar currents. Reliance on these conclusions, however, is doubtful due to the severe wall effects. Hauenstein and Dracos [6] investigated the phenomenon of plunging 3-D currents in a large basin 10x6 m and proposed an integral model based on the concept of a radial source of buoyancy. They found out that the assumption of linear growth of the current's lateral boundaries was not satisfactory. Alavian [1] presented limited experimental results obtained in a 2 m long tank and suggested that 3-D currents tend to attain a normal state with a constant Richardson number, where the depth and width of the current remain nearly constant, their subsequent growth depending only on the (small) entrainment rate. Tsihrintzis [7] presented more extensive results obtained in the same experimental facility leading to the same conclusion; he also distinguished three flow regimes, i.e. laminar, transitional and turbulent. According to his results the generation of turbulent currents requires at the inlet Reynolds numbers in excess of about 1000. The evolution of 3-D currents was also studied numerically by Tsihrintzis [7] and Tsihrintzis and Alavian [8]. Christodoulou [3] attempted to generalize in non-dimensional form Alavian's [1] results concerning the normal width.

The objective of the present study is a systematic examination of the basic characteristics of 3-D currents by means of extensive experiments in a large experimental basin, so that (i) Reynolds numbers are sufficiently high for turbulent flow to occur in most cases and (ii) interference with side or end walls is avoided. The

experimental study is supplemented by theoretical model development, extending previous investigations. In this paper, results concerning plume growth as obtained through photographic records are presented and discussed.

2. The Experiments

The experiments were conducted in the Applied Hydraulics Laboratory of the NTU of Athens, in a large basin 7 m long, 5 m wide and 0.7 m deep. One of its sidewalls was made of plexiglass, allowing a side view of the flowing current. The dense fluid was supplied through a small channel and released at the top edge of a metal slab which was positioned inside the basin at the desired slope. The slab consisted of corrugated steel sheets which were placed together and properly supported on aluminum legs so as to form flat rigid surfaces 4 m wide and 2 m long. By adjusting the height of the supporting legs, the slope of the slab could be varied. For small slopes a second 2 m long slab was added, so that the total length was 4 m. Before placement the slabs were painted white and had a 10x10 cm grid drawn on them, to facilitate visual observation.

The dense fluid consisted of a saltwater solution which was well mixed to the desired density, measured at the beginning and end of each experiment to an accurancy of $\pm$ 0.001 gr/cm^3. The saltwater solution was supplied to the inflow channel from a nearly constant head tank through a plastic pipe equipped with vanes for controlling the flow and with a specially designed orifice meter, connected to a precalibrated carbon tetrachloride differential manometer for flow measurement. Before each run, the basin was slowly filled with tap water, and allowed to rest for more than one hour to avoid residual ambient circulation. Then the dense fluid was introduced from the inflow channel onto the bottom slab. Preliminary runs indicated that 1 to 3 minutes were required for the dense front to travel the entire slab length depending on the bottom slope, slab length and initial discharge; therefore, colour was injected after the respective time, so that the behaviour of the desired steady part of the current was observed. The colour was supplied through a separate reservoir and a series of photographs were being taken from a moving platform suitably located at 6 m above ground level. The colour consisted of a kalium permanganate solution and its flowrate was taken into account in the value of initial discharge, being of the order of 5% of the dense inflow.

Figure 1 shows schematically the experimental setup. Excluding preliminary runs, a total of 63 experiments were carried out in four series, corresponding to different bottom slopes, i.e. 15°, 10°, 7.5^o and 5°; further experiments on a 2° slope are presently underway. Table I presents a summary of the experiments, indicating the range of parameters examined. For comparison, available similar data from previous studies are also shown.

3. Results and Discussion

Figures 2 and 3 show samples of the photographs taken, which illustrate consecutive stages of the coloured dense plumes. Analysis of the photographic records allows quantitative estimates of the longitudinal velocity on the axis u(x), and the width of the current, b(x). The thickness of the current, h(x), was observed only qualitatively by side view of the coloured plume in selected runs. In general it was seen that the current upon entrance to the basin undergoes a rapid lateral spreading and at the same time a severe reduction of height, in a way resembling the plunging phenomenon. Further downstream, the current height changes only slightly, whereas the width continues to increase significantly, but at an ever decreasing rate. In the experimental series carried out on the 2 m long slab it was often not clear whether a "normal" width has been reached by the end of the slab, i.e. a width with slight (approaching zero) linear further growth. In the experiments carried out on the 4 m

long slab it was evident that such a normal width condition was indeed reached at a distance usually 2.0 to 2.5 m from the origin: specifically, the increase of width db/dx beyond this distance was estimated at 0.1 or less.

Previous research [1,7] suggests that the increase of width at the normal stage of the 3-D current should be related to the entrainment rate, as follows:

$$db/dx = 3E \qquad (1)$$

where E depends on the normal Richardson number Ri_n. To an order-of-magnitude approximation, the value of Ri_n may be obtained as [1,2]:

$$Ri_n = c_d/(c_i \tan\theta) \qquad (2)$$

where c_d is the bottom friction factor, c_i is a shape factor and θ is the bottom slope. In the present experiments on a smooth bottom, a value of c_d of the order of 0.01 was found appropriate. Therefore, using $c_i = 0.75$ [1], and for $\theta = 5^o$ to 15°, the range of Ri_n is, approximately, $Ri_n = 0.15$ to 0.05. According to Christodoulou [4], the entrainment rate for $Ri_n<1$ may be estimated by

$$E = 0.007\ Ri_n^{-1/2} \qquad (3)$$

Therefore, for Ri_n between 0.15 and 0.05, the respective range of E is E = 0.018 to 0.031. Consequently, based on eq.(1), the predicted rate of increase of the width is at most 0.1, i.e. of the same order as experimentally found, taking into account the accuracy of the method used. While the detailed analysis of the records is still in progress, the width of the plume at the beginning of small linear increase as discussed above was considered as the "normal" width b_n. It was attempted to correlate this normal width to the initial width of inflow, b_o, or to other flow variables. By comparing results with $b_o = 5.0$ cm and $b_o = 2.8$ cm it became clear that b_n does not depend on the initial width; instead, b_n correlates very well with the buoyancy flux and the initial density difference. Through dimensional considerations, the following expression was established:

$$b_n / (B^2/g'^3)^{1/5} = K \qquad (4)$$

where $g' = g\Delta\rho_o/\rho$ is the effective intensity of gravity based on the density difference of inflow ($\Delta\rho_o$), and $B = g'Q$ is the buoyancy flux.

Figure 4 shows the correlation of experimental data with eq.(4). Despite the experimental scatter, it may be seen that eq.(4) represents well all experiments, with a different value of the constant K for each bottom slope. The value of K, determined by least-squares analysis, is found to increase with decreasing bottom slope, as follows:

$\theta = 15^o$	K = 33.5	(5.1)
$\theta = 10^o$	K = 36.4	(5.2)
$\theta = 7.5^o$	K = 39.8	(5.3)
$\theta = 5^o$	K = 45.0	(5.4)

It is to be noted that even experiments with relatively small Reynolds numbers, which may conceivably belong to the transitional or even laminar regime, are also well described by the above general expression, within the observed experimental scatter. Besides, in Fig 4 the experimental data of Alavian [1] are included, which clearly represent laminar currents. Those data are also in fair agreement with the proposed expression.

It may therefore be concluded that the width b_n at the beginning of the normal state of a 3-D current on a smooth surface depends uniquely on the length scale $(B^2/g'^3)^{1/5}$ and the bottom slope; the initial width, b_o, has no influence as long as it remains small, i.e. $b_o<(B^2/g'^3)^{1/5}$.

4. Conclusions

Results are presented from an experimental investigation of mostly turbulent 3-D density currents, carried out in a large laboratory basin. Analysis of photographic records tends to support earlier evidence about the attainment of a normal state, in which the current dimensions grow only marginally. The current width at the beginning of the normal state is found to depend mainly on a length scale consisting of the buoyancy flux and the effective gravity, as given by eq. (4). The constant K depends on the bottom slope but not on other experimental variables in the ranges studied. Further work on the behaviour of 3-D currents is in progress.

Acknowledgment

This study was supported by a research grant from the General Secretariat of Research and Technology of the Hellenic Ministry of Industry, Research and Technology.

References

1. Alavian V., "Behavior of density currents on an incline", J. Hydraulic Engrg., ASCE, Vol 112, No 1, Jan 1986, 27-42

2. Alavian V., Jirka, G.H., Denton, R.A., Johnson, M.C. and Stefan, H.G., "Density currents entering lakes and reservoirs", J. Hydraulic Engrg, ASCE, Vol. 118, No 11, Nov. 1992, 1464-1489

3. Christodoulou, G.C., "Dilution of dense effluents on a sloping bottom", J. Hydraulic Research, Vol 29, No 3, 1991, 329-339

4. Christodoulou, G.C., "Interfacial mixing in stratified flows", J. Hydraulic Research, Vol 24, 1986, 77-92

5. Fietz, T.R. and Wood, I.R., "Three dimensional density current", J. Hydraulics Div, ASCE, Vol 93, No HY6, Nov. 1967, 1-23

6. Hauenstein, W. and Dracos, Th., "Investigation of plunging density currents generated by inflows in lakes", J. Hydraulic Research, Vol 22, No 3, 1984, 145-156

7. Tsihrintzis, V.A., "Theoretical and experimental investigation of three dimensional boundary-attached gravity currents", Ph.D. Thesis presented at the University of Illinois at Urbana-Champaign, U.S.A, 1988

8. Tsihrintzis, V.A. and Alavian, V., "Mathematical modeling of boundary attached gravity plumes", Proceedings Intern. Symposium on Buoyant Flows, Frame Publ. Co, Athens, 1986, 289-300

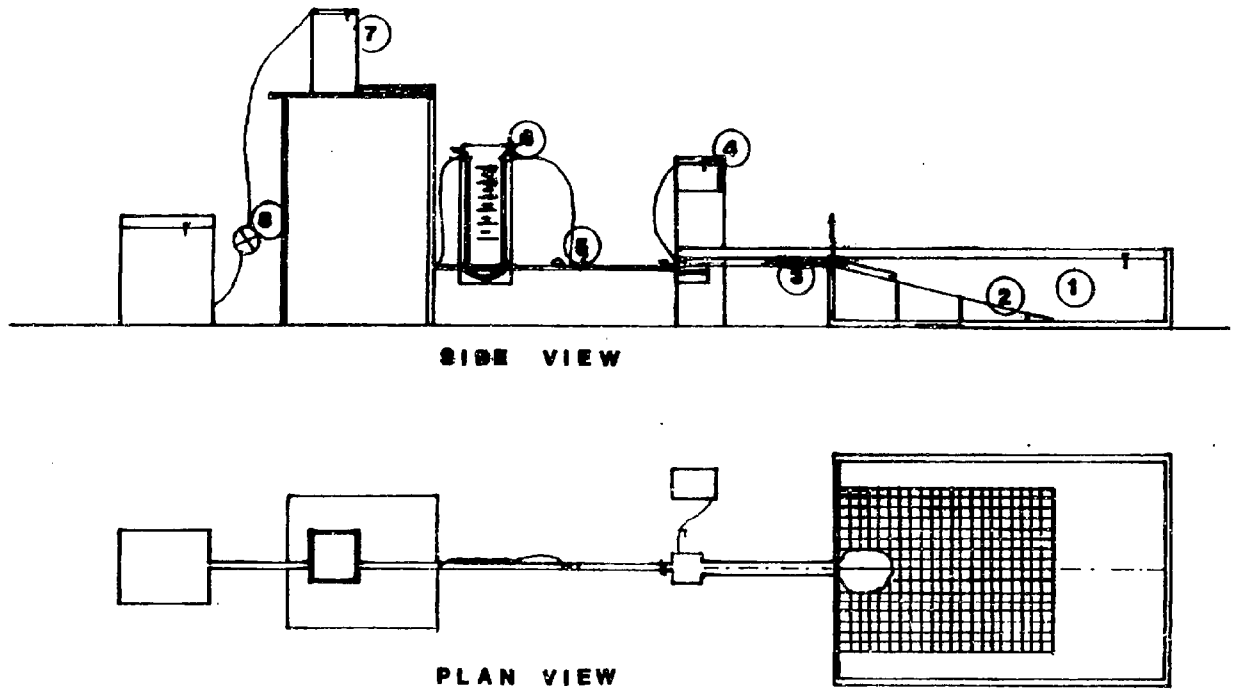


Figure 1. The experimental setup

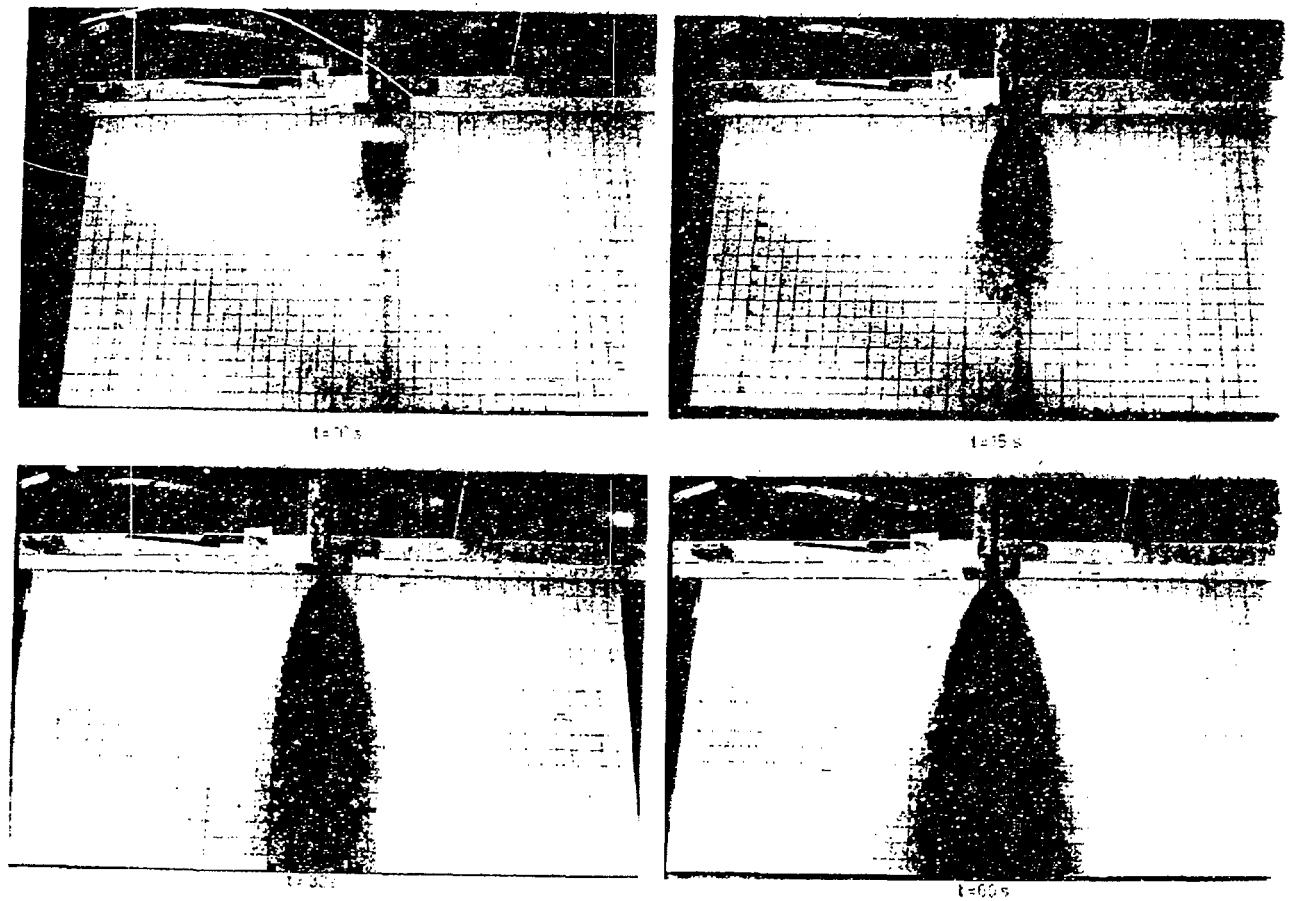


Figure 2. Views of a density current on a 15° slope at various times after the injection of colour; $Q=51{,}2\ cm^3/s$, $\Delta\rho_o/\rho=0.030$, $B_o=1506\ cm^4/s^3$, $Re_o=1024$



Figure 3. Views of a density current on a 5°slope at various times after the injection of colour; $Q=100cm^3/s$, $\Delta\rho_o/\rho = 0.030$, $B_o = 2943\ cm^4/s^3$, $Re_o = 2000$

Table I: Range of basic parameters

Study	No of runs	$\Delta\rho_o/\rho$ (‰)	Q_o (cm^3/s)	B_o (cm^4/s^3)	Re_o	Ri_o
Present	63	5-32	25-200	245-6121	500-7143	0.014-1.05
Alavian [1]	3	4	2.4-14.9	9.4-58.5	55-390	0.15-5.9
Tsihrintzis [7]	75	2.1-14.7	3.5-33.2	12-140	38-5533	10^{-4}-8.5
Fietz&Wood [5]	22	10-85	4.8-39	50-3194	1800-14900(*)	$2.6.10^{-4}$ -$10.7.10^{-4}$(*)
Hau+Dracos [6]	-	1-25	240-3850	$280-16.10^4$	-	-

(*) Based on the hydraulic radius

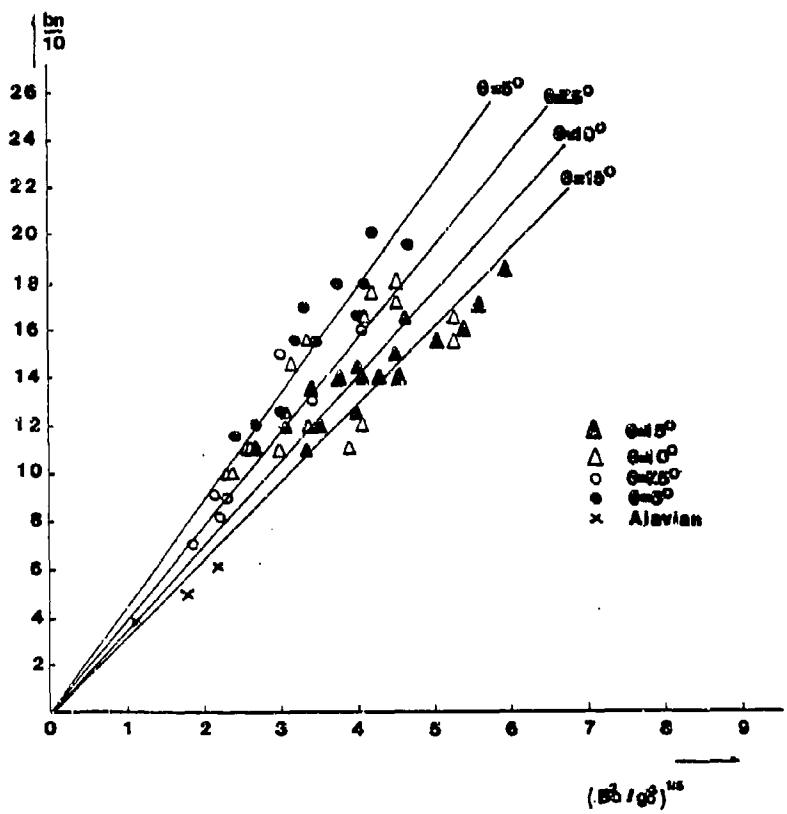


Figure 4. Correlation of the normal width with the buoyancy-based length scale (eq.4)

MIXING AT THE FRONT OF GRAVITY CURRENTS

Marcelo H. García and Jeffrey D. Parsons
Department of Civil Engineering
University of Illinois at Urbana-Champaign
Urbana, Illinois 61801, USA

INTRODUCTION

Mixing at the front of a gravity current such as a saline flow or a turbidity current depends on two main processes. They consist of (a) Kelvin-Helmholtz billows which roll up in the region of velocity shear above the front of the dense current, and (b) a complex shifting pattern of lobes and clefts which form near the bottom at the lower part of the leading edge (Simpson, 1987). It has been suggested that mixing at the front of turbidity currents plays an important role on the dynamics of such flows, regulating their capacity to transport sediment for long distances as well as the characteristics of the sedimentary structures that they generate along their path (Allen, 1971). However, our present ability to quantify the impact of frontal mixing on the dynamics of dense bottom currents is quite limited. Probably the main reason for the limited amount of data obtained through laboratory experiments and field work is the unsteady nature of the phenomenon under consideration. The fact that a current front is continuously moving as the flow evolves with distance, renders the measuring of its internal structure a very difficult task, both in the laboratory (Altinakar et al., 1990) and in nature (Hay et al, 1982). If the issue of unsteadiness could be resolved, the potential for obtaining quantitative data and detailed observations on fluid-sediment dynamics would be vastly increased. This has motivated the experiments reported herein, which are part of a long-term program to study the dynamics of gravity currents in continental shelves and slopes.

EXPERIMENTAL APPARATUS

An experimental tank specially designed to freeze the motion of unsteady gravity current fronts was constructed for the experiments. The tank is similar to but larger than the one used by Simpson and Britter (1979). A schematic of the facility is shown in Figure 1. The apparatus includes: a channel fabricated with clear Plexiglass having a moving conveyor-floor portion and a fixed-bed portion, a headbox with flow conditioners, a tailbox reservoir with an adjustable weir, a sediment-water mixing reservoir with a constant-head tank, two pumps, valves and piping with flow meters, and a supporting structure. The working channel is 300 cm long, 30 cm wide, and 50 cm deep. The upstream end of the channel has a 150 cm long "moving bed" conveyor floor. The belt speed can be varied from virtually no motion up to 20 cm per second. Downstream of the conveyor belt, a 75 cm long portion of the 150 cm long fixed-bed region of the channel has a false floor that allows for placement of a sediment bed to enable erosion studies. A sliding slot valve is installed at the downstream end of the flume to regulate the flow of dense fluid. A 2500 liter working capacity reservoir is used to prepare the dense fluid by mixing salt or sediment with water. A pump conveys the dense fluid to a 500 liter constant head tank from were it is delivered at a controlled rate to the slot valve. A broad crest weir mounted just behind the slot valve, regulates the water depth along the working channel anywhere from 10 cm up to 48 cm. The water that flows over the weir goes into a tank with a 2000 liter capacity from were it is pumped back to the upstream end of the channel. The flow rates of dense fluid and fresh water are monitored with the help of Venturi flow meters.

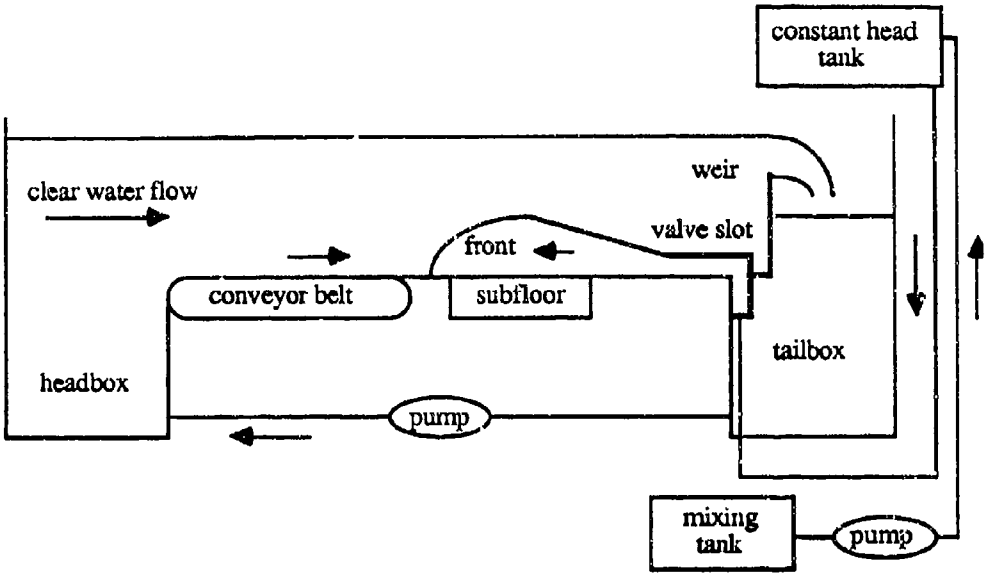


Figure 1. Schematic of experimental apparatus (not to scale)

EXPERIMENTAL TECHNIQUE

In this set of experiments only conservative saline currents have been studied. Their behavior can be expected to be quite similar to that of turbidity currents laded with very fine sediment (Garcia, 1993). The experiments were started by setting the conveyor belt to a desired speed and by adjusting the discharge of fresh water over the weir and the weir height so as to produce a mean flow velocity in the channel equal in direction and magnitude to that of the belt (i.e. slip velocity condition). Dense water, previously prepared in the mixing tank by adding salt, was then introduced through the slot valve at a measured rate, thus creating a density current. The discharge of dense fluid was varied until reaching a steady state in which the current front was arrested just in front of the end of the conveyor belt but still on the fixed-bed portion of the channel. At this point the front characteristics were measured. Such equilibrium configuration inhibited the formation of lobes and clefts near the bottom at the lower part of the leading edge and isolated the effect of the Kelvin-Helmholtz billows at the upper edge of the density current front.

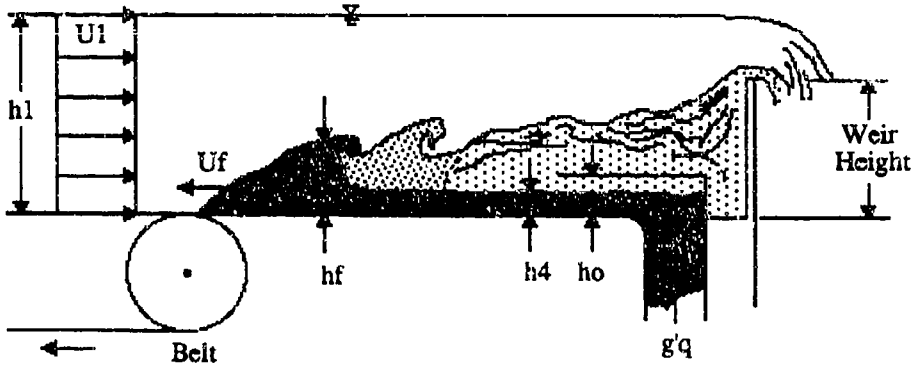


Figure 2. Definition diagram

EXPERIMENTAL RESULTS

Main results of the experiments conducted are presented in Tables 1a and 1b. Other data (e.g. aspect ratios) can be calculated from the data given in the tables, but were not included for the sake of brevity.

Exp. Number	Reduced Gravity g' (cm/s^2)	Weir Height (cm)	Body Height h4 (cm)	Front Velocity U1 (cm/s)	Flow Depth h1 (cm)
1	11.77	30	4.0	9.03	38.97
2	11.77	30	3.5	7.57	38.05
3	17.66	30	3.0	9.41	39.09
4	13.73	30	3.5	9.89	39.37
5	19.62	30	2.0	10.22	39.40
6	15.70	38	2.5	8.88	46.84
7	9.81	38	3.3	8.30	46.67
8	7.85	38	4.5	8.59	46.91
9	29.43	22	3.0	9.50	29.20
10	28.45	22	2.5	10.44	29.75
11	26.49	22	2.4	11.39	30.79
12	25.51	22	4.5	12.33	30.91
13	29.43	22	3.4	11.72	30.33
14	29.43	22	3.6	12.52	30.75

Table 1a. Experimental initial conditions and results

Front Height hf (cm)	Buoyancy Flux g'q (cm^3/s^3)	Reynolds Number U1hf/v	Richardson Number g'qs/U1^3	Froude Number U1/(g'h4)^1/2
15.0	230.3	11951	0.313	1.32
12.0	93.4	7892	0.215	1.18
8.5	137.1	7057	0.165	1.29
13.0	225.2	11001	0.233	1.43
6.0	115.1	5093	0.108	1.63
9.0	92.1	6737	0.132	1.42
14.0	96.8	9683	0.169	1.47
18.0	163.8	12885	0.258	1.45
7.5	121.9	6479	0.142	1.01
8.0	152.2	7593	0.134	1.24
7.5	155.4	7765	0.105	1.01
13.0	562.8	14572	0.300	1.09
11.0	330.6	10652	0.205	1.17
12.0	372.8	13657	0.190	1.22

Table 1b. Additional experimental results

ANALYSIS

Consider the situation described in Figure 2. The independent variables are the flow velocity in the channel (U1), the total flow depth (h1), the reduced gravity (g') due to excess fractional density, and the discharge per unit width of dense fluid (q). The dependent variables of interest are the density current velocity (Uf) and the depth of the body (h4). Following Britter and Simpson (1978), dimensional analysis can be used to obtain the relation:

$$\frac{Uf}{U1}, \frac{h4}{h1} = \Phi_{1,2}\left(\frac{g'q}{U1^3}, \frac{U1^2}{g'h1}\right) \qquad (1)$$

For given U1 and h1, the buoyancy discharge g'q can be adjusted, as it was done in the experiments, until the velocity of the front (Uf) is equal to zero. This yields:

$$\Phi_1\left(\frac{g'q}{U1^3}, \frac{U1^2}{g'h1}\right) = 0 \qquad (2)$$

From (1) and (2) it follows that:

$$\frac{U1^2}{g'h1} = \Phi_3\left(\frac{h4}{h1}\right) \qquad (3)$$

and

$$\frac{g'q}{U1^3} = \Phi_4\left(\frac{h4}{h1}\right) \qquad (4)$$

For the purpose of comparison with the observations of both Britter and Simpson (1978) and Simpson and Britter (1979), (3) is modified to

$$\frac{U1^3}{g'h4} = \Phi_5\left(\frac{h4}{h1}\right) \qquad (5)$$

where $\Phi 5 = \Phi 3(h1/h4)$, without any loss of generality. Figure 3 shows a plot of observations corresponding to the relationship implied by (5). The data fall between the limits set by the observations of Britter and Simpson (1978) and Simpson and Britter (1979) which correspond to slip and no-slip velocity conditions; respectively. This suggests that the formation of lobes and clefts may not have been totally inhibited during the present experiments as corroborated by casual observation.

The most important parameter for the present study is the dimensionless mixing rate; g'q/U1^3. A plot of the observed values of mixing rates is shown in Figure 4. For the sake of comparison, the data of Britter and Simpson (1978) obtained under similar conditions are also included in the graph.

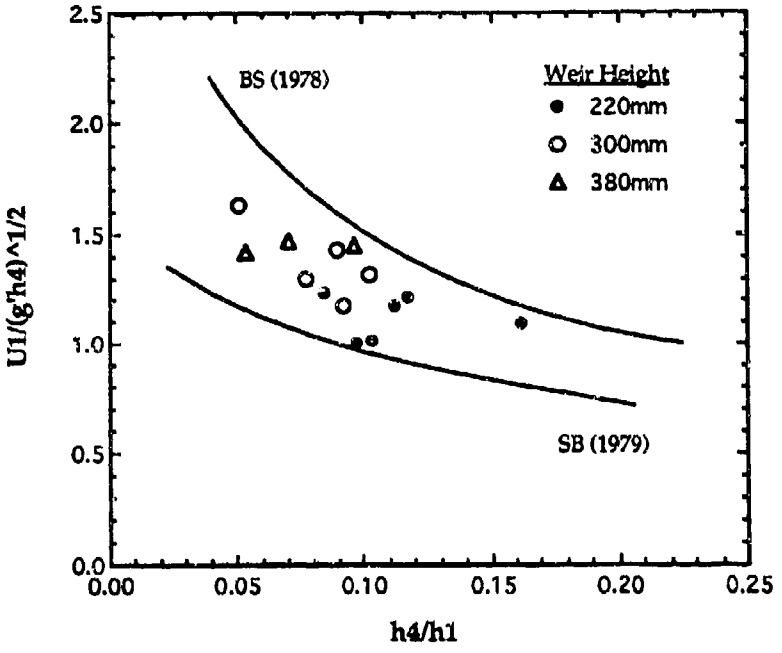


Figure 3. Froude comparison

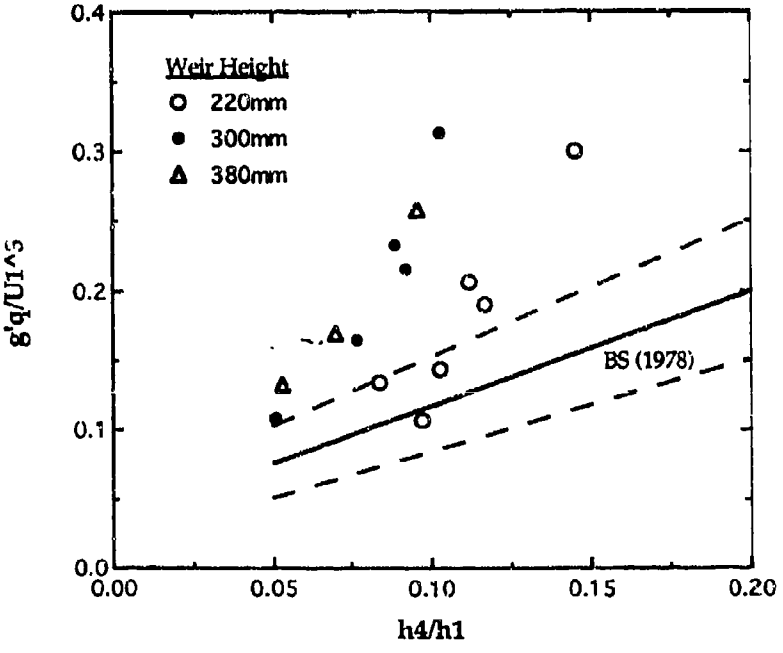


Figure 4. Dimensionless mixing rates

The data range is restricted by the amount of saline flow that can be measured accurately in the experimental facility at low mixing rates, and by a critical condition at the upper end. Such an upper limit is interesting because the data in this study, Britter and Simpson (1978) and Simpson and Britter (1979) suggest a critical dimensionless entrainment rate of about 0.3. Above this level it was found that all fronts could not exist as such and became unstable, mixing up completely with the clear water.

The observed dimensionless mixing rates display a pattern that seems to be influenced by the depth of the clear water, as determined by the clear water discharge and the height of the weir. After careful inspection of the data, it was found that a different parameter, that is not dimensionless, can account for such behavior. This parameter is the velocity of a given front moving through a still water body divided by the depth of the water body (Uf/h1). Such a parameter, gives a measure of the amount of time the front takes to travel a distance equal to the depth of the body it is intruding. In this fashion, short travel times would be characteristic of shallow environments and long travel times would be representative of deep water bodies. In these experiments, the travel time of the front is fairly constant (within 10%) for each of the weir heights considered in the present experiments. What is even more unique about the behavior of the travel time, as it can be observed in Figure 5, is that the differences between each subset of experiments is representative of the differences in the rates of mixing for a given height ratio (h4/h1). Also of interest, is the fact that the slope of the mixing rate lines are relatively constant and equal to about three for all the weir heights considered. On the other hand, the different mixing rate lines in Figure 5, give different values of (h4/h1) for no mixing. Such values would imply that there is a condition for which a dense bottom layer of a certain height (h4) could exist without entraining the clear water above. This condition, in which a density wedge forms at the corner of the channel, has been observed in these experiments when the supply of dense fluid was suppressed and the clear water flow velocity was small.

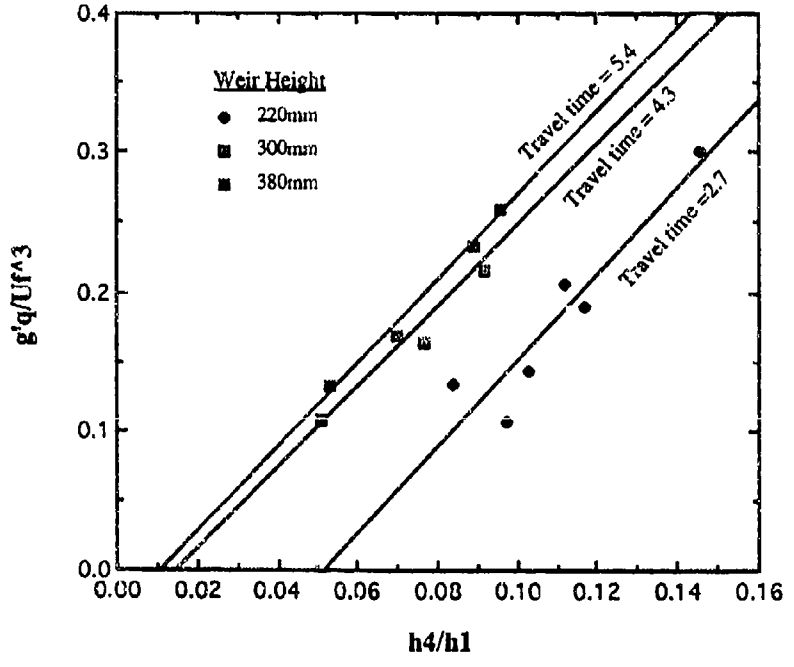


Figure 5. Relation between travel time and mixing rate lines

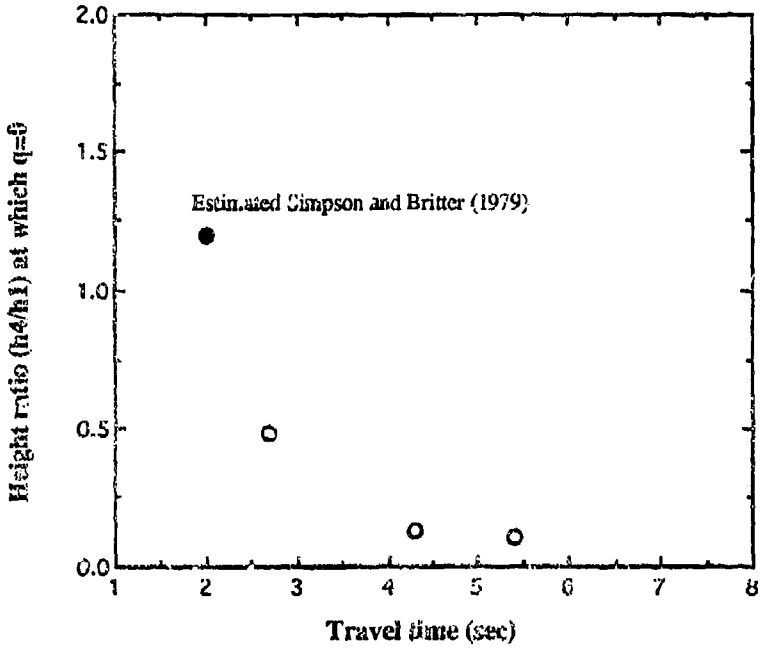


Figure 6. Trend of the mixing rate intercept with travel time

IMPLICATIONS FOR BOTTOM CURRENTS IN NATURE

In Figure 6, the variation of the height ratio (h4/h1) for which there is no mixing in the experiments is seen to decrease exponentially with travel time. On continental shelves, where water depths are on the order of 100 meters and current velocities are of about 1 m/s (Garcia, 1992), characteristic travel times will be on the order of 100 seconds. Assuming that the exponential decay displayed in Figure 6 is valid for large scale flows, the dimensionless mixing rate for density current fronts in continental shelves will be equal to three times the ratio between the current body height and the total water depth (h4/h1). Observations suggests that current depths are approximately equal to 5 meters (Garcia, 1992), thus the dimensionless mixing rate would be given by

$$\frac{g'q}{Uf^3} = 0.15 \qquad (6)$$

From Figure 3 and using h4/h1 = 0.05, a Froude number Uf/(g'h4)^1/2 = 1.7 results. Further reduction gives a value of g' = 0.07 m/s^2 and an excess fractional density of 0.7 % which is quite reasonable for dilute currents as the ones being considered herein.

ACKNOWLEDGEMENTS

The support of the Marine Geology and Geophysics Program (Grant N00014-93-1-0044) of the U.S. Office of Naval Research is gratefully acknowledged. The help of Sigurd Anderson, Engineering Design Inc., Lake City, Minnesota, was instrumental for the construction of the experimental apparatus. Thanks are also due to Chris Dagiantis for his help with the experiments.

REFERENCES

Allen, J. R. L. 1971. Mixing at turbidity current heads, and its geologic implications. *Journal of Sedimentary Petrology* 41: 97-113.

Altinakar, S., Graf, W., Hopfinger, E. 1990. Weakly depositing turbidity current on a small slope. *Journal of Hydraulic Research* 28: 55-80.

Britter, R. E., and Simpson, J. E. 1978. Experiments on the dynamics of a gravity current head. *Jounal of Fluid Mechanics* 88: 223-240.

Garcia, M. H. 1992. Turbidity currents. *Encyclopedia of Earth System Science*, Academic Press, Inc. 4: 399-407

Garcia, M. H., 1993. Hydraulic Jumps in sediment-driven bottom currents. *Journal of Hydraulic Engineering*, ASCE 119(10): 1094-1117.

Hay, A., Burling, R., and Murray, J. 1982. Remote acoustic detection of a turbidity current surge. *Science* 217: 833-835.

Simpson, J. E., and Britter, R. E. 1979. The dynamics of the head of a gravity current advancing over a horizontal surface. *Journal of Fluid Mechanics* 94: 477-495.

Simpson, J. E. 1987. Gravity currents in the environment and in the laboratory. New York, John Wiley and Sons, p.244.

LABORATORY OBSERVATIONS OF GRAVITY CURRENTS AND INTERNAL BORES

by
Sherrill Mausshardt, Harry Yeh, & Cami Grandinetti

Department of Civil Engineering, FX-10
University of Washington
Seattle, WA 98195
USA

A gravity current is a gravity-driven flow by the current's fluid-density difference from that of its surroundings. When a similar flow advances into a quiescent two-layer fluid of which the thinner layer has the same fluid density as the advancing current and distinct wave breaking is formed at the leading wave, the flow is called an internal bore. Salient features of gravity currents and internal bores are investigated in a horizontal flume with a lock-exchange device, i.e. by lifting a partition that initially separates fresh water from saline water.

Up-to-date understanding of physical features of gravity currents are summarized in Simpson's book (1987). As a gravity current advances, a characteristic 'head' is formed at the leading edge of the gravity current, which is approximately twice as deep as the following flow. The characteristics of the head are considered to be the ones that control the entire flow behavior. The head profile is sensitive to the Reynolds number ($R = Uh/\nu$), the internal Froude number ($F = U/\sqrt{g'h}$), and the ambient flow conditions, e.g. the total flow depth, and the ambient flow velocity, its direction and turbulence intensity. (Note that in the Reynolds number and the internal Froude number, U is the velocity of the front advancement, h is the depth of the current behind the head, ν is the kinematic viscosity of the fluid, g' is the buoyant acceleration, $g' = (\rho_2 - \rho_1)g/\rho_1$, ρ_1 and ρ_2 are the fluid densities of the ambient and the current, respectively, and g is the acceleration of gravity.)

There are, according to Simpson (1987), two types of instabilities that are responsible for the mixing associated with gravity currents: 1) billows which roll up in the region of velocity shear above the advancing front and 2) a complex shifting pattern of 'lobes and clefts' located on the face of the head. Simpson suggested that the billow formation on the upper surface of the head is similar to the Kelvin-Helmholtz instability. Simpson also indicated that the formation of 'lobes and clefts' develops from the lighter fluid that is overrun by the gravity current's foremost leading edge. (The foremost leading edge of the current is located slightly above the bed; approximately 1/8 of the total height of the head.) Some ambient fresh water is trapped under the head and entrained into the current from the bottom. This trapped lighter fluid is convected upward through the denser fluid to form a complicated shifting pattern of 'lobes and clefts' on the front face of the head.

Experiments

Our laboratory experiments were performed in a 16.2 m long, 0.61 m wide and 0.45 m deep tank. The tank was initially divided into two separate chambers with an aluminum gate: the front chamber is 8.9 m long and the back chamber is 7.3 m long. For the gravity current experiments, uniformly mixed saline water filled the back chamber, while fresh water filled the front chamber. For the internal bore experiments, a thin layer of saline water was placed beneath the fresh water in the front chamber, and the fluid density of the thin layer was identical to that of the saline water in the back chamber. A sharp interface was established by introducing saline water slowly through a diffuser along the bottom against the side wall.

Throughout the series of experiments, the total depth of both front and back chambers was set at 36 cm. A gravity current or an internal bore was created as a lock-exchange flow by lifting the aforementioned aluminum gate to 20 cm from the bed; this partial gate opening is a similar generation scheme as that used by Wood & Simpson (1984), which minimizes the free-surface disturbance created at the gate and controls the current depth to approximately 9 cm.

Observations by laser-induced fluorescence were made in the front-chamber area at 4.5 m downstream from the gate, approximately 50 times the average saline-water flow depth; all the transient disturbances caused by the gate motion should have sufficiently subsided in the area of

the observation and measurements. It is also noted that the length of the back chamber is long enough so that flows in the observation area are not disturbed by the reflection from the back-chamber end wall. In addition to the flow visualization, fluid density profiles were measured by vertically traversing a conductivity-thermistor probe.

The saline water densities used in the experiments are 1002, 1005, and 1025 kg/m^3. For the internal bore experiments, the initial saline-layer thicknesses in the front chamber are 0.5, 1.0, 2.0, and 3.0 cm. The cases with 1002 kg/m^3 saline densities are focused on in this paper because the results with other densities are qualitatively similar; the complete set of data and the results were reported in Grandinetti (1992).

Features of Gravity Currents

Figures 1a and 2 show our laser-induced-fluorescence flow images of a gravity current in a longitudinal vertical plane at the center of the tank and in a horizontal plane 10.5 cm above the bed, respectively. For the images shown in Fig. 2, a sketch to identify the locations of the laser illuminating planes are depicted in Fig. 2c. Only the saline water (ρ_2 = 1002 kg/m^3) was dyed with fluorescein, and appear as green-yellow regions, having been illuminated by an Argon-ion laser sheet.

The flow image in Fig. 1a shows the formation of billows on the front face; these small-scale billows are found to be three-dimensional. This can be verified in Fig. 2 where the front's flow pattern in the horizontal plane is irregular. This is, however, different from typical Kelvin-Helmholtz instability features in a plain shear flow created, for example, by a splitter plate; the billows associated with the Kelvin-Helmholtz instability are at least initially two-dimensional, i.e. the roll-up features of billows are long-crested. Instead, the three-dimensional front formation observed here is consistent with the 'lobes and clefts' pattern indicated by Simpson (1987).

There are several intriguing features in Figs. 1a and 2 that need to be addressed. The underside entrainment of the lighter fluid at the front of the gravity current is clearly seen in Fig. 1a where the entrapped fresh water ascends due to its buoyancy. The leading edge is irregular as seen in Fig. 2, including the formation of counter-rotating eddies (Fig. 2a), which are presumably associated with the formation of U-shaped vortex loops on the front face. In the flow following the front (see Fig. 2b), the pattern is irregular, although it appears to be an alternating pattern of saline and fresh water rows in the propagation direction indicating periodic formation of large-size eddies.

Features of Internal Bores

Differences in initial conditions between the gravity current and internal bore phenomena are minute: whether or not a thin layer of denser fluid is present initially. A limited number of previous studies on internal bores are found, for example, in Wood and Simpson (1984), Wallace and Wilkinson (1988), and Denton (1990).

Our experimental results in Fig. 1 show that the flow characteristics of the gravity current and internal bore are significantly different from each other, even when the pre-existing front layer of the denser fluid for the internal bore is thin (0.5 cm for Fig. 1b, i.e. approximately 1.4 percent of the total depth). Unlike a gravity current, the front face of an internal bore is smooth, and turbulence is generated at the rear side of the 'head' by flow instability. Figure 1 shows that the thinner the initial front layer, the steeper the front face and the earlier the formation of billow roll-ups. Contrary to the case of gravity currents, the billow formation of an internal bore resembles that of the Kelvin-Helmholtz instability, which appears to be two-dimensional at least initially, i.e. the flow pattern is uniform in the direction transverse to the flow, which will be verified later.

The distinct differences in the features between gravity currents and internal bores might be explained by Simpson's (1987) 'lobes and clefts' formation at a gravity current's foremost leading edge. Such formations are not possible in an internal bore because ambient fresh water cannot be trapped along the bottom where the denser fluid already occupies. Further explanation is given here based on the vorticity creation mechanisms. The rate of change in flow circulation Γ moving with the fluid can be expressed as:

$$\frac{D\Gamma}{Dt} = \int_S \left[\frac{1}{\rho^2}(\nabla\rho \times \nabla p) + \frac{\mu}{\rho}\nabla^2\omega - \frac{1}{\rho^2}\left(\nabla\rho \times \mu\nabla^2 u\right) \right] \cdot dA \qquad (*)$$

for the fluid with uniform viscosity μ, which can be justified since viscosity variation is negligible in our saline-fresh water experiments. In (*), u is the fluid velocity, ω is the vorticity (i.e. curl u), ρ is the fluid density, Γ is the flow circulation, and A is the area vector of the surface s whose boundary is a single closed curve c. Based on (*), there are only two mechanisms to create fluid rotation within the fluid domain (excluding the surface at the solid boundary). These are baroclinic torque (the first integrand term) and viscous-shear torque (the last integrand term) (Yeh, 1991) both of which require the presence of a density gradient. Note that the second integrand in (*) represents the transfer of fluid rotation by vorticity diffusion from fluid parcels adjacent to the boundary of the integration surface s, and does not represent creation of new fluid rotation within the fluid domain.

In the case of the internal bore, the fluid parcels along the interface are initially quiescent and irrotational. Fluid rotation must be created at the interface by baroclinic torque: the pressure gradient must be close to that of hydrostatic condition while the density gradient is normal to the interface; note that it was shown by an order-of-magnitude analysis that viscous-shear torque plays an insignificant role compared with the role of baroclinic torque (Yeh, 1991). Once fluid rotation was created by baroclinic torque, the rotationality is advected with the fluid motion (Helmholtz's theorem) and diffuses by viscous effects. This property manifests itself in the formation of billows behind the ridge of the bore front.

On the other hand, in a gravity current, the fluid parcels along the interface are advected from inside of the advancing current. The fluid within the current is already vortical due to turbulence induced by a) wave breaking behind the head, b) entrapped fresh water under the leading edge or nose (Fig. 1a), c) the bottom (no-slip) boundary condition, and d) flow disturbance caused by the gate opening; hence, fluid parcels along the interface are originally vortical. This initially vortical flow results in three-dimensional and complicated patterns at the interface of the head. The nature of inherently vortical flow at the gravity-current head can be an explanation for 'lobe-and-cleft' formations as well as the reason for three-dimensional small-scale billow formations.

It appears in Fig. 1 and in other images not presented here, that the vortex formation behind the head of the internal bore resembles that of a separation eddy associated with a flow expansion of the fresh water along a fictitious saline wall (i.e. the saline-fresh water interface). Furthermore, roll-ups form a periodic pattern of turbulent regions at somewhat uniform intervals. The periodic features of turbulence patches might be related to the intermittent nature of the flow. We conjecture that turbulence patches are formed by a "generation-advection" cycle of the roll-up formation: as soon as the roll-up is formed, the large vortex of the roll-up is advected behind the head, then the next roll-up is created, and this process is repeated. Note that Yeh and Mok (1989) pointed out that turbulence-patch formations behind bores at the air-water interface also result from the generation-advection cycle. In order to test this hypothesis, the periodic turbulence-patch formation is quantified by the frequency of its generation; the generation frequency can be measured directly from the video images of our experiments. This measured frequency should be related to the frequency associated with the excursion time of a fluid parcel traveling around the vortex. Assuming the vortex size L (say the diameter of the orbital motion) is comparable with the difference in height between the head and the current depth behind the head (the actual length scale of the vortex is somewhat smaller than this estimation), and using the vortex-velocity scale to be the bore propagation velocity U, then the time scale for roll-up is found to be $T_r \approx \pi L/U$. Computed frequencies $1/T_r$ shown in Fig. 3 are in surprisingly good agreement with the measured frequency from the video images; the error bars in the figure represent the 90 % confidence limit for the frequency measurements. The excellent agreement in Fig. 3 strongly supports our conjecture that the periodic behavior of the turbulence patches in internal bores is closely related to the cyclic behavior of the roll-up formation between its generation and advection.

Another dye-tracing experimental result is shown in Fig. 4; only the initially thin (1.0 cm) saline-water layer was dyed with fluorescein but the saline water with the same density behind the lock gate was kept without dye. Note that this supplemental experiment was performed in a

smaller scale apparatus. It is evident in Fig. 4 that the main portion of core fluid in the internal bore consists of the saline water originally placed behind the gate. The fluid initially placed in the thin layer is advected to form the mixed layer behind the head between the fresh-water and the advancing saline water, and also to form the boundary layer along the bottom bed. This clearly demonstrates the shortcomings of one-dimensional-flow models: flow velocity of each layer would be uniform in the vertical direction in a one-dimensional-flow model, hence the fluid of the leading bore was supposed to be made of the fluid picked up from the thin layer initially placed in front of the advancing bore: the result in Fig. 4 evidently shows that this is not the case. Another important point from Fig. 4 is that the fluid originally located behind the lock gate is capable of intruding through the thin layer of fluid without significant mixing: as shown later the fluid mixing is limited to a certain depth between the fresh water and saline water.

Nearly two-dimensional wave breaking patterns in the internal bore can be confirmed in Fig. 5 which presents flow patterns in a horizontal plane at 10.5 cm from the bed. (The same visualization plane was used to obtain Fig. 2 -- see Fig. 2c for the position of the laser sheet). It is emphasized that only saline water was dyed with fluorescein, i.e. the bright portions in the figures represents the saline water and the black portions represent the fresh water. The bore is propagating from left to right. A fuzzy broad band seen in the figure represents the head of the bore. The initial roll-up can be seen as a thin black line within the fuzzy broad band. Once the vortex is detached from the head on the illuminated plane, the roll-up tube breaks apart and appears as a series of elliptic rings in the image of Fig. 5b. The ring appearance indicates that even though the initial roll-up formation is two-dimensional (just like the Kelvin-Helmholtz instability), once it is formed, the roll-up immediately possesses transverse variations. Such transverse wave formations resemble the manifestation of longitudinal (streamwise) vortex formations in the Kelvin-Helmholtz instability reported by Bernal (1981), Lin & Corcos (1983), Lasheras & Maxworthy (1987), and others. It is not clear, however, whether the transverse variations shown here are created by the formation of longitudinal vortices.

The occurrence of this transverse perturbation can be found in the results presented in Fig. 4. The sequence of flow images in Fig. 4 evidently demonstrates the cyclic behavior of the roll-up formation between its generation and advection, which was discussed previously. It appears that the initial roll-up formation is two dimensional as shown in Fig. 4a, but the clean roll-up pattern is immediately perturbed in Fig. 4b within a few seconds and becomes three-dimensional. At the time of the three-dimensional vortex formation, the fluid mixing rate must increase drastically according to the mixing-transition process proposed by Breidenthal (1981). (Note that later Lasheras, et al. (1987) demonstrated in their well controlled laboratory environment that the mixing transition does not necessarily coincide with the initial formation of streamwise vortices; the mixing transition can be delayed well after the formation of organized three-dimensional features.) Figures 4 and 5 show that the three-dimensional vortex formation appears to occur immediately after the roll-up eddy is advected behind the head, which implies that fluid mixing takes place immediately at the rear face of the internal bore. In fact, the rapid mixing process will be verified later with the discussion of density-profile data.

This immediate perturbation shown in Fig. 5 suggests that the three-dimensional features (transverse variations of the vortex tube) could be caused by a mechanism other than the formation of longitudinal vortices. Consider the fact that rotational motions which initially have rotational axes perpendicular to the density gradient are not stable and cannot maintain their orientation due to an adverse buoyancy-force gradient created by the overturning motion itself (just like the Rayleigh-Taylor instability); all the rotational motions tend to become those which have axes parallel to the density gradient (i.e. pancake-like turbulence patches). Hence, the initially created roll-up with the horizontal axis tends to bend, which causes transverse variations. This explanation for the three-dimensional variations is plausible for the present case. To see this more clearly, consider the time scales of the vortex motion and the buoyancy effect. The buoyancy time scale T_b can be estimated as the traversing time for a fluid-parcel to ascend through the vortex length scale L by the buoyancy force: $T_b \approx \sqrt{L/g'}$. Assuming the vortex size is comparable with the difference in height between the head and the current depth behind the head and using the buoyant acceleration, $g' = (\rho_2 - \rho_1)g/\rho_1$, the time scale for the buoyancy effect is found to be $T_b \approx 1.15$ sec. The roll-up time scale can be estimated as before: an excursion time for a fluid parcel to travel around the vortex. Using the vortex velocity scale to be the bore propagation velocity U, the time scale for roll-up is found to be $T_r \approx \pi L/U = 3.80$ sec.

These rough estimates demonstrate that the order of magnitude of the buoyancy-effect time scale and of the vortex-motion time scale are comparable, which supports the explanation for three-dimensional variations discussed above. Hence, the transverse perturbation of vortices, which appear in Figs. 4 and 5, could be caused by gravitational instability rather than the manifestation of longitudinal (streamwise) vortex formations in the Kelvin-Helmholtz instability.

Density Profiles

In our laboratory experiments, quantitative data for mixing processes were obtained by vertically traversing the conductivity/thermistor probe. The results show the mixing phase caused by overturning billows; small-scale density inversions in the profiles are interpreted as the presence of small active eddies. Approximately 10 sec. after the passage of the head, these small-scale density inversions are diminished. At this point, the region of overturning billows is considered to be mixed, i.e. appreciable fluid mixing has already taken place in the vicinity of the head. The results appear to be consistent with our discussion made for Figs. 4 and 5, indicating that fluid mixing at the head is immediate and efficient in comparison to mixing in the current far behind the head.

Two separate mixing processes are represented by the appearance of two distinguishable gradients in the density profile plots. The upper portion of a profile has a uniform density gradient caused by large-scale mixing of overturning billows. As mentioned, this mixing process takes place directly behind the head. In the second gradient, the mixing process is attributed to the continual shear flow created by the fast-moving dense water under the nearly stationary mixed-fluid region. This fast-moving fluid layer is vortical due to the boundary-layer effect which gradually erodes the layer, as do the combined effects of shear instability and small-scale eddies within the lower layer fluid. The variations of mixed-layer thickness are measured by the ratio of fluid density difference to the maximum density gradient, i.e. the parameter

$$\delta = \frac{\rho_2 - \rho_1}{\left|\partial\rho/\partial z\right|_{max}}$$

, for the two separate mixing processes and are plotted in Fig. 6 versus downstream distance from the head. The mixing right behind the head is immediate and very efficient but once this process takes place, the subsequent mixing process due to shear is very slow, in fact the thickness of the mixed layer decreases, instead, due to the buoyancy effect. All the mixing is completed at the head. Figure 6 also indicates that the thinner the initial front saline-water layer, the thicker the mixed layer.

REFERENCES

Bernal, L.P. 1981. The coherent structure of turbulent mixing layers. I. Similarity of the primary vortex structure; II. Secondary streamwise vortex structure. Report, Graduate Aeronautical Laboratories, California Institute of Technology, Pasadena, Calif. 92 pp.

Breidenthal, R. 1981. Structure in turbulent mixing layers and wakes using chemical reaction. J. Fluid Mech. 189, 1-24.

Denton, R.A. 1990. Accounting for density front energy losses. J. Hydr. Engr. 116: 270-275.

Grandinetti, C. 1992. Gravity current and internal bores. M.S. thesis, Univ. of Washington, Seattle, pp. 82.

Lasheras, J.C., Cho, J.S., and Maxworthy, Y. 1986. On the origin and evolution od streamwise vortical structures in a plane, free shear layer. J. Fluid Mech. 172, 231-258.

Lin, S.J. and Corcos, G.M. 1983. The mixing layer: deterministic models of a turbulent flow. Part 3. the effect of plane strain on the dynamics of streamwise vortices. J. Fluid Mech. 141, 139-178.

Simpson, J.E. 1987. Gravity currents: In the environment and the laboratory. Ellis Horwood Ltd.: Chichester.

Wallace, B.C. and D.L. Wilkinson. 1988. Run-up of internal waves on a gentle slope in a two-layered system. J. Fluid Mech. 191: 419-442.

Wood, I.R. and I.E. Simpson. 1984. Jumps in layered miscible fluids. J. Fluid Mech. 140: 329-342.

Yeh, H., 1991. Vorticity-Generation Mechanisms in Bores. Proc. Roy. Soc., Lond. A., 432: 215-231.

Yeh, H.H. and Mok, K.-M. 1990. On turbulence in bores. Phys. Fluids A, 2, 821-828.

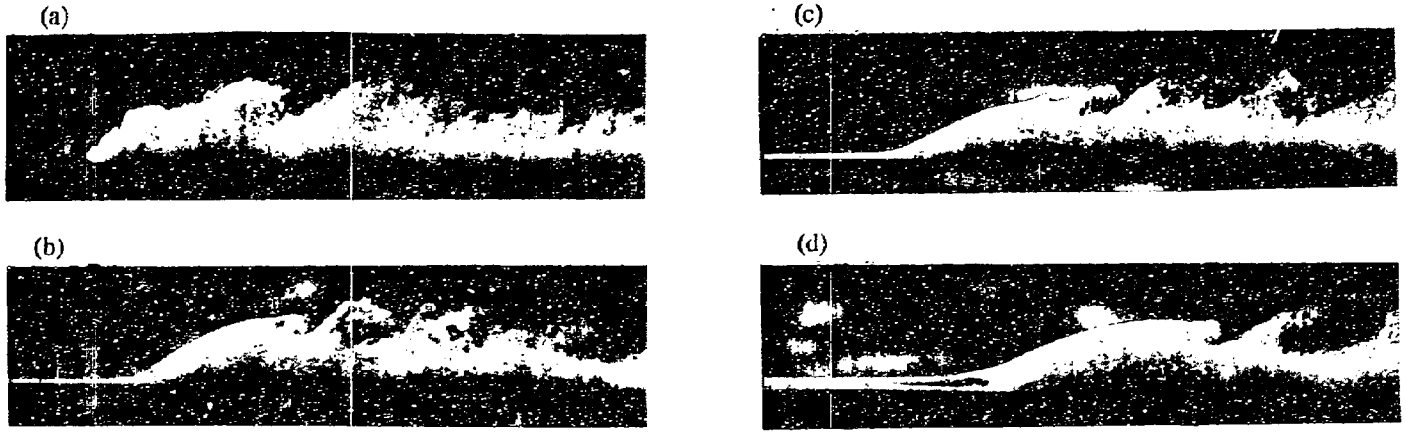


Figure 1. Flow patterns of a) a gravity current: R = 1450, F = 0.995, and internal bores with the initial layer thickness of b) 0.5 cm: R = 1440, F = 1.00, c) 1.0 cm: R = 1730, F = 1.29, and d) 2.0 cm: R = 1230, F = 0.861. ρ_2 = 1002 kg/m^3.

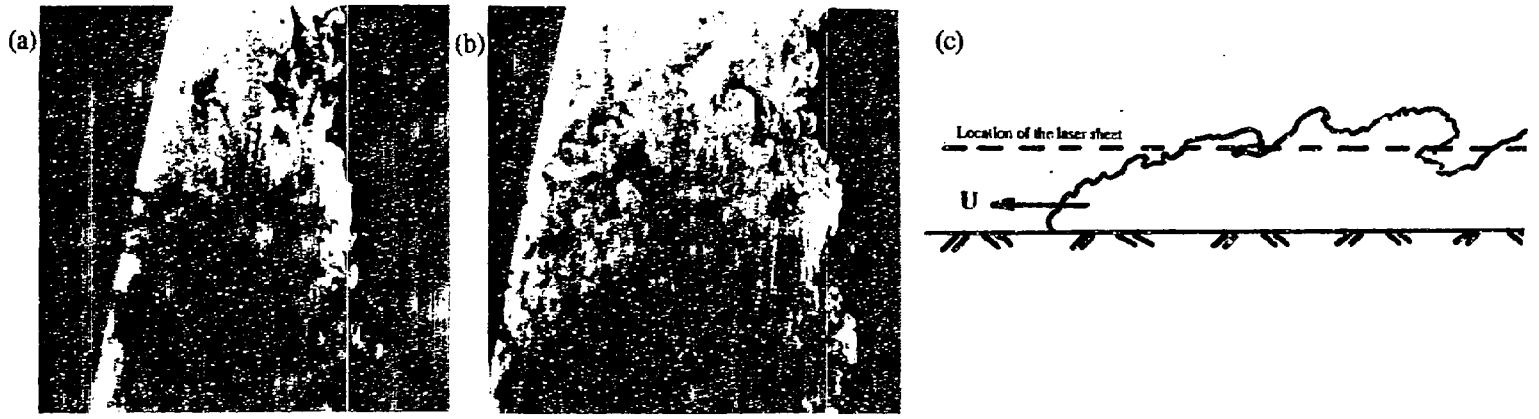


Figure 2. Gravity-current images on a horizontal plane at 10.5 cm from the bed. Only saline portion is dyed. ρ_2 = 1002 kg/m^3; R = 1450; F = 0.995. The current motion is from left to right. Time interval between a) and b) is 5.6 sec. c) A sketch of the flow pattern and the imaging plane.

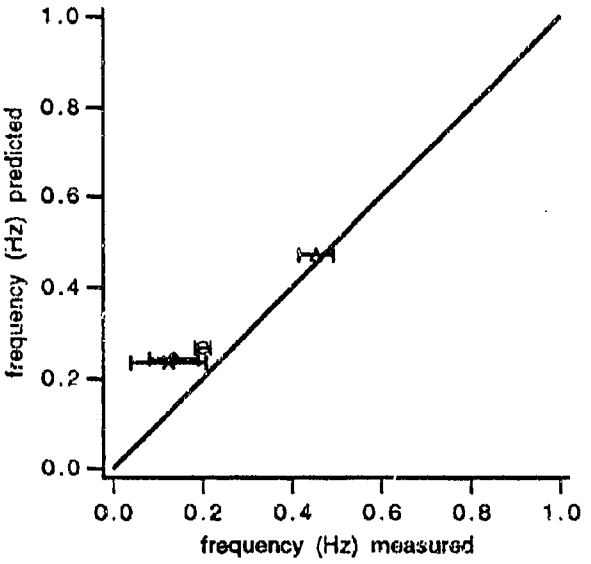


Figure 3. Predicted and measured generation frequencies of the large-scale eddies: ◊, gravity current shown in Fig. 1a; the internal bores shown in Fig. 1b-d. ×: h = 0.5 cm. *: h = 1 cm. ×: h = 2 cm. The error bars represent 90 % confidence limits.

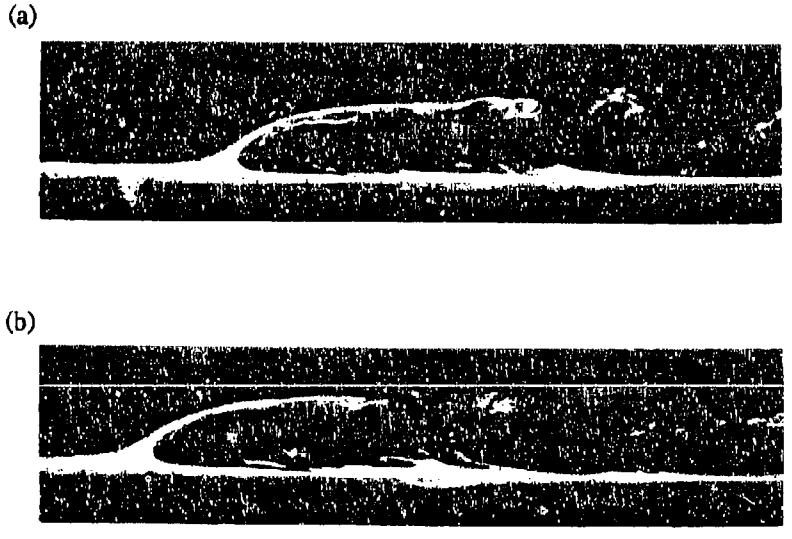


Figure 4. Flow pattern of an internal bore with the initial layer thickness of 1.0 cm: R = 1050, F = 0.70, ρ_2 = 1002 kg/m^3. Only the saline water initially placed in front of the gate was dyed with fluorescein, while the saline water behind the gate was left without dye. a) $t = t_0$, b) $t = t_0 + 2.8$ sec.

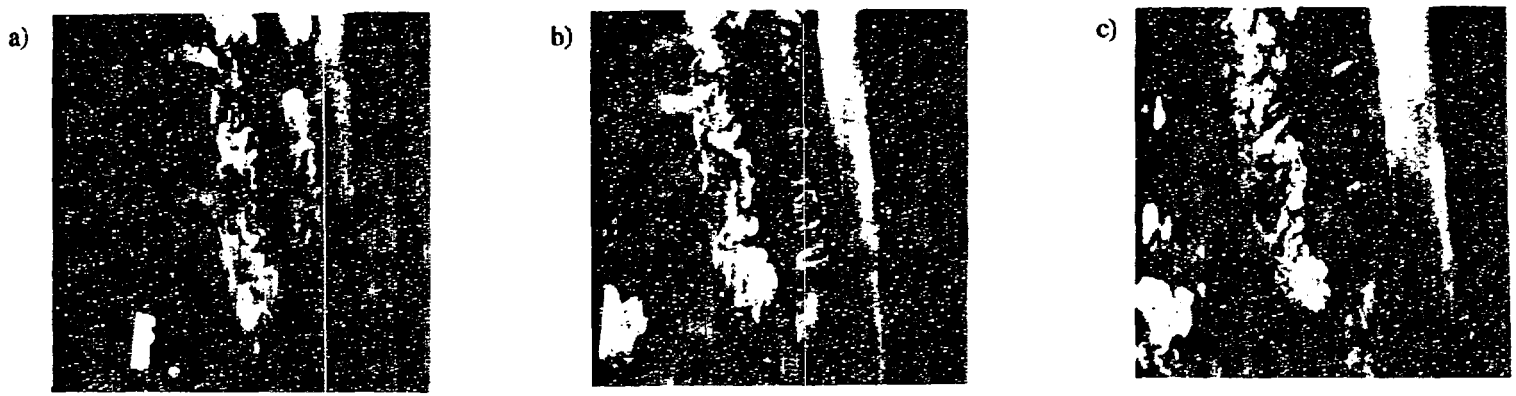


Figure 5. A sequence of the internal-bore images on a horizontal plane at 10.5 cm from the bed. The flow condition is identical to that in Fig. 1d. The bore advancement is from left to right. The time intervals between a) - b) and b) - c) are 1.6 sec.

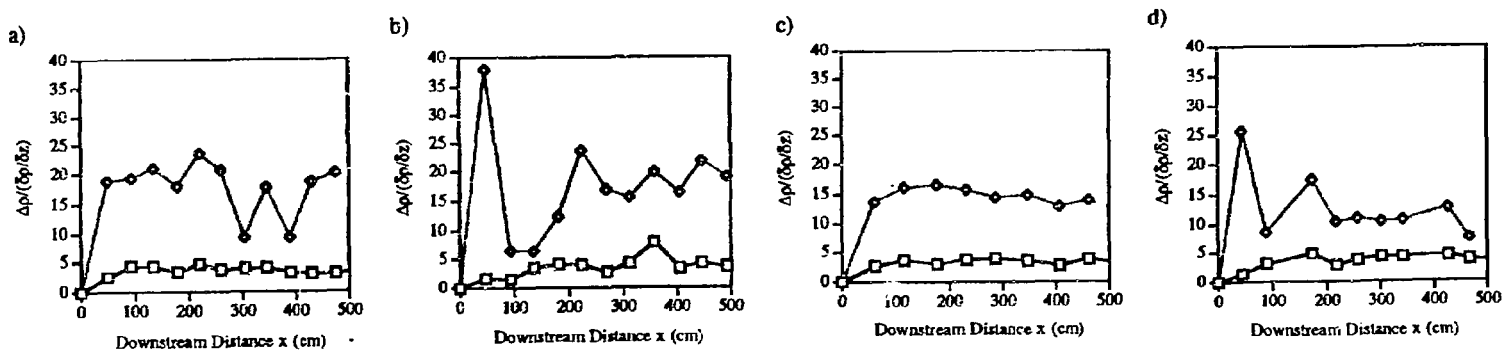


Figure 6. Measured variations of the mixed layer thickness, $\delta = \Delta\rho \Big/ \left(\frac{\delta\rho}{\delta z}\right)$, of the gravity current and the internal bores shown in Fig. 1:

a) a gravity current: R = 1450, F = 0.995, and internal bores with the initial layer thickness of b) 0.5 cm: R = 1440, F = 1.00, c) 1.0 cm: R = 1730, F = 1.29, and d) 2.0 cm: R = 1230, F = 0.861. ρ_2 = 1002 kg/m^3. The head location is at x = 0.
- - - -◊- - - -: the upper mixed layer, ----□ -----: the lower mixed layer

Shear Instabilities in Arrested Salt-Wedge Flows

Noboru Yonemitsu*, Gordon E. Swaters**,
Naliamuthu Rajaratnam*** and Gregory A. Lawrence*

* Environmental Fluid Mechanics,
Dept. of Civil Engineering,
University of British Columbia, Vancouver
B.C., V6T 1Z4, CANADA

** Institute of Applied Mathematics,
Dept. of Mathematics,
University of Alberta, Edmonton,
Alberta, T6G 2G1, CANADA

*** Department of Civil Engineering,
University of Alberta, Edmonton,
Alberta, T6G 2G7, CANADA

ABSTRACT

"One-sidedness" in arrested salt-wedge flows is investigated with theoretical models based upon two-layer approximations. These models include the effects of rigid bottom boundaries and the effects of density interface displacement with respect to the centre of the shear layer. The results indicate that inclusion of both interface displacement and rigid boundaries in the model greatly contribute to the "one-sidedness" phenomenon and influence the wave characteristics, especially their stability criteria. Data from laboratory experiments agreed well with the results produced by these models.

1. INTRODUCTION

"One-sidedness" (Keulegan 1966, Browant and Winant 1973) is a classic problem in the study of mixing processes in two-layered stratified flows. This phenomenon, which is associated with the breaking of the density interface, tends to be confined to the high-speed side of the flow, and is commonly observed in arrested salt wedges. Figure 1 shows a schematic of a salt wedge. The longitudinal sub-divisions are defined by Sargent and Jirka (1987) using the force balances. Two different kinds of interfacial waves (positive and negative waves) are observed; they propagate in opposite directions. The positive waves cusp upwards and occasionally break down into the upper layer. They appear near the tip region and propagate in the downstream direction. In contrast, the negative waves cusp towards the lower layer, and are commonly observed near the exit region. This is the one-sidedness phenomenon in salt-wedge flows. Although many attempts have been made to interpret this phenomenon as shear instability, they fail to clarify its mechanism, due mainly to the lack of appropriate models.

One of the problems associated with analysis of this type of flow is the modeling of the velocity profile. Most models employ time-averaged velocity profiles which are generally anti-symmetric to the density interface. Interfacial waves, however, are known to be intermittent and consequently must be considered as events dependent on the instantaneous velocity distribution. Our observations show that instantaneous velocity profiles often have a displacement between the centre of the shear layer and the density interface, and the stability characteristics of such flows are known to be quite different from those of anti-symmetric

cases (Lawrence *et al.* 1991). Another modeling problem is that most of the stability analyses have neglected the existence of rigid boundaries for simplicity. It is obvious that the bottom boundary effects on salt-wedge flows are not negligible.

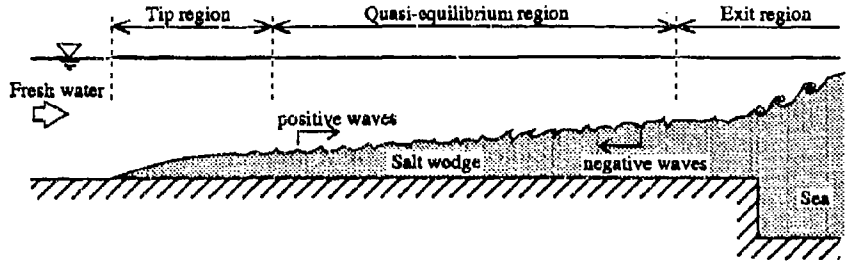


Fig. 1. Schematic structure of a salt-wedge flow with three longitudinal subdivisions (based upon its force balance) and its typical interfacial waves.

The effects of rigid boundaries were first investigated by Howard (1963), and Hazel (1972) in inviscid theory. This study was followed by Lalas and Einaudi (1976), Lindzen and Rosenthal (1976), and Fua and Einaudi (1984), to solve atmospheric boundary layer problems. Hazel showed, in one of his models (continuous velocity and density profiles), that flows were stable for $0<ZR<1.195$-1.205, despite some numerical instability problems. These models are, however, designed for atmospheric boundary layers, and hence their results, owing to their density profiles, are not directly applicable to the salt-wedge flows.

In this paper, we report first on the experiments we performed to obtain detailed information on the flow field, which is often three-dimensional. These experiments determined the appropriate functions for modeling the velocity profile for two-layered stratified flow; we then calculated the stability characteristics assuming the existence of rigid boundaries, interface displacements and viscosity.

2. EXPERIMENTS

The aim of our experiments was to identify the relationships among three-dimensional flow structures, velocity profiles, interfacial displacements, lower layer thickness, and associated interfacial waves. Sixty-three salt wedge experiments were conducted in the flume shown in Figure 2. Flow visualization was employed to obtain the flow structure and wave characteristics, while LDA and dye injection (see Yoshida 1980) were used to measure the velocity profiles. Density interface position and thickness were measured by using conductivity probes, and throughout the experiments the interface thickness was found to be less than 1/10 of the shear layer thickness. This result justifies the use of two-layered models.

The results of the flow visualization can be summarized as shown in Figure 3. It was impossible to eliminate side and bottom boundary effects from our experiments, and consequently the flows in this channel exhibited a three-dimensional structure. The secondary flows, induced by several pairs of stream-wise vortices in the upper layer, cause a wave-like variation of U velocity in the lateral direction. For our convenience, we shall introduce transverse subdivisions such as the high-speed region (HSR) and the low-speed region (LSR), according to the U velocity in the upper layer. In the HSR, the lower layer tends to be thin because of higher shear stress, *i.e.* higher entrainment at the density interface. In this region, the volume of entrained salt water is much larger than that of the back flow in the lower layer; therefore mass-balance is not valid in a two-dimensional sense. Similarly, in the LSR the velocity profile indicates less interfacial shear stress, which causes less entrainment than back flow. By summing the fluxes of the HSR and the LSR, the salt wedge maintains its stationary position, *i.e.* mass is conserved. Therefore, transverse subdivisions must be considered when the experimental data are analyzed and interpreted.

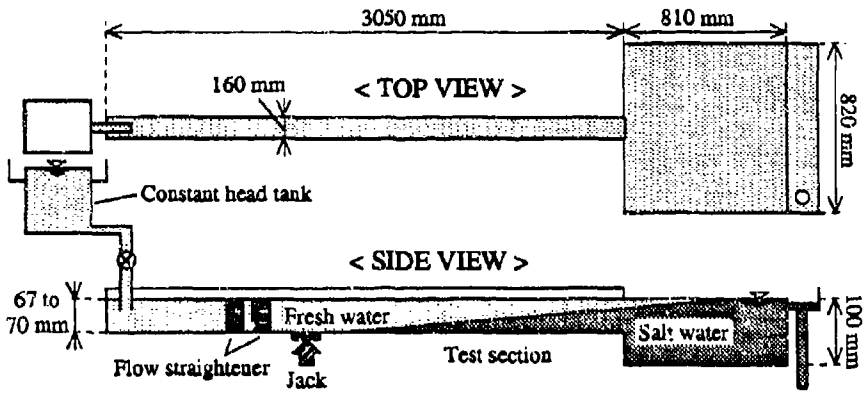


Figure 2. Experimental apparatus. The bed slope of the channel can be adjusted with the hydraulic jack. The conductivity probes, wave sensors and LDA optics are located in the test section.

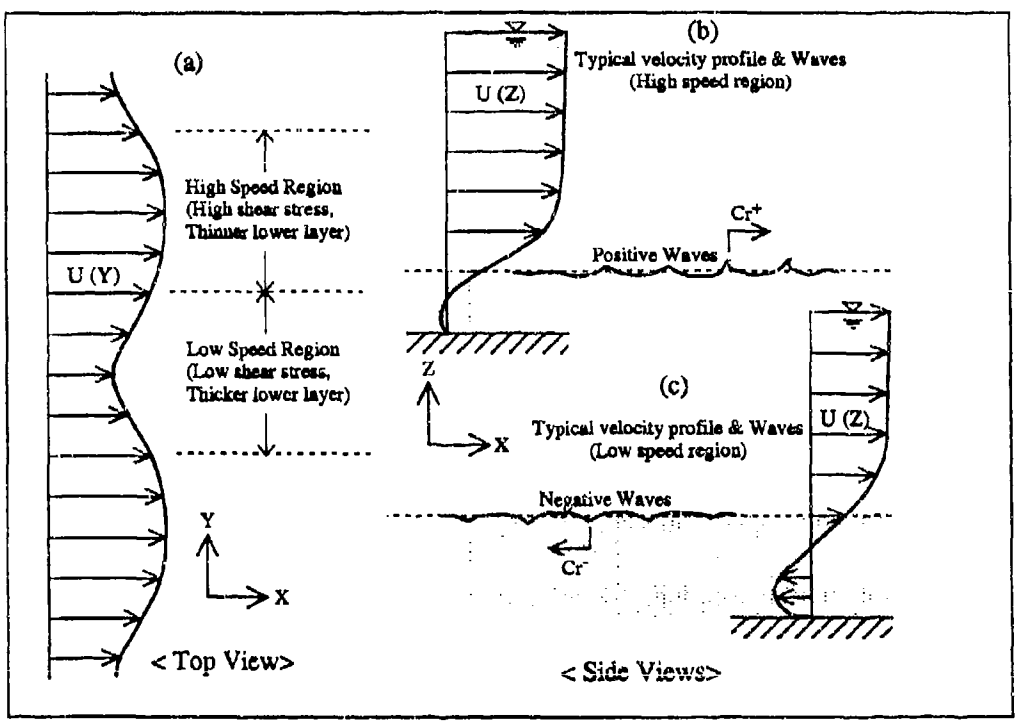


Figure. 3. Three-dimensional flow structure, velocity profiles and interfacial waves created mainly by the secondary flow (steam-wise vortex pairs) in an experimental channel. X,Y,Z are Cartesian coordinates corresponding to the longitudinal, lateral and vertical directions. U in this Figure is velocity in the X direction. Note that the inflection point of the velocity profiles is located above the density interface in the High Speed Region (b), and below in the Low Speed Region (c).

Flow visualization also revealed the existence of two different kinds of interfacial waves. These waves are known as Holmboe instabilities (Holmboe 1962), consisting of positive and negative instabilities of equal strength traveling at the same speed, but in opposite directions with respect to the mean flow (Tsubaki *et al.* 1969, Murota and Hirata 1978, Yoshida 1980). Our study differs from previous work in that the positive and the negative waves appear in different locations on the salt wedge. This is the one-sidedness phenomenon in salt-wedge flows. The positive waves, which are induced by vortex tubes just above the density interface, cusp upwards. They are observed most of the time in the HSR near the tip region, and propagate in the downstream direction. The negative waves, which cusp towards the lower layer, can be found in the LSR near the exit region, and propagate slowly upstream. Interaction between these two waves occurs somewhere in the quasi-equilibrium region.

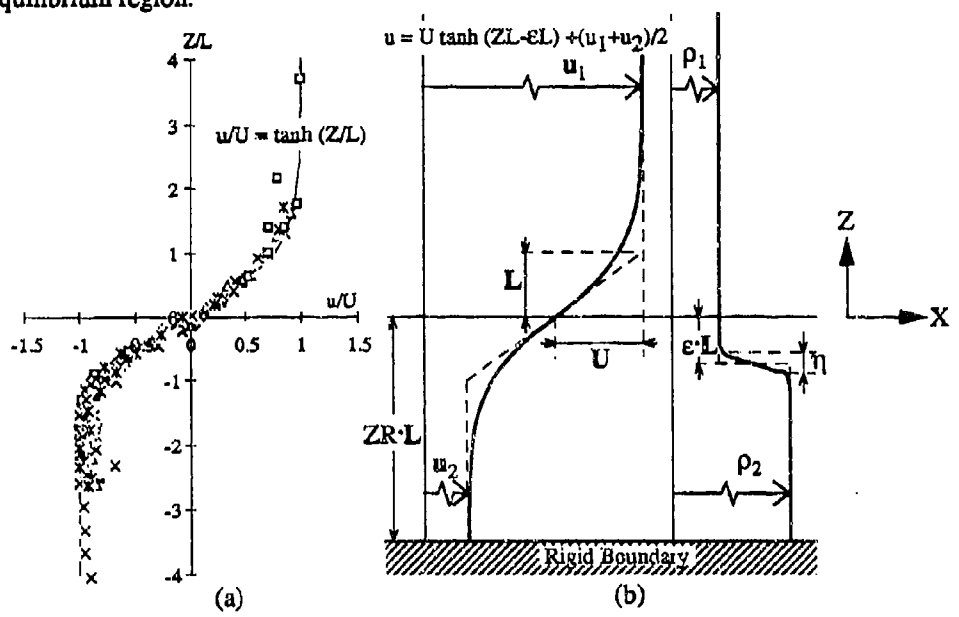


Figure 4. (a) Observed Velocity profiles and (b) definition of velocity and length scale. The interfacial displacement ε is removed in (a). Notations are: x, z = Cartisian coordinatye system located at the density interface with u_1, u_2 = velocity in upper and lower layer; ρ_1, ρ_2 = density in upper and lower layer; ZR = the lower layer thickness; L, U = the characteristic length and velocity scales; ε = the displacement of the centre of shear layer and density interface (non-dimensionalized); η = the density interface thickness.

Vertical velocity distributions measured in both the HSR and the LSR are shown in Figure 4. In Figure 4(a), length and velocity scales are non-dimensionalized based upon the definition given in (b), and the displacement ε is removed. The results in Figure 4(a) indicate that velocity profiles can be approximated by the TANH function very well, and therefore the non-dimensionalization by the length scale L and velocity scale U is justified. The non-dimensional parameters are defined as:

$$\alpha = \frac{2\pi L}{\lambda}, \qquad \gamma = \frac{\rho_1}{\rho_2}, \qquad Ri = \frac{(1-\gamma)gL}{U^2}, \qquad Re = \frac{UL}{\nu}, \tag{1}$$

where Ri is the overall Richardson number, Re is the Reynolds number, α is the wave number, λ is the wave length, ν is the kinematic viscosity of water and g is gravitational acceleration.

Figure 5 shows observations of interface displacement ε with the Richardson number Ri and the lower layer thickness ZR. These plots imply that: 1) most of the positive waves occur where the values of ε are positive, 2) the Ri for positive waves tends to be large when the corresponding ε is large, 3) the negative waves have very small Ri and relatively large ZR, and 4) there is no specific value of ε for the negative waves. It is especially interesting that some positive unstable waves have much larger Ri than 1.4, which is predicted as the stability boundary by Nishida and Yoshida (1987).

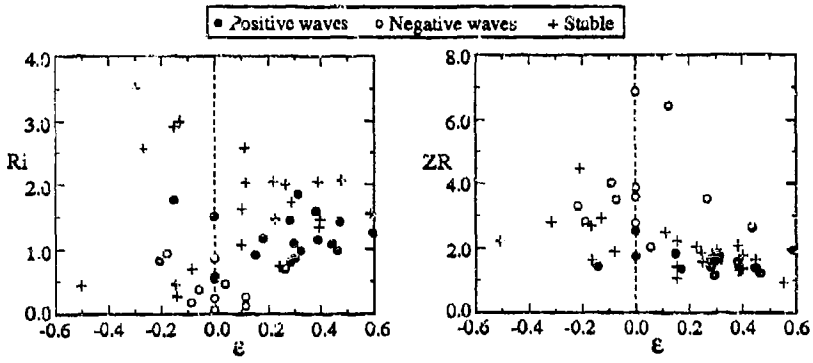


Figure 5. Interfacial displacement ε vs. Richardson number Ri and lower layer thickness ZR.

It can be concluded that the interfacial waves on the salt wedge flows must be analyzed by appropriate models based upon more realistic velocity profiles and boundary conditions than have been used in existing theories. The following theoretical analysis is therefore designed to evaluate the effects of interfacial displacement and rigid boundaries on the stability characteristics of two-layered stratified flows.

3. THEORETICAL DEVELOPMENT

Hino and Hung (1982) analyzed the stability characteristics of salt-wedge flows by solving equations for viscous-diffusive systems, with realistic velocity (TANH function for the upper-layer velocity profile and second-order polynomial function for the lower-layer velocity profile) and density profiles ($\rho(z) = \exp[-\gamma \tan(Rz)/R]$ where R is the ratio of shear layer to density interface thickness), and having a rigid bottom boundary. Their analysis failed, however, to provide any unstable solutions, and it could not distinguish the effects of viscosity, diffusivity, rigid boundary and velocity profiles, owing to their complicated models.

In the model described here we employed relatively simple and realistic velocity (TANH function) and density (two-layer approximation) profiles to avoid any further complexity, then evaluated the effects of the rigid boundary and the interfacial displacement separately. Two models are examined by the linear stability theory. One of them was designed to test the effects of a rigid boundary and the other to investigate the interfacial displacement. Their velocity and density profiles are shown in Figures 6 and 7. The governing equation is derived by applying infinitesimally small monochromatic perturbations to the two-dimensional, incompressible flow system. A two-layer approximation of density distribution is made for simplification. The stream function of the perturbation is defined as $\Phi(z)\exp[i\alpha(x-ct)]$, where $\Phi(z)$ is the complex amplitude. This stream function is governed by the Orr-Sommerfeld (O-S) equation:

$$(u(z)-c)\left(\frac{d^2}{dz^2}-\alpha^2\right)\Phi(z)-\frac{d^2u(z)}{dz^2}\Phi(z)=\frac{1}{i\alpha Re}\left(\frac{d^4}{dz^4}-2\alpha^2\frac{d^2}{dz^2}+\alpha^4\right)\Phi(z) \qquad , \quad (2)$$

where i is $\sqrt{-1}$. The lower and upper boundary conditions are given by:

$$\Phi(z) = \frac{d\Phi(z)}{dz} = 0 \quad \text{at } z = -ZR, \infty. \tag{3}$$

The matching conditions at the density interface, *i.e.* the continuity of both normal and shear stress, can be written as:

$$\Phi_1 = \Phi_2,$$

$$\frac{d\Phi_1}{dz} - \frac{du/dz}{u-c}\Phi_1 = \frac{d\Phi_2}{dz} - \frac{du/dz}{u-c}\Phi_2,$$

$$\gamma\frac{d^2\Phi_1}{dz^2} - \gamma\left[\frac{d^2u/dz^2}{u-c} - \alpha^2\right]\Phi_1 = \frac{d^2\Phi_2}{dz^2} - \left[\frac{d^2u/dz^2}{u-c} - \alpha^2\right]\Phi_2 \ ,$$

$$i\gamma\frac{d^3\Phi_1}{dz^3} + \gamma\alpha[Re\,(u-c) - 3i\,\alpha]\frac{d\Phi_2}{dz} - \gamma\alpha\,Re\,\frac{du}{dz}\Phi_1 =$$

$$i\frac{d^3\Phi_2}{dz^3} + \alpha[Re\,(u-c) - 3i\,\alpha]\frac{d\Phi_2}{dz} - \alpha\,Re\,\frac{du}{dz}\Phi_1 - \frac{\alpha\,Re\,Ri}{u-c}\Phi_2 \ ,$$

$$\text{at } z = 0, \tag{4}$$

where subscripts 1, 2 correspond to the upper and lower layer, respectively. Details can be found in Nishida and Yoshida (1987). The Runge-Kutta-Gill numerical integration and the filtered method (*e.g.* Betchov and Criminale 1967, Gersting and Jankowski 1972) have been employed to solve the system (2), (3), (4). The eigenvalues c are obtained by the shooting method. The results are plotted along with the experimental data in Figures 6 and 7. Re=100 is chosen as a typical value to match the range of experimental data (29.4< Re <549.0).

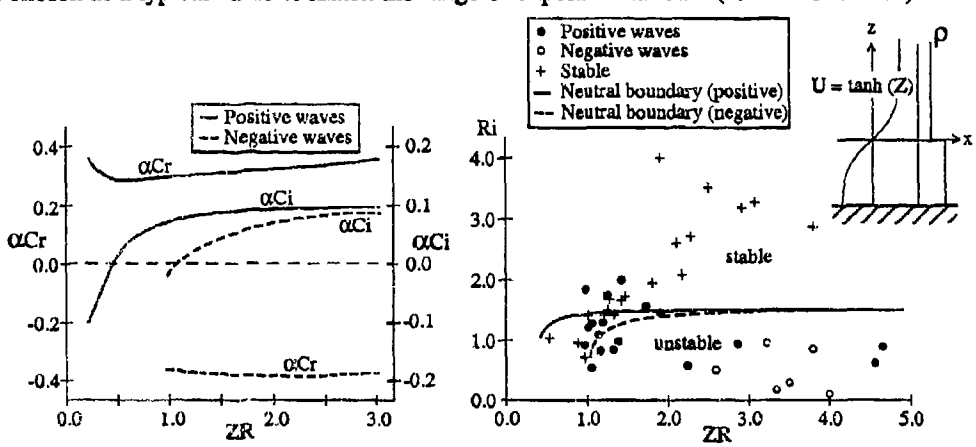


Figure 6. ZR effects on the stability of positive and negative waves. (a) Growth rate αCi and phase velocity Cr of Re=100, Ri=0.4, α=0.8 solutions, (b) comparison of the neutral boundaries (αCi=0.0) for Re=100 and experimental results.

Figure 6 shows that the presence of a rigid boundary greatly stabilizes the negative instabilities when ZR< 2.0. By contrast, the positive instabilities are only weakly influenced by variations of ZR. For the positive instabilities, the only noticeable difference between the un-bounded case (*i.e.* ZR=∞) and ZR< 5.0 is that the wave number of the most unstable waves tends to be smaller (longer wave length) as ZR decreases. Similar results were found in the inviscid theories (Yonemitsu 1991). For the case Re=100, the stability criteria predicted by our analysis for positive and negative waves are ZR=0.46 and 1.10, respectively. This means that no wave can be found for 0<ZR<0.46, only positive waves can exist for 0.46<ZR<1.10, and both positive and negative waves may be observed for 1.10<ZR cases. In

salt-wedge flows, the tip region (where ZR is very small) shows no waves; then positive waves appear as the lower layer thickness increases. Further downstream, where ZR is large enough, both positive and negative waves are observed. Therefore these observations are consistent with a theoretical analysis which includes consideration of rigid boundary effects.

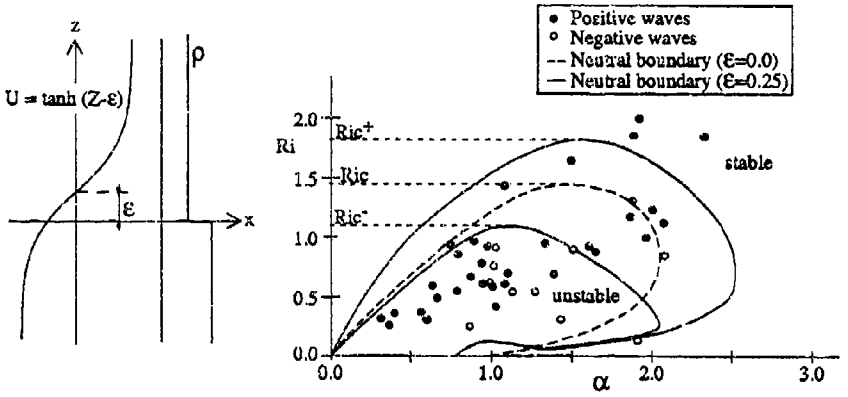


Figure 7. Stability boundaries with interface displacements (Re=100) and experimental results. Ric⁺ and Ric⁻ correspond to the critical Richardson number for the positive and negative instabilities, respectively.

Nishida and Yoshida (1987) show that the critical Richardson number Ric (which is defined as the maximum Richardson number for unstable waves) is relatively insensitive to the variation of the Reynolds number Re (for 20< Re <1000) and remains constant (Ric≈1.4). The experimental values of Ric for positive waves (Ric^+) are, however, larger than our model's prediction as shown in Figure 6. This problem can be clarified by considering the effects of the interfacial displacement ε. In Figure 7, ε=0.0 and ε=0.25 are chosen as examples. Similarly to the results of Lawrence *et al.* (1991), the stability boundaries for the positive and negative instabilities bifurcate and stability characteristics change drastically as ε increases. Ric^+ gets larger as ε increases (for example, $Ric^+ \approx 2.2$ when ε=0.5) and therefore the relatively large Ric for positive waves from our experiments can be understood as a result of the interfacial displacement. In a somewhat similar way, the negative waves with large wave numbers can be unstable when interfacial displacement effects are included.

Analyses of both rigid boundary effects and displacement effects indicate that the positive instability always has the greater predicted growth rate for any given Ri. It means that the Holmboe (1962) instability can occur only when ZR=∞ and ε=0. For salt-wedge flows, 'one-sidedness' is therefore the natural state of the wave phenomenon because of the existence of rigid boundaries and interfacial displacement.

4. CONCLUSIONS

The "one-sidedness" phenomenon is explained by a hydrodynamic stability theory including the effects of rigid boundary and interfacial displacement. Our viscous models show the significant details of the salt-wedge flows such as the critical Richardson number (Ric) and unstable wave numbers. In the case of Re=100, the stability criteria are given as ZR=0.46 for positive waves and ZR=1.1 for negative waves, *i.e.* 0<ZR<0.46 means no waves, 0.46<ZR<1.10 means only positive waves, and 1.10<ZR means both positive and negative waves can be found. Also the critical Richardson number is determined as Ric=1.6 for ε=0.25 and Ric=2.2 for ε=0.5. Our experimental data verify these theoretical results. Because the characteristics of Holmboe instabilities are very sensitive to the parameters ZR and ε, experimental data must be analyzed and interpreted carefully. For salt-wedge flows,

'one-sidedness' is the natural state of the wave phenomenon because of the existence of rigid boundaries and interfacial displacement.

REFERENCES

Browand, F.K. and C.D. Winant (1973): Laboratory observations of shear-layer instability in a stratified fluid. *Boundary Layer Meteorology*. **5**, 67-77.

Betchov, R. and W.O. Criminale (1967): Stability of parallel flows. *Academic Press, London*.

Fua, D. and F. Einaudi (1984): On the effect of dissipation on shear instabilities in the stable atmospheric boundary layer. *J. Atmospheric Sci.*, **41**, 888-900.

Gersting, J.M. and D.F. Jankowski (1972): Numerical methods for Orr-Sommerfeld problems. *Int. J. Numerical Methods Eng.*, **4**, 195-206.

Hazel, P. (1972): Numerical studies of the stability of inviscid stratified shear flow, *J. Fluid Mech.*, vol. **51**, 39-61.

Hino, M. and N.G. Hung (1982): The stability and interfacial waves of viscous-diffusive stratified two-layer flows. *Proceedings of the 26th Japanese Conference on Hydraulics*. 513-519. (in Japanese).

Holmboe, J. (1962): On the behavior of symmetric waves in stratified shear layers. *Geofysiske Publikasjoner*. **24**, 67-113.

Howard, L.N. (1963): Neutral curves and stability boundaries in stratified flow. *J. Fluid Mech.*, **16**, 333-342.

Keulegan, G. (1966): The mechanism of an arrested saline wedge, *Estuary and Coastline Hydrodynamics*. ch11. A.T. Ippen Ed., McGraw Hill, 546-574.

Lalas, D.P. and F. Einaudi (1976): On the characteristics of gravity waves generated by atmospheric shear layers. *J. Atmospheric Sci.*, **33**, 1248-1259.

Lawrence, G.A., F.K. Browand and L.G. Redkopp (1991): The stability of a sheared density interface. *Physics of Fluids A*, **3** (10), 2360-2370.

Lindzen, R.S. and J. Rosenthal (1976): On the instability of Helmholtz velocity profiles in stably stratified fluids when a lower boundary is present. *J. Geophysical Res.*, **81**, 1561-1571.

Murota, A. and K. Hirata (1978): Properties of internal waves and mixing mechanisms on density stratified flows. *Proc. 22nd Symp. of Hydraulics, JSCE*, 107-112. (in Japanese).

Nishida, S. and S. Yoshida (1987): Stability and eigenfunctions of disturbances in stratified two-layer shear flow. *Proceedings of 3rd International Symposium on Stratified Flows*. 28-34.

Sargent, F.E. and G.H. Jirka (1987): Experiments on saline wedge, *Journal of Hydraulic Engineering*. **113 (10)**, 1307-1324.

Tsubaki, T., M. Hamamura and M. Hashimoto (1969): On the statistical properties of internal waves formed at the interface of arrested saline wedges. *Proc. 13th Congress of IAHR*, **C17**, 63-74.

Yonemitsy, N. (1991): The stability and interfacial phenomena of a salt wedge flow. *Ph.D. thesis, University of Alberta*.

Yoshida, S. (1980): Mixing mechanisms of density current system at a river mouth. *2nd Int. Symp. on Stratified Flows,Trondheimn, Norway*, 1062-1073.

Dilution of dense bottom plumes in turbulent currents

by

Ole Petersen[1] and Torben Larsen

Department of Civil Engineering, Aalborg University, Sohngaardsholmsvej 57,
DK-9000 Aalborg, Denmark
[1]presently at International Research Centre for Computational Hydraulics at Danish Hydraulic Institute, Agern Alle 5, DK-2970 Horsholm, Denmark.

Abstract

The dilution of negatively buoyant discharges released into a turbulent current has been studied both in the laboratory and by means of advanced numerical models. The experiments showed that the dilution is mainly due to vertical turbulent mixing and depends on a buoyancy induced dispersion og the plume. These findings have been incorporated into a calibrated integral description of the dilution. A 3-D numerical model with a k-ϵ parameterisation of the turbulent mixing has been applied to the problem and a comparison between this model and the experiments been made. The conclusions are that the dilution can be realistically described by the model.

1 Introduction

Co-flowing negatively buoyant plumes may be formed when dense waste water is continously released from point sources near the bed into a turbulent current, as for example when industrial waste water with large concentrations of salts are released into marine environments. Although the density difference between the discharge and the receiving water may be relatively small, when seen from a hydrodynamical point of view, the nature of these wastes often require that concern is given to the dilution in the immediate vicinity of the discharge. The propagation and dilution of dense bottom plumes may also be of theoretical interest as the situation with a continous release of negatively bouyant water constitutes one of the simpler steady experiments with turbulent mixing across a density interface.
Dense bottom plumes have traditionally been studied in the context of spills of heavy gases in the atmosphere (Puttock et al., 1984; Zumsteg and Fannelop, 1987), while the opposite situation with a light surface plume is more often encountered in the marine environment (Petersen, 1992; Thomas and Simpson, 1985; Weil and Fischer, 1974); a situation which has some similarities with dense bottom plumes.
The aim of the present study is to investigate the dilution of dense bottom plumes. First, a

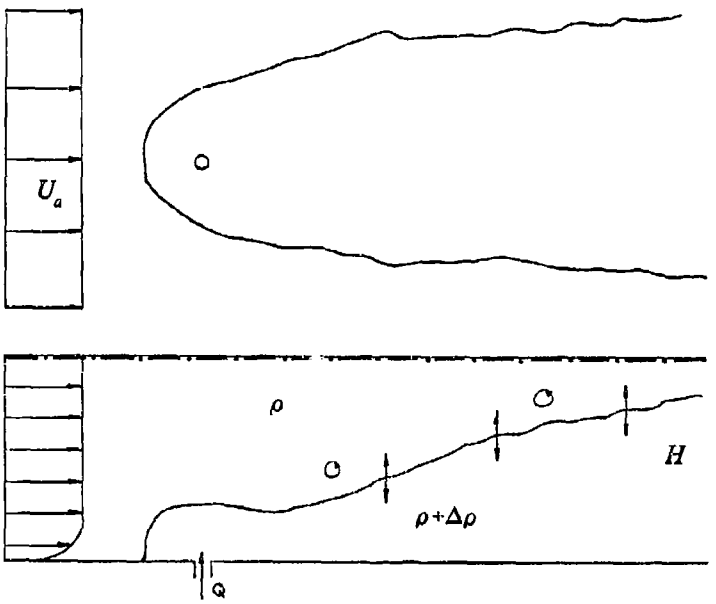


Fig. 1 Dense bottom plume.

series of laboratory experiments is discussed using an idealized integral theory that describes the dilution of the plume. Next, a 3-D numerical model is established and the results are compared to the experiments in order to validate the models in this specific case and to incorporate the data in a more general frame. Finally are the conclusions summarized.

2 Dense bottom plumes

To guide the analysis of the experiments an idealized theory where the dilution depends on a bouyancy induced spread and vertical turbulent mixing is developed below. The distribution of buoyancy in each cross section is characterized by a plume height and width, that both are defined as integral scales. If the local time average density difference is denoted $\Delta\rho_l$, the excess mass m in the cross section may be defined from

$$m = \int\int \Delta\rho_l \, dydz \tag{1}$$

where y and z are lateral and vertical cartesian coordinates, respectively.

The plume height h and width b may be defined from the second moments of the density difference distribution as for example

$$h^2=\frac{1}{m}\int\int \Delta\rho_i\, z^2 dydz \tag{2}$$

for the plume height and similarly for the width. The dilution of the plume can now be described in terms of the downstream development of these cross sectional characteristics. Assuming that the plume is conveyed downstream with the ambient velocity U_a the lateral expansion some distance from the source may be approximated by a bouyancy induced front (Larsen and Sorensen, 1968) with celerity

$$V_f=\alpha\sqrt{gh\Delta\rho/\rho} \tag{3}$$

where x is the streamwise coordinate; g is gravitational acceleration; ρ is the density; α is an empirical correction and $\Delta\rho=m/(8\ m\ h)$. Applying continuity and assuming the dilution to follow a Fickian diffusion law and postulating that the dispersion and the frontal motion are independent the two processes can be combined to

$$\frac{db}{dx}=\frac{V_f}{U_a}+\frac{K_y}{U_a b} \tag{4}$$

$$\frac{dh}{dx}=-\frac{h}{b}\frac{V_f}{U_a}+\frac{K_z}{U_a h} \tag{5}$$

where K_y and K_z are turbulent dispersion coefficients. The vertical dispersion is assumed to depend on the stability through a Richardson number as

$$K_z=K_{zo}/(1+\beta R_{io}) \qquad \text{where} \quad R_{io}=\frac{g}{\rho}\frac{\Delta\rho h}{u_f^2} \tag{6}$$

K_{zo} is the dispersion coefficient in the neutral situation; u_f the friction velocity and β is an empirical factor.

3 Laboratory experiments

The experiments were carried out in a recirculating hydraulic flume, 20 m long and 1.5 m wide, with a flat epoxy painted bed. A dense bottom plume was established by vertically discharging colder tap water with low velocity through a 2.8 cm diameter nozzle located 5.0 m from the downstream end of the flume and in level with the bed. The metered discharge

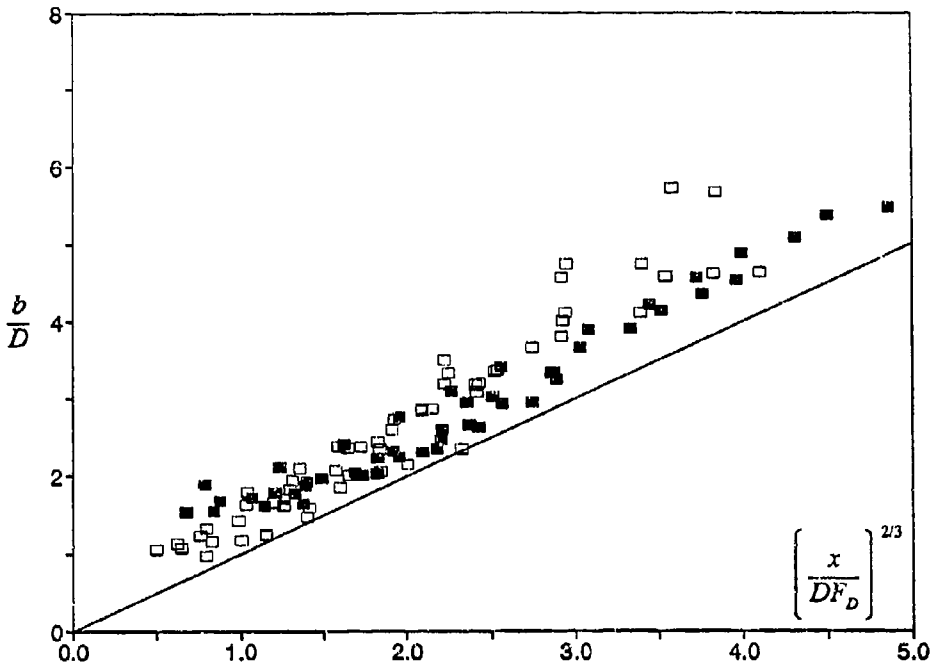


Fig. 2. Measured (open symbols) and calculated by numerical model (filled symbols) relative plume width as a function of a relative downstream distance from the source. The full line corresponds to data from (Weill and Fischer, 1974). Here D is a virtual source diameter and $F_D = U_a / \sqrt{gD\Delta\rho/\rho}$.

went through a storage tank and had a temperature at 6 - 7 °C. The ambient temperature in the flume was app. 18 °C with a drift during experiment at 0.5 °C/hour.
The temperature difference between the plume and the ambient water was measured by means of a vertical array of 8 thermocouples, connected to a PC through an AD converter. The thermocouples were mounted on a step-motor controlled carriage which could automatically traverse the plume. The resolution of the temperature measurement was 0.02 °C and the accuracy of the order 0.05 °C. By means of a standard table implemented on the PC each measurement of temperature was converted into a density-difference in order to allow for non-linearities in the conversion when the temperature fluctuates. Further details of the setup can be found in (Petersen, 1994; Petersen and Larsen, 1992).

4 Results

In each experiment the time average density difference in 15 verticals evenly distributed over the plume cross section was measured in 6 cross sections located with 0.5 m intervals. These

# ()	U_a (cm/s)	H (cm)	T_c (C)	Q_o (l/min)	T_oC (C)
1	7.1	17.0	18.7	4.4	7.1
2	7.1	17.2	18.4	2.1	7.2
3	9.4	17.0	19.0	3.0	7.6
4	9.4	17.0	19.0	4.8	7.5
5	15.0	17.2	18.5	4.8	6.5
6	15.0	17.2	18.3	7.4	6.4
7	20.5	17.0	18.0	9.4	6.6
8	20.5	17.0	17.5	2.7	6.0

Table 1. Experimental conditions

data allowed for a direct estimation of the integral scales the excess mass, the width and the height previously defined. A number of 8 experiment were carried out, covering a range of ambient velocities, discharges and density differences as shown in Table 1. These values ensures that the flow and mixing processes appear as fully turbulent. The downstream development of the plume widths are shown in Figure 2 in a form suggested by Weill and Fischer (1974), which is suitable for immiscible surface plumes (full line). It appears that due to the turbulent dispersion the measured plumes are wider than predicted by the simple theory and that the development of dense bottom plumes largely follows the pattern seen for surface plumes.

The experimental results are reduced by means of a calibration of the integral relations (4) and (5). The transverse dispersion coefficient is found to $K_y = 0.12\, u_f H$ from a tracer experiment and the vertical dispersion coefficient is estimated using a numerical model of the downstream development of a neutral plume in a logarithmic boundary layer to $K_z = 1.35\, u_f h\, (0.57\text{-}h/H)$. Summing the difference in the calculated and measured change in dilution between two cross sections the error as a function of the two empirical constants can be estimated. The combination of the constants $\alpha = 1.2$ and $\beta = 1.0$ minimises this error and agreement between the calibrated model and the experiments illustrated in terms of the average density difference.

5 Numerical experiments

The dilution in the near field is the result of a 3-dimensional and fully turbulent flow with pronounced buoyancy effects. The mathematical model consists of the 3-dimensional hydrodynamical equations where buoyancy effects are included through an equation of state and a transport equation for temperature. Turbulent stresses and transports are described using an eddy viscosity concept. Boundary conditions are symmetry conditions at the surface

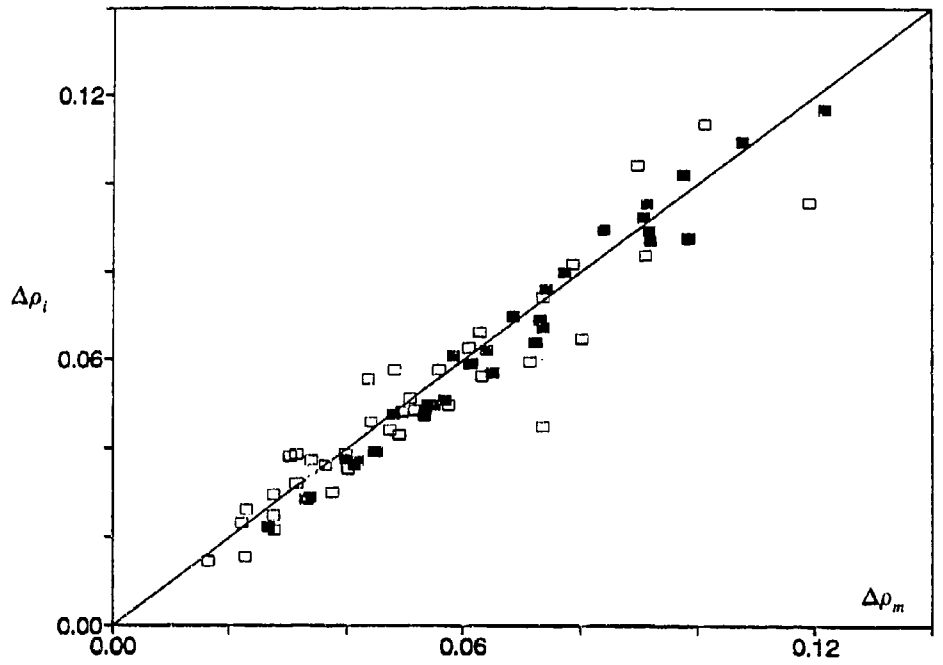


Fig. 3. Density difference obtained from measurements (open squares) or numerical model (filled squares) vs. integral description.

the two sides, prescribed distributions of velocity (logarithmic law) and temperature at the upstream end, simple outflow at the downstream end. The bottom boundary layer is described using a logarithmic wall law. The discharge is here described as a point source of flow and buoyancy, thus the complex details around the discharge is not resolved.
The resulting set of equations are solved using the system Phoenics which is based on a Simple type coupling between pressure and momentum and an iterative solution procedure (Rosten and Spalding, 1987) and here used in combination with a standard k-ϵ turbulence closure. The influence of buoyancy on the turbulence is in the k-ϵ model incorporated as additional sinks in the equations for k and ϵ (see Rodi, 1987). The resolutions used are .06 x .03 x .01 m in the three cartesian directions.

6 Results of the numerical experiments

The theoretical basis for the model has been extensively tested in turbulent boundary layers and also in some cases where buoyancy is important (Rodi, 1987) so only dense bottom plumes will be discussed here. A number of calculations with the k-ϵ model set up as close as possible to the conditions in the experiments has been made and the results treated in a similar manner as the results from the experiments. In Figure 2 are the plume widths from

the numerical calculation displayed where it appears that the transverse propagation is reasonably reproduced. In order to verify the dilution the plume scales obtained from the numerical model are used to recalibrate the integral description discussed previously. Following the same procedure as above, this yields $\alpha=1.2$ and $\beta=1.25$. In Figure 3 is the agreement between the numerical model and the calibrated integral description shown; the variance is in this case not due to randomness but can only be attributed to differences between the theories. If the two empirical factors summarize the experimental data the recalibration indicates that the numerical model slightly overestimates the vertical mixing as a larger damping factor β is needed.

7 Discussion and conclusions

The study has examined the dilution of co-flowing dense bottom plumes in a turbulent boundary layer and shown that the dilution can be described as the result of two important factors that are a buoyancy induced spread, which in principle changes the area subject to mixing, and a vertical turbulent mixing that is attenuated by the density gradient.
It has also been demonstrated that a 3-D hydrodynamical model can reproduce these processes.
A general comment is that the study has shown that the dilution depends on a few fundamental processes and as the problem as posed here is steady and has relatively well-defined boundaries it may be well suited as one benchmark case for testing of models for mixing across density gradients.
The more specific conclusions may be summarized as follows :
i) Within the range of ambient velocities and density differences used here the dilution of a co-flowing dense bottom plume can be described using the integral model discussed above, with two constants $\alpha=1.2$ and $\beta=1.0$ both empirically derived in the laboratory.
ii) The numerical model with a k-ϵ turbulence closure gives a realistic description of the dilution.

Acknowledgements

Parts of this work was founded by the Danish National Research Foundation. Their support is greatly appreciated.

Litterature

Larsen, I. and Sorensen, T. (1968). Buoyancy spread of waste water in coastal regions. *Proc. 11th Conf. on Coastal Engrng.*, London, 1397-1402.

Petersen, O. (1994). Laboratory and numerical experiments on the dilution of buoyant surface plumes. in : Davies, P. A. and Valente Neves, M. J. (eds.). *Recent Research Advances in the Fluid Mechanics of Turbulent Jets and Plumes*, Kluwer Academic Publishers, Dordrecht, The Netherlands, 223-236.

Petersen, O. and Larsen, T. (1992). Laboratory study of dispersion of buoyant surface plumes. *Proc. Int. Conf. on Physical Modeling of Transport and Dispersion*, ASCE., Mass., USA.

Puttock, J. S., Colenbrander, G. W. and Blackmore, D. R. (1984). Dispersion results from continous releases of refrigerated liquid. In : Wispelaere, C. D. (ed.). *Air pollution modelling and its applications III*. Plenum Publishers Corp. Ltd.

Rodi, W. (1987). Examples of calulations methods for flow and mixing in stratified fluids. *J. Geophysical Res.*, **92**(C5), 5305-5328.

Rosten, H. I. and Spalding, D. B. (1987). *The Phoenics reference manual*. CHAM Ltd., London.

Thomas, N. H. and Simpson, J. E. (1985) Mixing of gravity currents in turbulent surroundings : laboratory studies and modelling implications. In : Hunt, J. C. R. *Turbulence and diffusion in stable environments*. Clarendon Press, Oxford, 61-96.

Weill, J. and Fischer, H. B. (1974). Effect of stream on heater water plumes. *J. Hydraul. Div.*, ASCE, **100**(HY7), 951-970.

Zumsteg, F. and Fannelop, T. K. (1987). Large scale experiments on the spreading and dilution of cold gasclouds in a controlled environment. In : List, E. J. and Jirka, G. H. (eds.). *Stratified flows*. ASCE, N.Y., 613-622.

Mixing in lock-release gravity currents

J. Hacker, P.F. Linden and S.B. Dalziel

Department of Applied Mathematics and Theoretical Physics
Silver Street, Cambridge, CB3 9EW, UK.
ph. (+44 223) 337900 fax. (+44 223) 337918 Email: jh156@amtp.cam.uk.ac

The density front bounding a gravity current is usually highly unstable and this leads to mixing between the fluid of the gravity current and that of the surroundings. We describe a new experimental technique to determine the synoptic density structure of gravity currents, and to examine these mixing processes. We find that substantial mixing occurs in the early stages of the evolution of lock-release gravity currents and that this results in a complex internal density structure. We present analyses of three experiments, for three different values of lock aspect ratio. By comparing these gravity currents we build up a picture of the processes of mixing and detrainment. We also quantify the mixing and determine the overall entrainment rate.

1. Introduction

Gravity currents are produced when fluid of a given density is released into fluid of a different density at a horizontal boundary. The buoyancy forces are constrained by the boundary to produce a horizontal pressure gradient which drives a flow along the boundary. The simplest configuration, often referred to as a 'lock-release', consists of two fluids of different densities initially separated by a vertical barrier. When the barrier is removed the denser fluid flows along the boundary underneath the less dense fluid.

This flow occurs in many situations of practical interest. For example, when a door is opened between two rooms containing air at different temperatures, the air from the colder room enters the warmer room and flows along the floor as a gravity current. Another example occurs when a dense gas is released (possibly accidentally) from a storage container. While these two examples closely resemble the lock-release flow, other naturally occurring gravity currents demonstrate similar dynamics, for example the sea breeze and turbidity currents (Simpson 1987). An understanding of the simpler lock-release flow is also an essential prerequisite to modelling a wide range of more complex flows.

An aspect of these flows which is of much practical interest, and which is poorly understood, is the mixing of the current with the ambient fluid and the consequent dilution of the fluid within the gravity current. Simpson & Britter (1979) quantified the bulk mixing rates for steady state currents, but did not determine the details of the density structure. Recent work by Hallworth *et al.* (1993) suggests that the fluid within the head of the gravity current is well mixed, and that the mixing rate depends on the phase of the evolution of the current. When the barrier is removed the current quickly accelerates and enters a constant velocity 'slumping phase'. During this phase the fluid is still draining from the lock and the current effectively has a constant supply of fluid from the rear. Once all the fluid has drained from the lock, and a bore on the interface reflected from the back of the lock reaches the front of the current, the flow enters a 'similarity phase' in which the velocity decreases with distance. Hallworth *et al.* (1993) claim that no mixing takes place during the slumping phase, and that all dilution takes place downstream of the transition to the similarity phase.

In this paper we use a new experimental technique to measure the density structure within gravity currents generated by lock-release in a channel by use of a passive dye and image processing techniques. These measurements provide a synoptic picture of the dye concentra-

tion averaged across the channel. The molecular diffusivities of the dye and of salt are comparable, so dye concentrations may be taken to be equal to salt concentrations. From these measurements we are able to determine the internal structure of the gravity currents and to investigate how the ambient fluid is entrained. We examine the dependence of the mixing and the internal structure on the aspect ratio of the lock, contrasting tall, narrow locks with shallow wide ones. In §2 the experiments and the measurement technique are described, and in §3 the results are presented. The results are discussed and the conclusions given in §4.

2. The experiments

The experiments described in this paper were carried out in a rectangular perspex channel 205 mm wide, 500 mm deep and 3480 mm long. On one side of the channel four fluorescent strip lights were mounted horizontally behind a diffusing screen to provide back-lighting.

Each experiment was performed as follows. The channel was filled with tap water to a depth H. A vertical perspex gate was then positioned at a distance x_0 from one end of the channel to form a lock. A quantity of salt was dissolved into the water in the lock to create the density difference. A measured quantity of dye was also added to the water in the lock to enable flow visualisation. The gate was then smoothly withdrawn, leaving the dense fluid to flow out along the floor and form a gravity current. The progress of each experiment was recorded using a video camera and video tape recorder. For practical reasons the camera was kept at a fixed position for all the experiments, and the field of view was restricted to the first half of the channel. For different experiments the aspect ratio $R = H/x_0$ of the lock was varied by changing the distance x_0 of the gate from the end wall and the height H of the water in the channel. For the three experiments reported here the values of these parameters were i) x_0 = 300 mm, H = 200 mm, R = 0.78; ii) x_0 = 400 mm, H = 400 mm, R = 1.0; ii) x_0 = 150 mm, H = 267 mm, R = 1.78. The reduced gravity was 120 mm s^{-2} for all the experiments.

Measurements of density structure were made by digitally analysing the video tapes using Dig*Image*, an image processing system developed at DAMTP (Dalziel 1993). The attenuation of the back-lighting was measured and related to the cross-channel dye concentration. The measurement process involved two stages of processing.

The first stage is to measure the attenuation of the background lighting. If I_0 is the light intensity of a point in the video image when no dye is present in the flow, and I is the intensity at the same point when dye is present, the attenuation is defined to be the ratio I/I_0. The image processing system digitises a frame of video tape by recording the light intensity at 512×512 pixel points across a video frame, and can be used to measure I/I_0. Due to the nature of the measuring system the digitised intensities do not correspond directly to actual light intensities but, if I represents actual light intensity and i represents digitised intensity, there exists a smooth, single-valued function f such that

$$I = f(i) \tag{1}$$

and the system may be calibrated. The calibration was carried out by using a grey scale for which the optical transmittance of each level of grey had been determined.

The second stage of the measurement process is to infer the concentration of dye in the flow from the attenuation measurements. If the flow is taken to be two-dimensional, i.e. there are no variations in the cross-channel direction, and the light received by the video camera is assumed to have passed through the flow in a direction perpendicular to the channel walls, then the concentration of dye is constant along each ray of light received by the camera. The attenuation per unit width of the channel is therefore also constant, and the cross-stream dye concentration, C, can be related to the attenuation by an equation of the form,

$$C = C_0 g(I/I_0) \qquad (2)$$

where C_0 is a reference concentration. To determine the function g in (2) the channel was filled with water, measured volumes of dye were added and the ratio I/I_0 was determined for each concentration of dye solution.

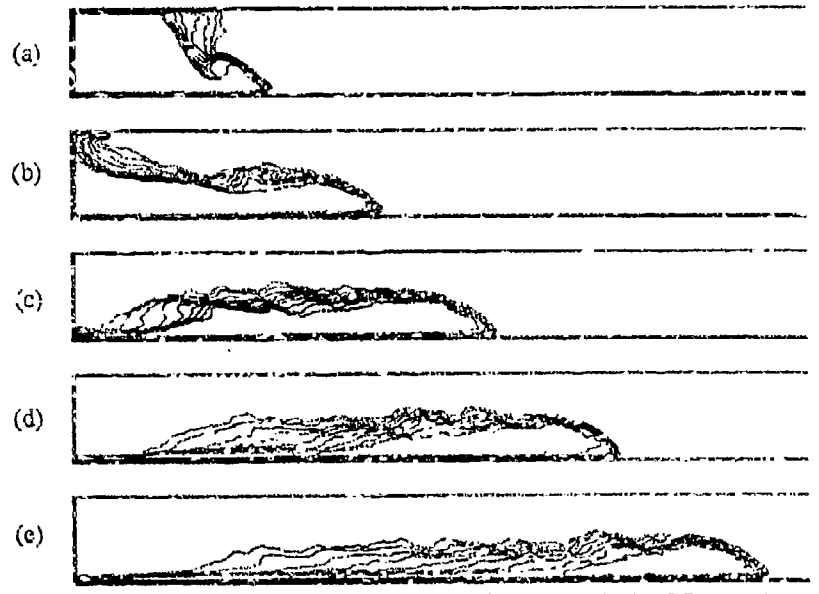


Figure 1: Evolution of iso-concentration contours for aspect ratio R = 0.76, at values of non-dimensional front position $I = (x_f - x_0)/x_0$ (a) I=0.47, (b) I=1.33, (c) I=2.20, (d) I=3.15, (e) I=4.30.

In order to estimate the errors involved in the two stages of processing two checks were made. If the channel is filled with a uniform concentration of dye solution, (2) implies that the value of I/I_0 determined from (1), should be constant across the whole image, regardless of variations in the intensity of the back-lighting. This was found to be the case, to an error within the noise level of the system (± 2%). In order to check the dye calibration function in (2), the total amount of dye in the flow, which is conserved, was determined from the digitised images at successive times during an experiment. It was found that the total quantity of dye remained constant to within 10%.

Measurements were also made from the digitised images of the speed of advance of the gravity current along the channel, and of the height of the head. The spatial resolution was ± 5 mm and the temporal resolution was ± 0.04 s.

3. Results

Figures 1 to 3 show iso-concentration contours for the three experiments with aspect ratios R = 0.67, 1.00 and 1.78, respectively. Iso-concentration contours are plotted in each figure for concentration values of 0.8, 0.7, 0.6, 0.5, 0.4, 0.3, 0.2, 0.1, and 0.05 of the initial concentration. Figures 1 and 2 show the evolution of the current over a propagation distance of approximately four lock lengths, while figure 3 shows the evolution of the larger aspect ratio lock as it propagates to nearly ten lock lengths.

The initial development of the flow is quite similar for all three cases with the vertical interface released by the withdrawal of the lock gate collapsing downwards and producing an outflow along the floor of the channel. The collapse is initiated at the base of the column of dense fluid, where a formative gravity current 'head' develops, which is bounded downstream by a sharp front. The head immediately rolls-up to form a vortex-like structure which engulfs less dense fluid from the rear. Above the outflow the contours are spread horizontally with the

area of mixed fluid increasing with increasing lock aspect ratio. This increased mixing may be due to the increase in influence, at higher aspect ratios, of the initial disturbance produced by the withdrawal of the lock gate.

Corresponding to the outflow of dense fluid at the base of the tank there is counter flow of fresh fluid towards the rear wall at the higher levels. This causes the interface to be sheared over towards the horizontal as can be seen in figures 1(a)-(c), 2(a)-(c) and 3(a)-(c). Note that the density front bounding the head of the counter flow is much weaker than that bounding the outflow. By the time the current has propagated approximately 2-3 lock lengths (figures 1(c), 2(c) and 3(c)) the fresh water has reached the end of the wall of the lock and the whole volume of the dense fluid is now propagating along the tank. This transition represents the end of the slumping phase during which the gravity current is evolving from the lock and behaves as though the lock were infinite in horizontal extent. After this phase the finite volume of the lock becomes important.

Figures 1 to 3 (c)-(e) show the subsequent evolution of the flow, which is quite different for each of the three aspect ratio cases. The low aspect ratio case (figure 1) develops a classical gravity current shape with a raised head and thin trailing flow (Simpson 1987). The whole volume of the flow moves downstream with the front moving faster than the rear, so that the length of the current extends. Waves form and break at the rear of the head (figure 1(d)) and this causes ambient fluid to be entrained. The mixed fluid is left behind the head and a region of stratification develops in the trailing part of the current. In figure 1(e) it can be seen that a stratification has developed over almost the complete length of the current, although the region in the head remains well mixed. Fluid which is mixed and left behind at the head is replaced by dense fluid from the rear, so that the concentration of the fluid in the head remains fairly constant over the propagation distance shown in this figure.

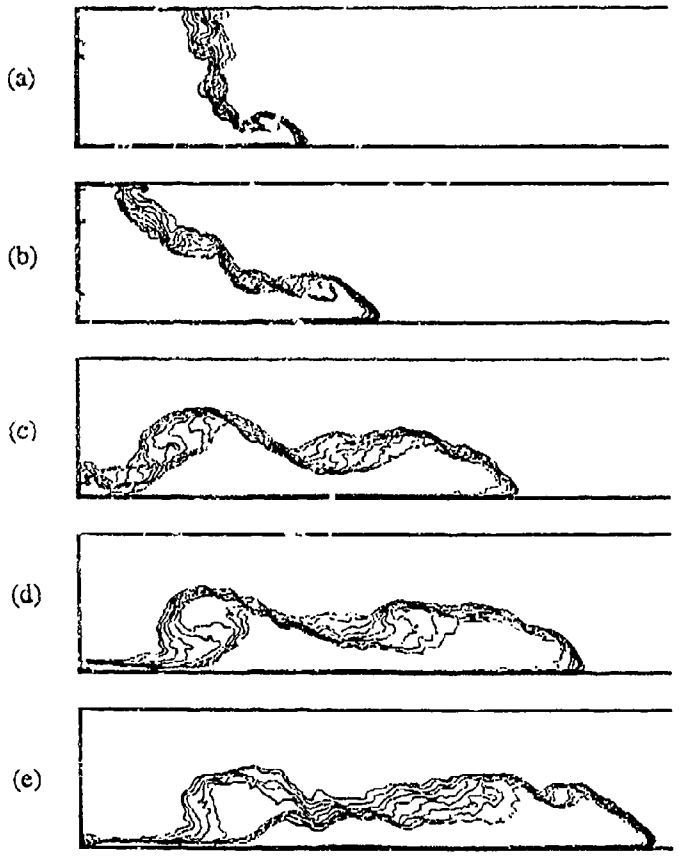


Figure 2: Evolution of iso-concentration contours for aspect ratio R = 1.00 at values of non-dimensional front position $l = (x_f - x_0)/x_0$ (a) l=0.60, (b) l =1.11, (c) l=2.10, (d) l=2.56, (e) l=3.08.

The evolution of the flow for unit aspect ra-

tio, shown in figures 2(c)-(e) is quite different. When the fresh water reaches the rear of the lock (figure 2(c)) a large vortex occurs at the trailing edge of the current. The origin of this vortex is a shear instability that grows, from an initial disturbance caused by the gate, on the strongly sloping interface of the slumping dense fluid (figure 2(b)). This vortex is seen to persist throughout the remainder of the experiment. Dense fluid is drawn upwards into the vortex resulting in a large amount of mixing within this structure (figures 2(c)-(e)). The leading edge of the current is again bounded by a sharp front, but the structure of the current is different from that shown in figure 1 as the trailing flow is of comparable depth to the head. Waves form at the head and evidence can be seen of these breaking in figure 2(d). Rather than leading to the formation of a stratified trailing flow, as in figure 1, the wave breaking leads to the formation of a stratified region between the vortex structure and the head (figure 2(e)). The fluid within the head region itself remains relatively uniform and at the initial concentration of the lock over this small propagation distance.

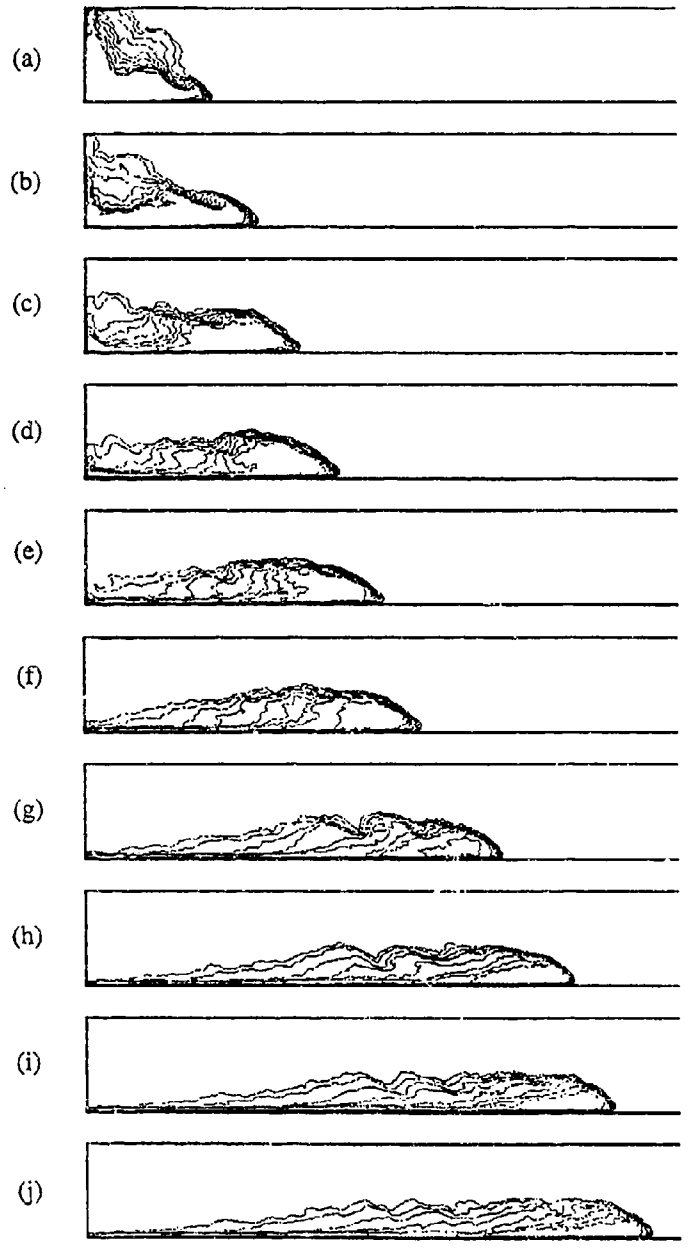


Figure 3: Evolution of iso-concentration contours for aspect ratio $R = 1.78$. at values of non-dimensional front position $l = (x_f - x_0)/x_0$ (a) l=1.33, (b) l=2.17, (c) l=3.00, (d) l=3.73, (e) l=4.53, (f) l=5.27, (g) l=6.80, (h) l =8.13, (i) l=8.93, (j) l =9.60.

The high aspect ratio case is shown in figure 3. The frontal structure again has the form of a sharp transition and a distinct head, but the internal structure of the

current is different again. Once the counter flow has reached the back wall of the lock, the region of fluid of initial concentration in the head is of horizontal extent comparable to its depth (figure 1(c)), so that there is no longer a supply of dense fluid from the rear. The waves formed at the head now break directly into mixed fluid and this produces a strong horizontal stratification, which can be seen developing in figures 3 (d)-(e).There is little evidence of the strong vortex structure observed in figure 2. This may be a result of the increased mixing in the earliest phase of the flow (figure 3(b)), which produces a diffuse density structure behind the head.

By the time the current has progressed about five lock lengths (figure 3 (e)) all of the fluid in the current has been mixed to some extent with the ambient fluid and there is virtually none remaining at the initial concentration. The densest fluid in the current is now confined to the immediate region of the nose and, consequently, the flow is no longer frontogenic. The horizontal density gradient in the rear of the current is now tending to weaken the horizontal density gradients, rather than to sharpen them. Since fluid detrained from the head is now replaced by less dense fluid from the rear, the head now becomes progressively diluted, as can be seen in figure 3(f)-(j). The stratified region continues to develop in a similar way to that described in the case of the low aspect ratio lock. However it can be seen in figure 3(j) that by the time the current has propagated ten lock lengths, the region of stratification extends almost up to the front, with appreciable vertical stratification within the head.

Despite these differences in the internal structure the velocities of propagation of the three currents were very similar, and constant, over the common propagation range of the three experiments, with the Froude numbers based on the total water depth H taking the values 0.45, 0.45, 0.44 for aspect ratios of 0.67, 1.00, 1.78, respectively. These values agree closely with the 'universal' value of 0.46 determined by Barr (1967). In the high aspect ratio experiment, the current began to decelerate after it had propagated approximately 8 lock-lengths. The head heights also behaved in a similar fashion for each flow. The maximum height of the 0.05 isoconcentration contour within the head increased to a value somewhere between 0.45 and 0.55 of the total depth for each experiment . This value was maintained for a time and then began to slowly decrease. It is worth noting that a steady dissipationless current would occupy half the total depth, and it would not be possible to produce such a flow with greater fractional depth (Benjamin 1968).

We can further quantify the mixing by examining in more detail the amounts of fluid at different concentrations as the flow develops. Figure 4 shows the total area (the volume per unit width of channel) of the current *below* a given concentration level, for the three different aspect ratio lock-release flows shown in figures 1 to 3. The areas are non-dimensionalised with respect to the initial area of the lock. The concentrations are non-dimensionalised with respect to the initial concentration of the fluid in the lock. The lowest set of points on each graph correspond to a concentration threshold equal to the initial concentration, with further sets of points plotted at 0.8, 0.6, 0.4, 0.2 and 0.05 of initial concentration. We shall refer to each set of points as an isocline. The ordinate values of the 1.0 isocline then correspond to the amount of fluid remaining at the initial concentration, which is fluid that has not undergone any mixing. The 0.05 isocline may be taken to nominally define the boundary of the current, so that the ordinate values of the points correspond to the total volume of the current, and the slope of the isocline corresponds to the rate of entrainment.

As can be seen from the figures, at the initial instant all the points lie on the value of 1.0 (with slight scatter due to experimental error) indicating that the total volume of fluid in the lock is at the initial concentration. As the current progresses and mixes with the ambient fluid,

fluid with concentration between 1.0 and 0.05 is formed and so the isoclines diverge. The divergence of the isoclines is constrained by the condition that the total amount of salt in the flow is conserved. For example the mixing of a given volume dense fluid could either result in the production of a large amount of dilute fluid, and so strong convergence of low concentration isoclines, or in the production of a smaller volume of higher concentration fluid, and so less divergence of higher concentration isoclines.

Considering the three graphs in figure 4 we can see that in each case the 'total volume' of the current increases almost linearly with distance propagated, which indicates that the initial 'slumping phase' and the subsequent flow produce very similar rates of overall entrainment of ambient fluid. The slopes of the 0.05 isoclines are comparable in all three cases with the common value being approximately 0.17 $A_0 x_c^{-1}$.The graphs also show that there are qualitative and quantitative differences in the way in which the mixed fluid is distributed across the concentration range.

In the low aspect ratio experiment (figure 4(a)) most of the mixed fluid is of concentration between 0.05 and 0.43, with progressively less fluid at higher concentrations. This indicates that the mixing occurred primarily at the edges of the current to produce dilute fluid. In the unit aspect ratio experiment (figure 4(b)) most of the mixed fluid has concentration between 0.6 and 0.4, with there being progressively less fluid at lower concentrations. This indicates that ambient fluid was mixed more deeply into the current, which is consistent with the qualitative features of the mixing due to the strong vortex and deep wave breaking, shown in figure 2. In the high aspect ratio case (figure 4(c)) the mixed fluid is evenly distributed across the whole range of concentrations indicating that the mixing is deeper still in this case. This is consistent with the mixing due to the wave breaking in the horizontal stratification, shown in figure 3. In this case the lower concentration isoclines decrease sharply and it can be seen that there is no fluid remaining at the initial concentration after the current has propagated five lock lengths, and almost none at 0.8 of initial concentration after the current has propagated 9.6 lock lengths.

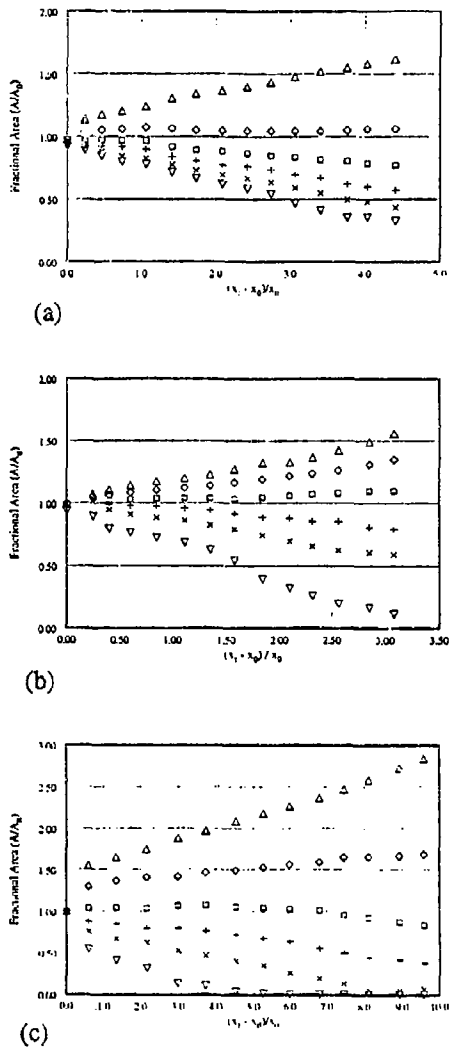


Figure 4. Fractional areas A/A_0 below given concentration thresholds as a function of non-dimensional front position $(x_f-x_0)/x_0$, for different values of lock aspect ratio R: (a): R=0.78; (b): R=1.00 ; (c): R=1.78. Non-dimensional concentration thresholds denoted by: Δ, 0.05; ◊, 0.2; , 0.4;+, 0.6; ×, 0.8; ∇, 1.0. (Note the differences in the scales of the axes.)

4. Discussion and conclusions

In this paper we have presented a new experimental technique to determine the cross-stream averaged density structure of gravity currents. The three cases described in §3 indicate that there is a broad range of structure associated with the initial development of lock-release gravity currents, and that this structure is influenced by the aspect ratio of the lock. A common underlying process by which the fluid of the current is mixed with the ambient fluid is the detrainment of dense fluid from the head by wave breaking, which leads to the production of a stratified following layer. As the current progresses the fluid mixed at the head is displaced upwards and back into the following stratified fluid by dense fluid moved forward into the head by frontogenic motions. Once all of the initial dense fluid of the release has been mixed in this way the wave breaking continues, but the fluid mixed out of the head is now replaced by less dense fluid from the tail, so that the head becomes progressively diluted.

The fractional height of the head was similar in the three cases considered, so one consequence of the changes in aspect ratio was that the higher aspect ratio currents had relatively shorter, higher heads. This resulted in more rapid dilution of the head in these cases. Further exploration of the parameter space will be needed in order to quantify this effect, and the other features discussed in §3. It is thought that some of the features described, such as the persistent vortical structure in the unit aspect ratio case, are not a direct result of change of aspect ratio. Changes in the overall height of the lock may be important since these influence the amount of baroclinic vorticity introduced into the flow, and the relative importance of the initial disturbance produced by removal of the gate. It will also be interesting to determine the extent to which gravity currents originating from different lock geometries develop self-similar behaviour at large times.

Since the experimental technique used here can only resolve cross-stream averaged structure, we are not able to directly investigate the role played by the three-dimensional structures important in the mixing, such as the 'lobes and clefts' which form at the nose (Simpson, 1987). We have only considered lock-releases where the initial height of the dense fluid equals the depth of the ambient fluid, but we expect that differences in initial fractional depth will effect the mixing. Another class of gravity current are currents generated by constant flux releases of dense fluid. In constant-flux gravity currents the process of replenishment of dense fluid at the head will persist as there is always a supply of dense fluid from the rear. We would expect the density structure to consist of a homogeneous head and tail, with stratified fluid lying above the tail. In naturally occurring situations the form of gravity currents often lies somewhere between the lock releases case and the constant flux case, and so the mixing and the density structure produced will be correspondingly influenced.

References

Barr, D.I.H 1967 Densimetric exchange flow in rectangular channels III: Large scale experiments. *Houille-Blanche* 6/1967 619-631

Benjamin, T.B. 1968 Gravity Currents and related phenomena, *J. Fluid Mech.* **31** 209-243.

Dalziel, S.B. 1993 Rayleigh-Taylor instability: Experiments with image analysis. *Dyn. Atmos. Oceans* **20** 127-153.

Hallworth, M.A., Phillips, J.C., Huppert, H.E. & Sparks, R.S.J, 1993 Entrainment in turbulent gravity currents. *Nature* **362** 829-831.

Simpson, J.E.. & Britter, R.E. 1979 The dynamics of a gravity current advancing over a horizontal surface. *J. Fluid Mech.* **94**, 447-495.

Simpson, J.E. 1987 Gravity Currents in the Environment and in the Laboratory. (Ellis-Hornwood / Halstead Press).